Université Bordeaux I
UMR EPOC 5805

Modélisation et analyse physique des processus hydro-sédimentaires contrôlant l'évolution des littoraux sableux

Mémoire d'Habilitation à Diriger des Recherches présenté par

Bruno Castelle

Chargé de Recherche au CNRS
Soutenue le 20 novembre 2012 devant le jury composé de:

M	Antoire Grémare	PR, Université Bordeaux I	(Président)
M.	Stéphane Abadie	PR, Université de Pau et des Pays de l'Adour	(Rapporteur)
M.	Vincent Rey	PR, Université du Sud - Toulon - Var	(Rapporteur)
M.	Dano Roelvink	PR, UNESCO - Institute for Water Education	(Rapporteur)
M.	Hervé Michallet	CR, Université de Grenoble	(Examinateur)
M.	Philippe Bonneton	DR, Univsersité Bordeaux I	(Examinateur)

Aux dépressions de l'Atlantique Nord et au vent d'est...

Remerciements

J'exprime ma gratitude aux membres du jury et en particulier aux rapporteurs pour avoir accepté cette tâche, c'est un honneur pour moi.

Le chemin est long avant d'en arriver là, et même si on a coutume de dire qu'il s'agit d'un chemin semé d'embuches, mon sentiment est que c'est plutôt un chemin parsemé de rencontres, d'échanges... et de chance. C'est pourquoi si j'en suis là, à passer ces dernières semaines à rédiger ce manuscrit, c'est grâce en particulier à un professeur de physique au collège, M. Courtois, qui m'a donné à vie le gout de la physique ; une note éliminatoire en maths à un concours pour une grande école d'ingénieur française à cause d'un bug interne encore à ce jour inexplicable sur un énoncé pourtant limpide, et qui m'a fait bifurquer vers la moins prestigieuse ISITV ; la découverte des cours de Vincent Rey qui m'a fait préférer la dynamique littorale à la météorologie qui jusque-là occupait toutes mes pensées ; les cours de Master 2 de Pierre le Hir dont la passion communicatrice m'a révélé ma vocation de chercheur ; la rencontre avec Philippe Bonneton qui m'a permis de me lancer dans la morphodynamique littorale et m'a fait confiance depuis le début, ce qui n'est pas gagné quand, à l'époque, on est un chevelu vivant une partie du temps dans son camion de manouche.

Un travail de recherche est un travail collectif. Je remercie donc avant tout les doctorants que j'ai encadrés ou pour lesquels j'ai pris une part active à l'encadrement (Nicolas Bruneau, Rafael Almar, Mounir Hakkou, Florent Birrien, Benjamin Dubarbier et Timothy Price) ainsi que les différents étudiants que j'ai encadrés en Master 1 et 2. Je remercie également tous les membres de l'équipe METHYS et mes collaborateurs français et étrangers favoris avec parmi d'autres Gerben Ruessink, Giovanni Coco, Ian Turner, Gerd Masselink, Hervé Michallet, Xavier Bertin. Un grand merci aux collègues français avec qui j'ai eu moins l'occasion de collaborer mais avec qui les discussions ne sont pas moins enrichissantes, en particulier mes collègues et amis des labos d'Anglet, Perpignan, Toulon, La Rochelle et ailleurs : Florent, Raphael, Nicolas, Denis, Stéphane, Vincent, Damien, Déborah, Rodrigo, Roland et bien d'autres.

Merci à tous les collègues d'EPOC avec qui je partage des pauses café, le repas au resto CNRS... ou au pub.

J'ai le devoir de remercier Vincent Marieu, que j'avais oublié de remercier dans mon manuscrit de thèse et qui me le rappelle tous les matins au café, merci pour les discussions, le soutien en calcul numérique mais surtout pour les vidéos improbables de toi qui trainent sur le web et qui égayent nos journées d'hiver. Rien à voir avec les vidéos, je remercie le service informatique d'EPOC, Jean-Michel et Hubert, qui me permet de faire de la modélisation numérique dans de très bonnes conditions.

Comment ne pas remercier Mathias, McFly, Marcus et Jonah pour les soirées à taper le boeuf, sans oublier les voisins pour leur surdité.

Enfin, je souhaite remercier ma famille, en particulier mes parents et ma soeur, ma femme Sophie et nos enfants Timéo et Eloi pour ces moments de bonheur partagés à quatre.

La Pesca, Chili, le 7 décembre 2012

Préambule

De tous les environnements côtiers, les côtes sableuses sont de nos jours parmi les zones les plus attractives, générant des revenus importants du tourisme et des milliers d'emplois. Des plages sableuses larges, peu dangereuses et peu soumises à l'érosion et à la submersion sont ainsi un atout majeur en termes d'activité économique et récréative. Les littoraux sableux exposés à la houle sont pourtant parmi les environnements les plus énergétiques, les plus dynamiques, les plus complexes, les moins bien compris et donc les moins prédictibles. L'évolution des plages sableuses est régie par des processus hydro-sédimentaires complexes et très non-linéaires impliquant de fortes rétroactions entre l'hydrodynamique (vagues et courant), le transport sédimentaire et l'évolution du fond sableux. La compréhension et la modélisation de la dynamique des vagues, des courants et tout particulièrement de l'évolution de la morphologie des littoraux sableux représentent encore un véritable défi scientifique.

L'objectif de mes travaux depuis 11 ans a été de contribuer à l'amélioration de la compréhension des processus hydro-sédimentaires contrôlant l'évolution des littoraux sableux en associant de façon étroite la modélisation théorique et numérique avec la modélisation physique en laboratoire et la télédétection par imagerie vidéo dans le cadre de collaborations nationales et internationales et, plus ponctuellement, l'analyse de mesures *in-situ* haute fréquence. Cette originalité dans le paysage de la recherche française en dynamique littorale s'est également manifestée plus récemment à travers le développement innovant de méthodes d'assimilation de données issues de la télédétection (vidéo et/ou radar) dans les modèles numériques. Un autre caractère original de mes recherches réside dans ma stratégie de modélisation. En effet, en modélisation de la morphodynamique littorale, on peut facilement augmenter le degré de complexité de la représentation de chaque processus hydro-sédimentaire. Toutefois, céder à cette tentation aboutit la plupart du temps à un modèle qui s'apparente à une grosse boîte noire, de laquelle il n'est pas possible d'identifier les processus moteurs des évolutions morphologiques. Le modélisateur peut aussi obtenir avec ce type de modèle des évolutions morphologiques similaires aux observations de terrain, tout en ayant une description fausse de l'hydrodynamique sédimentaire. Je me suis donc orienté vers une réduction de la complexité des modèles morphodynamiques afin de favoriser la compréhension en identifiant les processus et rétroactions clés déterminant la réponse des littoraux.

Mes recherches en dynamique hydro-sédimentaire ont jusqu'à présent couvert une assez large gamme d'échelles spatio-temporelles. Les plus grandes échelles ont été abordées en 2005 et 2006 lorsque j'étais chercheur au Griffith Centre for Coastal Management (Griffith University, Australie). Depuis mon intégration au CNRS en octobre 2007, en accord avec le projet de recherche sur lequel j'ai été recruté, j'ai pris la responsabilité des activités de modélisation morphodynamique en domaine

littoral au sein de l'équipe thématique METHYS de l'UMR EPOC (mon CV complet est donné en Annexe B). Pour être concis et se focaliser sur les travaux qui ont eu le plus d'impact sur la communauté scientifique internationale, mes contributions sur le comportement hydro-sédimentaire des littoraux à grande échelle qui sont à l'heure actuelle à la marge de mes activités ne sont pas abordées dans ce mémoire (un résumé de ces activités est donné en Annexe A), ni ceux abordant des problématiques plutôt méthodologiques. Les travaux qui ont eu le plus d'impact sur la communauté scientifique internationale concernent les circulation induites par les vagues et la morphodynamique des plages sur des échelles de temps de l'ordre de quelques heures à l'échelle d'une tempête jusqu'à plusieurs mois à l'échelle d'un nombre important de changements de régimes de houle. Pendant ces travaux j'ai notamment contribué à 2 changements de paradigme scientifiques au sein de la communauté littorale internationale. Ces travaux ont été réalisés grâce à l'élaboration d'un réseau de collaborations nationales et internationales dans le cadre de nombreux projets, mais aussi le (co-)encadrement de nombreux stagiaires et doctorants. Cet encadrement de la recherche et ces collaborations seront explicités tout au long de ce mémoire. Celui-ci s'articule autour de 5 chapitres :

Le *premier chapitre* présente le contexte général et le positionnement de mes recherches.

Le *deuxième chapitre* présente les recherches menées sur les circulations induites par les vagues en domaine littoral. De notre expérience en campagnes de mesures *in-situ*, je montre qu'on peut favoriser le développement de campagnes de mesures courtes, flexibles, ciblées et déterminées en fonction de questions scientifiques précises au détriment de grosses campagnes de mesures parfois rigides, souvent coûteuses, qui ne permettent pas toujours d'avancées scientifiques importantes à cause de conditions naturelles hostiles et non-maîtrisées. D'un point de vue théorique, nous dérivons un terme de forçage de la vorticité verticale permettant, à partir d'un champ de vagues simulé, de prédire l'intensité et le signe de la nature rotationnelle des circulations littorales sans avoir à utiliser un modèle de circulation, ce qui était jusqu'à présent nécessaire avec l'approche des tensions de radiations. Nous montrons que notre approche est non seulement plus pratique que la théorique classique, mais qu'elle a aussi des bases théoriques beaucoup plus solides puisqu'elle ne fait pas intervenir d'empirisme. Enfin, nous expliquons comment à partir de la modélisation physique en laboratoire nous avons participé à un changement important de perception de la dynamique instationnaire des courants d'arrachement : d'un comportement ouvert vers un comportement semi-fermé des cellules de circulation associées. Ce changement a de fortes implications pour le mélange en domaine littoral et la sécurité de la baignade.

Le *troisième chapitre* synthétise les travaux d'observation de la morphodynamique des plages sableuses qui amènent un grand nombre de questionnements scientifiques stimulant des travaux de modélisation théorique et numérique. Nous développons un modèle conceptuel de la dynamique des plages d'Aquitaine avec la volonté d'intégrer leur comportement dans la modélisation conceptuelle universelle. J'émets également pour la première fois l'hypothèse que les interactions entre les différentes entités du système plage peuvent jouer un rôle crucial dans la morphodynamique du système composite. Ces travaux sont aussi à l'origine du montage du projet BARBEC (ANR Jeunes Chercheurs) que je coordonne depuis fin 2010. Mes travaux sur le littoral

aquitain puis ceux sur le littoral australien soulignent le rôle tampon essentiel des barres sableuses pré-littorales et des dunes végétalisées dans la réponse de la plage aux événements de tempête.

Le *quatrième chapitre* présente les travaux menés en modélisation théorique et numérique de la morphodynamique des plages sableuses. Nous montrons comment mes travaux ont contribué au changement de paradigme de la théorie des motifs vers la théorie de l'auto-organisation pour expliquer la formation et la dynamique des corps sableux tridimensionnels en zone de déferlement. Les travaux les plus récents en modélisation morphodynamique non-linéaire permettent enfin d'expliquer un nombre important de comportements des plages sableuses qui jusque-là n'avaient encore jamais été compris puisque la communauté internationale s'obstinait dans la théorie des motifs ou n'utilisait pas toutes les possibilités de la modélisation morphodynamique non-linéaire. Nous montrons finalement comment, récemment, nous contribuons fortement à la réconciliation de la théorie avec les observations.

Le *cinquième chapitre* synthétise ces travaux et expose les principaux axes de recherche que je privilégierai ces prochaines années.

Ces travaux de recherche ont été largement valorisés à travers de nombreuses publications et communications (liste complète fournie en Annexe C) avec par exemple 45 publications internationales de rang A, dont 19 en 1^{er} auteur (les 12 plus représentatives sont fournies en Annexe D).

x

Table des matières

Liste des figures

Introduction

1

Sommaire

1.1 Contexte

1.1.1 Enjeux

Depuis plusieurs dizaines d'années, la densité de la population le long des côtes a augmenté de manière drastique. Désormais, près de la moitié de la population mondiale habite en zone côtière et on prévoit une accélération de cette tendance ces prochaines décennies. Cette migration de population a été motivée par divers facteurs, notamment l'accès plus facile à la nourriture, aux transports, un climat généralement plus doux et, plus récemment, pour le style de vie. Parmi tous les environnements côtiers, les côtes sableuses sont de nos jours l'une des zones les plus attractives, générant des revenus importants du tourisme et des milliers d'emplois. C'est également un environnement permettant la pratique de nombreuses activités récréatives (*e.g.*, baignade, surf, planche à voile). Des plages sableuses larges, peu dangereuses et peu soumises à l'érosion et à la submersion sont ainsi un atout majeur en termes d'activité économique et récréative.

Les interventions humaines, principalement au cours du dernier siècle, ont considérablement diminué le volume de sédiment atteignant les littoraux (*e.g.*, diversion des rivières, construction de barrages, aménagement des berges). L'Homme a également perturbé les cellules sédimentaires naturelles et, par conséquent, l'évolution morphologique des côtes (*e.g.*, structures en "dur" d'ingénierie côtière telles que les digues, jetées, épis et brise-lames) en défigurant progressivement certains littoraux (pour un panorama de l'histoire des aménagements en "dure", voir *Charlier et al.* 2005). Alors que ces derniers aménagements avaient pour but initial de stabiliser les plages et fixer le trait de côte en tentant de maîtriser la nature, force est de constater que ces ouvrages sont parfois inefficaces face au caractère inexorable de la dynamique littorale [1]. Ainsi, les techniques de protection dites "souples" (*e.g.*, rechargements de plage, accompagnement de la mobilité des dunes, géotextiles, drainage de plage, *e.g.*, *Hamm et al.* 2002, *Hanson et al.* 2002) sont progressivement apparues à la fin du siècle dernier. Cette prise de conscience s'est également matérialisée par la mise en place de Gestion Intégrée des Zones Côtières (GIZC) qui est une démarche des territoires littoraux promouvant une gestion et une utilisation durable des zones côtières, prenant en compte simultanément la fragilité des écosystèmes et des paysages côtiers, la diversité des activités et des usages et leurs interactions. Heureusement donc, de nos jours les directives européennes (EUROSION), nationales (Comité interministériel d'aménagement et de développement du territoire, CIADT) et régionales recommandent que la gestion des zones côtières ne repose plus uniquement sur l'utilisation de structures en dure. Ainsi, la GIZC combine le plus souvent les mesures dures avec des mesures souples, traduisant une évolution de la doctrine du génie côtier. Toutefois, les interventions humaines devraient encore augmenter dans le futur et ainsi continuer d'impacter l'évolution naturelle des littoraux.

Un autre phénomène résultant de l'activité humaine est le changement climatique [2], à travers ses activités telles que l'industrie, la circulation automobile ou l'agri-

1. Les structures en "dures" ont la particularité de souvent déplacer le problème d'érosion aux littoraux adjacents. D'autre part, les méthodes rigides ne garantissent pas toujours une protection absolue des populations contre les risques de submersion marine, certaines tempêtes pouvant dépasser en intensité les hypothèses de dimensionnement des ouvrages (*e.g.*, tempête Xynthia).

2. Sans rentrer dans les controverses, dans son quatrième rapport (*IPCC* 2007) le GIEC conclut que la probabilité que le réchauffement climatique soit dû aux activités humaines est supérieur à 90%, reléguant les causes naturelles, *e.g.* fluctuations de l'activité solaire et les émissions volcaniques, au second plan.

culture qui produisent des gaz qui amplifient l'effet de serre naturel. Le changement climatique induit une augmentation du niveau moyen des mers (*e.g.*, *Cazenave and Nerem* 2004), modifie les climats de houle régionaux (*e.g.*, *Mori et al.* 2010) et l'intensité et la fréquence des tempêtes (*IPCC* 2007). Cela risque de conduire à une modification significative des paysages littoraux, un remodelage du trait de côte et une augmentation de la menace qui pèse sur la gestion durable du littoral. Toutefois, à l'heure actuelle le flou règne encore sur l'évolution des climats de houle le long de nos littoraux et, dans une moindre mesure, sur l'augmentation du niveau moyen des mers. Ainsi les projections se matérialisent le plus souvent sous la forme de scénarii qui, du plus pessimiste au plus optimiste, peuvent diverger de manière significative.

Une connaissance extensive de la dynamique hydro-sédimentaire le long des littoraux sableux et de leur évolution pourrait donc répondre à des enjeux sociétaux majeurs. Comme nous l'avons vu ci-dessus, l'un des principaux enjeux concerne l'érosion. A titre d'exemple, 35% du linéaire côtier métropolitain est en recul. Parmi ces 35%, près de 70% concerne les littoraux sableux (*EUROSION* 2004). Cette érosion, qui a souvent des conséquences catastrophiques d'un point de vue économique, peut se manifester de différentes manières en bouleversant le paysage littoral et parfois l'écosystème (*e.g.*, Figures 1.1b, c). Certains littoraux sont également exposés à la menace de submersion. Le dernier exemple en date est celui du passage de la tempête Xyn-

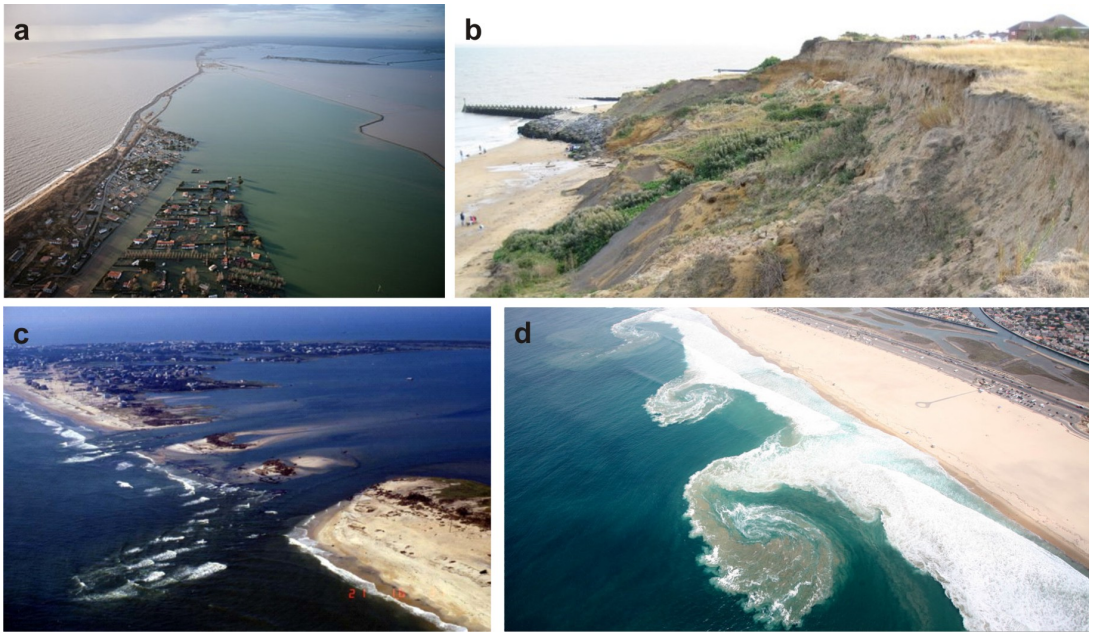

FIGURE 1.1 – *Illustration de la liste (non-exhaustive) des enjeux sociétaux affectant la gestion durable des littoraux sableux. (a) Submersion du littoral vendéen au passage de la tempête Xynthia laissant un bilan catastrophique de 53 morts et de plus de 2,5 milliards d'euros de dommages. (b) Gestion discutable des problèmes d'érosion avec des structures en dur. Les épis en haut de la photo captent une partie du sable induisant un déficit sédimentaire important de la plage en bas de la photo. Dans ce cas l'érosion de la plage sableuse livre la falaise aux assauts des vagues induisant un recul rapide (à l'échelle géologique) de celle-ci. (c) Ouverture d'une brèche à travers un cordon sableux au passage d'une tempête. Dans ce cas la dynamique hydro-sédimentaire du système peut changer de manière drastique. Dans certains cas l'intrusion massive d'eaux salines dans les eaux douces ou saumâtres peut bouleverser l'écosystème. (d) Courants d'arrachement (déduits des panaches sédimentaires) induits par les vagues le long d'une plage sableuse soumise à l'action de la houle. Les courants d'arrachement sont de loin la principale cause mondiale de noyades et de sauvetages le long des plages.*

thia (*Bertin et al.* 2012) le long des littoraux vendéens et charentais (Figure 1.1a) qui s'est traduit par un bilan économique et humain très lourd. Enfin, les mouvements des masses d'eau induits par le déferlement de la houle peuvent se manifester sous la forme de courants d'arrachement (Figure 1.1d) qui sont internationalement la cause principale des noyades et des sauvetages le long des plages (*e.g.*, *Scott et al.* 2009).

1.1.2 Motivations

La mauvaise compréhension du comportement des littoraux sableux et l'incapacité actuelle de prévoir correctement leur évolution contrastent avec leurs atouts économiques, en particulier quand on considère le besoin urgent de mieux comprendre leur réponse aux changements des conditions de forçage des vagues dans le cadre du changement climatique. En effet, de tous les environnements littoraux (sableux, vaseux et rocheux), les littoraux sableux dominés par l'action de la houle sont parmi les plus dynamiques, les plus complexes, les moins bien compris et donc les moins prédictibles. L'évolution des plages sableuses est régie par des processus hydro-sédimentaires complexes et très non-linéaires impliquant de fortes rétroactions entre l'hydrodynamique (vagues et courant), le transport sédimentaire et l'évolution du fond sableux. C'est pourquoi mes travaux de recherche se sont essentiellement portés sur les processus hydro-sédimentaires contrôlant l'évolution des littoraux sableux et la morphodynamique.

La grande quantité de données (*in-situ* et laboratoire) collectées pendant ces dernières décennies, combinée avec le développement de nouvelles techniques permettant de caractériser la morphologie littorale et son évolution, a permis une récente renaissance de la théorie et de la modélisation numérique. L'océanographie physique littorale moderne se nourrit désormais de son histoire riche en termes d'observations tout en profitant de l'émergence de méthodes de suivi spécifiques au domaine littoral (*e.g.*, imagerie vidéo). L'amélioration récente des modèles numériques et la quantité de données qui peuvent être collectées en temps réel (principalement par imagerie vidéo) rendent aussi désormais envisageable la mise en place de méthode d'assimilation de données dans les modèles numériques pour la prévision des évolutions morphodynamiques.

1.2 Positionnement de mes recherches

1.2.1 Problématique scientifique

La dynamique des corps sableux littoraux couvre une vaste gamme d'échelles temporelles et spatiales (Figure 1.2). Cette dynamique va de l'évolution rapide des petites rides sableuses jusqu'à l'évolution sur plusieurs années à plusieurs siècles du prisme littoral et du trait de côte. Ces deux échelles aux extrémités du spectre ont été peu abordées dans mes travaux. Pour les échelles de temps de l'ordre de quelques heures (*i.e.*, à l'échelle d'une tempête) à quelques mois (*i.e.*, à l'échelle d'un nombre important de changements de régimes de houle), on observe la dynamique du profil de plage. Celui-ci est caractérisé par la présence d'un certain nombre de corps sableux qui ont la particularité de présenter la plupart du temps des structures tridimensionnelles, avec des longueurs d'onde longitudinales allant de quelques mètres jusqu'à plusieurs kilomètres.

La Figure 1.3 présente les différents compartiments du système plage, ainsi que les principaux processus hydro-sédimentaires et corps sédimentaires typiquement

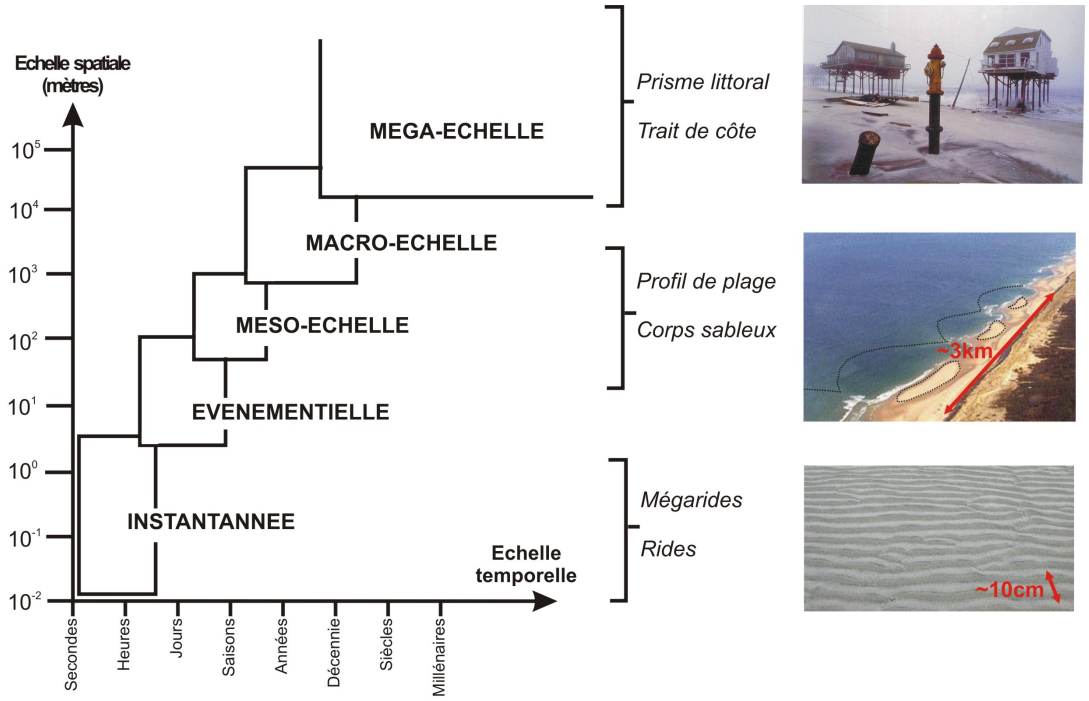

FIGURE 1.2 – *Schéma des échelles spatio-temporelles associées à la dynamique des littoraux sableux dominés par l'action de la houle.*

observés le long des plages sableuses naturelles dominées par l'action de la houle et en présence de la marée. Les terminologies indiquées dans ce schéma seront couramment utilisées tout au long de ce mémoire. Parmi ces corps sableux, on note tout d'abord l'omniprésence des barres sableuses en zone subtidale et/ou intertidale, typiquement entre 0 et 10 m de fond, et qui sont une composante essentielle de la dynamique littorale (*Stive and Reniers* 2003). Ces barres de déferlement ont été étudiées depuis plusieurs décennies (*e.g.*, *Shepard* 1952, *Hom-ma and Sonu* 1962, *Sonu* 1973, *Goldsmith et al.* 1982, *Aleman et al.* 2011). Ces barres sont observées le long des plages de type 'intermédiaire' d'après la classification conceptuelle de *Wright and Short* (1984), c'est à dire pour les plages où $1 < \Omega < 6$ où $\Omega = H_b/w_s T$ avec H_b la hauteur des vagues, w_s la vitesse de chute du sédiment et T la période des vagues. Cela correspond à l'immense majorité des plages sableuses dans le monde.

Les barres agissent comme une protection naturelle pour la plage en dissipant l'énergie des vagues de tempête au large par déferlement bathymétrique (Figure 1.4a), ce qui induit une réduction à la fois de l'intensité des processus en zone de jet de rive au niveau de la plage et des problèmes de submersion et d'érosion des dunes et des falaises. La géométrie des barres sableuses impacte aussi parfois la géométrie du haut de plage (Figure 1.4b) et les oscillations du trait de côte (la définition du trait de côte utilisée en Figure 1.3b est la limite de végétation de la dune bordière, mais celle-ci n'est pas universelle [3]) ou encore la présence de pics d'érosion intense et très localisée (appelés *hot-spots* dans la littérature anglo-saxonne, correspondant souvent à la

3. Il existe un grand nombre de définitions du trait de côte, suivant par exemple les échelles de temps appréhendées, l'approche utilisée (photos aériennes ou satellitaires, imagerie vidéo, relevés topographiques), la géomorphologie et la présence ou pas de dune ou de végétation, ou encore le marnage. Par exemple, en domaine microtidal on tendra plutôt à utiliser la ligne d'eau, tandis que dans les environnements micro-tidaux on préférera par exemple la limite de végétation. Pour une liste extensive des définitions du trait de côte, le lecteur est invité à consulter *Boak and Turner* (2005).

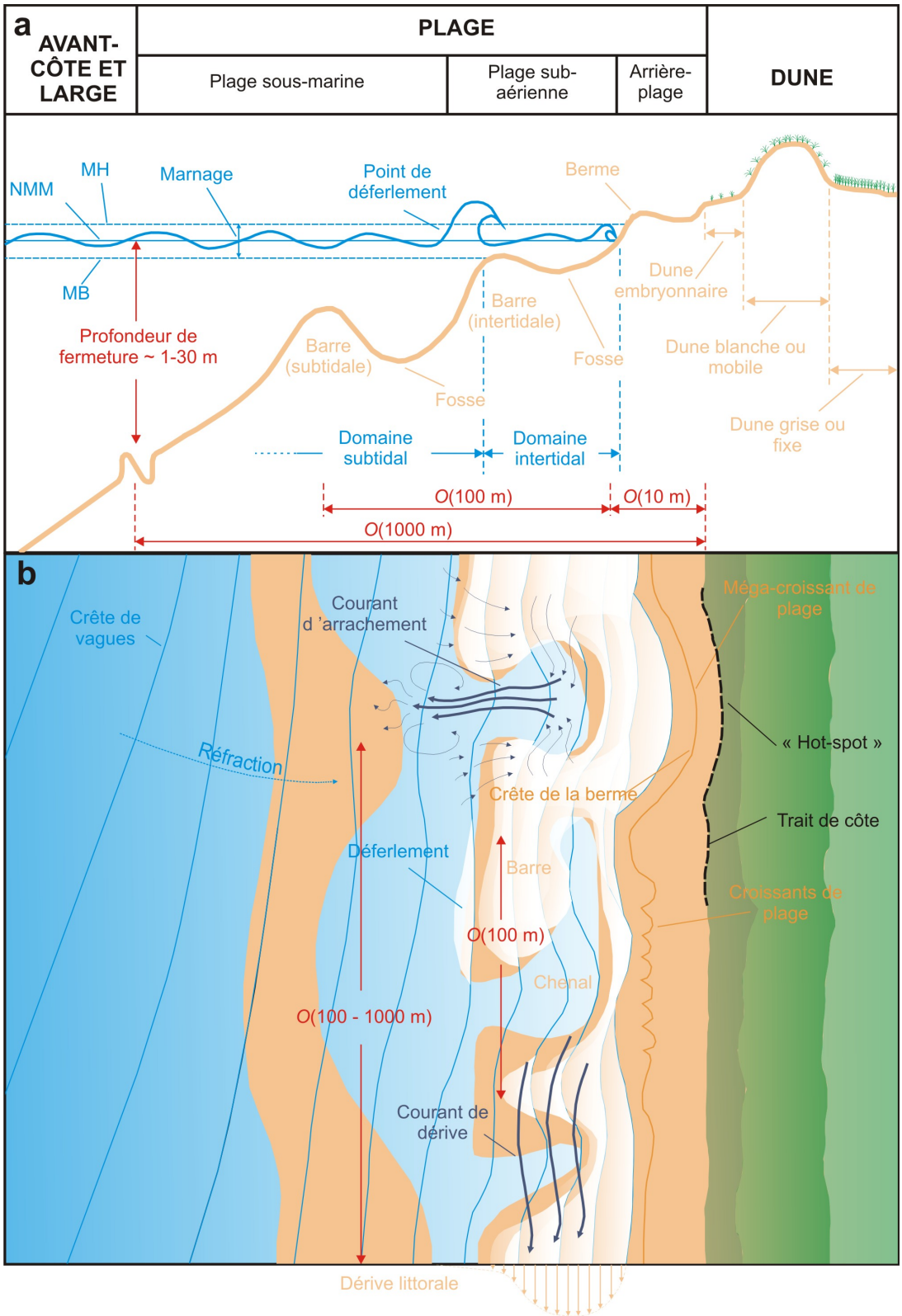

FIGURE 1.3 – *Croquis de définitions des différents compartiments du domaine littoral, des processus hydro-sédimentaires et corps sédimentaires typiquement observés le long des plages sableuses naturelles dominées par l'action de la houle en présence de la marée. Le profil de plage peut présenter une ou plusieurs barre(s). MH : marée haute, NMM : niveau moyen des mers ou niveau de mi-marée, MB : marée basse. Les ordres de grandeur indiqués globalement augmentent avec l'énergie du climat de houle auquel la plage est exposée.*

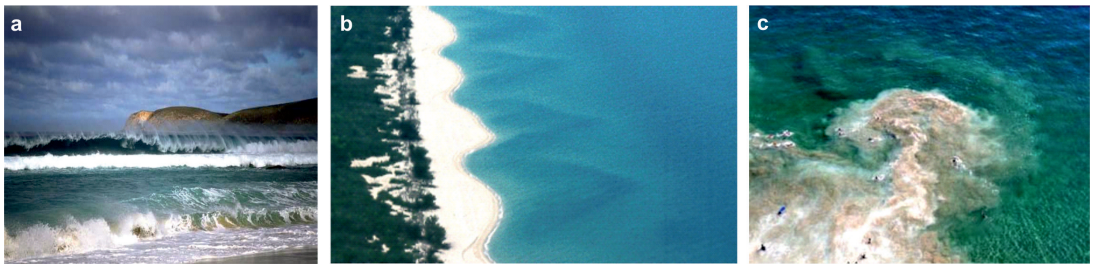

FIGURE 1.4 – *Illustration de l'importance des barres pré-littorales en dynamique littorale : (a) protection de la plage aérienne par dissipation de l'énergie des vagues au large par déferlement bathymétrique, (b) les oscillations du trait de côte sont souvent couplées à la géométrie des barres et (c) 'grappe' de baigneurs pris dans un courant d'arrachement induit par le déferlement des vagues au-dessus d'une barre pré-littorale tridimensionnelle.*

présence des méga-croissants de plage, *i.e. megacusps Thornton et al.* 2007). La tridimensionnalité des barres sableuses guide les circulations horizontales induites par les vagues en zone de déferlement. Ces cellules de circulation sont une composante essentielle en dynamique littorale puisqu'elles sont supposées participer activement aux échanges hydro-sédimentaires entre le plateau continental et les franges littorales, et sont moteur du mélange des masses d'eau (*e.g., Smith and Largier* 1995). Ces cellules ont donc des implications importantes dans les problématiques de transport et de dispersion des polluants ou des nutriments. Enfin, ces cellules de circulation sont associées à des courants d'arrachement (Figure 1.4c, courants intenses et étroits dirigés vers le large, *e.g., MacMahan et al.* 2006, *Dalrymple et al.* 2011). Le comportement instationnaire de ces courants d'arrachements a fait récemment l'objet d'un important changement de perception qui sera traité plus loin dans ce document.

Les barres sableuses ont un comportement extrêmement complexe qui contraste avec la simplicité apparente de leur géométrie. La plupart du temps les barres sableuses présentent une structuration cohérente, rythmique ou quasi-rythmique, le long de la plage. En partant d'une barre rectiligne, typique des épisodes de tempête, des structures tridimensionnelles se développent pendant les périodes accrétives (post-tempêtes). Parmi ces morphologies, on peut distinguer les systèmes de barres en croissant et les systèmes barres/chenaux (Figure 1.3b), ce dernier étant parfois qualifié de système barre/baïne par le grand public sur le littoral aquitain. Malgré un nombre important d'objections soulevées dans la littérature (*e.g., Sonu* 1972a, *Bryan and Bowen* 1997, *Van Enckevort et al.* 2004), depuis les années 70 jusqu'à très récemment les ondes infragravitaires de bord stationnaires (*e.g., Bowen and Inman* 1971, *Holman and Bowen* 1982, *Komar* 1998) étaient supposées contrôler la formation et la dynamique de ces barres sableuses tridimensionnelles rythmiques. Récemment, il a été montré que la rétroaction positive entre l'hydrodynamique (vagues et courants induits), le transport sédimentaire et l'évolution du fond sableux pouvait jouer un rôle majeur dans la génération spontanée des structures tridimensionnelles des barres sableuses (*e.g., Damgaard et al.* 2002, *Calvete et al.* 2005, *Garnier et al.* 2006). Ce changement de paradigme scientifique de la théorie des motifs vers les théories d'auto-organisation, qui est synthétisé dans *Coco and Murray* (2007), sera traité plus loin dans ce document.

Bien que des progrès importants aient été réalisés depuis une vingtaine d'années sur le plan international, **la compréhension et la modélisation de la dynamique des vagues, des courants induits et de l'évolution des littoraux sableux dominés par l'action de la houle représentent encore un véritable défi scientifique.** Pour faire avancer les modèles théoriques puis numériques, il faut mieux comprendre les

processus physiques. Pour cela, il faut faire interagir étroitement la théorie, la modélisation physique puis l'observation qui valide ou pas les concepts élaborés. D'une manière générale, les modèles sont capables en partie de simuler les épisodes d'accrétion de plage sur des temps courts, de l'ordre de quelques jours à quelques semaines. Ils sont par contre à l'heure actuelle incapables de simuler la dynamique des plages dans leur globalité pendant les épisodes de tempête et sur des échelles de temps plus grandes. En d'autres termes, **la modélisation de la réponse, très non-linéaire, des plages aux changements de régimes de houle reste un problème ouvert. D'autre part, l'avancée des connaissances en océanographie physique littorale a été caractérisée pendant la dernière décennie par un nombre important de changements de paradigmes scientifiques auxquels mes travaux ont contribué. Nous verrons aussi que, récemment, mes travaux ont réconcilié la théorie avec les observations qui allient pourtant à l'encontre du nouveau paradigme.**

1.2.2 Approche méthodologique

Mon domaine de recherche couvre la dynamique des plages sableuses dominées par l'action de la houle avec une approche basée sur la modélisation des processus physiques (ma stratégie de modélisation est détaillée dans la prochaine sous-partie 1.2.3). Mes études ont porté sur les évolutions des corps sableux littoraux sur des échelles de temps de l'ordre de quelques heures à quelques années, en réponse aux changements de régimes de houle, le but à terme étant d'intégrer ces processus hydro-sédimentaires complexes dans des modèles à plus grande échelle, notamment dans le cadre du réchauffement climatique. Un point fort de ma démarche est d'associer de façon étroite la modélisation théorique et numérique avec l'analyse de mesures *in-situ* hautes fréquences et tout particulièrement, dans le cadre de collaborations nationales et internationales, la modélisation physique en laboratoire et la télédétection par imagerie vidéo. Enfin, depuis peu je pilote le développement innovant de méthodes d'assimilation de données dans les modèles numériques.

Une des originalités de mon approche est donc de sortir du schéma classique en océanographie physique littorale qui consiste, le plus souvent, à ne combiner que les mesures *in-situ* et la modélisation numérique pour appréhender la dynamique hydro-sédimentaire d'un nombre limité de sites. De plus, l'étude d'une plage donnée (souvent celle proche du laboratoire) présente des spécificités qui ne permettent pas, dans beaucoup de cas, d'en sortir des leçons génériques sur les comportements morphodynamiques limitant parfois l'approche à une simple étude de cas. Pour éviter cela, j'ai plutôt travaillé dans le cadre de collaborations nationales et internationales sur un grand nombre des plages dans le monde afin de couvrir une vaste gamme de forçages de vagues et de marée, de morphologies et de granularités de sable[4]. J'ai également le plus souvent utilisé l'imagerie vidéo[5], outil extrêmement bien adapté à la dynamique littorale, pour caractériser les évolutions morphodynamiques haute-fréquence en complément des données *in-situ* ou en unique source de données. Les

4. Par exemple, participation aux campagnes de mesures PNEC 2001 et ECORS'08 sur le littoral aquitain en collaboration avec des laboratoires nationaux et internationaux ; campagne DRIBS à Perranporth, UK avec l'University of Plymouth ; Gold Coast Shoreline Management Plan sur les plages de la Gold Coast, Australie, au sein de Griffith University ; les plages du littoral charentais en collaboration avec l'Université de La Rochelle ; les plages du littoral de Bouknadel-Kénitra au Maroc en collaboration avec l'Université Ibn-Tofail.

5. Travaux réalisés dans le cadre de nombreuses collaborations comme avec l'University of New South Wales (Australie), Utrecht University (Pays-Bas), la Pontificia Universidad Catolica de Chile (Chili) et en France avec le CASAGEC et l'IVS (UPPA).

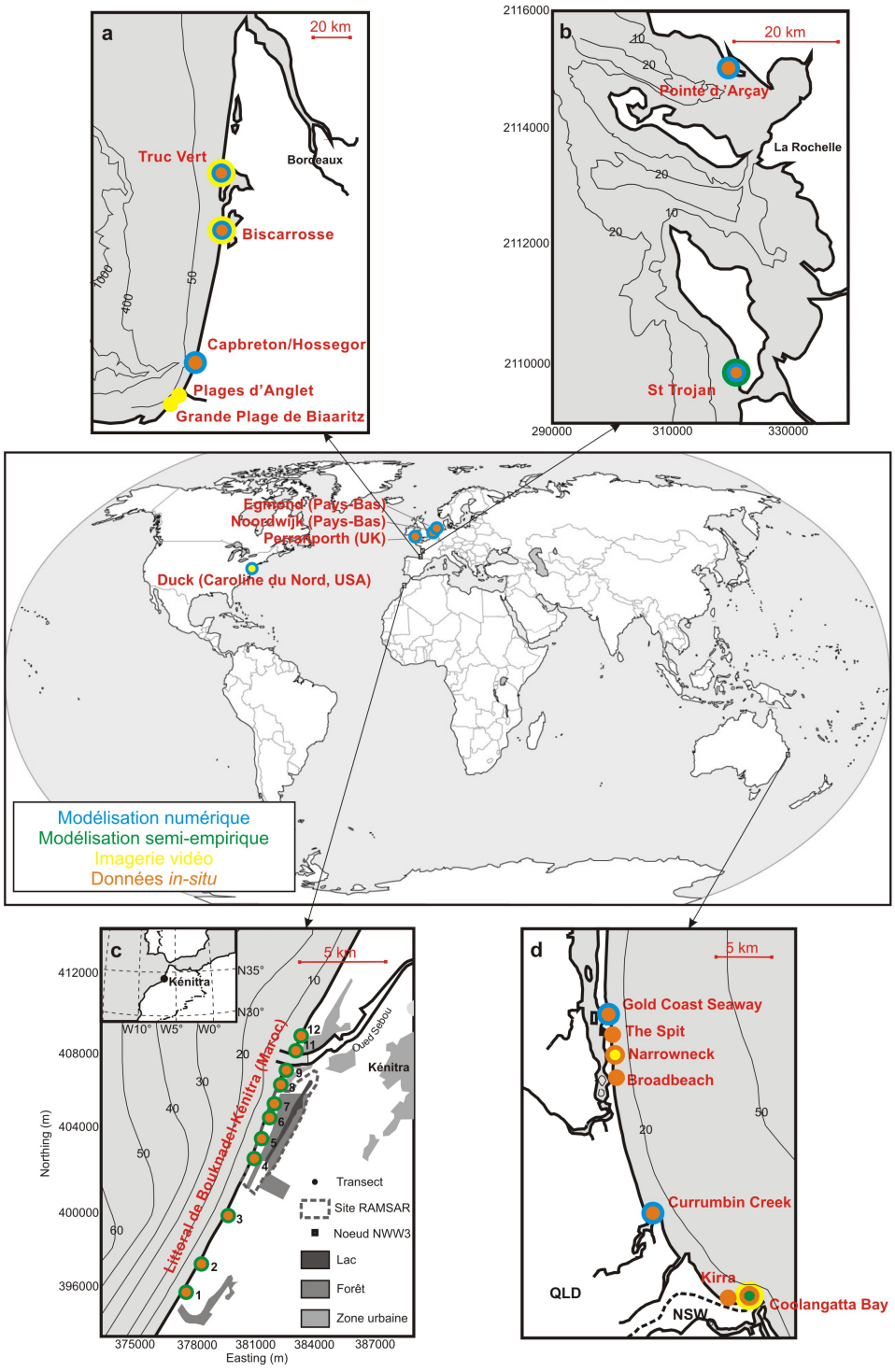

FIGURE 1.5 – *Localisation des principaux sites étudiés pendant mes recherches, avec discrimination des approches de modélisation numérique, semi-empirique, d'imagerie vidéo et de mesures in-situ. Sites internationaux avec zooms sur certaines régions : (a) le littoral aquitain, (b) le littoral charentais et vendéen, (c) le littoral de Bouknadel-Kénitra (Maroc) et (d) la Gold Coast (Australie).*

plages sur lesquelles j'ai travaillé sont montrées en Figure 1.5 [6], avec discrimination des approches de modélisation numérique, semi-empirique, d'imagerie vidéo et de mesures *in-situ*.

Une autre approche que j'ai privilégiée ces dernières années est la modélisation physique en laboratoire. En effet la modélisation physique permet d'effectuer des expériences pour des conditions contrôlées ce qui permet de réaliser des scénarii et élaborer des expériences en fonction de questions scientifiques précises. Ces travaux ont été réalisés principalement dans le cadre d'une collaboration étroite avec nos collègues de l'équipe HOULE du LEGI sur des modèles réduits [7]. Plus récemment en juin 2012, dans le cadre du projet européen BARDEX II (HYDRALAB-IV, University of Plymouth, UK), j'ai également pu profiter de simulations en canal à houle avec fond sableux à l'échelle 1 afin de s'affranchir des problèmes de similitudes.

1.2.3 Stratégie de modélisation

La démarche de modélisation passe typiquement par une étape d'identification et de hiérarchisation des processus physiques, puis une phase de modélisation explicite des processus et finalement par une intégration des processus dans des modèles de plus grande échelle, le plus souvent sous forme de paramétrisation. D'autre part, les modèles de plus grande échelle permettent d'obtenir des conditions limite pour les modèles à plus petite échelle. Cette démarche appliquée aux modèles de morphodynamique littorale est schématisée en Figure 1.6. Par exemple, pour appréhender la morphodynamique d'une plage sableuse sur des échelles de temps de l'ordre de quelques jours à quelques mois, les modèles côtiers de vagues et/ou de circulation permettent de forcer le modèle de morphodynamique littorale aux conditions limites. D'autre part, les modèles hydrodynamiques fins basés par exemple sur les équations de Navier-Stokes ou de type Boussinesq permettent d'obtenir des informations sur les processus hydrodynamiques à l'échelle de la vague qui doivent être rigoureusement paramétrés dans les modèles morphodynamiques [8].

Ma démarche est donc basée sur la modélisation des processus physiques. Sur de plus grandes échelles, certains modèles sont basés essentiellement sur des lois de comportement. Par exemple, le modèle de *Bruun* (1962) est basé sur une hypothèse de profil statique qui permet d'estimer le recul du trait de côte en fonction de l'élévation du niveau moyen des mers [9]. D'autres sont des modèles hybrides basés à la fois sur

6. A ces sites viennent s'ajouter, dans le cadre de campagnes de mesures avec imagerie vidéo, La Pesca au Chili (décembre 2012) et la plage de Grand Popo au Benin (Février 2013).

7. (1) Dans le canal à houle du LEGI de 36 m de long, considérant un rapport d'échelle d'environ 1 :10 en longueur et 1 :3 en temps dont l'originalité réside dans l'utilisation d'un sédiment de faible densité permettant de satisfaire les lois de similitude en transport sédimentaire afin d'obtenir des comportements des plages expérimentales cohérents avec celui des plages naturelles (*e.g.*, *Michallet et al.* 2007, *Grasso et al.* 2009; 2011) et (2) le bassin 2D du LHF fin 2008 qui nous a permis d'étudier pour la première fois en laboratoire la morphodynamique des plages tridimensionnelles et les circulations horizontales induites par les vagues.

8. Par exemple, les asymétries en vitesse et accélération des mouvements orbitaux du fluide ne sont pas simulés explicitement dans les modèles morphodynamiques à phase moyennée. Le transport sédimentaire étant une fonction non-linéaire des vitesses du fluide, les flux sédimentaires et par conséquent les évolutions morphologiques induites par ces asymétries sont significatives (*e.g.*, *Drake and Calantoni* 2001, *Hoefel and Elgar* 2003).

9. Les hypothèses sous-jacentes à la loi de Bruun sont extrêmement fortes, et dans la plupart des utilisations elles ne sont pas respectées. Même si ce modèle est encore largement et abusivement utilisé (à cause de sa facilité d'utilisation, de l'absence de modèle alternatif et parfois la méconnaissance de ses très nombreuses limitations), il est fortement recommandé d'abandonner ce modèle (*e.g.*, *Cooper and Pilkey* 2004).

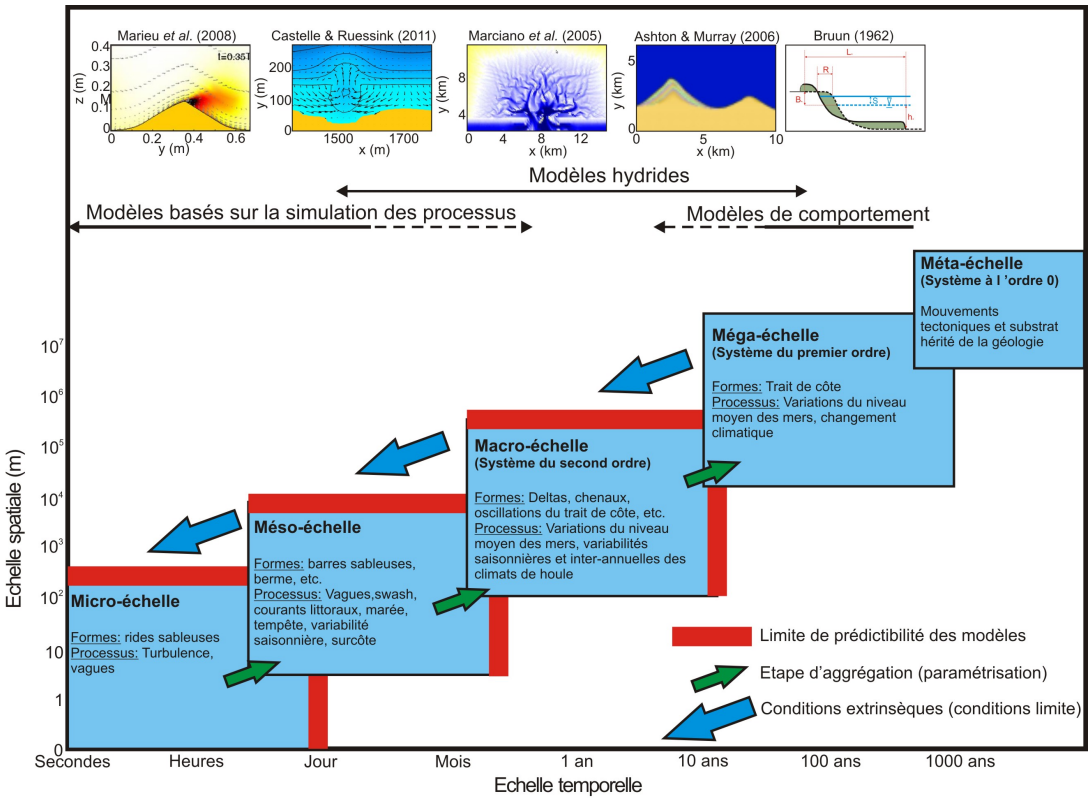

FIGURE 1.6 – *Croquis simplifié illustrant le type de modèle couramment utilisé en fonction du type de corps sableux dont on veut simuler la dynamique. Des plus petites aux plus grandes échelles spatio-temporelles (de gauche à droite), les modèles basés sur la simulation des processus sont utilisés pour étudier la formation et l'évolution des rides sableuses (e.g., Marieu et al. 2008), des barres sableuses de déferlement ou des réseaux de chenaux dans les bassins tidaux (e.g., Marciano et al. 2005). Pour simuler sur plusieurs années à plusieurs siècles les instabilités du trait de côte on peut utiliser un modèle hybride : on simule de manière semi-empirique la dérive littorale, puis l'évolution de la position du trait de côte est obtenue en combinant les gradients longshore de dérive littorale et un modèle de comportement qui considère une translation du profil actif de la plage (e.g., Ashton and Murray 2006a). Enfin, le modèle de comportement basé sur la loi de Bruun (1962) considère une translation du profil de plage en réponse à l'évolution du niveau moyen des mers S qui permet d'obtenir une relation linaire entre le recul du trait de côte R et S. L'hypothèse principale dans ce modèle de comportement (où aucun processus n'est simulé) est que la forme du profil de plage ne change pas : on parle de modèle statique.*

les processus physiques et des lois de comportement. Ces derniers ont notamment permis des avancées scientifiques majeures dans la compréhension des instabilités du trait de côte (*e.g.*, *Ashton et al.* 2001, *Ashton and Murray* 2006a, *Idier et al.* 2011). Comme nous le verrons par la suite, la combinaison de lois de comportement avec une description plus complète d'autres processus physiques est une approche que j'ai utilisée (voir approche du *basis state*). Si les hypothèses sont bien posées et que les simulations sont réalisées dans la gamme de validité des approximations, alors ce type d'approche peut permettre de réaliser des avancées scientifiques marquantes dans la compréhension de la morphodynamique littorale.

Une originalité de ma stratégie de modélisation, qui découle aussi en partie de l'utilisation de lois de comportement, et d'éviter une complexification parfois abusive des modèles morphodynamiques. En effet, les évolutions morphologiques simulées par ces modèles sont régies par les interactions entre différents processus hydrodynamiques et sédimentaires très non-linaires, que l'on peut chacun décrire avec cer-

tains degrés de complexités. Le danger en augmentant le degré de complexité de la représentation de chaque processus est de se retrouver avec un modèle qui s'apparente finalement à une grosse boite noire, de laquelle il n'est plus possible d'identifier les processus moteurs des évolutions morphologiques. Un exemple frappant, réalisé pourtant sur un cas très simplifié (évolution d'un profil de plage, pas de courant de marée, pas d'onde infragravitaire, pas de description de la variabilité du courant dans la colonne d'eau), est un de ceux documentés dans *Ruessink and Kuriyama* (2008). Les auteurs ont montré qu'ils pouvaient obtenir le même type d'évolution du profil de plage (même profil final) en utilisant plusieurs combinaisons de paramètres déterminant par exemple l'intensité des flux sédimentaires par suspension, les caractéristiques du courant dans la couche limite, etc. En résumé, en modélisation morphodynamique on peut facilement se retrouver avec une évolution morphologique assez réaliste tout en ayant une description fausse de l'hydrodynamique sédimentaire [10], pouvant réduire les interprétations à de pures spéculations. Ces dernières années, ma stratégie de modélisation s'est orientée vers une épuration de l'approche de modélisation afin d'identifier précisément les mécanismes responsables des évolutions. D'autres part, en s'affranchissant des difficultés liées aux cas d'application (nécessité de données bathymétriques et de forçages aux conditions limite précis), l'application des modèles sur des cas idéalisés permet d'identifier le comportement des corps sableux littoraux en réponse aux différents forçages et d'en sortir des lois génériques. Mon approche, qui constitue une originalité dans le paysage de la recherche française en dynamique littorale, consiste donc globalement à réduire la complexité des modèles afin de favoriser la compréhension en identifiant les processus et rétroactions clés déterminant la réponse de la plage. Ce choix de stratégie de modélisation est, dans un cadre plus général, extrêmement bien documenté dans *Murray* (2007).

Les avancées scientifiques sont réalisées dans 2 codes de recherche dont je coordonne le développement. Le premier est un modèle morphodynamique non-linaire entièrement couplé permettant de décrire l'évolution des barres sableuses tridimensionnelles. C'est à l'heure actuelle le seul modèle permettant de simuler la formation, l'évolution non-linéaire et la saturation des barres 3D et l'évolution du trait de côte associées. Le deuxième code de calcul, dont le développement a débuté plus tardivement, est un modèle de profil de plage entièrement couplé permettant de décrire la dynamique *cross-shore* des barres sableuses sur des échelles de temps longs (jusqu'à quelques années). **Les avancées scientifiques réalisées dans ces codes de recherche sont progressivement implémentées dans des modèles opérationnels** (*e.g.*, MARS2D-3D, *Lazure and Dumas* 2008).

1.2.4 Objectifs et organisation du mémoire

Mes recherches en dynamique hydro-sédimentaire ont jusqu'à présent couvert une assez large gamme d'échelles spatio-temporelles. Les plus grandes échelles ont été abordées pendant mon séjour postdoctoral en Australie au Griffith Centre for Coastal Management (Griffith University). Depuis mon intégration au CNRS en octobre 2007, en accord avec le projet de recherche sur lequel j'ai été recruté, j'ai pris la responsabilité des activités de modélisation morphodynamique en domaine littoral au sein de l'équipe thématique METHYS de l'UMR EPOC. Les travaux décrits dans ce mémoire sont le fruit de nombreuses collaborations avec des laboratoires français et étrangers, mais aussi des travaux de doctorants et stagiaires que j'ai (co-)encadrés.

10. Les mauvaises langues affirment qu'on peut sortir ce qu'on veut des modèles morphodynamiques en tournant les 'boutons' dans tous les sens... et elles ont raison !

Ces contributions seront explicitées tout au long du mémoire. L'ensemble des **publications internationales issues de ces travaux** seront indiquées en gras, avec une coloration pour les stagiaires et doctorants dans la liste bibliographique. De plus, afin de se concentrer sur les domaines où ma contribution a été la plus importante, ne seront pas abordés les travaux réalisés à l'échelles de la vague (***Bonneton et al.*** 2006, ***Tissier et al.*** 2011), ni les travaux sur les embouchures tidales (***Castelle et al.*** 2007b, ***Sennes et al.*** 2007, dans le cadre des travaux des stagiaires de Master Nathalie Molnar, Julien Bourget et Gilles Sennes), ceux sur la profondeur de remaniement du sédiment (***Bertin et al.*** 2008a), le mascaret (***Bonneton et al.*** 2011) et l'estimation de la hauteur des vagues par imagerie vidéo (***Almar et al.*** 2012).

Afin d'éviter l'effet catalogue, mes travaux qui, à mon goût, ont eu le moins d'impact sur la communauté internationale ne seront pas détaillés ici. C'est notamment le cas de mes travaux sur le comportement hydro-sédimentaire des littoraux sableux à grande échelle (O(1-10 km), O(1-10 ans)) qui consistaient à estimer les conditions de vagues à la côte et la dérive littorale dans le but de diagnostiquer les évolutions du trait de côte observées. Ces travaux impliquaient des collaborations avec avec Xavier Bertin (LIENSS, Université de La Rochelle / LNEC, Portugal) sur les plages du littoral charentais (***Bertin et al.*** 2008b) et avec le Griffith Centre of Coastal Management et la School for Information and Communications Techonology de Griffith University (Australie) dans le cadre de l'application de l'intelligence artificielle pour l'estimation des vagues à la côte (***Browne et al.*** 2006; 2007). Les approches de modélisation semi-empirique développées ont été ensuite appliquées aux plages du littoral de Bouknadel-Kénitra (Maroc, ***Hakkou et al.*** 2011) et au système de *bypass* permanent de sédiment dans la baie de Coolangatta (***Castelle et al.*** 2009a) respectivement à travers le co-encadrement de la thèse de Mounir Hakkou (Université de Ibn-Tofail, Kénitra, Maroc) et une collaboration avec Ian Turner de l'Université du New South Wales (Australie). **Pour une synthèse de mes travaux réalisés sur le comportement hydro-sédimentaire à grande échelle des littoraux sableux, le lecteur est invité à consulter l'Annexe A.**

Dans ce mémoire l'accent sera donc mis sur mes travaux qui ont eu le plus d'impact sur la communauté internationale et, notamment, sur ma contribution dans deux changements de paradigme scientifique. En effet, selon *Kuhn* (1962) l'évolution des connaissances dans une discipline scientifique peut typiquement se décomposer en trois phases : les premiers balbutiements, la maturité et l'âge avancé (Figure 1.7a). Seulement parfois le paradigme scientifique est infondé et, lorsque la communauté s'obstine dans ce dernier, cela peut même conduire à un déclin des connaissances. Le changement de paradigme intervient lorsqu'au fil des années il y ait eu à la fois la découverte de faits nouveaux ou l'invention de nouvelle(s) théorie(s) qui ne cadre(nt) pas avec le paradigme existant, et la candidature convaincante d'un nouveau paradigme [11]. Le changement de paradigme de la théorie des motifs vers les théories d'auto-organisation pour expliquer la dynamique des corps sableux tridimensionnels littoraux et, dans une moindre mesure, celui d'un comportement ouvert

11. D'après *Kuhn* (1962) cette étape de transition d'un paradigme scientifique à un autre peut prendre des décennies, l'ancien paradigme pouvant résister même s'il est contredit par de nombreux travaux. C'est le cas en morphodynamique littorale pour le changement de paradigme de la théorie des motifs vers les théories d'auto-organisation. Comme nous le verrons plus loin dans ce mémoire, la théorie des ondes de bord (motif dans l'hydrodynamique) introduite à la fin des années soixante a mis près de 40 ans à être renversée, même si dès les années 70 certains auteurs soulevaient déjà des incohérences frappantes (*e.g.*, *Sonu* 1972a). A l'heure de rédiger ce mémoire, il ne reste plus qu'un tout petit nombre d'irréductibles (souvent gaulois) qui pensent que les ondes de bord contrôlent la présence et la dynamique des barres sableuses tridimensionnelle rythmiques.

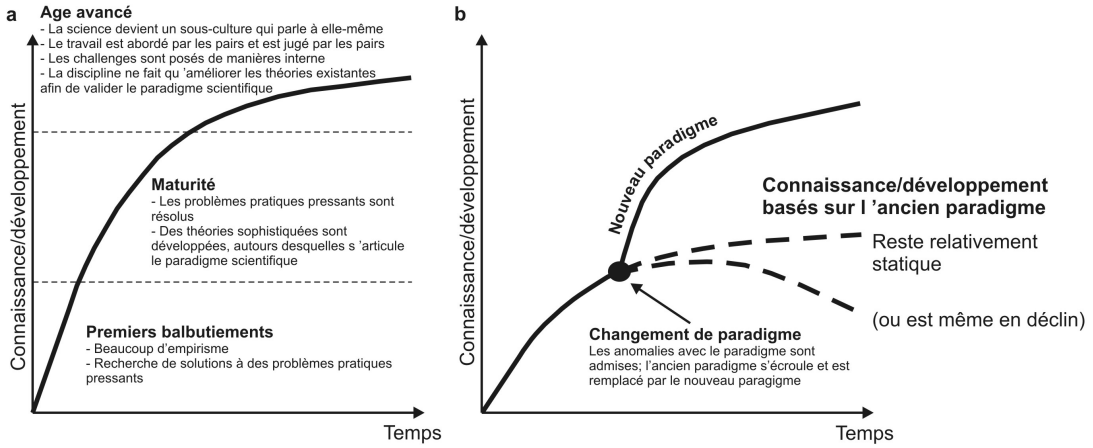

FIGURE 1.7 – *(a) Évolution des connaissances et du développement d'une discipline et (b) impact d'un changement de paradigme scientifique d'après Kuhn (1962; 1977) et Kamphuis (2011).*

vers un comportement semi-fermé des cellules de circulation associées aux courants d'arrachement ont permis des avancées scientifiques majeures en océanographie physique littorale. J'ai activement participé à ces changements, et mes contributions seront détaillées respectivement dans le chapitre 2 et 4.

Le Chapitre 2 traite des circulations induites par les vagues en domaine littorale à travers les approches *in-situ*, de modélisation théorique et numérique et de modélisation physique. La contribution de nos expériences en laboratoire au changement important de perception de la dynamique instationnaire des courants d'arrachement d'un comportement ouvert vers un comportement semi-fermé des cellules de circulation associées sera discutée. Le Chapitre 3 synthétise l'ensemble des travaux sur l'observation de la morphodynamique des plages sableuses par mesures *in-situ* et imagerie vidéo en distinguant les travaux sur les plages d'Aquitaine et les études sur l'impact de la succession des tempêtes sur l'érosion des plages. Le Chapitre 4 expose les travaux en modélisation de la morphodynamique des plages sableuses. Une partie de ce chapitre traite de ma contribution au changement de paradigme scientifique de la théorie des motifs vers la théorie d'auto-organisation. Ce chapitre montre surtout comment mes travaux ont récemment contribué à réconcilier la théorie avec les observations. Dans le chapitre 5, ces travaux sont synthétisés et les principaux axes de recherche que je privilégierai ces prochaines années sont discutés.

Circulations induites par les vagues en domaine littoral

2

Sommaire

Dans ce chapitre, nous traitons des circulations induites par les vagues en domaine littoral et en particulier des courants d'arrachement. Ces derniers sont des courants intenses, étroits et dirigés vers le large qui sont importants à de nombreux points de vue, *e.g.*, la morphodynamique court à moyen terme des plages, les échanges hydro-sédimentaires entre le plateau et les franges littorales, le mélange en zone littorale ou encore la sécurité de la baignade. Nous traitons ici des courants d'arrachement établis, *i.e.* qui ont ont une position relativement fixe le long de la plage et qui sont donc essentiellement contrôlés par la topographie locale du fond sableux ou une variabilité de la bathymétrie plus au large. Ne sont pas traités ici

les courants d'arrachement dits "transitoires" (*flash rips*), beaucoup plus rares et observés préférentiellement le long des plages bidimensionnelles. Ces derniers ont un caractère épisodique et peuvent migrer le long de la plage. Ils peuvent être, par exemple, forcés par les groupes d'ondes (*e.g.*, *Dalrymple* 1975, *Johnson and Pattiaratchi* 2004, *Reniers et al.* 2004, *Long and Ozkan-Haller* 2009) générés par interactions vagues à vagues ou par des instabilités de cisaillement du courant de dérive (*e.g.*, *Allen et al.* 1996, *Ozkan-Haller and Kirby* 1999) sachant qu'en fait, le long des plages naturelles, ces deux mécanismes coexistent (*Haller et al.* 1999).

Dans un premier temps (Section 2.1) nous présentons le cadre théorique qui permettra d'introduire notre stratégie de modélisation basée sur le couplage d'un modèle de vagues à phase moyennée et d'un modèle de circulation. Dans un deuxième temps (Section 2.2), nous décrivons l'analyse des observations des circulations en zone littorale réalisées dans le cadre de plusieurs campagnes de mesure. La pertinence de la modélisation numérique pour caractériser et quantifier la dynamique des circulations est ensuite démontrée (Section 2.3). En particulier, nous montrons que l'intensité et la nature rotationnelle des circulations peuvent être estimées à partir du champ de vagues, sans avoir à utiliser un modèle de circulation comme c'était traditionnellement le cas dans la littérature. Enfin, les difficultés rencontrées sur le terrain pour acquérir des jeux de données complets et exploitables, combinées au manque de données pour la validation extensive des modèles nous amènent (Section 2.4) à décrire une expérience innovante en bassin à houle visant à reproduire l'hydrodynamique sédimentaire au-dessus de plages tridimensionnelles réalistes. Nous montrons que l'analyse des données Lagrangiennes a permis de contribuer au changement de paradigme sur les cellules de circulation associées aux courants d'arrachement d'un comportement complètement ouvert à un comportement semi-fermé. Les implications pour la sécurité de la baignade et les échanges hydro-sédimentaires entre le plateau et les franges littorales sont discutées.

Une partie importante des travaux ci-dessous a été réalisée dans le cadre de mes travaux de thèse puis à travers l'encadrement des stages de Master 1 de Benjamin Dubarbier et Fabien Leckler et d'une participation active à l'encadrement de la thèse de Nicolas Bruneau (Dirigé par P. Bonneton, EPOC et Rodrigo Pedreros, BRGM). Les campagnes de mesures ont été réalisées dans le cadre des programmes PNEC et ECORS, et ce en collaboration avec des équipes nationales et internationales. Enfin, les travaux décrits sur la modélisation physique dans le cadre du projet MODLIT (RELIEFS/INSU, PI P. Bonneton) et d'une collaboration avec plusieurs laboratoires français n'auraient pu se faire sans l'équipe du LEGI et tout particulièrement sans la forte implication de Hervé Michallet qui a piloté cette expérience particulièrement innovante et ambitieuse.

2.1 Cadre théorique

Ci-dessous nous décrivons le cadre théorique qui permettra de mieux appréhender les avancées scientifiques réalisées dans la compréhension de la dynamique des circulations induites par les vagues en domaine littoral et, plus loin dans le chapitre 4, sur la morphodynamique des plages. Les équations et les simulations seront par la suite traitées dans le système de notations donné en Figure 2.1. L'approche décrite ci-dessous est basée sur un très grand nombre de travaux de la communauté internationale au cours des dernières décennies, que l'on peut retrouver synthétisés dans certains ouvrages de référence (*e.g.*, *Dean and Dalrymple* 1991, *Mei* 1983, *Svendsen* 2006).

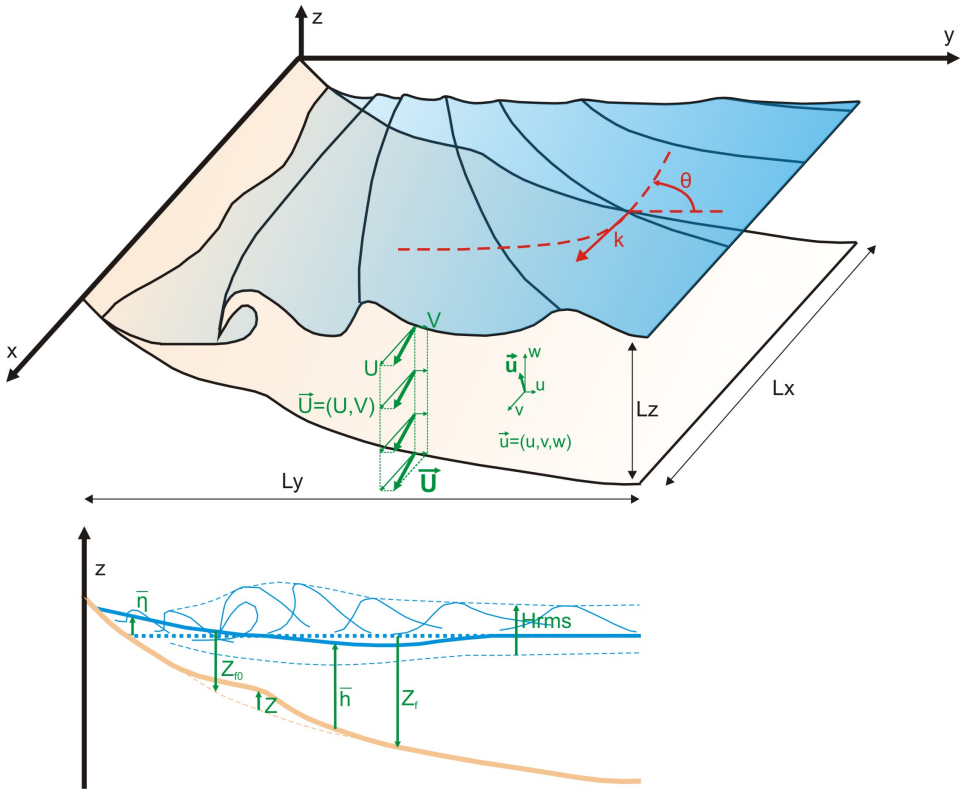

Figure 2.1 – *Système hydrodynamique et morphodynamique et notations associées*

2.1.1 Notions de base en dynamique des fluides

Equations locales du mouvement

En dynamique des fluides appliquée au domaine littoral, les équations aux dérivées partielles non-linéaires de conservation de la masse et du moment sont des axiomes fondamentaux. En faisant l'hypothèse d'incompressibilité du fluide ($\partial\rho/\partial t = 0$ où ρ est la masse volumique du fluide) l'équation de conservation de la masse devient :

$$\frac{\partial u}{\partial x} + \frac{\partial v}{\partial y} + \frac{\partial w}{\partial z} = 0 \tag{2.1}$$

Les deux équations de conservation de la quantité de mouvement horizontale peuvent s'écrire de la manière suivante :

$$\frac{\partial u}{\partial t} + u\frac{\partial u}{\partial x} + v\frac{\partial u}{\partial y} + w\frac{\partial u}{\partial z} = -\frac{1}{\rho}\frac{\partial p}{\partial x} + \frac{1}{\rho}\left(\frac{\partial \tau_{xx}}{\partial x} + \frac{\partial \tau_{yx}}{\partial y} + \frac{\partial \tau_{zx}}{\partial z}\right) \tag{2.2}$$

$$\frac{\partial v}{\partial t} + u\frac{\partial v}{\partial x} + v\frac{\partial v}{\partial y} + w\frac{\partial v}{\partial z} = -\frac{1}{\rho}\frac{\partial p}{\partial y} + \frac{1}{\rho}\left(\frac{\partial \tau_{xy}}{\partial x} + \frac{\partial \tau_{yy}}{\partial y} + \frac{\partial \tau_{zy}}{\partial z}\right) \tag{2.3}$$

où p est la pression et τ_{ij} sont les tensions de cisaillement dans le fluide.

Les vagues

Pour des vagues linéaires progressives se propageant dans le plan horizontal avec un angle θ à la côte (Figure 2.1), le potentiel de vitesse Φ est donné par :

$$\Phi(x, y, z, t) = -\frac{ga}{\omega}\frac{\cosh k(h+z)}{\cosh kh}\sin\left(-k\cos\theta y + k\sin\theta x - \omega t\right) \tag{2.4}$$

où g est la constante gravitationnelle, $a = H/2$ est l'amplitude de la vague, H la hauteur de la vague, h est la profondeur d'eau, $\omega = 2\pi/T$ est la pulsation, T est la période, $k = 2\pi/L$ est le nombre d'onde et L est la longueur d'onde. La pulsation ω et le nombre d'onde sont reliés à la profondeur d'eau par l'équation de dispersion :

$$\omega^2 = gk\tanh kh \tag{2.5}$$

Plusieurs caractéristiques importantes des vagues, qui seront utilisées dans la suite du document, peuvent être dérivées de ces équations :

- La vitesse de phase du champ de vagues :

$$c = \sqrt{\frac{g}{k}\tanh kh} \tag{2.6}$$

- La vitesse de groupe du champ de vagues, qui est la vitesse à laquelle l'énergie des vagues E_t est transportée :

$$c_g = \frac{c}{2}\left(1 + \frac{2kh}{\sinh 2kh}\right) \tag{2.7}$$

  où on note que $c_g \to c/2$ par grands fonds et $c_g \to c$ par petits fonds.
- La densité spatiale de l'énergie des vagues :

$$E_t = \frac{\rho g a^2}{2} \tag{2.8}$$

Lorsque les vagues se propagent à la côte, elles subissent des transformations importantes comme la réfraction par les variations de la bathymétrie ou des courants, la diffraction, la réflexion et la levée. De plus, des phénomènes de génération et de dissipation d'énergie sont observés tels que la génération par le vent ou la dissipation par moutonnement. Lorsqu'on s'intéresse au domaine littoral, la transformation la plus frappante est la dissipation d'énergie par déferlement bathymétrique. Ce déferlement bathymétrique est le principal moteur du mouvement des masses d'eau le long des plages sableuses.

2.1.2 Circulations moyennes induites par les vagues en domaine littoral : approche 2DH

Le mouvement des masses d'eau en domaine littoral couvre une vaste gamme d'échelles spatio-temporelles et qui sont aussi bien de nature ondulatoire (mer de vent, houle et ondes infragravitaires) que tourbillonnaire (turbulence tridimensionnelle à petite échelle et tourbillons quasi-bidimensionnels associés aux instabilités de cisaillement des courants induits par les vagues). Puisque, par la suite, notre objectif est de modéliser la morphodynamique des plages sur des échelles de temps de l'ordre de quelques heures à quelques mois, on doit pour garder des temps de calcul raisonnables traiter de façon déterministe les processus lents, et de façon statistique les processus rapides. On définit alors les courants moyens comme les courants moyennés sur une période T_c supérieure à celle des ondes infragravitaires mais suffisamment inférieure aux échelles temporelles associées aux changements de régime de houle ou à une évolution significative du niveau de marée. Pour plus d'informations sur les échelles temporelles caractéristiques et les différentes stratégies de modélisation en domaine littoral, le lecteur est invité à consulter *Bonneton* (2003). D'autre part, en domaine littoral, les échelles horizontales sont très grandes devant l'échelle verticale. Ainsi, dans l'approximation des milieux peu profonds on peut considérer que l'on peut obtenir une représentation satisfaisante de l'écoulement en considérant que la vitesse de l'écoulement varie peu sur la verticale et en intégrant le mouvement sur la colonne d'eau.

Prenons ici la définition du courant moyen proposée par *Mei* (1983) [1] et qui s'écrit :

$$U = \frac{1}{T_c(h+\bar{\eta})} \int_t^{t+T_c} \int_{-h}^{\eta(t)} u dz dt \tag{2.9}$$

En faisant la moyenne temporelle et sur la colonne d'eau des équations locales du mouvement (équations 2.1, 2.2 et 2.3) on obtient :

$$\frac{\partial \bar{\eta}}{\partial t} + \frac{\partial U(h+\bar{\eta})}{\partial x} + \frac{\partial V(h+\bar{\eta})}{\partial y} = 0 \tag{2.10}$$

$$\begin{aligned} \frac{\partial U}{\partial t} + U\frac{\partial U}{\partial x} + V\frac{\partial U}{\partial y} = & - g\frac{\partial \bar{\eta}}{\partial x} - \frac{1}{\rho(h+\bar{\eta})}\left(\frac{\partial S_{xx}}{\partial x} + \frac{\partial S_{xy}}{\partial y}\right) \\ & + \frac{1}{\rho(h+\bar{\eta})}\left(\frac{\partial \mathcal{T}_{xx}}{\partial x} + \frac{\partial \mathcal{T}_{yx}}{\partial y} + \mathcal{T}_x(\eta) - \mathcal{T}_x(-h)\right) \end{aligned} \tag{2.11}$$

$$\begin{aligned} \frac{\partial V}{\partial t} + U\frac{\partial V}{\partial x} + V\frac{\partial V}{\partial y} = & - g\frac{\partial \bar{\eta}}{\partial y} - \frac{1}{\rho(h+\bar{\eta})}\left(\frac{\partial S_{xy}}{\partial x} + \frac{\partial S_{yy}}{\partial y}\right) \\ & + \frac{1}{\rho(h+\bar{\eta})}\left(\frac{\partial \mathcal{T}_{xy}}{\partial x} + \frac{\partial \mathcal{T}_{yy}}{\partial y} + \mathcal{T}_y(\eta) - \mathcal{T}_y(-h)\right) \end{aligned} \tag{2.12}$$

où $\vec{\mathcal{T}}(-h)$ et $\vec{\mathcal{T}}(\eta)$ sont respectivement les cisaillements au fond et en surface, et le tenseur $\mathcal{T}_{ij}$ s'apparente à un terme de mélange horizontal des masses d'eau. Le mouvement des masses d'eau est forcé par les gradients de tensions de radiation $S_{i,j}$ qui s'écrivent :

1. Celle-ci diffère légèrement de celle de *Philipps* (1977) dont une description complète est donnée dans *Bruneau* (2009)

$$S_{xx} = E\left(n(\cos\theta^2+1)-\frac{1}{2}\right) \quad (2.13)$$

$$S_{yy} = E\left(n(\sin\theta^2+1)-\frac{1}{2}\right) \quad (2.14)$$

$$S_{xy}=S_{yx} = \frac{En\sin 2\theta}{2} \quad (2.15)$$

où $n = c_g/c$

Avec cette approche, il convient de constater qu'on doit découpler le mouvement des vagues de ceux des circulations. En d'autres termes, on doit effectuer le couplage d'un modèle de vagues à phase moyennée avec un modèle de circulation par l'intermédiaire des tensions de radiation.

Les vagues observées le long des plages ne sont pas monochromatiques, il faut donc décrire le spectre directionnel du champ de vagues. Une approche permettant de modéliser ces phénomènes consiste à résoudre l'équation de la conservation de densité spectro-angulaire d'énergie des vagues $N(\sigma_r,\theta)/\sigma_r$ (*WAMDI Group* 1988, *Tolman* 1991, *Booij et al.* 1999) où σ_r représente la fréquence relative des vagues :

$$\frac{\partial N}{\partial t}+\frac{\partial C_x N}{\partial x}+\frac{\partial C_y N}{\partial y}+\frac{\partial C_\sigma N}{\partial \sigma}+\frac{\partial C_\theta N}{\partial \theta}=\frac{S}{\sigma_r} \quad (2.16)$$

où C_x et C_y sont les vitesses de transfert de densité d'action des vagues (incluant les courants moyens) dans le plan (x,y), C_{σ_r} et C_θ les vitesses transfert fréquentiel et angulaire de densité d'action des vagues et S la somme des termes source et puits. Par la suite S se limitera principalement à la dissipation par déferlement bathymétrique en utilisant des modèles basés sur l'analogie avec le ressaut hydraulique (*e.g.*, *Battjes and Janssen* 1978, *Thornton and Guza* 1983). Enfin, par soucis de souplesse des notations, les équations données dans ce mémoire sont formulées pour des houles monochromatiques. Pour les houles aléatoires qui seront étudiées par la suite, on prendra naturellement la hauteur moyenne quadratique (aussi appelée hauteur énergétique) des vagues H_{rms} (au lieu de H) et les valeurs directionnelles et fréquentielles seront basées sur le pic spectral.

Des solutions analytiques simples peuvent être obtenues de ces équations pour connaître, sur les plages planes, le courant de dérive et le courant de retour. **Dès qu'on s'intéresse aux plages tridimensionnelles, le couplage d'une modèle numérique de vagues et d'un modèle numérique de circulation est nécessaire pour simuler les circulations induites par les vagues.**

2.2 Observation des circulations induites par les vagues

Les circulations induites par les vagues ont été observées principalement dans le cadre de 4 campagnes de mesures intensives auxquelles j'ai participé avec, dans l'ordre chronologique : la campagne PNEC 2001 (plage du Truc Vert), la campagne Biscarrosse 2007 (plage de Biscarrosse), la campagne ECORS'08 (plage du Truc Vert) et DRIBS (plage de Perranporth, UK, en collaboration avec l'University of Plymouth). Ici nous ne discuterons pas de cette dernière campagne dont le traitement de données piloté par l'University of Plymouth est en cours [2].

2. A terme, c'est cette campagne qui fournira de loin le jeu de données le plus complet sur les courants d'arrachement, notamment grâce à l'utilisation intensive de bouées Lagrangiennes et la mise en oeuvre de relevés topo-bathymétriques récurrents.

2.2.1 Principaux résultats et difficultés rencontrées pendant les Campagnes PNEC 2001 et ECORS'08

Les campagnes PNEC 2001 (*Sénéchal et al.* 2004) et ECORS'08 (*Sénéchal et al.* 2011) ont été réalisées sur la plage aquitaine du Truc Vert. Lors de la campagne PNEC 2001, aucun relevé bathymétrique n'a été réalisé, la bathymétrie subtidale a donc été estimée par imagerie satellitaire (***Castelle et al.*** 2006b). Plusieurs courantomètres et capteurs de pression ont été déployés, mais aucun n'a pu être installé dans le chenal de vidange, rendant les interprétations sur le comportement du courant d'arrachement difficiles. Toutefois, nous avons pu pour la première fois décrire et quantifier les circulations induites par les vagues sur une plage d'Aquitaine. Parmi les principaux résultats, nous avons montré que (1) les courants sont fortement modulés par la marée avec, et contrairement à la plupart des autres sites à marée documentés (*e.g.*, *Brander* 1999, *Brander and Short* 2000), des circulations les plus intenses entre la mi-marée et la marée basse pour les conditions de houle faiblement à modérément énergétiques (***Castelle et al.*** 2006b) et (2) la présence d'oscillations très basse fréquence (sur des périodes de l'ordre de 25 minutes) des courants à priori causées par des instabilités de cisaillement des courants.

La campagne ECORS'08 est celle qui a très largement mobilisé le plus de temps et le plus de moyens humains et financiers. Toutefois, à cause des conditions fortement énergétiques rencontrées pendant les 5 semaines de la campagne, aucun relevé bathymétrique n'a pu être réalisé pendant les mesures intensives, le seul relevé pendant la campagne ayant été réalisé la dernière semaine lorsque nous retirions la plupart des instruments. A cause du fort *set-up*, la plupart des relevés topographiques n'ont pu couvrir que la partie haute du domaine intertidal. De plus, les conditions de houle très obliques ont favorisé l'omniprésence du courant de dérive et ont très largement limité la présence de courants d'arrachement. Même si la campagne a produit de très bonnes données sur d'autres aspects (*e.g.*, zone de *swash*, érosion et accrétion du haut de plage, turbulence en zone de déferlement), une interprétation rigoureuse des données eulériennes de circulation est impossible pour la campagne ECORS'08. Toutefois, à la fin de la campagne de mesures, pendant le relevé complet topo-bathymétrique (voir plus loin dans le mémoire la Figure 3.3b) nous avons déployé un ADCP Horizontal (HADCP) pour étudier le profil horizontal du courant d'arrachement qui commençait à se mettre en place au-dessus d'un chenal intertidal bien développé (***Castelle et al.*** 2009b). Les données de l'HADCP ont été validées avec les données acquises par un ADV localisé à 5 m en face de l'HADCP. Nous avons ainsi montré que, même si la mise en oeuvre de ce type d'instrument peut s'avérer difficile (*e.g.*, nécessité d'une horizontalité parfaite de l'instrument, nécessité de viser une zone où il y a peu de déferlement bathymétrique pour ne pas réduire la portée de l'instrument à cause des bulles d'air), l'HADCP peut permettre d'obtenir des données précises sur la structure horizontale des circulations (***Castelle et al.*** 2009b).

2.2.2 Campagne Biscarrosse 2007 :

Dans le cadre d'une participation active à l'encadrement de la thèse de Nicolas Bruneau, pendant la campagne Biscarrosse 2007 nous avons caractérisé les courants induits par les vagues au-dessus d'un système barre/chenal bien développé et soumis à des houles longues et frontales, favorisant la présence d'un courant d'arrachement intense. La Figure 2.2 montre la morphologie de la plage de Biscarrosse pendant la campagne de mesure ainsi que la localisation des différents instruments déployés autour du système barre/chenal. Parmi les courantomètres, on note la présence du

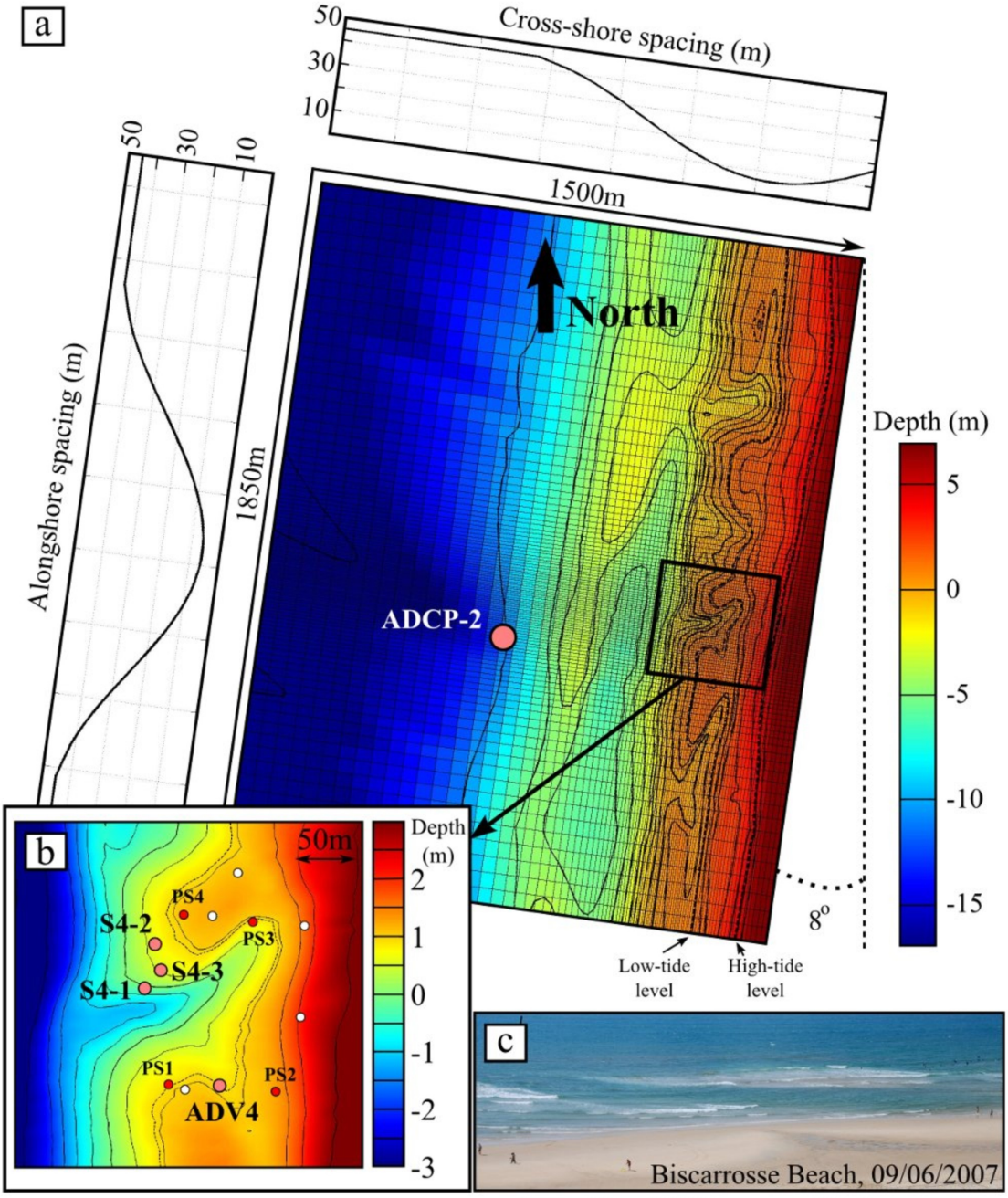

FIGURE 2.2 – *Configuration de la plage de Biscarrosse pendant la campagne de mesure Biscarrosse 2007. (a) Topo-bathymétrie grande échelle de la plage (bathymétrie levée par le SHOM) avec superposé le maillage utilisé pour la modélisation numérique dans* ***Bruneau et al.*** *(2011). (b) Zoom sur le système barre/chenal instrumenté pendant la campagne avec localisation des différents instruments analysés dans* ***Bruneau et al.*** *(2009b). (c) Photo montrant le chenal de vidange (****Bruneau et al.*** *2011).*

courantomètre S4-1 qui était déployé dans le chenal de vidange (Figure 2.2b). Celui-ci nous a permis d'obtenir les premières données aquitaines sur les vitesses dans le cou du courant d'arrachement. L'étude extensive de l'hydrodynamique et de la morphodynamique pendant la campagne est documentée dans ***Bruneau et al.*** (2009b). La Figure 2.3 montre le forçage des vagues au large et les courants mesurés par différents courantomètre. On note la modulation tidale intense du courant d'arrache-

ment avec, notamment, les courants les plus intenses mesurés entre la mi-marée et la marée basse pour les houles avec $H_s \approx 1$ m, confirmant ainsi les résultats obtenus pendant la campagne PNEC 2001 (***Castelle et al.*** 2006b). De plus, pendant cette campagne je me suis laissé emporter une dizaine de fois dans le courant d'arrachement muni d'un GPS afin d'obtenir les premières données Lagrangiennes de courant d'arrachement sur littoral aquitain. Les données (décrites dans ***Bruneau et al.*** 2009a) ont montré (1) des vitesses moyennes atteignant 1.2 m/s dans le cou du courant d'arrachement, (2) que les trajectoires passaient systématiquement à moins de 20 m du S4-1, confirmant ainsi l'excellent positionnement du courantomètre et (3) que sur la dizaine de trajectoire, je fus expulsé seulement 2 fois à environ 200 m au large de la zone de déferlement. Ce dernier point suggère, comme nous le verrons plus loin dans le cadre de la modélisation physique en laboratoire (***Castelle et al.*** 2010d), une rétention importante des cellules de circulation associées aux courant d'arrachement. Pour les houles énergétiques ($H_s \approx 2.5$ m), on remarque que le maximum d'intensité du courant d'arrachement se déplace vers la marée haute (Figure 2.3d), confirmant les résultats théoriques antérieurs (***Castelle and Bonneton*** 2006a). Comme nous le verrons plus loin dans ce mémoire, ce large set de données a été ensuite utilisé pour valider l'approche de modélisation numérique (***Bruneau et al.*** 2011).

2.3 Modélisation numérique des circulations en zone de déferlement

2.3.1 Validation des approches de modélisation

Nous avons tout d'abord validé l'approche de modélisation par le couplage d'un modèle de vagues avec un modèle circulation à travers les tensions de radiation. Nous avons pour cela utilisé les données de la campagne de mesures intensives PNEC 2001 sur la plage du Truc Vert, qui a la particularité de présenter des structures sédimentaires complexes et un marnage important, impliquant une forte variabilité de l'hydrodynamique pendant un cycle de marée et donc un défi pour la modélisation (***Castelle et al.*** 2006b). Cette étude a surtout permis de décrire pour la première fois la dynamique des courants induits par les vagues le long du littoral aquitain. Nous avons notamment caractérisé la dynamique des courants d'arrachement en fonction des conditions de houle et de hauteur de marée. Cette étude s'est poursuivie de manière plus théorique sur la modulation tidale des courants d'arrachement et des cellules de circulation associées (***Castelle and Bonneton*** 2006a) qui n'est pas décrite ici.

Les résultats de modélisation documentés dans ***Castelle et al.*** (2006b) et ***Castelle and Bonneton*** (2006a), en particulier ceux sur la modulation tidale des courants et l'impact de l'énergie des vagues sur l'occurrence du maximum de courant d'arrachement, ont été ensuite (comme nous l'avons vu dans la partie précédente) confirmés par les données issues de la campagne de mesures Biscarrosse 2007. L'approche de modélisation, utilisant ensuite le système d'équation de *Smith* (2006) qui sera discutée plus loin, a également été validée (voir par exemple la comparaison des simulations avec les observations en Figure 2.3) dans le cadre de la thèse de Nicolas Bruneau.

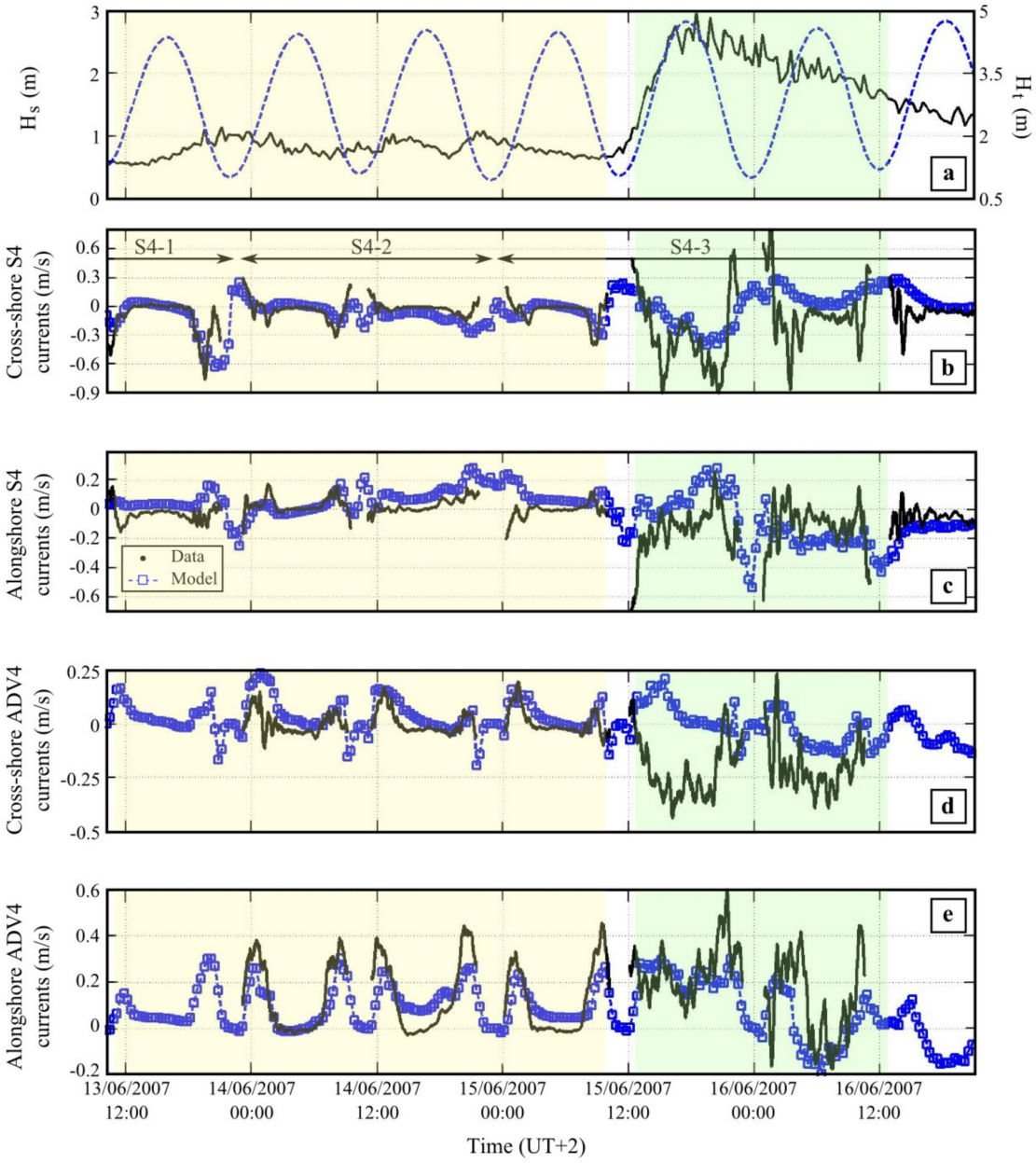

FIGURE 2.3 – *Conditions hydrodynamiques pendant la campagne Biscarrosse 2007 avec les séries temporelles de (a) la hauteur significative de vagues H_s et de hauteur de marée H_t mesuré par l'ADCP au large du système par environ 10 m de fond (Figure 2.2a), (b) vitesse cross-shore et (c) longshore mesurées par le S4 et (d) vitesse cross-shore et (e) longshore mesurées par l'ADV4. Sont superposés les résultats des simulations numériques dans* ***Bruneau et al.*** *(2011) qui seront discutées un peu plus loin dans ce document.*

2.3.2 Mécanisme de génération des courants d'arrachement : notion de terme de forçage de vorticité et comparaison à l'approche classique

Il est communément admis dans la littérature que ce sont les gradients de pression $-\rho g \partial\eta/\partial x$ qui génèrent les courants d'arrachement. En fait, comme nous l'avons montré dans ***Castelle and Bonneton*** (2006a), c'est la somme des gradients de tensions de radiation et des gradients de pression, définie comme le forçage résiduel $\vec{F}_r$ (*Haas and Svendsen* 2002, ***Castelle and Bonneton*** 2006a), qui détermine de forçage

net disponible pour mettre en mouvement les masses d'eau. Ce forçage résiduel s'exprime en utilisant la convention de sommation d'Einstein dans le plan horizontal :

$$F_{ri} = -gh\frac{\partial \eta}{\partial x_i} - \frac{1}{\rho}\frac{\partial S_{ij}}{\partial x_j} \tag{2.17}$$

Toujours dans le cadre de la thèse de Nicolas Bruneau, en dérivant les équations de conservation de la quantité de mouvement intégrées sur la colonne d'eau et sur une période supérieure à celle des vagues proposées par *Smith* (2006), nous avons identifié un terme de forçage de la vorticité verticale des circulations littorales qui est contrôlé par les gradients spatiaux d'intensité de déferlement bathymétrique (***Bruneau et al.*** 2011). L'équation que vérifie la vorticité verticale s'écrit (***Bonneton et al.*** 2010) :

$$\frac{\partial \Gamma}{\partial t} + \vec{\nabla}.(\Gamma \vec{U}) = \left(\vec{\nabla} \wedge (D\vec{e}_k)\right).\vec{e}_z + \tau_t \tag{2.18}$$

où $\Gamma = \left(\vec{\nabla} \wedge \vec{U}\right).\vec{e}_z$ est la vorticité moyenne verticale ; $\vec{e}_z = \vec{k}/k$ est le vecteur unitaire dans le sens de propagation des vagues ; $D = D_b k/\sigma_r$ est l'intensité de la force de dissipation d'énergie par déferlement bathymétrique (***Bonneton et al.*** 2010) avec D_b la dissipation d'énergie des vagues par déferlement bathymétrique ; σ_r est la fréquence relative des vagues et τ_t est un terme de diffusion turbulente de la vorticité. Pour des circulations quasi-stationnaires ($\partial\Gamma/\partial t \approx 0$), le terme advectif $\vec{\nabla}.(\Gamma\vec{U})$ devient petit par rapport à $\left(\vec{\nabla} \wedge (D\vec{e}_k)\right).\vec{e}_z$ (***Bruneau et al.*** 2011). On obtient alors un équilibre entre les gradients de dissipation d'énergie des vagues et la diffusion turbulente de la vorticité $\tau_t \sim \nu_t \vec{\nabla}^2\Gamma$. Ainsi, le sens et l'intensité de la nature rotationnelle des circulations induites par le déferlement des vagues sont essentiellement contrôlés par un terme de forçage de la vorticité verticale F_v qui s'écrit :

$$F_v = \left(\vec{\nabla} \wedge (D\vec{e}_k)\right).\vec{e}_z \tag{2.19}$$

Le calcul simple du terme de forçage de la vorticité verticale permet, à partir d'un champ de vague simulé, de prédire l'intensité et le signe de la nature rotationnelle des circulations littorales, sans avoir à utiliser un modèle de circulation. Cette prédiction était jusqu'à présent impossible à travers l'approche des tensions de radiation traditionnellement utilisée dans la littérature (*Longuett-Higgins and Stewart* 1964) puisqu'elle nécessitait le couplage avec un modèle de circulation. **Notre approche est non seulement plus pratique que la théorie classique, mais elle a aussi des bases théoriques beaucoup plus fortes puisque le terme de dissipation *D* peut s'obtenir directement par la théorie, alors que les tensions de radiations sont obtenues empiriquement.** Nous avons ensuite démontré la pertinence de ce terme de forçage de la vorticité verticale en appliquant l'approche sur la campagne de mesures Biscarrosse 2007 (***Bruneau et al.*** 2011).

Plus tard, dans ***Castelle et al.*** (2012) nous avons montré que les termes F_v et le forçage résiduel $\vec{F}_r$ était similaires, confirmant définitivement la pertinence de l'approche. A titre d'exemple, la Figure 2.4 montre la simulation d'un courant d'arrachement et de son estimation à travers le terme de forçage de vorticité et l'approche des tensions de radiation. Ici on a choisi le cas d'un courant d'arrachement induit par des gradients *longshore* de déferlement bathymétrique non pas dus à la bathymétrie locale, mais dus à des zones de focalisation d'énergie des vagues causées par la réfraction au large au-dessus d'une anomalie bathymétrique. Comme on le voit dans les Figures

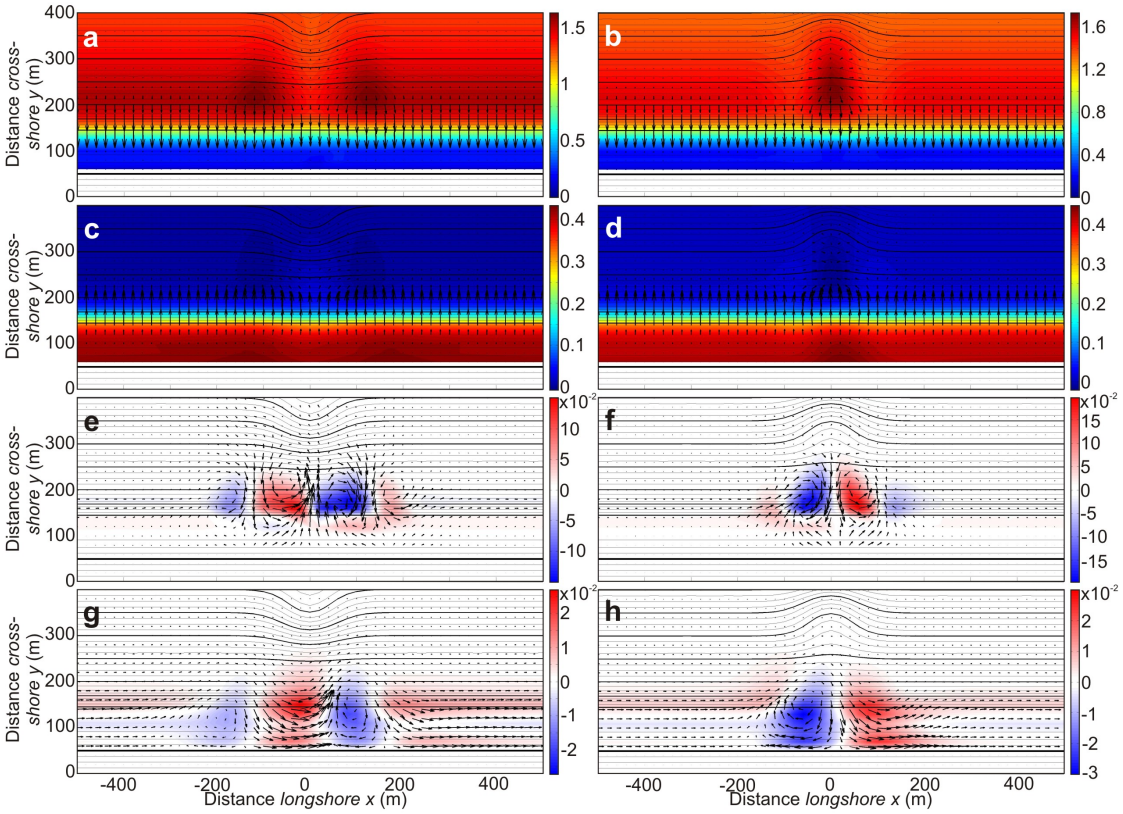

FIGURE 2.4 – *Hydrodynamique pour des vagues au large avec H_s = 1.2 m, T_p = 10 s et θ = 1° pour une plage plane présentant au large une anomalie bathymétrique à une distance d_b = 350 m du trait de côte et une hauteur A = -1 m (fosse, panels de gauche) et A = 1 m (bosse, panels de droite). (a,b) Champs de hauteur significative de vagues avec superposés les gradients de tension de radiation (flèches). (c,d) Gradients de pression $\vec{F}_p$ ($m^2.s^{-2}$) (flèches) superposés au champ de surface libre moyenne η. (e,f) Forçage résiduel $\vec{F}_r = \vec{F}_p + \vec{F}_w$ (flèches) superposé au terme de forçage de la vorticité verticale $F_v = \left(\vec{\nabla} \wedge (D\vec{e}_k)\right).\vec{e}_z$ ($kg.m^{-2}.s^{-2}$). (g,h) Champs de courants moyens résultant $\vec{U}$ (flèches) et champs de vorticité $\Gamma = \left(\vec{\nabla} \wedge \vec{U}\right).\vec{e}_z$ (s^{-1}). D'après* **Castelle et al.** *(2012).*

2.4e et 2.4f, les 2 théories donnent les mêmes résultats. On note aussi sur cette figure que la vorticité du champ de courant simulé (Figures 2.4g et 2.4h) a des motifs un peu différents de ceux de F_v et $\vec{F}_r$. En effet, en présence de vagues obliques, la diffusion de la vorticité peut devenir significative et l'estimation de la position des cellules de circulation par F_v ou $\vec{F}_r$ seul peut être faussée. Dans ce cas il devient nécessaire d'avoir recours à un modèle de circulation [3].

2.4 Modélisation physique des courants d'arrachement

Une grande difficulté des études *in-situ* sur les courants d'arrachement est de devoir faire face à l'évolution permanente des régimes de houle, de la hauteur de marée et de la morphologie du fond (*e.g.*, *Aagaard et al.* 1997, *Brander* 1999, *Brander and Short* 2000; 2001, *MacMahan et al.* 2004a;b, ***Bruneau et al.*** 2009b, *Austin et al.* 2010), ce qui rend extrêmement difficile la quantification des courants d'arrachement en fonction

3. Il devient aussi nécessaire d'avoir recours à un modèle de circulation pour les plages contraintes par des caps ou des épis.

de la morphologie du fond et des conditions de houle. D'autre part, les mesures de courants d'arrachement en laboratoire (*e.g.*, *Hamm* 1992, *Haller and Dalrymple* 2001, *Haas and Svendsen* 2002, *Kennedy and Thomas* 2004, *Kennedy et al.* 2006) ont été réalisées au-dessus de morphologies de barre ne correspondant pas au milieu naturel. Parmi d'autres limitations de toutes ces expériences, (1) la profondeur relative du chenal était d'un ordre de grandeur supérieur à celle mesurée couramment sur le terrain et (2) les fortes discontinuités de fond dur généraient le décollement permanent de tourbillons instationnaires pouvant fortement perturber la dynamique du courant d'arrachement et des cellules associées (*Chen et al.* 1999).

Afin de s'affranchir des conditions énergétiques et fortement instationnaires des régimes de houle et de marée sur le terrain, une expérience en laboratoire visant à étudier les courants d'arrachement au-dessus de plages réalistes était nécessaire pour améliorer les connaissances sur la dynamique des courants d'arrachement. Ce besoin a été identifié dans le cadre du projet MODLIT (RELIEFS/INSU, PI Philippe Bonneton, EPOC) pendant lequel une expérience de 5 semaines pilotée par le LEGI (PI Hervé Michallet) a été réalisée dans le bassin de la SOGREAH au-dessus d'un fond mobile (***Michallet et al.*** 2010; en préparation). Dans ce mémoire nous ne traiterons que des travaux réalisés à partir des données Lagrangienne que je pilotais et dont les principaux résultats sont donnés dans ***Castelle et al.*** (2010d; 2011). L'analyse détaillée des nombreuses données Eulériennes et des évolutions morphodynamiques est en cours (***Michallet et al.*** en préparation).

2.4.1 Présentation de l'expérience MODLIT 2D

L'expérience MODLIT 2D a été réalisée dans le bassin de 30 m par 30 m du Laboratoire d'Hydraulique de France (G-INP-Sogréah, Figure 2.5). Le dimensionnement des expériences considère une échelle de longueur de 1/10 ce qui, par similitude de Froude, impose une échelle de temps de l'ordre de 1/3 (***Michallet et al.*** 2010). Les expériences consistaient à générer des séquences de 20 minutes de houle de spectre de Jonswap caractérisées par une hauteur de vague significative H_s et une période pic T_p. La mise en place de circulations a été forcée par une houle frontale avec un déficit d'énergie au centre du bassin en imposant diverses lois d'amortissement aux batteurs.

La plage de sable couvrait la largeur du bassin (30 m en *longshore*) pour un profil total de 20 m *cross-shore*, sur une épaisseur d'environ 15 à 20 cm au-dessus d'un soubassement de gravier recouvert de géotextile. Une sonde laser placée sur une passerelle pilotée pour couvrir l'essentiel de la plage a permis de lever régulièrement les bathymétries. Ici nous décrivons uniquement les résultats obtenus pendant une partie de l'expérience où le caractère tridimensionnel de la plage s'est fortement accentué (Figure 2.6). A noter que, d'une part, ces morphologies sont typiques des systèmes de barres sableuses observées sur le terrain et que, d'autre part, la séquence morphodynamique correspond à une séquence accrétive quasi-complète des états intermédiaires suivant la modélisation conceptuelle de *Wright and Short* (1984). On observe en effet une morphologie de type 'Rhythmic Bar and Beach' (RBB, Figure 2.6a, b et c) avec une barre en croissant qui vient se connecter au haut de plage et ainsi former une morphologie de type 'Transverse Bar an Rip' (TBR, Figures 2.6d, e et f) avec 2 chenaux en x = 11 m et x = 22 m. Enfin, les chenaux se comblent progressivement pour former une morphologie faiblement tridimensionnelle de type 'Low Tide Terrace' (LTT, Figures 2.6g et h).

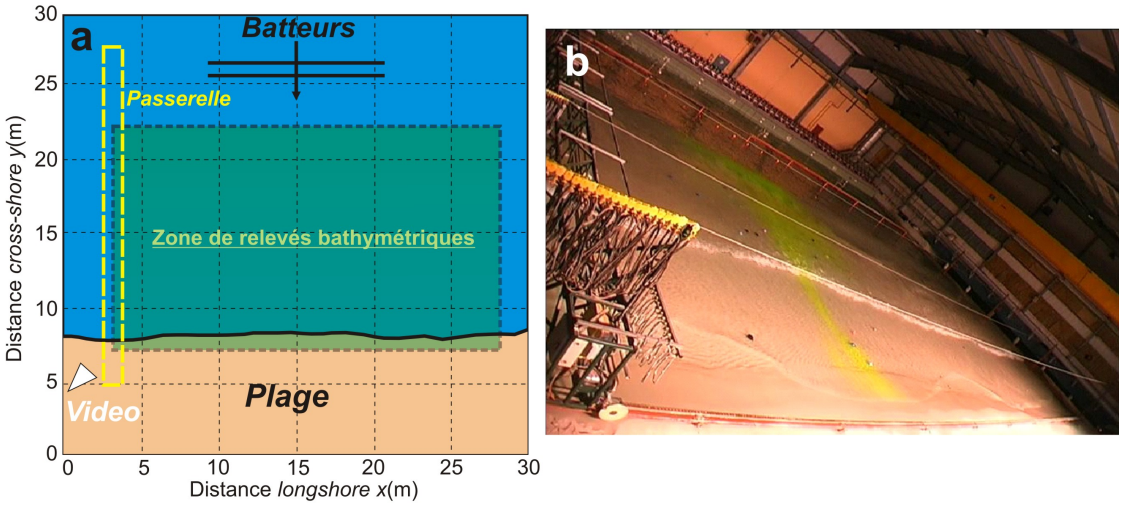

FIGURE 2.5 – *Schématisation de l'expérience MODLIT 2D avec (a) les dimensions de la plage avec l'emplacement des batteurs et des relevés bathymétriques et (b) une image de la vidéo montrant la présence des drifters dans la zone de déferlement (**Castelle et al.** 2010d).*

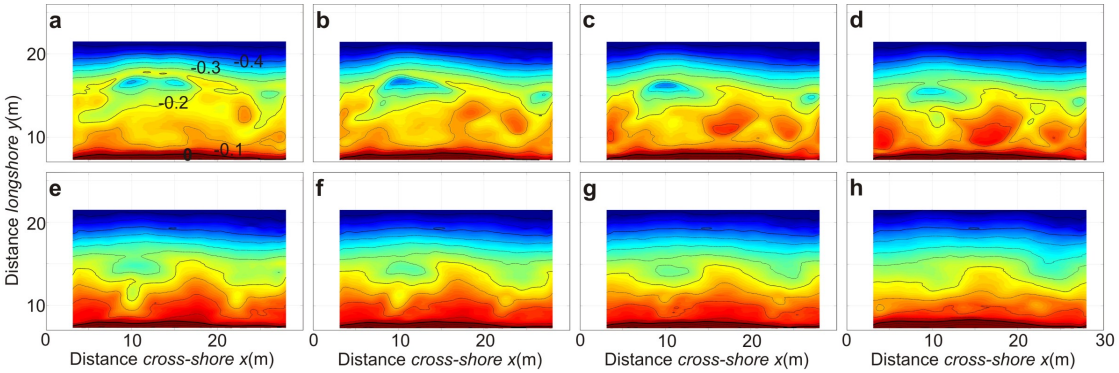

FIGURE 2.6 – *Les 8 configurations pendant l'expérience MODLIT 2D pour lesquelles les courants d'arrachement ont été quantifiés. Les caractéristiques de ces morphologies et leur correspondance dans la classification de Wright and Short (1984) sont décrites dans le texte (**Castelle et al.** 2010d).*

2.4.2 Comportement général des bouées Lagrangiennes

Les *drifters* (ou bouées Lagrangiennes) devaient flotter pour pouvoir être suivis par la caméra sans subir l'action des vagues (phénomène de *surf*, c'est-à-dire emportés par le rouleau de déferlement). Après plusieurs essais, la solution adoptée a été de simples ballons de baudruche remplis d'eau. Ceux-ci présentaient l'avantage d'avoir une masse volumique quasi-identique à celle de l'eau, ayant donc le même comportement que les masses d'eau les entourant, tout en présentant une faible surface immergée. Entre 20 et 39 *drifters* ont été déployés dans le bassin et ont été filmés pendant environ une heure pour chaque morphologie.

La position de chaque *drifter* fut ainsi détectée toutes les 6 secondes et transformée de leur position en pixel à celle dans le repère de coordonnées locales liées au bassin. L'évolution de cette position a ensuite été interpolée en temps et en espace afin d'obtenir l'évolution de la vitesse de chaque *drifter*. La Figure 2.7 montre les données issues d'un seul *drifter*. On voit que le *drifter* réalise plusieurs boucles dans la cellule de circulation avant d'être éjecté définitivement de la zone de déferlement à $t \approx 2400$ s. Ce comportement était très fréquemment observé durant toute l'expérience

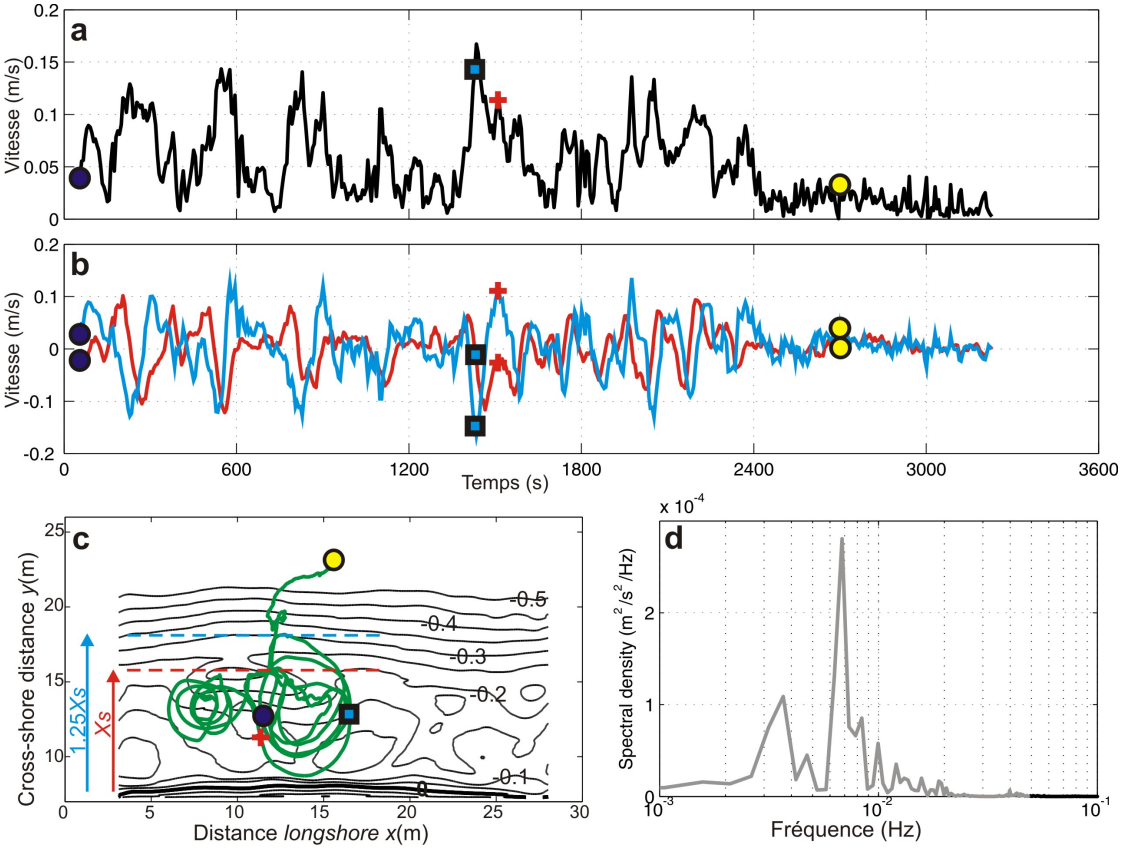

FIGURE 2.7 – *Données issues d'un seul drifter au-dessus de la morphologie donnée en Figure 2.6d avec la série temporelle de (a) la vitesse du drifter, (b) la vitesse cross-shore (bleu) et longshore (rouge) du drifter, (c) la trajectoire du drifter et (d) le spectre d'énergie de la vitesse cross-shore (**Castelle et al. 2010d**).*

et, comme nous le verrons plus tard, contraste avec l'idée reçue qu'un corps flottant pris dans un courant d'arrachement est systématiquement emporté vers le large.

2.4.3 Courants moyens issus de l'approche Lagrangienne

Le domaine du bassin a été divisé en mailles carrées de 1 mètre de côté. Pour chaque maille, les données de vitesse des *drifters* traversant celle-ci ont été triées et stockées. Pour les mailles comportant plus de 5 données, des valeurs statistiques ont été calculées : courant moyen et écart type en intensité et direction du courant. La figure 2.8 montre les circulations moyennes calculées à partir des données Lagrangiennes. Les circulations montrent l'omniprésence de courants d'arrachement pour toutes les morphologies avec, visuellement et sans surprise, une intensité des courants d'arrachement qui augmente avec la tridimensionnalité de la plage. Par la suite, nous nous sommes focalisés sur le courant d'arrachement situé en $x \approx 10$ m puisque c'est dans celui-ci que le jeu de données acquis est le plus complet. Une caractéristique importante du courant d'arrachement pendant l'expérience est que celui-ci était parfois symétrique (Figures 2.8d, e, f, g et h) et parfois asymétrique (Figure 2.8a, b et c), et ce malgré les conditions de houle toujours frontales. Nous verrons que cela semble avoir un impact sur le taux de rétention des courants d'arrachement.

Pour la première fois, l'intensité du courant d'arrachement a été quantifiée en

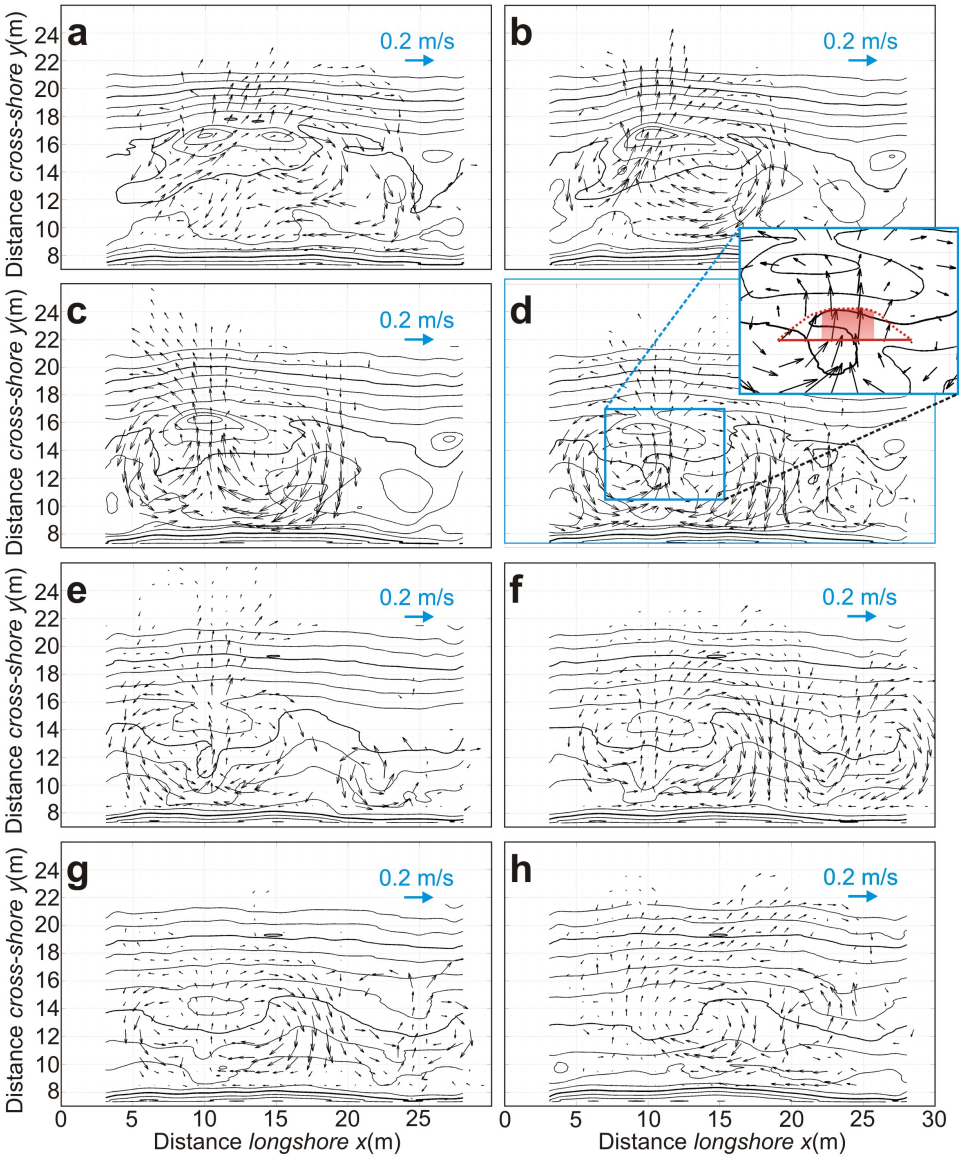

FIGURE 2.8 – *Champ de courants moyens calculés à partir des données Lagrangiennes pour les 8 morphologies présentées en Figure 2.6. L'échelle des vitesses est donnée en haut à droite de chaque panel (**Castelle et al.** 2010d).*

fonction de la tridimensionnalité de la plage. Celle-ci a été estimée d'après *Feddersen and Guza* (2003) autour du chenal situé en $x \approx 10$ m par la formule :

$$\sigma_z(y) = \sqrt{\frac{1}{x_2 - x_1} \int_{x_1}^{x_2} \left(Z_f(x,y) - \langle Z_f(y) \rangle_x \right)^2 dx} \tag{2.20}$$

pour 7.16 m $< y <$ 22 m, avec $x_1 = 3.12$ m et $x_2 = 18$ m, et où la notation $\bar{(.)}$ désigne la moyenne *longshore* entre x_1 et x_2. Nous avons ensuite défini la moyenne *cross-shore* $\bar{\sigma_z}$ comme la mesure de la tridimensionnalité du système barre/chenal centré en $x \approx 10$ m. Comme aucune définition cohérente de l'intensité du courant d'arrachement U_{rip} n'est donnée dans la littérature, nous l'avons défini en se basant sur la géométrie des cellules de circulations : U_{rip} est la moyenne du courant entre les 2 centres des cellules de circulation, le long de la section de 2 m où il est maximum

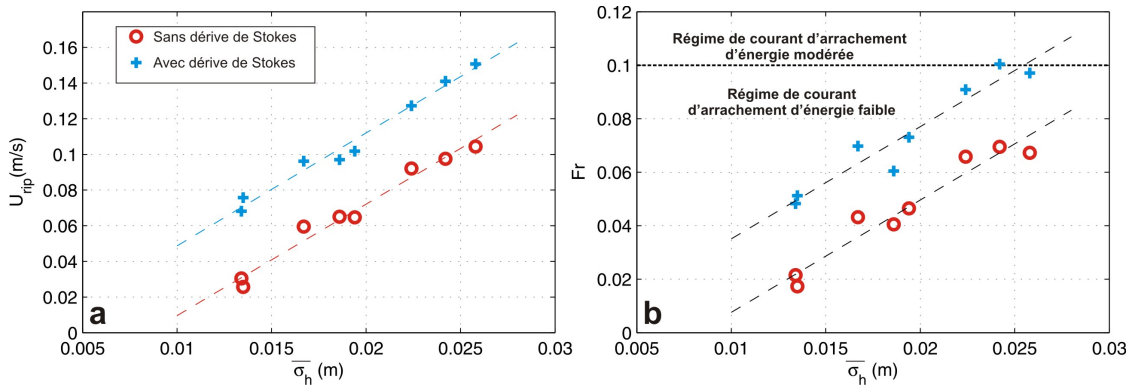

FIGURE 2.9 – *Intensité du courant d'arrachement (a) U_{rip} et (b) F_r en fonction de la tridimensionnalité de la plage $\bar{\sigma}_z$ avec le seuil $F_r = 0.1$ délimitant les régimes de courant d'arrachement d'énergies faible et modérée selon MacMahan et al. (2006).*

(Figure 2.8d). Nous avons enfin utilisé le nombre de Froude $F_r = U_{rip}/\sqrt{gh}$ comme mesure adimensionnée du courant d'arrachement afin de classifier le régime hydrodynamique. Les résultats sont synthétisés en figure 2.9 avec et sans prise en compte de la dérive de Stokes. De manière surprenante, une relation presque parfaitement linéaire est obtenue entre l'intensité du courant d'arrachement et la tridimensionnalité de la plage pour une houle donnée. En outre, les courants d'arrachement les plus intenses ont été mesurés pour des morphologies de type RBB alors que dans la modélisation conceptuelle de *Wright and Short* (1984) les courants d'arrachement sont supposés être les plus intenses pour les morphologies de type TBR. Cela se justifie par le fait que, jusqu'à présent, aucune mesure Eulérienne ou Lagrangienne de courant d'arrachement au-dessus d'un système RBB n'avait été réalisée, ni sur le terrain ni en laboratoire.

2.4.4 Rétention des cellules de circulation associées aux courants d'arrachement

Les circulations moyennes présentées en Figure 2.8 étaient très instables tout au long de l'expérience. Par exemple, en quelques minutes le courant d'arrachement pouvait passer assez rapidement d'une forme asymétrique (vers la droite ou vers la gauche) à une forme symétrique sans raison apparente. Une autre caractéristique frappante est que les *drifters* pris dans le courant d'arrachement restaient piégés dans les cellules de circulation avant de rentrer à nouveau dans le courant d'arrachement et ainsi de suite (*i.e.*, Figure 2.7). En de plus rares occasions, les *drifters* étaient expulsés de la zone de déferlement jusqu'à la zone en face des batteurs à houle. Pour chacune

	Run a	Run b	Run c	Run d	Run e	Run f	Run g	Run h
Morphologie	RBB	RBB	TBR	TBR	TBR	TBR	LTT	LTT
U_{rip} (m/s)	0.0650	0.1044	0.0975	0.0921	0.0647	0.0595	0.0304	0.0256
N_r	47	74	79	329	135	283	218	40
N_e	12	22	35	27	16	30	10	17
R (%)	74.5	70.3	55.7	91.8	88.1	89.4	95.5	57.5

TABLE 2.1 – *Pour les 8 morphologies montrées en Figure 2.6 : vitesse du courant d'arrachement U_{rip} mesurée d'après* ***Castelle et al.*** *(2010d) ; morphologie de la plage d'après la classification de Wright and Short (1984) ; N_r le nombre de drifters entrant dans le courant d'arrachement ; N_e le nombre de drifters étant expulsés de la zone de déferlement et R taux de rétention résultant (****Castelle et al.*** *2011)*

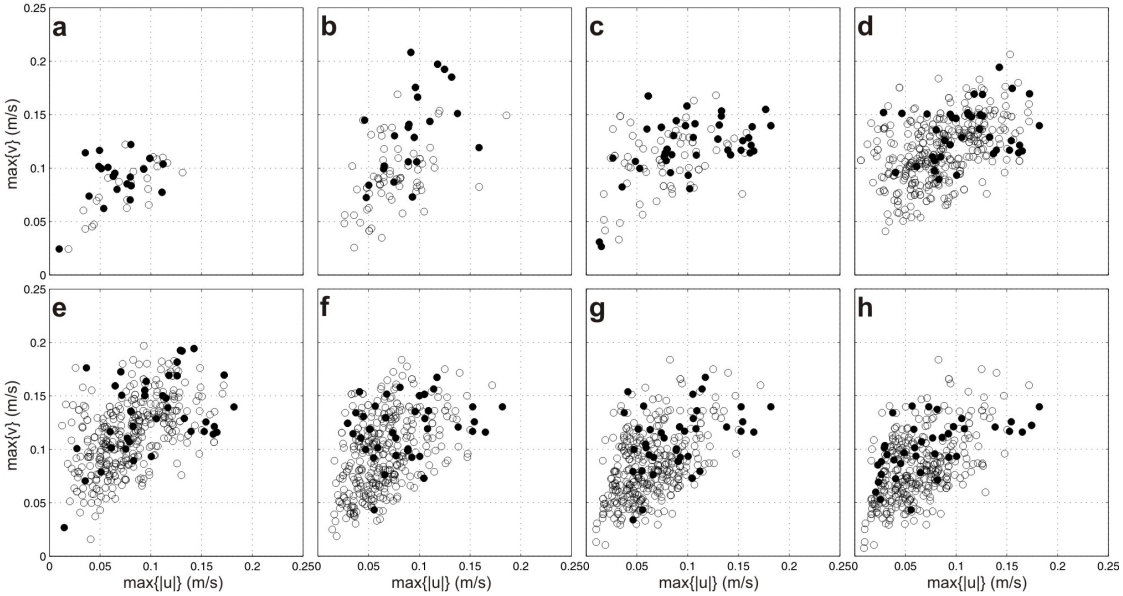

FIGURE 2.10 – *Pour chaque drifter et pour chacune des 8 morphologies présentées en Figure 2.6 est indiqué la vitesse maximum cross − shore $max\{|v|\}$ en fonction de la vitesse maximum longshore $max\{|u|\}$ qu'a connu le drifter dans la circulation pendant sa dernière rotation. Les drifter ayant été éjectés de la zone $1.25X_s$ sont les cercles remplis en noir (**Castelle et al.** 2011).*

des 8 expériences nous avons compté automatiquement le nombre de *drifters* entrant dans le courant d'arrachement et ceux expulsés (*i.e.*, traversant la limite $y = 1.25X_s$ où X_s est la largeur de la zone de déferlement d'après *MacMahan et al.* 2010) afin de calculer le taux de rétention des cellules de circulation associées au courant d'arrachement. Ils sont synthétisés dans le Tableau 2.1. Les résultats montrent que, la plupart du temps, le taux de rétention calculé est de l'ordre de 90%, ce qui est en accord avec les mesures réalisées par *MacMahan et al.* (2010) la même année sur une plage californienne. Toutefois, le taux de rétention chute lorsque le courant d'arrachement moyen est asymétrique (expériences a, b et c). En outre, l'analyse des pulsations du courant d'arrachement n'a pas mis en évidence de lien avec l'expulsion des *drifters*, contrairement à ce qui est avancé dans la littérature. En effet, la Figure 2.10 montre que les *drifters* expulsés ne sont pas ceux nécessairement pris dans une pulsation (forte vitesse *cross-shore* en traversant le chenal). Enfin, durant l'expérience (h) le taux de rétention est très faible alors que le courant d'arrachement est à la fois faible et symétrique. Nous pouvons expliquer ce faible taux de rétention par l'apparition de courants d'arrachement dits 'transitoires' qui, par définition, ne retiennent que très peu les masses d'eau, puisque la bathymétrie autour de $x \approx 10$ m était devenue quasiment homogène.

2.4.5 Implications pour le mélange en domaine littoral et la sécurité de la baignade : un changement de perception

Il était jusqu'à présent admis par la communauté internationale que les courants d'arrachement produisent en permanence des échanges hydro-sédimentaires importants entre les franges littorales et le plateau continental. Nous avons mis en évidence que les systèmes de courants d'arrachement (et des cellules de circulations associées) sont en fait des systèmes quasi-fermés. Seulement sporadiquement, des échanges importants peuvent être observés, notamment à travers l'expulsion de vortex instation-

naires se décollant du courant d'arrachement et migrant ensuite vers le large (***Castelle et al.*** 2011). Nos résultats issus de la modélisation physique en laboratoire (***Castelle et al.*** 2010d; 2011) sont en accord avec les résultats publiés la même année à partir de la modélisation numérique (*Reniers et al.* 2010) et des mesures de terrain (*MacMahan et al.* 2010). Ce rapide revirement de paradigme sur le comportement des courants d'arrachement a de fortes implications sociétales et scientifiques.

Nos recherches ont des implications fortes pour la sécurité de la baignade. Ces résultats, qui ont été présentés aux autorités américaines en février 2010 au cours du 1st International Rip Current Symposium, ont reçu un accueil très positif par les sauveteurs en mer. Ces avancées scientifiques contredisent en effet les conseils 'traditionnels' des sauveteurs ('si vous êtes pris dans un courant d'arrachement, nagez parallèlement à la côte', au risque de s'épuiser). En effet, nos mesures en laboratoire (***Castelle et al.*** 2010d; 2011), et les études numériques (*Reniers et al.* 2010) et expérimentales (*MacMahan et al.* 2010) montrent qu'**un baigneur pris dans un courant d'arrachement a 80-90% de chance de revenir au bord en moins de 10 minutes juste en se laissant flotter, alors que l'on a une chance sur deux de nager dans le mauvais sens si l'on nage parallèlement à la côte.** Ces avancées stimulent ainsi actuellement une discussion à l'échelle internationale sur les recommandations à donner aux touristes le long des plages dominées par l'action de la houle. Ce fut notamment l'objet d'une session spéciale de discussion à la conférence Coastal Sediment'11 pour laquelle j'étais invité comme membre du panel international d'experts avec S. Leathermann, B. Dean, J.H. MacMahan et A.J.H.M. Reniers. Nous devrons pendant ces prochaines années amorcer des discussions avec les sauveteurs en mer et CRS aquitains et français puisque, sur le littoral aquitain comme sur les autres plages dans le monde, la majorités des sauvetages et des noyades ont lieu à cause d'un courant d'arrachement [4].

Conclusion du chapitre

Nous avons montré que l'approche consistant à coupler un modèle de vagues à phase moyennée et un modèle de circulation permet de simuler très correctement les circulations induites par les vagues au-dessus de bathymétries complexes. En effet, cette approche a été validée avec des données hydro-sédimentaires acquises pendant plusieurs campagnes de mesures intensives le long des plages aquitaine (*e.g.*, ***Castelle et al.*** 2006b, ***Bruneau et al.*** 2011). En particulier, **la combinaison de la modélisation et de l'analyse de données *in-situ* nous a permis pour la première fois de caractériser et quantifier les circulations induites par les vagues au-dessus des plages d'Aquitaine** (***Castelle and Bonneton*** 2006a, ***Castelle et al.*** 2006b; 2009b, ***Bruneau et al.*** 2009b;a; 2011). Toutefois, pendant ces campagnes de mesures, souvent coûteuses financièrement, nous avons souvent subi des conditions naturelles hostiles et non maîtrisées. Comme nous pouvons le voir dans l'Annexe 2 pour la campagne de mesure menée sur la plage de St Trojan (***Bertin et al.*** 2008b) et comme nous le verrons dans le chapitre suivant sur les plages de la Gold Coast (***Castelle et al.*** 2007c; 2008), des campagnes de mesures ponctuelles, flexibles, déterminées en fonction de questionnements scientifiques précis et mises en oeuvre lorsque les bonnes conditions (en termes de morphologie de plage et de conditions de houle) sont combinées, permettent souvent des avancées scientifiques similaires à celle réalisées pendant les

4. L'été 2012 fut d'ailleurs une année noire sur le littoral aquitain. Toutes les noyades ont eu lieu en dehors des zones surveillées démontrant que le manque de conscience du danger des baigneurs.

campagnes de mesures 'lourdes'. Ces prochaines années, **il apparaît important de favoriser le développement de campagnes de mesures courtes, flexibles, ciblées et déterminées en fonction de questions scientifiques précises au détriment de grosses campagnes de mesures rigides, coûteuses, qui parfois ne permettent pas d'avancées scientifiques importantes à cause de conditions naturelles hostiles et non-maîtrisées** (*e.g.*, morphologie de plage bidimensionnelles, climats de houles non représentatifs ou empêchant les relevés topo-bathymétriques couvrant un domaine suffisant).

A travers l'approche de modélisation des processus physiques, les équations du mouvement ont été dérivées de manière à faire apparaître un terme de forçage du mouvement des masses d'eau déterminé uniquement par les gradients de dissipation d'énergie des vagues par déferlement bathymétrique (***Bonneton et al.*** 2010). La pertinence de ce terme de forçage de la vorticité verticale des circulations moyennes induites par les vagues en domaine littoral a été démontrée pendant la campagne de mesure de Biscarrosse 2007 (***Bruneau et al.*** 2011) et lors de la comparaison obtenue théoriquement avec l'approche des tensions de radiation (***Castelle et al.*** 2012). En résumé, **le calcul simple du terme de forçage de la vorticité verticale permet, à partir d'un champ de vagues simulé, de prédire l'intensité et le signe de la nature rotationnelle des circulations littorales avec des bases théoriques solides et sans avoir à utiliser un modèle de circulation contrairement à ce qui s'est fait jusqu'à présent dans la littérature.** En effet, cette prédiction était jusqu'à présent impossible à travers l'approche des tensions de radiation (*Longuett-Higgins and Stewart* 1964) qui nécessite le couplage avec un modèle de circulation.

Comme indiqué ci-dessus, l'inconvénient majeur des campagnes de mesure *in-situ* est que nous sommes typiquement soumis aux conditions naturelles qui souvent peuvent être hostiles et empêcher la démarche scientifique de se mettre en place. Partant de cette constatation et de celle que les mesures en laboratoires aient été jusqu'à présent réalisées au-dessus de morphologie irréalistes, une expérience en laboratoire innovante visant à étudier les courants d'arrachement au-dessus de plages sableuses tridimensionnelles dynamiques a été réalisée dans le cadre du projet MODLIT (***Michallet et al.*** 2010; en préparation). Dans le cadre de l'utilisation intensive de mesures Lagrangiennes (***Castelle et al.*** 2010d; 2011), nous avons pu quantifier pour la première fois de manière expérimentale les vitesses du courant d'arrachement en fonction de la tridimensionnalité de la plage. **Nous avons participé au changement de paradigme d'un comportement ouvert vers un comportement semi-fermé des cellules de circulation associées aux courants d'arrachement qui a de fortes implications pour le mélange en domaine littoral et la sécurité de la baignade.** Nos résultats issus de la modélisation physique en laboratoire ***Castelle et al.*** (2010d; 2011), en accord avec les résultats publiés la même année à partir de la modélisation numérique (*Reniers et al.* 2010) et les mesures *in-situ* (*MacMahan et al.* 2010), suggèrent en plus que le taux de rétention de ces cellules de circulation n'est pas nécessairement de l'ordre de 90% et que, dans des cas assez rares cas qui restent à explorer théoriquement, ces taux peuvent descendre jusqu'à 50%.

3 Observation de la morphodynamique des plages sableuses

Sommaire

Dans ce chapitre, nous présentons dans un premier temps une synthèse de la morphodynamique des plages d'Aquitaine en se concentrant sur le comportement des barres sableuses (section 3.1) puis nous présentons les résultats obtenus sur la réponse des plages soumises à une successions de tempête en présence, ou non, d'aménagements côtiers. De ces résultats découlent un nombre important de questionnements scientifiques et des leçons génériques sur le rôle tampon des barres pré-littorales et des systèmes dunaires végétalisés dans la réponse des plages soumises à des événements extrêmes. Une partie importante de ces travaux a été réalisée en collaboration avec mes collègues de l'équipe METHYS à EPOC sur les plages d'Aquitaine et, sur les plages australiennes, avec Gerben Ruessink (Utrecht University, Pays-Bas), Ian Turner (University of New South Wales, Australie) et mes collègues du Griffith Centre for Coastal Management (Australie). Une partie de ces travaux ont été aussi réalisés dans le cadre d'une participation active à l'encadrement de la thèse de Rafael Almar, et l'encadrement des stages de Master 2 de Yann Le Corre et Camille Enjalbert.

3.1 Dynamique des plages d'Aquitaine

3.1.1 Synthèse sur la morphodynamique des plages ouvertes d'Aquitaine

Une partie significative de mes travaux en début de carrière ont consisté à synthétiser nos connaissances sur le comportement des plages sableuses d'Aquitaine. Ce travail s'est appuyé sur les mesures réalisées par l'équipe METHYS depuis 1998, date des premiers relevés de terrain pilotés par Hélène Howa, dans le cadre des thèses de *De Melo Apoluceno* (2003) et *Desmazes* (2005). Mon implication dans cette synthèse était stimulée par la volonté d'intégrer le comportement des plages d'Aquitaine dans la modélisation conceptuelle universelle de *Wright and Short* (1984). En effet, celle-ci était utilisée par l'ensemble de la communauté internationale, mais était écartée au niveau aquitain. Je me suis également appuyé sur les travaux réalisés en imagerie satellitaire sur l'observation du système interne de barre/baïne (*Lafon et al.* 2002) et du système externe de barre en croissant (*Lafon et al.* 2004, ***Lafon et al.*** 2005), et sur l'analyse d'archives de photos aériennes du littoral aquitain. Ces travaux de synthèse se sont également très largement basés sur les travaux de modélisation numériques et plus particulièrement sur mes observations personnelles réalisées dans le cadre des campagnes de mesures et surtout de mes activités extra-professionnelles afin de combler l'absence de données sur la morphodynamique des barres pendant les conditions de houle énergétiques.

Cette synthèse a abouti à un article de revue de la morphodynamique des plages d'Aquitaine (***Castelle et al.*** 2007a) dont les conclusions ont très largement dépassé le cadre local. Nous avons par exemple développé un modèle conceptuel de la morphodynamique des plages sableuses ouvertes d'Aquitaine (Figure 3.1). Ce modèle a aussi été élaboré et discuté en fonction des extensions de la classification originale de *Wright and Short* (1984) aux environnements à marée (*Masselink and Short* 1993) ou aux systèmes à plusieurs barres (*e.g.*, *Short* 1992, *Short and Aagaard* 1993, *Lippmann and Holman* 1990).

Nous avons également déduit un certain nombre de questions scientifiques génériques comme par exemple celle sur l'origine du caractère ponctuellement asymétrique des barres sableuses tridimensionnelles. Plus particulièrement, nous avons pour la première fois émis l'hypothèse que les interactions entre les différentes entités du système plage pouvait jouer un rôle crucial dans la morphodynamique du système composite. A titre d'exemple, la Figure 3.2 montre trois types de couplage observés sur le littoral aquitain (***Castelle et al.*** 2007a) [1]. Ces couplages morphologiques ont toutefois été rarement observés, d'une part parce que ce type de couplage est difficile à identifier *in-situ* et d'autre part parce qu'il faut pouvoir (et vouloir) déconvoluer les informations. Malgré cela, nous avons fait le choix de chercher à comprendre les mécanismes à l'origine de ces couplages. Comme nous le verrons dans la suite de ce mémoire, un nombre important d'études se sont appuyées sur cette découverte sur les couplages morphologiques (*e.g.*, ***Castelle et al.*** 2010b;c, ***Almar et al.*** 2010, *Price and Ruessink* 2011, *Thiébot et al.* 2012, ***Castelle et al.*** 2012, *Price and Ruessink* in press, ***Price et al.*** soumis). Une partie de ces travaux ont été réalisés dans le cadre de l'ANR Jeune Chercheur BARBEC (Role of morphological interactions in governing the whole wave-dominated sandy BARred-BEaCh system) que je coordonne depuis fin 2010. Nous verrons notamment plus tard que le fait que les couplages soient rarement ob-

1. Les couplages morphologiques ont également fait l'objet d'une étude publiée plus tard la même année sur les plages de la Gold Coast (Australie) à partir de l'imagerie vidéo (*Ruessink et al.* 2007a).

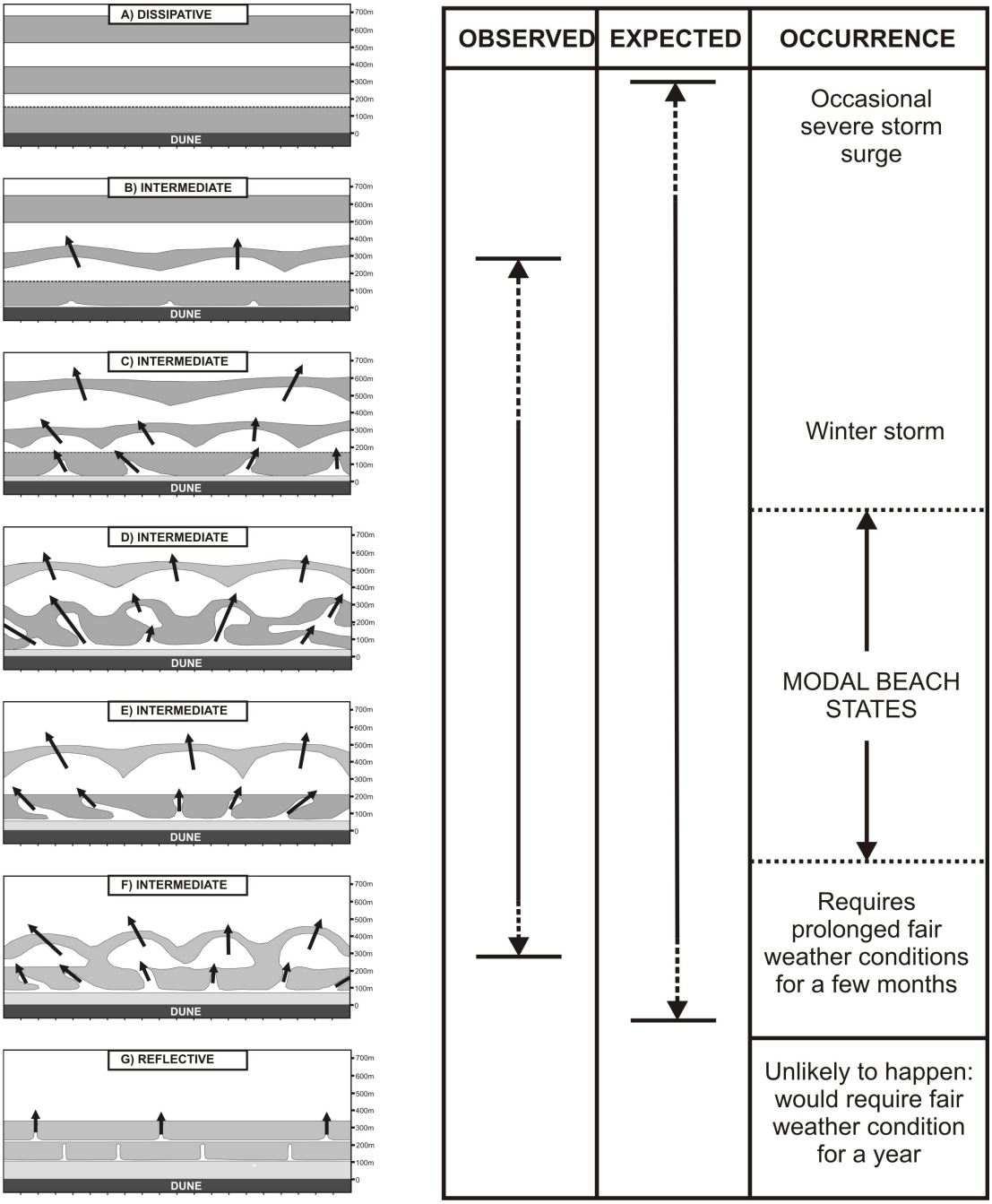

FIGURE 3.1 – *Proposition d'un modèle conceptuel de morphodynamique des plages sableuses ouvertes d'Aquitaine montrant la gamme de morphologies du système double barre pouvant être observées aux alentours de la plage du Truc Vert (**Castelle et al.** 2007a). Il est supposé que le type (A) est observé pour de très rares événements extrêmes avec surcote, et le type (B) après des tempêtes hivernales très énergétiques. Du plus dissipatif au plus réflectif, les types (C), (D), (E) et (F) ont été observées à travers des photographies aériennes et l'imagerie satellitaire. Le type (G) n'est possible qu'après une période prolongée (≈ 1 an) de conditions peu énergétiques et ne peut donc pas être théoriquement observé sur les plages aquitaines similaires à celles du Truc Vert. Les flèches indiquent la présence de courants d'arrachement lorsqu'ils sont actifs, i.e. pour des conditions de vagues suffisamment énergétiques et frontales.*

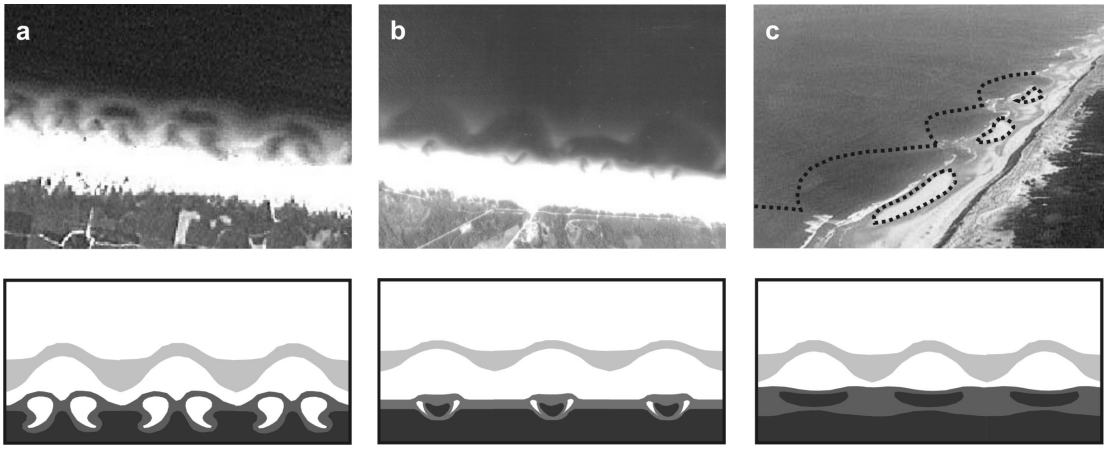

FIGURE 3.2 – *Couplages morphologiques observés sur le littoral aquitain dans* ***Castelle et al.*** *(2007a) : (a,b) couplage à la demi longueur d'onde et (c) couplage en opposition de phase.*

servés ne signifie pas que les barres n'interagissent pas, bien au contraire (***Castelle et al.*** 2010c).

3.1.2 Confrontation du modèle conceptuel aux données acquises à partir de 2007

Les interprétations sur la morphodynamique des barres basées sur des observations essentiellement visuelles (fréquence d'observation des morphologies, comportements des barres pendant les tempêtes) ont été confirmées par des travaux postérieurs. Ces travaux ont été basés sur la mesure directe ou la télédétection vidéo le long du littoral aquitain dans le cadre d'une participation active à l'encadrement de la thèse de Rafael Almar (codirigé par P. Bonneton et N. Sénéchal). C'est notamment le cas des résultats issus de l'exploitation des données vidéo de la station pérenne de Biscarrosse (seuils de hauteur de barres pour le raidissement des vagues pendant les épisodes de tempête, ***Almar et al.*** 2009, voir aussi Figure 3.3), et de la campagne de mesure Truc Vert'08 (rôle des interactions entre les différentes entités morphologiques de la plage pendant un épisode de tempête décennal, ***Almar et al.*** 2010) et de l'exploitation des données topographiques (fréquence d'observation des différentes morphologies de système barre/baïne, ***Sénéchal et al.*** 2009). Ceci montre que **l'observation visuelle, avertie et récurrente, des plages et des zones de déferlement peut permettre des avancées scientifiques importantes sans avoir à s'appuyer sur des moyens techniques et humains importants**. En effet, cela s'avère moins coûteux, souvent plus instructif et pertinent que le traitement parfois aveugle de données topographiques ponctuelles. Ceci n'est pas nouveau puisque des avancées scientifiques importantes dans la compréhension de l'évolution de la morphologie des plages ont été réalisées à travers l'observation uniquement visuelle des chercheurs 'plagistes' [2] (parmi d'autres *Short* 1999).

3.1.3 Dynamique des plages sableuses d'Aquitaine contraintes par la géologie héritée : exemple de la Grande Plage de Biarritz

Intuitivement, la dynamique des plages sableuses anthropisées et/ou affectées par l'héritage géologique (falaises, caps, substratum rocheux) doit contraster avec

2. Un chercheur 'plagiste' étant plus souvent dans l'eau que devant son ordinateur, c'est-à-dire, malheureusement, un chercheur en voie d'extinction.

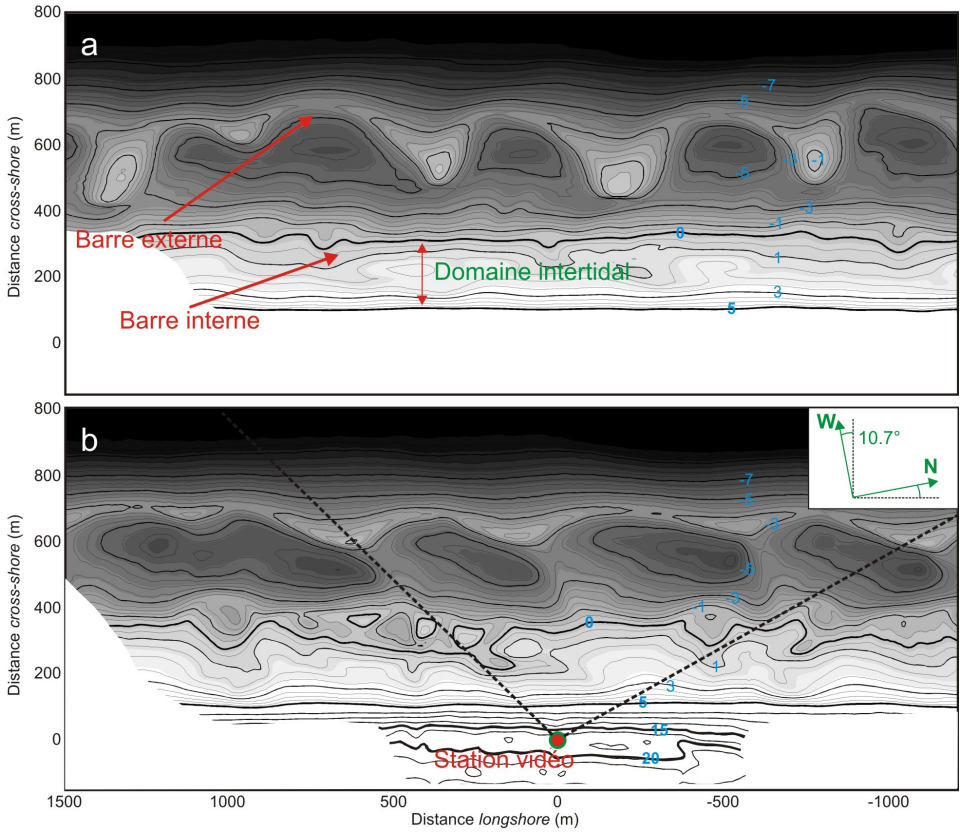

FIGURE 3.3 – *Morphologie (bathymétrie mesurée par un navire océanographique du SHOM et topographie mesurée par les chercheurs d'EPOC) de la plage du Truc Vert (a) le 15 février 2008 avant le début de la campagne et (b) le 5 avril 2008 à la fin de la campagne ECORS-Truc Vert'08 (modifié d'après* ***Almar et al.*** *2010). Les iso-contours 0 et 5 m correspondent respectivement au niveau des plus basses mers et au niveau des plus hautes mers. On note la présence d'une barre externe en croissant et d'une barre interne découpée par des chenaux de vidange : la morphologie (a) correspond à l'état de plage (F) dans la Figure 3.1 et la morphologie (b) à l'état (E). Cette évolution vers un état de plage plus dissipatif est accord avec les conditions énergétiques rencontrées pendant la campagne. Une description de la méthodologie mise en place pour obtenir ces relevés topo-bathymétriques est donnée dans* ***Parisot et al.*** *(2009).*

celle des plages ouvertes telles que celles décrites dans la section ci-dessus. Toutefois l'étude de ces contraintes a jusqu'à présent été peu abordée dans la littérature. Par exemple, *Jackson et al.* (2005) ont montré sur 25 plages irlandaises, pour la plupart délimitées par des caps rocheux, que la géologie héritée pouvait être plus déterminante pour l'état de plage que le forçage des vagues combiné à la granularité (*Wright and Short* 1984). Ceci a été confirmé sur des plages australiennes par *Short* (2006). Toutefois, l'impact de la géologie héritée sur la morphodynamique haute-fréquence des plages a été très peu étudié (*Gallop et al.* 2011).

En collaboration avec la cellule de transfert CASAGEC et dans le cadre du stage de Master 2 de Camille Enjalbert nous avons étudié l'évolution haute-fréquence de la dynamique des barres sableuses sur la Grande Plage de Biarritz qui est fortement contrainte par la géologie (délimitée par deux caps rocheux, substratum rocheux affleurant en zone intertidale pendant les épisodes érosifs, présence de deux petites îles rocheuses au large). Nous avons montré que l'héritage géologique était déterminant pour la réponse de la plage. En particulier, on observe une rapide tridimensionnalisation de la bathymétrie littorale pendant les épisodes de tempête à cause des

contraintes géologique (***Enjalbert et al.*** 2011) alors que, sur les plages ouvertes, une rapide bidimensionnalisation est typiquement observée (*e.g.*, *Wright and Short* 1984, *Van Enckevort et al.* 2004). En effet, la tridimensionnalisation des barres pendant les événements énergétiques ne peut être observée que si les conditions énergétiques, préférentiellement frontales, persistent pendant plusieurs jours/semaines (*Van Enckevort et al.* 2004, *Splinter et al.* 2011). Il a également été montré sur la Grande Plage de Biarritz qu'on pouvait observer la formation de chenaux de vidange transitoires se formant près des caps rocheux et migrant ensuite vers d'autres chenaux avant de s'apparier, cette migration n'étant visiblement pas contrôlée par l'incidence des vagues (***Enjalbert et al.*** 2011).

3.1.4 Questions scientifiques amenées par ces travaux

Ces observations sur la dynamique des barres sableuses de déferlement ont soulevé un nombre important de questions scientifiques. Nos travaux en modélisation morphodynamique non-linéaire se sont largement inspirés de ces questions et, comme nous le verrons dans la suite de ce mémoire (chapitre 4) des réponses seront apportées. Parmi les principales questions, on peut citer les suivantes :

- Quel est le mécanisme qui gouverne la présence des couplages morphologiques frappants observés en Figure 3.2 ?
- Ces couplages étant finalement assez rarement observés, ce mécanisme est-il important si l'on veut appréhender la dynamique des plages à double barre ?
- Est-il pertinent d'étudier la morphodynamique d'une barre interne en ignorant volontairement celle de la barre externe ou encore la morphologie du plateau interne ?
- Quels est le mécanisme responsable de la bidimensionnalisation des barres sableuses pendant les épisodes de tempête ?
- Quels sont les mécanismes sous-jacents qui induisent des comportements de barres sableuses si contrastés entre les plages ouvertes et les plages délimitées par des caps rocheux ou des épis (*i.e.*, plages de poche) ?
- Quel sont les mécanismes pouvant expliquer la formation puis la migration des chenaux transitoires observés le long des plages fortement contraintes par la géologie ?

3.2 Réponse des plages sableuses aux événements de tempête

L'une des lacunes au travail de synthèse réalisé sur le littoral aquitain résidait à l'époque dans l'absence de données quantitatives pendant les épisodes de tempête. Dans le cadre de mon séjour postdoctoral j'ai organisé deux campagnes de mesures sur 3 mois combinant relevés de terrain pour suivre l'évolution du haut de plage et l'imagerie vidéo pour suivre l'évolution des barres sableuses. Quatre plages ont été sélectionnées en fonction de leurs différents degrés d'exposition aux aménagements côtiers. L'une des caractéristiques de cette campagne était sa flexibilité. En

effet nous avons attendu l'arrivée d'un événement extrême afin de commencer les mesures immédiatement avant l'arrivée de cet épisode. L'objectif était de suivre ensuite son impact à court terme (et potentiellement à plus long terme) sur l'évolution morphologique de la plage, ainsi que le rôle des barres sableuses et des aménagements côtiers sur l'intensité de l'érosion du haut de plage. Ces travaux ont été en partie réalisés dans le cadre du stage de Master 2 de Yann Le Corre et en collaboration avec Gerben Ruessink de l'Université d'Utrecht (Pays-Bas), Ian Turner de l'University of New South Wales (Australie) et Rodger Tomlinson du Griffith Centre for Coastal Management (Australie).

3.2.1 Réponse d'une plage sableuse à une succession de tempêtes

Les conditions de houle pendant la campagne Broadbeach 2006 et les résultats obtenus ont très largement répondu à nos attentes (***Castelle et al.*** 2007c). La Figure 3.4 montre l'évolution du volume de plage de la position des 2 barres sableuses pendant une partie de la campagne sur la plage de Broadbeach (Gold Coast, Australie). Le début de la campagne a été caractérisé par le passage d'une tempête d'une rare intensité (cyclone hybride) avec une houle décennale et, sans surprise, une érosion intense de la plage. Les taux d'érosion exceptionnellement élevés mesurés pendant les

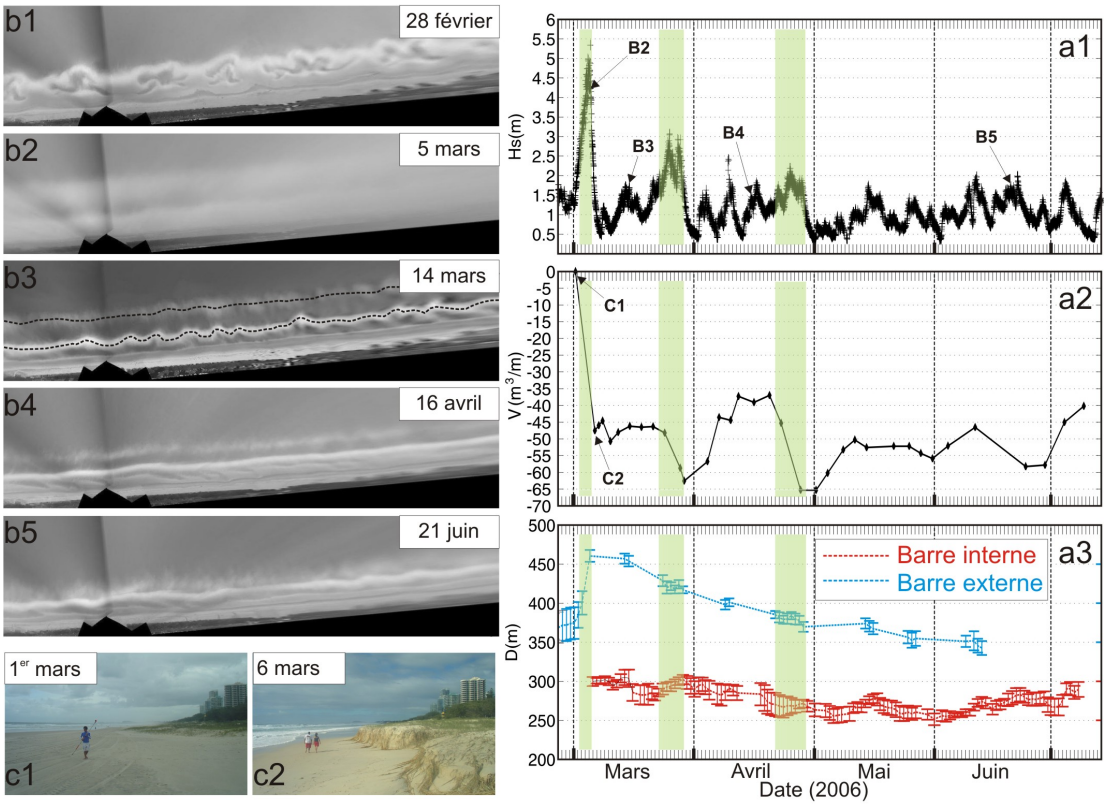

FIGURE 3.4 – *Résultats issus de la campagne Broadbeach 2006 (**Castelle et al.** 2007c). Série temporelle de la hauteur significative H_s (a1), du volume de la plage V (a2) et des distances de la barre interne et de la barre externe D à la côte avec superposées les déviations standards (mesure de la tridimensionnalité de la barre) de ces positions (a3). Les résultats montrent que l'événement décennal (première zone grisée des séries temporelles) du début de la campagne a généré une intense érosion de la plage (C1-C2) associé à une dégénérescence de la barre externe visible par imagerie vidéo (B2-B5) pendant la suite de la campagne (d'après **Castelle et al.** 2007c, **Castelle** 2009).*

deuxième et troisième tempêtes (considérées comme annuelles) ont pu être expliqués par la dégénérescence de la barre externe observée pendant la première tempête. En effet, la barre ayant migré anormalement loin au large pendant l'événement décennal, celle-ci est ensuite restée rectiligne et profonde pendant le reste de la campagne de mesure, ne permettant pas une dissipation suffisante par déferlement bathymétrique au large des houles énergétiques. Le haut de plage a alors été exposé à des processus hydro-sédimentaires agressifs en zone de jet de rive. La barre a ainsi perdu son rôle de protection plusieurs mois après la première tempête. Cet événement a été associé à un épisode NOM (pour *Net Offshore Migration*, voir *Bailey and Shephard* 1999, *Kuriyama* 2002) ici favorisé par la succession de tempêtes (*Ruessink et al.* 2009). Cette notion importante d'effet de seuil dans les épisodes de tempête a été mise en évidence dans des étude plus récentes (*e.g.*, *Almeida et al.* 2012, *Gervais et al.* 2012). Notre étude a notamment mis en évidence des liens importants entre la dynamique des barres pré-littorales et la réponse du haut de plage ainsi que l'impact que peut avoir un événement extrême sur la dynamique de la plage, et ce même plusieurs mois après

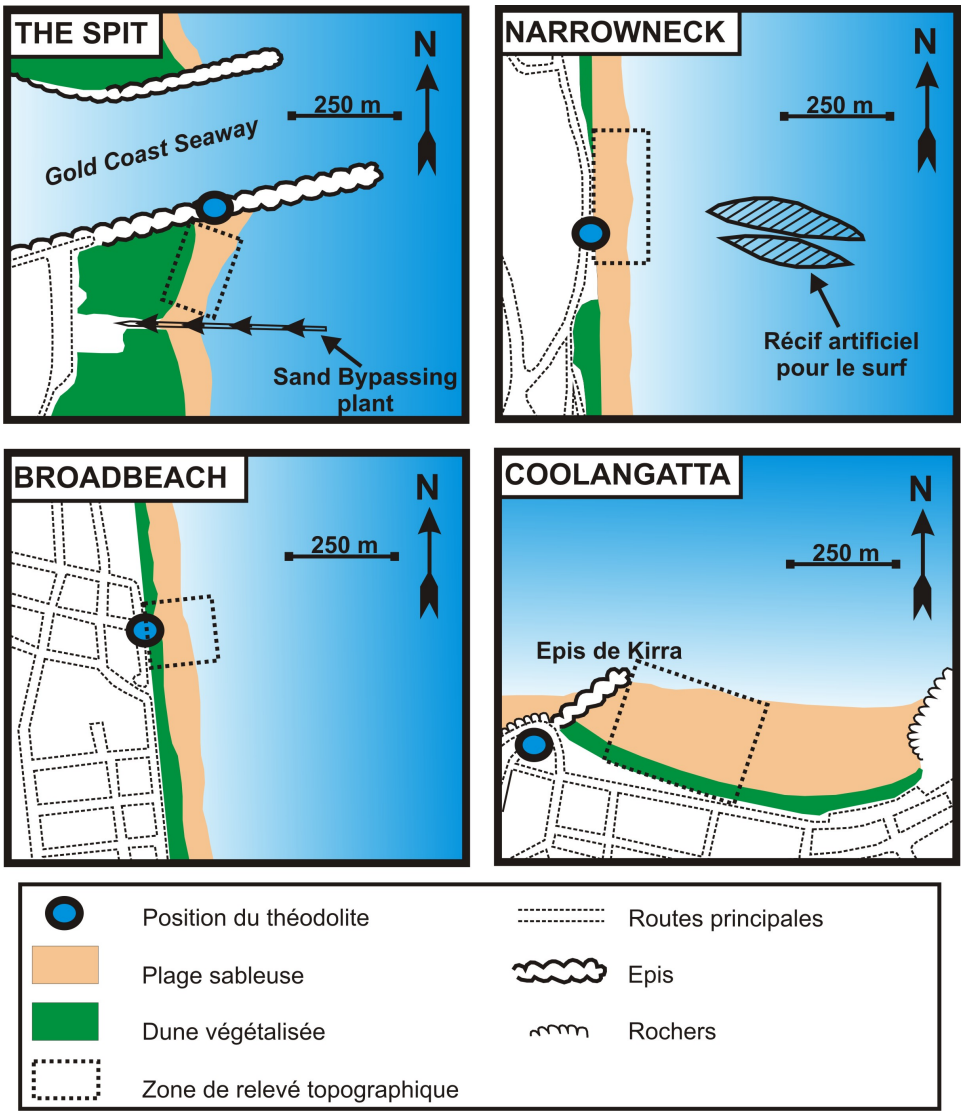

FIGURE 3.5 – *Localisation des 4 plages étudiées dans* ***Castelle et al.*** *(2008) avec les principales caractéristiques des systèmes dunaires et aménagements côtiers.*

l'événement (***Castelle et al.*** 2007c). Ces résultats sont importants notamment avec le spectre du changement climatique et de la modification probable de l'intensité et de la fréquence des tempêtes.

3.2.2 (In)efficacité des aménagements littoraux pour la protection des plages face aux tempêtes

Cette étude fut complétée par des mesures pendant la même période sur d'autres plages de la Gold Coast (***Castelle et al.*** 2008) présentant des aménagements (récif artificiel, digues, système de *bypass* de sédiment). La Figure 3.5 décrit les 4 plages étudiées pouvant être localisées sur la Figure 1.5d, qui sont du nord au sud : la plage du Spit située juste en aval de la jetée instrumentée par le système de *bypass* de sédi-

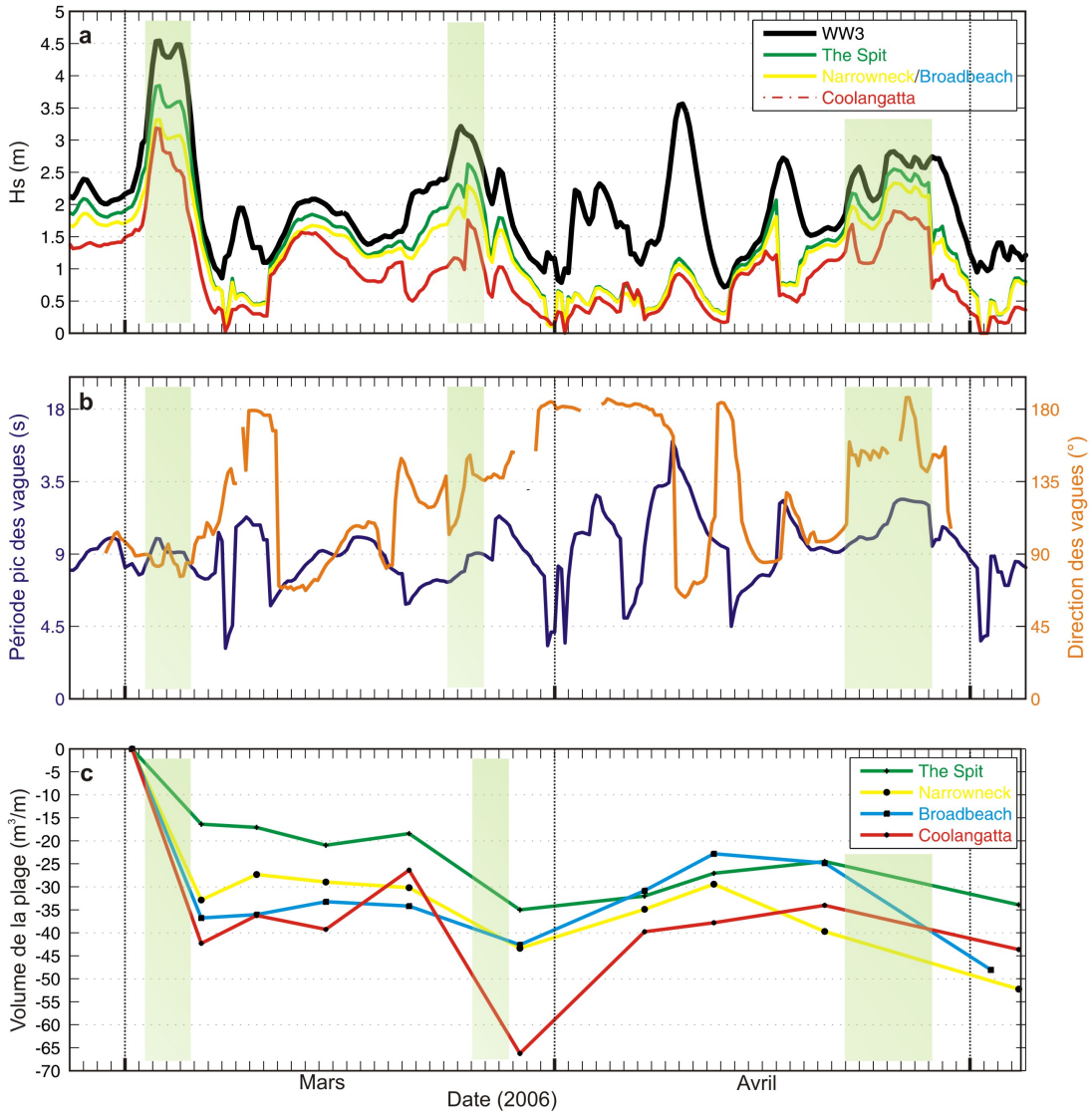

FIGURE 3.6 – *Série temporelle (a) des hauteurs significatives des vagues H_s au niveau des 4 plages décrites en Figure 3.5 simulées en emboîtant le modèle SWAN (Booij et al. 1999) dans le modèle global WW3 (Tolman 1991), (b) de la période pic des vagues T_p et de l'angle d'incidence θ et (c) des volumes de plage mesurés (**Castelle et al.** 2008). Les 3 zones grisées indiquent les 3 épisodes énergétiques discuté dans **Castelle et al.** (2007c) et **Castelle et al.** (2008).*

ment permanent du Gold Coast Seaway (***Sennes et al.*** 2007), en amont de la digue sud de l'embouchure, et bordée par une large dune végétalisée ; la plage de Narrowneck caractérisée par la présence d'un récif artificiel (*Turner* 2006), bordée par une dune non-végétalisée et qui a une longue histoire de rechargements de plages ; la plage de Broadbeach (***Castelle et al.*** 2007c) située 3.5 kilomètres au sud de Narrowneck qui n'a pas de récif artificiel et est bordée par une dune végétalisée ; la plage de Coolangatta située en aval du système permanent de *bypass* de sédiment de la Tweed River (***Castelle et al.*** 2009a) et délimitée par un épis bloquant une partie du transit sédimentaire dans le but de stabiliser le trait de côte. La Figure 3.6 montre la série temporelle correspondante des vagues et des volumes de plage. Les détails de l'étude sont donnés dans ***Castelle et al.*** (2008). En résumé, l'étude a montré que les plages aménagées (récifs artificiels plus au large, système de *bypass* de sédiment plus en amont ou présence d'épis) s'érodaient plus pendant les épisodes de tempête que les plages qui n'avaient juste subi qu'une végétalisation de la dune (plage de Bradbeach). Ainsi, **de manière similaire au rôle des barres sableuses pré-littorales, les dunes végétalisées jouent un rôle tampon essentiel dans la réponse de la plage aux événements de tempête.** En outre, notre étude suggère que la plupart des plages de la Gold Coast seraient complètement érodées si une succession de cyclones similaire à 1967 venaient à toucher cette portion du littoral australien.

Conclusion du chapitre

Même si mon approche peut parfois apparaître focalisée sur la modélisation numérique et théorique, je me suis en fait très largement investi ces 11 dernières années dans l'observation (visuelle ou issue de mesures) de la morphodynamique des plages. Ces travaux ont permis des avancées scientifiques significatives dans la compréhension de la dynamique des barres sableuses et de la réponse du haut de plage aux événements de tempête. Ces avancées ont suscité un grand nombre de questions scientifiques qui ont, comme nous le verrons dans le prochain chapitre, stimulé des projets et de nombreuses collaborations en modélisation numérique de la morphodynamique des plages.

Un modèle conceptuel de la morphodynamique du système double barre des plages de la côte aquitaine a été proposé (***Castelle et al.*** 2007a) en se basant sur une large base de données existantes et des observations visuelles récurrentes et averties. J'ai réalisé cette synthèse avec la volonté d'intégrer le comportement des plages d'Aquitaine dans la modélisation conceptuelle universelle de *Wright and Short* (1984) afin d'en tirer des conclusions et des questions scientifiques génériques. Ce modèle a été plus tard confirmé par les études basées sur l'exploitation des données vidéo (***Almar et al.*** 2009; 2010) et les relevés topographiques récurrents (***Sénéchal et al.*** 2009). Dans ***Castelle et al.*** (2007a) nous avons pour la première fois émis l'hypothèse que les interactions entre les différentes entités du système plage ont le potentiel de jouer un rôle crucial dans la morphodynamique du système composite. Plus récemment, nous avons montré que la morphodynamique haute-fréquence des plages sableuses contrainte par la géologie héritée (*e.g.*, caps rocheux) a un comportement qui contraste avec celui des plages ouvertes (***Enjalbert et al.*** 2011). D'où les interrogations suivantes : **Quels sont les mécanismes contrôlant les couplages morphologiques entre les différentes entités morphologiques du système plage et ceux contrôlant la bidimensionnalisation des barres pendant les épisodes de tempête ? L'étude isolée d'un corps sableux peut-il aboutir à une analyse erronée de sa dynamique et une mauvaise compréhension des données de terrain ? Quels sont les mécan-**

ismes induisant les comportements morphodynamiques contrastés entre les plages ouvertes et celles influencées par la géologie héritée ? Comme nous le verrons plus loin dans le chapitre 4, nous avons à travers la modélisation morphodynamique non-linéaire répondu en grande partie à l'ensemble de ces questions.

Nos études sur la réponse de la plage aux événements extrêmes ont mis en évidence des liens entre la dynamique des barres pré-littorales et la réponse du haut de plage ainsi que l'impact d'un événement extrême sur la dynamique de la plage même plusieurs mois après l'événement (***Castelle et al.*** 2007c). Nous avons montré que les barres pré-littorales agissent comme une protection essentielle de la plage pendant les épisodes de tempête mais que, si la tempête dépasse un certain seuil, la barre pré-littorale peut dégénérer et ainsi n'offrir plus aucune protection en livrant le haut de plage aux assauts de processus hydro-sédimentaires intenses en zone de jet de rive. Ces résultats sont importants notamment dans le cadre du changement climatique et de la possible augmentation de l'intensité et de la fréquence des tempêtes. Cette étude fut complétée par des mesures pendant la même période sur d'autres plages de la Gold Coast (***Castelle et al.*** 2008) présentant des aménagements (récif artificiel, digues, système de *bypass* de sédiment). Nous avons montré que les plages aménagées s'érodaient davantage pendant les épisodes de tempête que les plages qui n'avaient juste subi qu'une végétalisation de la dune. Ces travaux furent une composante essentielle du projet 'Gold Coast Managament Plan' qui visait à terme à établir une politique durable de gestion du trait de côte à 30 ans par le Gold Coast City Council. En résumé, **nous avons montré que les barres pré-littorales et les systèmes dunaires jouent un rôle crucial dans le comportement des plages aériennes en réponse aux événements de tempête.**

4 Modélisation théorique et numérique de la morphodynamique des plages sableuses

Sommaire

Dans ce chapitre, nous traitons de la modélisation numérique et théorique de la morphodynamique des plages, et tout particulièrement de la morphodynamique des barres pré-littorales. En effet, comme nous l'avons rappelé dans le chapitre 1, la dynamique de la plage aérienne (épisodes d'érosion/accrétion, oscillations du trait de côte) est en grande partie contrôlée par la dynamique de la plage sous-marine et tout particulièrement celle des barres pré-littorales (cf Figure 1.4).

Dans un premier temps (Section 4.1), nous présenterons le cadre théorique et particulièrement la théorie des motifs et la théorie d'auto-organisation qui ont progressivement vu le jour pour expliquer la formation et l'évolution des corps sableux tridimensionnels en zone de déferlement. Mon implication dans le changement de paradigme scientifique (de la théorie des motifs vers les théories d'auto-organisation) sera discutée. Le modèle morphodynamique non-linéaire dont je coordonne le développement ainsi que les différents outils d'analyse seront succinctement présentés en Section 4.2. La Section 4.3 présentera les principaux résultats obtenus ces 3 dernières années. Nous montrerons ainsi que ces études ont répondu aux questionnements scientifiques découlant des observations et soulevés dans le chapitre précédent, et que nos travaux ont récemment réconcilié la théorie avec les observations.

Ces travaux en modélisation de la morphodynamique des plages sableuses ont débuté pendant ma thèse de doctorat, et ont repris lors de mon recrutement au CNRS en 2007 après une pause de 2 ans pendant mon séjour postdoctoral. Ils ont été réalisés dans le cadre de plusieurs projets, notamment le PNEC ART 7, MODLIT et plus récemment l'ANR BARBEC que je coordonne. J'ai été moteur de l'ensemble de ces travaux mis à part ceux sur l'impact de la marée sur la dynamique de barres (***Dubarbier and Castelle*** 2011) dans le cadre du stage de Master 2 de Benjamin Dubarbier et l'analyse de stabilité linéaire des systèmes à double barre (***Brivois et al.*** 2012), qui ne seront pas abordés ici. Ces travaux sont également le fruit de nombreuses collaborations nationales et internationales avec, en particulier, Gerben Ruessink, Timothy Price et Florent Grasso (Utrecht University, Pays-Bas), Giovanni Coco (Universidad de Cantabria, Espagne), Nicolas Bruneau (LNEC, Portugal) et Philippe Bonneton et Vincent Marieu de METHYS/EPOC.

4.1 Cadre théorique

Il est important de rappeler ci-dessous le cadre théorique permettant de comprendre le changement de paradigme scientifique de la théorie des motifs vers la théorie de l'auto-organisation pour expliquer la présence et la dynamique des barres sableuses rythmiques de type barre/chenal et barre en croissant. En effet, au début de mes travaux de recherche en 2001 (stage de Master et début la thèse de doctorat), l'ancien paradigme (théorie des motifs) était encore admis. Mes travaux de recherche en thèse se sont orientés sur la candidature du nouveau paradigme (l'auto-organisation), et mes travaux ont ainsi contribué à ce très important changement de paradigme scientifique en morphodynamique littorale. La suite de mes travaux, en particulier depuis mon recrutement au CNRS en 2007, se sont ancrés dans ce nouveau paradigme.

4.1.1 Théorie des motifs

On part ici des équations (2.1,2.2 et 2.3) du mouvement moyen des masses d'eau que nous avons décrit dans le chapitre 2. En linéarisant les équations et en négligeant la présence des vagues (ondes courtes), du frottement au fond et en surface, on obtient alors le système d'équations suivant :

$$\frac{\partial \bar{\eta}}{\partial t} + \frac{\partial Uh}{\partial x} + \frac{\partial Vh}{\partial y} = 0 \tag{4.1}$$

$$\frac{\partial U}{\partial t} = -g\frac{\partial \bar{\eta}}{\partial x} \tag{4.2}$$

$$\frac{\partial V}{\partial t} = -g\frac{\partial \bar{\eta}}{\partial y} \tag{4.3}$$

qui peut alors être simplifié en :

$$\frac{\partial^2 \bar{\eta}}{\partial t^2} = \frac{\partial}{\partial x}\left(gh\frac{\partial \bar{\eta}}{\partial x}\right) + \frac{\partial}{\partial y}\left(gh\frac{\partial \bar{\eta}}{\partial y}\right) \tag{4.4}$$

Cette dernière est une équation d'onde hyperbolique que vérifient les ondes longues (infragravitaires). Si on considère une plage de pente constante telle que $Z_f = -my$ et une onde de fréquence angulaire ω, alors il existe une solution qui s'écrit :

$$\bar{\eta} = a_n e^{-k_e y} L_n(2k_e y)\cos(k_e x)\cos(\omega t) \tag{4.5}$$

où L_n est le polynôme de Laguerre au mode n, qui peut avoir différentes formes selon n ($L_0(x) = 1$; $L_1(x) = 1 - x$; $L_2(x) = 1 - 2x + x^2/2$), a_n est l'amplitude de l'onde longue, $k_e = 2\pi/\lambda_e$ est le nombre d'onde avec la longueur d'onde longitudinale $\lambda_e = (1+2n)mgT_e^2/(4\pi)$ où T_e est la période de l'onde longue. Prenons ici par exemple le mode $n = 1$ ($\bar{\eta} = Ae^{-k_e y}(1 - 2k_e y)\cos(k_e x)\cos(\omega t)$). Cette solution correspond à une onde longue de bord stationnaire (non propagative). En effet, des ondes longues sont liées aux groupes d'ondes (courtes, *i.e.*, les vagues) au large et sont libérées lorsque les ondes courtes déferlent. Les ondes longues ne déferlent pas et sont réfléchies à la plage et, si elles arrivent avec un angle d'incidence suffisant, peuvent être piégées par réfraction. Si 2 ondes longues de même ω et d'incidence opposées arrivent à la côte, alors on a formation d'un onde de bord stationnaire. La Figure 4.1 montre l'enveloppe de cette onde longue stationnaire à un temps t avec une longueur d'onde λ_e = 200 m obtenue pour n = 1, T = 65 s et m = 0.02.

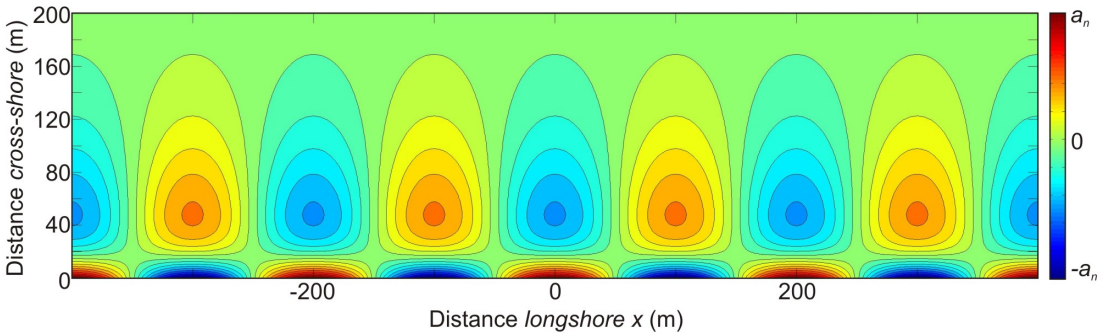

FIGURE 4.1 – *Enveloppe d'une onde longue de bord stationnaire à un instant t ayant une longueur d'onde λ_e = 200 m obtenue pour n = 1, T = 65 s et m = 0.02.*

La théorie des ondes de bord a été établi dans les années 50 (*e.g.*, *Eckart* 1951). La cohérence de ces motifs hydrodynamiques est apparue comme une candidate séduisante pour expliquer la structuration cohérente des barres sableuses pré-littorales telles que celle des barres en croissant (*e.g.*, *Bowen and Inman* 1971) ou les systèmes barre/chenal (*e.g.*, *Holman and Bowen* 1982). L'hypothèse de base est que **ce motif dans l'hydrodynamique (onde longue de bord stationnaire) peut se retrouver imprimé sur le fond sableux**. En calculant les courants induits par ces ondes de bord et en considérant que le transport sédimentaire se fait seulement proche du fond, alors il y a le potentiel pour un transport sédimentaire net permettant de former une bosse faisant face à chaque noeud de l'onde de bord stationnaire (*Carter et al.* 1973). Cette théorie de motif hydrodynamique a été très largement acceptée par la communauté, et ce, jusqu'à très récemment (en témoigne la place qui lui est faite dans certains ouvrages de référence *e.g.*, *Carter* 1988, *Komar* 1998, *Short* 1999).

4.1.2 Théorie de l'auto-organisation

Ecartons désormais la présence des ondes longues et ne considérons que les vagues et les courants $\vec{U} = (U, V)$ qu'elles induisent. Dans un premier temps, faisons l'hypothèse que les flux sédimentaires sont de la forme :

$$\vec{Q}_s = \alpha U^{a-1}\vec{U} - \gamma\vec{\nabla}Z \tag{4.6}$$

où a et γ sont des constantes positives et α un coefficient de mise en mouvement du sédiment. Les premier et deuxième termes du membre de droite sont respectivement un terme advectif et un terme de transport par effet de pente. Rappelons ici que $Z_f(x,y,t) = Z_f^0(y) + Z(x,y,t)$ (Figure 2.1) où Z_f^0 est le profil de plage à l'équilibre (le *basic state*) et Z est la perturbation du fond sableux par rapport à ce profil d'équilibre. A partir de ces flux sédimentaires, l'évolution du fond peut être calculée à partir de l'équation de la conservation du sédiment :

$$(1-p)\frac{\partial Z_f}{\partial t} + \nabla\cdot\vec{Q}_s = 0 \tag{4.7}$$

où p est la porosité du sédiment. En faisant l'hypothèse que les courants évoluent lentement et après quelques manipulations on obtient :

$$(1-p)\frac{\partial Z}{\partial t} = \vec{\nabla}\cdot(\gamma\vec{\nabla}Z) - \alpha U^{a-1}\vec{U}\cdot\vec{\nabla}\ln\frac{\alpha}{h} - (a-1)\alpha U^{a-2}a_T \tag{4.8}$$

où $a_T = \vec{U} \cdot \left(\vec{\nabla} \cdot \vec{U}\right) \cdot \vec{U}/U$. Pour simplifier considérons le cas $a = 1$, l'équation de l'évolution du fond devient :

$$(1-p)\frac{\partial Z}{\partial t} = \vec{\nabla} \cdot (\gamma \vec{\nabla} Z) - \vec{U} \cdot \vec{\nabla} \ln \frac{\alpha}{h} \tag{4.9}$$

Le premier terme est un terme de diffusion (amortissement, avec migration si $\vec{\nabla}\gamma \neq 0$, de la perturbation du fond Z par rapport au profil d'équilibre Z_f^0) et peut donc être écarté pour l'analyse de stabilité. En considérant de petites évolutions de Z ($\alpha = \alpha(x)$ et $h = h^0(x)$) l'équation revient à :

$$(1-p)\frac{\partial Z}{\partial t} = -V\frac{d}{dy}\ln\frac{\alpha}{h} \tag{4.10}$$

D'après l'équation 4.10, il y a accrétion ($\partial Z/\partial t > 0$) si le courant *cross-shore* s'oppose aux gradients de α/h et érosion ($\partial Z/\partial t > 0$) si le courant *cross-shore* est colinéaire aux gradients de α/h. Considérons maintenant une plage comprenant dans la zone de déferlement une succession de barres et de chenaux de faible amplitude (Figure 4.2). Comme nous l'avons vu dans le chapitre (2), sur la barre (chenal) il y a un déferlement bathymétrique plus (moins) intense, de telle sorte qu'un courant vers le rivage (large) est généré. Dans le cas classique d'une diminution de α/h du point de déferlement y_s vers la plage (Figure 4.2a), on observe alors une rétroaction positive : il y a accrétion ($\partial Z/\partial t > 0$) au niveau de la barre car le courant *cross-shore* s'oppose au gradients de α/h et érosion du chenal($\partial Z/\partial t > 0$) car le courant *cross-shore* est colinéaire aux gradients de α/h (Figure 4.2b). Le système plage est donc instable en présence de vagues frontales et la croissance de structures tridimensionnelles peut être observée. *Sonu* (1972b) a le premier suggéré que les rétroactions entre l'hydrodynamique et la morphologie pouvait être à l'origine des structures tridimensionnelles des barre sédimentaires. Les travaux théoriques de *Hino* (1974) ont confirmé que cette hypothèse est

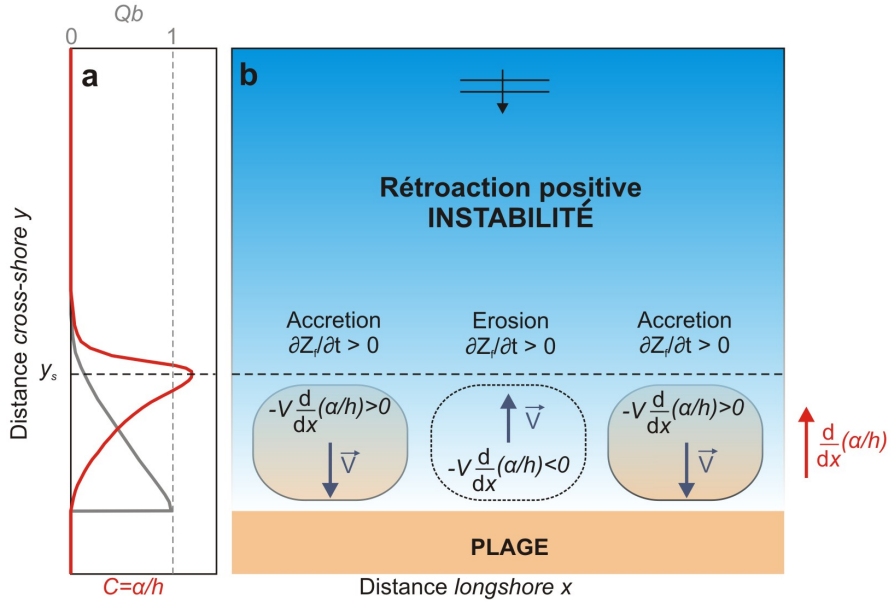

FIGURE 4.2 – *Schématisation de l'instabilité du système plage en présence de vagues frontales dont découle la théorie de l'auto-organisation. (a) Profil classique de fraction de vagues déferlée Q_b et de α/h^0. (b) Accrétion de la barre ($\partial Z/\partial t > 0$) et érosion du chenal ($\partial Z/\partial t < 0$) dans le cas classique d'une diminution de α/h^0 du point de déferlement y_s vers la plage.*

plausible. Toutefois, ce sont les travaux théoriques menés à l'UPC par Albert Falqués qui ont démontré pour la première fois que le mécanisme d'auto-organisation était essentiel. Ces travaux sont synthétisés dans *Falqués et al.* (2000), publication qui marque un tournant dans la communauté littorale travaillant sur la morphodynamique des plages.

La notion d'instabilité du système plage synthétisée ci-dessus n'est valable que pour des perturbations infinitésimales du fond sableux (pour une description détaillée du mécanisme, le lecteur est invité à consulter *Falqués et al.* 2000), c'est-à-dire pour la croissance initiale (régime linéaire) des instabilités qui peut être appréhendée par analyse de stabilité linéaire (*e.g.*, *Deigaard et al.* 1999, *Falqués et al.* 2000, *Calvete et al.* 2005, *Klein and Schuttelaars* 2006, ***Brivois et al.*** 2012). Ainsi, même si ici nous n'avons pas abordé les évolutions des corps sableux d'amplitude finie, il est montré que **la rétroaction positive entre l'hydrodynamique (vagues et courants induits), le transport sédimentaire et l'évolution du fond sableux peut expliquer la génération spontanée des structures tridimensionnelles des barres sableuses sans nécessiter la présence de motif dans l'hydrodynamique.**

4.1.3 Le changement de paradigme de la théorie des motifs vers la théorie de l'auto-organisation et implication/positionnement de nos travaux

La théorie de motif hydrodynamique a été très largement acceptée par la communauté, et ce, jusqu'à très récemment (*e.g.*, *Carter* 1988, *Komar* 1998, *Short* 1999). Pourtant, dès le début des années 70, un nombre important de limitations ont été pointées du doigt dans la littérature (*e.g*, *Sonu* 1972b, *Bryan and Bowen* 1997, *Bowen* 1997, *Holman* 2000, *Van Enckevort et al.* 2004). Parmi les principaux arguments, on peut lister : (1) la théorie des motifs de prend pas en compte le déferlement des vagues, or ces barres tridimensionnelles sont observées en zone de déferlement ; (2) l'intensité des courants induits par les ondes de bord stationnaires sont généralement un ordre de grandeur en dessous de celle des courants induits par la houle ; (3) l'énergie des ondes longues est la plus importante pendant les épisodes de tempête, or on observe plutôt la destruction des corps sableux tridimensionnels pendant les tempêtes et leur formation pendant les épisodes de post-tempête ; (4) les longueurs d'onde des ondes longues n'est que très rarement en accord avec celle des barres sableuses [1] ; (5) la présence d'onde de bord stationnaire peut paraître logique le long des plages délimitées par des caps, mais pas sur la plupart des plages sableuses ouvertes ; (6) pour $n = 2$ (équation 4.5) on obtient un système double barre en croissant, les 2 systèmes ayant systématiquement la même longueur d'onde, or ce cas est très rarement observé le long des plages naturelles ; (7) l'argument le plus important est certainement que **la théorie des motifs considère une réponse passive du fond sableux, ce qui incompatible avec le caractère dynamique et très non-linéaire démontré par les observations.**

Au début de mes travaux de recherche en 2001, l'ancien paradigme était encore admis. Mes travaux de recherches en thèse se sont orientés sur la candidature du nouveau paradigme. Plutôt que d'étudier la croissance initiale des barres (par l'analyse de stabilité linaire qui était déjà développée dans d'autres laboratoires, *e.g.*, *Deigaard et al.* 1999, *Falqués et al.* 2000, *Caballeria et al.* 2002), nous nous sommes orientés vers l'analyse de stabilité non-linaire, *i.e.*, en développant un modèle morphodynamique non-linéaire entièrement couplé s'appuyant sur le module de courant

1. Dans le cas où elles sont en accord, on peut se demander si les caractéristiques de l'onde de bord stationnaire seraient plutôt contrôlées par la morphologie, et pas l'inverse !

développé dans le cadre de la thèse de Frédéric Saint-Cast (*Saint-Cast* 2002). Ce type de modèle fut développé dans le même temps par d'autres équipes internationales (*Damgaard et al.* 2002, *Klein and Schuttelaars* 2006, *Garnier et al.* 2006, *Drønen and Deigaard* 2007, *Smit et al.* 2008, *Garnier et al.* 2008). **Mes travaux (*e.g.*, *Castelle et al.* 2006a) ont ainsi montré par la modélisation morphodynamique non-linéaire que les systèmes barre/chenal et en croissant pouvaient se former spontanément par le mécanisme d'auto-organisation et ont donc contribué au changement de paradigme**. Ce changement de paradigme scientifique de la théorie des motifs vers la théorie de l'auto-organisation fut notamment acté dans l'article de revue de *Coco and Murray* (2007) [2].

La suite de mes travaux s'est ancré dans ce nouveau paradigme scientifique dans le but : (1) de réconcilier la théorie avec certaines observations de terrain allant à l'encontre des résultats obtenus par l'analyse de stabilité linéaire ou non-linéaire et surtout (2) de répondre à un certain nombre de questions scientifiques que nous avions déduits de nos observations (voir paragraphe 3.1.4).

4.2 Description succincte du modèle morphodynamique non-linéaire

4.2.1 Structure du modèle

Mes travaux en modélisation morphodynamique se sont en grande partie basés sur le développement et l'utilisation d'un modèle morphodynamique non-linéaire au sein de l'équipe METHYS de EPOC. Ici je ne détaille pas le modèle (des descriptions assez complètes sont données dans ***Castelle et al.*** 2010b, ***Castelle and Ruessink*** 2011, ***Castelle et al.*** 2012, ***Castelle and Coco*** 2012). Ce modèle couple le modèle spectral SWAN (*Booij et al.* 1999) avec un modèle de circulations induite par les vagues (*Saint-Cast* 2002, ***Castelle et al.*** 2006b) à travers les tensions de radiation, un module de flux sédimentaires (dont un peu plus de détails sont donnés ci-dessous) et d'évolution du fond sableux calculée à partir de l'équation de conservation du sédiment (équation 4.7).

Le module sédimentaire permet de prendre en compte plusieurs formulations. La première approche consiste à utiliser une formule de type énergétique complète. L'une des plus utilisées est celle de *Bailard* (1981). L'utilisation de ce type de formule devient problématique lorsqu'on veut étudier la dynamique des barres sur des échelles de temps assez grandes (*i.e.*, quelques semaines à quelques mois). En effet, la croissance des corps sableux n'est pas amortie par des termes diffusifs et le modèle plante typiquement après quelques jours lorsque les barres sortent de l'eau et commencent à avoir des pentes trop raides (*e.g.*, ***Castelle et al.*** 2006a, *Drønen and Deigaard* 2007, *Smit et al.* 2008).

Encore une fois, il faut rappeler que l'on peut facilement augmenter le degré de complexité de la représentation de chaque processus hydro-sédimentaire, et ce même si l'on sait que la totalité de ces processus, certains étant pourtant à priori très importants, ne sont de toute façon pas pris en compte [3]. Trop complexifier les formules en

2. Même si les processus physiques hydro-sédimentaires mis en jeu dans le développement des instabilités sont différents (*swash*, tri sédimentaire, dérive littorale, etc.), *Coco and Murray* (2007) étendent ce changement de paradigme scientifique des théories de motifs vers l'auto-organisation à d'autres corps sableux comme les croissants de plage (*e.g.*, *Holland and Holman* 1996), les instabilités du trait de côte (*e.g.*, *Ashton and Murray* 2006a) et les *sorted bedforms* sur le plateau continental interne (*Coco et al.* 2007).

3. Les formules classiques de transport sédimentaires ne prennent par exemple pas en compte l'in-

modélisation morphodynamique aboutit à un modèle qui s'apparente à une grosse boîte noire, de laquelle il n'est pas possible d'identifier les processus et interactions moteurs des évolutions morphologiques. Ce type de modèle peut reproduire des évolutions morphologiques similaires aux observations de terrain tout en ayant une description fausse de toute l'hydrodynamique sédimentaire, ce qui devient dangereux pour les interprétations.

Une approche alternative doit donc être mise en oeuvre lorsqu'on veut réaliser des simulations sur des temps longs. Une solution efficiente et relativement facile à mettre en place est de faire l'hypothèse que le transport sédimentaire vers le bord induit par les non-linéarités (*e.g.*, *Drake and Calantoni* 2001, *Hoefel and Elgar* 2003, *Ruessink et al.* 2007b, *Grasso et al.* 2011) et celui vers le large induit par le courant de retour (*e.g.*, *Hoefel and Elgar* 2003, *Henderson et al.* 2004, *Ruessink et al.* 2007b) sont en équilibre avec le transport sédimentaire par effet de pente pour un profil de plage Z_f^0. Autrement dit, on fait ici l'hypothèse que les structures tridimensionnelles évoluent bien plus vite que les échelles de temps associées aux évolutions du profil moyen[4]. En outre, on peut faire l'hypothèse que l'hydrodynamique joue un rôle dominant de manière qu'une description très complexe (mais toujours incomplète) du transport sédimentaire (*e.g.*, *Van Rijn* 1989) n'est pas nécessaire pour explorer les mécanismes physiques gouvernant la dynamique des corps sableux en zone de déferlement (*e.g.*, *Schielen et al.* 1993, *Falqués et al.* 1996). Cette approche est utilisée en analyse de stabilité linéaire (*e.g.*, *Falqués et al.* 1996; 2000, *Calvete et al.* 2005) et l'est depuis plus récemment dans l'analyse de stabilité non-linéaire (*e.g.*, *Garnier et al.* 2006; 2008; 2010). Pour certains de nos travaux, nous avons donc adopté cette approche en utilisant la formulation suivante :

$$\vec{Q}_s = \alpha(\overline{\overline{|\vec{u}_b(t)|^3 \vec{u}_b(t)}} - \gamma u_{rms} \vec{\nabla} Z) \tag{4.11}$$

où $\vec{u}_b(t) = \vec{U} + (u_{rms}\cos\omega t)\vec{e}_k$ est la vitesse totale du fluide au fond et la notation $\overline{\overline{()}}$ définit la moyenne temporelle sur une période plus grande que celle des vagues. Le premier terme de l'équation (4.11) est un terme advectif (similaire au terme de transport par suspension de *Bailard* 1981) et le deuxième est un terme d'effet de pente par rapport au profil d'équilibre Z_f^0 qui introduit une diffusion morphodynamique et surtout une saturation de la croissance des structures tridimensionnelles. **Le modèle morphodynamique non-linéaire développé ici est sur le plan international le seul à pouvoir simuler la formation, l'évolution non-linéaire et la saturation des barres sableuses de déferlement tridimensionnelles ainsi que l'évolution du trait de côte (*megacusps*) associée** (le seul autre modèle pouvant simuler la saturation des barres, co-développé à l'UPC en Espagne et l'Université de Nottingham (UK), considère un mur au niveau de la ligne d'eau et ne prend pas en compte la marée).

jection de la turbulence sur le fond qui joue grandement sur la remise en suspension du sédiment en zone de déferlement (***Grasso et al.*** 2012), ni le transport en *Sheet Flow* de manière convenable, la compaction du sable au niveau de la barre de déferlement, etc.

4. Cette hypothèse est vraie pour les conditions de houle modérément énergétiques : pour les vagues peu énergétiques (pas ou peu de déferlement), on a typiquement une migration lente de la barre vers le bord et l'absence de développement tridimensionnel ; pendant les épisodes de tempête on observe une migration rapide de la barre vers le large avec une bidimensionnalisation de la barre. Ainsi, dans les 2 cas l'hypothèse mentionnée n'est pas valable et celle-ci doit être utilisée pour des conditions de houles modérément énergétiques et pour de faible changements de régimes de houle en termes de hauteur significative H_s.

4.2.2 Outils d'analyse de l'évolution morphodynamique

Deux types d'analyse ont été réalisés afin de quantifier l'évolution des barres sableuses :

Analyse 'locale'

L'analyse 'locale' consiste dans un premier à extraire un profil *longshore* du fond sableux représentatif de la morphologie tridimensionnelle des barres sableuse. Typiquement, on extrait le profil entre la crête de la barre et le trait de côte en $y = y_c$. L'étude de l'évolution spatio-temporelle $Z_b(x,t) = Z_f(x, y = y_c, t)$ permet alors d'appréhender la morphodynamique des barres sableuses. On peut ensuite quantifier la longueur d'onde du système à un instant t en utilisant la transformée de Fourier. Toutefois, comme nous le verrons plus tard, nos simulations sont souvent caractérisées par des longueurs d'onde qui présentent une variabilité significative le long de la plage. Cette variabilité ne pouvant pas être capturée par l'analyse de Fourier classique, nous avons plutôt utilisé une analyse en ondelette. La transformée en ondelette continue $W_n^z(s)$ discrète est définie comme la convolution d'une séquence discrète du profil *longshore* de plage z_n, ($n = 0,...,N-1$) avec une ondelette mère ψ_0 :

$$W_n^z(s) = \left(\frac{\mathrm{dz}}{s}\right)^{1/2} \sum_{n'=0}^{N-1} z_{n'} \psi_0^* \left(\frac{(n'-n)\mathrm{dz}}{s}\right) \tag{4.12}$$

où dz est l'espacement (constant) en z, n est la coordonnée *longshore* et s est l'échelle *longshore* (*Torrence and Compo* 1998) et $*$ est le complexe conjugué. De plus, pour étudier dans un système double-barre comment les barres peuvent avoir des comportements couplés ou découplés, nous avons utilisé l'extension bi-variée de la transformée en ondelette $R_n^2(s)$ (*Jevrejeva et al.* 2003, *Grinsted et al.* 2004) :

$$R_n^2(s) = \frac{|S(s^{-1}W_n^{zy}(s))|^2}{S(s^{-1}W_n^z(s)).S(s^{-1}W_n^y(s))} \tag{4.13}$$

où S est un opérateur de lissage détaillé dans *Torrence and Webster* (1999).

Analyse 'globale'

Contrairement à l'analyse 'locale', l'analyse globale consiste à intégrer les variables de sortie du modèle sur l'ensemble du domaine. Ainsi on définit la notation $\bar{()}$ comme la moyenne d'une fonction donnée $f = f(x,y,t)$ sur l'ensemble du domaine :

$$\bar{f}(t) = \frac{1}{L_x L_y} \int_0^{L_x} \int_0^{L_y} f(x,y,t) dx dy \tag{4.14}$$

où L_x et L_y sont respectivement la longueur *longshore* et *cross-shore* du domaine. En utilisant la définition de *Garnier et al.* (2010), le taux de croissance global des structures tridimensionnelles, σ, est donné par :

$$\sigma(t) = \frac{1}{2E_z(t)^2} \frac{dE_z(t)^2}{dt} \tag{4.15}$$

avec E_z, qui est une mesure du développement des instabilités, qui s'écrit :

$$E_z(t) = \sqrt{\overline{Z(x,y,t)^2}} \tag{4.16}$$

Une autre variable qui peut être considérée est la migration globale *longshore* instantanée V_L qui s'écrit (*Vis-Star et al.* 2008) :

$$V_L = -\frac{1}{\overline{(\partial Z/\partial x)^2}}\overline{\frac{\partial Z}{\partial x}\frac{\partial Z}{\partial t}} \tag{4.17}$$

L'analyse globale permet donc de quantifier l'évolution temporelle du développement des structures tridimensionnelles et leur migration le long de la plage.

4.3 Modélisation numérique et théorique des barres sableuses tridimensionnelles

Le modèle morphodynamique décrit ci-dessus a été utilisé dans de nombreuses études de dynamique des plages. Pour être concis, nous ne décrirons pas les études menées sur l'application du modèle au système double barre aquitain (***Castelle et al.*** 2006a) ni sur l'impact de la marée sur l'évolution des systèmes barre/chenal dans le cadre du stage de Master 2 de Benjamin Dubarbier (***Dubarbier and Castelle*** 2011), ou l'analyse de stabilité linéaire des systèmes double-barre (***Brivois et al.*** 2012).

4.3.1 Le couplage morphologique : théorie des motifs ou théorie d'auto-organisation ?

Comme nous l'avons vu précédemment, un récent changement de paradigme de la théorie des motifs vers les théories d'auto-organisation a eu lieu au sein de la communauté scientifique internationale. Le long des plages à double barre, il est admis que la dynamique de chacune des deux barres est contrôlée uniquement par les mécanismes d'auto-organisation qui émergent de la rétroaction positive entre les vagues, les courants induits et l'évolution du fond résultant des flux sédimentaires. Ceci est à première vue conforté par des observations récurrentes qui ne montrent l'immense majorité du temps aucune relation de rythmicité entre les deux barres (*e.g.*, *Hom-ma and Sonu* 1962, *Goldsmith et al.* 1982, *Bowman and Goldsmith* 1983, ***Lafon et al.*** 2005), justifiant souvent l'étude de la dynamique de la barre interne en ignorant volontairement la présence et la morphodynamique de la barre externe (*e.g.*, ***Sénéchal et al.*** 2009, *Poate et al.* 2009).

Toutefois, certaines observations montrent un couplage significatif entre la morphologie de la barre interne et la barre externe (*e.g.*, *Sonu* 1973, *Van Enckevort and Wijnberg* 1999, ***Castelle et al.*** 2007a, *Ruessink et al.* 2007a, *Quartel* 2009). En utilisant l'imagerie vidéo, *Ruessink et al.* (2007a) ont montré qu'en épisode post-tempête, la barre interne le long de la Gold Coast (Australie) passait d'un comportement découplé à un comportement couplé avec la barre externe en réponse à la tridimensionnalisation de la barre externe. Cette réponse était alors supposée être gouvernée par les circulations forcées par des variabilités *longshore* de la hauteur des vagues induites par la réfraction et le déferlement des vagues au-dessus de la barre externe en croissant, hypothèse la première fois formulée dans ***Castelle and Bonneton*** (2006b).

Dans ***Castelle et al.*** (2010b), nous avons exploré cette hypothèse en partant de cas idéalisés de systèmes double barre caractérisés par une barre externe en croissant de différentes longueur d'onde λ, amplitude verticale D_v et amplitude $cross-shore$ D_c (Figure 4.3) soumises à différentes hauteurs significatives de vagues H_s. L'ensemble des simulations ont été réalisées pour des houles frontales et avec la formulation énergétiques de *Bailard* (1981) pour les flux sédimentaires (*i.e.*, pas de saturation de

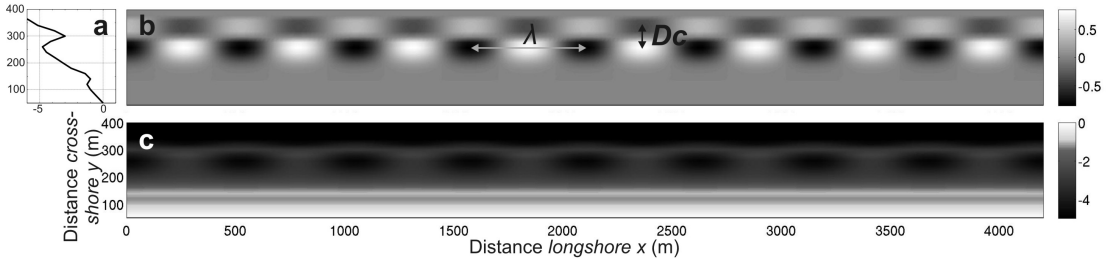

FIGURE 4.3 – *Exemple de bathymétrie initiale idéalisée d'un système double barre utilisé dans nos simulations avec (a) le profil moyen avec (b) superposée une séquence de cornes (bosses) et de baies (trous) donnant (c) une barre externe en croissant, ici avec λ = 525 m, D_c = 60 m et D_v = 1.7 m (**Castelle et al.** 2010b).*

la croissance des systèmes barre/chenal). Nous avons montré que **les contributions respectives de la réfraction des vagues, de la localisation et de l'intensité du déferlement au-dessus de la barre externe entrainent une modulation spatiale du champ de vagues au-dessus de la barre interne qui, en retour, forcent des circulations et des structures sableuses tridimensionnelles couplées à la morphologie plus au large.** Nous avons ainsi dépeint un mécanisme de couplage morphologique pouvant expliquer, en partant pourtant de cas idéalisés, la formation des couplages les plus observés jusqu'à présent le long des plages dans le monde.

La Figure 4.4 montre les 3 types de couplages qui ont pu être simulés : (1) un couplage en phase (Figure 4.4a, observé par exemple dans *Quartel* 2009) favorisé par les houles peu énergétiques (ne déferlant pas au-dessus de la barre externe) et une faible amplitude verticale D_v des croissants, (2) un couplage à la demi-longueur d'onde de la barre externe (Figure 4.4b, observé par exemple dans ***Castelle et al.*** 2007a, voir aussi Figure 3.2) observé en augmentant légèrement H_s, λ ou D_v et (3) un couplage en opposition de phase (Figure 4.3c, observé par exemple dans ***Castelle et al.*** 2007a, *Ruessink et al.* 2007a, ,voir aussi Figure 3.2) en continuant d'augmenter H_s, λ ou D_v et apparaissant typiquement lorsqu'un déferlement bathymétrique significatif

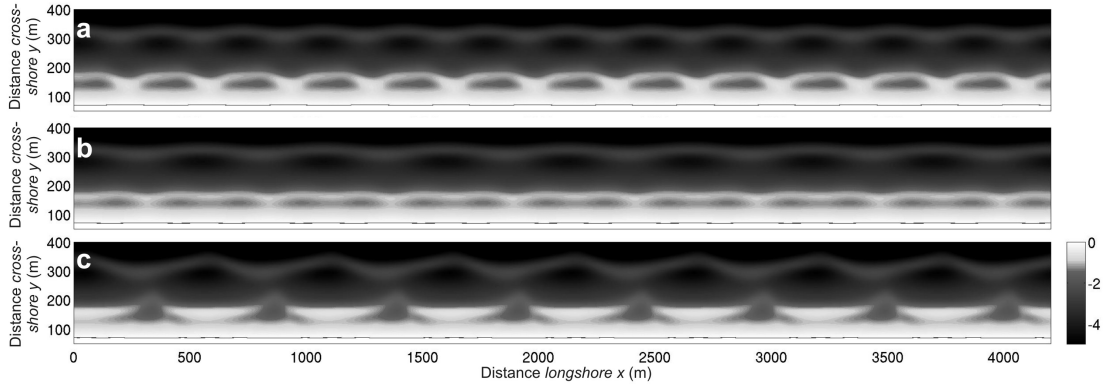

FIGURE 4.4 – *Exemple de couplages morphologiques simulés. (a) Couplage en phase à t = 7 jours en partant à t = 0 d'une barre en croissant avec λ = 350 m, D_v = 60 m et D_v = 1.35 m et des vagues frontales avec H_s = 0.8 m. (b) Couplage à la demi longueur d'onde à t = 7 jours en partant à t = 0 d'une barre en croissant avec λ = 525 m, D_v = 60 m et D_v = 1.7 m et des vagues frontales avec H_s = 0.8 m. (c) Couplage en opposition de phase à t = 3 jours en partant à t = 0 d'une barre en croissant avec λ = 525 m, D_v = 60 m et D_v = 1.7 m et des vagues frontales avec H_s = 1.2 m (**Castelle et al.** 2010b).*

intervient au-dessus des cornes de la barre externe. **Les couplages morphologiques observés dans la nature ont pu être simulés et les conditions hydrodynamiques et la morphologie de la barre externe donnant lieu à ces couplages ont été quantifiées.** A noter qu'un autre type de couplage a été récemment documenté (*Price and Ruessink* in press) et semble être très fréquent sur les plages de la Gold Coast (Australie). Nous venons récemment d'expliquer le mécanisme à l'origine de ce couplage en présence de houle oblique (***Price et al.*** soumis). Celui-ci n'est pas détaillé dans ce mémoire.

Ces couplages ne sont que très rarement observés ce qui pourrait suggérer finalement que ce mécanisme est peu important. Nous avons montré que ce n'était pas le cas (***Castelle et al.*** 2010c). En effet, un résultat encore plus important, issu d'une autre série de simulations et à travers une analyse en ondelettes, est que l'immense majorité du temps les mécanismes d'auto-organisation et de couplage morphologique coexistent. La Figure 4.5 montre un exemple de simulation avec une barre externe en croissant régulière, qui contraste avec une barre interne présentant un système barre/chenal très irrégulier. Ainsi, le fait que la barre interne présente dans l'immense majorité des observations une rythmicité beaucoup plus irrégulière que celle de la barre externe émerge en fait de la superposition des mécanismes d'auto-organisation et de couplage morphologique (une partie de cette analyse est montrée en Figure 4.6). Cette irrégularité de la barre interne qui contraste avec la régularité de la barre externe était jusqu'à présent supposée justifier dans la littérature qu'il n'y avait pas de couplage entre les 2 systèmes, sans toutefois justifier ce contraste dans la régularité des longueurs d'onde. Cela justifiait que, sur le terrain, beaucoup d'études se focalisent sur une entité morphologique (par exemple la barre interne) en ignorant volontairement la présence et la dynamique des autres entités morphologiques. **Ces résultats montrent que la dynamique des barres internes ne doit pas être étudiée en déconnection de celle de la barre externe, comme cela a été pourtant fait jusqu'à présent sur de nombreux sites. Ce constat s'applique également aux autres corps sableux comme les formes géologiques au large des barres ou les oscillations du trait de côte.** De plus, en partant d'un système double barre bidimensionnel, caractéristique d'un épisode de tempête, nous avons reproduit le comportement découplé passant progressivement à un comportement couplé du système double barre similaire aux observations de *Ruessink et al.* (2007a).

Une description complète de cette étude sur le rôle des couplages morphologiques dans les systèmes à double barre est présentée dans ***Castelle et al.*** (2010b) et ***Castelle et al.*** (2010c).

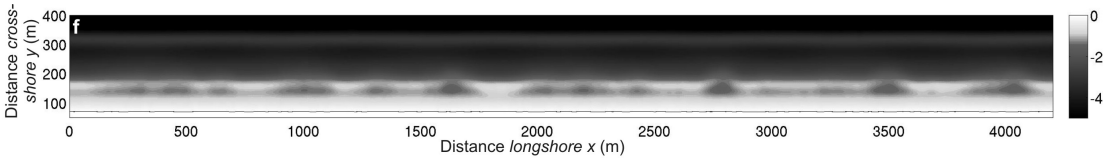

FIGURE 4.5 – *Evolution de la bathymétrie à t = 6 jours en partant à t = 0 d'une barre externe en croissant peu développée soumises à des vagues frontales avec H_s = 0.8 m. La morphologie montre un système de barre/chenal avec une forte variabilité longshore (**Castelle et al.** 2010b) qui est le résultat de la superposition des mécanismes d'auto-organisation et de couplage morphologiques dépeints par l'analyse en ondelette en Figure 4.6.*

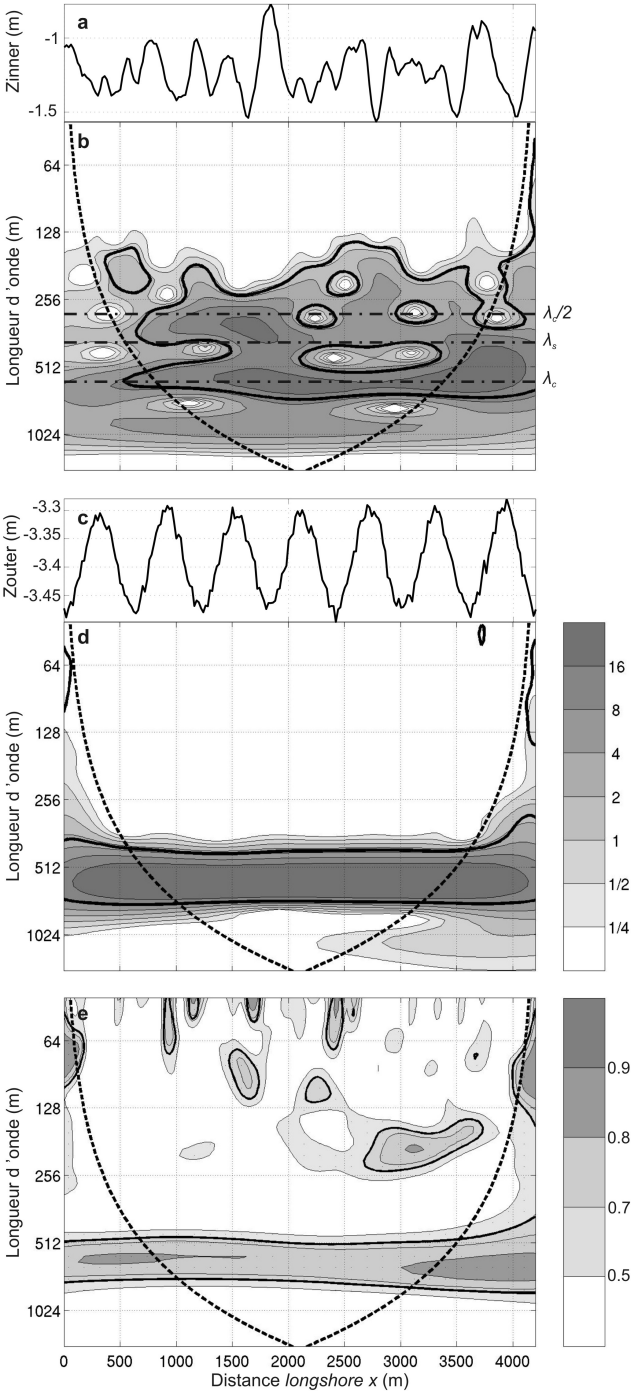

FIGURE 4.6 – *Analyse en ondelette de la morphologie du système à double barre montrée en Figure 4.5. (a) Profil longshore représentatif de la morphologie de la barre interne Z_{inner} ; (b) transformée en ondelette $W_n^z(s)$ de Z_{inner}, λ_c et λ_s étant respectivement les longueur d'onde du couplage et de l'auto-organisation ; (c) Profil longshore représentatif de la morphologie de la barre externe Z_{outer} ; (d) transformée en ondelette $W_n^z(s)$ de Z_{outer} et (e) extension bi-variée de la transformée en ondelette $R_n^2(s)$ entre Z_{outer} et Z_{inner}.*

4.3.2 Rôle de l'hypothèse classique du forçage stationnaire : vers une réconciliation des modèles et des observations ?

Ces dernières années, un nombre important d'études sur l'évolution haute-fréquence des barres sableuses ont été réalisées grâce à l'émergence de l'imagerie vidéo (*e.g.*, *Van Enckevort and Ruessink* 2003, *Holman et al.* 2006, *Turner et al.* 2007, *Ruessink et al.* 2007a, ***Almar et al.*** 2010, *Price and Ruessink* 2011, *Gallop et al.* 2011). Certaines de ces études ont essayé d'identifier des relations entre la longueur d'onde ou la migration *longshore* des chenaux avec les caractéristiques des régimes de houle moyens auxquels la plage est exposée. Ces études ont toutes montré de mauvaises relations. Ainsi les prédictions données par l'analyse de stabilité linéaire ou l'analyse de stabilité non-linéaire ne sont généralement pas en accord avec les observations, suggérant que les modèles seraient faux. Toutefois, il est important de noter que les travaux en modélisation n'ont été réalisés que pour des régimes de houle constants. C'est le cas pour l'analyse de stabilité linéaire qui est limitée à la croissance initiale des structures et, par conséquent, est limitée à une condition de vagues [5]. Il est beaucoup plus surprenant de constater que toutes les études d'analyse de stabilité non-linéaire ont été réalisées avec des forçages de vagues constants (*e.g.*, *Damgaard et al.* 2002, *Reniers et al.* 2004, *Drønen and Deigaard* 2007, *Smit et al.* 2008, ***Castelle et al.*** 2006a, *Garnier et al.* 2006; 2008; 2010, ***Castelle et al.*** 2010b;c, *Tiessen et al.* 2011) alors que ce type d'approche est pourtant appropriée pour la prise en compte de forçages de vagues instationnaires [6].

Ces constatations ont motivé l'étude de l'impact des forçages de vagues instationnaires sur la dynamique non-linéaire des systèmes barre/chenal. Ces travaux, publiés dans ***Castelle and Ruessink*** (2011), se sont basés sur l'utilisation de notre modèle morphodynamique non-linéaire avec la paramétrisation donnée dans l'équation (4.11) afin de suivre la formation, la dynamique non-linéaire et la saturation des systèmes barre/chenal. Dans un premier temps, des simulations avec des forçages stationnaires ont été réalisés. La Figure 4.7 montre un exemple d'évolution des systèmes barre/chenal avec la série temporelle du taux de croissance global σ et E_z pour un forçage stationnaire avec H_s = 1 m, T_p = 10 s et θ = 0. On remarque qu'après le régime linéaire (σ maximal et quasiment constant), certains chenaux s'apparient pendant le régime non-linéaire afin de s'auto-organiser dans une longueur d'onde la plus régulière possible jusqu'à la saturation du système ($\sigma \approx 0$ pour environ $t >$ 10 jours). Un ensemble de simulations avec forçage stationnaire (pour un H_s, T_p et θ donné) a été réalisé. Les résultats sont en accord avec les études précédentes et ont ainsi supporté l'utilisation de ce modèle pour des forçages instationnaires.

Plusieurs dizaines de simulations avec forçage instationnaire ont été réalisées et analysées. En particulier, ces simulations ont montré que les variabilités dans l'angle d'incidence impactent fortement les longueurs d'onde et le taux de migration *longshore* moyens. La Figure 4.8 montre 4 exemples de simulations avec un angle d'incidence instationnaire (variabilités avec une période de 4 jours et d'amplitude de 4°, Figure 4.8e) et une forme sinusoïdale (Figure 4.8a) en dents de scie (Figure 4.8b), en demi-dent de scie/sinusoïde (Figure 4.8c) et en créneaux (Figure 4.8c), toutes avec une moyenne temporelle $\bar{\theta} = 0$. Ces simulations montrent plusieurs résultats très im-

5. Une exception est l'étude de *Tiessen et al.* (2010) qui a combiné l'analyse de stabilité linéaire et un algorithme approprié identifiant les résultats du modèle les plus représentatifs physiquement, leur permettant d'appliquer l'analyse de stabilité linéaire à des changements de régime de houle.

6. Une exception est l'étude de *Smit et al.* (2005) publiée dans un acte de congrès, et qui était limitée à un très petit nombre de simulations. Une étude postérieure à la nôtre (***Castelle and Ruessink*** 2011) a ensuite confirmé nos résultats théoriques (*Smit et al.* 2012).

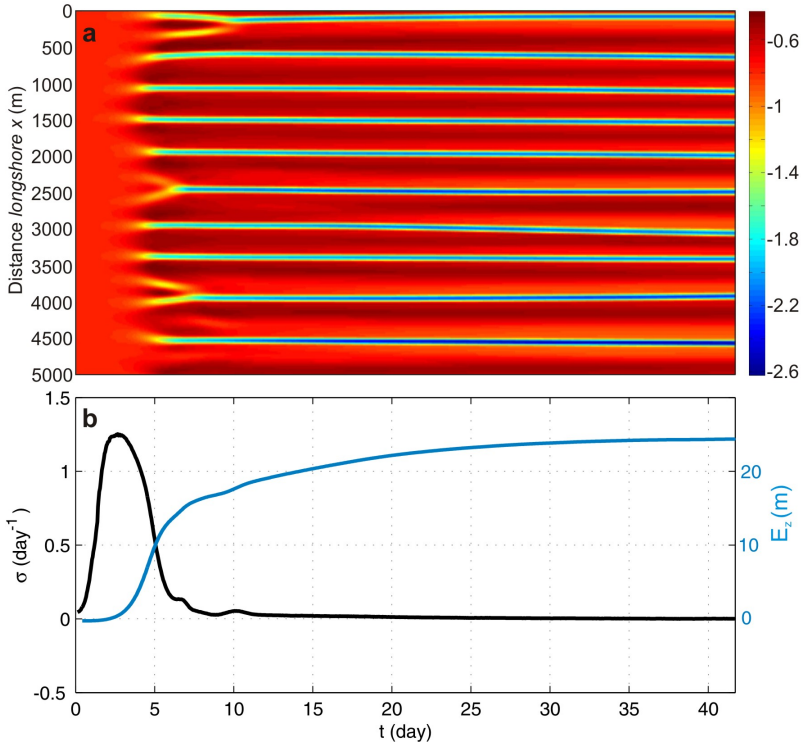

FIGURE 4.7 – *Simulation de la formation, de l'évolution non-linéaire et de la saturation d'un système barre chenal pour un forçage de vagues stationnaires avec $H_s = 1m$, $Tp = 10\ s$ et $\theta = 0$ avec (a) l'évolution temporelle du profil de longshore de plage Z_b et (b) du taux de croissance global σ et la densité d'énergie potentielle des perturbations E_z (**Castelle and Ruessink** 2011).*

portants : (1) un équilibre dynamique des système barre/chenal est observé pour l'ensemble des simulations avec θ instationnaire ; (2) les système barre/chenal sont systématiquement moins développés pour les forçages instationnaires que pour le forçage stationnaire (Figure 4.8f) ; (3) le forçage instationnaire excite le comportement non-linéaire des barres puisque, par rapport à la simulation avec forçage stationnaire (Figure 4.7), on observe une augmentation du nombre d'appariements de chenaux et surtout on a l'apparition de scissions (les chenaux apparaissant au milieu des barres ayant une longueur *longshore* plus importante que celles du reste du domaine, Figures 4.8a-c) ; (4) les longueurs d'onde moyennes sont différentes de celles obtenues avec le forçage stationnaire puisqu'on observe au cours du temps 10 à 13 chenaux pour le forçage instationnaire (Figures 4.8a-d), alors que 10 chenaux sont observés pour le forçage stationnaire (Figure 4.7a) ; (5) les longueur d'onde des systèmes ont systématiquement une variabilité *longshore* plus prononcée que pour le forçage stationnaire, ce qui est en accord avec les observations des barres sableuses naturelles ; (6) lorsque la variabilité de θ est asymétrique (Figures 4.8b et c), on observe une migration net des chenaux même si la moyenne temporelle de θ est nulle.

Ces travaux théoriques ont des implications importantes. En effet nous avons montré que l'instationnarité dans le forçage des vagues était critique pour le développement des systèmes barre/chenal en termes de morphologie, de dynamique non-linéaire (appariements et scissions des systèmes), de migration *longshore* et de longueur d'onde. Nos simulations avec forçage instationnaire montrent une forte variabilité *longshore* qui est en accord avec les observations de terrain et contraste avec les résultats obtenus jusqu'à présent dans la littérature avec un forçage stationnaire. Ainsi, **nos simulations réconcilient l'approche de modélisation numérique et la**

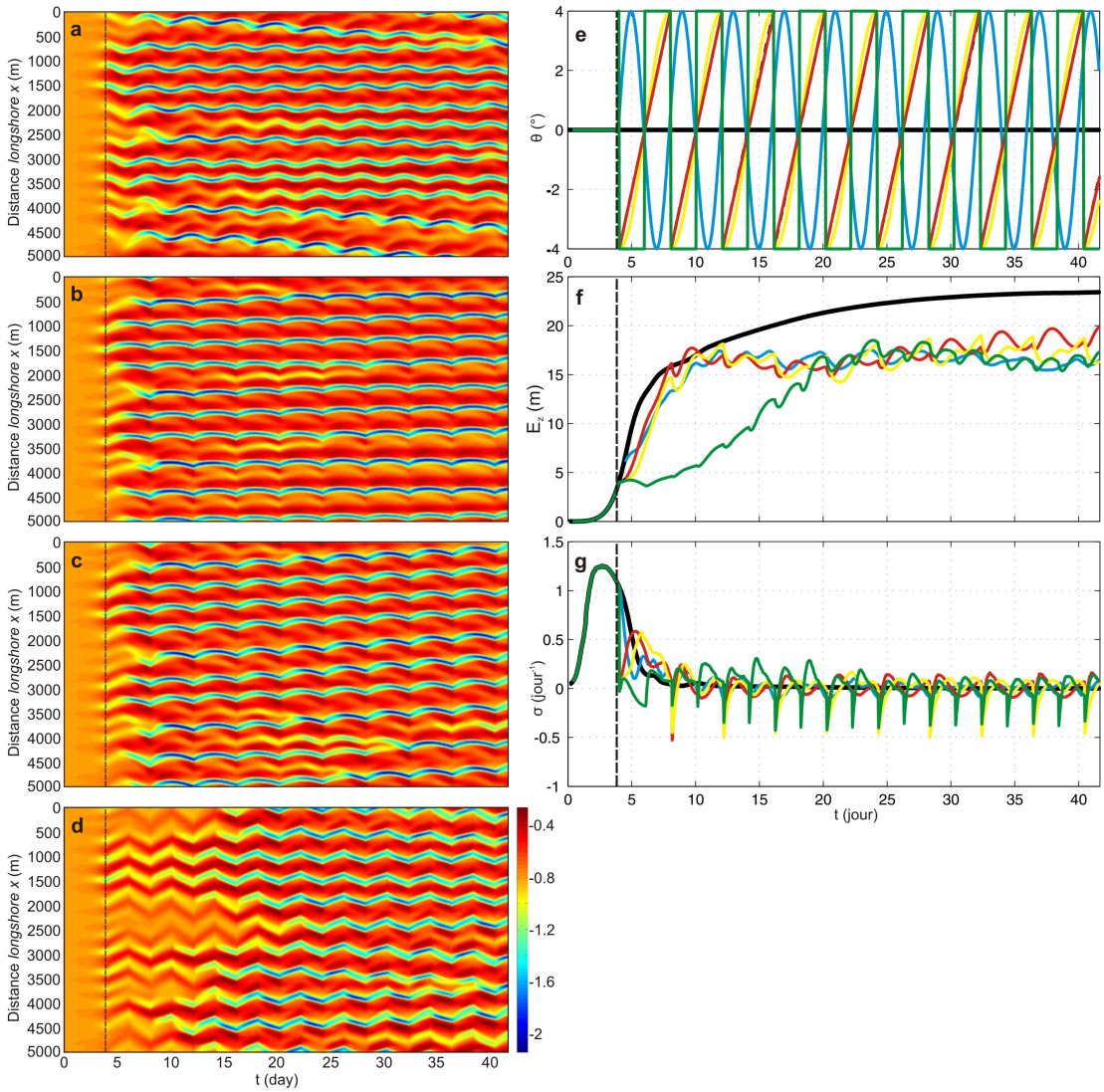

FIGURE 4.8 – *Influence du forçage instationnaire en angle d'incidence θ sur l'évolution non-linéaire des systèmes barre/chenal. La variabilité en θ, qui a une moyenne nulle, a une amplitude de 4° et une période de 4 jours. La hauteur significative des vagues H_s = 1 m et la période pic T_p = 10 s sont instationnaires. (a-c) Evolution temporelle du profil longshore de plage Z_b et série temporelle correspondante (e) de l'angle d'incidence θ, (f) de la densité d'énergie potentielle des perturbations E_z et (g) du taux de croissance global σ. Variabilité de θ sinusoïdale (panel a, en vert dans les panels (e-g)), en dents de scie (panel b, en rouge dans les panels (e-g)), en demi-dent de scie/sinusoïde (panel c, en jaune dans les panels (e-g)) et en créneaux (panel d, en vert dans les panels (e-g)).*

théorie de l'auto-organisation avec les observations par imagerie vidéo de la dynamique des systèmes barre/chenal et de barres en croissant et montrent que la prise en compte de l'instationnarité dans le forçage des vagues est crucial pour prédire les caractéristiques (morphologie, longueur d'onde et migration) des barres sableuses tridimensionnelles.

Une description extensive de cette étude sur le rôle des variabilités temporelles du forçage des vagues sur la dynamique des systèmes barre/chenal est donnée dans ***Castelle and Ruessink*** (2011).

4.3.3 Impact d'une anomalie bathymétrique sur la dynamique non-linéaire des chenaux de vidange

Dans le cadre de notre étude de l'impact d'une barre externe en croissant sur la dynamique du système barre/chenal de la barre interne (***Castelle et al.*** 2010b;c), nous avons montré que la dynamique d'une entité morphologique du système plage peut être en partie gouvernée par le comportement d'une autre entité morphologique. Ainsi, il semble qu'il faille considérer l'ensemble des entités morphologiques du système plage si l'on veut comprendre la morphodynamique du système composite. Immédiatement au large des systèmes de barres sableuses, au niveau du plateau interne, on peut trouver des corps sédimentaires tridimensionnels naturels comme des *sorted bedform* (*e.g.*, *Murray and Thieler* 2004, *Coco et al.* 2007) ou des canyons (*e.g.*, *Long and Ozkan-Haller* 2005, *Gaudin et al.* 2006), ou bien des corps formés par la main de l'homme comme, par exemple, les dépôts de dragage ou des fosses creusées pour des extractions de sable (*e.g.*, *Benedet and List* 2008). Des observations récentes montrent que ces morphologies peuvent impacter la variabilité *longshore* du trait de côte (*e.g.*, *Bender and Dean* 2003, *McNinch* 2004, *Schupp et al.* 2006) et les circulations induites plus près du rivage en zone de déferlement (*e.g.*, *Shepard and Inman* 1950, *Long and Ozkan-Haller* 2005, *Dalrymple et al.* 2011). Aucune étude n'a toutefois tenté d'explorer le rôle de ces anomalies bathymétriques sur la morphodynamique de la plage.

Dans ***Castelle et al.*** (2012) nous avons utilisé la modélisation numérique non-linéaire pour étudier l'impact d'une anomalie bathymétrique sur la morphodynamique des plages. Nous avons utilisé le modèle sur plusieurs dizaines de bathymétries caractérisées par la présence d'une anomalie bathymétrique ayant la forme d'une gaussienne de hauteur A (comprise en -1.5 et 1.5 m), à une distance d_b du trait de côte (Figure 4.9). Nous avons utilisé des forçages de vagues stationnaires

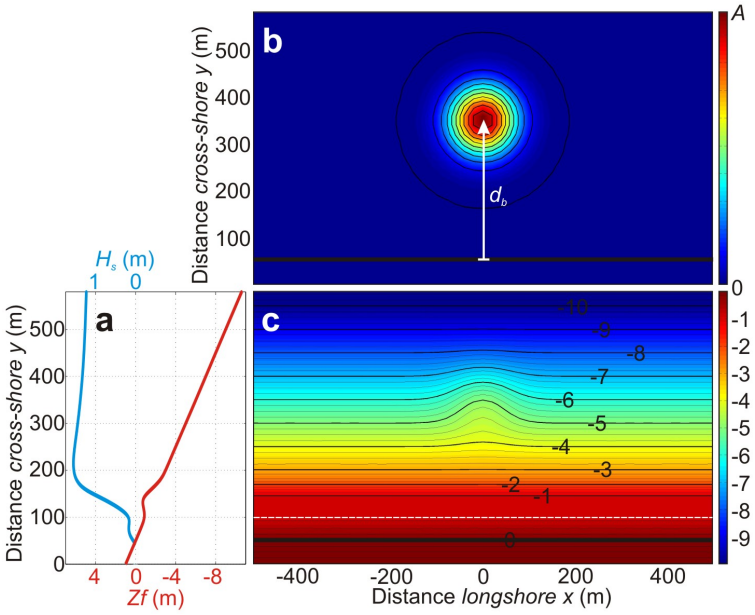

FIGURE 4.9 – *(a) Profil initial d'équilibre (rouge) avec la distribution spatiale de H_s (avec au large H_s = 1.2 m, T_p = 10 s et θ = 0). (b) Zoom à -500 m < x < 500 m de l'anomalie bathymétrique de hauteur A et située à une distance d_b du trait de côte. (c) Bathymétrie initiale d'équilibre (basic state) résultante avec la ligne blanche pointillée montrant la localisation du profil longshore de plage Z_b (**Castelle et al.** 2012).*

avec H_s = 1.2 m et T_p = 10 s avec plusieurs angle d'incidence des vagues θ. Au total, une centaine de simulations ont été réalisées et analysées par l'analyse globale et l'-analyse en ondelettes afin de discriminer le comportement des systèmes barre/chenal en amont et en aval (par rapport au sens de la dérive littorale dans le cas de houles oblique $\theta \neq 0$) de l'anomalie bathymétrique.

La Figure 4.10 montre un exemple de zoom à -2000 m $< x <$ 2000 m de l'évolution temporelle de la bathymétrie et des circulations induites par les vagues pour θ = 1.5° pour une anomalie de la bathymétrie au large caractérisée par A = - 1 m (trou) et d_b = 350 m. Il est frappant ici que les systèmes barre/chenal en amont ($x < 0$) et en aval ($x > 0$) de l'anomalie ont un comportement très contrasté. En effet, les systèmes barre/chenal ont une longueur d'onde plus grande et une migration plus lente en aval que ceux en amont de l'anomalie bathymétrique. Ceci fut systématiquement le cas pour les houles obliques, et ce, quelle que soit la valeur de A. La Figure 4.11 montre l'analyse en ondelette correspondant du profil *longshore* de la plage Z_b à saturation des instabilités (t = 9.73 jours). L'analyse montre une longueur d'onde en amont $\bar{\lambda}_m^u$ = 525 m plus petite qu'en aval $\bar{\lambda}_m^d$ = 742 m (la même analyse a été réalisée pour les taux de migration avec l'analyse globale).

Ce type d'analyse a été réalisé systématiquement pour la centaine de simulations effectuées dans cette étude. En résumé, nous avons démontré par la modélisation morphodynamique non-linéaire que la présence d'une anomalie bathymétrique affecte considérablement la formation et la dynamique non-linéaire des systèmes de barres sableuses tridimensionnelles. En présence de vagues obliques, un chenal de vidange forcé par la variabilité bathymétrique au large est systématiquement observé

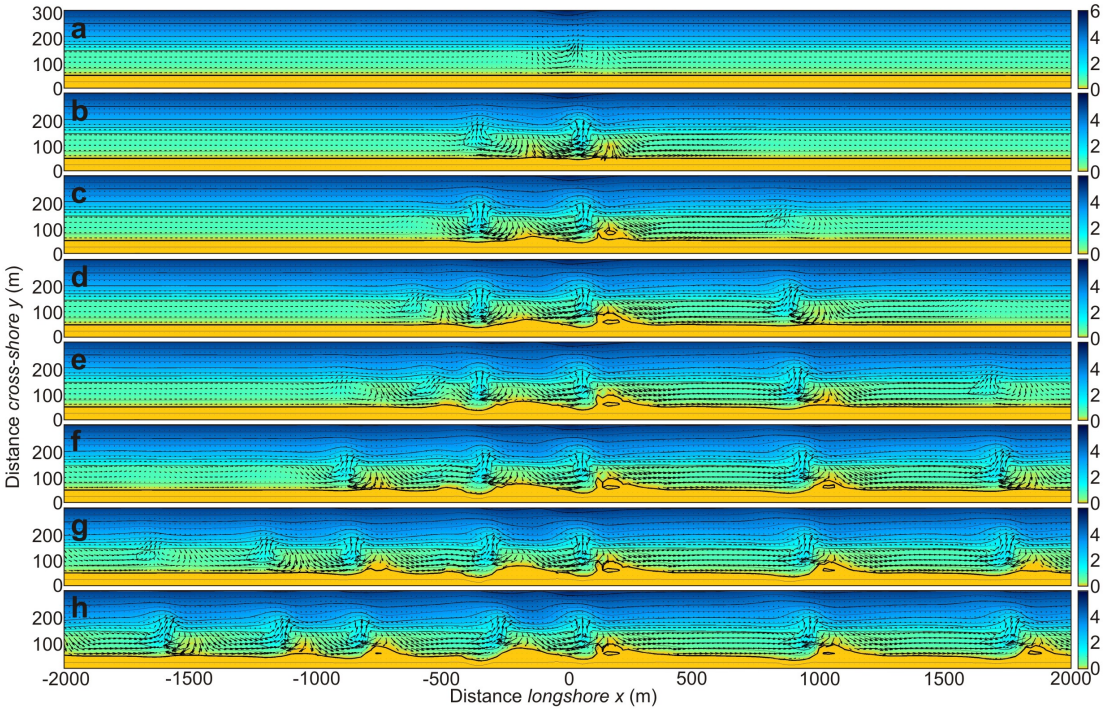

FIGURE 4.10 – *Zoom à -2000 m $< x <$ 2000 m et 0 $< y <$ 300 m la morphologie de la plage avec superposées les circulations induites par les vagues pour une forçage de vagues stationnaire avec H_s = 1.2 m, T_p = 10 s et θ = 1.5° et une anomalie de la bathymétrie au large centrée en x = 0 et caractérisée par A = - 1m (trou) et d_b = 350 m. (a) t = 0, (b) t = 1 jours, (c) t = 2 jours, (d) t = 3 jours, (e) t = 4 jours, (f) t = 5 jours, (g) t = 6 jours et (h) t = 7 jours (**Castelle et al.** 2012).*

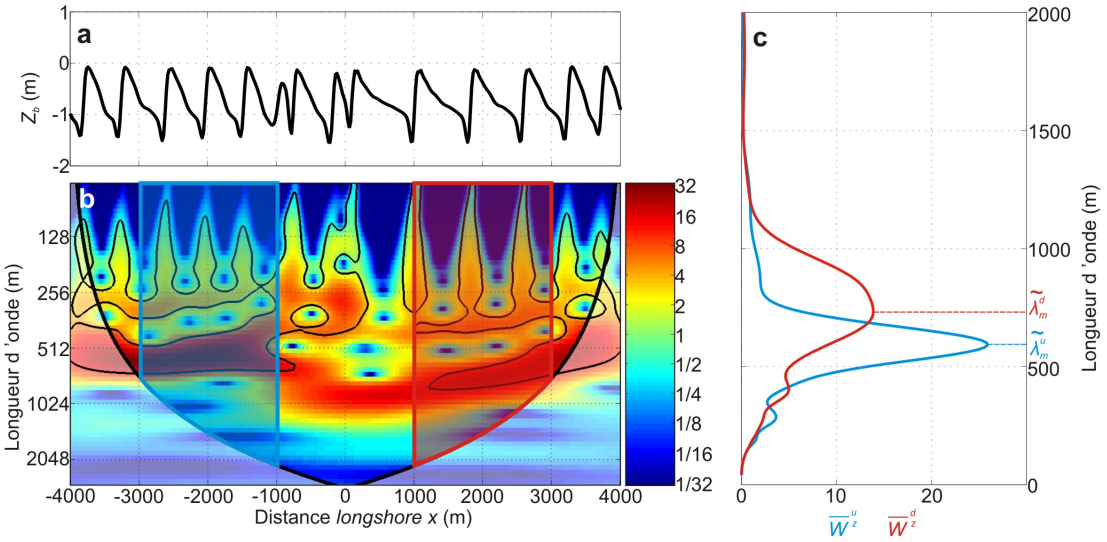

FIGURE 4.11 – *Profil longshore de plage Z_b à saturation (t = 9.73 jours) pour H_s = 1 m, T_p = 10 s et θ = 1.5° pour une simulation débutant avec une anomalie bathymétrie centrée en x = 0 caractérisée par A = -1 m (trou) et d_b = 350 m. (b) Transformée en ondelette de Z_b avec respectivement en bleu et rouge les zones où le spectre est moyenné pour calculer (b) la longueur d'onde moyenne des systèmes barre/chenal en amont $\bar{\lambda}_m^u$ = 525 m, plus courte qu'en aval $\bar{\lambda}_m^d$ = 742 m (**Castelle et al.** 2012).*

en face de l'anomalie bathymétrique. Le degré de forçage de ce chenal est contrôlé par les gradients de dissipation par déferlement bathymétriques induits par les zones de focalisation d'énergie des vagues par réfraction au-dessus de l'anomalie. La stabilité de ce chenal augmente avec l'amplitude de l'anomalie $|A|$ et diminue avec la distance de l'anomalie à la côte d_b et l'angle d'incidence des vagues θ. Nous avons en particulier montré que les comportements des systèmes barre/chenal en amont et en aval de la perturbation étaient très différents, avec les chenaux en aval de la dérive littorale ayant systématiquement des longueurs d'onde plus grandes et des taux de migration plus faibles que ceux en amont. Ainsi, nous avons montré que, pour une condition de vagues donnée, **les barres sableuses tridimensionnelles peuvent s'auto-organiser dans des motifs différents à cause d'une perturbation longitudinale du champ de vagues induite par la présence d'une anomalie bathymétrique**. Dans notre étude, nous avons montré que nos résultats théoriques étaient corroborés par des observations par imagerie vidéo sur la plage de Duck (USA) équipée d'une station ARGUS (*Holman and Stanley* 2007) et qui présente une anomalie bathymétrique au niveau de la jetée du Field Research Facility (*Lee and Birkemeier* 1993, *Plant et al.* 2006). Une description extensive de l'étude est donnée dans ***Castelle et al.*** (2012).

4.3.4 Dynamique des chenaux de vidange dans une plage de poche *versus* le long des plages ouvertes

Les plages de poche sont très largement observées le long des côtes vallonnées ou montagneuses (*e.g.*, *Short and Masselink* 1999, *Klein et al.* 2010, *Scott et al.* 2011). Ces plages sont généralement délimitées par des caps rocheux ou plus rarement des structures d'ingénierie côtière qui peuvent profondément impacter la morphodynamique de la plage. La dynamique des plages peut être caractérisée par une rotation de la plage à l'échelle des changements d'indice de l'oscillation australe (*e.g.*, *Ranasinghe et al.* 2004, *Harley et al.* 2011) ou à l'échelle saisonnière (*e.g.*, *Schyuer-Ming and Komar*

1994). A l'échelle des changements de régimes de houle (plusieurs jours à plusieurs semaines), la dynamique des plages de poche est caractérisée par la présence de systèmes barre/chenal et de barres en croissant dont la morphodynamique est affectée par les contraintes longitudinales de la plage (*Gallop et al.* 2011, ***Enjalbert et al.*** 2011). *Short and Masselink* (1999) ont synthétisé les circulations/morphologies typiquement observées le long des plages de poche : (1) 'circulation normale' caractérisée par des systèmes barre/chenal ayant un comportement similaire à celui observé sur les plages ouvertes (*e.g.*, *Holman et al.* 2006, *Gallop et al.* 2011), avec la probable présence d'un chenal contre chaque cap (*headland rip*) ; (2) 'circulation cellulaire' où l'on observe potentiellement un chenal contre les caps rocheux (*e.g.*, *Loureiro et al.* 2012), ou un chenal dans le centre de la plage ; (3) 'circulation transitoire', correspondant à la situation intermédiaire, où la topographie et l'hydrodynamique influencent le comportement des systèmes barre/chenal (*e.g.*, ***Enjalbert et al.*** 2011).

Alors que, comme nous l'avons vu plus tôt dans ce mémoire, les études numériques sur la formation et la dynamique des systèmes barre/chenal sont nombreuses le long des plages ouvertes, aucune modélisation morphodynamique n'a été entreprise afin d'expliquer les mécanismes qui contrôlent la formation et l'évolution des systèmes de barres le long des plages de poche. Pourtant, alors que l'on sait désormais que sur les plages ouvertes les ondes de bord stationnaires ne sont pas à l'origine de la présence des systèmes barre/chenal ou en croissant, mais que leur dynamique est contrôlée par des mécanismes d'auto-organisation (*Coco and Murray* 2007), le doute persiste pour les plages de poche. En effet, la présence des ondes de bord stationnaires est très largement favorisée par les caps rocheux aux deux extrémités de la plage.

Dans ***Castelle and Coco*** (2012) nous avons utilisé la modélisation morphody-

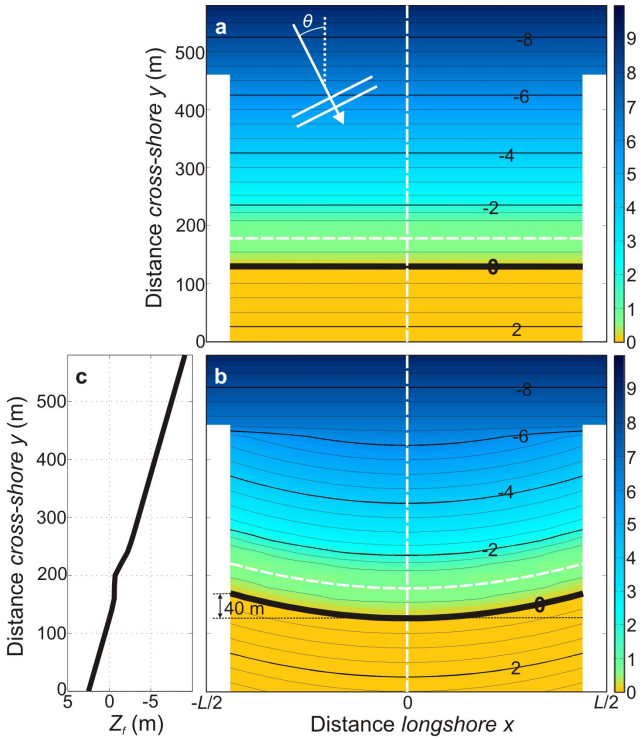

FIGURE 4.12 – *Bathymétries initiales (i.e., plages en équilibre, basic state) de plages de poche. (b) Plage rectiligne, (c) plage incurvée et (a) profil transversal (**Castelle and Coco** 2012).*

namique non-linéaire pour examiner pour la première fois la formation et la dynamique non-linéaire des systèmes barre/chenal le long des plages sableuses de poche. Nous utilisons ce modèle en partant d'un grand nombre de bathymétries idéalisées de plages de poche contraintes par 2 caps rocheux, caractérisées par une longueur L = 500, 1000, 2000, 4000 et 8000 m et différents degrés de courbure (Figure 4.12). Des forçages de vagues stationnaires avec une hauteur significative H_s = 1 m, une période pic T_p = 10 s et un angle d'incidence θ = 0, 5° et 10°, ainsi que des forçages de vagues instationnaires caractérisés par des variations sinusoïdales de θ sur une période de 4 jours et d'amplitude 5° ou 10° ont été considérés.

L'ensemble des circulations observées dans la littérature (*Short and Masselink* 1999) ont pu être obtenues par notre modèle en partant de plages et de forçages de vagues très idéalisés (Figure 4.13). Ces simulations ont également permis de proposer un paramètre adimensionné permettant de prédire le type de circulation à partir de paramètres simples comme la hauteur modale des vagues, la pente moyenne de la plage et la largeur de la plage de poche. Les valeurs obtenues par notre modèle sont en accord avec les observations de plages de poche (***Castelle and Coco*** 2012). Nos simulations montrent que les chenaux de cap sont préférentiellement observés pour les plages à faible courbure, sans claire dépendance de l'angle d'incidence des vagues, et sont favorisés par des vagues avec un étalement directionnel significatif. En effet, l'étude détaillée (voir ***Castelle and Coco*** 2012) montre que les courants d'arrachement de cap, et par conséquent la formation de chenaux de cap, est en grande par-

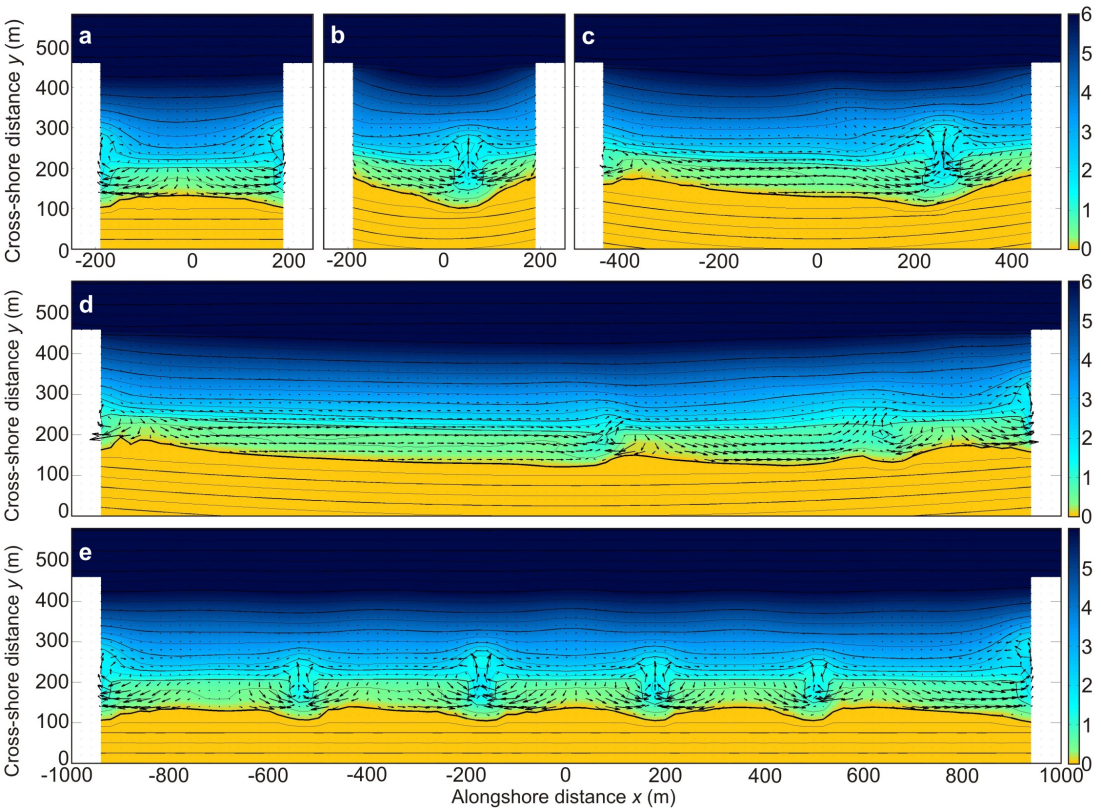

FIGURE 4.13 – *(a) Circulation cellulaire avec deux chenaux de cap (L = 500 m, plage linéaire, θ =5°), (b) circulation cellulaire avec un chenal central (L = 500 m, plage incurvée, θ = 5°), (c) circulation cellulaire avec un chenal de cap et un chenal central (L = 1000 m, plage incurvée, θ = 5°) (d) Circulation transitoire (L = 2000 m, plage incurvée, θ=5°) et (e) Circulation normale (L = 2000 m, plage linéaire, θ = 0) (**Castelle et al.** 2012).*

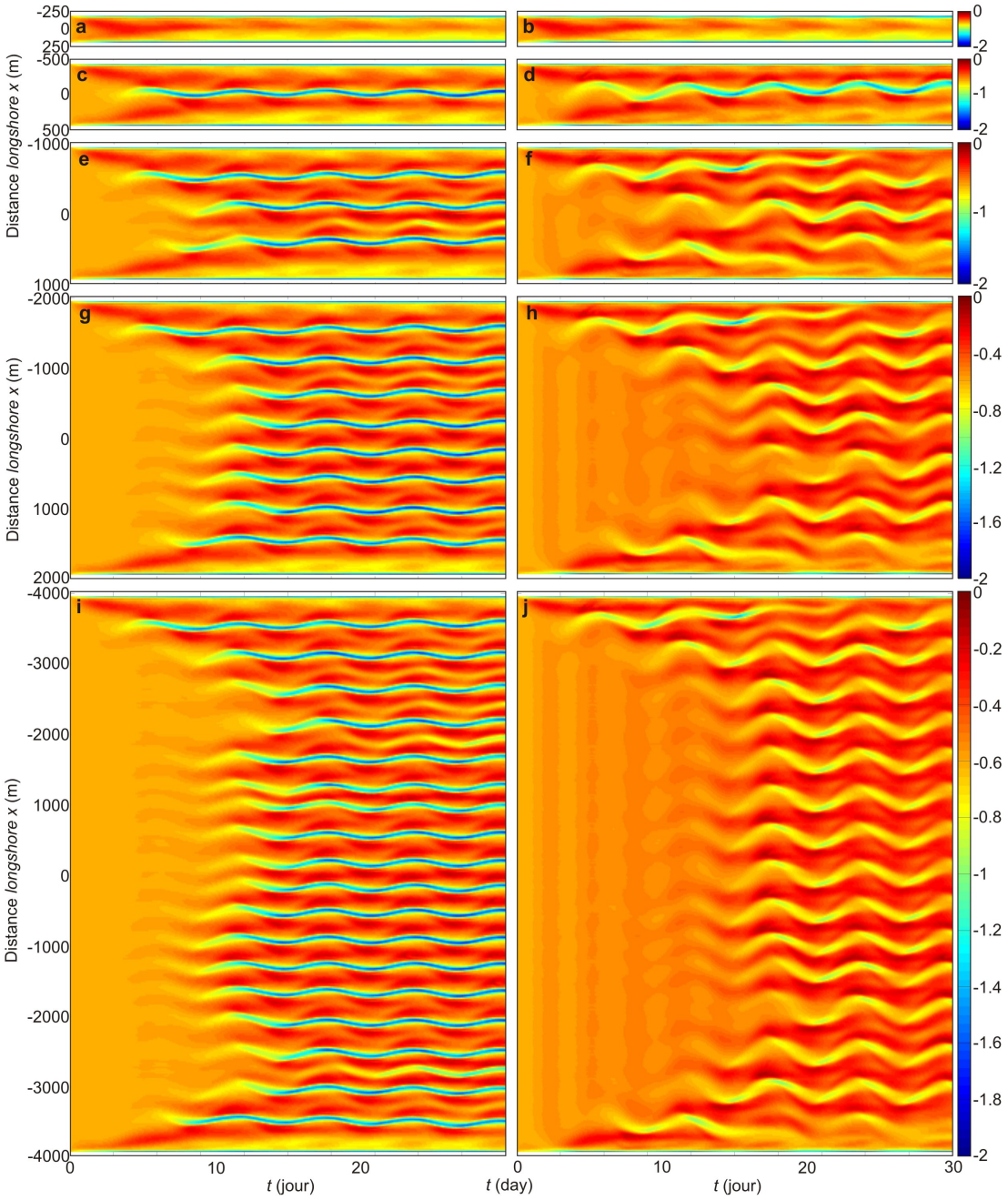

FIGURE 4.14 – *Evolution temporelle du profil longshore de plage Z_b pour un forçage de vague instationnaire en θ (amplitude de 5° et 10 ° respectivement à gauche et à droite) en partant de plages de poche rectilignes. (a-b) L = 500 m, (c-d) L = 1000 m, (e-f) L = 2000 m, (g-h) L = 4000 m et (i-j) L = 8000 m (**Castelle and Coco** 2012).*

tie contrôlée par les zones d'ombre énergétique des vagues au voisinage de chaque cap, induisant des gradients de dissipation d'énergie des vagues par déferlement bathymétrique. Les dimensions et l'intensité de ces zones d'ombre énergétique augmentent avec l'étalement directionnel des vagues au large, avec une influence très limitée des phénomènes de diffraction.

Nos simulations suggèrent également que, pour des forçages instationnaires ou pour des forçages stationnaires avec une forte obliquité des vagues, l'influence des caps sur la morphodynamique des barres peut se propager progressivement dans

l'ensemble du domaine. Lorsque les dimensions de la plage de poche sont suffisamment larges pour développer plusieurs chenaux de vidange et que la variabilité de θ est importante (*i.e.*, Figures 4.14f et h), on remarque que les chenaux proches des caps sont 'aspirés' par le chenal de cap. Cela, en cascade, implique des longueurs d'onde de système plus grandes au centre de la baie. Puisque, intrinsèquement, les systèmes auto-organisés tendent systématiquement à faire émerger une longueur d'onde régulière, cela implique des scissions de barres. Ainsi, **la dynamique non-linéaire (scissions et appariements) des systèmes barre/chenal est exacerbée par la présence des caps, ce qui implique également de fortes variabilités spatio-temporelles des longueurs d'onde. Cette variabilité le long de la plage est en accord avec l'hypothèse que les systèmes barre/chenal le long des plages de poche sont des motifs auto-organisés et est en accord avec de récentes observations de la dynamique des systèmes barre/chenal.**

4.3.5 Comment pourrait s'expliquer la bidimensionnalisation des structures tridimensionnelles pendant les épisodes de tempête ?

Nous avons vu précédemment que les structures tridimensionnelles des barres sableuses du système plage sont des instabilités du système plage qui naissent de la rétroaction positive entre l'hydrodynamique (vagues et courants induits), le transport sédimentaire et l'évolution du fond sableux. **Alors que la tridimensionnalisation des barres pendant les épisodes post-tempête est maintenant bien comprise, la bidimensionnalisation des structures pendant les épisodes de tempête reste un problème ouvert (aucune explication n'ayant été documentée à ce jour) alors que ces événements sont la principale source de variabilité de la morphologie des plages.** Nous sommes en train de réaliser des travaux pionniers à ce sujet.

En reprenant le concept du terme moteur de la vorticité introduit dans le chapitre 2, ce concept d'instabilité du système plage montré en Figure 4.2 peut être schématisé comme en Figure 4.15. Les gradients de dissipation d'énergie au-dessus d'un système barre/chenal de petite amplitude induit une vorticité verticale avec un courant d'arrachement dans le chenal et un courant vers le bord au-dessus des barres (Figure 4.15a). Cela induit une rétroaction positive ($\partial Z/\partial t > 0$ où $Z > 0$ et $\partial Z/\partial t < 0$ où $Z < 0$) et la barre sableuse est donc instable et va développer des structures tridimensionnelles (Figure 4.15c).

Prenons maintenant la cas d'une houle de tempête frontale au-dessus du même système barre/chenal (Figure 4.16). On considère alors un point de déferlement y_s situé très au large et une zone de déferlement saturée ($Q_b \approx 1$) au-dessus du système barre/chenal (Figures 4.16a et b). En zone de déferlement saturée $H_{rms} = \gamma h$ avec γ un paramètre de déferlement qui est typiquement une constante plus une fonction de la pente locale de la plage (*Raubenheimer et al.* 1996). Si on considère un système barre/chenal peu développé alors on peut faire l'hypothèse que $H_{rms} \propto h$. La dissipation d'énergie par déferlement bathymétrique ϵ peut par exemple s'exprimer comme (*Thornton and Guza* 1983) $\epsilon \approx \kappa H_{rms}^3 Q_b/h$, où κ est une constante qui dépend de la période des vagues. Puisqu'en zone de déferlement saturé on a $H_{rms} = \gamma h$ et $Q_b \simeq 1$, cela revient à $\epsilon \approx \kappa\gamma^2 h^2$. L'intensité de la force de dissipation d'énergie par déferlement bathymétrique (équation 2.19 ***Bonneton et al.*** 2010), en se considérant en domaine peu profond ($c = \sqrt{gh}$), est alors de la forme $D \approx \kappa\gamma^2 g^{-1/2} h^{1/2}$. Cette dernière équation signifie que, dans une zone de déferlement saturée, la force de dissipation par déferlement bathymétrique D augmente avec la profondeur d'eau locale. Par conséquent, F_v change de signe par rapport à la situation post-tempête (Figure

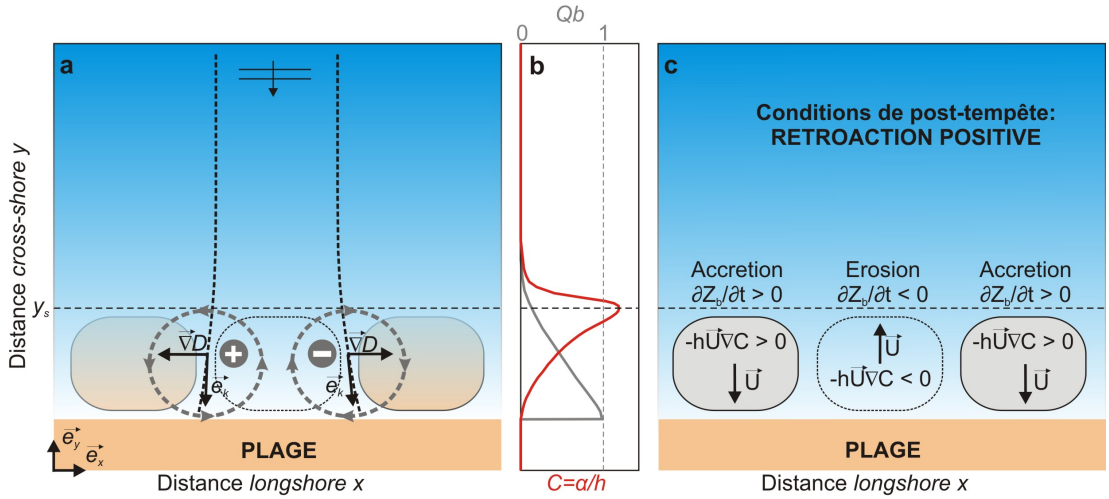

FIGURE 4.15 – *Schématisation de la rétroaction positive entre l'hydrodynamique, le transport sédimentaire et l'évolution du fond sableux pour des vagues de post-tempête (zone de déferlement non-saturée au-dessus du système barre/chenal) impliquant le développement des instabilités. (a) Terme de forçage de la vorticité verticale au-dessus du système barre/chenal avec y_s la position cross − shore du point de déferlement. (b) Profil classique de fraction de vagues déferlée Q_b et de α/h^0. (c) Accrétion de la barre ($\partial Z/\partial t > 0$) et érosion du chenal ($\partial Z/\partial t < 0$) dans le cas classique d'une diminution de α/h^0 du point de déferlement y_s vers la plage.*

4.15) et on a théoriquement un changement de signe de la vorticité verticale des circulations et donc un courant vers le large au-dessus de la barre et un courant vers le bord dans le chenal (Figure 4.16a). Cela induit une rétroaction négative ($\partial Z/\partial t > 0$ où $Z < 0$ et $\partial Z/\partial t < 0$ où $Z > 0$) et les structures tridimensionnelles sont amorties (Figure 4.16c). En résumé, **une zone de déferlement saturée au-dessus d'une barre sableuse tridimensionnelle peut induire théoriquement un changement de signe de la nature rotationnelle des circulations qui, en retour, induit une rétroaction négative entre l'hydrodynamique, le transport sédimentaire et l'évolution du fond sableux qui peut expliquer la bidimensionnalisation des barres sableuses pendant les épisodes de tempête.** Cette démonstration est développée dans ***Castelle and Bonneton*** (en préparation).

Cette analyse repose sur un certain nombre d'hypothèses. En particulier la démonstration ne marche que si on considère des structures tridimensionnelles préexistantes peu développées, or cette bidimensionnalisation a déjà été observée pour des structures tridimensionnelles bien développées (*e.g.*, *Van Enckevort et al.* 2004). L'existence de phénomène de 'SPAW' (pour *Shoreward Propagating Accretionary Wave*, *Wijnberg and Holman* 2007, ***Almar et al.*** 2010) couplé à cette bidimensionnalisation pourrait alors expliquer l'évolution des barres tridimensionnelles développées pendant les épisodes de tempête. Il est à noter également que ce changement de nature rotationnelle des cellules de circulation n'a jamais pu être mesuré sur le terrain, et à l'heure actuelle aucune modélisation numérique sur ce sujet n'a été documentée.

Ce changement de signe de vorticité n'est pas la seule théorie qui permette d'expliquer la bidimensionnalisation des barres pendant les tempêtes. En particulier, il est systématiquement fait l'hypothèse que α/h décroit du point de déferlement jusqu'à la ligne d'eau. Cela n'est pas prouvé, notamment puisque les formules qui prédisent cette décroissance ne prennent pas en compte l'injection de la turbulence générée par le déferlement bathymétrique jusqu'en bas de la colonne d'eau. Or celle-ci est connue pour fortement impacter la remise en suspension du sédiment (*e.g.*, *Nadaoka et al.*

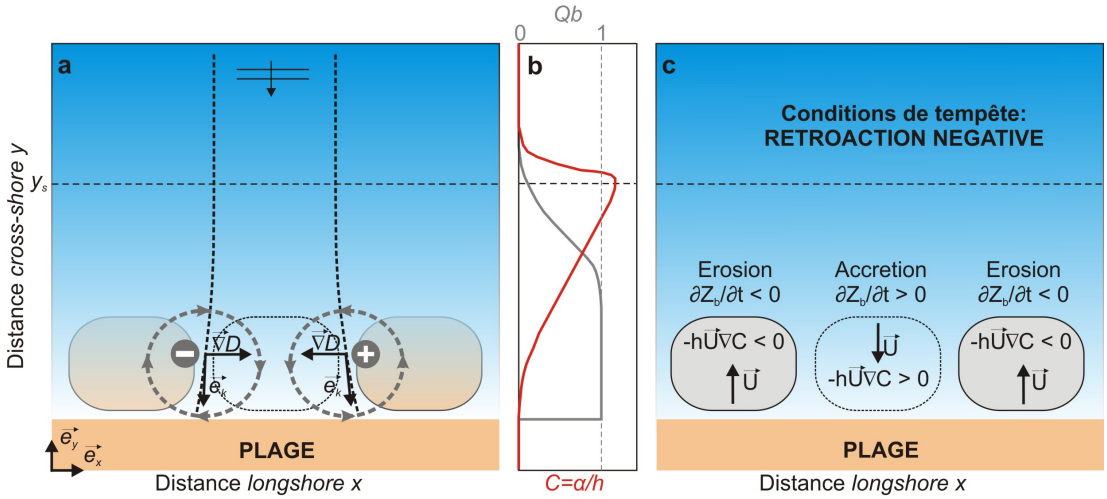

FIGURE 4.16 – *Schématisation de la rétroaction négative entre l'hydrodynamique, le transport sédimentaire et l'évolution du fond sableux pour des vagues de tempête (zone de déferlement saturée au-dessus du système barre/chenal) impliquant la bidimensionnalisation des barres. (a) Terme de forçage de la vorticité verticale au-dessus du système barre/chenal avec y_s la position cross − shore du point de déferlement. On observe un changement de la nature rotationnelle des circulations puisque qu'on peut faire l'hypothèse que la force de dissipation d'énergie par déferlement bathymétrique est de la forme $D \approx \kappa\gamma^2 g^{-1/2} h^{1/2}$ (démonstration dans le texte). (b) Profil classique de fraction de vagues déferlée Q_b et de α/h^0. (c) Erosion de la barre ($\partial Z/\partial t < 0$) et accrétion du chenal ($\partial Z/\partial t > 0$) dans le cas classique d'une diminution de α/h^0 du point de déferlement y_s vers la plage.*

1988, *Aagaard and Hughes* 2010). Récemment (***Grasso et al.*** 2012), nous avons montré *in-situ* que la structure verticale de la dissipation de la turbulence en zone de déferlement dépendait fortement de si on était placé au niveau des vagues déferlantes ou des ressauts (zone de déferlement interne). Cela suggère une structure *cross-shore* de α plus complexe que celle utilisée dans les différentes démonstrations. Cela est très important puisque qu'un changement de signe des gradients *cross-shore* de α/b pourrait induire une rétroaction négative entre l'hydrodynamique, les flux sédimentaires et l'évolution du fond sableux, sans nécessiter un changement de la nature rotationnelle des circulations. Enfin, le rôle du courant de retour et des asymétries des vagues sur les flux sédimentaires et l'évolution du fond n'est pas abordé ici mais pourrait également apporter des éléments de réponse quant à la bidimensionnalisation des barres sableuses pendant les épisodes de tempête. Dans le cadre de la thèse de Benjamin Dubarbier que j'encadre, un modèle d'évolution de profil de plage qui s'appuie essentiellement sur les contributions de ces deux processus hydro-sédimentaires est en cours de développement et de validation. Les avancées scientifiques réalisées dans ce code de calcul seront implémentées dans le modèle 2DH dans le cadre de cette thèse afin d'explorer le rôle potentiel des flux sédimentaires *cross-shore* dans la bidimensionnalisation des barres pendant les tempêtes.

CONCLUSIONS DU CHAPITRE

Les travaux de recherche réalisés au début de ma carrière, particulièrement pendant ma thèse de doctorat, ont largement contribué au changement de paradigme scientifique de la théorie des motifs vers les théorie d'auto-organisation pour expliquer la formation et la dynamique des barres pré-littorales tridimensionnelles (*e.g.*,

Castelle et al. 2006a). Ces travaux ont aussi permis d'expliquer d'autres caractéristiques des systèmes de barres en croissant, comme leur forme asymétrique, et ont nourri l'article de synthèse sur la dynamique des plages d'Aquitaine (***Castelle et al.*** 2007a). A travers cet article de synthèse et des observations sur les plages australiennes (voir chapitre 3), nous avions également développé un certain nombre de questions scientifiques auxquelles j'ai répondu en m'appuyant sur la modélisation numérique et théorique.

En particulier, le rôle potentiel des rétroactions morphologiques et des interactions entre les différents corps sableux littoraux n'avait commencé à être abordé que très récemment dans la littérature. Nos observations dans ce domaine étaient pionniers (*e.g.*, ***Castelle et al.*** 2007a, ***Almar et al.*** 2010). En s'appuyant sur la modélisation numérique, nous avons montré que le comportement individuel d'une entité morphologique du système plage contraste avec son comportement si on considère le système entier interconnecté, suggérant que l'étude isolée d'un corps sableux peut aboutir à une analyse erronée de sa dynamique et une mauvaise compréhension des données de terrain. Ces travaux ont concerné dans un premier temps la dynamique des plages à double barre (***Castelle et al.*** 2010b;c) et ont stimulé le montage du projet BARBEC (ANR Jeunes Chercheurs) que je coordonne et qui a débuté le 1er décembre 2010 et dont a déjà découlé un grand nombre d'avancées scientifiques importantes en morphodynamique littorale (*e.g.* ***Castelle and Ruessink*** 2011, ***Dubarbier and Castelle*** 2011, ***Castelle et al.*** 2012, ***Castelle and Coco*** 2012, ***Grasso et al.*** 2012, *Ruessink et al.* 2012, *Price and Ruessink* in press, ***Price et al.*** soumis).

En particulier, nous avons montré que la prise en compte de l'instationnarité du forçage des vagues est cruciale pour prédire les caractéristiques (morphologie, longueur d'onde et migration) des barres sableuses tridimensionnelles (***Castelle and Ruessink*** 2011) et que celui-ci excite considérablement la dynamique non-linéaire des systèmes (appariements et scissions). Cette dynamique non-linéaire implique alors une variabilité temporelle et spatiale des longueurs d'onde qui est en accord avec les observations. Nous avons également montré que les barres sableuses tridimensionnelles peuvent s'auto-organiser dans des motifs différents à cause d'une perturbation longitudinale du champ de vagues induites par la présence d'une anomalie bathymétrique (***Castelle et al.*** 2012), ces résultats théoriques étant corroborés par des observations par imagerie vidéo sur la plage de Duck (USA). Nous avons également montré que la dynamique non-linéaire des systèmes barre/chenal est exacerbée par la présence des caps, ce qui implique également de fortes variabilités spatio-temporelles des longueurs d'onde le long des plages de poche. Cette variabilité le long de la plage est consistante avec l'hypothèse que les systèmes barre/chenal le long des plages de poche sont aussi des motifs auto-organisés et permet d'écarter la théorie des ondes de bord pour les plages de poche. Cette étude a également permis de proposer un paramètre adimensionné permettant de prédire le type de circulation observée le long des plages de poche naturelles (***Castelle and Coco*** 2012). Globalement donc, **nos travaux ont récemment réconcilié la théorie avec les observations.** Enfin, nous sommes actuellement pionniers dans la recherche d'une explication pour la bidimensionnalisation des barres sableuses pendant les épisodes de tempête. Parmi les hypothèses les plus plausibles, nous devons explorer (1) le changement de nature rotationnelle des circulations en zone de déferlement saturée (***Castelle and Bonneton*** en préparation) ; (2) le changement de structure *cross-shore* des gradients de α/h par une meilleure prise en compte de la remise en suspension du sédiment par l'injection de la turbulence induite par déferlement bathymétrique jusqu'en bas de la colonne d'eau (***Grasso et al.*** 2012) ; (3) la prise en compte optimale des flux sédimentaires

induit vers le bord par les non-linéarités des vagues et vers le large par le courant de retour dans les modèles morphodynamiques de plage tridimensionnelle (thèse de Benjamin Dubarbier).

Il est important de rappeler que le code de recherche qui a permis d'aboutir à ces résultats, et dont je coordonne le développement, est désormais sur le plan international le seul à pouvoir simuler la formation, l'évolution non-linéaire et la saturation des barres sableuses de déferlement tridimensionnelles ainsi que l'évolution du trait de côte associée (le seul autre modèle pouvant simuler la saturation des barres, co-développé à l'UPC en Espagne et l'Université de Nottingham (UK), considère un mûr au niveau de ligne d'eau). Ce code est donc un outil particulièrement pertinent pour poursuivre les recherches sur, entre autres, les interactions entre les barres sableuses, le trait de côte, et la géologie (caps rocheux et/ou motifs géologiques sur le haut du plateau continental).

Synthèse

5

Conclusions sur les travaux

Depuis 11 ans mes travaux, tout particulièrement ceux menés au sein de l'UMR EPOC, ont largement contribué à **l'amélioration de la compréhension de la dynamique hydro-sédimentaire des littoraux sableux et des processus et interactions contrôlant leurs évolutions.** Ceci a pu se faire notamment à travers la mise en place d'une politique scientifique, sous l'impulsion de Philippe Bonneton, au sein de l'équipe METHYS visant à concentrer nos efforts dans la compréhension et la modélisation des processus physiques fondamentaux contrôlant la dynamique littorale, en laissant moins de place à l'observation parfois trop passive des évolutions. Ces travaux n'auraient pas abouti sans l'implication des nombreux étudiants dont j'ai (co-)encadré les recherches et celle des collègues de l'équipe METHYS dans le cadre des différents projets. Ces efforts font que mes travaux sont reconnus sur le plan national et international et que l'équipe METHYS est devenue en quelques années incontournable en morphodynamique littorale. **Les travaux qui ont été présentés dans ce mémoire sont donc aussi le produit du travail d'une équipe.**

Parmi les résultats les plus importants, **nos travaux ont alimenté les débats sur les changements de paradigme scientifique en morphodynamique et en hydrodynamique littorale** (1) de la théorie des motifs vers les théories d'auto-organisation pour expliquer la formation et la dynamique des barres sableuses de déferlement et, dans une moindre mesure, (2) du comportement ouvert vers un comportement semi-fermé des cellules de circulation des courants d'arrachement. Plus récemment, j'ai montré que le comportement individuel d'une entité morphologique du système plage (anomalie bathymétrique, barre(s), haut de plage, berme, etc.) contraste avec son comportement si on considère le système entier interconnecté, suggérant que l'étude isolée d'un corps sableux peut aboutir à une analyse erronée de sa dynamique et une mauvaise compréhension des données de terrain. Les travaux les plus récents en modélisation morphodynamique non-linéaire ont enfin permis d'expliquer un nombre important de comportements des plages sableuses qui jusque-là n'avaient encore jamais été compris puisque la communauté internationale s'obstinait dans la théorie des motifs ou n'utilisait pas toutes les possibilités de la modélisation morphodynamique non-linéaire (*e.g.*, forçage stationnaire, bathymétries homogènes, formulation des flux sédimentaires). **Nous avons ainsi récemment fortement contribué à la réconciliation de la théorie avec les observations en morphodynamique littorale.**

Ces travaux se sont appuyés sur la modélisation numérique et théorique mais aussi sur des données collectées sur des dizaines de sites (Figure 1.5) en combinant mesures hydro-sédimentaires et topo-bathymétriques. Plus que sur ces données *in-situ*, mes travaux se sont appuyés sur la télédétection par imagerie vidéo et plus

récemment la modélisation physique en laboratoire qui sont des approches particulièrement pertinentes pour l'étude de la morphodynamique littorale. Cette approche multidisciplinaire et la combinaison de méthodes à travers, par exemple, l'assimilation de données dans les modèles reste et restera essentielle.

Synthèse des perspectives de recherche

Globalement, l'orientation générale de mes recherches futures en dynamique hydro-sédimentaire littorale sera de **poursuivre sur la forte dynamique qui a été impulsée ces dernières années, la compréhension et la modélisation de la morphodynamique des littoraux sableux restant encore à l'heure actuelle limitée. Compte tenus des nombreux points bloquants dans l'observation et la modélisation de la morphodynamique des littoraux sableux, il n'est pas raisonnable d'être sur tous les fronts, et il faudra évidemment cibler les axes de recherche que je serai en mesure de piloter.** Ainsi, je ne serai pas moteur, par exemple, dans la description 3D de l'hydrodynamique induite par les vagues en domaine littoral (*e.g.*, *Ardhuin et al.* 2008, *Bennis et al.* 2011), qui peut impacter les flux sédimentaires ; la modélisation du transport *cross-shore* par des modèles à résolution de phase (*e.g.*, *Cienfuegos et al.* 2010, *Tissier et al.* 2012) ; la description détaillée de l'hydrodynamique (*e.g.*, *Desombre et al.* 2012) et des flux sédimentaires (*e.g.*, *Blenkinsopp et al.* 2011) en zone de jet de rive. Par contre, il est évident je suivrai de très près les recherches menées autours de ces thèmes, afin notamment d'implémenter les avancées scientifiques dans nos codes de recherche. Dans le cas d'une implication personnelle dans l'un de ces axes, celle-ci restera marginale.

D'un point de vue méthodologique, je continuerai de m'appuyer sur la modélisation des processus physiques. Toutefois, et comme ce fut déjà le cas dans mes recherches antérieures (*i.e.*, approche d'état de base en modélisation morphodynamique non-linéaires système barre/chenal, ***Castelle and Ruessink*** 2011), je chercherai à combiner celle-ci avec d'autres approches afin de m'affranchir des limitations des connaissances sur certains processus hydro-sédimentaires complexes (*e.g.*, *sheet flow*, transport sédimentaire en zone de jet de rive). Le couplage avec des lois de comportements (*e.g.*, *Yates et al.* 2009), les attracteurs dynamiques (*e.g.*, *Plant et al.* 2006), l'intelligence artificielle (*e.g.*, ***Browne et al.*** 2007) ou les automates cellulaires (*e.g.*, *Narteau et al.* 2009) est en cours de réflexion. Cette stratégie de modélisation qui privilégie la compréhension des comportements à la course à la complexification des modèles morphodynamiques, inspirée du discours de *Murray* (2007), sera la colonne vertébrale de mes futures recherches. L'assimilation de données dans les modèles numériques pour l'inversion bathymétrique (*e.g.*, *Wilson et al.* 2010, ***Birrien et al.*** 2011; 2012; soumis) mais aussi l'assimilation dynamique (*e.g.*, ***Dubarbier et al.*** 2012) sera également un axe méthodologique que je privilégierai. Enfin, en parallèle de ces aspects innovants, je poursuivrai mes activités en imagerie vidéo, modélisation physique en laboratoire et, ponctuellement, sur les mesures *in-situ*.

Parmi les axes de recherche que je privilégierai on peut distinguer les 4 domaines succinctement décrits ci-dessous. Deux de ces axes font actuellement l'objet de thèses de doctorat que j'encadre, et ces travaux seront bien sûr poursuivis.

Dynamique instationnaire des courants d'arrachement

Même si nous avons largement avancé sur la compréhension des courants d'arrachement, il existe encore un certain nombre de points bloquants. L'un des princi-

paux concerne les processus contrôlant la rétention des cellules associées au courant d'arrachement : nos mesures en laboratoires (***Castelle et al.*** 2011) ont montré que le taux de rétention pouvait varier de 50 à 95% sans pouvoir déterminer dans quelle mesure le forçage des vagues et la morphologie impactaient ces taux. Ces derniers sont cruciaux pour le mélange des masses d'eau ou la sécurité de la baignade, au même titre que l'intensité moyenne du courant d'arrachement qui est elle beaucoup mieux comprise et prédictible. Une étape importante consistera à modéliser les courants d'arrachement instationnaires avec des modèles à résolution de phase (*e.g.*, *Tissier et al.* 2012) ou à phase moyennée pour les vagues et à résolution de phase pour les ondes infragravitaires (*e.g.*, *Roelvink et al.* 2009). Il faudra tout d'abord travailler sur des cas idéalisés (à la manière de nos récentes études morphodynamiques, *e.g.*, ***Castelle and Ruessink*** 2011, ***Castelle et al.*** 2012, ***Castelle and Coco*** 2012) afin d'identifier les mécanismes moteur et en déduire des lois génériques. Un exemple préliminaire est donné en Figure 5.1 dans le cadre d'une collaboration tout juste initiée avec Ad Reniers (University of Miami, USA) et Jamie MacMahan (Naval Postograduate School, USA). L'acquisition de nouvelles données Lagrangiennes sur les plages naturelles (par exemple celles obtenues pendant la campagne DRIBS2 sur la plage de Perranporth, UK, pilotée par l'Université de Plymouth à laquelle j'ai participé) permettront de valider ces avancées.

D'autre part, toujours dans le souci de ne jamais dissocier la théorie de l'observation et pour répondre à la forte demande sociétale liée à la dangerosité des courants d'arrachement, nous devrons favoriser le développement d'outils capables de déterminer et/ou prédire la localisation et l'intensité des courants d'arrachement. Une piste à explorer, parmi d'autres en cours de réflexion, est le couplage de l'imagerie vidéo (par laquelle on peut quantifier en temps réel l'intensité du déferlement bathymétrique et sa répartition spatiale) et la théorie de la force de vorticité (***Bonneton et al.*** 2010, ***Bruneau et al.*** 2011) qui peut être complémentaire aux approches plus empiriques (*e.g.*, *Lascody* 1998). Cette approche peut procurer en effet une carte des courants d'arrachement. Ces recherches devront se faire en concertation notamment avec les services de sécurité des plages avec qui les contacts avec le milieu universitaire, contrairement aux pays anglo-saxons, restent très marginaux en France.

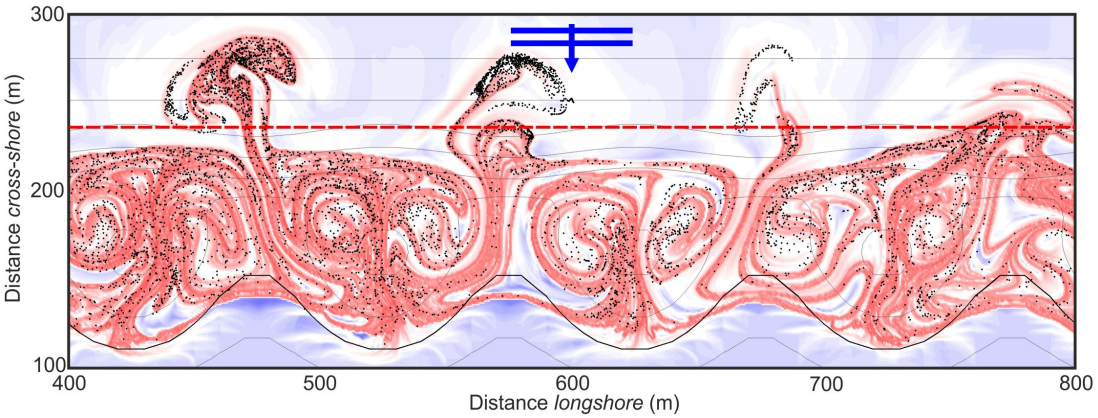

FIGURE 5.1 – *Exemple de simulation de courants d'arrachement pour une houle frontale avec H_s = 0.8 m et T_p = 10 s au-dessus d'un système idéalisé barre/chenal à t = 20 min. Plusieurs centaines de drifters (points noirs) déployés dans la zone de déferlement à t = 0 sont observés et présentent les mêmes motifs que les filaments des Structures Cohérentes Lagrangiennes (en rouge foncé). On remarque que seulement un petit nombre de drifters sont expulsés du compartiment de la zone de déferlement (délimité par les pointillés rouges).*

Amélioration des processus hydro-sédimentaires *cross-shore* en zones de déferlement et de jet de rive et évolution des profils de plage

La position des barres par rapport à la côte contrôle en grande partie la longueur d'onde de leurs structures tridimensionnelles, et leurs positions relatives semblent contrôler en partie leurs interactions. Toutefois, encore à l'heure actuelle aucun modèle de morphodynamique 3D littorale n'est capable de simuler correctement la migration transversale de ces barres. Ces constatations motivent le développement de modèle d'évolution de profil de plage afin de se concentrer essentiellement sur la dynamique des barres dans l'axe perpendiculaire à la côte sur des échelles de temps suffisamment longues (de l'ordre de quelques mois à quelques années), en réponse aux changements de régime de houle. Ce développement permettra (1) de disposer d'un modèle long terme d'évolution du trait de côte avec des temps de calcul très courts et (2) d'implémenter progressivement les avancées scientifiques dans les modèles 2DH.

J'ai ainsi débuté en 2008 le développement d'un modèle simple d'évolution de profil de plage sableuse (1DBeach) basé sur une approche à phase moyennée et sur un couplage vagues / transport sédimentaire / évolution bathymétrique (***Castelle et al.*** 2010a). Depuis début 2011, dans le cadre de la thèse de Benjamin Dubarbier que j'encadre, le développement du code s'est activement poursuivi avec la prise en compte de l'état de l'art en processus hydro-sédimentaires en zone de déferlement (*e.g.*, *Ruessink et al.* 2012). Les non-linéarités des vagues en milieu peu profond (asymétrie des vitesses et des accélérations proches du fond) induisent un transport net de sédiment qui est prédominant pendant les épisodes de temps calme, tandis que le courant de retour dirigé vers le large devient prédominant sur le transport sédimentaire pendant les épisodes énergétiques.

Le modèle a été confronté aux données issues des plages de Duck (USA), Egmond (Pays-Bas), Noordwijk (Pays-Bas) et des simulations dans le canal à houle du LEGI (*e.g.*, ***Dubarbier et al.*** 2012). Nous utiliserons les données issues de l'expérience en canal à houle à taille réelle BARDEX II (PI G. Masselink, University of Plymouth, UK, AO Européen HYDRALAB-IV) qui a eu lieu en juin-juillet 2012 dans laquelle Benjamin Dubarbier et moi-même ont été fortement impliqués. Des données très fines sur les évolutions morphologiques et sur la distribution *cross-shore* des processus hydro-sédimentaires ont été collectées et vont former une base de données unique pour le développement et la validation du modèle de profil de plage en fonction de la marée et de différentes conditions de houle. Ces avancées seront implémentées dans le code 2DH et permettra alors d'identifier le rôle des processus hydro-sédimentaires *cross-shore* sur la dynamique des barres tridimensionnelles et peut-être expliquer pourquoi jusqu'à présent ces modèles se comportaient mal pendant les épisodes de tempête. Ces avancées offriront aussi la possibilité de simuler la morphodynamique 3D de plages réelles en présence de changements de régimes de houle et de marée, ce qui n'a encore jamais été réalisé.

Assimilation de données dans les modèles numériques

Le fait d'avoir récemment réconcilié la théorie et l'observation implique que la modélisation numériques et les observations (*in-situ* ou par télédétection) sont devenues 'compatibles'. Comme indiqué dans ***Castelle*** (2009), les modèles hydro-sédimentaires et les méthodes mises en oeuvre en imagerie vidéo ont atteint un niveau de maturité qui a rendu depuis peu envisageable la mise en place de méthodes d'assimilation de données dans les modèles numériques. Les données vidéo

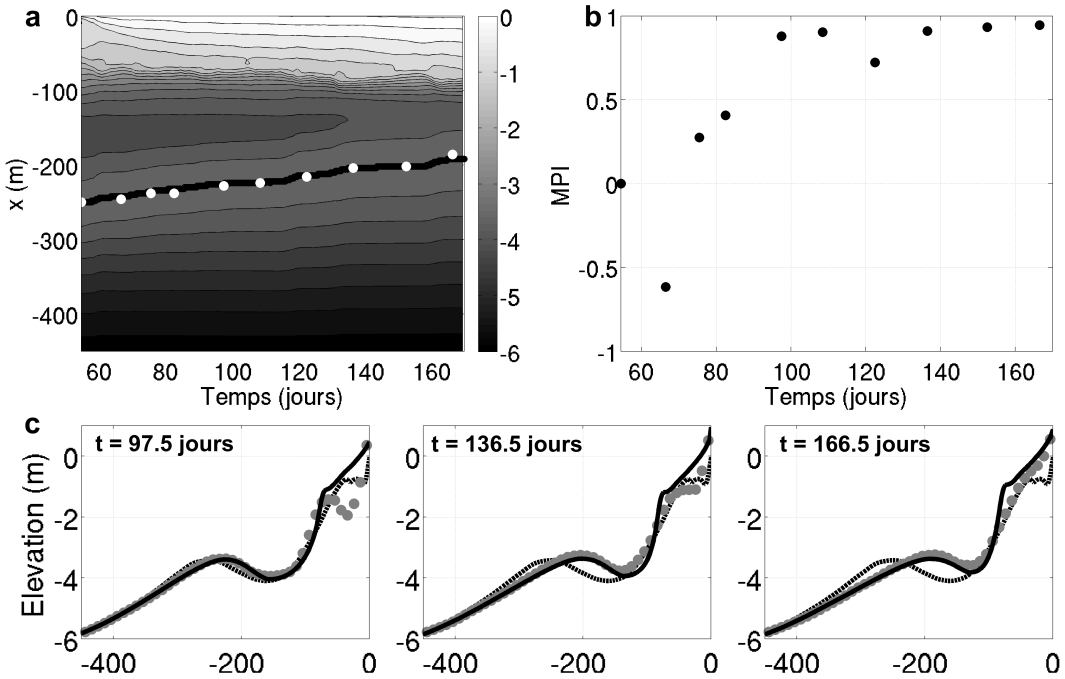

FIGURE 5.2 – *Exemple de simulation d'évolution du profil de plage à Duck (Caroline du Nord, USA) montrant la migration vers le bord d'une barre sableuse. (a) Evolution spatio-temporelle du profil, (b) évolution du skill du modèle et (c) comparaison du profil avec les mesures à différents temps de la simulation (**Dubarbier et al.** 2012).*

peuvent aussi être complétées ponctuellement par des données topo-bathymétriques ou hydrodynamiques par mesure directe (DGPS, capteur de pression, etc.). C'est dans cette optique qu'a débuté en octobre 2009 la thèse de Florent Birrien dont je suis l'encadrant et qui soutiendra fin 2012. Le but de ses travaux, qui seront à poursuivre ces prochaines années, est de développer une méthode d'assimilation de données inspirée de ce qui se fait par exemple en météorologie. L'approche consiste à combiner de manière optimale les informations disponibles sur le système plage (équations mathématiques, observations et statistiques d'erreur). En particulier, les observations sont souvent hétérogènes en nature, en quantité, en qualité mais aussi en répartition spatiale. Cela rend bien évidemment le problème extrêmement complexe.

Le développement, très innovant en océanographie physique littorale, de méthodes d'assimilation de données doit permettre à terme :

- d'avoir des méthodes d'inversion en assimilant les données dans les modèles hydrodynamique (vagues + courants) afin de quantifier la bathymétrie (***Birrien et al.*** 2011; 2012; soumis). L'utilisation de modèles à phase moyennée est ici privilégiée à celle de modèle non-linaires de type Boussinesq (***Almar et al.*** 2011). Notre approche diffère de la seule méthode d'inversion documentée (*Van Dongeren et al.* 2008) qui ne peut pas prendre en compte l'hétérogénéité des données et n'est pas compatible avec l'assimilation au sens strict. Les données bathymétriques qui peuvent être obtenues par l'inversion d'une part manquent cruellement aux modèles morphodynamiques pour leur validation, particulièrement pendant les épisodes de tempête, et d'autre part sont une approche alternative et peu coûteuse aux relevés bathymétriques qui permettront de mieux quantifier les évolutions morphologiques qui, jusqu'à présent, ont été appréhendées de manière géométrique.

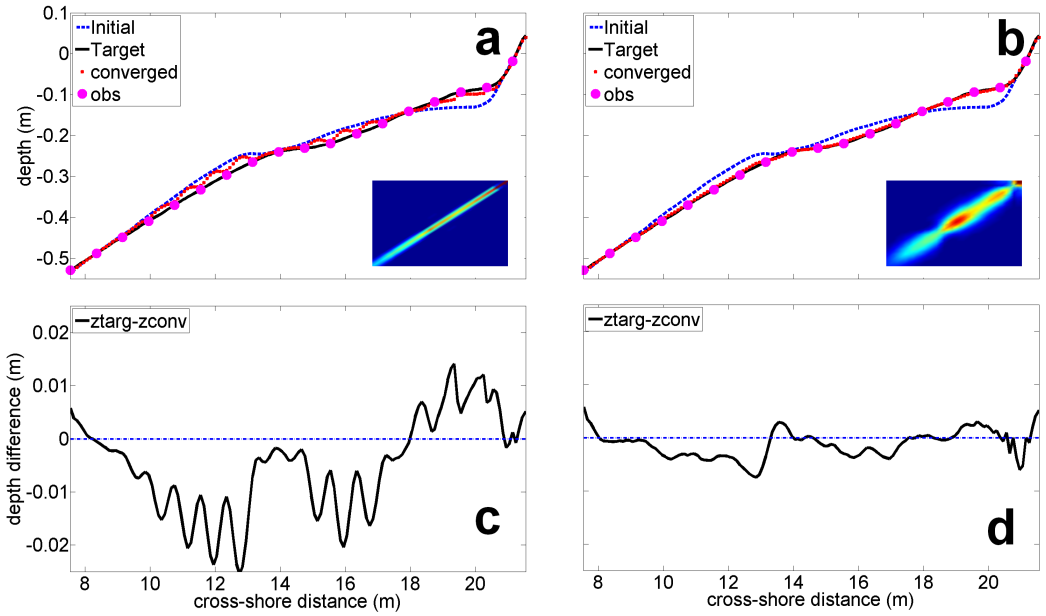

FIGURE 5.3 – *Exemple d'assimilation de données vidéo sur un cas synthétique pour inverser la bathymétrie en utilisant plusieurs méthodes de localisation (**Birrien et al.** soumis).*

- d'assimiler les données dans les modèles morphodynamiques afin de corriger en temps réel les évolutions simulées (assimilation au sens strict) et ainsi disposer d'un outil pertinent pour la prévision des évolutions morphologiques. Le succès de ces recherches devrait permettre de développer des outils de prévision à court terme (*e.g.*, quelques jours à quelques semaines) de l'évolution morphologique des littoraux sableux. Cela ouvrira également de grandes perspectives pour la modélisation morphodynamique opérationnelle des plages sableuses.

Application du modèle de morphodynamique littorale 3D aux cas réels

Jusqu'à présent, nous avons refusé du brûler les étapes en modélisation morphodynamique 3D littorale, *i.e.* nous avons cherché à comprendre des comportements observés qui n'avait jamais encore été expliqués, et ce en s'appuyant sur la modélisation morphodynamique pour en tirer des lois génériques, sans réaliser de comparaison quantitative. Cela se justifiait par (1) le fait que nous sommes conscients qu'il manque encore beaucoup de physique dans les modèles pour prétendre simuler la réalité (on peut bien sûr en 'tournant les boutons' obtenir des évolutions réalistes des barres, mais cela n'est pas satisfaisant) et (2) le manque de données haute-fréquence hydro-sédimentaires et surtout bathymétriques pour la validation. Grâce aux 2 derniers axes de recherches développés ci-dessus (processus hydro-sédimentaires *cross-shore* et assimilation de données) nous pouvons enfin envisager la modélisation morphodynamique 3D précise des plages réelles. Une première étape est en cours dans le cadre de la thèse de Timothy Price avec qui, sur les plages de la Gold Coast (Australie), nous avons utilisé XBeachWizard (*Van Dongeren et al.* 2008) pour reconstruire des bathymétries et réaliser des évolutions morphologiques sur temps courts (quelques jours et pour des conditions de vagues peu énergétiques) avec des résultats très encourageants (***Price et al.*** soumis). Nous ne pourrons réellement aborder les simulations à plus long terme et pour un grand nombre de changements de régimes de houle que lorsque les processus *cross-shore* auront été correctement implémentés. Cela

ouvrira ensuite un nombre incroyable de perspectives de recherche avec notamment l'amélioration des modèles à travers l'influence de la variabilité de la granularité des sédiments, la nappe sous-terraine, le substrat rocheux, et bien plus encore.

Bibliographie

Aagaard, T., and M. G. Hughes (2010), Breaker turbulence and sediment suspension in the surf zone, *Marine Geology*, *271*, 250–259. (Cité page 71.)

Aagaard, T., B. Greenwood, and J. Nielsen (1997), Mean currents and sediment transport in a rip channel, *Marine Geology*, *140*, 24–45. (Cité page 26.)

Aarninkhof, S. G. J., I. L. Turner, T. D. T. Dronkers, M. Caljouw, and L. Nipius (2003), A video-based technique for mapping intertidal beach bathymetry, *Coastal Engineering*, *49*, 275–289. (Cité page 110.)

Abadie, S., R. Butel, S. Mauriel, D. Morichon, and H. Dupuis (2006), Wave climate and longshore drift on the South Aquitaine coast, *Continental Shelf Research*, *26*, 1924–1939. (Cité page 113.)

Aleman, N., N. Robin, R. Certain, C. Vanroye, J. -P. Barusseau and F. Bouchette (2011), Typology of nearshore bars in the Gulf of Lions (France) using LIDAR technology, *Journal of Coastal Research*, *SI 64*, 721–725. (Cité page 5.)

Allen, J. S., P. A. Newberger, and R. A. Holman (1996), Nonlinear shear instabilities of alongshore currents on plane beaches, *Journal of Fluid Mechanics*, *310*, 181–213. (Cité page 16.)

Almar, R., **B. Castelle**, B. G. Ruessink, N. Sénéchal, P. Bonneton, and V. Marieu (2009), High-frequency video observation of a double sandbar system under high-energy wave forcing, *Journal of Coastal Research*, *SI 56*, 1706–1710. (Cité pages 38 et 44.)

Almar, R., **B. Castelle**, B. G. Ruessink, N. Sénéchal, P. Bonneton, and V. Marieu (2010), Two- and three-dimensional double-sandbar system behaviour under intense wave forcing and a meso-macro tidal range, *Continental Shelf Research*, *30*, 781–792. (Cité pages xvii, 36, 38, 39, 44, 60, 70 et 72.)

Almar, R., R. Cienfuegos, P. Catalan, F. Birrien, **B. Castelle**, and H. Michallet (2011), Nearshore bathymetric inversion from video using a fully nonlinear Boussinesq wave model, *Journal of Coastal Research*, *SI 64*, 20–24. (Cité page 79.)

Almar, R., R. Cienfuegos, P. A. Catalan, H. Michallet, **B. Castelle**, P. Bonneton, and V. Marieu (2012), A new breaking wave height direct estimator from video imagerye, *Coastal Engineering*, *61*, 42–48. (Cité page 13.)

Almeida, L. P., M. V. Vousdoukas, O. Ferreira, and A. Matias (2012), Thresholds for storm impacts on an exposed sandy coastal area in southern Portudal, *Geomorphology*, *143-144*, 3–12. (Cité page 42.)

Alvarez-Ellacuria, A., A. Orfila, M. Olabarrieta, L. Gomez-Pujol, R. Medina, and J. Tintore (2009), An alert system for beach hazard management in the Baleric Islands, *Coastal Management*, *37*, 569–584. (Cité page 108.)

Ardhuin, F., A. D. Jenkins, and K. A. Belibassakis (2008), Comments on "The three-dimensional current and surface wave equations", *Journal of Physical Oceanography*, *38*, 1340–1350. (Cité page 76.)

Ashton, A. D., and A. B. Murray (2006a), High-angle-wave instability and emergent shoreline shapes : 1. Modeling of sand waves, flying spits and capes, *Journal of Geophysical Research*, *111*, F04011, doi :10.1029/2005JF000422. (Cité pages xv, 11, 53 et 108.)

Ashton, A. D., and A. B. Murray (2006b), High-angle-wave instability and emergent shoreline shapes : 2. Wave climate analysis and comparisons to nature, *Journal of Geophysical Research*, *111*, F04012, doi :10.1029/2005JF000423. (Cité page 108.)

Ashton, A. D., A. B. Murray, and O. Arnault (2001), Formation of coastalines features by large-scale instabilities induced by high-angle waves, *Nature*, *414*, 296–300. (Cité pages 11 et 108.)

Austin, M., T. M. Scott, J. W. Brown, J. A. Brown, J. H. MacMahan, G. Masselink, and P. Russell (2010), Temporal observations of rip current circulation on a macro-tidal beach, *Continental Shelf Research*, *30*, 1149–1165. (Cité page 26.)

Bailard, J. A. (1981), An energetics total load sediment transport model for a plane beach, *Journal of Geophysical Research*, *86*(C11), 10,938–10,954. (Cité pages 53, 54 et 56.)

Bailey, R. D. S. D. G., and M. J. Shephard (1999), An inter-site comparison of net offshore bar migration characteristics and environmental conditions, *Journal of Coastal Research*, *15*, 750–765. (Cité page 42.)

Balouin, Y., H. Howa, R. Pedreros, and D. Michel (2005), Longshore sediment movements from tracers and models, Praia de Faro, South Portugal, *Journal of Coastal Research*, *21*, 146–156. (Cité page 109.)

Battjes, J. A., and J. Janssen (1978), Energy loss and set-up due to breaking in random waves, in *16th Int. Conf. on Coastal Eng.*, pp. 569–587, ASCE. (Cité page 20.)

Bender, C. J., and R. G. Dean (2003), Wave field modification by bathymetric anomalies and resulting shoreline changes : a review with recent results, *Coastal Engineering*, *49*, 125–153. (Cité page 63.)

Benedet, L., and J. H. List (2008), Evaluation of the physical process controlling beach changes adjacent to nearshore dredge pits, *Coastal Engineering*, *55*, 1224–1236. (Cité page 63.)

Bennis, A. C., F. Ardhuin, and F. Dumas (2011), On the coupling of wave and three-dimensional circulation models : Choice of theoretical framework, practical implementation and adiabatic tests, *Ocean Modelling*, *3-4*, 260–272. (Cité page 76.)

Bertin, X., **B. Castelle**, G. Anfuso, and O. Ferreira (2008a), Improvement of sand activation depth prediction under conditions of oblique wave breaking, *Geo-Marine Letters*, *28*, 65–75. (Cité page 13.)

Bertin, X., **B. Castelle**, E. Chaumillon, R. Butel, and R. Quique (2008b), Longshore transport estimation and inter-annual variability at a high energy dissipative beach : St Trojan beach, SW Oleŕon Island, France, *Continental Shelf Research*, *28*, 1316–1332. (Cité pages 13, 33, 107, 109 et 113.)

Bertin, X., N. Bruneau, J. P. Breilh, A. B. Fortunato, and M. Karpytchev (2012), Importance of wave age and resonnance in storm surges : The cas Xynthia, Bay of Biscay, *Ocean modelling*, *42*, 16–30. (Cité page 4.)

Birrien, F., **B. Castelle**, V. Marieu, R. Almar, and H. Michallet (2011), Application of a data-model assimilation method to a 3d surf zone sandbar physical experiment, *Journal of Coastal Research*, *SI 64*, 976–980. (Cité pages 76 et 79.)

Birrien, F., **B. Castelle**, B. Dubarbier, and V. Marieu (2012), Data-model assimilation for nearshore bathymetric inversion using heterogeneous video-derived observations, in *Proc. 33rd International Conference on Coastal Engineering*. (Cité pages 76 et 79.)

Birrien, F., **B. Castelle**, V. Marieu, and B. Dubarbier (soumis), On a data-model assimilation method to inverse wave-dominated beach bathymetry using heterogeneous video-derived observations, *Ocean Engineering*. (Cité pages xx, 76, 79 et 80.)

Blenkinsopp, C. E., I. L. Turner, G. Masselink, and P. E. Russell (2011), Swash zone sediment fluxes : Field observations, *Coastal Engineering*, *58*, 28–44. (Cité page 76.)

Boak, E. H., and I. L. Turner (2005), Shoreline Definition and Detection : A Review, *Journal of Coastal Research*, *21*, 688–703. (Cité page 5.)

Bonneton, P. (2003), Analyse physique et modélisation des processus hydrodynamiques en zone de surf, *Oceanis*, *29*, 157–179. (Cité page 19.)

Bonneton, P., V. Marieu, N. Seńećhal, and **B. Castelle** (2006), Wave transformation and energy dissipation in the surf zone : comparison between a non-linear model and field data, *Journal of Coastal Research*, *SI 39*, 329–333. (Cité page 13.)

Bonneton, P., N. Bruneau, **B. Castelle**, and F. Marche (2010), Large-scale vorticity generation due to dissipating waves in the surf zone, *Discrete and Continuous Dynamical Systems - Series B*, *13*(4), 729–738. (Cité pages 25, 34, 69 et 77.)

Bonneton, P., J. Van de Loock, J. P. Parisot, N. Bonneton, A. Sottolichio, G. Dedandt, **B. Castelle**, V. Marieu, and N. Pochon (2011), On the occurrence of tidal bores - The Garonne River case, *Journal of Coastal Research*, *SI 64*, 1462–1466. (Cité page 13.)

Booij, N., R. C. Ris, and L. H. Holthuijsen (1999), A third-generation wave model for coastal regions, Part 1, Model description and validation, *Journal of Geophysical Research*, *104*(C4), 7649–7666. (Cité pages xvii, 20, 43, 53 et 107.)

Bowen, A. J. (1997), Patterns in the water : Patterns in the sand ?, in *Proc. of Coastal Dynamics '97*, pp. 1–10, ASCE, New York. (Cité page 52.)

Bowen, A. J., and D. L. Inman (1971), Edge waves and crescentic bars, *Journal of Geophysical Research*, *76*, 8662–8671. (Cité pages 7 et 50.)

Bowman, D., and V. Goldsmith (1983), Bar morphology of dissipative beaches : an empirical model, *Marine Geology*, *51*, 15–33. (Cité page 56.)

Brander, R. W. (1999), Field observations on the morphodynamic evolution of a low-energy rip current system, *Marine Geology*, *157*, 199–217. (Cité pages 21 et 26.)

Brander, R. W., and A. D. Short (2000), Morphodynamics of a large-scale rip current system at Muriwai Beach, New Zealand, *Marine Geology*, *165*, 27–39. (Cité pages 21 et 26.)

Brander, R. W., and A. D. Short (2001), Flow kinematics of low-energy rip current systems, *Journal of Coastal Research*, *17*, 468–481. (Cité page 26.)

Brivois, O., D. Idier, J. Thiebot, **B. Castelle**, G. Le Gozannet, and D. Calvete (2012), On the use of linear stability model to characterize the morphological behaviour of a double sandbar system. Application to Trcu Vert Beach, France, *Comptes Rendus Geoscience*, *344*, 277–287. (Cité pages 48, 52 et 56.)

Browne, M., D. Strauss, **B. Castelle**, C. Lane, M. Blumenstein, and R. Tomlinson (2006), Empirical estimation of near-shore waves from a global offshore model, *IEEE Geoscience and Remote Sensing Letters*, *34*, 462–466. (Cité pages 13, 107, 108 et 113.)

Browne, M., **B. Castelle**, D. Strauss, and R. Tomlinson (2007), Estimating onshore break size from a global wind-wave model : An empirical approach using neural networks, *Coastal Engineering*, *54*, 445–460. (Cité pages 13, 76, 107, 108, 109 et 113.)

Bruneau, N. (2009), *Modélisation morphodynamique des plages sableuses*, These de doctorat de l'Université Bordeaux I. (Cité page 19.)

Bruneau, N., **B. Castelle**, P. Bonneton, and R. Pedreros (2009a), Very low frequency motions of a rip current system : observation and modeling, *Journal of Coastal Research*, *SI 56*, 1731–1735. (Cité pages 23 et 33.)

Bruneau, N., **B. Castelle**, P. Bonneton, R. Pedreros, R. Almar, N. Bonneton, P. Bretel, J. P. Parisot, and N. Sénéchal (2009b), Field observations of an evolving rip current on a meso-macrotidal well-developed inner bar and rip morphology, *Continental Shelf Research*, *29*, 1650–1662. (Cité pages xv, 22, 26, 33 et 107.)

Bruneau, N., P. Bonneton, **B. Castelle**, and R. Pedreros (2011), Modeling rip current circulations and vorticity in a high-energy meso-macrotidal environment, *Journal of Geophysical Research*, *116*(C07026), doi :10.1029/2010JC006693. (Cité pages xv, 22, 23, 24, 25, 33, 34, 77, 107 et 113.)

Bruun, P. (1962), Sea level rise as a cause of shore erosion, *Journal of Waterways and Harbours Division*, *88*, 117–130. (Cité pages xv, 10 et 11.)

Bryan, K. R., and A. J. Bowen (1997), Can bar-trapped edge waves cause bar formation, bar movement or bar growth ?, in *Proc. of Coasts and Ports*, pp. 1037–1042. (Cité pages 7 et 52.)

Caballeria, M., G. Coco, A. Falqués, and D. A. Huntley (2002), Self-organization mechanisms for the formation of nearshore crescentic and transverse bars, *Journal of Fluid Mechanics*, *465*, 379–410. (Cité page 52.)

Calvete, D., N. Dodd, A. Falqués, and S. M. Van Leeuwen (2005), Morphological development of rip channel systems : normal and near-normal wave incidence, *Journal of Geophysical Research*, *110*, C10006, doi :10.1029/2004JC002803. (Cité pages 7, 52 et 54.)

Carter, R. W. G. (1988), *Coastal Environments*, Academic Press. (Cité pages 50 et 52.)

Carter, T. G., P. L. Liu, and C. C. Mei (1973), Mass transport by waves and offshore bedforms, *Journal of the Waterways, Harbors and Coastal Engineering Division*, *99*, 165–184. (Cité page 50.)

Castelle, B. (2009), Dynamique des littoraux sableux dominés par l'action de la houle : les apports de la modelisation et de l'imagerie videó, *La Houille Blanche*, *1*, 64–70. (Cité pages xvii, 41 et 78.)

Castelle, B., and P. Bonneton (2006a), Modelling of a rip current induced by waves over a ridge and runnel system on the Aquitanian Coast, France, *Comptes Rendus Geoscience*, *338*, 711–717. (Cité pages 23, 24 et 33.)

Castelle, B., and P. Bonneton (2006b), Nearshore waves and currents over crescentic bars, *Journal of Coastal Research*, *SI 39*, 687–691. (Cité page 56.)

Castelle, B., and P. Bonneton (en préparation), On a negative feedback mechanism for surfzone sandbar behaviour during storms. (Cité pages 70 et 72.)

Castelle, B., and G. Coco (2012), The morphodynamics of rip channels on embayed beaches, *Continental Shelf Research*, *43*, 10–23. (Cité pages xix, 53, 66, 67, 68, 72 et 77.)

Castelle, B., and B. G. Ruessink (2011), Modeling formation and subsequent nonlinear evolution of rip channels : time-varying versus time-invariant wave forcing, *Journal of Geophysical Research*, *116*(F04008), doi :10.1029/2011JF001997. (Cité pages xviii, 53, 60, 61, 62, 72, 76 et 77.)

Castelle, B., P. Bonneton, and R. Butel (2006a), Modeling of crescentic pattern development of nearshore bars : Aquitanian Coast, France, *Comptes Rendus Geoscience*, *338*, 795–801. (Cité pages 53, 56, 60 et 72.)

Castelle, B., P. Bonneton, N. Sénéchal, H. Dupuis, R. Butel, and D. Michel (2006b), Dynamics of wave-induced currents over an alongshore non-uniform multiple-barred sandy beach on the Aquitanian Coast, France, *Continental Shelf Research*, *26*, 113–131. (Cité pages 21, 23, 33, 53, 107 et 113.)

Castelle, B., P. Bonneton, H. Dupuis, and N. Sénéchal (2007a), Double bar beach dynamics on the high-energy meso-macrotidal French Aquitanian Coast : a review, *Marine Geology*, *245*, 141–159. (Cité pages xvii, 36, 37, 38, 44, 56, 57 et 72.)

Castelle, B., J. Bourget, N. Molnar, D. Strauss, S. Deschamps, and R. B. Tomlinson (2007b), Dynamics of a wave-dominated tidal inlet and influence on adjacent beaches, Currumbin Creek, Gold Coast, Australia, *Coastal Engineering*, *54*, 77–90. (Cité page 13.)

Castelle, B., I. L. Turner, and B. G. Ruessink (2007c), Impact of storms on beach erosion : Broadbeach (Gold Coast, Australia), *Journal of Coastal Research*, *SI 50*, 534–539. (Cité pages xvii, 33, 41, 43, 44 et 45.)

Castelle, B., Y. Le Corre, and R. B. Tomlinson (2008), Can the Gold Coast beaches withstand extreme events, *Geo-Marine Letters*, *28*, 23–30. (Cité pages xvii, 33, 42, 43, 44, 45, 107, 110 et 113.)

Castelle, B., I. L. Turner, X. Bertin, and R. Tomlinson (2009a), Beach nourishment at coolangatta bay over the period 1987-2005, *Coastal Engineering*, *56*, 940–950. (Cité pages xx, xxi, 13, 44, 107, 109, 110, 111, 112, 113 et 114.)

Castelle, B., V. Marieu, P. Bonneton, N. Bruneau, and F. Grasso (2010a), Modelling beach profile evolutions, *La Houille Blanche*, *1*, 104–110. (Cité page 78.)

Castelle, B., B. G. Ruessink, P. Bonneton, V. Marieu, N. Bruneau, and T. D. Price (2010b), Coupling mechanisms in double sandbar systems, Part 1 : Patterns and physical explanation, *Earth Surface Processes and Landforms*, *35*, 476–486. (Cité pages xviii, 36, 53, 56, 57, 58, 60, 63 et 72.)

Castelle, B., B. G. Ruessink, P. Bonneton, V. Marieu, N. Bruneau, and T. D. Price (2010c), Coupling mechanisms in double sandbar systems, Part 2 : impact on alongshore variability of inner-bar rip channels, *Earth Surface Processes and Landforms*, *35*, 771–781. (Cité pages 36, 38, 58, 60, 63 et 72.)

Castelle, B., H. Michallet, V. Marieu, and P. Bonneton (2011), Surf zone retention in a laboratory rip current, *Journal of Coastal Research*, *SI 64*, 50–54. (Cité pages xvi, 27, 31, 32, 33, 34 et 77.)

Castelle, B., V. Marieu, G. Coco, P. Bonneton, N. Bruneau, and B. G. Ruessink (2012), On the impact of an offshore bathymetric anomaly on surfzone rip channels, *Journal of Geophysical Research*, *117*(F01038), doi :10.1029/2011JF002141. (Cité pages xvi, xix, 25, 26, 34, 36, 53, 63, 64, 65, 67, 72 et 77.)

Castelle, B., P. Bretel, S. Morisset, P. Bonneton, N. Bonneton, M. Tissier, C. Sotin, A. Nahon, N. Bruneau, J. -P. Parisot, S. Capo, S. Bujan, V. Marieu (2009b), Rip current system over string alongshore non-uniformities : on the use of HADCP for model validation, *Journal of Coastal Research*, *SI 56*, 1746–1750. (Cité pages 21, 33, 107 et 113.)

Castelle, B., H. Michallet, V. Marieu, F. Leckler, B. Dubarbier, A. Lambert, C. Berni, E. Barthélemy, F. Bouchette, P. Bonneton (2010d), Laboratory experiment on rip current circulations over a moveable bed : Drifter measurements, *Journal of Geophyical Research*, *115*(C12008), doi :10.1029/2010JC006343. (Cité pages xvi, 23, 27, 28, 29, 30, 31, 33 et 34.)

Cazenave, A., and R. S. Nerem (2004), Present-day sea level change : Observations and causes, *Reviews of Geophysics*, *42*, RG3001, doi :10.1029/2003RG3001. (Cité page 3.)

Charlier, R. H., M. C. P. Chaineux, and S. Morcos (2005), Panorama of the history of caostal protection, *Journal of Coastal Research*, *21*, 79–111. (Cité page 2.)

Chen, Q., R. A. Dalrymple, J. T. Kirby, A. B. Kennedy, and M. C. Haller (1999), Boussinesq modelling of a rip current system, *Journal of Geophysical Research*, *104*, 20,617–20,637. (Cité page 27.)

Cienfuegos, R., E. Barthélemy, and P. Bonneton (2010), Wave-breaking model for boussinesq-type equations including roller effects in the mass conservation equation, *Journal of Waterway, Port and Ocean Engineering*, *136*, 10–26. (Cité page 76.)

Coco, G., and A. B. Murray (2007), Patterns in the sand : from forcing templates to self-organization, *Geomorphology*, *91*, 271–290. (Cité pages 7, 53 et 66.)

Coco, G., A. B. Murray, and M. O. Green (2007), Sorted bed forms as self-organized patterns : 1. Model development, *Journal of Geophysical Research*, *112*(F03015), doi : 10.1029/2006JF000665. (Cité pages 53 et 63.)

Cooper, J. A. G., and O. H. Pilkey (2004), Sea-level rise and shoreline retreat : time to abandon the Bruun Rule, *Global and Planetary Change*, *43*, 157–171. (Cité page 10.)

Cowell, P. J., P. S. Roy, and R. A. Jones (1995), Simulation of large-scale coastal change using a morphological behavior model, *Marine Geology*, *126*, 45–61. (Cité page 108.)

Dalrymple, R. A. (1975), A mechanism for rip current generation on an open coast, *Journal of Geophysical Research*, *80*, 3485–3487. (Cité page 16.)

Dalrymple, R. A., J. H. MacMahan, A. J. H. M. Reniers, and V. Nelko (2011), Rip currents, *Annual Review of Fluid Mechanics*, *43*, 551–581. (Cité pages 7 et 63.)

Damgaard, J., N. Dodd, L. Hall, and T. Chesher (2002), Morphodynamic modeling of rip channel growth, *Coastal Engineering*, *43*, 199–221. (Cité pages 7, 53 et 60.)

De Melo Apoluceno, D. (2003), *Morphodynamique des plages a barres en domaine méso a macrotidal : exemple de la plage du Truc Vert, Gironde, France*, These de doctorat de l'Université Bordeaux I. (Cité page 36.)

Dean, R. G., and R. A. Dalrymple (1991), *Water Wave Mechanics for Engineers and Scientists*, World Scientific. (Cité page 17.)

Deigaard, R., N. Drønen, J. Fredsøe, J. H. Jensen, and M. P. Jørgensen (1999), A morphological stability analysis for a long straight barred coast, *Coastal Engineering*, *36*, 171–195. (Cité page 52.)

Desmazes, F. (2005), *Caractérisation des barres sableuses d'une plage de la cote aquitaine : exemple de la plage du Truc Vert*, These de doctorat de l'Université Bordeaux I. (Cité page 36.)

Desombre, J., D. Morichon, and M. Mory (2012), RANS v^2-f simulation of a swash event : Detailed flow structure, *Coastal Engineering*, *71*, 1–12. (Cité page 76.)

Drake, T., and J. Calantoni (2001), Discrete particle model for sheet flow sediment transport in the nearshore, *Journal of Geophysical Research*, *106*(C9), doi :10.1029/2000JC000611. (Cité pages 10 et 54.)

Drønen, N., and R. Deigaard (2007), Quasi-three-dimensional modelling of the morphology of longshore bars, *Coastal Engineering*, *54*, 197–215. (Cité pages 53 et 60.)

Dubarbier, B., and **B. Castelle** (2011), Numerical modeling investigation of the influence of tide on the formation andsubsequent nonlinear evolution of rip channels, *Journal of Coastal Research*, *SI 64*, 1018–1022. (Cité pages 48, 56 et 72.)

Dubarbier, B., **B. Castelle**, F. Birrien, V. Marieu, and B. G. Ruessink (2012), On a new beach profile evolution model on the timescales of weeks : simulations and preliminary results from the input of data assimilation, in *Proc. 33rd International Conference on Coastal Engineering*. (Cité pages xx, 76, 78 et 79.)

Duplantier, F. (1976), *Etude sédimentologique de la zone cotiere et du proche plateau continental de la région de Capbreton, paléographie et évolution actuelle*, These de Doctorat de l'Université Bordeaux I. (Cité page 113.)

Eckart, C. (1951), Surface waves in water of variable depth, in *Wave Rep. 100, S10 Ref 51-52*, p. 99pp., Univ. Calif. Scripps Inst. Oceanogra. (Cité page 50.)

Enjalbert, C., **B. Castelle**, D. Rihouey, and D. Dailloux (2011), High-frequency video observation of geologically-constrained barred-beach : La Grande Plage de Biarritz (France), *Journal of Coastal Research*, *SI 64*, 70–74. (Cité pages 40, 44 et 66.)

EUROSION (2004), *Living with coastal erosion in Europe : Sediment and Space for Sustainability*, rapport disponible sur www.eurosion.org. (Cité page 3.)

Falqués, A., A. Montoto, and V. Iranzo (1996), Bed-flow instability of the longshore current, *Continental Shelf Research*, *16*, 1927–1964. (Cité page 54.)

Falqués, A., G. Coco, and D. A. Huntley (2000), A mechanism for the generation of wave-driven rhythmic patterns in the surf zone, *Journal of Geophysical Research*, *105*, 24,071–24,088. (Cité pages 52 et 54.)

Falqués, A., D. Calvete, and F. Ribas (2011), Shoreline Instability due to Very Oblique Wave Incidence : Some Remarks on the Physics , *Journal of Coastal Research*, *27*, 291–295. (Cité page 108.)

Feddersen, F., and R. T. Guza (2003), Observations of nearshore circulation : alongshore uniformity, *Journal of Geophysical Research*, *108*(C1), doi :10.1029/2001JC001293. (Cité page 30.)

Froidefond, J. M., F. Duplantier, and O. Weber (1982), Estimation and flux of the theoretical sedimentary volume displaced during the Holocene transgression on the Bayonne inner-shelf (SW, France), *Marine Geology*, *46*, 101–116. (Cité page 113.)

Gallop, S. L., K. R. Bryan, G. Coco, and S. A. Stephens (2011), Storm-driven changes in rip channel patterns on an embayed beach, *Geomorphology*, *127*, 179–188. (Cité pages 39, 60 et 66.)

Garnier, R., D. Calvete, A. Falqués, and M. Caballeria (2006), Generation and nonlinear evolution of shore-oblique/transverse sand bars, *Journal of Fluid Mechanics*, *567*, 327–360. (Cité pages 7, 53, 54 et 60.)

Garnier, R., D. Calvete, A. Falqués, and N. Dodd (2008), Modelling the formation and the long-term behavior of rip channel systems from the deformation of a longshore bar, *Journal of Geophysical Research*, *113*, C07053, doi :10.1029/2007JC004632. (Cité pages 53, 54 et 60.)

Garnier, R., N. Dodd, A. Falqués, and D. Calvete (2010), Mechanisms controlling crescentic bar amplitude, *Journal of Geophysical Research*, *115*(F02007), doi :10.1029/2009JF001407. (Cité pages 54, 55 et 60.)

Gaudin, M., T. Mulder, P. Cirac, S. Berne, and P. Imbert (2006), Past and present sedimentary activity in the Capbreton Canyon, southern Bay of Biscay, *Geo-Marine Letters*, *26*, 331–345. (Cité pages 63 et 113.)

Gervais, M., Y. Balouin, and R. Belon (2012), Morphological response and coastal dynamics associated with major storm events along the Gulf of Lions Coastline, France, *Geomorphology*, *143-144*, 69–80. (Cité page 42.)

Goldsmith, V., D. Bowman, and K. Kiley (1982), Sequential stage development of crescentic bars : HaHoterim Beach, Southeastern Mediterranean, *Journal of Sedimentary Petrology*, *52*, 233–249. (Cité pages 5 et 56.)

Goodwin, I. D., M. A. Stables, and J. M. Olley (2006), Wave climate, sand budget and shoreline aligment evolution of the Iluka-Woody Bay sand barrier, northern New South Wales, Asuatralia, since 3000 yr BP, *Marine Geology*, *226*, 127–144. (Cité page 108.)

Grasso, F., H. Michallet, E. Barthélemy, and R. Certain (2009), Physical modeling of intermediate cross-shore beach morphology : Transient and equilibrium states, *Journal of Geophysical Research*, *114*, C09001, doi :10.1029/2009JC005308. (Cité page 10.)

Grasso, F., H. Michallet, and E. Barthélemy (2011), Sediment transport associated with morphological beach changes forced by irregular asymmetric skewed waves, *Journal of Geophysical Research*, *116*, C03020, doi :10.1029/2010JC006550. (Cité pages 10 et 54.)

Grasso, F., **B. Castelle**, and B. G. Ruessink (2012), Turbulence dissipation under breaking waves and bores in a natural surf zone, *Continental Shelf Research*, *43*, 133–141. (Cité pages 54, 71 et 72.)

Grinsted, A., J. C. Moore, and S. Jevrejeva (2004), Application of the cross wavelet transform and wavelet coherence to geophysical time series, *Nonlinear Processes in Geophysics*, *11*, 561–566. (Cité page 55.)

Haas, K. A., and I. A. Svendsen (2002), Laboratory measurements of the vertical structure of rip currents, *Journal of Geophysical Research*, *107*(C5), doi :10.1029/2001JC000911. (Cité pages 24 et 27.)

Hakkou, M. (2012), *Contribution a l'étude de la dynamique morphosédimentaire du littoral de Bouknadel-Kénitra*, These de Doctorat de l'Université Ibn Tofail. (Cité page 112.)

Hakkou, M., **B. Castelle**, A. Benmohammadi, and B. Zourarah (2011), Wave climate of morpho-sedimentary characteristics of the Keńitra-Bouknadel sandy coast, Morocco, *Environmental Earth Sciences*, *64*, 1729–1739. (Cité pages 13, 107, 109, 111, 112, 113 et 114.)

Haller, M. C., and R. A. Dalrymple (2001), Rip current instabilities, *Journal of Fluid Mechanics*, *433*, 161–192. (Cité page 27.)

Haller, M. C., U. Petrevu, J. Oltman-Shay, and R. A. Dalrymple (1999), Wave group forcing of low frequency surf zone motion, *Coastal Engineering*, *41*, 121–36. (Cité page 16.)

Hamm, L. (1992), Directional nearshore wave propagation over a rip channel : an experiment, in *Proc. of 23rd Int. Conf. on Coast. Eng.*, pp. 226–239, ASCE, New York. (Cité page 27.)

Hamm, L., M. Capobianco, H. H. Dette, A. Lechuga, R. Spanhoff, and M. J. F. Stive (2002), A summary of European experience with shore nourishment, *Coastal Engineering*, *47*, 237–264. (Cité pages 2 et 114.)

Hansen, J. E., and P. L. Barnard (2010), Sub-weekly to interannual variability of a high-energy shoreline, *Coastal Engineering*, *57*, 959–972. (Cité page 108.)

Hanson, H., A. Brampton, M. Capobianco, H. H. Dette, L. Hamm, C. Laustrup, A. Lechuga, and R. Spanhoff (2002), Beach nourishment projects, pratices, and objectives - a European overview, *Coastal Engineering*, *47*, 81–111. (Cité page 2.)

Harley, M. D., I. L. Turner, A. D. Short, and R. Ranasinghe (2011), A reevaluation of coastal embayment rotation : The dominance of cross-shore versus alongshore sediment transport processes, Collaroy-Narrabeen Beach, southeast Australia, *Journal of Geophysical Research*, *116*(F04033), doi :10.1029/2010JF001989. (Cité page 65.)

Henderson, S. M., J. S. Allen, and P. A. Newberger (2004), Nearshore sandbar migration predicted by an addy-diffusive boundary layer model, *Journal of Geophysical Research*, *109*(C06024), doi :10.1029/2003JC002137. (Cité page 54.)

Hino, M. (1974), Theory on formation of rip-current and cuspidal coast, in *Proc. of the 14th Conference on Coastal Engineering*, pp. 901–919, ASCE, New York. (Cité page 51.)

Hoefel, F., and S. Elgar (2003), Wave-induced Sediment Transport and Sandbar Migration, *Science*, *299*, 1885–1887. (Cité pages 10 et 54.)

Holland, K. T., and R. A. Holman (1996), Field observations of beach cusps and swash motions, *Marine Geology*, *134*, 77–93. (Cité page 53.)

Holman, R. A. (2000), Pattern formation in the nearshore, in *Proc. of River, Coastal and Estuarine Morphodynamics*, pp. 141–162, Springer-Verlag, New York. (Cité page 52.)

Holman, R. A., and A. J. Bowen (1982), Bars, bumps and holes : models for the generation of complex beach topography, *Journal of Geophysical Research*, *87*, 457–468. (Cité pages 7 et 50.)

Holman, R. A., and J. Stanley (2007), The history and technical capabilities of argus, *Coastal Engineering*, *54*, 477–491. (Cité pages 65 et 110.)

Holman, R. A., G. Symonds, E. B. Thornton, and R. Ranasinghe (2006), Rip spacing and persistence on an embayed beach, *Journal of Geophysical Research*, *111*, C06006, doi :10.1029/2005JC002965. (Cité pages 60 et 66.)

Hom-ma, M., and C. Sonu (1962), Rhythmic pattern of longshore bars related to sediment characteristics, in *Proc. of 8th Int. Conf. on Coast. Eng.*, pp. 248–278, ASCE, New York. (Cité pages 5 et 56.)

Idier, D., A. Flaqués, B. G. Ruessink, and R. Garnier (2011), Shoreline instability under low-angle wave incidence, *Journal of Geophysical Research*, *116*(F4), doi : 10.1029/2010JF001894. (Cité page 11.)

IPCC (2007), *IPCC Fourth Assessment Report : Climate Change 2007*, Cambridge, United Kingdom and New York, NY, USA. (Cité pages 2 et 3.)

Jackson, D. W. T., J. A. G. Cooper, and L. D. Rio (2005), Geological control of beach morphodynamic state, *Marine Geology*, *216*, 297–314. (Cité page 39.)

Jevrejeva, S., J. C. Moore, and A. Grinsted (2003), Influence of the Arctic Oscillation and El Niño-Southern Oscillation (ENSO) on ice conditions in the Baltic sea : The wavelet approach, *Journal of Geophysical Research*, *108*(D21), doi :10.1029/2003JD003417. (Cité page 55.)

Johnson, D., and C. Pattiaratchi (2004), Transient rip currents and nearshore circulation on a swell-dominated beach, *Journal of Geophysical Research*, *109*(C02026), doi : 10.1029/2003JC001798. (Cité page 16.)

Kaczmarek, J. M., R. Ostrowski, Z. Pruszak, and G. Rozynski (2005), Selected problems of sediment transport and morphodynamics of a multi-bar nearshore zone, *Estuarine Coastal and Shelf Science*, *62*, 415–425. (Cité page 109.)

Kamphuis, J. W. (1991), Alongshore Sediment Transport Rate, *Journal of Waterway, Port, Coastal, and Ocean Engineering*, *117*, 624–640. (Cité page 109.)

Kamphuis, J. W. (2011), Coastal Engineering - Theory and Practice, in *Proc. of Coastal Sediments '11*, vol. 1, pp. 1–14, ASCE, New York. (Cité pages xv et 14.)

Kennedy, A. B., and D. Thomas (2004), Drifter measurements in a laboratory rip current, *Journal of Geophysical Research*, *109*(C08005), doi :10.1029/2003JC001927. (Cité page 27.)

Kennedy, A. B., M. Brocchini, L. Soldini, and E. Gutierrez (2006), Topographically controlled, breaking-wave-induced macrovortices. Part 2. Changing geometries, *Journal of Fluid Mechanics*, *559*, 57–80. (Cité page 27.)

Klein, A. H. F., O. Ferreira, J. M. A. Dias, M. G. Tessler, L. F. Silveira, L. Benedet, J. T. de Menezes, and J. G. N. de Abreu (2010), Morphodynamics of structurally controlled headland-bay beaches in southeastern Brazil : A review, *Coastal Engineering*, *57*, 98–111. (Cité page 65.)

Klein, M. D., and H. M. Schuttelaars (2006), Morphodynamic evolution of double-barred beaches, *Journal of Geophysical Research*, *111*, C06017, doi :10.1029/2005JC003155. (Cité pages 52 et 53.)

Komar, P. D. (1971), The mechanics of sand transport on beaches, *Journal of Geophysical Research*, *76*. (Cité page 109.)

Komar, P. D. (1998), *Beach processes and sedimentation*, Prentice Hall. (Cité pages 7, 50 et 52.)

Kostanic, F. M. H. I. (2001), *Principles of Neurocomputaing for Science and Engineering*, McGraw Hill. (Cité page 108.)

Kuhn, T. S. (1962), *The structure of scientific revolutions*, University of Chicago Press. (Cité pages xv, 13 et 14.)

Kuhn, T. S. (1977), *The essential tension : selected studies in scientific tradition abd change*, University of Chicago Press. (Cité pages xv et 14.)

Kuriyama, Y. (2002), Medium-term bar behavior and associated sediment transport at Hasaki, Japan, *Journal of Geophysical Research*, *107*, doi :10.1029/JC2001JC000899. (Cité page 42.)

Lafon, V., H. Dupuis, H. Howa, and J. M. Froidefond (2002), Determining ridge and runnel longshore morphodynamics using SPOT imagery, *Oceanologica Acta*, *25*, 149–158. (Cité page 36.)

Lafon, V., D. De Melo Apoluceno, H. Dupuis, D. Michel, H. Howa, and J.-M. Froidefond (2004), Morphodynamics of nearshore rhythmic sandbars in a mixedenergy environment (SW France) : I. Mapping beach changes using visible satellite imagery, *Estuarine, Coastal and Shelf Science*, *61*, 289–299. (Cité page 36.)

Lafon, V., H. Dupuis, R. Butel, **B. Castelle**, D. Michel, H. Howa, and D. De Melo Apoluceno (2005), Morphodynamics of nearshore rhythmic sandbars in a mixed energy environment (SW France) : II. Physical forcing analysis, *Estuarine, Coastal and Shelf Science*, *65*, 449–462. (Cité pages 36 et 56.)

Lascody, R. L. (1998), East central Florida rip current program, *National Weather Digest*, *22*, 25–30. (Cité page 77.)

Lazure, P., and F. Dumas (2008), An external-internal mode coupling for a 3D hydrodynamical model for applications at regional scale (MARS), *Advances in Water Ressources*, *31*, 233–250. (Cité page 12.)

Lee, G., and W. A. Birkemeier (1993), Beach and nearshore survey data : 1985-1991 CERC Field Research Laboratory, in *Tech. Rep. CERC-93-3*, U.S. Army Corps of Engineers, Waterways Experiment Station, Vicksburg, Miss. (Cité page 65.)

Lippmann, T., and R. Holman (1990), The spatial and temporal variability of sand bar, *Journal of Geophysical Research*, *95(C7)*, 11,575–11,590. (Cité page 36.)

Long, J. W., and H. T. Ozkan-Haller (2005), Offshore controls on nearshore rip currents, *Journal of Geophysical Research*, *110*(C12007), doi :10.1029/2005JC003018. (Cité page 63.)

Long, J. W., and H. T. Ozkan-Haller (2009), Low-frequency characteristics of wave group-forced vortices, *Journal of Geophysical Research*, *114*(C08004), doi :10.1029/2008JC004894. (Cité page 16.)

Longuett-Higgins, M. S., and R. W. Stewart (1964), Radiation stress in water waves, a physical discussion with applications, *Deep Sea Research*, *11*(4), 529–563. (Cité pages 25 et 34.)

Loureiro, C., O. Ferreira, and J. A. G. Cooper (2012), Extreme erosion on high-energy embayed beaches : Influence of megarips and storm grouping, *Geomorphology*, *139-140*, 155–171. (Cité page 66.)

MacMahan, J. H., A. J. H. M. Reniers, E. B. Thornton, and T. P. Stanton (2004a), Infragravity rip current pulsations, *Journal of Geophysical Research*, *109*, C01033, doi : 10.1029/2003JC002068. (Cité page 26.)

MacMahan, J. H., A. J. H. M. Reniers, E. B. Thornton, and T. P. Stanton (2004b), Surf zone eddies coupled with rip current morphology, *Journal of Geophysical Research*, *109*, C07004, doi :10.1029/2003JC002083. (Cité page 26.)

MacMahan, J. H., E. B. Thornton, and A. J. H. M. Reniers (2006), Rip current review, *Coastal Engineering*, *53*, 191–208. (Cité pages xvi, 7 et 31.)

MacMahan, J. H., et al. (2010), Mean lagrangian flow behavior on an open coast rip channeled beach : a new perspective, *Marine Geology*, *268*, 1–15. (Cité pages 32, 33 et 34.)

Marciano, R., Z. B. Wang, A. Hibma, H. J. de Vriend, and A. Defina (2005), Modeling of channel patterns in short tidal basins, *Journal of Geophysical Research*, *110*, F01001, doi :10.1029/2003JC000092. (Cité pages xv et 11.)

Marieu, V., P. Bonneton, D. L. Foster, and F. Ardhuin (2008), Modeling of vortex ripple morphodynamics, *Journal of Geophysical Research*, *113*, C09007, doi : 10.1029/2007JC004659. (Cité pages xv et 11.)

Masselink, G., and A. D. Short (1993), The effect of tide range on beach morphodynamics and morphology : a conceptual model, *Journal of Coastal Research*, *9*, 785–800. (Cité page 36.)

McNinch, J. E. (2004), Geologic control in the nearshore : shore-oblique sandbars and shoreline erosion hotspots, Mid-Atlantic Bight, USA, *Marine Geology*, *211*, 121–141. (Cité page 63.)

Mei, C. C. (1983), *The Applied Dynamics of Ocean Surface Waves*, World Scientific. (Cité pages 17 et 19.)

Michallet, H., F. Grasso, and E. BarthÍemy (2007), Long waves and beach profile evolutions, *Journal of Coastal Research*, *SI 50*, 221–225. (Cité page 10.)

Michallet, H., **B. Castelle**, F. Bouchette, A. Lambert, C. Berni, E. Barthélemy, P. Bonneton, and D. Sous (2010), ModeĺIisation de la morphodynamique d'une plage barreé tridimensionnelle, in *Proc. Journeé Nationales de Geńie Cotier et Geńie Civil*, pp. 379–386. (Cité pages 27 et 34.)

Michallet, H., **B. Castelle**, C. Berni, E. Barthélemy, and P. Bonneton (en préparation), Physical modeling of three-dimensional intermediate beach morphodynamics, *Journal of Geophysical Research*. (Cité pages 27 et 34.)

Mori, N., T. Yasuda, H. Mase, T. Tom, and Y. Oku (2010), Projection of Extreme Wave Climate Change under Golbal Warming, *Hydrological Research Letters*, *4*, 15–19. (Cité page 3.)

Murray, A. (2007), Reducing model complexity for explanation and prediction, *Geomorphology*, *90*, 178–191. (Cité pages 12 et 76.)

Murray, A., and E. Thieler (2004), A new hypothesis for the formation of large-scale inner-shelf sediment sorting and rippled scour depressions, *Continental Shelf Research*, *24*, 295–315. (Cité page 63.)

Nadaoka, K., S. Ueno, and Y. Igarashi (1988), Sediment suspension due to large scale eddies in the surf zone, in *Proc. of the 21st International Conference on Coastal Engineering*, pp. 1646–1660, ASCE, New York. (Cité page 70.)

Narteau, C., D. Zhang, O. Rozier, and P. Claudin (2009), Setting the length and time scales of a cellular automaton dune model from the analysis of superimposed bed forms, *Journal of Geophysical Research*, *114*, F03006, doi :10.1029/2008JF001127. (Cité page 76.)

Ozkan-Haller, H. T., and J. T. Kirby (1999), Nonlinear shear instabilities of the longshore current : A comparison of observations and computations, *Journal of Geophysical Research*, *104*, C11, doi :10.1029/1999JC900104. (Cité page 16.)

Pape, L., and B. G. Ruessink (2011), Neural-network predictability experiments for nearshore sandbar migration, *Continental Shelf Research*, *31*, 1033–1042. (Cité page 108.)

Parisot, J. P., et al. (2009), Evolution of a multi-barred sandy beaches in presence of very energetic events, *Journal of Coastal Research*, *SI 56*, 1786–1790. (Cité pages xvii et 39.)

Peterson, C. D., P. L. Jackson, D. J. O'Neil, C. L. Rosenfield, and A. J. Kimerling (1990), Lirroral cell response to inter-annual climatic forcing 1983-1987 on the central Oregon coast, USA, *Journal of Coastal Research*, *6*, 87–110. (Cité page 108.)

Philipps, O. M. (1977), *The dynamics of the upper ocean*, Cambridge University Press. (Cité page 19.)

Plant, N. G., K. T. Holland, and R. A. Holman (2006), A dynamical attractor governs beach response to storms, *Geophysical Research Letters*, *33*(L17697), doi :10.1029/2006GL027105. (Cité pages 65 et 76.)

Poate, T., K. Kingston, G. Masselink, and P. Russell (2009), Response of High-energy, Macrotidal Beaches to Seasonal Changes in Wave Conditions : Examples from North Cornwall, UK, *Journal of Coastal Research*, *SI 56*, 747–751. (Cité page 56.)

Price, T. D., and B. G. Ruessink (2011), State dynamics of a double sandbar system, *Continental Shelf Research*, *31*, 659–674. (Cité pages 36 et 60.)

Price, T. D., and B. G. Ruessink (in press), Observation and conceptual modellin of morphological coupling in a double sandbar system, *Earth Surface Processes and Landforms*. (Cité pages 36, 58 et 72.)

Price, T. D., **B. Castelle**, R. Ranasinghe, and B. G. Ruessink (soumis), Coupled sandbar patterns and obliquely incident waves, *Journal of Geophysical Research*. (Cité pages 36, 58, 72 et 80.)

Quartel, S. (2009), Temporal and spatial behaviour of rip channels in a multiple-barred coastal system, *Earth Surface Processes and Landforms*, *34*, 163–176. (Cité pages 56 et 57.)

Ranasinghe, R., R. McLoughlin, A. D. Short, and G. Symonds (2004), The Southern Oscillation Index, wave climate, and beach rotation, *Marine Geology*, *204*, 273–287. (Cité page 65.)

Raubenheimer, B., R. T. Guza, and S. Elgar (1996), Wave transformation across the inner surf zone, *Journal of Geophysical Research*, *101*(C1), 25,589–25,597. (Cité page 69.)

Reniers, A. J. H. M., J. A. Roelvink, and E. B. Thornton (2004), Morphodynamic modeling of an embayed beach under wave group forcing, *Journal of Geophysical Research*, *109*, C01030, doi :10.1029/2002JC001586. (Cité pages 16 et 60.)

Reniers, A. J. H. M., J. H. MacMahan, F. J. Beron-Vera, and M. J. Olascoaga (2010), Rip-current pulses tied to lagrangian coherent structures, *Geophysical Research Letters*, *37*, doi :10.1029/2009GL041443. (Cité pages 33 et 34.)

Ripley, B. D. (1996), *Pattern Classification and Neural Networks*, Cambridge. (Cité page 108.)

Ris, R. C., L. H. Holthuijsen, and N. Booij (1999), A third-generation wave model for coastal regions 2. Verification, *Journal of Geophysical Research*, *104*(C4), 7667–7681. (Cité page 107.)

Roelvink, J. A., A. J. H. M. Reniers, A. van Dongeren, J. V. de Vries, and R. McCall and J. Lescinski (2009), Modelling storm impacts on beaches, dunes and barrier islands, *Coastal Engineering*, *56*, 1133–1152. (Cité page 77.)

Rosati, J. D., T. L. Walton, and K. Bodge (2002), Longshore sediment transport, in *Coastal Engineering Manual, Part II : Coastal Sediment Processes*, edited by D. B. King, U.S. Army Corps of Engineering, Washington, D.C. (Cité page 109.)

Ruessink, B. G., and Y. Kuriyama (2008), Numercial predictability experiments of cross-shore sandbar migration, *Geophysical Research Letters*, *35*(L01603), doi : 10.1029/2007GL032530. (Cité page 12.)

Ruessink, B. G., G. Coco, R. Ranasinghe, and I. L. Turner (2007a), Coupled and non-coupled behavior of three-dimensional morphological patterns in a double sandbar system, *Journal of Geophysical Research*, *112*, C07002, doi :10.1029/2006JC003799. (Cité pages 36, 56, 57, 58 et 60.)

Ruessink, B. G., Y. Kuriyama, A. J. H. M. Reniers, and J. A. Roelvink (2007b), Modeling cross-shore sandbar behavior on the timescales of weeks, *Journal of Geophysisical Research*, *112*(F03010), doi :10.1029/2006JC000730. (Cité page 54.)

Ruessink, B. G., L. Pape, and I. L. Turner (2009), Daily to interannual cross-shore sandbar migration : Observatuions from a multiple bar system, *Continental Shelf Research*, *29*, 1663–1677. (Cité page 42.)

Ruessink, B. G., G. Ramaekers, and L. C. van Rijn (2012), On the parametrization of the free-stream non-linear wave orbital motion in nearshore morphodynamic models, *Coastal Engineering*, *65*, 56–63. (Cité pages 72 et 78.)

Ruggiero, P., M. Buijsman, G. M. Kaminsky, and G. Gelfenbaum (2010), Modeling the effects of wave climate and sediment supply variability on large-scale shoreline change, *Marine Geology*, *273*, 127–140. (Cité page 108.)

Saint-Cast, F. (2002), *Modélisation de la morphodynamique des corps sableux en milieu littoral*, These de doctorat de l'Université Bordeaux I. (Cité page 53.)

Schielen, R., A. Doelman, and H. E. De Swart (1993), On the dynamics of free bars in straight channels, *Journal of Fluid Mechanics*, *252*, 325–356. (Cité page 54.)

Schupp, C. A., J. E. McNinch, and J. H. List (2006), Nearshore shore-oblique bars, gravel outcrops, and their correlation to shoreline change, *Marine Geology*, *233*, 63–79. (Cité page 63.)

Schyuer-Ming, S., and P. D. Komar (1994), Sediments, beach morphology and seacliff erosion within an Oregon Coast littoral cell, *Journal of Coastal Research*, *10*, 144–157. (Cité page 65.)

Scott, T. M., P. Russell, G. Masselink, and A. Woolers (2009), Rip current variability and hazard along macro-tidal coast, *Journal of Coastal Research*, *SI 56*, 895–898. (Cité page 4.)

Scott, T. M., G. Masselink, and P. E. Russell (2011), Morphodynamic characteristics and classification of beaches in England and Wales, *Marine Geology*, *286*, 1–20. (Cité page 65.)

Sénéchal, N., H. Dupuis, and P. Bonneton (2004), Preliminary hydrodynamic results of a field experiment on a barred beach, Truc Vert beach on October 2001 , *Ocean Dynamics*, *54*, 408–414. (Cité pages 21 et 107.)

Sénéchal, N., T. Gouriou, **B. Castelle**, J.-P. Parisot, S. Capo, S. Bujan, and H. Howa (2009), Morphodynamic response of a meso- to macro-tidal intermediate beach based on a long-term dataset, *Geomorphology*, *107*, 263–274. (Cité pages 38, 44 et 56.)

Sénéchal, N., et al. (2011), The ECORS-Truc Vert'08 nearshore field experiment : presentation of a three-dimensional morphologic system in a macro-tidal environment during consecutive extreme storm conditions, *Ocean Dynamics*, *61*, 2073–2098. (Cité pages 21 et 107.)

Sennes, G., **B. Castelle**, X. Bertin, H. Mirfenderesk, and R. B. Tomlinson (2007), Modeling of the Gold Coast Seaway tidal inlet, Australia, *Journal of Coastal Research*, *SI 50*, 1086–1091. (Cité pages 13 et 44.)

Shepard, F. P. (1952), Revised nomenclature for depositional coastal features, *Bulletin - American Association of Petroleum Geologists*, *36*, 1902–1912. (Cité page 5.)

Shepard, F. P., and D. L. Inman (1950), Nearshore circulation related to bottom topography and refraction, *Transactions - American Geophysical Union*, *31*, 196–212. (Cité page 63.)

Short, A. D. (1992), Beach systems of the central netherlands coast : processes, morphology and structural impacts in a storm driven multi-bar system, *Marine Geology*, *107*, 103–137. (Cité page 36.)

Short, A. D. (1999), *Handbook of Beach and Shoreface Morphodynamics*, Wiley, Chichester. (Cité pages 38, 50 et 52.)

Short, A. D. (2006), Australian Beach Systems - Nature and Distribution, *Journal of Coastal Research*, *22*, 11–27. (Cité page 39.)

Short, A. D., and T. Aagaard (1993), Single and multi-bar beach change models, *Journal of Coastal Research*, *SI 15*, 141–157. (Cité page 36.)

Short, A. D., and G. Masselink (1999), Embayed and structurally controlled embayed beaches, in *Handbook of Beach and Shoreface Morphodynamics*, edited by A. D. Short, pp. 230–250, Wiley, Chichester. (Cité pages 65, 66 et 67.)

Smit, M. W. J., A. J. H. M. Reniers, and M. J. F. Stive (2005), Nearshore bar response to time-varying conditions, in *Proc. of Coastal Dynamics '05*, pp. [CD–ROM], ASCE, New York. (Cité page 60.)

Smit, M. W. J., A. J. H. M. Reniers, B. G. Ruessink, and J. A. Roelvink (2008), The morphological response of a nearshore double sandbar system to constant wave forcing, *Coastal Engineering*, *55*, 761–770. (Cité pages 53 et 60.)

Smit, M. W. J., A. J. H. M. Reniers, and M. J. F. Stive (2012), Role of morphological variability in the evolution of nearshore sandbars, *Coastal Engineering*, *69*, 19–28. (Cité page 60.)

Smith, J. (2006), Wave-current interactions in finite depth, *Journal of Physical Oceanography*, *36*, 1403–1419. (Cité pages 23 et 25.)

Smith, J. A., and J. L. Largier (1995), Observation of nearshore circulation : Rip currents, *Journal of Geophysical Research*, *100*(C6), 10,967–10,975. (Cité page 7.)

Sonu, C. J. (1972a), Field observation of nearshore circulation and meandering currents, *Journal of Geophysical Research*, *77*, 3232–3247. (Cité pages 7 et 13.)

Sonu, C. J. (1972b), Comments on paper by A.J. Bowen and D.L. Inman "Edge Wave and Crescentic Sandbars", *Journal of Geophysical Research*, *77*, 6629–6631. (Cité pages 51 et 52.)

Sonu, C. J. (1973), Three-dimensional Beach Changes, *Journal of Geology*, *81*, 42–64. (Cité pages 5 et 56.)

Splinter, K. D., R. A. Holman, and N. G. Plant (2011), A behavior-oriented dynamic model for sand bar migration and 2DH evolution, *Journal of Geophysical Research*, *116*, C01020, doi :10.1029/2010JC006382. (Cité page 40.)

Stive, M. J. F., and A. J. H. M. Reniers (2003), Sandbar in Motions, *Science*, *299*(5614), 1855–1856. (Cité page 5.)

Svendsen, I. A. (2006), *Introduction to nearshore Hydrodynamics*, World Scientific. (Cité page 17.)

Thiébot, J., D. Idier, R. Garnier, A. Falqués, and B. G. Ruessink (2012), The influence of wave direction on the morphological response of a double sandbar system, *Continental Shelf Research*, *32*, 71–85. (Cité page 36.)

Thornton, E. B., and R. T. Guza (1983), Transformation of wave height distribution, *Journal of Geophysical Research*, *88*, 5925–5938. (Cité pages 20 et 69.)

Thornton, E. B., J. H. MacMahan, and A. H. Sallenger Jr (2007), Rip currents, megacusps, and eroding dunes, *Marine Geology*, *240*, 151–167. (Cité page 7.)

Tiessen, M. C. H., S. M. Van Leeuwen, D. Calvete, and N. Dodd (2010), Field test of a linear stability model for crescentic sandbar, *Coastal Engineering*, *57*, 41–51. (Cité page 60.)

Tiessen, M. C. H., N. Dodd, and R. Garnier (2011), Development of crescentic bars for a periodically perturbated initial bathymetry, *Journal of Geophysical Research*, *116*(F04016), doi :10.1029/2011JF002069. (Cité page 60.)

Tissier, M., P. Bonneton, R. Almar, **B. Castelle**, N. Bonneton, and A. Nahon (2011), Field measurements and non-linear prediction of wave celerity in the surf zone, *European Journal of Mechanics - B/Fluids*, *30*, 589–597. (Cité page 13.)

Tissier, M., P. Bonneton, F. Marche, F. Chazel, and D. Lannes (2012), A new approach to handle wave breaking in fully non-linear Boussinesq models, *Coastal Engineering*, *67*, 54–66. (Cité pages 76 et 77.)

Tolman, H. L. (1991), A third generation model for wind waves on slowly varying, unsteady and inhomogeneous depths and currents, *Journal of Physical Oceanography*, *21*, 782–797. (Cité pages xvii, 20, 43 et 107.)

Torrence, C., and G. P. Compo (1998), A practical guide to wavelet analysis, *Bulletin of the American Meteorological Society*, *79*, 61–78. (Cité page 55.)

Torrence, C., and P. J. Webster (1999), Interdecadal changes in the ENSO-Monsoon system, *Journal of Climate*, *12*, 2679–2690. (Cité page 55.)

Turner, I. L. (2006), Discriminating modes of shoreline response to offshore-detached structures, *Journal of Wateway Port Coastal and Ocean Engineering*, *132*, 180–191. (Cité page 44.)

Turner, I. L., D. Whyte, B. G. Ruessink, and R. Ranasinghe (2007), Observations of rip spacing, persistence and mobility at a long, straight coastline, *Marine Geology*, *236*, 209–221. (Cité page 60.)

Van Dongeren, A. R., N. G. Plant, A. B. Cohen, J. A. Roelvink, M. C. Haller, and P. Catalán (2008), Beach Wizard : Nearshore bathymetry estimation through assimilation of model computations and remote observations, *Coastal Engineering*, *55*, 1016–1027. (Cité pages 79 et 80.)

Van Enckevort, I. M. J., and B. G. Ruessink (2003), Video observation of nearshore bar behaviour. Part 2 : alongshore non-uniformity variability, *Continental Shelf Research*, *23*, 513–532. (Cité page 60.)

Van Enckevort, I. M. J., and K. M. Wijnberg (1999), Intra-annual changes in bar plan shape in a triple bar system, in *Proc. of Coastal Sediments '99*, pp. 2548–2558. (Cité page 56.)

Van Enckevort, I. M. J., B. G. Ruessink, G. Coco, K. Susuki, I. L. Turner, N. G. Plant, and R. A. Holman (2004), Observations of nearshore crescentic sandbars, *Journal of Geophysical Research*, *109*, C06028, doi :10.1029/2003JC002214. (Cité pages 7, 40, 52 et 70.)

Van Maanen, B., G. Coco, K. R. Bryan, and B. G. Ruessink (2010), The use of artificial neural networks to analyze and predict alongshore sediment transport, *Nonlinear Processes in Geophysics*, *17*, 395–404. (Cité page 108.)

Van Rijn, L. C. (1989), *Handbook of Sediment Transport by Currents and Waves*, Delft Hydraulics, Delft, The Netherlands. (Cité page 54.)

Vis-Star, N., H. de Swart, and D. Calvete (2008), Patch behaviour and predictability properties of modelled finite-amplitude sand ridges on the inner shelf, *Nonlinear Processes in Geophysics*, *15*, 943–955. (Cité page 56.)

WAMDI Group (1988), The WAM model - a third generation ocean wave prediction model, *Journal of Physical Oceanography*, *18*, 603–674. (Cité pages 20 et 107.)

Wijnberg, K. M., and R. A. Holman (2007), Video-observation of shoreward propagating accretionary waves, in *Proc. of River, Coastal and Estuarine Morphodyanmics '07*, pp. 737–743, ASCE, New York. (Cité page 70.)

Wilson, G. W., H. T. Ozkan-Haller, and R. A. Holman (2010), Data assimilation and bathymetric inversion in a two-dimensional horizontal surf zone model, *Journal of Geophysical Research*, *115*(C12057), doi :10.1029/2010JC006286. (Cité page 76.)

Wright, L. D., and A. D. Short (1984), Morphodynamic variability of surf zones and beaches : A synthesis, *Marine Geology*, *56*, 93–118. (Cité pages xvi, 5, 27, 28, 31, 36, 39, 40 et 44.)

Yates, M. L., R. T. Guza, and W. C. O'Reilly (2009), Equilibrium shoreline response : Observations and modeling, *Journal of Geophysical Research*, *114*(C09014), doi :10. 1029/2009JC005359. (Cité page 76.)

Annexes

Comportement hydro-sédimentaire à grande échelle

A

Sommaire

Dans cette annexe sont succinctement présentées les différentes méthodes développées et appliquées dans le but d'estimer les conditions de vagues à la côte (Section A.1) et la dérive littorale (Section A.2) dans le but de diagnostiquer les évolutions du trait de côte observées. Les avantages et limitations des différentes approches sont discutés. Outre les travaux réalisés sur le littoral aquitain au sein du laboratoire EPOC, les travaux discutés ici ont été en partie réalisés dans le cadre de collaborations développées pendant mon séjour postdoctoral. En particulier, j'ai collaboré avec Xavier Bertin (LIENSS, Université de La Rochelle / LNEC, Portugal) sur les plages du littoral charentais et vendéen et avec le Griffith Centre of Coastal Management et la School for Information and Communications Techonology de Griffith University (Australie) dans le cadre de l'application de l'intelligence artificielle pour l'estimation des vagues à la côte. Enfin, les approches de modélisation semi-empirique ont été appliquées aux plages du littoral de Bouknadel-Kénitra (Maroc) et au système de *bypass* permanent de sédiment dans la baie de Coolangatta respectivement à travers le co-encadrement de la thèse de Mounir Hakkou (Université de Ibn-Tofail, Kénitra, Maroc) et une collaboration avec Ian Turner de l'Université du New South Wales (Australie). Enfin les limitations de l'approche semi-empirique sont abordées sur le cas du Gouf de Capbreton dans le cadre d'une collaboration récemment initiée avec

Hervé Gillet de l'équipe SEDIMENTOLOGIE d'EPOC, et ce, dans le cadre de la thèse de Alaïs Mazières.

A.1 Comment estimer simplement les conditions de vagues à la côte ?

Les vagues sont le moteur du mouvement des masses d'eau en milieu littoral. Les caractéristiques des vagues à la côte sont donc essentielles pour le calcul des courants littoraux, du transport sédimentaire littoral et des mécanismes d'érosion et d'accrétion associés. Ce constat est d'autant plus vrai pour les côtes sableuses exposées à des houles particulièrement énergétiques. Les mesures $in - situ$ à long terme dans la zone de déferlement sont pratiquement impossibles à mettre en oeuvre. D'autres méthodes, développées dans le cadre de mes recherches, ont été mises en place afin de connaître en permanence le forçage des vagues à la côte, et ainsi estimer le transit littoral le long des côtes sableuses.

A.1.1 Emboîtement de modèles spectraux

Les modèles numériques permettent d'estimer les conditions de houle à la côte. On peut distinguer 2 types de modèle : les modèles globaux (O(10 000 km), *e.g.*, WAM et WW3, *Tolman* 1991, *WAMDI Group* 1988) et les modèles régionaux (O(100 km), *e.g.*, SWAN *Booij et al.* 1999, *Ris et al.* 1999). Ces derniers permettent de simuler la propagation des vagues en domaine côtier en présence de déferlement bathymétrique, de réfraction (bathymétrique ou par les courants) et de diffraction. Dans ce contexte nous avons couplé le modèle spectral régional SWAN avec les données de spectre directionnel de houle directement mesuré par des bouées par 20 à 50 m de fond (***Castelle et al.*** 2006b; 2009b, ***Bruneau et al.*** 2011) afin d'estimer le forçage à la côte et de simuler les circulations induites par les vagues en domaine littorale pendant les campagnes PNEC 2001 (*Sénéchal et al.* 2004), Biscarrosse 2007 (***Bruneau et al.*** 2009b) et ECORS-Truc Vert'08 (*Sénéchal et al.* 2011). Nous avons ainsi pu montrer que la prise en compte de l'ensemble de l'information sur l'état de mer, à travers le spectre directionnel, améliore considérablement les résultats obtenus classiquement en utilisant simplement l'information spectrale (hauteur significative H_s, période pic T_p et incidence θ).

Comme les données de houle ne sont pas systématiquement disponibles au large d'une zone d'étude donnée, nous avons également utilisé ce type d'approche en couplant SWAN avec le modèle global WW3 sur différentes zones en France, en Australie et au Maroc (***Browne et al.*** 2006; 2007, ***Castelle et al.*** 2008, ***Bertin et al.*** 2008b, ***Castelle et al.*** 2009a, ***Hakkou et al.*** 2011). Nous avons ainsi montré que l'emboîtement de modèles de vagues régionaux avec un modèle global permet d'affiner considérablement l'estimation des vagues à la côte, en particulier en présence de côtes découpées (voir plus loin le Tableau A.1). Des erreurs significatives peuvent être obtenues, notamment en présence d'états de mer complexes. Même si ces résultats ne sont pas vraiment surprenants, nous avons montré que ce type de couplage était particulièrement adapté aux littoraux où les données sont rares ou inexistantes (*e.g.*, ***Hakkou et al.*** 2011), puisque des estimations correctes des hauteurs de vagues au déferlement peuvent être obtenues sans avoir à calibrer le modèle régional de vagues (paramétrisations par défaut, ***Browne et al.*** 2007).

A.1.2 Intelligence artificielle

La modélisation numérique pour une estimation très fine des vagues à la côte présente certaines difficultés (nécessité de données bathymétriques, temps de cal-

cul parfois longs, calibration intensive des paramètres ajustables si nécessaire). Par conséquent, des méthodes alternatives doivent être développées sans la nécessité de représenter tous les processus physiques affectant les vagues ni l'acquisition de données bathymétriques. L'intelligence artificielle (*e.g.*, *Ripley* 1996, *Kostanic* 2001) apparaît naturellement comme une solution adaptée. Pendant mon séjour postdoctoral nous avons développé des réseaux artificiels de neurones afin de connaître les conditions de vagues à la côte à partir du modèle global WW3 (***Browne et al.*** 2006; 2007). Les résultats le long de 17 plages australiennes (Tableau A.1) montrent que **l'intelligence artificielle est systématiquement plus performante que la modélisation numérique pour prévoir la hauteur des vagues à la côte**. On constate, comme déjà discuté ci-dessus, que SWAN améliore de manière très significative les prévisions par rapport aux données WW3 au noeud le plus proche de la côte, particulièrement le long des côtes découpées. L'intelligence artificielle améliore les résultats en termes de corrélation r avec les observations, mais surtout en terme d'erreur moyenne absolue qui diminue typiquement à 10-30 cm le long de toutes les plages australiennes étudiées.

Les principaux désavantages de l'intelligence artificielle sont qu'il est impossible de connaître la houle en d'autres points que ceux où les données existent et que la qualité du réseau artificiel de neurones dépend essentiellement de la qualité du jeu de données sur lequel il est entraîné. En outre, l'intensité des événements extrêmes est systématiquement sous-estimée par les réseaux artificiels de neurones. L'intelligence artificielle était jusqu'à notre étude relativement peu utilisée en océanographie physique littorale. Par la suite, cette approche a été reprise, notamment pour la mise en place de système d'alerte opérationnel (*e.g.*, *Alvarez-Ellacuria et al.* 2009), pour la dynamique des profils de plages (*e.g.*, *Pape and Ruessink* 2011) ou encore l'estimation des flux sédimentaires en zone de déferlement (*e.g.*, *Van Maanen et al.* 2010).

A.2 Dérive littorale et évolution du trait de côte : méthode semi-empirique

L'un des intérêts des approches discutées ci-dessus est de pouvoir ensuite estimer la dérive littorale qui est le flux de sédiment transporté le long de la plage par les houles obliques (Figure 1.3). De nombreuses études ont montré que les gradients *longshore* de dérive littorale sont le principal moteur des évolutions du trait de côte sur de grandes échelles de temps (O(10-100 ans) *e.g.*, *Peterson et al.* 1990, *Goodwin et al.* 2006, *Ruggiero et al.* 2010, *Hansen and Barnard* 2010), à tel point qu'un déficit de 1 % de dérive littorale peut avoir un impact similaire à celui d'une augmentation de 0.5 m du niveau moyen des mers (*Cowell et al.* 1995). Dans le cas des côtes exposées aux vagues très obliques, la rétroaction positive entre la dérive littorale et l'évolution du trait de côte donne également naissance à des instabilités du trait de côte tels que les *cuspates* et *flying sandspits* (*e.g.*, *Ashton et al.* 2001, *Ashton and Murray* 2006a;b, *Falqués et al.* 2011). Comprendre et estimer la dérive littorale est donc essentiel lorsqu'on s'intéresse aux évolutions des côtes sableuses sur de grandes échelles spatio-temporelles.

A.2.1 Approche méthodologique et validation sur un site naturel

Plutôt que de simuler en détail la dynamique sédimentaire, on force des formules empiriques de dérive littorale qui sont gouvernées par les caractéristiques des vagues

Region	Plage	WW3		SWAN		ANN l		ANN nl	
		MAE	*r*	MAE	*r*	MAE	*r*	MAE	*r*
QLD	Surfer's Paradise	91.77	.49	32.31	.72	17.84	.71	16.12	.79
	Sunshine Coast	96.33	.46			16.77	.71	15.51	.80
WA	Margaret River	102.89	.77	65.51	.73	34.74	.78	26.69	.86
	Trigg Beach	244.11	.79	62.77	.72	13.80	.80	12.05	.85
SA	Seaford	245.64	.67	15.20	.63	14.49	.61	12.83	.70
	Chiton Rocks	152.84	.58	40.93	.40	20.64	.64	17.42	.74
NNSW	Mid Coast	127.92	.72			22.97	.73	19.62	.80
	North Coast	90.93	.34			19.98	.52	18.15	.68
SNSW	Bondi	59.54	.81			21.73	.76	19.41	.82
	Cronulla	60.26	.80			21.85	.75	20.25	.79
	Manly	60.18	.80	50.06	.76	21.40	.75	19.49	.81
	Palm Beach	58.97	.81			22.26	.75	19.75	.81
	South Coast	64.73	.69			27.45	.70	24.20	.76
VIC	Woolamai	89.94	.67	38.72	.62	28.30	.68	25.64	.74
	Portsea	83.22	.70			28.72	.69	26.61	.74
	Torquay	143.57	.68	34.98	.70	24.34	.71	21.03	.78
	Warranambol	141.49	.59			25.96	.64	25.29	.69

TABLE A.1 – *Tableau récapitulatif de la comparaison des données WW3 au noeud le plus proche de la côté, des simulations par emboîtement du modèle régional SWAN, des réseaux artificiel de neurone (ANN) linaire (ANN l) et de l'ANN non-linéaire (ANN nl) avec les données de vagues observées le long de 17 plages australiennes (QLD : Queensland, WA : Western Australia, SA : South Australia, NNSW : nord du New South Wales, SNSW ; sud du New South Wales et VIC : Victoria). Les comparaisons sont données en termes d'erreur moyenne absolue (MAE, donnée en cm) et de coefficient corrélation r (**Browne et al.** 2007).*

au déferlement, la pente de plage et la granularité du sédiment. Cette approche permet d'identifier les cellules sédimentaires, de quantifier les gradients *longshore* de dérive littorale ou encore d'estimer l'impact de potentiels aménagements littoraux. Il existe un grand nombre de formules empiriques pour estimer la dérive littorale. Parmi les plus connues, on peut citer celles du CERC (*Rosati et al.* 2002), de *Komar* (1971) ou de *Kamphuis* (1991). Puisque ces formules nécessitent la calibration d'un certain nombre de paramètres ajustables et qu'elles sont parfois très sensibles à de petites variations dans le forçage des vagues (*e.g.*, *Balouin et al.* 2005), nous nous sommes appuyés sur la formulation proposée par *Kaczmarek et al.* (2005) plus robuste et qui ne nécessite la calibration que d'un paramètre. Celle-ci est détaillée dans ***Bertin et al.*** (2008b), ***Castelle et al.*** (2009a) et ***Hakkou et al.*** (2011).

Cette approche a été validée sur la plage dissipative de St Trojan (Ile d'Oléron, Figure 1.5b) avec des mesures de flux sédimentaires par traçage fluorescent pour trois climats de houle caractéristiques (pour plus de détails sur la méthode et la validation, le lecteur est invité à consulter ***Bertin et al.*** 2008b). Cette étude a également permis de remettre à jour les estimations de la dérive littorale et ses variabilités interannuelles le long de ces plages qui connaissent depuis plusieurs années une forte érosion.

A.2.2 Application à des sites antropisés : littoral de Bouknadel-Kénitra (Maroc) et baie de Coolangatta (Australie)

Système de *bypass* artificiel : Baie de Coolangatta (Australie)

La baie de Coolangatta est située au sud de la Gold Coast (Australie) à la bordure des états du New South Wales et du Queensland (Figure 1.5d). L'érosion des plages de cette baie est devenue problématique après l'extension des digues de la Tweed River réalisée au début des années 60 afin d'améliorer les conditions de navigation de l'embouchure. Ces digues ont constitué un piège pour la dérive littorale qui était la source principale de sédiment vers la baie. Au début des années 90, et ce malgré les nombreux rechargements de plage et de dragage, les plages de la baie étaient d'une part complètement érodées, et d'autre part tout le sable accumulé en amont des digues était à nouveau disponible pour combler l'embouchure, rendant les conditions de navigation catastrophiques. Le Tweed River Entrance Sand Bypassing Project (TRESBP) a alors été mis en oeuvre en 1995 afin de proposer une solution durable pour à la fois recréer les plages de la baie de Coolangatta et assurer de bonnes conditions de navigation. L'aspect très novateur de ce projet fut la mise en place d'un système de *bypass* de sédiment en 2001 (Figure A.1a).

Afin de suivre l'évolution du trait de côte, les relevés bathymétriques réalisés par différentes organisations ont été regroupés et uniformisés. Huit profils de référence ont été choisis pour leur représentativité de la morphologie de la baie (Figure A.1b). D'autre part, depuis mi-avril 2002, un réseau de stations ARGUS (*Holman and Stanley* 2007) opère en continue en couvrant l'ensemble de la baie de Coolangatta avec un total de 6 caméras. La méthode PIC ("Pixel Intensity Clustering", *Aarninkhof et al.* 2003) a été utilisée pour déterminer chaque semaine la position du trait de côte au niveau des différents profils (Figure A.2b).

La rapide sédimentation de la baie à partir de 2002 est due aux quantités de sable surpompé pendant le TRESBP par rapport à la dérive littorale naturelle estimée par la méthode semi-empirique (Figure A.2, ***Castelle et al.*** 2009a). Cela est visible sur les échelles annuelles, mais aussi à plus haute fréquence où les avancées et reculs rapides du trait de côte peuvent être corrélés avec les quantités de sable surpompé calculées. Les wagons sédimentaires se propagent ensuite le long de la baie avant de combler la plage de Kirra (la réponse du trait de côte est quasi-instantanée au niveau du profil RB5, tandis que l'influence du surpompage se fait ressentir 5 à 6 mois après au niveau du profil CG6, Figure A.2). **Cette approche pourrait donc être utilisée afin de mieux gérer les quantités de sable pompé par le système de *bypass* en fonction des prévisions de houle et ainsi reproduire au plus proche la dérive littorale naturelle**. Les résultats de cette étude (pour une description complète voir ***Castelle et al.*** 2009a) ont également montré que le système de *bypass* est bien plus performant que les rechargements réalisés avec les dépôts de dragage. En effet le sable déposé en eau peu profonde par le système de pompage est immédiatement transporté par le courant de dérive et nourrit les bancs de sable puis le haut de plage de la baie, ce qui est au plus proche de ce qui se produirait naturellement. Ce système a rendu ces plages les plus à même à résister à une succession d'épisodes cycloniques tels que l'a connu la Gold Coast en 1967 (***Castelle et al.*** 2008). Alors que Coolangatta Beach et Rainbow Bay se sont relativement stabilisées, la plage de Kirra continue à sédimenter rapidement et une grande partie du sable pompé vient s'accumuler dans cette zone. Cela n'est pas complètement surprenant car la plage de Kirra était la zone qui avait été la plus affectée par le piégeage de la dérive littorale

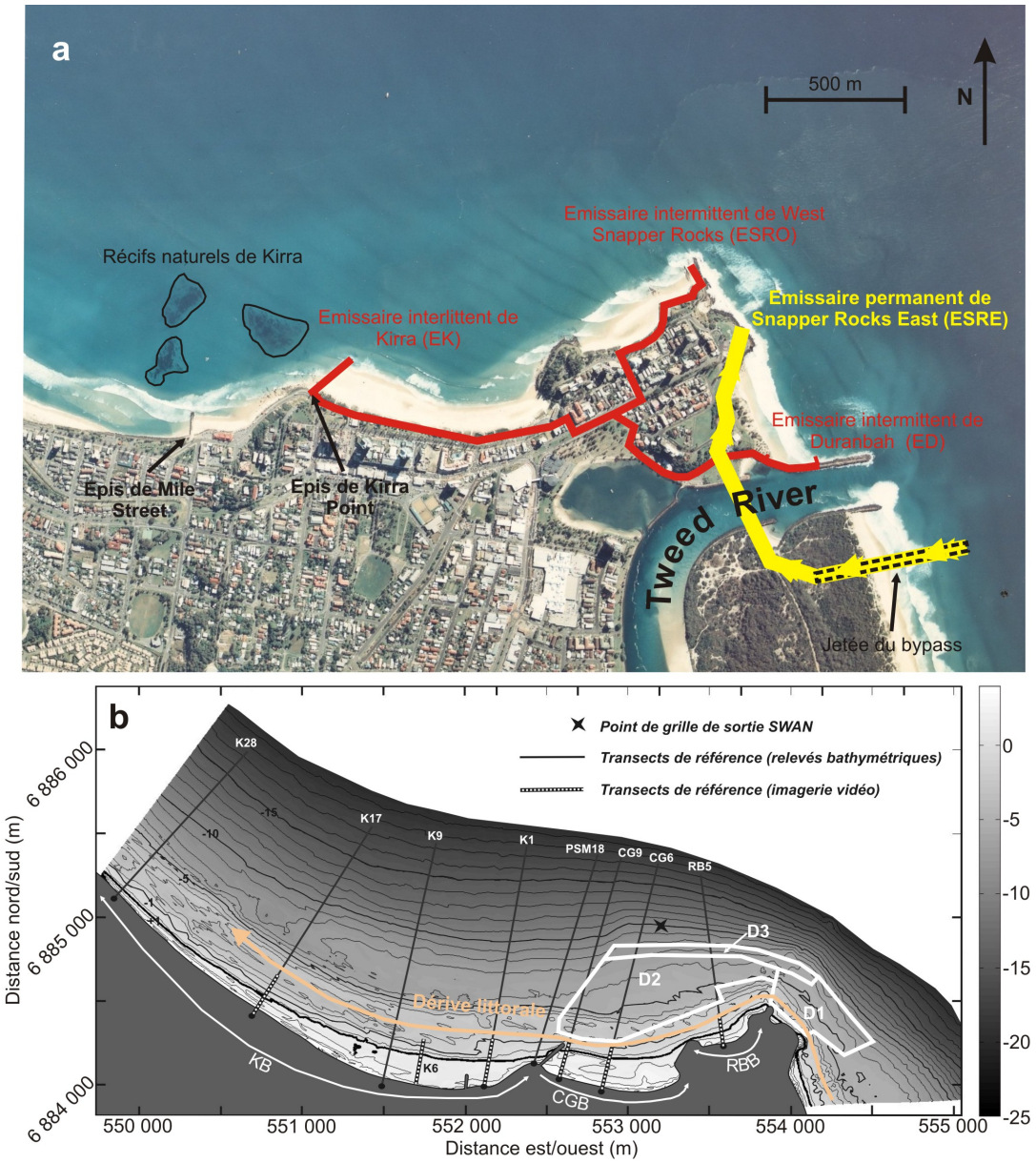

FIGURE A.1 – *(a) Photo aérienne de la baie de Coolangatta (Gold Coast, Australie) avec superposée la schématisation du système de bypass. (b) Morphologie de la baie de Coolangatta en 1997 avec localisation des profils de référence de relevés bathymétriques et d'imagerie vidéo, et indication des zones de dépôt (D1, D2 et D3) du sable dragué dans l'embouchure (**Castelle et al.** 2009a).*

par les aménagements de la Tweed River, et présentait donc le déficit sédimentaire le plus significatif.

Système de digues bloquant la dérive littorale : littoral de Bouknadel-Kénitra (Maroc)

L'approche développée ci-dessus a aussi l'avantage de pouvoir être appliquée à des zones peu documentées où les données sont quasi-inexistantes. Cela a été réalisé sur les plages sableuses énergétiques de Bouknadel-Kénitra au Maroc (***Hakkou et al.*** 2011) qui s'étendent sur environ 20 km de linéaire côtier (Figure 1.5c). Les plages sableuses sont interrompues au Nord par l'embouchure du Sébou fixée par deux

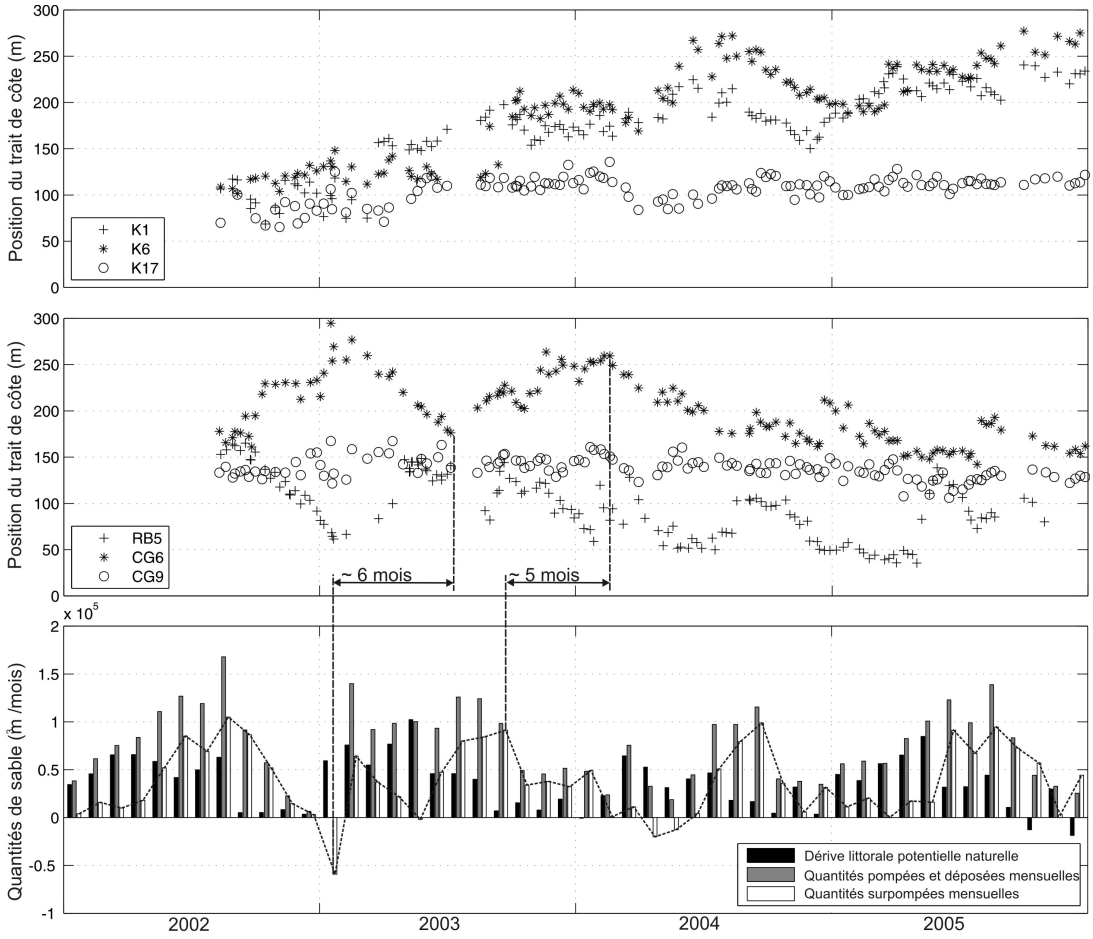

FIGURE A.2 – *Evolution de la position du trait de côte dans la baie de Coolangatta (Gold Coast, Australie) déduite de l'imagerie vidéo au niveau des profils indiqués en Figure A.1 et des quantités de sable surpompé (histogramme blanc) déduites de la dérive littorale calculée par la modélisation semi-empirique soustraite aux quantités de sable pompées par le TRESBP (**Castelle et al.** 2009a).*

digues s'étendant environ 600 m vers le large. Le littoral encourt un risque sérieux de dégradation sous l'effet des perspectives de son occupation touristique et résidentielle et des extractions de sable sauvages directement sur la dune, tous ces facteurs étant susceptibles de déséquilibrer ses unités morphologiques fragiles. Nous avons combiné un suivi biannuel de profils de plage le long de ce littoral, l'analyse granulométrique des sables relevés le long des profils, des photos aériennes permettant de connaître l'évolution du trait de côte ces 40 dernières années, les données sur 9 ans du modèle de vagues global WW3 et la modélisation semi-empirique du transit sédimentaire. Nous avons ainsi pu étudier l'impact des aménagements côtiers sur les états de plage et l'accrétion et l'érosion inexorable du trait de côte mesurées respectivement en amont et en aval des digues du Sébou. Nous avons également pu identifier certains secteurs plus vulnérables et avons relié cette fragilité aux gradients de dérive littorale (***Hakkou et al.*** 2011, *Hakkou* 2012).

A.2.3 Limites de l'approche semi-empirique : exemple de la zone du gouf de Capbreton (France)

La principale approximation de l'approche traitée ici est qu'elle fait l'hypothèse que les iso-contours de la plage sous-marine sont parallèles à la plage. Ce n'est évidemment pas toujours le cas. On peut ici prendre l'exemple du Gouf de Capbreton qui se démarque entre autre par sa très profonde incision du plateau continental (il prend naissance à environ 250 m du rivage), et où le comportement de la dérive littorale fait débat depuis plusieurs décennies (*Duplantier* 1976, *Froidefond et al.* 1982, *Gaudin et al.* 2006).

La Figure A.3 montre un exemple de simulation numérique [1] des courants induits par les vagues à marée haute pour des conditions de houle de nord-ouest modérément énergétiques. On remarque plusieurs changements de direction du courant de dérive (moteur de la dérive littorale) dus aux différentes zones de focalisation d'énergie des vagues par réfraction au-dessus de la tête du canyon de Capbreton. La principale zone de focalisation d'énergie étant localisée sur le banc de sable de 'La Nord' qui correspond à l'extrémité sud de la barre externe en croissant tombant dans la tête de canyon. L'étude en cours montre des effets de seuil très importants sur la hauteur de marée et la hauteur des vagues, et un impact faible de l'angle d'incidence des vagues. En particulier, la plupart du temps la dérive littorale est dirigée vers le nord et, dans de rares occasions (favorisées par les houles énergétiques et des niveaux de marée bas), la dérive littorale peut alimenter massivement en sable la tête du canyon. Ce phénomène ne pourrait pas être dépeint par la méthode semi-empirique. Cette étude permettra notamment de compléter celle de *Abadie et al.* (2006) qui avaient mis en évidence une complexification importante de la dérive littorale à proximité de Capbreton et qui encourageaient des études plus fines sur cette zone.

Conclusions du chapitre

Les conditions de vagues à la côte peuvent être estimées classiquement par l'emboîtement de modèles régionaux de vagues. Ceux-ci peuvent être forcés par un modèle global (***Browne et al.*** 2007, ***Bertin et al.*** 2008b, ***Castelle et al.*** 2008; 2009a) ou des données mesurées par une bouée directionnelle plus au large (***Castelle et al.*** 2006b; 2009b, ***Bruneau et al.*** 2011). Cette dernière approche ne permet toutefois pas la prévision (alors que les modèles globaux peuvent donner des prévisions précises de forçage sur plusieurs jours). Dans les deux cas, la prise en compte de l'ensemble de l'information sur l'état de mer (spectre directionnel) augmente considérablement la qualité des simulations. Des résultats bien meilleurs peuvent être obtenus par l'intelligence artificielle (***Browne et al.*** 2006; 2007). Toutefois, avec cette approche il est (1) impossible de connaître la houle en d'autres points que ceux où les données existent et (2) la qualité du réseau artificiel de neurones dépend essentiellement de la qualité du jeu de données sur lequel il est entraîné.

La modélisation semi-empirique développée pour l'estimation de la dérive littorale a été validée par des mesures de flux sédimentaires par traçage fluorescent (***Bertin et al.*** 2008b) et d'accumulation de sable en amont de digues bloquant le transit (***Castelle et al.*** 2009a, ***Hakkou et al.*** 2011). L'approche permet de caractériser le comportement morpho-sédimentaire d'une section du littoral particulièrement vulnérable afin par exemple de mieux évaluer les dangers liés à des projets immobiliers et

1. Une description du modèle (*e.g.*, ***Castelle et al.*** 2006b) est donnée dans le chapitre 2

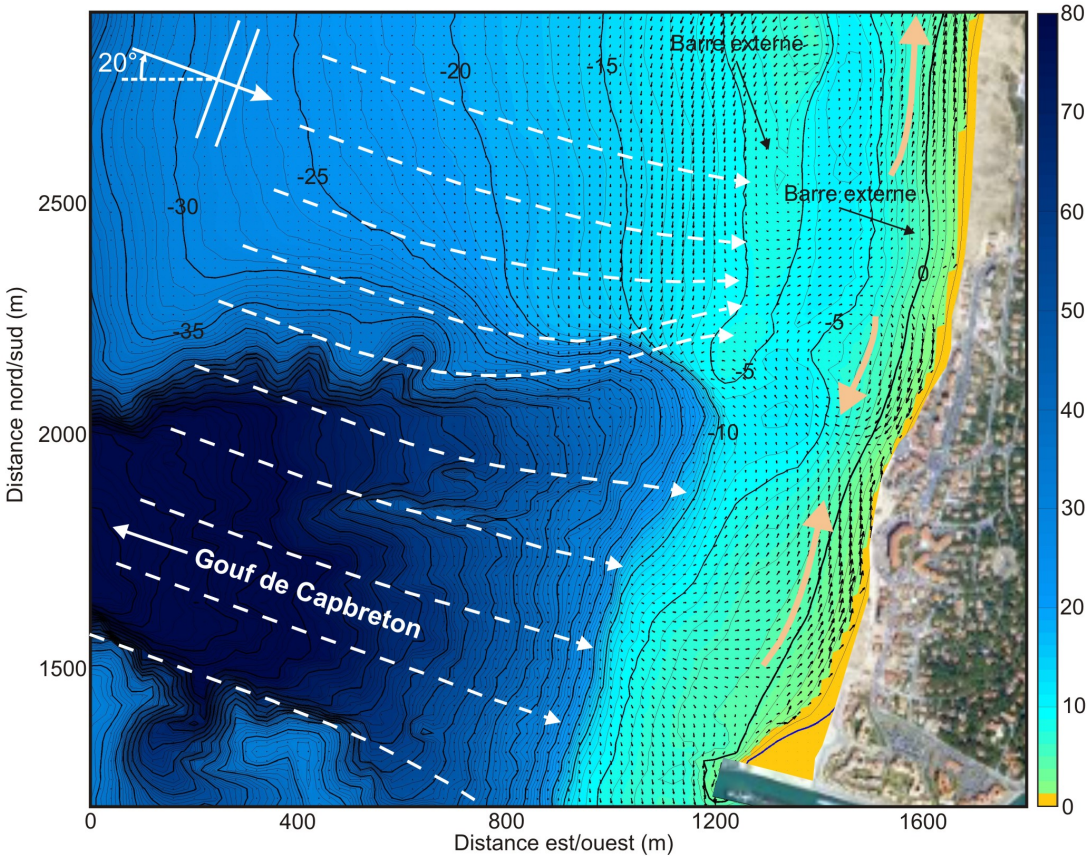

FIGURE A.3 – *Zoom sur la zone de Capbreton d'une simulation des courants induits par les vagues à marée haute avec au large une houle de hauteur significative H_s = 2.5 m, une période pic T_p = 12 s et une incidence nord-ouest. Les flèches blanches en pointillés montrent la convergence des rayons de houle sur le banc de sable de La Nord / La Gravière (dans une moindre mesure, le même phénomène est observé plus au sud sur la plage de La Piste, alors que les rayons de houle divergent sur la plage du Prévent ; ceci n'est pas visible sur ce zoom). On note plusieurs changements de direction du courant de dérive.*

d'extraction de sable directement sur la dune qui menacent ce type d'environnement (***Hakkou et al.*** 2011). Ce type d'approche peut aussi être utilisée pour le développement d'aménagements côtiers novateurs pour, en temps réel, nourrir une plage par des quantités de sable comparables aux quantités de sable que cette plage devrait recevoir si la côte n'avait pas été aménagée, et ainsi artificiellement reproduire les conditions naturelles (*i.e.*, système permanent de *bypass* de sédiment, ***Castelle et al.*** 2009a). Cette approche combinée à l'imagerie vidéo et aux suivis bathymétriques réguliers est en accord avec les recommandations sur les nouvelles pratiques à développer en ingénierie côtière (*Hamm et al.* 2002).

Curriculum Vitae

B

CASTELLE Bruno
Né le 17 avril 1977 à La Rochelle
Nationalité française, pacsé, 2 enfants
CR1 à l'UMR CNRS EPOC 5805, Equipe METHYS, Université Bordeaux I
Page web : http ://www.epoc.u-bordeaux.fr/indiv/Castelle/

B.1 Expérience professionnelle et formation

B.1.1 Carrière

Octobre 2011 -

CR1/CNRS, UMR EPOC (équipe METHYS).

Octobre 2007 - Octobre 2011

CR2/CNRS, UMR EPOC (équipe METHYS).

Février 2007 - Septembre 2007

Post-doctorant, UMR EPOC (équipe METHYS) : *Circulations induites par les vagues en domaine littoral* (ECORS, DGA/SHOM).

Janvier 2005 - Janvier 2007

Senior Research Assistant à Griffith Centre for Coastal Management (Griffith University, Australie). *Climatologie de houle et comportement morpho-sédimentaire de la Gold Coast* (Gold Coast Shoreline Management Plan).

Octobre 2004 - Décembre 2004

Post-doctorant, UMR EPOC : Valorisation des travaux de thèse.

Septembre 2001 - Septembre 2004

Doctorant, UMR EPOC
Titre de la thèse : *Modélisation de la dynamique hydro-sédimentaire au-dessus des plages sableuses dominées par l'action de la houle : application à la côte aquitaine.*
Directeur de thèse : Philippe Bonneton.
Soutenue le 4 Octobre 2004, mention très honorable
Prix scientifique 2004 décerné par IAA (Identités et Ambitions Aquitaines)

B.1.2 Diplômes

2004

Doctorat de l'Université Bordeaux I.

2001

Diplôme d'ingénieur, option « Ingénierie Marine » (ISITV, Université de Toulon et du Var).

2001

DEA en Sciences de l'Environnement Marin, option « Océanographie physique côtière littorale » (Université Aix-Marseille II).

B.2 Production scientifique

- (Co-)auteur de 45 publications (dont 19 en 1^{er} auteur) depuis 2005 dans des revues à comité de lecture.
- (Co-)auteur de 36 publications (dont 18 en 1^{er} auteur) depuis 2002 dans des actes de congrès nationaux et internationaux avec comité de lecture.

B.3 Enseignement, formation et diffusion de la culture scientifique

B.3.1 Encadrement de thèses

Officiel

- Benjamin Dubarbier, thèse de l'Université Bordeaux I, co-encadrée par Jean-Paul Parisot (HDR), débutée en décembre 2010 (financement ANR BARBEC) : *Modélisation physique et numérique de l'évolution des profils de plage*.
- Florent Birrien, thèse de l'Université Bordeaux I, co-encadrée par Jean-Paul Parisot (HDR) débutée en octobre 2009 (financement ministériel) : *Assimilation de données vidéo dans les modèles numériques hydro-sédimentaires pour l'inversion bathymétrique*.
- Timothy Price, thèse de l'Université d'Utrecht (Pays-Bas) débutée en septembre 2008 (financement NWO) encadrée par Gerben Ruessink : *The finite amplitude behaviour of nearshore crescentic sandbars*. J'encadre l'étudiant sur les aspect de modélisation numérique de la morphodynamique des barres en croissant abordés pendant la fin de sa thèse.
- Mounir Hakkou, thèse de l'Université Ibn-Tofail (Kénitra, Maroc) débutée en 2008, co-encadrée avec Aïcha Benmohammadi et soutenue le 25 février 2012 : *Etude morpho-sédimentaire de la dynamique du littoral de Kénitra-Bouknadel (Maroc)*.

Participation active à l'encadrement

- Rafael Almar, thèse de l'Université Bordeaux I débutée en septembre 2006 (Bourse DGA) et soutenue septembre 2009, co-encadrée par Philippe Bonneton et Nadia Sénéchal (EPOC) : *Modélisation de l'hydrodynamique littorale et suivi de la morphodynamique par imagerie video*.

- Nicolas Bruneau, thèse de l'Université Bordeaux I débutée en décembre 2005 (Financement BRGM) et soutenue en janvier 2009, encadrée par Philippe Bonneton (EPOC) et co-encadrée par Rodrigo Pedreros (BRGM) : *Modélisation morphodynamique des plages sableuses*.

B.3.2 Encadrement de stagiaires

- (Co-)supervision de 4 stagiaires de master 1, 6 de master 2. La majorité des stages a fait l'objet d'une publication internationale de rang A.

B.3.3 Participation à l'enseignement

Master OACOS (Ecole des ponts ParisTech ; Ecole nationale supérieure de techniques avancées (ENSTA ParisTech) ; UPMC Pierre-et-Marie-Curie))

- Contribution au cours E4 depuis 2007 « Hydrodynamique sédimentaire, géomorphologie et qualité de l'eau » (12,5 heures).

Master ENVOLH (Université Bordeaux 1)

- Contribution aux cours de Master 1 et 2 depuis 2007 (3 à 7 heures suivant les années).

B.3.4 Organisation de conférences

- Membre du comité d'organisation de la conférence internationale Coastal Dynamics 2013 (Palais des Congrès d'Arcachon, 23-28 juin 2013) co-organisée par l'UMR EPOC et le SHOM. Site web : http ://www.coastaldynamics2013.fr

B.3.5 Vulgarisation/communication

Vulgarisation

- Plusieurs interventions de communication auprès du grand public pour expliquer les décisions d'aménagement (ou de retraits d'aménagements) littoraux par le Gold Coast City Council (Australie, 2005-2006)

- Conseiller scientifique pour l'exposition interactive et itinérante *Vagues et Littoral* (Association Cap Sciences, Bordeaux) : Conception d'un canal à houle, et vulgarisation de l'océanographie physique littorale (2003).

- Conférencier pour l'Association *Océans* (interventions sur les plages d'Aquitaine et les courants de baïne, 2003).

- Entre 2001 et 2004 : membre Actif de l'Association *Océans* (Médiation des Sciences et de l'Histoire de l'Environnement). Vulgarisation auprès du grand public et sorties estuaires / expériences scientifiques pour les enfants.

Communication dans la presse écrite et audiovisuelle

- Interview dans la dépêche AFP *Les "baïnes", le piège meurtrier du littoral aquitain* du 10 août 2012 relayée sur des dizaines de sites internet et dans la presse écrite suite au nombre anormalement haut de noyades survenues en juillet le long des plages d'aquitaine

- Interview dans le webdocumentaire *La côte en Aquitaine* pour la Banque numérique du savoir d'Aquitaine (2012) lié à la dynamique des barres sableuses du littoral aquitain et leur impact sur les vagues (http ://web-doc.bnsa.aquitaine.fr/)

- Interview dans l'article du journal Sudouest *Les baïnes, piège de l'Océan* par Jean-Denis Renard (31 juillet 2011)

- Conseiller scientifique pour l'ouvrage *Vagues : Le fabuleux spectacle de l'Océan* (157 pages, Editions Hermé, 2004)

- Auteur de l'article *Le mur de l'Atlantique* dans le magazine *Surf Session* Hors Série n°52 (p. 24-30) traitant des bancs de sable aquitains (2004).

- Conseiller scientifique pour le magazine *Surf Session* Hors Séries n°47 et 50 Spécial Environnement (2003-2004)

Ouvrages de communication vers les pouvoirs publics

- Co-rédacteur du chapitre *Dynamique littorale* (coordinateur Philippe Bonneton) pour le livre *Changement climatique en Aquitaine : un état des lieux scientifique* demandé par la Région Aquitaine et coordonné par Hervé Le Treut.

B.3.6 Participation à des travaux d'expertise

Rapporteur pour des projets et publications

- Reviewer pour des actes de congrès de plusieurs conférences nationales et internationales.

- Reviewer pour des projets soumis au Netherlands Organisation for Scientific Research (NWO).

- Reviewer pour un projet INSU/OA.

- Reviewer pour de nombreux articles (*e.g.*, 13 en 2012) soumis aux journaux suivants :
Geophysical Research Letters
Journal of Geophysical Research - Earth Surface
Journal of Geophysical Research - Oceans
Marine Geology
Continental Shelf Research
Coastal Engineering
Journal of Climate
Estuarine, Coastal and Shelf Science
Nonlinear Processes in Geophysics
Water Ressources Research
Journal of Coastal Research
Ocean Engineering
Environmental Earth Sciences
Comptes Rendus Geoscience

Participation à des jurys de thèse

- Membre du jury de thèse de Florent Grasso, soutenue le 26 octobre 2009 à Grenoble, thèse de l'Université Joseph Fourier - Grenoble I. *Modélisation physique de la dynamique hydro-sédimentaire des plages*.

- Membre du jury de thèse de Pierre Ferrer, soutenue le 20 juillet 2010 à Perpignan, thèse de l'Université de Perpignan Via Domitia. *Morphodynamique à multi-échelles du trait de côte (prisme sableux) du Golfe du Lion (Languedoc-Roussillon) depuis le dernier optimum climatique*.

- Membre du jury de thèse de Mathieu Gervais, soutenue le 9 novembre 2012 à Perpignan, thèse de l'Université de Perpignan Via Domitia. *Impacts morphologiques des surcotes et vagues de tempêtes sur le littoral méditerranéen*.

Participation a des comités de pilotage de thèse

- Jean-Françcois Breilh (2010-2013), encadré par Eric Chaumillon et Xavier Bertin (Université de La Rochelle), *Mesure et modélisation à haute résolution des surcotes et de la submersion marine : Les enseignements de Xynthia en Charente-Maritime et en Vendée*.

- Camille Enjalbert (2010-2013), encadrée par Nadia Sénéchal (EPOC) *Etude de la dynamique du swash et impact sur la dynamique du haut de plage*.

- Nicolas Aleman (2010-2013), encadré par Nicolas Robin et Raphael Certain (Université de Perpignan Via Domitia), *Morphodynamique du milieu littoral du Languedoc-Roussillon à l'aide de la technologie LiDAR.*

- Matthias Delpey (2009-2012), co-encadré par Pantxika Otheguy (CTL / Lyonnaise des Eaux) et Fabrice Ardhuin (IFREMER), *Etude de la dispersion horizontale en zone littorale sous l'effet de la circulation tridimensionnelle forcée par les vagues : Application à la baie de Saint Jean de Luz et au littoral de Guethary-Bidart.*

- Elodie Charles (2008-2011), encadrée par Déborah Idier (BRGM) *Impact du changement climatique sur la morphologie côtière par régionalisation dynamique des vagues : application aux plages sableuses de la côte aquitaine* (soutenue le 6 février 2012 à l'Université Toulouse III - Paul Sabatier).

Participation à des comités scientifiques

- Membre du comité scientifique du projet LOREA (2008-2011) *Littoral, Océan, Rivières, Euskadi, Aquitaine.*

B.4 Transfert technologique, relations industrielles et valorisation

Participation à des contrats de recherche

- Participation à des programmes nationaux et internationaux : PNEC ART7, PATOM, LEFE/IDAO (INSU), Gold Coast Shoreline Management Plan, ECORS (DGA/SHOM), VULSACO (ANR), EPIGRAM (ANR), MODLIT (RELIEFS/INSU, DGA), Finite-amplitude behaviour of nearshore crescentic sandbars (NWO), ECOS-CONICYT, BARCAN (INSU), BARDEXII (HYDRALAB-IV/EU).

- Coordinateur de BARBEC (ANR Jeunes Chercheurs, http ://barbec.epoc.u-bordeaux1.fr/) : *Role of morphological interactions in governing the whole wave-dominated sandy BARred-BEaCh system* (décembre 2010 - novembre 2013, 155 Keuros).

Participation à des campagnes de mesures

- Participation à 5 campagnes de mesures dont 1 comme responsable en Australie, Angleterre et France (PNEC 2001, BROADBEACH 2006, BISCA 2007, ECORS-Truc Vert'08, DRIBSB2).

Participation à des expériences de modélisation physique en laboratoire

- Expérience MODLIT réalisée dans le bassin de 30 m par 30 m du Laboratoire d'Hydraulique de France (G-INP-Sogréah), novembre-décembre 2008, PI : Hervé Michallet, LEGI.

- Expérience BARDEX II dans le canal Delta Flume (Deltares, Pays-Bas) de 230 m de long (projet européen HYDRALAB-IV, http ://bardex2.blogspot.fr/), juin-juillet 2012, PI : Gerd Masselink, University of Plymouth.

Consulting

- Divers activités de consulting entre janvier 2005 et janvier 2007 au Griffith Centre for Coastal Management (Griffith University) pour le compte du Gold Coast City Council sur, entre autres : la politique de rechargement en sable et de retrait des épis (enrochements) dans la baie de Coolangatta, la faisabilité du retrait d'un enrochement sur la plage de Burleigh, la politique de dragage des embouchures de Tallebudgera et Currumbin. Ces travaux sont compilés dans les rapports pour le Council dont je suis (co-)auteur (Research Report GCCM N° 51, 52 et 59).

- Activité de consulting en 2006 pour le compte de la société CAPSE : Modélisation hydro-sédimentaire de la baie de Bourail (Nouvelle-Calédonie).

Transfert technologique

- Transfert du code de recherche 1DBeach (dont je coordonne le développement) à la société ACTIMAR en 2010 pour le développement d'un démonstrateur de morphodynamique des plages sableuses, dans le cadre du PEA ECORS (volet Marine) de la DGA.

B.5 Encadrement, animation et management de la recherche

Encadrement et Management

- Depuis 2009 : animateur de l'axe 2 de recherche de l'équipe METHYS *Modélisation et analyse physique des processus hydro-sédimentaires.*

Autres

- Depuis 2009 : organisateur et animateur des séminaires scientifiques EPOC (20 à 40 par an) faisant intervenir des chercheurs français et étrangers sur les thématiques scientifiques abordées au sein d'EPOC (océanographie, paléoenvironnements, Sédimentologie, Bio-géochimie, etc.).

- 2005-2007 : Officier de liaison à Griffith University (Australie) pour l'ambassade de France (programme FEAST - France, réseau Franco-Australien pour la Coopération Scientifique et Technologique).

B.6 Réseau de collaborations [1]

Collaborations nationales

- UMR 5519, Laboratoire des Ecoulements Géophysiques et Industriels (UJF-INPG-CNRS), Université de Grenoble.

1. impliquant des expérimentations communes passées ou en cours, avec échanges de données et/ou des publications communes parues ou soumises.

- UMR 7266, LIttoral ENvironnement et Sociétés, Université de La Rochelle
- Laboratoire de Sciences Appliquées au Génie Civil et Côtier, Anglet
- UMR 5243, Geoscience Montpellier, Université Montpellier II
- Institut de Mathématiques et de Modélisation de Montpellier, Université Montpellier II
- BRGM (Bureau de recherches géologiques et minières), Orléans
- UMR 5566 Laboratoire d'Etudes en Géophysique et Océanographie Spatiales, Toulouse
- CASAGEC, Anglet

Collaborations internationales

- Department of Physical Geography, Faculty of Geosciences, Institute for Marine and Atmospheric Research, Utrecht University, Pays-Bas
- Department of Water Engineering, UNESCO-IHE, Delft, Pays-Bas
- Environmental Hydraulics Institute, IH Cantabria, Universidad de Cantabria, Espagne
- Departamento de Geología, Facultad de Ciencias del Mar y Ambientales, Universidad de Cádiz, Espagne
- Departement de Geologie, Faculte des Sciences, Universite Ibn-Tofail, Maroc
- Laboratoire de Geosciences Marines et Science du Sol (URAC 45), Faculté des Sciences, Universite Chouaib Doukkali, Maroc
- Griffith Centre for Coastal Management, Griffith University, Australie
- Water Research Laboratory, School of Civil and Environmental Engineering, University of New South Wales, Australie
- School of Information and Communications Technology, Griffith University, Australie
- CoastalWatch Australia, Australie

- Laboratório Nacional de Engenharia Civil, Lisbon, Portugal
- FCMA/CIMA, Universidade do Algarve, Portugal
- School of Marine Science and Engineering (Faculty of Science and Technology), Plymouth University, UK
- Departamento de Ingeniería Hidráulica y Ambiental, Escuela de Ingeniería, Pontificia Universidad Catolica de Chile, Chili
- Departamento de Obras Civiles, Universidad Técnica Federico Santa Maria, Valparaíso, Chili

Liste complète des publications

C

Les noms des doctorants ou stagiaires de Master que j'ai (co-)encadrés apparaissent en couleur dans la liste, et ce uniquement pour les articles publiés spécifiquement sur leurs travaux de thèse ou stage.

Revues à comité de lecture
(45 dont 19 en 1^{er} auteur)

[Art-45] Dehouck, A., Lafin, V., Sénéchal, N., Froidefond, J.-M., Almar, R., **Castelle, B.**, Martiny, N. (2012). Evolution morphodynamique interannuelle du littoral sud de la Gironde. *Revue Française de Photogrammétrie et de Télédétection*, 197, 31-42.

[Art-44] Grasso, F., **Castelle, B.**, Ruessink, B.G. (2012). Turbulence dissipation under breaking waves and bores in a natural surf zone. *Continental Shelf Research*, 43, 133-141.

[Art-43] Castelle, B., Coco, G. (2012). The morphodynamics of rip channels on embayed beaches. *Continental Shelf Research*, 43, 10-23.

[Art-42] Brivois, O., Idier, D., Thiébot, J., **Castelle, B.**, Le Gozannet, G., Calvete, D. (2012). On the use of linear stability model to characterize the morphological behaviour of a double bar system. Application to Truc Vert Beach (France). *Comptes Rendus Geoscience*, 344, 277-287.

[Art-41] Castelle, B., Marieu, V., G. Coco, Bonneton, P., Bruneau, N., Ruessink, B.G. (2012). On the impact of an offshore bathymetric anomaly on surfzone rip channels. *Journal of Geophysical Research - Earth Surface*, 117, F01038, doi :10.1029/2011JF002141.

[Art-40] Almar, R., Cienfuegos, R., Catalan, P.A., Michallet, H., **Castelle, B.**, Bonneton, P., Marieu, V. (2012). A new breaking wave height direct estimator from video imagery. *Coastal Engineering*, 61, 42-48.

[39-Art] Hakkou, M., **Castelle, B.**, Benmohammadi, A., Zourarah, B. (2011). Wave climate and morphosedimentary characteristics of the Kénitra - Bouknadel sandy coast, Morocco. *Environmental Earth Sciences*, 64, 1729-1739.

[38-Art] Tissier, M., Bonneton, P., Almar, R., **Castelle, B.**, Bonneton, N., Nahon, A. (2011). Field measurements and non-linear prediction of wave celerity in the surf zone. *European Journal of Mechanics / Fluids*, 30, 589-597.

[37-Art] Castelle, B., Ruessink, B.G. (2011). Modeling formation and subsequent nonlinear evolution of rip channels : time-varying versus time invariant wave forcing. *Journal of Geophysical Research - Earth Surface*, 116, F04008, doi :10.1029/2011JF001997.

[36-Art] Bruneau, N., Bonneton, P., **Castelle, B.**, Pedreros, R. (2011). Modeling rip current circulations and vorticity in a high-energy meso-environment, *Journal of Geophysical Research -*

Oceans, 116, C07026, doi : 10.1029/2010JC006693.

[35-Art] Castelle, B., Michallet, H., Marieu, V., Bonneton, P. (2011). Surf zone retention in a laboratory rip current. *Journal of Coastal Research*, SI 64, 50-54.

[34-Art] Almar, R., Cienfuegos, R., Catalan, P., Birrien, F., **Castelle, B.**, Michallet, H. (2011). Nearshore bathymetric inversion from video using a fully non-linear Boussinesq wave model. *Journal of Coastal Research*, SI 64, 20-24.

[33-Art] Bonneton, P., Van de Lock, J., Parisot, J.-P., Bonneton, N., Sottolichio, A., Dedandt, G.., **Castelle, B.**, Marieu, V. (2011). On the occurrence of tidal bore : The Garonne River case. *Journal of Coastal Research*, SI 64, 1462-1466.

[32-Art] Dubardier, B., **Castelle, B.** (2011). Numerical modeling investigation of the influence of tide on the formation and subsequent nonlinear evolution of rip channels. *Journal of Coastal Research*, SI 64, 1018-1022.

[31-Art] Enjalbert, C., **Castelle, B.**, Rihouey, D., Dailloux, D. (2011). High-frequency video observation of a geologically-constrained barred-beach : La Grande Plage de Biarritz (France). *Journal of Coastal Research*, SI 64, 70-74.

[30-Art] Birrien, F., **Castelle, B.**, Marieu, V., Almar, R., Michallet, H. (2011). Application of a data-model assimilation method to a 3D surf zone sandbar physical experiment. *Journal of Coastal Research*, SI 64, 976-980.

[29-Art] Castelle, B., Michallet, H., Marieu, V., Leckler, F., Dubarbier, B., F., Lambert, A., Berni, C., Barthélemy, E., Bouchette, F., Bonneton, P. (2010). Laboratory experiment on rip current circulations over a moveable bed : drifter measurements. *Journal of Geophysical Research - Oceans*, 115, C12008, doi :10.1029/2010JC006343.

[28-Art] Castelle, B., Ruessink, B.G., Bonneton, P., Marieu, V., Bruneau, N., Price, T.D. (2010). Coupling mechanisms in double sandbar systems, Part 2 : impact on alongshore variability of inner-bar rip channels. *Earth Surface Processes and Landforms*, 35(4), 476-486.

[27-Art] Castelle, B., Ruessink, B.G., Bonneton, P., Marieu, V., Bruneau, N., Price, T.D. (2010). Coupling mechanisms in double sandbar systems, Part 1 : Physical explanation and coupling patterns. *Earth Surface Processes and Landforms*, 35(7), 771-781.

[26-Art] Almar, R., **Castelle, B.**, Ruessink, B.G., Sénéchal, N., Bonneton, P., Marieu, V. (2010). Two- and three-dimensional double-sandbar system behaviour under intense wave forcing and meso-macro tidal range. *Continental Shelf Research*, 30, 781-792.

[25-Art] Bonneton, P., Bruneau, N., **Castelle, B.**, Marche, F. (2010). Large-scale vorticity generation due to dissipating waves in the surf zone. *Discrete and Continuous Dynamical Systems Series B*, 13(4), 719-738.

[24-Art] Castelle, B., Marieu, V., Bonneton, P., Bruneau, N., Grasso, F. (2010). Modélisation des évolutions de profil de plage. *La Houille Blanche*, 1, 104-110.

[23-Art] Castelle, B., Turner, I.L., Bertin, X., Tomlinson, R.B. (2009). Beach nourishments at Coolangatta Bay over the period 1987-2005 : impacts and lessons. *Coastal Engineering*, 56, 940-950.

[22-Art] Almar, R., **Castelle, B.**, Ruessink, B.G., Sénéchal, N., Bonneton, P., Marieu, V. (2009). High-frequency video observation of a double sandbar system under high-energy wave forcing. *Journal of Coastal Research*, SI 56, 1706-1710.

[21-Art] Bruneau, N., **Castelle, B.**, Bonneton, P., Pedreros, R., Almar, R., Bonneton, N., Bretel, P., Parisot, J-P. and Sénéchal, N. (2009) Field observations of an evolving rip current on a meso-macrotidal well-developed inner bar and rip morphology. *Continental Shelf Research*, 29, 1650'1662.

[20-Art] **Castelle, B.**, Bretel, P., Morisset, S., Bonneton, P., Bonneton, N., Tissier, M., Sotin, C., Nahon, A., Bruneau, N., Parisot, J.-P., Capo, S., Bujan, S., Marieu, V. (2009). Rip current system over strong alongshore non-uniformities : on the use of HADCP for model validation. *Journal of Coastal Research*, SI 56, 1746-1750.

[19-Art] Parisot, J.P., Capo, S., **Castelle, B.**, Bujan, S., Moreau, J., Gervais, M., Réjas, A., Hanquiez, V., Almar, R., Marieu, V., Gaunet, J., Gluard, L., George, I., Nahon, A., Dehouck, A., Certain, R., Barthe, P., Le Gall, F., Bernardi, P.J., Le Roy, R., Pedreros, R., Delattre, M., Brillet, J., Sénéchal, N. (2009). Evolution of a multi-barred sandy beaches in presence of very energetic events. *Journal of Coastal Research*, SI 56, 1786-1790.

[18-Art] Bruneau, N., **Castelle, B.**, Bonneton, P. and Pedreros, R. (2009). Very Low Frequency motions of a rip current system : observations and modeling. *Journal of Coastal Research*, SI 56, 1731-1735.

[17-Art] Sénéchal, N., Gouriou, T., **Castelle, B.**, Parisot, J.-P., Capo, S., Bujan, S., Howa H. (2009) Morphodynamic response of a meso- to macro-tidal intermediate beach based on a long-term data-set, *Geomorphology*, 107, 263-274.

[16-Art] **Castelle, B.** (2009) Dynamique des littoraux sableux dominés par l'action de la houle : les apports de la modélisation et de l'imagerie vidéo. *La Houille Blanche*, 1, 64-70.

[15-Art] **Castelle B.**, Le Corre Y., Tomlinson R.B. (2008) Can the Gold Coast beaches withstand extreme events ? *Geo-Marine Letters*, 28, 23-30.

[14-Art] Bertin, X., **Castelle, B.**, Chaumillon, E., Butel, R., Quique, R. (2008) Longshore transport estimation and inter-annual variability at a high energy dissipative beach : St Trojan beach, SW Oléron Island, France, *Continental Shelf Research*, 28, 1316.1332.

[13-Art] Bertin, X., **Castelle, B.**, Anfuso, G., Ferreira, O. (2008) Improvement of sand activation depth prediction under conditions of oblique wave breaking, *Geo-Marine Letters*, 28, 65.75.

[12-Art] **Castelle B.**, Bonneton P., Dupuis H., Sénéchal N. (2007). Double bar beach dynamics on the high-energy meso-macrotidal French Aquitanian coast : a review. *Marine Geology*, 245, 141-159.

[11-Art] **Castelle, B.**, Turner, I.L., Ruessink, B.G., Tomlinson, R.B. (2007) Impact of storms on beach erosion : Broadbeach (Gold Coast, Australia), *Journal of Coastal Research*, SI 50, 534-539.

[10-Art] Sennes, G., **Castelle, B.**, Bertin, X., Mirfenderesk, H., Tomlinson, R.B. (2007) Modeling of the Gold Coast Seaway tidal inlet, Australia, *Journal of Coastal Research*, SI 50, 1086-1091.

[9-Art] Browne, M., **Castelle, B.**, Strauss, D., Tomlinson R.B. (2007) Estimating onshore break size from a global wind-wave model : An empirical approach using neural networks, *Coastal Engineering*, 54 (5), 445-460.

[8-Art] **Castelle, B.**, Bourget, J., Molnar, N., Strauss, D., Deschamps, S., Tomlinson, R.B. (2007) Dynamics of a wave-dominated tidal inlet and influence on adjacent beaches, Currumbin Creek, Gold Coast, Australia, *Coastal Engineering*, 54 (1), 77-90.

[7-Art] Browne, M., Strauss, D., **Castelle, B.**, Lane, C., Blumenstein, M., Tomlinson, R.B. (2006) Empirical estimation of near-shore waves from a global offshore model, *IEEE Geoscience and*

Remote Sensing Letters, 34, 462-466.

[6-Art] Castelle, B., Bonneton, P., Sénéchal, N., Dupuis, H., Butel, R., Michel, D. (2006). Dynamics of wave-induced currents over a multi-barred beach on the Aquitanian coast. *Continental Shelf Research*, 26, 113-131.

[5-Art] Bonneton, P., Marieu, V., Dupuis, H., Sénéchal, N., **Castelle, B.** (2006). Wave transformation and energy dissipation in the surf zone : comparison between a non-linear model and field data. *Journal of Coastal Research*, SI 39, 329-333.

[4-Art] Castelle, B., Bonneton, P. (2006). Nearshore waves and currents over crescentic bars. *Journal of Coastal Research*, SI 39, 687-691.

[3-Art] Castelle B., Bonneton P., Butel R. (2006). Modeling of crescentic pattern development of nearshore bars : Aquitanian Coast, France. *Comptes Rendus Geosciences*, 338, 795-801.

[2-Art] Castelle, B., Bonneton, P. (2006). Modeling of a rip current induced by waves over a ridge and runnel system on the Aquitanian Coast, France. *Comptes Rendus Geosciences*, 338 (10), 711-717.

[1-Art] Lafon, V., Dupuis, H., Butel, R., **Castelle, B.**, Michel, D., Howa, H., De Melo Apoluceno, D. (2005). Morphodynamics of nearshore rhythmic sandbars in a mixed-energy envornment, 2 : Physical forcing analysis. *Estuarine, Coastal and Shelf Science*, 65, 449-462

Conférencier invité

[1-Inv] Castelle, B. (2011). Invitation au panel d'experts sur les courants d'arrachement pour la session spéciale : *Rip Current Processes and Morphology : Future Direction in Research and Outreach* avec Stephen Leathermann, Robert Dean, Jamie MacMahan et Ad Reniers pendant la conférence internationnale Coastal Sediment'11, 2-6 mai, Miami, Floride, USA.

Actes de colloques avec à comité de lecture
(36 dont 18 en 1^{er} auteur)

[36-Act] Castelle, B., Coco, G. (2012). Numerical simulations of rip channel development on embayed beaches. Proc. 33rd Int. Conf. On Coastal Eng., Juillet 1-6, Santander, Espagne.

[35-Act] Price, T.D., **Castelle, B.**, Ruessink, B.G. (2012). Straightening of nearshore sandbars by obliquely incident waves : observations and modelling. Proc. 33rd Int. Conf. On Coastal Eng., Juillet 1-6, Santander, Espagne.

[34-Act] Dubarbier, B., Birrien, F., **Castelle, B.**, Marieu, V., Ruessink, B.G. (2012). A new beach profile evolution model on the timescales of weeks : simulations and preliminary results from the input of data assimilation. Proc. 33rd Int. Conf. On Coastal Eng., Juillet 1-6, Santander, Espagne.

[33-Act] Birrien, F., **Castelle, B.**, Dubarbier, B., Marieu, V. (2012). Data-model assimilation of nearshore bathymetry using heterogeneous video-derived observations. Proc. 33rd Int. Conf. On Coastal Eng., Juillet 1-6, Santander, Espagne.

[32-Act] Almar, R., Cienfuegos, R., Gonzales, E., Catalan, P.A., Michallet, H., Bonneton, P., **Castelle, B.**, Suarez, L. (2012). Barred beach morphological control on infragravity motion. Proc. 33rd Int. Conf. On Coastal Eng., Juillet 1-6, Santander, Espagne.

[31-Act] Castelle, B., Coco, G. (2012). Morphodynamique des barres sableuses de déferlement le long des plages en baie. Proc. XIIèmes Journées Nationales Génie Côtie Génie Civil, 12-14 juin, Cherbourg, France.

[30-Act] Dubarbier, B., **Castelle, B.**, Birrien, F., Marieu, V., Ruessink, B.G. (2012). Modélisation de l'évolution des profils de plage sableuse sur plusieurs mois et apports de l'assimilation de données. Proc. XIIèmes Journées Nationales Génie Côtie Génie Civil, 12-14 juin, Cherbourg, France.

[29-Act] Birrien, F., **Castelle, B.**, Dailloux, D., Marieu, V., Rihouey, D., Price, T.D. (2012). Observation vidéo de la dynamique des méga-croissants de plage : plages d'Anglet (Pays Basque). Proc. XIIèmes Journées Nationales Génie Côtie Génie Civil, 12-14 juin, Cherbourg, France.

[28-Act] Bonneton, P., J.-P. Parisot, Bonneton, N., Sottolichio, A., **Castelle, B.**, Marieu, V., Pochon, N., Van De Lock, J. (2011). Modélisation physique de la morphodynamique d'une plage barrée tridimensionnelle. Proc. The 21st International Offshore (Ocean) and Polar Engineering Conference, 19-24 juin, Maui, Hawai, USA.

[27-Act] Idier, D., Boulahya, F., Brivois, O., **Castelle, B.**, Larroudé, P., Romieu, E., Le Gozannet, G., Delvallée, E., Thiebot, J. (2011). Sensitivity of beach morphodynamics to climate variability, Application to Truc Vert Beach (France). Proc. Coastal Sediment'11, 2-6 mai, Mimai, Floride, USA.

[26-Act] Castelle, B., Ruessink, B.G. (2011). Modeling formation and subsequent nonlinear evolution of rip channels : time-varying versus time-invariant wave forcing. Proc. Coastal Sediment'11, 2-6 mai, Mimai, Floride, USA.

[25-Act] Michallet, H., **Castelle, B.**, Bouchette, F., Lambert, A., Berni, C., Barthélemy, E., Bonneton, P., Sous, D. (2010). Modélisation physique de la morphodynamique d'une plage barrée tridimensionnelle. Proc. XIèmes Journées Nationales Génie Côtie Génie Civil, 22-24 juin, Les Sables d'Olonne, France.

[24-Act] Dailloux, D., Rihouey, D., Dugor, J., **Castelle, B.** (2010). Analyse critique de l'utilisation des techniques de mesure topographique vidéo comme outil de gestion des plages sableuses Proc. XIèmes Journées Nationales Génie Côtie Génie Civil, 22-24 juin, Les Sables d'Olonne, France.

[23-Act] Hakkou, M., **Castelle, B.**, Benmohammadi, A., Zourarah (2010). Climat de houle et caractéristiques morpho-sédimentaires du littoral de Bouknadel-Kénitra (Maroc). Proc. XIèmes Journées Nationales Génie Côtie Génie Civil, 22-24 juin, Les Sables d'Olonne, France.

[22-Act] Castelle, B., Michallet, H., Marieu, V., Leckler, F., Dubardier, B., Lambert,A., Berni, C., Barthélemy, E., Bouchette, F., Bonneton, P., Kimmoun, O., Sous, D. and Almar, R. (2010). Modélisation physique des courants d'arrachement : apport des mesures lagrangiennes. Proc. XIèmes Journées Nationales Génie Côtie Génie Civil, 22-24 juin, Les Sables d'Olonne, France.

[21-Act] Castelle, B., Michallet, H., Marieu, V., Leckler, F., Dubardier, B., Lambert,A., Berni, C., Bouchette, F., Bonneton, P., Kimmoun, O., Sous, D. and Almar, R. (2009). A large-scale laboratory experiment of rip current circulations over a moveable bed : drifter measurements. Proc. Coastal Dynamics'09, Tokyo, Japon.

[20-Act] Tissier, M., Bonneton, P., Almar, R., **Castelle, B.**, Bonneton, P. (2009). Etude expérimentale de la célérité des vagues en zone de surf. Proc. 11ème Congrès Français de Mécanique, Marseille, 24-28 aout, France.

[19-Act] Bruneau, N., Bonneton, P., **Castelle, B.**, Pedreros, R., Parisot, J-P., Sénéchal, N. (2008). Modeling of the dynamics of a high energy rip current system during Biscarosse 2007 field

experiment (Aquitanian Coast, France). Proc. 31st Int. Conf. On Coastal Eng., Aout 31 - Sept 5, Hambourg, Allemagne.

[18-Act] Castelle, B., Ruessink, B. G., Bonneton, P., Bruneau, N., Marieu, V. (2008). Modeling of coupled and noncoupled behaviour of a double sandbar system : self-organization and morphological forcing. Proc. 31st Int. Conf. On Coastal Eng., Aout 31 - Sept 5, Hambourg, Allemagne.

[17-Act] Castelle, B. (2008). Dynamique des littoraux sableux dominés par l'action de la houle : les apports de la modélisation et de l'imagerie vidéo. Proc. Colloques sur les nouvelles approches sur les risques côtiers : aléas, vulnérabilité, changement climatique, variations du trait de côte, Jan 30-31, Paris, France.

[16-Act] Castelle, B., Grasso, F., Marieu, V., Bonneton, P., Bruneau, N. (2008). Développement d'un nouveau modèle d'évolution de profil de plage. Proc. Xèmes Journées Nationales Génie Côtie Génie Civil, 14-16 octobre, Sophia Antipolis, France.

[15-Act] Castelle, B., Turner, I.L., Tomlinson, R.B., Bertin, X. (2008). Evolution de la baie de Coollangatta (Gold Coast, Australie) : impact des rechargements de plage et du système permanent de bypass de sédiment. Proc. Xèmes Journées Nationales Génie Côtie Génie Civil, 14-16 octobre, Sophia Antipolis, France.

[14-Act] Sénéchal, N., Ardhuin, F., **Castelle B.**, et al. (2008). ECORS-Truc Vert'08 : Qualification des modeles de houle et de morphodynamique. Proc. Xèmes Journées Nationales Génie Côtie Génie Civil, 14-16 octobre, Sophia Antipolis, France.

[13-Act] Almar, R., **Castelle, B.**, Sénéchal, N., Bonneton, P. (2008). Video observation of a rapid post-storm accretionnary beach state transition on the Aquitanian Coast. Proc. 11ème International Symposium on Oceanography of Bay of Biscay, 2-4 Avril, Espagne.

[12-Act] Castelle, B., Almar, R., Bonneton, N., Bonneton, P., Bretel, P., Bujan, S., Bruneau, N., Parisot, J.-P., Pedreros, R., Sénéchal, N. (2008). Dynamics of a moderate energy rip current over a Transverse Bar and Rip morphology : Biscarrosse 2007 field experiment (Aquitanian Coast, France). Proc. 11ème International Symposium on Oceanography of Bay of Biscay, 2-4 Avril, Espagne.

[11-Act] Castelle, B., Lazarow, N., Marty, G., Tomlinson, R.B. (2006). Impact of beach nourishmenton Coolangatta Bay morphology over the period 1995-2005. Proc. 15th NSWCoastal Conference, Nov 7-9, Coffs Harbour, NSW.

[10-Act] Bonneton, N., Bonneton, P., Sénéchal, N., **Castelle, B.** (2006). Very Low Frequency rip current pulsations during high-energy wave conditions on a meso-macro-tidal beach. Proc. 30th ICCE, Sept 4-8, San Diego, USA.

[9-Act] Castelle, B., Cope, M., Abbs, D., Tomlinson, R.B. (2006). Wave Modeling for the Gold Coast : down-sizing from global to near-shore. Proc. 13th National Conference of the Australian Meteorological and Oceanographic Society : Climate, Water and Sustainability, Feb 6-8, Newcastle, NSW, Australia.

[8-Act] Castelle, B., Bonneton, P., Butel, R. (2005). Morphodynamic modelling of nearshore crescentic bar dissymmetry on an open coast : Aquitanain Coast, France. Proc. 5th International Conference on Coastal Dynamics '05, Barcelona, Spain, April 11-15.

[7-Act] Castelle, B., Bonneton, P. (2004). Modélisation de la morphodynamique des plages d'Aquitaine. Proc. 8èmes Journées Nationales de Génie Côtier - Génie Civil, Compiègne, France.

[6-Act] Castelle, B., Bonneton, P. (2004). Nearshore crescentic bars along the French Aquitanian Coast : observation, physical mechanism and modeling. Proc. 9th International Symposium on Oceanography of the Bay of Biscay, Pau, France.

[5-Act] Castelle, B., Bonneton, P. (2004). Modeling of tidal modulation and magnitude of wave-induced currents over the intertidal transverse bar systems on the french aquitanian coast. Proc. 9th International Symposium on Oceanography of the Bay of Biscay, Pau, France.

[4-Act] Castelle, B., Saint-Cast, F., Bonneton, P. (2003). 2DH Modelling of wave-induced current and sediment transport over a high energy barred-beach. Proc. Coastal Sediment '03, Floridia, USA.

[3-Act] Castelle, B., Saint-Cast, F., Bonneton, P. (2003). 2DH Modelling of wave-induced current and sediment transport in a rip current channel. Proc. 3rd IAHR Symposium on River, Coastal and Estuarine Morphodynamics, Barcelona, Spain.

[2-Act] Sénéchal, N., Abadie, S., Bonneton, N., Bonneton, P., Brière, C., Butel, B., Capobianco, R., **Castelle, B.**, Chapalain, G., Desmazes, F., Dulou, C., Dupuis, H., Howa, H., Larroude, P., Maron, P., Malengros, D., Michel, M., Mory, M., Oggian, G., Pedreros, R., Rey, V., Rihouey, D. (2002). Présentation de la campagne de mesures hydro-sédimentaires du PNEC : Truc Vert 2001. Proc. 7èmes Journées Nationales de Génie Côtier - Génie Civil, Anglet, France.

[1-Act] Saint-Cast, F., **Castelle, B.**, Bonneton, P., Caltagirone, J.-P. (2002). Modélisation des écoulements induits par la houle sur les plages d'Aquitaine. Proc. 7èmes Journées Nationales de Génie Côtier - Génie Civil, Anglet, France.

Communication à des congrès, symposium
(20 dont 10 en 1^{er} auteur)

[20-Com] Birrien, F., **Castelle, B.**, Dailloux, D., Marieu, V., Rihouey, D., Michallet, H. (2011). Implementing data-model assimilation techniques to the Basque Coast Neaches : preliminary results. Vulnérabilité des écosystèmes côtiers au changement global et aux évènements extrêmes, 18-21 octobre, Biarritz, France.

[19-Com] Barbara, L., **Castelle, B.**, Schmidt, S., Massé, G., Crosta, X. (2011). Sea ice variability and teleconnection between ENSO and SAM in north Antarctic Peninsula during the Historic period. 11th International Symposium on Antarctic Earth Sciences, 10-15 juillet, Edinburgh, Ecosse.

[18-Com] Gillet, H., Guyot, C., **Castelle, B.**, Moreau, J., Bujan, S., Cirac, P. (2010). Analyse morpho-sédimentaire de la tête du canyon de Capbreton : relations avec la dérive littorale aquitaine et l'activité turbiditique du canyon. MNT et imagerie à 50 cm de résolution (V/O Haliotis). 23èmes Réunions des Sciences de la Terre, 25-29 octobre, Bordeaux, France.

[17-Com] Hakkou, M., **Castelle, B.**, Benmohammadi, A. (2010). Dynamique morphosédimentaire et évolution du trait de côte de Bouknadel-Kénitra. 2èmes Journées Internationales sur la dégradation des littoraux, 2-3 uillet, Kénitra, Maroc.

[16-Com] Castelle, B. (2010). Barre(s) de déferlement : une élément crucial de la dynamique des plages sableuses dominées par l'action de la houle et de leur vulnérabilité. 2èmes Journées Internationales sur la dégradation des littoraux, 2-3 juillet, Kénitra, Maroc.

[15-Com] Dehouck, A., Sénéchal, N., Lafon, V., Almar, R., **Castelle, B.**, Froidefond, J.-M. (2010). Yearly to decennial beach morphodynamics south the Arcachon inlet (France) from satellite observations. EGU General Assembly, Vienne, Autriche.

[14-Com] Castelle B., Michallet, H., Marieu, V., Bonneton, P., Dubardier, J., Leckler, F. (2010). Surf zone retention in rip current systems and implications for beach safety : a laboratory experiment. 1st International Rip Current Symposium, 17-19 Fèv., Miami, Flordide, USA.

[13-Com] Bonneton, P., Bruneau, N., **Castelle, B.**, Almar, R., Bonneton, N. (2010). Alongshore differential topographically controlled wave-breaking and rip current circulation. 1st International Rip Current Symposium, 17-19 Fèv., Miami, Flordide, USA.

[12-Com] Dehouck, A., Lafon, V., Sénéchal, N., **Castelle, B.**, Froidefond, J.-M. (2009). Evolution interannuelle du littoral sud-gironde. 12ème Congrès ASF, Rennes, France.

[11-Com] Idier, D., Falquès, A., Mallet, C., **Castelle, B.**, Parisot, J.-P., Le Gozannet, G., Devallée, E. (2009). Shoreline sandwaves along the Aquitanian Coast (France) : influence of Climate Change. EGU General Assembly, 19-24 avril, Vienne, France.

[10-Com] Bruneau, N., **Castelle, B.**, Pedreros, R., Bonneton, P. (2007). Modélisation morphodynamique des littoraux sableux dominés par l'action de la houle : vers un modèle opérationnel. 11ème Congrès ASF, Oct 21-27, Caen, France.

[9-Com] Castelle, B., Turner, I.L., Ruessink, B.G., Tomlinson, R.B. (2007). Erosion de la plage aérienne et comportement des barres pré-littorales pendant des événements extrêmes : Broadbeach (Australie). 11ème Congrès ASF, Oct 21-27, Caen, France.

[8-Com] Bruneau, N., Pedreros, R., Bonneton, P., **Castelle, B.**, Parisot, J.-P. (2007). Résultats préliminaires et faisabilité des mesures altimétriques haute fréquence en zone de déferlement. 11ème Congrès ASF, Oct 21-27, Caen, France.

[7-Com] Castelle, B., Bonneton, P., Sénéchal, N. (2007). Note sur une classification des morphologies barre/baïne. 11ème Congrès ASF, Oct 21-27, Caen, France.

[6-Com] Castelle, B., Bonneton, P., Bruneau, N., Marieu, V. (2007). Modélisation du couplage morphologique entre barre interne et barre externe : mécanisme d'auto-organisation ou forçage morphologique ? 11ème Congrès ASF, Oct 21-27, Caen, France.

[5-Com] Browne, M., Tomlinson, R.B., **Castelle, B.**, Strauss S. (2005). Estimating onshore break size from a global wind-wave model : An empirical approach using neural networks networks. Coastal CRC Conference : Research for Coastal Management, Coolangatta, Australia, 14 Sept.

[4-Com] Bertin, X., Chaumillon, E., Quique, R., Butel, R., **Castelle, B.** (2005). Estimation et variabilité interannuelle de la dérive littorale sur une plage dissipative, SW Oléron, France. 10ème Congrès ASF, Presqu ile de Giens, France.

[3-Com] Michel, D., Bonneton, P., Bretel, P., Bujan, S., **Castelle, B.**, De Melo, D., Desmazes, F., Dupuis, H., Howa, H., Lafon, V., Oggian, G., Sénéchal, N. (2003). Morphodynamique d'une plage sableuse : Plage du Truc Vert, côte aquitaine. 9ème Congrès ASF, Bordeaux, France.

[2-Com] Castelle, B., Bonneton, P. (2003). Calibrage et couplage du code MORPHODYN sur la plage aquitaine du Truc Vert campagne PNEC 2001. 9ème Congrès ASF, Bordeaux, France.

[1-Com] Castelle, B., Bonneton, P. (2002). Wave-induced currents over the Aquitanian Coast sand bars. 8th International Symposium on Oceanography of the Bay of Biscay, Gijon, Spain.

Séminaires / Workshops
(17 dont 10 en 1^{er} auteur)

[17-SWo] Castelle B. (2012). Modélisation physique des courants d'arrachement induits par les vagues le long des plages sableuses. Séminaire de la demi-journée d'animation scientifique de l'école doctorale Science et Environnements, 29 mai, Bordeaux France.

[16-SWo] Castelle B. (2012). Changement de stratégie et de paradigme scientifique en modélisation de la morphodynamique des plages sableuses : vers une réconciliation de la théorie avec la réalité ? Séminaire aux Journées Scientifiques JEST EPOC, 4 mai, Arcachon, France.

[15-SWo] Castelle B. (2012). Modélisation numérique de la morphodynamique des plages sableuses dominées par l'action de la houle. Séminaire scientifique du laboratoire LIENNs de l'Université de La Rochelle, 21 mars, La Rochelle, France.

[14-SWo] Marieu, V., Birrien, F., **Castelle, B.**, Bonneton, P. (2010). Bathymetry inversion and modelling. Workshop ECORS, 6-8 juillet, Bordeaux, France. Workshop ECORS, 6-8 juillet, Bordeaux, France.

[13-SWo] Castelle, B., Ruessink, B.G, Bonneton, P., Bruneau, N., Marieu, V., Price, T.D. (2010). Coupling mechanisms in double sandbar systems : coupling patterns and impact on alongshore variability of inner-bar rip channels. Workshop ECORS, 6-8 juillet, Bordeaux, France.

[12-SWo] Tissier, M., Bonneton, P, Almar, R., Postacchini, M., **Castelle, B.**, Bonneton, N., Parisot, J.-P., Bretel, P. (2010). Field measurements of wave celerity in the surf zone, analysis of nonlinear and very low frequency processes. Workshop ECORS, 6-8 juillet, Bordeaux, France.

[11-SWo] Thiebot, J., Pedreros, R., Bruneau, N., Marieu, V., **Castelle, B.**, Dumas, F., Garnier, V. (2010). Implementation of cross-shore processes in the MARS - SWAN modeling platform. Workshop ECORS, 6-8 juillet, Bordeaux, France.

[10-SWo] Castelle, B., Michallet, H., Marieu, V., Leckler, F., Dubardier, B., Lambert, A., Berni, C., Bouchette, F., Bonneton, P., Kimmoun, O., Sous, D., Almar, R. (2010). Laboratory experiment of rip current circulations over a moveable Bed : drifter Measurements. Workshop ECORS, 6-8 juillet, Bordeaux, France.

[9-SWo] Bruneau, N., Bonneton, P., **Castelle, B.**, Pedreros, R., Bertin, X. (2010). Modeling of topographically-controlled wave-driven circulations : Application to Biscarrosse Beach. Workshop ECORS, 6-8 juillet, Bordeaux, France.

[8-SWo] Grasso, F., Michallet, H., Barthélemy, E., **Castelle, B.** (2010). Morphological changes of cross-shore beach profiles. Workshop ECORS, 6-8 juillet, Bordeaux, France.

[7-SWo] Michallet, H., **Castelle, B.**, Bouchette, F., Lambert, A., Berni, C., Barthélemy, E., Bonneton, P., Sous, D. (2010). Physical modelling of the morphodynamics of a 3D barred beach. Workshop ECORS, 6-8 juillet, Bordeaux, France.

[6-SWo] Michallet H., **Castelle B.**, Bouchette F., Lambert A., Berni C., Barthélemy E., Bonneton P., Sous D. (2010). Presentation of the LHF experiment and preliminary hydrodynamic results. Workshop ECORS, 6-8 juillet, Bordeaux, France.

[5-SWo] Castelle, B. (2010). Coupling mechanisms in double sandbar systems : coupling patterns and impact on alongshore variability of inner-bar rip channels. 2nd Workshop on Mathematics and Oceanography, Montpellier, 1-3 Fèv.

[4-SWo] Castelle, B., Ruessink, B.G., Bonneton, P., Marieu, V., Bruneau, N., Price, T.D. (2010). Coupling mechanisms in double sandbar systems : coupling patterns and impact on alongshore variability of inner-bar rip channels. Workshop on : Linear stability analysis in coastal morphodynamics : essential or useless ?, 21-22 Janv., Barcelone, Espagne.

[3-SWo] Castelle B. (2008). Impact respectif des mécanismes de couplage et d'auto-organisation sur la dynamique des plages sableuses à double barre. Séminaire MAMNO ("Modélisation et Analyse Mathématique et Numérique en Océanographie"), 15 déc, Bordeaux, France.

[2-SWo] Castelle B. (2008). Dynamique des plages sableuses soumises à l'action de la houle. Séminaire scientifique de l'Université Ibn-Tofail, 26 fèv., Kénitra, Maroc.

[1-SWo] Castelle B. (2005). Dynamique hydro-sédimentaire d'un littoral sableux anthropisé : la Gold Coast (Australie). Séminaire EPOC, 19 déc, Bordeaux, France.

Chapitre d'ouvrage
(1 dont 0 en 1^{er} auteur)

[1-Chap] Actuellement co-rédacteur du chapitre *Dynamique littorale* (coordinateur Philippe Bonneton) pour le livre *Changement climatique en Aquitaine : un état des lieux scientifique* demandé par la Région Aquitaine et coordonné par Hervé Le Treut.

Codes de recherche
(Coordinateur du développement de 2 codes de recherche)

[2-Log] MORPHODYN : Modèle hydro-sédimentaire permettant de calculer les vagues, les circulations induites et la morphodynamique des plages sableuses. Les récents développements font que ce code est désormais sur le plan international le seul à pouvoir simuler la formation, l'évolution non-linéaire et la saturation de l'amplitude des barres sableuses de déferlement tridimensionnelles ainsi que l'évolution du trait de côte associée.

[1-Log] 1DBeach : Modèle d'évolution des profils de plage permettant de calculer les évolutions de profil de plage sur des temps longs (plusieurs années) avec des temps de calcul très faibles. Une des originalités de ce code est qu'il est couplé à un module d'assimilation de données permettant (1) d'inverser la bathyémtrie et (2) d'assimiler les données pour corriger en temps réel les évolutions simulées.

Publications représentative de mon activité de recherche

D

Sommaire

Dans cette annexe sont compilées les publications les plus représentatives de mes activités de recherche ces 11 dernières années. Ces publications sont listées dans un ordre chronologique et non thématique.

D.1 Dynamics of wave-induced currents over an alongshore non-uniform multiple-barred sandy beach on the Aquitanian Coast, France

Bruno Castelle, Philippe Bonneton, Nadia Sénéchal, Hélène Dupuis, Rémi Butel, Denis Michel

Continental Shelf Research, Vol. 26, pp. 113-131, 2006

Available online at www.sciencedirect.com
SCIENCE DIRECT®
Continental Shelf Research 26 (2006) 113–131
CONTINENTAL SHELF RESEARCH
www.elsevier.com/locate/csr

Dynamics of wave-induced currents over an alongshore non-uniform multiple-barred sandy beach on the Aquitanian Coast, France

Bruno Castelle*, Philippe Bonneton, Nadia Sénéchal, Hélène Dupuis, Rémi Butel, Denis Michel

Department of Geology and Oceanography, UMR CNRS 5805 EPOC, University of Bordeaux I, 33405 Talence cedex, France

Received 9 April 2004; received in revised form 11 August 2005; accepted 23 August 2005
Available online 15 November 2005

Abstract

This paper presents field investigation and numerical modelling of waves and wave-induced currents on a wave-dominated and non-alongshore uniform multiple barred beach. This study aims at establishing the first analysis of the dynamics of horizontal flows on the French Aquitanian coast. The spectral wave program SWAN is coupled with the time- and depth-averaged (2DH) coastal area model MORPHODYN. This coupled-model is applied to Truc Vert Beach, and results are compared with field data. From the 14th to the 19th of October 2001, a field experiment was carried out in order to characterize hydrodynamics and sediment transport over a complex bathymetry in the presence of oceanic wave conditions. From this data we calibrated three parameters: the bottom friction for wave propagation from the Aquitanian continental shelf to the nearshore zone, the spatially constant bottom friction coefficient due to waves and currents, and lateral mixing. Despite model approximations and the fact that the offshore wave boundary condition was located 15 km off the coast, the model is in good agreement with measurements. During weak wind conditions, computed waves and longshore currents fit well with field data on the ridge and runnel system. The strong tidal modulation of surf zone processes over this system is revealed. Hydrodynamics are strongly controlled by the beach morphology. For near-normally incident swells, the ridge and runnel system is responsible for a strong rip current located at the runnel outlet, associated with a circulation cell. Prediction of the tidal modulation and the sensitivity of the rip current to offshore wave conditions are in agreement with observations. Maximum rip current flow velocities occur approximately at mid-tide, which differs from what most researchers have found in other environments.

Keywords: France; Aquitanian coast; Nearshore dynamics; Rip currents; Longshore current; Field measurements; Modelling; Ridge and runnel system

1. Introduction

Ocean waves are the primary cause of sediment transport and morphological change in the nearshore. During the past three decades, knowledge of the physical processes related to waves, wave-induced currents and sediment transport has

*Corresponding author. Now at Griffith Centre for Coastal Management, Gold Coast, Australia. Tel.: +61 (0)7 5552 8520; fax: +61 (0)7 5552 8067.
E-mail address: b.castelle@griffith.edu.au (B. Castelle).

0278-4343/$ - see front matter © 2005 Elsevier Ltd. All rights reserved.
doi:10.1016/j.csr.2005.08.027

improved. However, on natural beaches, accurate prediction of wave-induced current circulations which control the nearshore sediment transport rate remains an open issue. In particular, the determination of longshore current structure and rip current behaviour are important topics for further research. In this paper, waves and wave-induced currents are investigated using measurements and numerical modelling over the Aquitanian beaches, which have not received much attention in the literature previously. In this environment, the longshore non-uniform topography and wave climate are responsible for complex rip currents, nearshore cell circulations and longshore currents. These are discussed herein and compared with other environments.

Cross-shore variability and magnitude of longshore currents have been investigated for a long time using different approaches. Laboratory experiments were undertaken by Visser (1991), Hamilton and Ebersole (2001) among others, to improve methods for predicting wave-induced currents and nearshore sediment transport rates. For barred and planar beaches, laboratory experiments show that the maximum longshore current velocity is located where breaking is most intense, i.e. on the bar and near the shoreline. Early longshore current models were reduced to one dimension (Longuet-Higgins, 1970) and predict the magnitude and location of the maximum longshore current at the breaking point. For alongshore uniform barred-beaches, the maximum of longshore current can be expected to occur at the point of most intense wave breaking (Ruessink et al., 2001; Feddersen and Guza, 2003), i.e. on the bar, consistent with the laboratory results of Reniers and Battjes (1997). When a barred-beach has strong alongshore non-uniformities, the maximum of longshore current is located in the trough (Church and Thornton, 1993; Kuriyama and Nakatsukasa, 2000). Several mechanisms were examined to explain this spatial lag. Roller effects on the longshore distribution were investigated by Reniers and Battjes (1997) as well as turbulent eddy viscosity. Church and Thornton (1993) examined the effects of wave-induced turbulence on the bottom shear stress and resulting longshore current profiles. However, the longshore pressure gradient due to longshore bathymetry inhomogeneities is the only mechanism able to shift enough the velocity maximum away from the bar crest (Petrevu et al., 1995; Reniers and Battjes, 1997; Feddersen et al., 1998).

The rip current is another common horizontal flow pattern which occurs on natural beaches. Rips are strong and narrow seaward oriented currents, responsible for significant sediment transport (Cook, 1970; Inman et al., 1971; Brander, 1999) and morphology change in the nearshore (Sonu, 1972; Short, 1979, 1992; Wright and Short, 1984). Recently, field studies have been undertaken to improve knowledge of this nearshore circulation pattern (Aagaard et al., 1997; Brander, 1999; MacMahan et al., 2003). The tidal modulation of the rip current velocity, with maximum velocities occurring at low-tide, were investigated by Brander (1999). A first scaling relationship between incoming waves and rip current dimension was established by Brander (2000). Haas and Svendsen (2002) investigated the vertical structure of the rip current from laboratory experiments in comparison with quasi-3D numerical simulations. They found that the vertical profile of the rip current varies from a depth uniform pattern in the channel to depth varying pattern further offshore, with maximum velocity at the surface.

The present study aims at investigating the structure and magnitude of longshore current and rip currents on a type of beach which behaves differently than others reported in the literature. The French Aquitanian coast beaches exhibit strongly longshore non-uniform multiple bars, resulting in complex horizontal wave-induced current patterns which are poorly understood. The lack of data is due both to a very energetic wave climate and difficult access to the study area, which makes intensive measurements in the field a challenging task, particularly in the shallow subtidal zone. Before PNEC 2001 experiment, measurements of rips and nearshore cell circulation were few, and virtually non-existent in the environment described in this paper. The present study paves this gap with a quality dataset. Combination of modelling, field measurements analysis and satellite imagery is used to investigate the random wave transformation and wave-induced currents. A two-dimensional depth-averaged motion approach (2DH) is undertaken to predict longshore current structure and rip currents. The two-dimensional structure, magnitude, tidal modulation and sensitivity to offshore wave conditions of wave-induced currents are then analysed.

2. Study area

The French Aquitanian coast is a 230 km high energy meso-macrotidal straight coast between the Gironde estuary and the Adour estuary (Fig. 1).

The high meso-macro tidal range is about 5 m at spring tides, along with a relatively broad intertidal region of approximately 200 m. This coast is bordered by high aeolian dunes and the sediment consists of fine to medium sand ($200\,\mu m < d_{50} < 350\,\mu m$). The coast is exposed to almost continuous high energy swells. Statistical analysis of non-directional Datawell wave rider times series (in 26 m water depth) shows that this coast is mainly concerned by very low steepness swell waves (mean annual H_s and period of 1.4 m and 6.5 s), travelling mainly from W–NW directions (Butel et al., 2002). During storms, offshore significant wave height can reach 10 m. The mean wave incidence induces a strong southerly longshore drift (Michel and Howa, 1994). In the area situated outside the influence of the Arcachon lagoon and Gironde estuary, tidal currents are not significant in comparison with wave-induced currents.

Following the beach state classification of Short (1992) and Short and Aagaard (1993), Aquitanian coast beach state is mainly an intermediate (d) double-barred beach. The nearshore is characterized by two distinct sand bar patterns: the crescentic bar system in the subtidal zone and the ridge and runnel system in the intertidal zone (Michel and Howa, 1999). After long periods of fair weather conditions, ridges are regularly interrupted by down-current oriented runnels with a mean wavelength of about 400 m (year-average), i.e. a rip density (RD) of 2.5. This value of RD characterizes west coast swell environments (Short and Brander, 1999), going against the world wave environment classification of Davies (1980) in which the Aquitanian coast is defined as a storm wave environment. Fig. 2 shows an aerial view of a ridge and runnel system on the Aquitanian Coast. Rip channel migration is about 3 m per day during summer (Lafon et al., 2002). After the occurrence of high energy wave conditions, random direction runnels with a large range of rip spacing are observed. The nearshore zone exhibits large scale crescentic bars (Froidefond et al., 1990) whose shape can vary from typically crescentic to a seldom observed lunate shape with a mean wavelength of about 700 m (Lafon et al., 2005). Fig. 3 shows a SPOT image of a regular nearshore crescentic bar system from Truc Vert Beach to the end of the sand spit. Sometimes a third bar system inshore of the crescentic bars can be connected to the ridge and runnel system. This system has a crescent shape, and it results in a shifting of the beach state to intermediate (e) following the classification of Short (1992). The morphodynamics of these intertidal and nearshore bar systems are still not well understood, and a state of the art of our knowledge is given by Castelle et al. (2005).

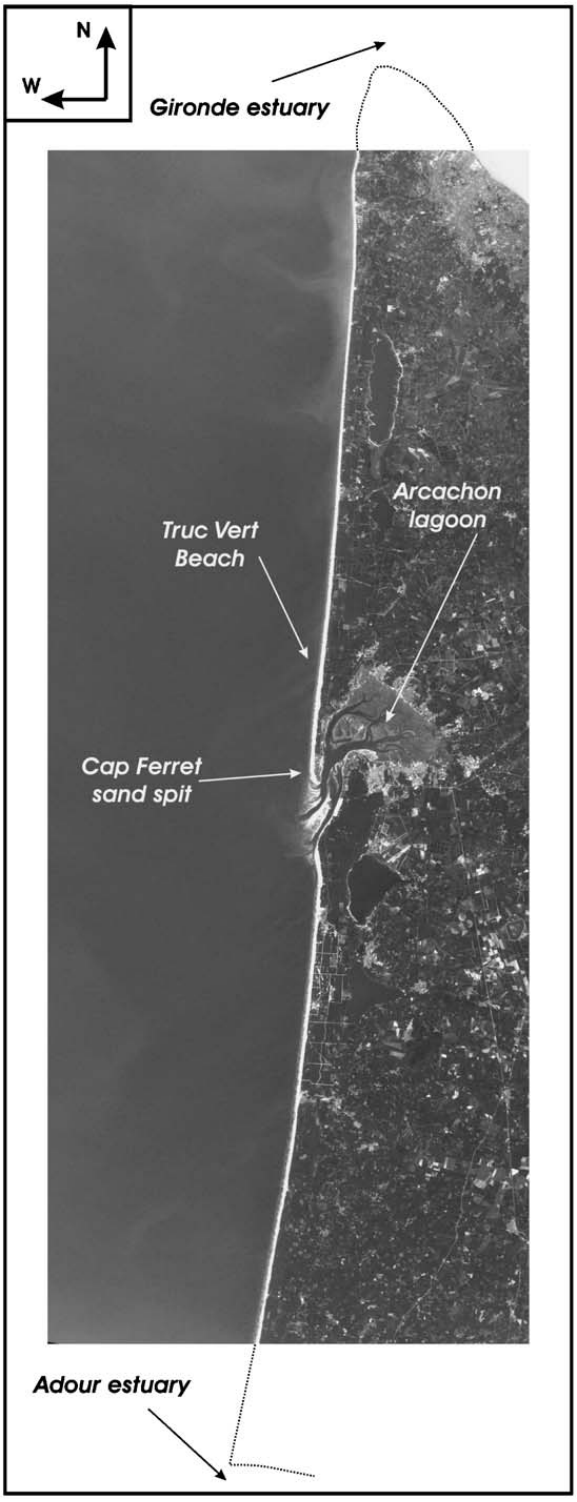

Fig. 1. Satellite image (SPOT XS1) of the Aquitanian Coast between the Gironde estuary and the Adour estuary. Location of Truc Vert Beach on the upper part of the Cap Ferret sand spit.

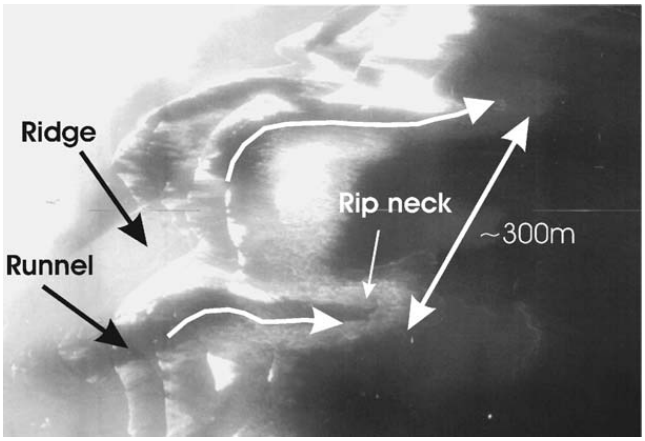

Fig. 2. Aerial photograph of a regular ridge and runnel system in the intertidal domain, Aquitanian Coast. Location of rip currents located at the runnel outlets with two sediment plumes is highlighted.

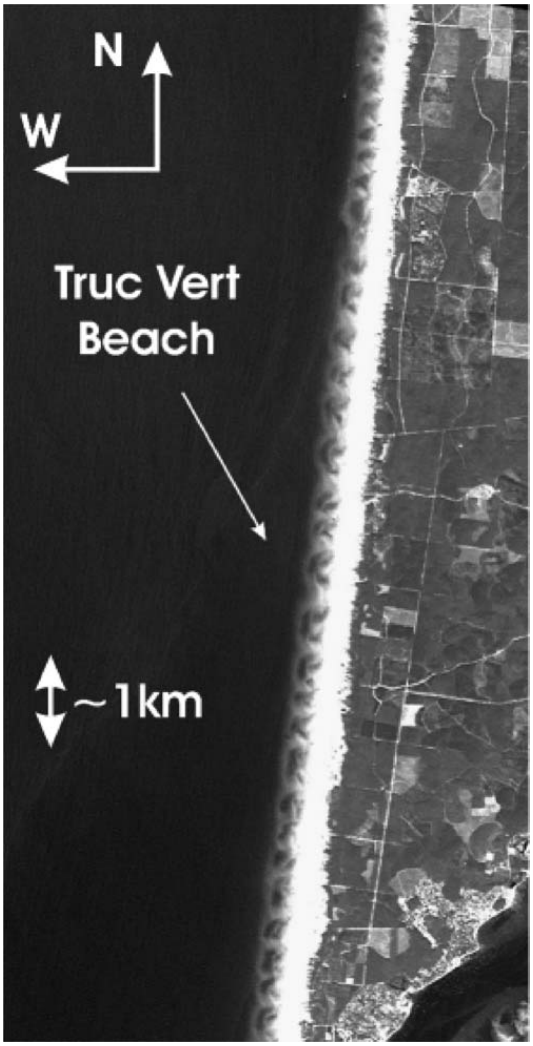

Fig. 3. SPOT image around Truc Vert Beach of regular crescentic bar patterns in the nearshore zone with a mean wavelength of approximately 600 m, SPOT XS1, 15/05/01@CNES-DGO-UMR EPOC.

This nearshore morphology is responsible for complex horizontal water circulations. According to fishermen, lifeguards and surfers, strong tidal modulated rip currents are observed at the runnel outlet, causing several drownings each summer, with maximum flow velocities occurring at mid-tide. This goes against recent studies on other environments (Brander, 1999, 2000) which showed maximum flow velocities occurred at low-tide. Such currents are also responsible for strong water and sediment exchanges between the nearshore and the intertidal zones (Fig. 2). Further offshore, rip currents are also observed over the nearshore crescentic bar systems. For mid- to high-energy conditions, large circulation cells and rip currents are supposed to be induced by waves over this system (Castelle and Bonneton, in press).

In this paper, field measurements of nearshore cell circulation and numerical modelling are combined to investigate the dynamics of waves and wave-induced currents. This study provides the first quantitative description of horizontal circulations on the Aquitanian coast beaches during real conditions.

3. Methods

3.1. PNEC 2001 field measurements

A field experiment was conducted at Truc Vert beach on the French Aquitanian coast from the 14th to the 19th of October 2001. The large tidal range allowed instruments to be deployed and recovered safely at low tide while measurements were obtained from mid-tide to high-tide on different swell and tide conditions (Sénéchal et al., 2004). Aerial photographs, satellite images and accurate topography surveys were used to monitor nearshore morphology. The beach profiles were measured at least daily, covering an area extending from the dune to about 200 m offshore, on a longshore distance of about 1 km. The average alongshore spacing between each beach profile was approximately 25 m. A Triaxys directional wave rider moored approximately 15 km off the Cap Ferret on the continental shelf provided incident swell conditions each hour (*http://www.epoc.u-bordeaux.fr/fr/Methys/zone_mouillage.html*).

From the 6th to the 9th of October, Truc Vert Beach was exposed to an intense storm. A very energetic quasi-normally incident swell lasted for four days with offshore significant wave heights ranging from 2 to 5 m (Fig. 4). It resulted in a strong

seaward sediment transport and the formation of random direction runnels. The storm was followed by 4 days of relative weak wave conditions resulting in the formation of a berm in the upper part of the beach. The beach area chosen for measurements was strongly alongshore non-uniform and exhibited a ridge and runnel system oriented W–SW in the intertidal domain (Fig. 5). The ridge and runnel system was connected to a small inner crescentic bar system, which can also be defined as a rip head bar following Wright and Short (1984). The nearshore area exhibited an approximately 600 m wavelength crescentic bar system (Desmazes and Michel, 2002). A cusp shape berm was observed in the upper part of the intertidal domain. By the end of the experiment, the beach morphology had changed significantly with the welding of the ridge to the beach face and smoothing of the upper part of the intertidal domain. Quantitatively, between the 16th and the 18th of October, erosion of the berm reached 1.3 m, and the ridge onshore migration was approximately 25 m.

In terms of hydrodynamics, we positioned two cross-shore transects along which four pressure sensors were deployed to provide the alongshore variability of the cross-shore distribution of wave heights. Three bottom-mounted directional wave current meters were deployed: two S4 InterOcean instruments (S1 and S2 on Fig. 5) positioned at the end of each transect and one Acoustic Doppler Velocimeter (ADV Vector) in between. Instruments were deployed like this in order to study the horizontal circulations over the ridge and runnel systems and to give the alongshore variability of waves and currents. Data were sampled at 8 Hz for the pressure sensors, 2 Hz for the S4 current meters, and 8 Hz for the ADV (Sénéchal et al., 2004). Due to the large tidal range at Truc Vert Beach, the intertidal domain is about 200 m and instruments then can be located alternatively during a tide cycle in the swash, the surf and the shoaling zone.

During the experiment, wave conditions were energetic. Significant wave height (H_s) ranged from 1 to 3.1 m (Fig. 4), significant wave period (T_s) ranged from 7 to 14 s, with peak swell period reaching 20 s on the 16th. The surf zone was generally wide, reaching a maximum width of 500 m on the 18th. Strong rip currents were observed during medium wave energy conditions at mid-tide at the runnel outlet, and inshore of

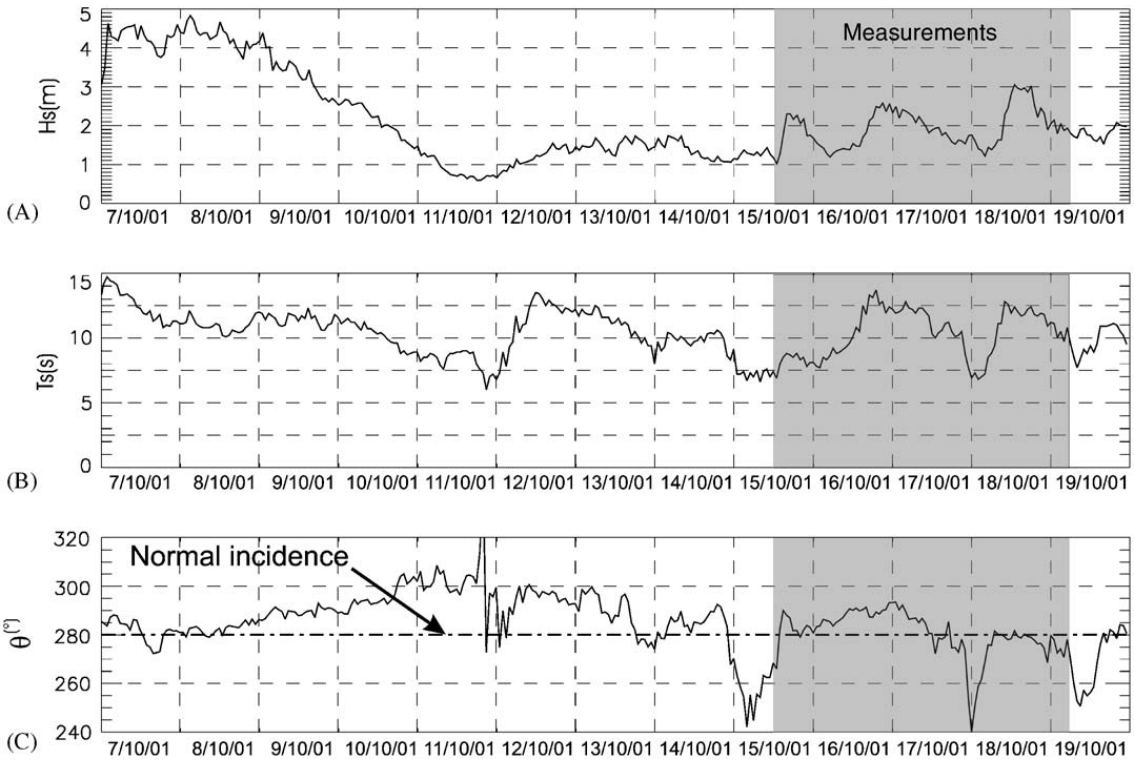

Fig. 4. Offshore wave conditions from eight days before field experiment to the end, the grey area corresponds to the measurement period; (A) Significant wave height H_s; (B) significant wave period T_s; (C) mean wave incidence θ. Data from the Triaxys buoy moored approximately 15 km off the coast.

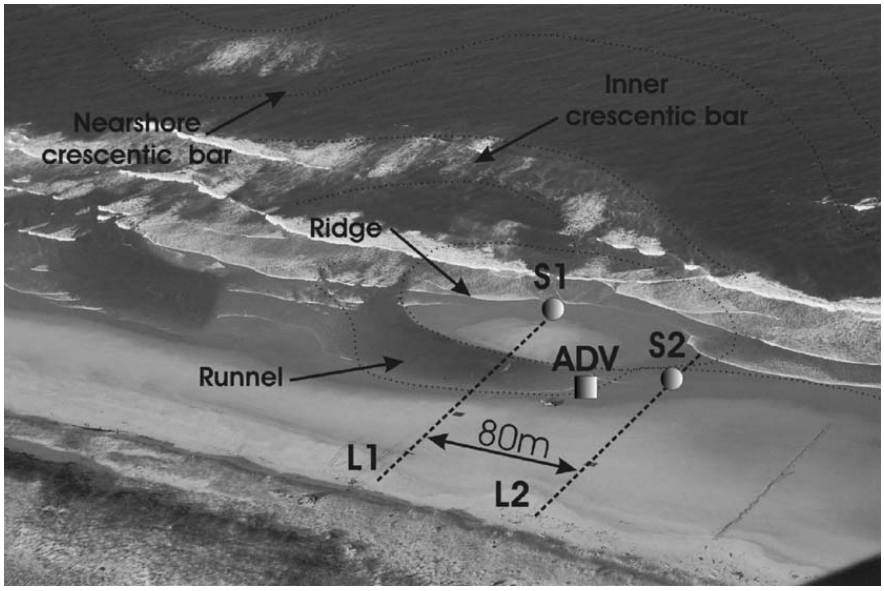

Fig. 5. Section of beach chosen for the field experiment indicating both instrument location and sand bar systems. All instruments are emerged during low tide and immersed during high tide. Two Directional Wave Current Meters S1 and S2, one Acoustic Doppler Velocimeter ADV and two lines of pressure sensors L1 and L2 are shown.

nearshore crescent horns at low tide. The current meters were not positioned near the rip neck in case the instruments were lost.

3.2. Numerical model

In this section the equations and underlying assumptions used to model the random wave transformation, the set-up/set-down and the two-dimensional wave-induced current velocities will be briefly presented.

3.2.1. Time- and depth-averaged wave-induced current model

The MORPHODYN model is based on the time average of the depth-integrated mass and momentum conservation equations. The average duration of about 10 min is chosen to be much longer than those for wave groups, but significantly shorter than time scales associated with changes in incident wave conditions. Hydrodynamics are solved using an implicit method to obtain quasi-steady mean water depth $\bar{h}$ and water volume fluxes $\bar{Q}_i$:

$$\bar{Q}_i(x,y,t) = \overline{\int_{Z_f}^{\eta} v_i(x,y,z,t)\,\mathrm{d}z}, \tag{1}$$

where $\bar{\cdot}$ is the time average, x the longshore axis, y the cross-shore axis, z the vertical axis, v_i the water particle velocity, Z_f the bed elevation and η the free surface elevation. The governing equations are (Phillips, 1977)

$$\frac{\partial \bar{Q}_i}{\partial t} + \frac{\partial}{\partial x_j}\left(\frac{\bar{Q}_i \bar{Q}_j}{\bar{h}}\right) = -g\bar{h}\frac{\partial \bar{\eta}}{\partial x_i} - \frac{1}{\rho}\frac{\partial S_{ij}}{\partial x_j} - \frac{1}{\rho}\frac{\partial R_{ij}}{\partial x_j} + \frac{1}{\rho}\frac{\partial T_{ij}}{\partial x_j} - \frac{\tau_i^b}{\rho}, \tag{2}$$

$$\frac{\partial \bar{\eta}}{\partial t} + \frac{\partial \bar{Q}_j}{\partial x_j} = 0. \tag{3}$$

In the conservation equations of momentum (2) and mass (3) g is the gravitational acceleration, ρ the mass density of water, S_{ij} the radiation stress components, R_{ij} the excess of momentum flux due to the wave roller, τ_i^b the time-averaged bed stress and T_{ij} the mixing term.

Wave velocity is separated into two components: a fluctuating velocity $\hat{v}_i$ (i.e. wave and turbulence) and a mean current velocity $U_{ci} = U_{ci}(x,y,t)$:

$$v_i(x,y,z,t) = U_{ci}(x,y,t) + \hat{v}_i(x,y,z,t). \tag{4}$$

According to Phillips (1977) the mean velocity U_{ci} is defined as

$$U_{ci} = \bar{v}_i. \tag{5}$$

Eqs. (4) and (5) lead to $\bar{\hat{v}}_i = 0$, $\bar{Q}_i$ can be written as

$$\bar{Q}_i = \overline{\int_{Z_f}^{\eta} U_{ci}\,\mathrm{d}z} + \overline{\int_{Z_f}^{\eta} \hat{v}_i(x,y,z,t)\,\mathrm{d}z} = \bar{h}U_{ci} + \hat{Q}_i, \tag{6}$$

where $\hat{Q}_i$ is the mean volume flux associated with the fluctuating motion. Due to the distinct physical nature of wave and turbulence, the fluctuating velocity $\hat{v}_i$ can be separated into two components:

$$\hat{v}_i(x,y,z,t) = v_i'(x,y,z,t) + v_i''(x,y,z,t), \tag{7}$$

where v_i' is the wave fluctuating velocity and v_i'' the turbulence fluctuating velocity. Then $\hat{Q}_i$ can be decomposed into

$$\hat{Q}_i = \overline{\int_{Z_f}^{\eta} v_i'(x,y,z,t)\,\mathrm{d}z} + \overline{\int_{Z_f}^{\eta} v_i''(x,y,z,t)\,\mathrm{d}z} = \hat{Q}_{wi} + \hat{Q}_{ri}, \tag{8}$$

where $\hat{Q}_w$ is the mean volume flux associated with the wave motion and $\hat{Q}_r$ is the mean volume flux associated with turbulence. The mean current velocity U_{ci} then becomes

$$U_{ci} = \frac{\bar{Q}_i - \hat{Q}_{wi} - \hat{Q}_{ri}}{\bar{h}}. \tag{9}$$

3.2.2. The spectral wave model

For a two-dimensional arbitrary beach topography, the computation of the forcing terms requires the wave field to be specified everywhere. To satisfy this condition, we use the wave program SWAN (Booij et al., 1999) which solves the spectral action balance equation. This wave driver is supposed to simulate accurately the wave field over Aquitanian beaches where reflection and diffraction are not significant (Ris et al., 1998). Triad interaction is taken into account in the computations, but wave–current and quadruplet interactions are not included in the wave modelling.

The breaking wave model chosen herein is the bore-based model of Battjes and Janssen (1978) with a constant breaker parameter $\gamma = 0.73$ following Battjes and Stive (1985). We apply the bottom friction formulation given by Madsen et al. (1988), which defines the bottom friction coefficient C_{Madsen} as

$$C_{Madsen} = f_w \frac{g}{\sqrt{2}} U_{rms}, \tag{10}$$

where U_{rms} is the root-mean-square value of the orbital motion near the bottom, and f_w is a non-dimensional friction factor estimated by using the formulation of Jonsson (1966):

$$\frac{1}{4\sqrt{f_w}} + log_{10}\left[\frac{1}{4\sqrt{f_w}}\right] = m_f + log_{10}\left[\frac{a_b}{K_N}\right], \tag{11}$$

where $m_f = -0.08$, a_b is a representative near-bottom excursion amplitude, and K_N the bottom roughness length scale.

The driving terms of the hydrodynamic model are computed from the SWAN outputs: H_{rms}, the mean wave direction θ, and the mean wave period T. The roller area in the surf zone is estimated following Kuriyama and Nakatsukasa (2000). According to Dally (2001), the roller terms are written as

$$\hat{Q}_{ri} = \frac{1}{\rho}\left(\frac{\rho_r A}{T}\right)\frac{k_i}{k}, \tag{12}$$

$$R_{xx} = c\left(\frac{\rho_r A}{T}\right)\left(\cos\,\theta^2 + \frac{1}{2}\right), \tag{13}$$

$$R_{yy} = c\left(\frac{\rho_r A}{T}\right)\left(\sin\,\theta^2 + \frac{1}{2}\right), \tag{14}$$

$$R_{xy} = c\left(\frac{\rho_r A}{T}\right)\cos\,\theta\,\sin\,\theta, \tag{15}$$

where ρ_r is the mass density of the roller, C is the phase velocity and k_i is the mean wave number. In shallow water the wave motion is characterized by weak advection of fluid particles. The linear theory gives the volume flux associated with the organized wave motion Q_{wi} and the random wave energy E:

$$\hat{Q}_{wi} = \overline{\int v_i'\,\mathrm{d}z} = \frac{1}{8}\frac{gH_{rms}^2}{c}\frac{k_i}{k} = \frac{E}{\rho c}\frac{k_i}{k}, \tag{16}$$

$$E = \frac{1}{8}\rho g H_{rms}^2. \tag{17}$$

The radiation stress components S_{ij} associated with wave motion are given by Svendsen and Petrevu (1996):

$$S_{ij} = \frac{E}{2}\left\{\frac{k_i k_j}{k^2}\frac{2C_g}{C} + \delta_{ij}\left(\frac{2C_g}{C} - 1\right)\right\} - \rho\frac{\hat{Q}_i\hat{Q}_j}{\bar{h}}, \tag{18}$$

where C_g is the group velocity.

The eddy viscosity v_t associated with mixing T_{ij} is determined using combination of a constant eddy viscosity v_0 and the formulation of Battjes (1975), which assumes that mixing in the surf zone is primarily due to the turbulence generated by breaking waves.

$$v_t = Mh\left(\frac{D}{\rho}\right)^{1/3} + v_0, \tag{19}$$

where D is the rate of energy loss due to depth-induced breaking for the organized wave motion and M is a dimensionless coefficient.

The final part of the closure problem is the determination of the bed shear stress τ_i^b, which is a crucial element in the prediction of horizontal circulations. According to the weak flow approximation (Liu and Dalrymple, 1978), the bottom shear stress due to wave and currents is

$$\tau_i^b = \rho C_f U_w U_{ci}, \tag{20}$$

where U_w is the bottom oscillatory velocity and C_f the spatially constant bottom friction coefficient.

This coupled numerical model computes both wave and wave-induced currents. To apply this model to field data, two-dimensional bathymetry and offshore incident wave conditions are required. With these inputs, the model can predict wave characteristics and quasi-steady currents across the entire nearshore zone.

3.3. Model inputs

Each hour the offshore wave rider buoy computed the directional wave spectrum, which was used as an offshore boundary condition for the SWAN model. First, the wave field was computed from the wave buoy to 9 m under the Lowest Astronomical Tide (LAT) level. Waves and currents were computed on a refined grid from the 9 m depth isobath to the shoreline on the beach area chosen for the field experiment. The buoy location and the two computational grids used for simulations are shown in Fig. 6. The bathymetry of the continental shelf was provided by the SHOM (Service Hydrographique et Océanographique de la Marine). The size of the regular computational grid is $40 * 80$, with 400 m mesh steps. The numerical bathymetry of the beach area was derived from the topographic survey of the intertidal domain undertaken on the 16th, and from the 16th satellite SPOT image for the subtidal zone. It is extended to a periodic bathymetry (wavelength equal to a crescent length: 600 m), enabling computation of the mean current field. The computational grid consists of 10 m meshes with periodic lateral boundary conditions in the longshore direction.

During the experiment, static water pressures were converted to water surface elevation, and for each sensor the root-mean-square wave height H_{rms} was estimated from a zero down-crossing analysis, defined as $H_{rms} = (\sum_{i=1}^{n} H_i^2)^{1/2}/n$. Measurements were not taken when the mean water depth ($\bar{h}$) is less than 70 cm, i.e. when they are positioned around the wave trough and occasionally emerge. Root-mean-square wave heights and current velocities were computed each hour over 30-min intervals during the experiment concurrent with the Triaxys buoy data input. During the 18th of October, energetic wave conditions were responsible for a strong morphological evolution of the beach area. Consequently, the last 30 h of measurements is not taken into account because the

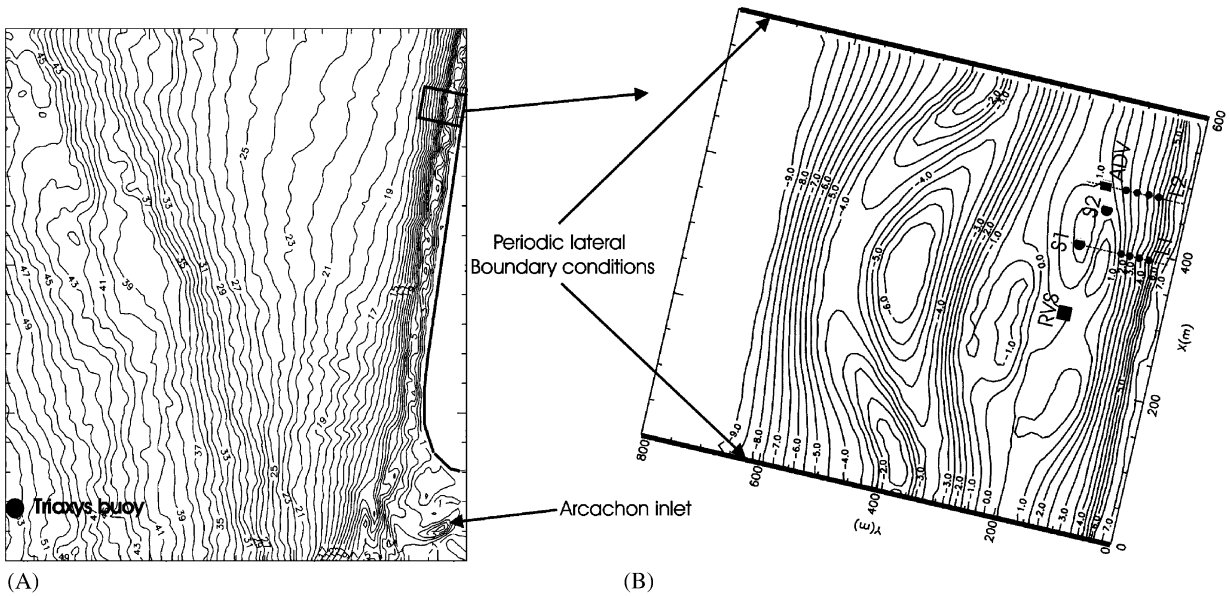

Fig. 6. Coupling of the two numerical bathymetries used for the computation. Bathymetry of the Aquitanian shelf off the field experiment area (copyright SHOM) with the Triaxys buoy location (A), and periodic lateral boundary condition bathymetry of the measurement site, with instrument locations (B).

numerical bathymetry was not accurate enough. Wave heights were computed on the beach area, and the bottom roughness length scale K_N (Eq. (11)) on the continental shelf was calibrated using the most seaward sensor data (S1). Then hydrodynamic free parameters of MORPHODYN C_f, v_0 and M, are tuned to give the best agreement of the simulations with field data in the nearshore zone.

4. Results

4.1. Data

During the experiment, measured mean currents ranged from 0.05 to 1.2 m/s, with instantaneous velocities often reaching 3 m/s (Castelle and Bonneton, 2002). The experiment was characterized by two distinct swell classes. The first (during the three first days of the experiment) is characterized by incident swell at about 10° to the beach, and generating a southward longshore current with a peak of approximately 1 m/s. The second (on the 18th) is characterized by an energetic swell with a shore-normal incidence generating circulation cells and rip currents.

Fig. 7 shows the 150 min time series at station S1, located in the breaker zone, of the low pass filtered signals (frequency cut-off: 0.01 Hz) of water depth h, cross-shore and longshore velocities during the 17th of October. This period was characterized by offshore incident waves at about 8° to the beach

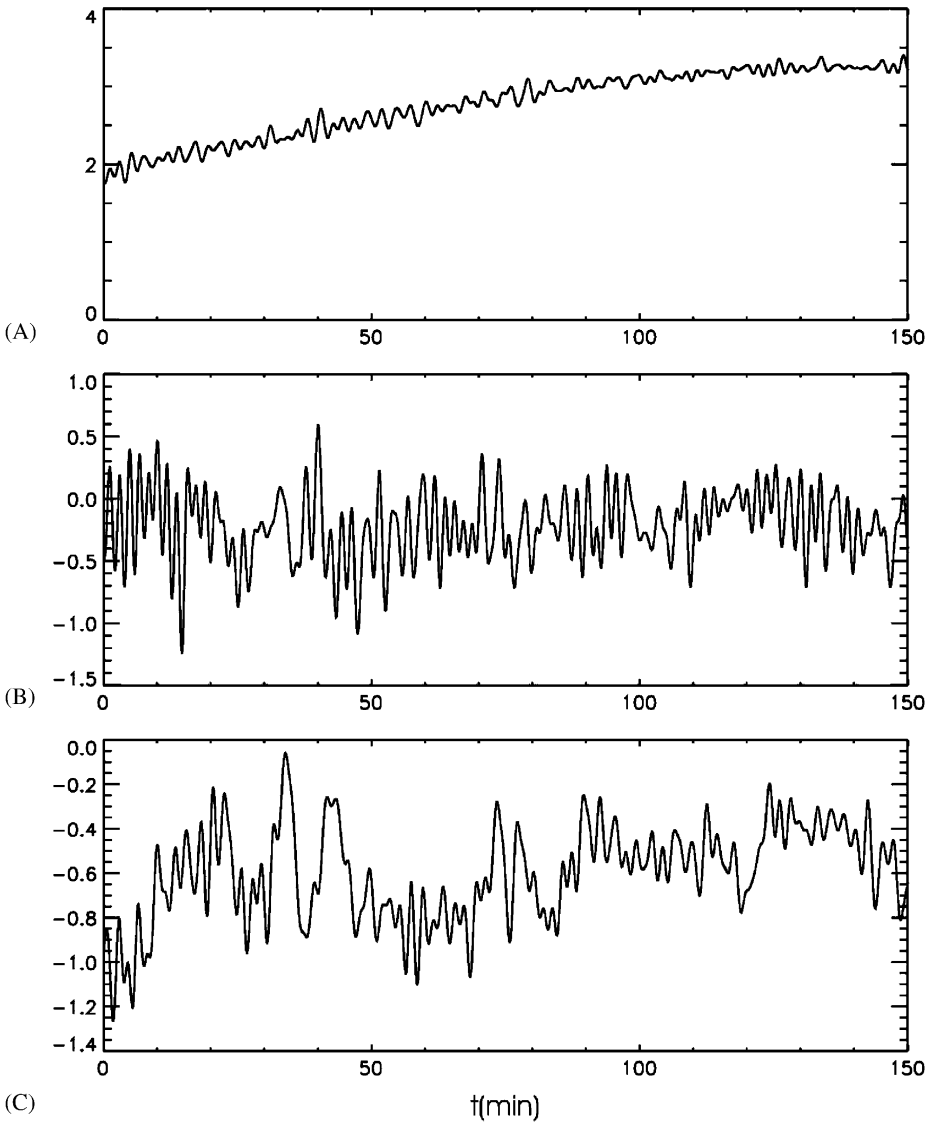

Fig. 7. Times series of 150 min on the 17th of October (t_0 = 1h00) at station S1 of low-passed filtered signals (cut-off frequency 0.01 Hz) of (A) water depth (m); (B) cross-shore velocities (m/s); (C) longshore velocities (m/s).

with root-mean-square wave height H_{rms} of about 2 m resulting in the generation of a southward longshore current on the order of 0.5–1 m/s. Unsteady longshore flows are observed (Fig. 7), with two strong low frequency modulations: infragravity wave motions (0.004–0.01 Hz) (Bonneton et al., in press), and very low frequency motions (frequencies less than 0.004 Hz). Quasi-steady and unsteady cross-shore flows are weaker, which means longshore current was predominant during this period. Fig. 8 shows the energy spectra associated of the surface elevation h, cross-shore and longshore velocities during the same period. This figure shows the peak wave energy frequency was about 0.06 Hz (peak wave period of approximately 17 s), while a large amount of longshore velocity energy was located in the infragravity and far infragravity bands (<0.01 Hz).

Very low frequency motions are obvious during the 18th. Fig. 9 shows the 150 min time series at station S2, located in the breaker zone, of the low pass filtered signals (frequency cut-off: 0.01 Hz) of water depth h, cross-shore and longshore velocities during the 18th of October. Measured longshore velocities inside the surf zone fluctuate aperiodically with temporal scales of approximately 30 min. This kind of very low frequency motions has been associated with rip current instabilities (Haller and Dalrymple, 2001), but recent studies show that very low frequency surf zone eddies forced by waves are responsible for these low frequency motions (MacMahan et al., 2004). These data confirm that

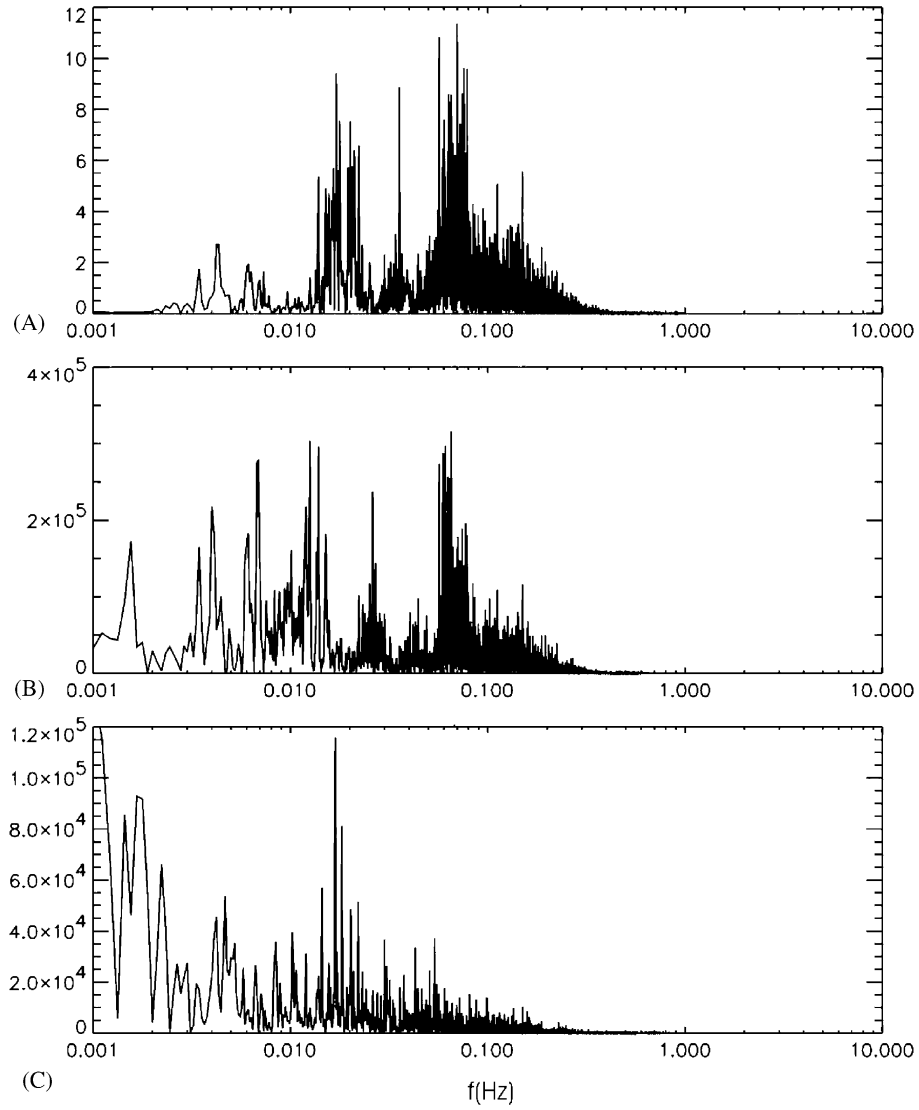

Fig. 8. Energy spectra at station S1 for the time series presented in Fig. 7. (A) Water depth (m^2/Hz); (B) cross-shore velocities (m/s^2/Hz); (C) longshore velocities (m/s^2/Hz).

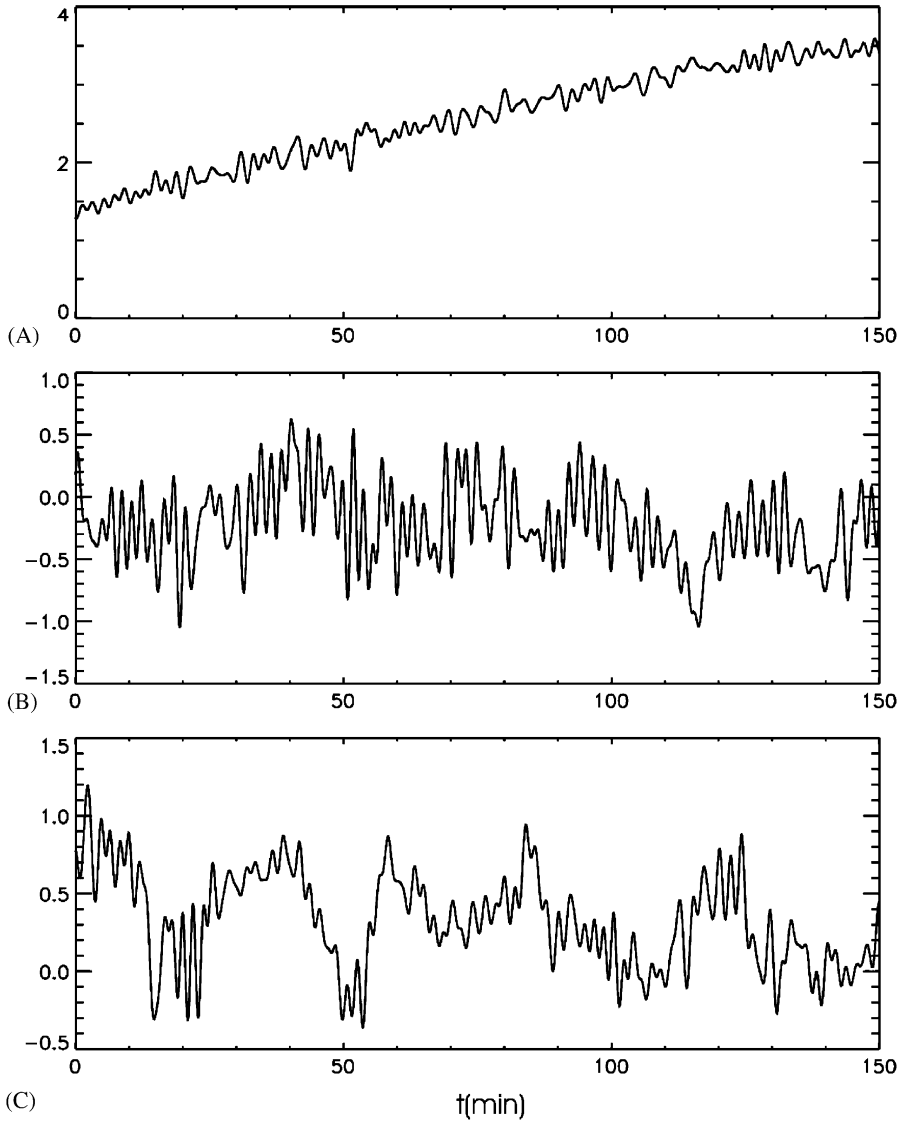

Fig. 9. Times series of 150 min on the 18th of October ($t_0 = 15$h00) at station S2 of low-passed filtered signals (cut-off frequency 0.01 Hz) of (A) water depth (m); (B) cross-shore velocities (m/s); (C) longshore velocities (m/s).

the amount of very low frequency motion energy increases with swell energy.

These data show the strong control of offshore wave conditions on wave-induced current velocities. A significant amount of velocity energy is in the very low frequency band.

4.2. Comparison of field data and model output

4.2.1. Waves

The input directional wave spectrum, given by the Triaxys buoy, is specified as the offshore boundary condition of our model. The comparison between computed H_{rms} and measured H_{rms} showed scattered results (Fig. 10A). Analysis of meteorological data clearly indicates that the results were most scattered when the wind was the strongest. Therefore for the calibration of K_N, only the measurements performed during periods of weak wind and wind sea were taken into account. Particularly, during the 16th of October a long and energetic long swell occurred with non-existent wind, which permitted us to accurately calibrate bottom friction. Then computed and measured wave heights were compared at the S1 location. Best agreement with field data is obtained using $K_N = 0.085$ for the Madsen model of bottom friction, while the default value in SWAN was $K_N = 0.05$. Fig. 10 shows the comparison of the root-mean-square wave height H_{rms} measured and computed for $K_N = 0.085$, for the entire experiment and during weak wind conditions. For the whole experiment, the model is

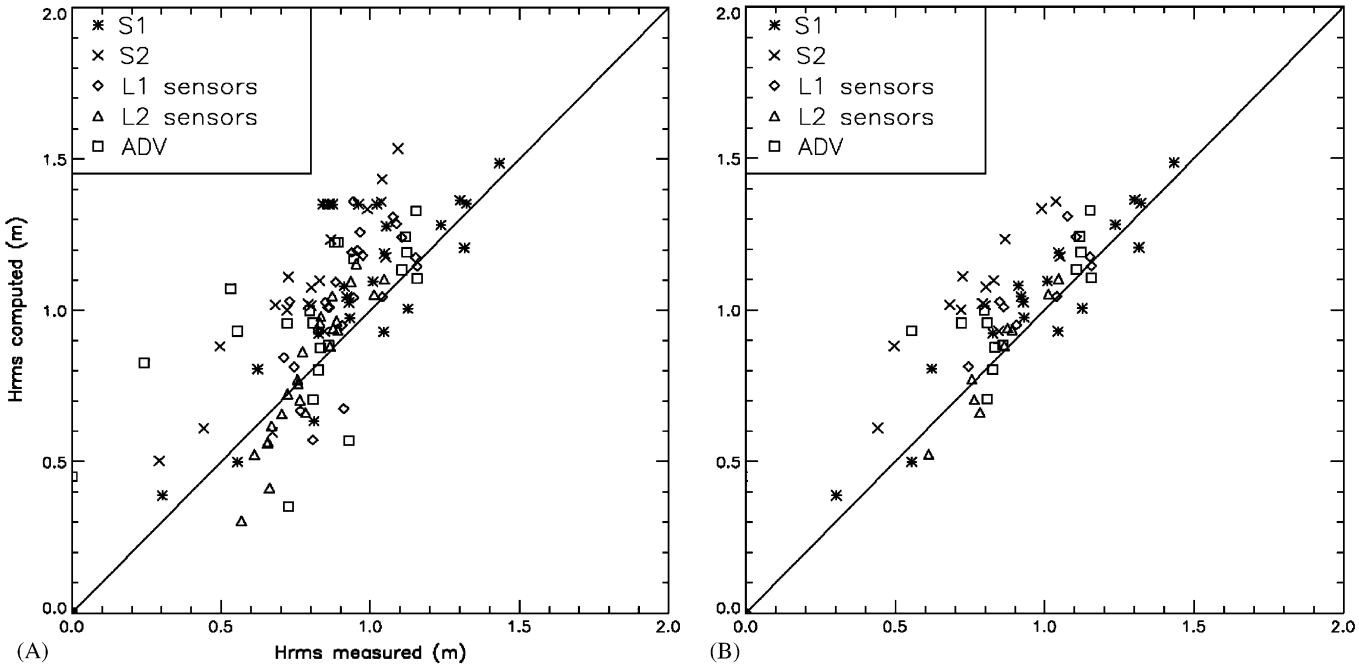

Fig. 10. Comparison between root-mean-square wave height H_{rms} measured and computed at all the sensor locations, for the whole experiment (A), and during weak wind conditions (B).

in agreement with field data for S1 while the model is less accurate at the other pressure sensor locations deployed on the upper part of the beach. Results are scattered and the model often overestimates wave heights. When only measurements during weak wind conditions are used, the model fits very well with field data for S1, and with good agreement for the other sensors inside and outside the surf zone.

4.2.2. *Wave-induced currents*

The driving terms of the hydrodynamic module were computed from SWAN outputs. To test the ability of the model to accurately simulate wave-induced currents in the nearshore zone, the value of the depth-averaged longshore current U_{cx} is compared with the measured longshore currents. We assume that the longshore current velocity measured by current meter (located about 30 cm up to the bottom) is representative of the depth-averaged current velocity. This assumption cannot be applied to the cross-shore current, because its vertical variations are much more important than for the longshore current. The spatially constant bottom friction coefficient C_f which controls the strength of the wave-induced currents is tuned, and mixing terms v_0 and M, which control the shape of horizontal circulations and cross-shore thickness of longshore current. Best agreement with field data during weak wind conditions is found for $C_f = 0.0048$, $v_0 = 10$ and $M = 5$. The value of lateral mixing is an order of magnitude larger than for Ozkan-Haller and Kirby (1999) because a large part of low frequency motions are filtered herein. The value of the bottom friction coefficient C_f is almost within the range of value given by Whitford and Thornton (1996). Fig. 11 shows the comparison between the mean longshore current U_{cx} measured and computed for the whole experiment and for only weak wind conditions. We can observe from Fig. 11 that the results are scattered for the whole experiments. However, the model fits very well with field data during weak wind conditions, considering the mathematical approximations of the model and the fact that the wave field was computed 15 km off Truc Vert beach.

Fig. 12 shows simulated two-dimensional current patterns and the comparison of H_{rms} and U_{cx} with field data on the crossshore transects L1 and L2 on the 16th of October averaged between 16h30 and 17h00. During this day, the wind and the wind sea were non-existent, and an energetic, long and narrow banded swell occurred (peak swell period between 16 and 20 s). All day long, the model fits very well with measurements for the wave height and the longshore current. A relevant feature of

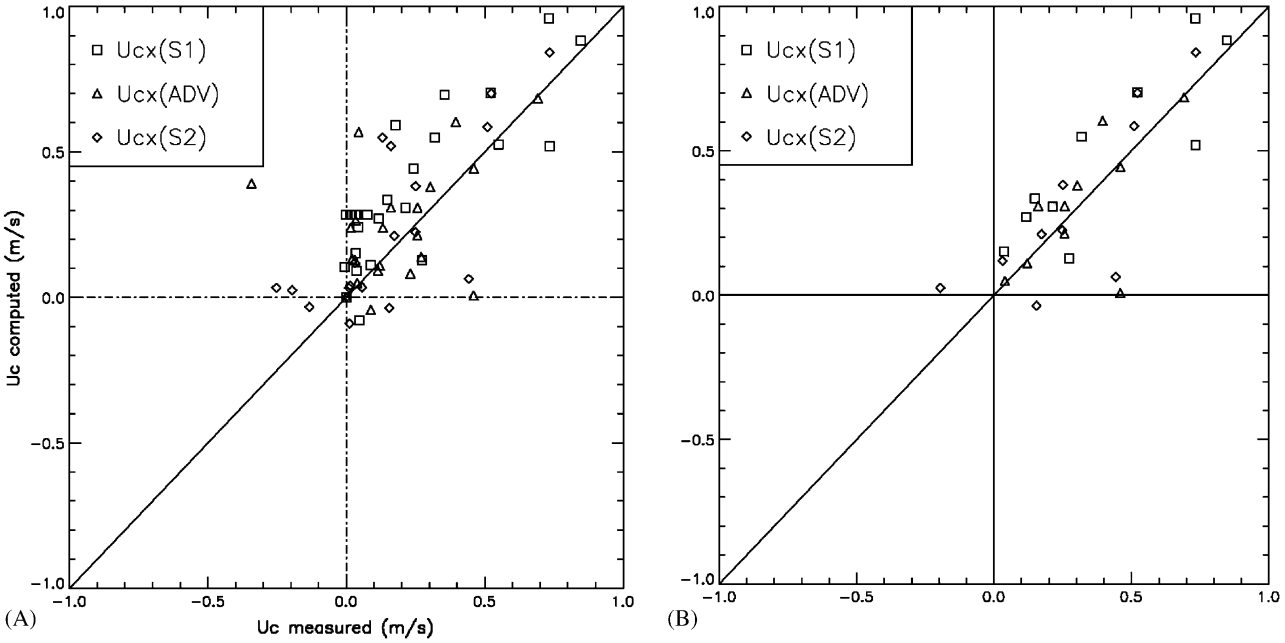

Fig. 11. Comparison between the longshore current (U_{cx}) measured and computed, for the whole experiment (A), and during weak wind conditions (B). Model free parameters: $C_f = 0.0015$, $v_0 = 10$ and $M = 5$.

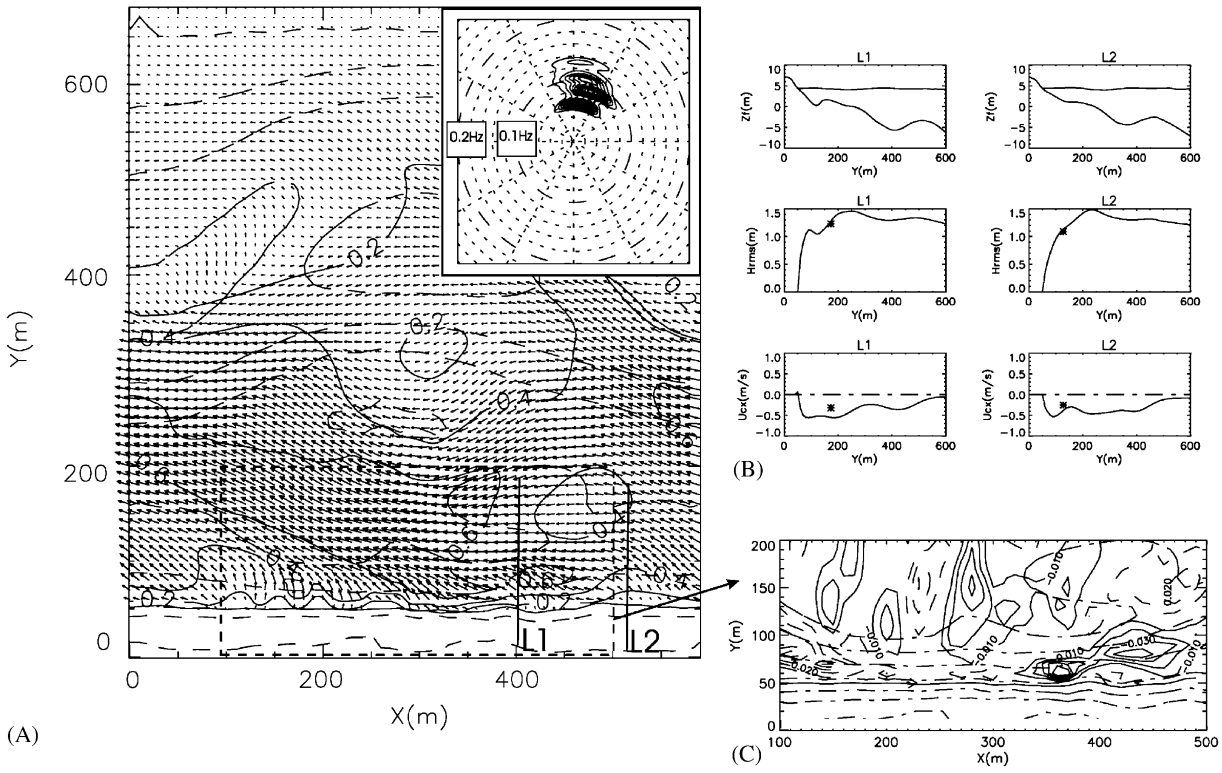

Fig. 12. (A) Simulation of mean wave-induced current $\vec{U}_c$ over the PNEC 2001 bathymetry the 16th of October 2001 (time-averaged between 16h30 and 17h00) with the directional wave spectrum given by the Triaxys wave rider. The solid lines represent the iso-values of mean current velocities $\bar{U}_c$ in m/s and the dashed lines correspond to the bathymetry (2 m contour, concurrent with the thick line of Fig. 6). (B) Comparison of the model results with field data at the cross-shore transects $L1$ and $L2$ for the mean longshore current $\bar{U}_{cx}$ and root-mean-square wave height H_{rms}. (C) Zoom of the longshore pressure gradient field $-\rho g\bar{h}(\partial\bar{\eta}/\partial x)$ inshore the ridge and runnel system.

simulations is the location of the maximum longshore current in the bar trough (Fig. 12B). This is due to longshore pressure gradients induced by the fully three-dimensional behaviour of the beach area (Fig. 12C). These longshore pressure gradients inshore of the ridge and runnel system induce an intensification of the longshore current in the runnel.

It was found that results are correct for strong longshore current velocities, but are less accurate for low longshore current with velocity smaller than 0.4 m/s. It is possible that our computational grid is not accurate enough to reproduce under-scaled phenomena, which can be predominant under low energy conditions.

4.3. Horizontal circulation patterns over the ridge and runnel system

4.3.1. Background

Both the ridge and runnel system and the nearshore crescentic bar are responsible for complex horizontal circulations depending on the tide level and the offshore wave conditions. Castelle and Bonneton (in press) investigated the circulations induced by the nearshore crescentic bar system. They showed that circulation cells and strong rip currents occurred in intertidal and subtidal zones, with strong tidal modulation of surf zone processes. The sensitivity of the horizontal circulation, and especially the rip current behaviour at the runnel outlet, to the tide level and the offshore wave conditions will be investigated.

Rip currents are common on beaches exhibiting three-dimensional topography and exposed to normal or near-normal incident swells (Aagaard et al., 1997; Brander, 2000). Rip cell circulations are controlled by topographic feed-back and are supposed to be responsible for strong water and sediment exchanges between the surf zone and the nearshore zone (Short, 1985), resulting in a strong influence on the beach morphology. On the Aquitanian coast, these rip currents occur at each runnel outlet and their intensity depends on the length, the shape of the system, the offshore wave conditions and the tide level. No current meter was placed in the rip neck during the field measurement, and no previous data are available in rip currents in these environments. However, tidal modulation is known by locals to occur with maximum rip velocities occurring more or less at mid-tide. The mechanism leading to the formation of a rip current can be summarized studying the ridge and runnel system during the PNEC 2001 field measurements. Let us assume that incoming wave field is longshore uniform. Waves approaching the bar will break before waves approaching the runnel, the induced set-up in the runnel will then begin further inshore, inducing longshore pressure gradients inshore the ridge and runnel system. These longshore pressure gradients drive the feeder currents which lead to a rip current system associated with horizontal circulation cells. These longshore pressure gradients have been successfully measured in laboratory (Haller and Dalrymple, 1999), and more recently in the field (Haas et al., 2002).

4.3.2. Simulation of a rip current

Fig. 13 shows the two-dimensional current patterns simulated during a normally incident swell on the 18th of October 2001. A strong narrow, seaward oriented current (maximum mean flow on the order of 1 m/s) is located at the runnel outlet, associated with a large circulation cell. The onshore flow of this circulation is located on the bar and is broader and weaker, on the order of 0.5 m/s. The computed longshore pressure gradient field $-\rho g\bar{h}(\partial\bar{\eta}/\partial x)$ over the ridge and runnel system during the same period is given in Fig. 13B. On the upper part of the beach (less than 1 m water depth), the longshore pressure gradients force the feeder currents. Water convergence inshore the runnel outlet results in the formation of a seaward oriented current which balances the water mass conservation equation inshore the runnel outlet. The computed rip current system is in agreement with the Lagrangian rip flow measurements of Brander (1999): flow velocities at the base of the feeders are relatively weak and quickly increase in the body of the rip up to 0.9 m/s before decreasing in the rip head.

4.3.3. Model to data comparison

For normal to near-normal incoming swells, rip currents are always associated with circulation cells. The wave-induced currents on the bar are also tidally modulated because they are associated with the broad flow of the circulation cell. Fig. 14 shows the variations of the mean current U_{cx} during two tidal cycles from mid-tide to high-tide on the 16th of October, for a wave incidence of about 6°. This figure shows the tidal modulation of mean longshore flow measured at S1 and S2, with stronger currents at mid-tide. The tidal modulation on the

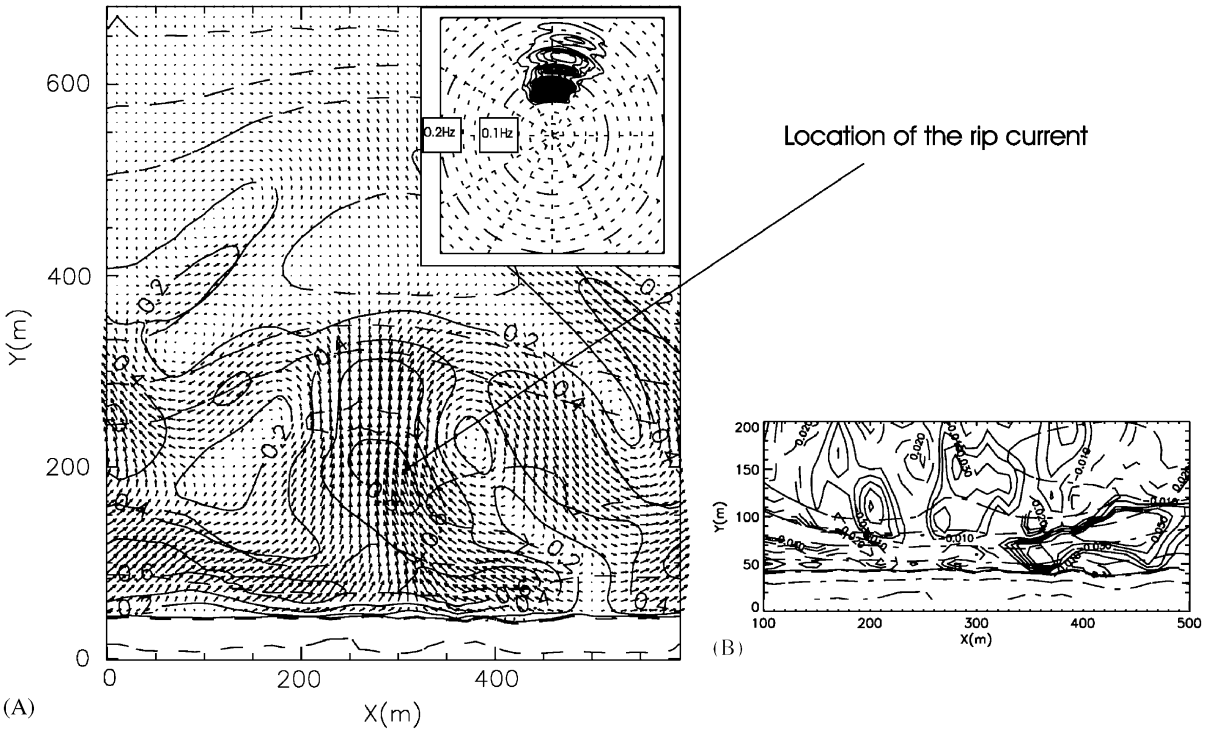

Fig. 13. Simulation of mean wave-induced current $\vec{U}_c$ over the PNEC 2001 bathymetry during a frontal swell $H_s = 3$ m at mid-high tide, the 18th of October 2001, 15 h (with the directional wave spectrum given by the Triaxys wave rider). The solid lines represent the iso-values of mean current velocities $\bar{U}_c$ in m/s and the dashed lines correspond to the bathymetry (2 m contour, concurrent with the thick line of Fig. 6). Visualization of a strong and narrow seaward oriented rip current which maximum flow velocity is located at the runnel outlet. (B) Zoom of the longshore pressure gradient field $-\rho g\bar{h}(\partial\bar{\eta}/\partial x)$ inshore the ridge and runnel system.

bar (station S1) is stronger than the modulation measured on the side of the bar (station S2). The model reproduces this tidal modulation very well (Fig. 14), except for the peak velocity at 17h30, with a good sensitivity to the increasing offshore wave conditions.

4.3.4. Model analysis

Simulations with stationary offshore wave conditions during one tidal cycle are required for a better understanding of this rip current. A virtual sensor station VS was defined at the runnel outlet where strong rip current velocities are supposed to occur. Incident wave angle is the main offshore wave characteristic controlling rip current shape. On October 16 at 15 h (Fig. 12) the 8° incoming swell is responsible for a strong longshore current from the shoreline to about 400 m offshore and no circulation cell or rip current is observed. For normal incidence swell the rip is oriented seaward, very intense and confined. Normally incident swells are used for the rip current simulations.

Wave period controls strength and shape of the rip currents. Indeed, longer swells lead to stronger and narrower rip currents (Fig. 15). Longer swells induce stronger spatial radiation stress gradients which force more intense circulation cells. For $T_p = 12$ s, rip velocity at station VS is almost double than for $T_p = 6$ s. For $T_p > 14$ s the rip velocity lightly decreases with increasing wave period.

Offshore wave height is the main wave characteristic controlling the rip velocities. Fig. 16 shows the location of the virtual sensor VS and the simulations of rip current velocities U_c at the station VS during one tidal cycle for normally incident swell with significant wave heights H_s ranging from 0.5 to 2 m. Results reveal that maximum rip current velocity occurs between mid-tide and high-tide. For H_s up to 2 m the maximum of rip velocity occurs at high-tide, while it occurs at mid-tide for $H_s = 1$ m. Changes in the breaking pattern control the rip current characteristics. From mid-low tide to high-tide, waves are breaking on the ridge and runnel system, which leads to a longshore pressure gradient inshore then inducing the rip current. During a tidal cycle, the temporal occurrence of maximum rip current velocity depends on both the longshore pressure

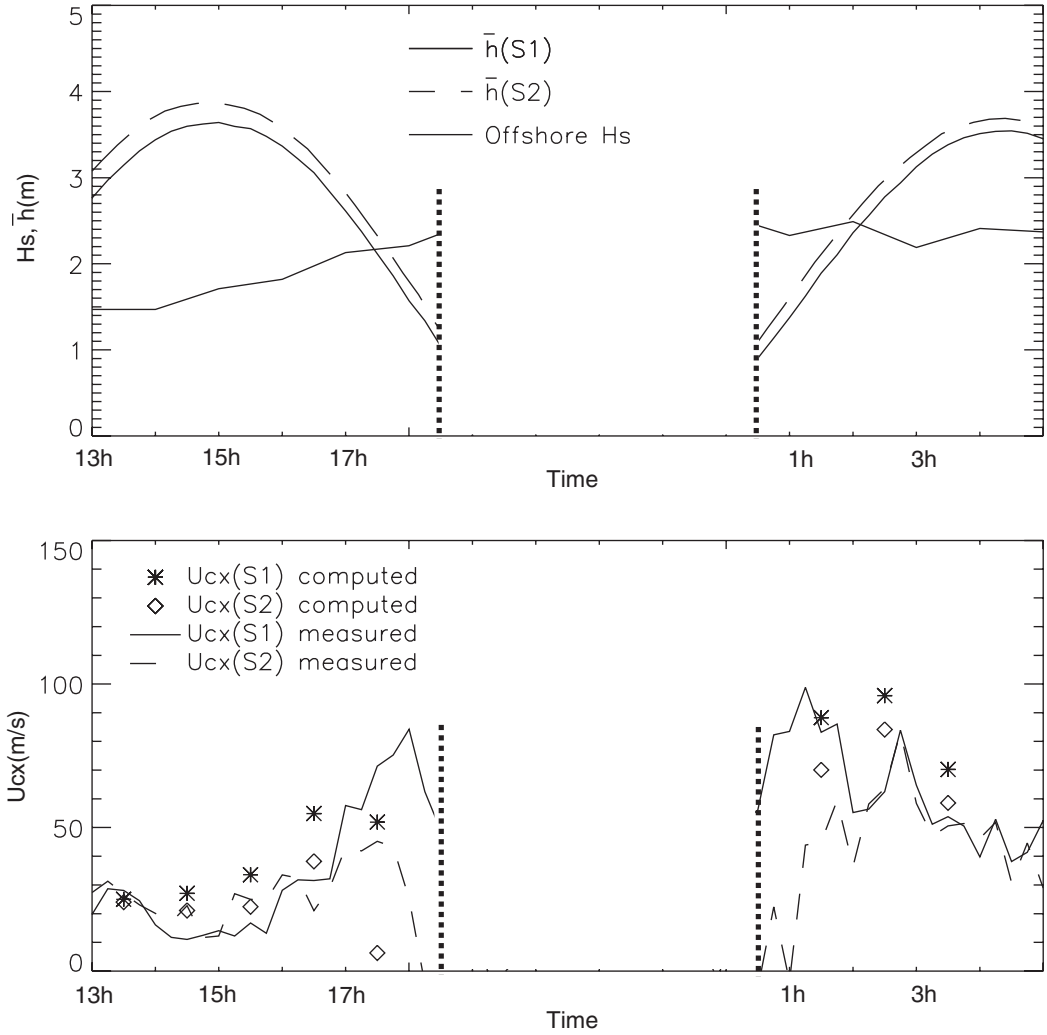

Fig. 14. Comparison between the longshore current $\bar{U}_{cx}$ measured and computed during two tide cycles, with offshore significant wave height H_s and mean water level $\bar{h}$ at stations $S1$ and $S2$. The 16th of October 2001.

gradient intensity inshore the ridge and runnel system and the cross-sectional area of the runnel outlet available for rip flow.

Consequently, it appears that the ridge and runnel morphology is a key parameter for rip current characteristics and especially the temporal occurrence of maximum flow velocities. Comparison with other rip studies reveals the Aquitanian coast rip currents behave differently from rip systems in low-energy environments (Aagaard et al., 1997; Brander, 1999), or other case studies in high energy environments (Brander, 2000). The morphology of these environments strongly differs from the Aquitanian coast beach morphology. The main reason is that the Aquitanian ridge and runnel system is almost uncovered at low-tide, and totally uncovered at spring low-tide, and thus cannot enable longshore pressure gradients likely to drive feeders.

5. Conclusion

Field measurements of waves and longshore currents were obtained on a ridge and runnel system at Truc Vert Beach under a range of incident wave conditions. Field data were compared with a time- and depth-averaged numerical model formulated for an irregular wave field. Computed offshore root-mean-square wave heights are in good agreement with field data inside and outside the surf zone during weak wind conditions. Considering the mathematical approximations involved, the model fits well with data and quantitatively simulates the tidal modulation of flow velocities on the bar.

A first description of the dynamics of wave-induced currents on Aquitanian ridge and runnel systems has been done. Longshore pressure gradients induced are responsible for the location of maximum longshore currents in the trough and

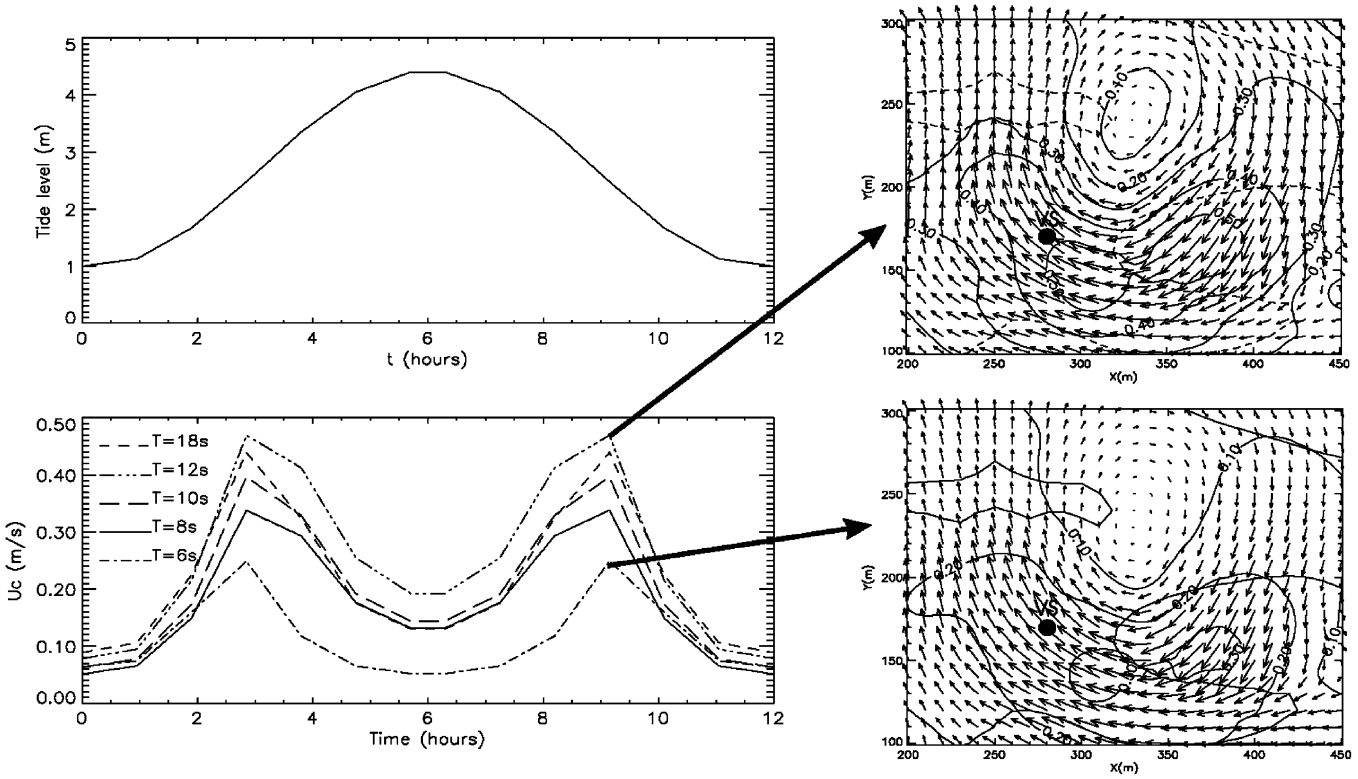

Fig. 15. (A) Tide cycle used for the simulations. (B) Simulation of rip current velocities U_c at VS during one tide cycle; boundary wave conditions: normal incoming swell, $H_s = 1$ m, different wave period T. (C) Zoom of the rip current feature for $T = 6$ s. (D) Zoom of the rip current feature for $T = 12$ s.

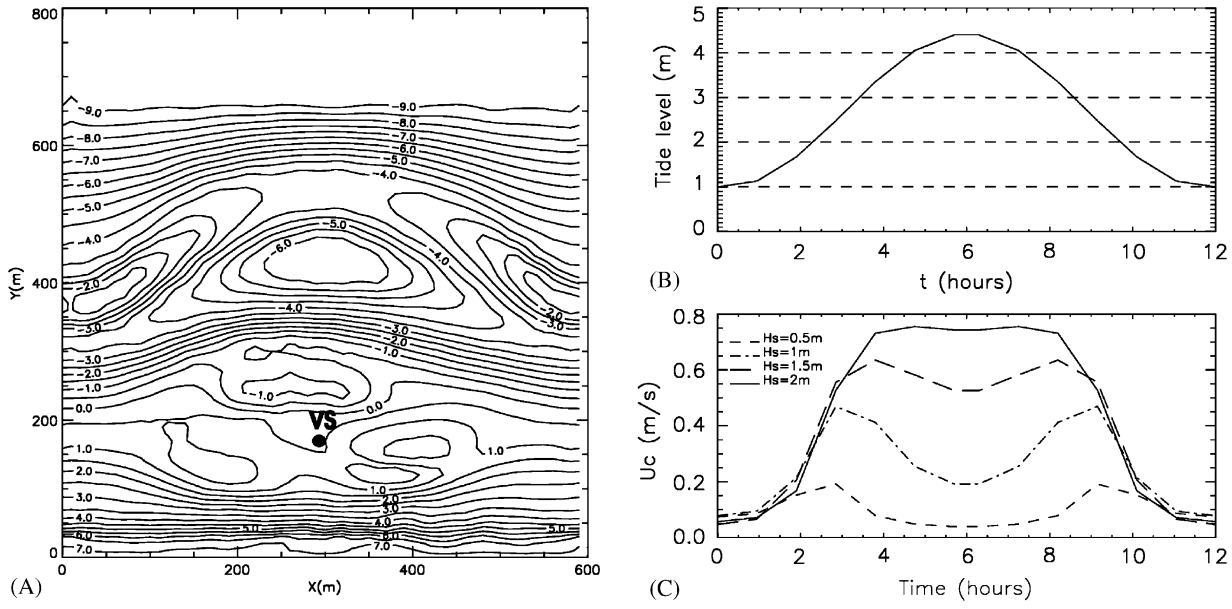

Fig. 16. (A) Location of the virtual station *VS* on the PNEC 2001 bathymetry. (B) Tidal cycle used for the simulations. (C) Simulation of rip current velocities U_c at VS during one tide cycle; offshore wave conditions: normal incoming swell, mean wave period $T = 10$ s, significant wave heights H_s ranging from 0.5 and 2 m.

drive the feeder which leads to rip currents. This paper emphasizes both the tidal modulated behaviour of the rip velocities and rip current sensitivity to offshore wave conditions. Results show that maximum rip current flows occur at mid-tide which differs from previous results observed in other beach environments. A strong coupling exists between bed morphology and hydrodynamics.

Results would be quite different for developed ridge and runnel system like those observed at the end of summer, just before the September first energetic swells.

This study constitutes the first stage of knowledge of the dynamics of waves and currents on the Aquitanian high energy beaches. It puts in evidence some mechanisms which should be investigated in more detail during further experiments. Further investigations (modelling and measurements) on different ridge and runnel morphologies are required for a full understanding. Given the strong currents observed on the Aquitanian coast beaches, wave–current interaction also has to be included in the modelling approach.

Acknowledgements

This study was performed within the framework of the Programme National d'Environnement Côtier, project ''Hydrodynamique sédimentaire en zone côtière'', sponsored by the CNRS/INSU. Bruno Castelle was financially supported by EPSHOM and DGA for his Ph.D. studies. The authors would like to thank G. Oggian, F. Desmazes, H. Howa, V. Rey, D. Rihouey, C. Brière, S. Abadie, V. Rey, R. Pedreros, P. Larroude among others for their help and support during PNEC2001 field measurements. We acknowledge the constructive criticism by R. W. Brander and an anonymous reviewer which significantly improved the contents of the paper.

References

Aagaard, T., Greenwood, B., Nielsen, J., 1997. Mean currents and sediment transport in a rip channel. Marine Geology 140, 25–45.

Battjes, J., 1975. Modelling of turbulence in the surf zone. In: Symposium on Modeling Techniques, ASCE, pp. 1050–1061.

Battjes, J., Janssen, J., 1978. Energy loss and set-up due to breaking of random waves. In: Proceedings of the 16th International Conference on Coastal Engineering, ASCE, pp. 569–587.

Battjes, J., Stive, M., 1985. Calibration and verification of a dissipation model for random breaking waves. Journal of Geophysical Research 90 (C5), 9159–9167.

Bonneton, P., Marieu, V., Dupuis, H., Sénéchal, N., Castelle, B. Wave transformation and energy dissipation model for random breaking waves. Journal of Coastal Research SI 39, in press.

Booij, N., Ris, R., Holthuijsen, L., 1999. A third-generation wave model for coastal regions, part i: model description and validation. Journal of Geophysical Research 104 (C4), 7649–7666.

Brander, R., 1999. Field observations on the morphodynamic evolution of low-energy rip current system. Marine Geology 157, 199–217.

Brander, R., 2000. Morphodynamics of a large-scale rip current system at Muriwai Beach, New Zealand. Marine Geology 165, 27–39.

Butel, R., Dupuis, H., Bonneton, P., 2002. Spatial variability of wave conditions on the French Aquitanian Coast using in-situ data. Journal of Coast Research SI 36, 96–108.

Castelle, B., Bonneton, P., 2002. Wave-induced currents over the Aquitanian Coast sand bars. In: 8th International Symposium on Oceanography of the Bay of Biscay.

Castelle, B., Bonneton, P. Nearshore waves and currents over crescentic bars. Journal of Coast Research SI 39, in press.

Castelle, B., Bonneton, P., Dupuis, H., Michel, D., Howa, H., Senechal, N. The French Aquitanian Coast: a high energy environment. Marine Geology, submitted.

Church, J., Thornton, E., 1993. Effects of breaking wave induced turbulence within a longshore current model. Coastal Engineering 20, 1–28.

Cook, D., 1970. The occurrence and geologic work of rip current off Southern California. Marine Geology 9, 173–186.

Dally, W., 2001. Modeling nearshore currents on reef-fronted beaches. In: Proceedings of Coastal Dynamics.

Davies, J., 1980. Geographical Variation in Coastal Development, second ed. Longman, London.

Desmazes, F., Michel, D., 2002. Sedimentation of a high energetic lower shoreface: example of Truc Vert Beach. In: Proceedings of the 8th International Symposium on Oceanography of the Bay of Biscay, p. 45.

Feddersen, F., Guza, R., 2003. Observation of nearshore circulation: alongshore uniformity. Journal of Geophysical Research 108 (C1), 15667–15676.

Feddersen, F., Guza, R., Elgar, S., Herbers, T., 1998. Alongshore momentum balances in the nearshore. Journal of Geophysical Research 103 (C8), 15667–15676.

Froidefond, J.-M., Gallissaires, J.-M., Prud'homme, R., 1990. Spatial variation in sinusoidal on a crescentic nearshore bar: application to the Cap Ferret Coast. Journal of Coastal Research 6, 927–942.

Haas, K., Svendsen, I., 2002. Laboratory measurements of the vertical structure of rip current. Journal of Geophysical Research 107 (C5).

Haas, K., Svendsen, I., Brander, R., Nielsen, P., 2002. Modeling of a rip current system on Moreton Island, Australia. In: Proceedings of International Conference on Coastal Engineering, ASCE.

Haller, M., Dalrymple, R., 1999. Rip currents dynamics and nearshore circulation. Center of Applied Coastal Research, University of Delaware.

Haller, M., Dalrymple, R., 2001. Rip current instabilities. Journal of Fluid Mechanics 433, 161–192.

Hamilton, D., Ebersole, B., 2001. Establishing uniform longshore currents in a large-scale sediment transport facility. Coastal Engineering 42, 199–218.

Inman, D., Tait, R., Nordstrom, C., 1971. Mixing in the surf zone. Journal of Geophysical Research 76 (C15), 3493–3514.

Jonsson, I., 1966. Wave boundary layers and friction factors. In: Proceedings of the 10th International Conference on Coastal Engineering, pp. 109–152.

Kuriyama, Y., Nakatsukasa, T., 2000. A one-dimensional model for undertow and longshore current on a barred beach. Coastal Engineering 40, 39–58.

Lafon, V., Dupuis, H., Howa, H., Froidefond, J.-M., 2002. Determining ridge and runnel longshore migration rate using spot imagery. Oceanologica Acta 25, 149–158.

Lafon, V., Dupuis, H., Butel, R., Michel, D., Howa, H., De Melo Apoluceno, D., 2005. Rhythmic sub-tidal and inter-tidal bar morphology and dynamics in a mixed-energy environment. Part II: Physical forcing analysis. Estuarine Coastal and Shelf Science 65(3), 449–462.

Liu, P., Dalrymple, R., 1978. Bottom frictional stresses and longshore currents due to waves with large angle of incidence. Journal of Marine Research 36, 357–375.

Longuet-Higgins, M., 1970. Longshore current generated by obliquely incident sea waves. Journal of Geophysical Research 75, 6778–6801.

MacMahan, J., Thornton, E., Stanton, T., Reniers, A., Dean, R., 2003. Ripex: rip-current pulsation measurements. Coastal Engineering 2002: Solving Coastal Conundrums, 736–746.

MacMahan, j., Reniers, A., Thornton, E., Stanton, T., 2004. Surf zone eddies coupled with rip current morphology. Journal of Geophysical Research C07004, doi:10.1029/2003JC002083.

Madsen, O., Poon, Y.-K., Graber, H., 1988. Spectral wave attenuation by bottom friction: theory. In: Proceedings of the 21st International Conference on Coastal Engineering, pp. 492–504.

Michel, D., Howa, H., 1994. Morphological evolution of a littoral sand bank, modelisation of its dynamics. Annals Geophysical, European Geophysical Union, Part II 12, 240.

Michel, D., Howa, H., 1999. Short-term morphodynamic response of a ridge and runnel system on a mesotidal sandy beach. Journal of Coastal Research 15, 428–437.

Ozkan-Haller, H.T., Kirby, J.T., 1999. Nonlinear evolution of shear instabilities of the longshore current: a comparison of observations and computations. Journal of Geophysical Research 104 (C11), 953–984.

Putrevu, U.J., Oltman-Shay, J., Svendsen, I.A., 1995. Effect of alongshore non uniformities of longshore current predictions. Journal of Geophysical Research 100 (C16), 119–130.

Phillips, O., 1977. The Dynamics of the Upper Ocean. Cambridge University Press, Cambridge.

Reniers, A., Battjes, J., 1997. A laboratory study of longshore currents over barred and non-barred beaches. Coastal Engineering 30, 1–22.

Ris, R., Booij, N., Holthuijsen, L., 1998. A third-generation wave model for coastal regions, part ii: Verification. Journal of Geophysical Research 104 (C4), 7649–7666.

Ruessink, B., Miles, J., Feddersen, F., Guza, R., Elgar, S., 2001. Modeling the alongshore current on barred beaches. Journal of Geophysical Research 106, 22451–22463.

Sénéchal, N., Dupuis, N., Bonneton, P., 2004. Preliminary hydrodynamic results of a field experiment on a barred beach, Truc Vert Beach on October 2001. Ocean Dynamics 54, 408–414.

Short, A., 1979. Three-dimensional beach-stage model. Journal of Geology 87, 553–571.

Short, A., 1985. Rip current type, spacing and persistence, Narrabeen Beach, Australia. Marine Geology 65, 103–137.

Short, A., 1992. Beach systems of the Central Netherlands Coast: processes, morphology and structural impacts in a storm driven multi-bar system. Marine Geology 107, 103–137.

Short, A., Aagaard, T., 1993. Single and multi-bar beach change models. Journal of Coastal Research SI 15, 141–157.

Short, A., Brander, R., 1999. Regional variations in rip density. Journal of Coastal Research 15 (3), 813–822.

Sonu, C., 1972. Field observation on nearshore circulation and meandering currents. Journal of Geophysical Research 77, 3232–3247.

Svendsen, I., Petrevu, U., 1996. Surf-Zone hydrodynamics, Advances in Coastal and Ocean Engineering, vol. 2. World Scientific, Singapore.

Visser, P., 1991. Laboratory measurements of uniform longshore current. Coastal Engineering 15, 563–593.

Whitford, D., Thornton, E., 1996. Bed shear stress coefficients for longshore currents over a barred profile. Coastal Engineering 27, 243–262.

Wright, L., Short, A., 1984. Morphodynamic variability of surf zone and beaches: a synthesis. Marine Geology 56, 93–118.

D.2 Double bar beach dynamics on the high-energy meso-macrotidal French Aquitanian Coast : A review

Bruno Castelle, Philippe Bonneton, Hélène Dupuis, Nadia Sénéchal
Marine Geology, Vol. 245, pp. 141-159, 2007

ELSEVIER

Marine Geology 245 (2007) 141 – 159

MARINE GEOLOGY
INTERNATIONAL JOURNAL OF MARINE GEOLOGY, GEOCHEMISTRY AND GEOPHYSICS

www.elsevier.com/locate/margeo

Double bar beach dynamics on the high-energy meso-macrotidal French Aquitanian Coast: A review

Bruno Castelle *, Philippe Bonneton, Hélène Dupuis, Nadia Sénéchal

UMR CNRS EPOC 5805, Université Bordeaux 1, Avenue des Facultes, 33405 Talence Cedex, France

Received 6 June 2006; received in revised form 23 April 2007; accepted 3 June 2007

Abstract

The French Aquitanian Coast is an approximately 250 km long straight low coast exposed to high energy conditions in a meso-macrotidal setting. Offshore wave conditions are seasonally modulated, predominantly with a WNW incidence, with offshore significant wave height likely to reach 10 m during winter. Truc Vert Beach, representative of most of the Aquitanian Coast beaches, commonly exhibits two distinct sandbar systems. The inner bar can go through all the states within the intermediate classification and usually exhibits a Tansverse Bar and Rip morphology. After a few weeks of lower energy conditions during summer, the inner bar commonly becomes a Low Tide Terrace with a mean wavelength of 400 m and a mean southerly migration rate of about 2–3 m/day. Crescentic bars have been reported in the literature in nontidal to microtidal settings. Long term persistent crescentic patterns are, however, exhibited at a narrow range of wavelength (mean of 700m) by the outer bar at the meso-macrotidal Truc Vert Beach. Most of the time, the outer bar is inactive and stagnates as offshore waves of $H_s > 3$ m are required to induce a significant morphological change. The crescent shape varies from a symmetric shape to a strongly asymmetric shape, likely to be the result of a long period of NW wave conditions. A strong, and rarely observed elsewhere, morphological coupling between the inner and outer bars can sometimes be observed, and may be the result of the combined effects of the initial presence of a well-developed outer crescentic bar and a long period of shore–normal low energy conditions. A synthesis of all the data available on the area combined with observations on other environments leads to a Truc Vert Beach state model ranging from a modal double bar configuration to an occasional triple bar configuration. This work also identifies knowledge gaps to be explored by further numerical and field studies in tidal double sandbar environments.

Keywords: crescentic bar; transverse bar and rip; low tide terrace; morphological coupling; field measurements; numerical modelling; satellite imagery

Contents

* Corresponding author.
E-mail address: b.castelle@epoc.u-bordeaux1.fr (B. Castelle).

0025-3227/$ - see front matter © 2007 Elsevier B.V. All rights reserved.
doi:10.1016/j.margeo.2007.06.001

1. Introduction

Coastal systems are highly variable due to temporally variable inputs of wave and tidal energy forcing. Wave-dominated sandy beaches are one of the most variable and unpredictable coastal systems. Many conceptual models have been designed to predict variations in beach morphology in terms of environmental conditions. The sequential morphologic state models (Wright and Short, 1984; Wright et al., 1985; Lippmann and Holman, 1990) predict the temporal and spatial evolution of single bar beaches under varying incident wave conditions. These models rely on a small number of environmental parameters, commonly the breaker height, the wave period, the sediment fall velocity and the local beach slope. From these parameters, three main beach states were identified as dissipative, intermediate and reflective states (Wright and Short, 1984). Intermediate beaches were further divided into four sub-states. Immediately below the high energy dissipative state is the Longshore Bar and Trough (LBT), then the Rhythmic Bar and Beach (RBB), next Transverse Bar and Rip (TBR) and finally the Low Tide Terrace (LTT) or ridge and runnel system (Short, 1979; Wright and Short, 1984; Short, 1999). Bauer and Greenwood (1988), (Anthony, 1998) and (Ranasinghe et al., 2004) showed that the environmental parameters were sufficient to discriminate between reflective and dissipative extreme beach states but not adequate to characterize inter mediate situations. Furthermore, the processes associated with morphological changes within the intermediate beach state transitions are still poorly understood. Only recently, with a numerical approach, Ranasinghe et al. (2004) gave a better understanding of the morphodynamic processes governing the down-state transition from idealised RBB and TBR morphologies. This down state transition was also only surveyed by Brander (1999) during a 12day field measurement.

Multiple bar beaches have long been investigated (King, 1972) and are present on a large range of sandy coastlines. Their behaviour is much less understood than single bar beach dynamics. Generally speaking, the bar number increases as the beach gradient and/or the wave period decrease (Short and Aagaard, 1993). Multiple bars are also more prevalent in tideless environments with the inner bar always being the most mobile (King, 1972). Indeed, each bar can go through the same states within the intermediate classification with a hierarchy of bar type, i.e. with the outer bar being of the highest energy type (Short, 1999). The outer bar can be dissipative only during high waves and is commonly quasi-inactive during low energy conditions, while the inner bar(s) can occasionally be reflective (Short, 1999). Among the multiple bar systems, triple bar beaches (Short, 1992; Short and Aagaard, 1993) and double bar beaches (Short and Aagaard, 1993; Short, 1999; Van Enckevort et al., 2004) were particularly focussed on. Short and Aagaard (1993) proposed a double bar model with indication of the observed frequency for each double bar configuration on the open, swell-dominated New South Wales coast (Australia). In other environments, changes in beach slope, sediment grain size or wave forcing may produce additional bar combinations and different frequencies of occurrence (Short, 1999), or produce the occurrence of single bar (Van Enckevort et al., 2004) or triple bar (Ruessink and Terwindt, 2000) configurations. Interaction between the outer and inner bars are not taken into account in this kind of model, neither is directly the tidal range. Indeed, despite tides

contributing to beach morphodynamic processes and types (Short, 1991; Masselink and Short, 1993), such studies occurred in rather micro-mesotidal environments.

The Aquitanian Coast commonly displays double bar beaches with very dynamic rhythmic features in a high energy meso-macrotidal environment. Since 1998, most of the field experiments along the Aquitanian Coast took place at Truc Vert beach, located a few kilometres northward of the Cap Ferret sand spit (Fig. 1). It is considered as being representative of most of the Aquitanian Coast beaches. Different approaches have been undertaken: hydrodynamic data (Sénéchal et al., 2001, 2003; Butel et al., 2002; Bonneton et al., 2004; Castelle et al., 2006b); sedimentary and topographic data (Howa and De Resseguier, 1994; De Melo Apoluceno et al., 2002); satellite imagery (Lafon et al., 2002, 2004, 2005); and numerical

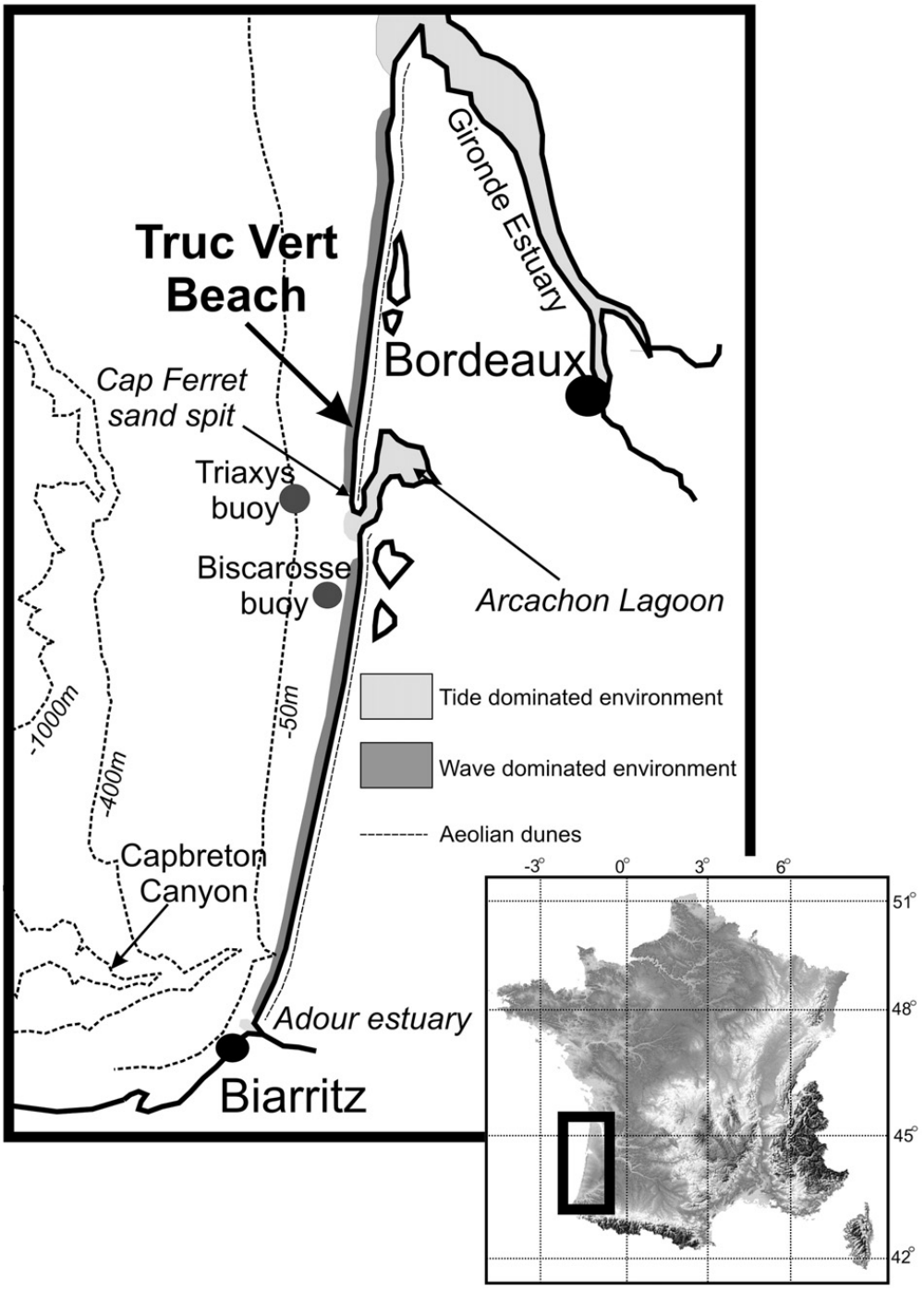

Fig. 1. Study area (Truc Vert Beach) on the Aquitanian Coast with location of wave-dominated and tide-dominated environments.

modelling exercises with direct application to the Aquitanian Coast beaches (Bonneton et al., 2004; Castelle et al., 2006a,b; Castelle and Bonneton, 2006).

The present paper aims at providing a synthesis of our knowledge about the meso-macrotidal high energy Aquitanian double bar beach system and to improve our understanding of double bar system dynamics. Knowledge gaps on the Aquitanian Coast beaches are identified and discussed. We begin with a description of the field site in Section 2. A review of previous works done on Truc Vert beach double bar dynamics is given in Section 3. In Section 4, a Truc Vert Beach state model is proposed, and the different findings are discussed. The findings are summarized and conclusions are stated in Section 5.

2. Field site description

2.1. General settings

The Aquitanian Coast (Fig. 1) is an approximately 250 km long straight low coast bordered by high aeolian dunes (Pedreros, 2000). This coast is located between the Gironde and Adour estuaries, and is interrupted by the approximately 5 km wide Arcachon lagoon tidal inlet, containing complex sandbar and inlet systems (Michel et al., 1995; Cayocca, 2001). The sediment consists of fine to medium quartz sand with mean grain sizes ranging from 200 to 400 μm (Pedreros et al., 1996). The tide is of meso-macro type, with a tidal range of 3.2 m on average which can reach 5 m during spring tides. Tidal currents are intense close to the Arcachon lagoon inlet. Flow velocities can reach 2m/s southward of the Cap Ferret sand spit (Cayocca, 2001). Outside of the Arcachon lagoon inlet, Adour and Gironde estuary influence, tidal currents are not significant in comparison with wave-induced currents (Castelle, 2004).

The coast is exposed to high energy North Atlantic swells travelling mainly from the W–NW sector (Butel et al., 2002), generating a strong southerly longshore drift of approximately 700,000 m^3 of sediment per year (Michel and Howa, 1994). During the past few years, a mean erosion of 1 to 2m/year has been observed (Aubié and Tastet, 2000). Beaches are mainly intermediate double-barred following the classification of Short (1992), Short and Aagaard (1993). Periodic sandbar features are observed in the intertidal domain and in the nearshore zone, which migrate southward at different rates (Lafon et al., 2004). Fig. 2 shows a typical double sandbar configuration at Truc Vert Beach. The inner bar in the intertidal domain commonly exhibits a TBR morphology (Fig. 2) with a mean alongshore averaged wavelength of about 400 m (Lafon et al., 2002). Most of the time, the bars are not shore–normal oriented but skewed, also referred to as oblique (Ribas et al., 2003). The outer bar exhibits crescentic patterns (Froidefond et al., 1990; Lafon et al., 2005), i.e. a RBB morphology, with a yearly averaged wavelength of about 700 m (Lafon et al., 2004). A berm often forms on the upper part of the beach after fair weather conditions, sometimes displaying beach cusps.

2.2. Wave climate

Waves arriving on the Aquitanian Coast are generated by W–E tracking subpolar deep low pressure

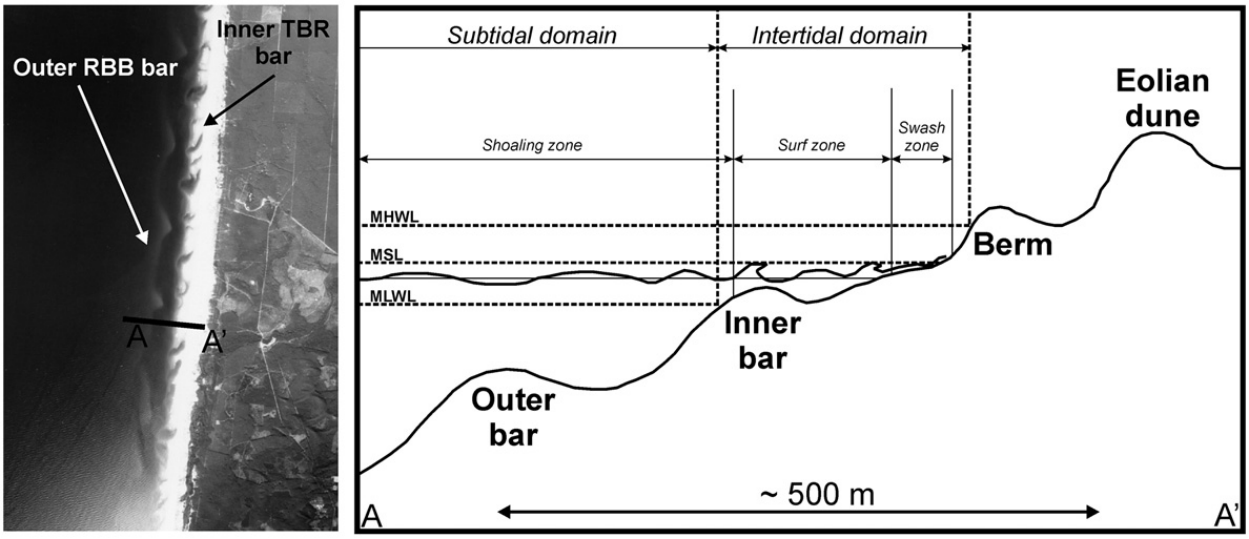

Fig. 2. Aerial photograph (IGN) of a section of the Aquitanian Coast displaying a double bar system, with typical Aquitanian Coast beach profile.

Table 1
Simulated annealing classification for Biscarosse

N	Occurrence	H_s	T_m	θ	Sea state
1	13.92	0.87	5.76	302.01	Summer WNW swell
2		12.14	7.87	296.41	Annual WNW swell
3	11.04	0.65	4.24	328.43	Summer NW swell
4	9.91	0.58	3.84	51.58	Annual E swell
5	9.88	1.58	5.90	286.58	Annual W swell
6	9.48	2.42	6.85	289.56	Annual WNW swell
7	9.05	0.99	5.42	8.87	Annual N swell
8	7.31	0.88	3.96	277.24	Summer W wind wave sea
9	5.52	1.75	10.36	294.76	Winter WNW swell
10	5.20	3.29	8.55	288.26	Winter WNW swell
11	5.09	0.81	5.25	192	Annual S swell
12	1.39	4.66	12.66	291.8	Winter big swell, WNW

The class 4 does not affect the coast (modified from Butel et al. (2002)).

systems over the North Atlantic Ocean and are, therefore, strongly seasonally modulated. A significant interannual variability of the wave climate also exists and could be related to the NOA Index (Dupuis et al., 2006). Recently, Butel (2000) developed a statistical toolbox to undertake a wave classification on the Aquitanian Coast (Butel et al., 2002) from the Biscarosse Buoy moored in 26 m water depth (Fig. 1). It was shown that significant wave height ranges from 0.1 to about 10 m, with the most energetic conditions occurring during winter with 25% of significant wave height larger than 2 m (Butel et al., 2002). Table 1 displays the 12 wave classes obtained with the toolbox (Butel et al., 2002). This classification shows that the Truc Vert beach area is mainly concerned with very low steepness waves associated with long distance swell travelling from the W–NW direction. The forcing varies from summer NW lower waves and occasional storms with a mean NW direction to very high energy winter W to WNW swells. Winds are generally weak in summer with a NW sea breeze in the afternoon. During winter, gusty W to NW winds are common. There is a significant spatial variability of the wave climate along the Aquitanian Coast as wave incoming directions are mostly about 290° around Biscarosse, while they are about 300° at the southern end of the coast with a narrower angular sector (Abadie et al., 2005, 2006).

2.3. Nearshore hydrodynamics

The field measurements of wave-induced currents along the Aquitanian Coast were predominantly obtained from a cross-shore array (Bonneton and Dupuis, 2001; Bonneton et al., 2004; Sénéchal et al., 2002). More recently, further field measurements were undertaken to assess the horizontal circulation behaviour in the intertidal domain (Sénéchal et al., 2003; Castelle et al., 2006b). According to fishermen, lifeguards and surfers, strong tidally modulated rip currents are observed over the intertidal TBR morphology, causing drownings each summer. Fig. 3 shows an aerial photograph of a TBR morphology downdrift oriented (oblique bars) in the intertidal domain on the Aquitanian coast (Castelle et al., 2006b). Two rip currents are easily observed associated with two sediment plumes. Maximum rip current flows occur from mid-tide for lower waves to high tide for high energy conditions, with no significant difference between ebb and flood (Castelle et al., 2006b; Castelle and Bonneton, 2006). This behaviour differs from other environments reported in the literature on both low-energy environments (Aagaard et al., 1997; Brander, 1999) and high energy environments (Brander, 2000) where maximum flow velocities occurred around low tide. Very low frequency (VLF) motions associated with those rip current circulations were observed during 6 day PNEC 2001 field measurements (Castelle et al., 2006b; Bonneton et al., 2007), with temporal scales of approximately 25min.

Due to the predominant W–NW wave direction, an intense longshore current is often observed. For example, during PNEC 2001 field measurements, a 2 m incidence swell at about 8° to the shore generated a southward mean longshore current ranging from 0.5 to 1m/s over a tidal cycle Castelle et al. (2006b). Given that offshore significant wave height can reach 10 m on the Aquitanian Coast, it is reasonable to assume that the longshore current velocity can reach very high values.

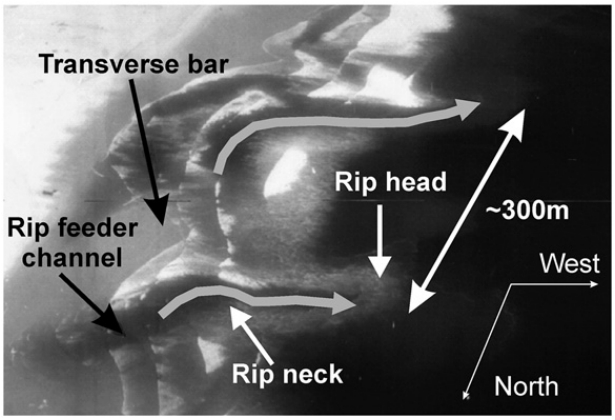

Fig. 3. Aerial photograph of the inner bar exhibiting a TBR morphology with regular downdrift oriented rip channels on the Aquitanian Coast. Visualisation of two rip current associated with two sediment plumes (Castelle et al., 2006b).

3. Sandbar systems

3.1. Inner bar

3.1.1. Morphology

Many previous studies on the French Aquitanian coast referred to the intertidal bar system as a ridge and runnel system (Michel and Howa, 1999; De Melo Apoluceno et al., 2002; Lafon et al., 2002; De Melo Apoluceno, 2003; Castelle and Bonneton, 2006), i.e. LTT, because these investigations were often undertaken after fair weather conditions. Actually, a TBR morphology is observed most of the time in the intertidal domain. Fig. 4 displays an example of 3 different inner bar morphologies from aerial photographs taken around low tide on the Aquitanian Coast. Fig. 4.A displays a LTT morphology. The bar is cut every several hundreds of meters by shallow shore–normal rip channels. On Fig. 4.B, a TBR morphology is observed with bars perpendicular to the shore and regularly spaced every few hundred meters. In the lower part of this photograph, the morphology almost looks like a LTT morphology as rips are very shallow. Fig. 4.C shows a typical Aquitanian Coast TBR morphology observed after a period of high energy conditions. Rip channels are deep and oriented with no preferred direction. Complex breaker patterns reveal that the inner bar is connected to alongshore irregular rip head bars.

3.1.2. Dynamics

In other environments reported in the literature, a few days of fair weather conditions are required to allow the formation of a LTT morphology. 46 surveys composed of high resolution topographic cross-shore profiles, shoreline maps (i.e. shoreline at low tide) and visual observation of the breaker zones were undertaken between 1998 and 2001 (De Melo Apoluceno, 2003). Fig. 5 shows a 5-phase conceptual model of the accretionary sequence of the inner bar proposed by De Melo Apoluceno (2003), associated with a downdrift migration of the system. The presence of the outer bar is

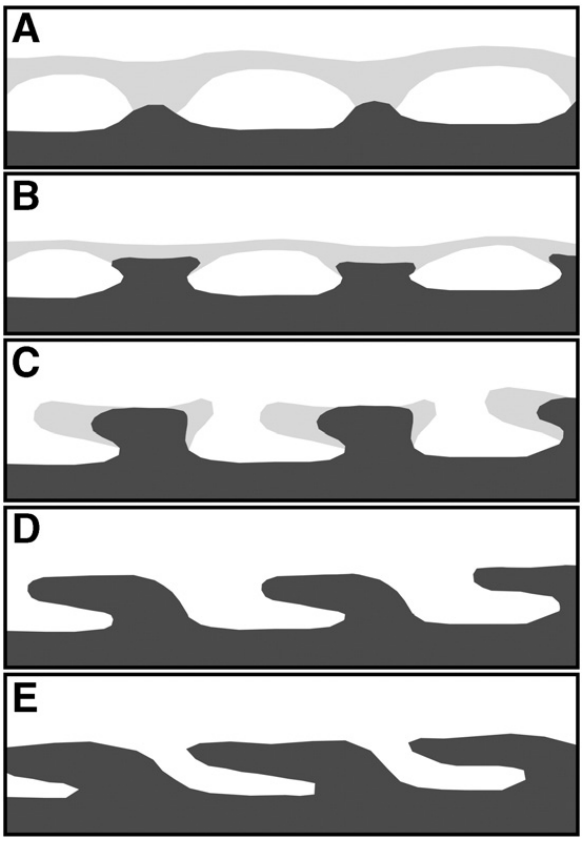

Fig. 5. Phases of a conceptual model for the LTT formation (modified from De Melo Apoluceno (2003)).

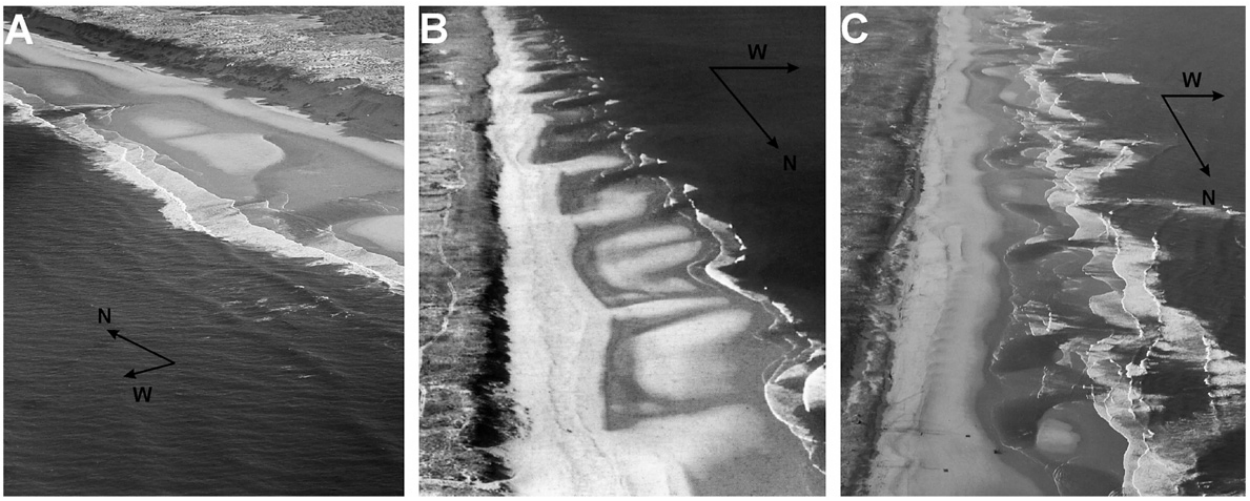

Fig. 4. Aerial photographs of different intertidal bar morphology during low-tide, Aquitanian Coast. (A) : Typical LTT morphology; (B) regular TBR morphology; (C) : TBR morphology with rip channels oriented in no preferred direction.

not taken into account. Starting from a LBT-RBB beach type, the morphology progressively reaches a TBR type associated with a shoreward migration of both the bar and the rip head bar (Fig. 5.A–B–C). Rip channels become well-developed, downdrift-oriented, resulting in an oblique bar configuration (Fig. 5.D). The rips progressively infill as the whole bar moves shoreward and the LTT morphology is eventually reached (Fig. 5.E). This conceptual model is actually similar to the conceptual model proposed by Brander (2000) which provides in more details of the mechanisms responsible for the accretive down-state transition. At Truc Vert Beach, it was found that 10 to 40 days of low energy conditions were required to reach a LTT morphology (Fig. 5.E) from the LBT TBR starting point (Fig. 5.A). It was also found that the LTT morphology could subsist for storm events with $H_s<3$ m, and that the TBR morphology could subsist during high energy storms with $H_s>5$ m.

A higher sample rate and higher resolution surveys of the inner bar were undertaken during 4days of the PNEC 2001 measurements during autumn (Fig. 6). At

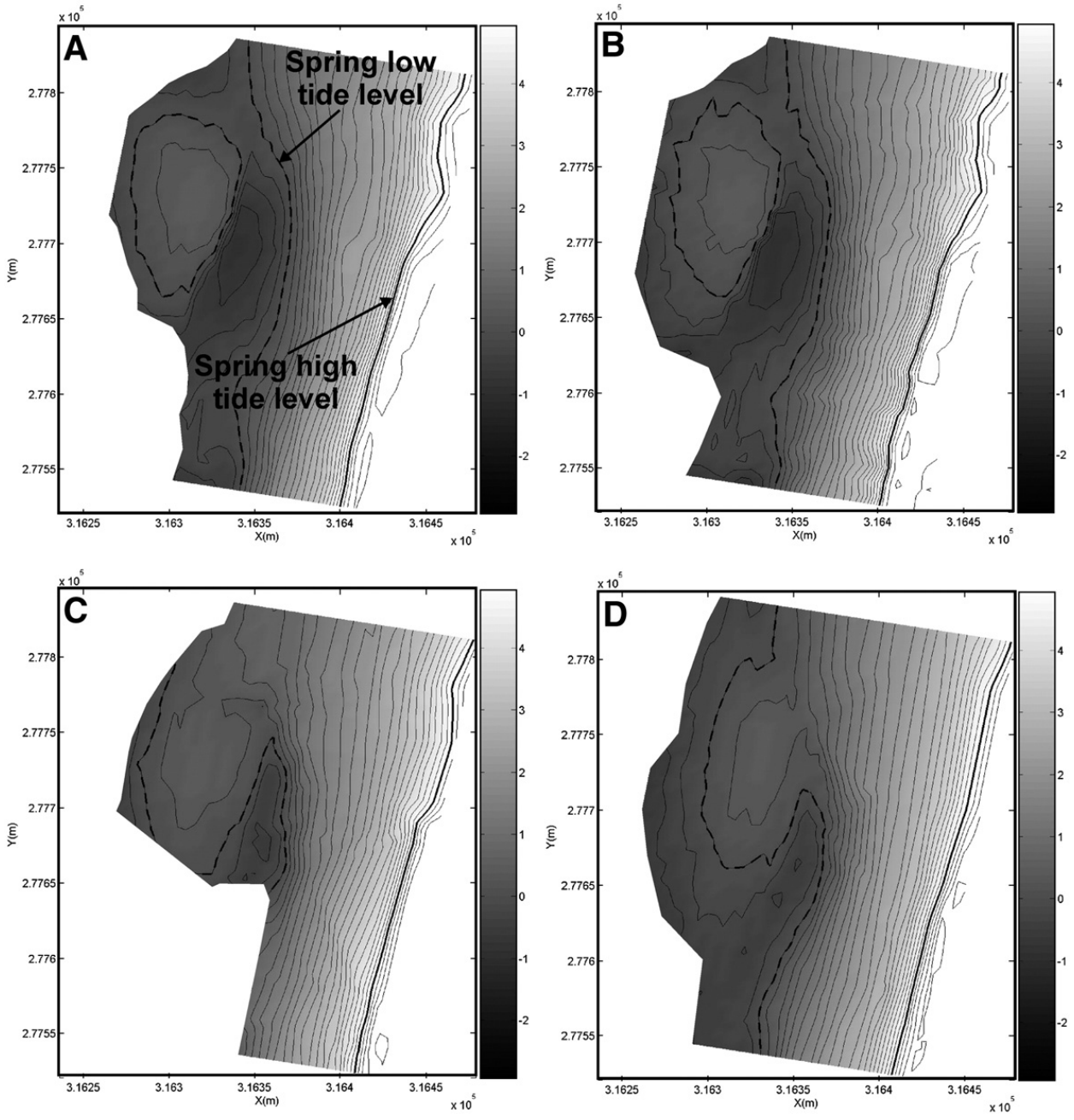

Fig. 6. Topographic surveys of the intertidal domain during PNEC 2001 field experiment showing the welding of the bar to the upper part of the associated with the opening up of a downdrift channel. A: October 15; B: October 16; C: October 17; D: October 18.

Table 2
Size distribution of the inner bar LTT morphology measured on SPOT image, after Lafon et al. (2004)

Date	Mean (m)	S.D. (m)	Med. (m)	Min. (m)	Max. (m)
16/07/86	370	146	342	102	852
02/09/86	427	131	401	146	840
29/07/89	435	211	389	142	1480
04/10/89	430	203	384	181	1303
04/10/90	390	166	343	127	1101
08/09/91	426	170	400	122	895
18/05/92	462	188	420	171	1315
05/10/94	419	150	385	181	849
28/06/95	421	149	406	158	697
23/08/97	440	144	417	197	858
24/06/98	404	136	369	165	948
16/07/99	410	170	400	90	866
01/08/00	463	205	436	85	1158

the starting point (Fig. 6.A), the bar is unwelded to the foreshore, with two channels. The bar was also welded to a rip head bar with a crescent shape (Castelle et al., 2006b). The day after (Fig. 6.B), the bar migrated a few meters onshore associated with a significant accretion of the upper part of the beach. During the third day (Fig. 6.C), the bar welded to the upper part of the beach, closing the northward oriented channel. On the last day (Fig. 6.D), the complete bar welded ashore. Prior to the field experiment, Truc Vert Beach was exposed to a 3 day storm with $H_s \approx 4$–4.5 m which can explain why the energetic wave conditions (1.2 m $< H_s <$ 3 m) resulted in an accretionary adjustment of the beach during the experiment, from a RBB TBR morphology to a TBR morphology. Two main findings can be deduced from those 4 days of observations. Firstly, rapid down-state transitions can be observed during high wave events. Secondly, the accretionary aspect of the commonly used accretionary conceptual models for intermediate beaches (Wright and Short, 1984) is not observed on Fig. 6: the main rip channel exhibits distinct sequential adjustments with a decrease in channel depth, an increase in the cross-sectional area available for rip flow and a reduction in the morphological relief. The lack of data on the morphological evolution of the crescent shape rip head bar connected intertidal system restricts the description of a conceptual model for the accretionary state, as rip head bars are thought to be a key component of rip system morphology evolution (Brander, 1999).

3.1.3. Wavelength and migration rate

Wavelengths and migration rates of the inner bar system were investigated using both shoreline maps (De Melo Apoluceno et al., 2002; De Melo Apoluceno, 2003) and satellite images (Lafon et al., 2002, 2004). The data was obtained during calm weather conditions, during the spring and summer periods, i.e. when the inner bar exhibited a LTT morphology. Based on satellite SPOT imagery from 1986 to 1999, and defining the wavelength as the average rip spacing, Lafon et al. (2004) showed that the inner bar alongshore averaged wavelength ranged from 370 to 463 m (Table 2). Using shoreline maps, De Melo Apoluceno et al. (2002) also found a ridge and runnel alongshore averaged wavelength ranging from 360 to 470 m.

Ridge and runnel alongshore movements were found to occur whenever fair weather conditions and oblique waves prevailed (De Melo Apoluceno et al., 2002; Lafon et al., 2004), which allows the persistence of the bar. Two pairs of SPOT images (16/07/86-02/09/86 and 29/07/89-04/10/89) were used to investigate the average longshore migration rate during low energy wave conditions with rare morphological changes. During the summers of 1986 and 1989, the southward migration rate of the inner bar was found to be respectively 3.1 m/day and 2.4 m/day. Based on 5 consecutive shoreline maps, De Melo Apoluceno et al. (2002) showed that, during the summer of 1999, the southward migration ranged from 0.5 to 4.3 m/day with an average of 1.7 m/day without relating these rates to wave forcing. Offshore wave data can be used to compute the longshore component of the offshore wave energy flux P_{long} which can be approximated (Ruessink and Terwindt, 2000) by:

$$P_{\text{long}} = \frac{\rho g^2}{64\pi} H_s^2 T_p \sin\theta_0 \cos\theta_0 \quad (1)$$

where ρ is the water density, g the gravitational acceleration, H_s the offshore significant wave height, T_p the peak wave period and θ_0 the offshore wave angle to the shore. Results (Table 3) show that the longshore migration rates are weakly correlated to P_{long}, which was also the case at Egmond aan Zee for weak longshore migration rates (Ruessink and Terwindt, 2000). The

Table 3
Measured longshore migration rate of the inner bar measured by De Melo Apoluceno (2003) compared to the longshore component of the off shore energy wave energy flux P_{long}

Period	Longshore migration rate (m/day)	Mean P_{long} (W/m)
05/03/99–01/07/99	0.8	854.6
01/07/99–16/07/99	2.4	583.7
16/07/99–31/07/99	0.4	521.0
31/07/99–01/09/99	0.5	176.3
01/09/99–13/09/99	4.3	1031.7

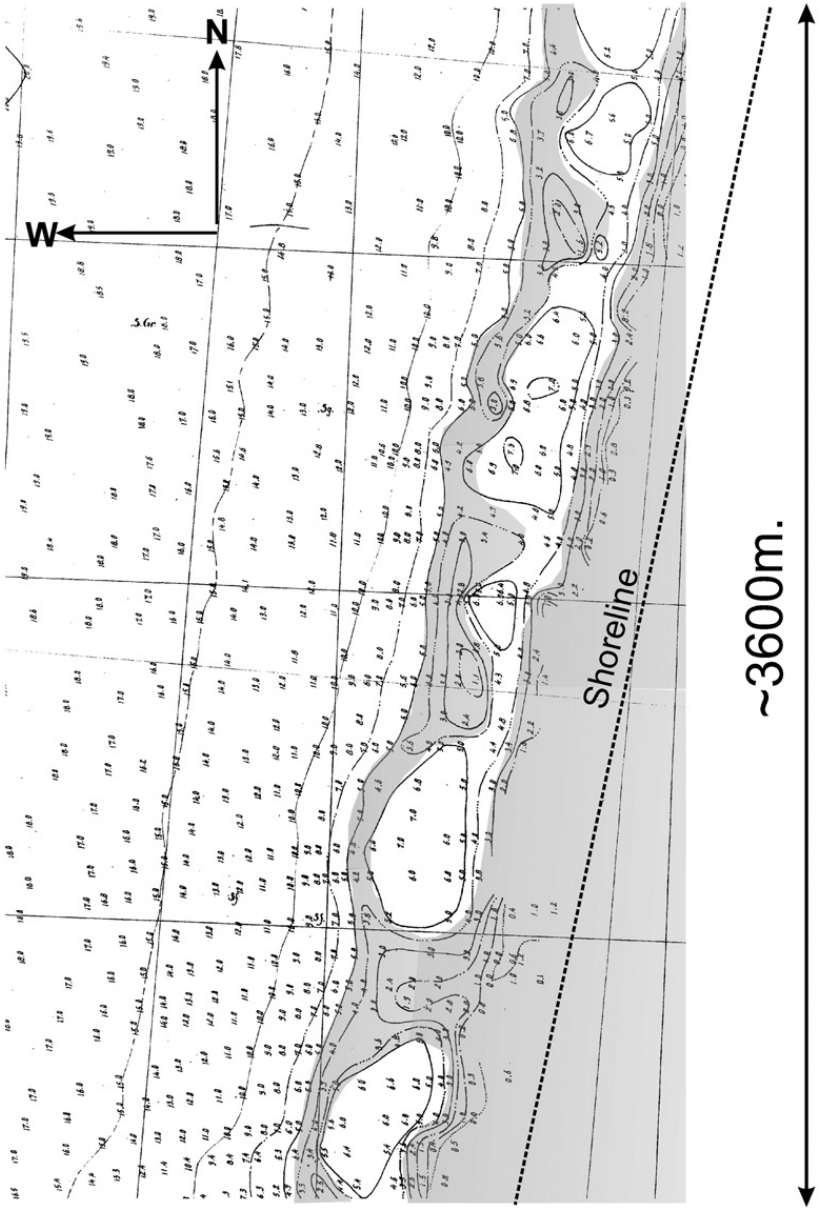

Fig. 7. Bathymetric chart deduced from a bathymetry survey carried out by the SHOM (1967) around Truc Vert Beach with a crescentic bar longshore averaged wavelength of about 700 m. The isobaths are given such as the Lowest Astronomical Tide (LAT) is 0.

measured longshore migration rates are of the same order of magnitude as those measured by Ruessink and Terwindt (2000) at Egmond aan Zee Beach for similar offshore wave conditions. Given that the longshore migration rate can reach 150 m/day at Egmond aan Zee, it is reasonable to assume that the Aquitanian Coast inner bar migration rate could reach such a value during energetic NW waves.

3.2. Outer bar

3.2.1. Morphology

Crescentic bars, also known as lunate bars (Shepard, 1952), are observed on a large range of sandy coasts all around the world (Van Enckevort et al., 2004). They can be found in embayed beaches (Short, 1979; Nafaa and Frihy, 1993) and along straight sandy coasts (Sallenger et al., 1985), and therefore play a key role in beach morphodynamics. These bars have been found in predominantly nontidal to microtidal settings (see for instance the listing in Van Enckevort et al. (2004)). However, on the meso-macrotidal Aquitanian Coast beaches, the outer bar commonly exhibits regular crescentic patterns (Froidefond et al., 1990; Lafon et al., 2005), i.e. a RBB morphology following Wright and Short (1984). Fig. 7 shows a bathymetric chart deduced from a bathymetric survey carried out by SHOM ("Service Hydrographique et Oceanographique de la

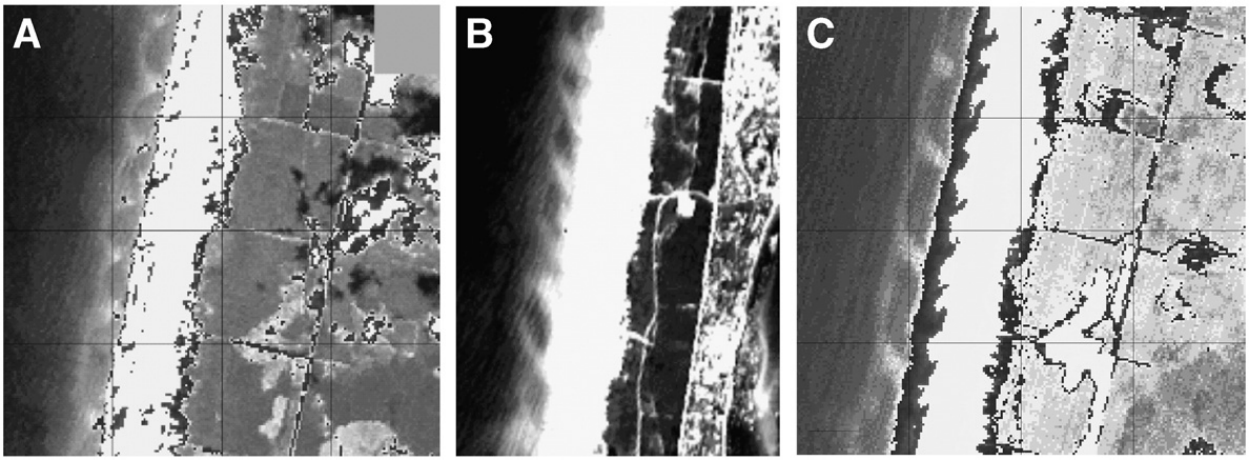

Fig. 8. Satellite SPOT images. Different nearshore crescentic bar morphologies are observed due to water transparency during fair weather conditions, Truc Vert beach area (Castelle et al., 2005). A: Symmetric shape; B: quasisymmetric shape; C: Asymmetric shape.

Marine") around Truc Vert Beach displaying an outer crescentic bar with an alongshore averaged wavelength of about 700m. On average, the shallower landward-protruding section of the bar, the deeper seaward-protruding section of the bar and the trough are respectively 2 m, 4.5 m and 6 m above the Lowest Astronomical Tide (LAT). These values are likely to vary a lot given the high energy highly variable wave conditions that the Aquitanian Coast is exposed to.

Fig. 8 shows that the crescentic bar shape can vary from a typical crescent shape (Fig. 8.A) to a strong asymmetric shape (Fig. 8.C) with the landward part of the bar being linear transverse oriented NW–SE. This asymmetric shape can also be referred as 'skewed' by Wright and Short (1984), Short (1999). Based on numerical wave model outputs and SPOT images, Lafon et al. (2005) suggested that an increased percentage of SW waves seemed to be able to alter the bar symmetry. However, in this particular case, asymmetric bars derived from the superimposition of SW and NW waves, with the NW waves always remaining dominant features. Based on numerical modelling, Castelle et al. (2005) showed that, starting from well developed crescentic patterns, long periods of oblique incidence swells were responsible for the nearshore crescentic bar shape, associated with a longshore migration of the system. Fig. 9 displays the asymmetric behaviour of nearshore crescentic bars and inner bar morphology as a function of the wave-induced current, circulation cell patterns and wave angle. It shows that long periods of NW swells on the Aquitanian Coast can result in the asymmetric shape sometimes observed around Truc Vert Beach.

3.2.2. Wavelength and migration rate

Table 4 shows the size distribution of the crescents measured on SPOT imagery by Lafon et al. (2005) around Truc Vert Beach area. The alongshore averaged wavelength ranges from 579 m to 818 m, with an average of 715 m. This suggests that the alongshore averaged wavelength covers a narrow range of wavelength around Truc Vert Beach, although previous studies on other sites suggest that crescents develop at a wide range of wavelengths after a storm event (Van Enckevort et al., 2004). Therefore, the outer bar behaviour after storm event at Truc Vert Beach remains an open question. Individual crescent wavelength ranges from 250 to 1570 m, with crescents longer than 1000 m observed on every SPOT image. This order of

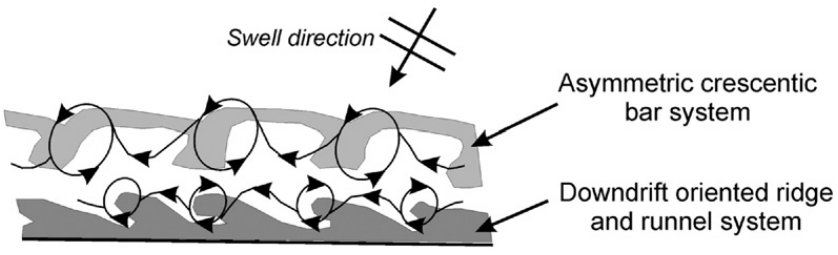

Fig. 9. Asymmetric behaviour of the outer nearshore crescentic bar and inner bar LTT morphology as a function of wave-induced currents, circulation cell patterns and wave angle (Castelle et al., 2005).

Table 4
Size distribution of the nearshore crescentic bar systems measured on SPOT image, after Lafon et al. (2004)

Date	Mean (m)	S.D. (m)	Med. (m)	Min. (m)	Max. (m)
16/07/86	804	200	804	399	1155
29/07/89	777	211	793	380	1428
27/05/91	818	214	767	440	1569
08/09/91	706	169	688	441	1122
18/05/92	726	193	700	361	1050
24/06/98	579	200	539	362	1353
16/07/99	633	236	568	248	1313

wavelength is quite common for a straight beach, all around the world crescentic bar wavelength on straight coasts varies from 100 to 3000 m (Van Enckevort et al., 2004).

Estimating the crescentic bar longshore migration is a challenging task without both high spatial and temporal resolution imagery. The only available data comprises two pairs of SPOT images during the summers of 1991 and 2000 (Lafon et al., 2004). Between May and September 1991, the outer bar morphology did not significantly change except for a restricted zone showing the splitting of two crescents into three crescents. This splitting occurred where the longest crescents were observed, similar to the crescent splittings observed by Van Enckevort et al. (2004), which indicates once again the attempt of the crescentic bar systems to self-organize into a more uniform pattern. A 1 m/day southerly migration rate of the outer bar was observed over this period with no significant morphological change outside the splitting area. Between April and August 2000, neither modification of the crescent morphology nor significant longshore migration of the crescentic bar system was observed. During the summer 2000 period, H_s was always below 3 m, with a mean P_{long} of 799.2W/m and a maximum of 10,432.1W/m. During the summer of 1991, H_s exceeded 3 m for 2.3% of the time, but without accurate wave angle information, P_{long} cannot be computed. This suggests that only offshore wave conditions with $H_s > 3$ m with a W–NW incidence are likely to induce a significant southerly longshore migration of the crescentic bar system.

3.3. Interaction

Crescentic bars have occasionally been associated with similar rhythmic protuberances in the shoreline (Sonu, 1973; Dolan et al., 1985; Thornton et al., 2007) and have been thought to have a strong influence on the location of erosion hot spots (Castelle, 2004; Thornton et al., 2007). Double-barred systems featuring inner bar spacings approximately half the spacing of the outer bar were already documented by Short and Aagaard (1993) and Van Enckevort et al. (2004). However, there is no existing aerial photograph or bathymetric survey showing evidence of complete coupling between each morphology. On the Aquitanian coast during the summer period and dominant NW low energy swells, average migration rates and wavelengths of each of the systems were different, suggesting uncoupled systems. Lafon et al. (2004) showed that for all the images, the mean number of ridge and runnel systems included in one single crescent ranged from 1.43 to 2.17. Between 65 and 90% of the crescents were associated with either one or two inner bar rip channel(s).

However, Fig. 10 shows 3 distinct evidences of a strong morphological coupling, suggesting a strong morphological control of the outer bar on the inner bar can sometimes occur. In the first configuration (Fig. 10.A), the inner bar exhibits TBR morphology welded to rip head bars with a crescent shape, typical of rip cell systems. Two rips are associated with one crescent wavelength and each rip is oriented in the opposite direction. On Fig. 10.B, the aerial photograph taken at low tide shows a LTT inner bar morphology with the uncovered part of the bar located just shoreward of the crescent crest. On the last configuration (Fig. 10.C), for one crescent wavelength, two small rip channels are observed in the intertidal domain, each one being oriented in the opposite direction. Their shape and length scales are completely different from those observed on Fig. 10.A.

Self-organization mechanisms (Falquès et al., 1996, 2000; Damgaard et al., 2002; Reniers et al., 2004; Calvete et al., 2005) or different mode edge waves (Bowen and Inman, 1971) cannot explain such a length scale factor as the aerial photographs presented in Fig. 10 show an obvious morphological coupling, suggesting that the inner bar rips did not form by themselves. The common point between each configuration is the presence of a well developed crescentic morphology of the outer bar, i.e. welded or almost welded to the inner bar with strong three-dimensional characteristics. This is in agreement with a recent investigation undertaken by Ruessink et al. (2006, 2007) using continuous wavelet and cross-wavelet transforms of a double sandbar system on the Gold Coast (Australia). They showed that, initially, inner and outer bar variability develops independently and that, eventually, the inner bar variability becomes slaved to the outer bar variability. Lafon et al. (2005) did not observe any morphological coupling despite the presence of well

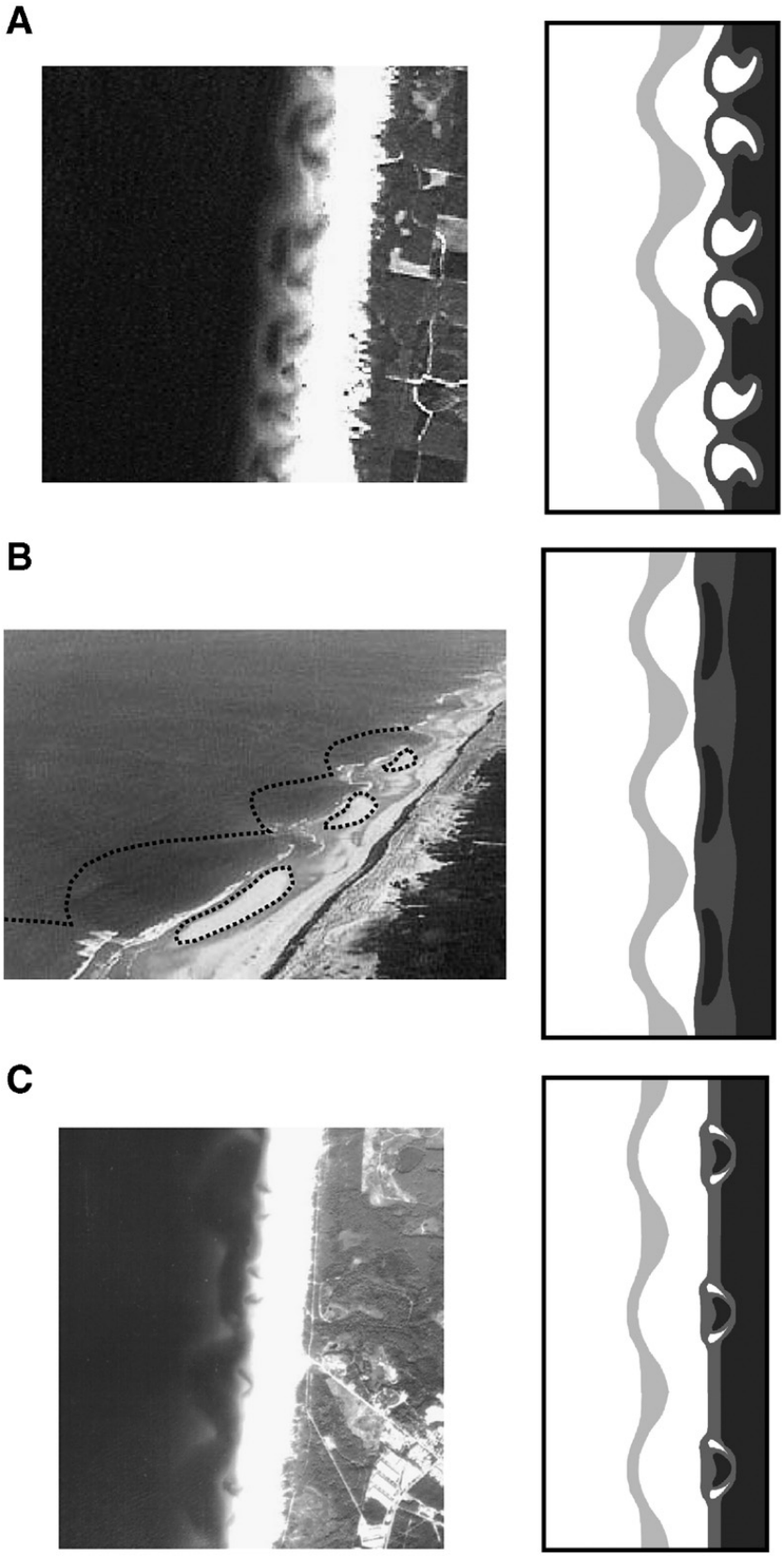

Fig. 10. Evidence of strong morphological coupling between the inner and outer bars (Castelle, 2004). A: Satellite SPOT image (15/10/2001@CNES UMR EPOC 5805); B: Aerial photograph (1999); C: Aerial photograph (IGN, 1978).

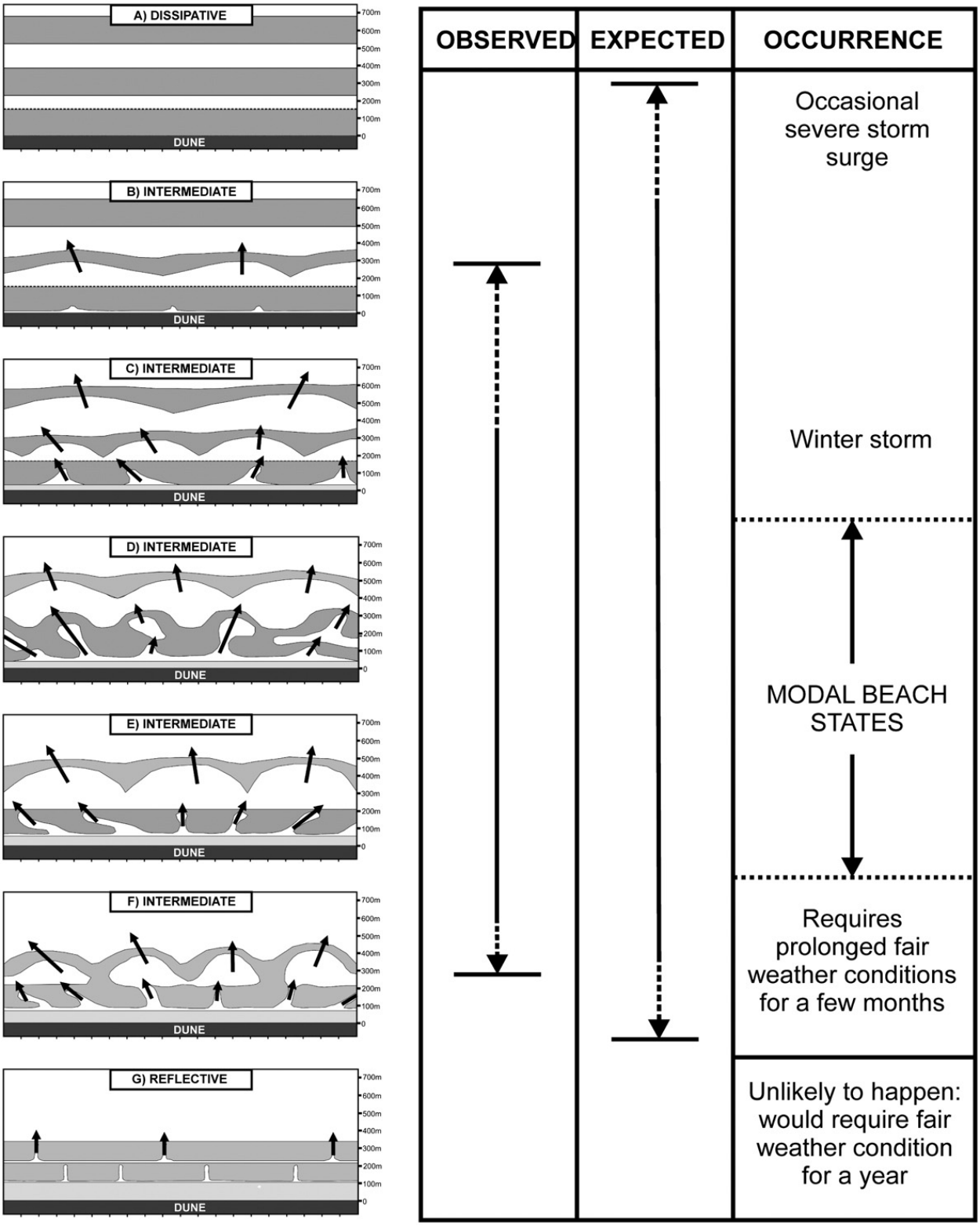

Fig. 11. Preliminary beach state model exhibiting the possible range of beach state around Truc Vert Beach area. Type (A) is expected following severe storms and storms surges, as type (B) after a sever winter storm. Type (C), (D), (E) and (F) were observed on aerial photographs and/or satellite images. Type (F) is only possible following extreme period of low energy conditions (≈year), and then impossible to occur on the Aquitanian coast. Arrows indicate rip current when active under sufficient wave energy conditions.

developed crescentic patterns, suggesting other key parameters for morphological coupling occurrence. Off shore wave conditions prior the morphological couplings on Fig. 10 have in common : more than 10days of low energy shore–normal swell just prior the photograph and high energy shore–normal swell a few weeks before the photograph. The fact that rip channels are almost shore–normal in Fig. 10 confirms that shore–normal waves may play a key role in this morphological coupling. Moreover, with a numerical approach, Castelle and Bonneton (2004) showed that, for $H_s < 1.5$ m, wave refraction over an idealized Aquitanian coast near shore crescentic bar system and the resulting energy focalization shoreward could generate stable and regularly spaced rip currents in the intertidal domain over a tide cycle. Further investigations, including the use of a nonlinear morphodynamic model, may explain more rigorously this morphological coupling.

4. Discussion

4.1. Truc Vert Beach state model

All the sandbar investigations presented above are considered to build a beach model for the Truc Vert Beach area. Fig. 11 displays this beach model with 7 beach states. This beach model is restricted to the available database, and extended to expected configurations following previous works on beach morphology (Lippmann and Holman, 1990; Aagaard, 1991; Short, 1992; Short and Aagaard, 1993; Van Enckevort et al., 2004). Beach states range from a dissipative state (A) to a reflective state (G), with 5 intermediate beach states in-between.

The dissipative state (A) exhibits a dissipative beach system containing three shore-parallel bars, with rip circulations expected to be weak in comparison with the bed return flow. This shore-parallel nearshore bar configuration has never been observed at Truc Vert Beach, and should have therefore a very low occurrence frequency, i.e. would require a decadal storm. Truc Vert Beach usually exhibits an intermediate state. After individual extreme winter storms, the beach is likely to exhibit a high energy intermediate beach state (B) and (C), with a continuous outer bar either straight (LBT, (B)) or rhythmic (LBT RBB,(C)). These beach states could also be part of an accretionary state sequence, developing from straight shore-parallel bars (A) within a few hours or days following a period of severe storm waves and surges. Under continuing low or moderate energy conditions, the intermediate crescent horns weld to the inner bar (D), causing the disappearance of the alongshore continuous trough and the separation of the bays into isolated narrow channels with strong rip currents. This beach state configuration is commonly observed on the Aquitanian coast (for instance on Fig. 4.C), sometimes after a common storm type. Then, as the bars move shoreward under post-storm conditions increasing rhythmicity leads to (D), (E) and (F) Truc Vert modal beach states. The outer bar is located about 400–500 m from the shoreline and regularly broken by widely spaced rips (with a wavelength of about 600–800 m), which is the so-called nearshore crescentic bar commonly observed on Truc Vert Beach. The inner bar is highly rhythmic and attaches to the beach, with a wavelength of about 300–500 m. The inner bar is dominated by detached or attached (TBR-RBB) bars and rip systems (D). Under continuing low energy conditions, the inner bar attaches to the beach as TBR (E), and eventually welds to the beach as a ridge and runnel system (LTT, F). The intermediate beach state (E) can be observed on Fig. 2, and (F) on Fig. 8.C. For a long period of particular offshore wave conditions, a coupling between the inner and outer bars could be observed within the states (D), (E) and (F), as described in Section 3.3. An unusually long period of low waves could produce the fully reflective beach state (G) when all the bars weld to the beach. Such configuration would require a period of the order of a year of $H_s < 1$ m which is obviously impossible on the Aquitanian coast, but needs to be taken into account in this beach state model, as all the bars in a beach state model can theoretically go through all the states of a single bar (Short and Aagaard, 1993).

This beach state model is in-between the generalised two and three bar beach systems proposed by Short and Aagaard (1993), despite some significant differences. Firstly, the present model goes from a double bar to a triple bar configuration. This single-double or double triple bar configuration has already been observed (Ruessink and Kroon, 1994; Van Enckevort et al., 2004), while Short and Aagaard (1993) distinguished single, double and multi-bar beach systems. Despite the Truc Vert Beach morphology most of the time exhibiting double bar morphology, this triple bar configuration could play a key role during severe storms. Secondly, this model, for a meso-macrotidal environment, differs also in terms of frequency of outer and inner bar combinations. Indeed, an outer bar LBT morphology is observed about 40% of the time by Short and Aagaard (1993) on the east coast of Australia, while investigations at Truc Vert Beach suggest that it is an occasional configuration. Investigations in other environments suggested that crescentic bar lifetime was on the order

of a few days to several weeks (Wright et al., 1985; Lippmann and Holman, 1990). For example, the outer bar on the Gold Coast (Australia) exhibited a LBT morphology during each high energy event, with typically $H_{rms}>1.5-2$ m (Van Enckevort et al., 2004). It differs considerably for Noordwijk (The Netherlands) where crescentic features of the outer bar had a lifetime of 0.5–37months (Van Enckevort and Ruessink, 2003). Certain and Barusseau (2005) also showed that a decadal storm was required to straighten the outer bar at the microtidal Sètes Beach. Truc Vert Beach outer bar lifetime may be of the same order as the latest as crescentic patterns deduced from breakers were still clearly observed on an aerial photograph during high energy conditions with $H_s \approx 6$ m (Castelle, 2004), suggesting *Hs* on the order of 10 m (i.e. decadal storm) may be required to straighten the outer bar. An outer bar decay, as observed by Ruessink and Terwindt (2000), Castelle et al. (2007), may also occur during a decadal storm, which is not taken into account in the present Truc Vert Beach model.

Morphological coupling, as described in Section 3.3., may be observed for the states (D), (E) and (F) but is not included in this conceptual model due to significant

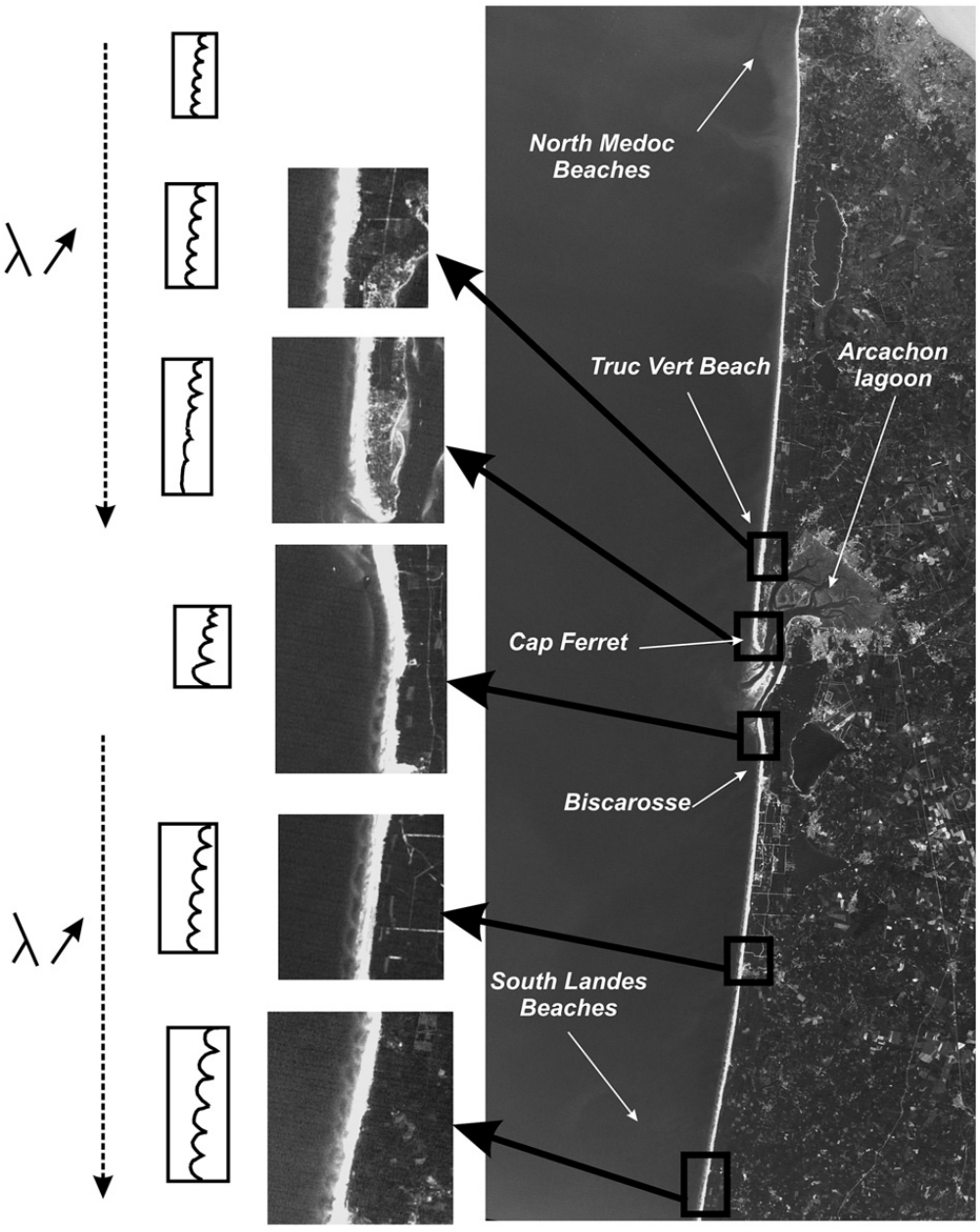

Fig. 12. Variation of the outer crescentic bar morphology along the Aquitanian Coast. Crescentic bars are not observed around the Arcachon lagoon inlet where tidal currents are intense, and the outer bar alongshore averaged wavelength Λ slightly increases to the south, after Castelle (2004).

knowledge gaps in this behaviour. This beach state model must be considered as a starting point for further investigations on the Truc Vert Beach morphodynamics. Video imagery and higher sample rate satellite imagery are likely to provide a more rigorous analysis. Conclusions reached in this study need to be rigorously discussed to build a more robust beach state model and to assess the impact of the meso-macrotial settings on the bar dynamics.

4.2. Extension to the whole Aquitanian Coast

Field measurements, satellite imagery and numerical works presented above focussed on Truc Vert Beach area. Truc Vert Beach is not entirely representative of all the other beaches of the Aquitanian Coast. Sediment grain size (Pedreros, 2000), seaward shelf width, wave climate (Abadie et al., 2005) and beach slope can be significantly different. It results in an alongshore variability of the sandbars which have not been discussed previously.

High energy swells have a peak direction of about 300° in the southern part of the Aquitanian Coast Abadie et al. (2005), while in Truc Vert Beach area swells are distributed on a wider angular sector, usually between 280° and 300° (Butel et al., 2002). This is because the southern part of the Aquitanian coast is more sheltered by Spain from the SW–W swells than for the northern Aquitanian coast. The continental shelf is also significantly narrower in the southern Aquitanian Coast, and ends in front of the Capbreton Canyon (see Fig. 1). It results in weaker wave attenuation on the continental shelf due to bottom friction, and significantly more energetic waves on the southern beaches.

Occasional satellite images cover the entire Aquitanian cost. Fig. 12 shows a LANDSAT image of the Aquitanian coast displaying alongshore variations of the nearshore crescentic bar morphology. Crescentic bars are present, with a significantly shorter mean wavelength than around Truc Vert Beach, in the far northern part of the Coast despite the high turbidity making the crescentic bar identification a challenging task. In the Southern part of the Cap Ferret sand spit, crescent patterns start straightening, and then are interrupted by the Arcachon inlet tidal banks. Tidal currents are thought to be responsible for the straightening of the crescent patterns, disturbing and interacting with the circulation cells in the surf zone which are a key component in the crescentic bar development. At the southern extremity of the Arcachon lagoon inlet, crescentic patterns start to form, with irregular wavelengths and shapes. Then, outside the influence of the tidal currents, crescentic bars become rhythmic down to the southern part of the Aquitanian coast. The most important feature is that the crescentic bar wavelength significantly increases from the northern to the southern part of the Aquitanian coast. A factor of about 2 exists between the two wavelengths. This would mean that the mean crescentic bar wavelength in the southern Aquitanian coast is of the order of 1500m. The whole Aquitanian Coast could then afford a natural laboratory to investigate crescentic bars. Further investigations must be undertaken to provide accurate data on the alongshore variability of the different parameters (the sediment grain size, mean beach slope, local wave climate, etc) in order to accurately explain this longshore variability of the nearshore crescentic bar morphology, and to quantify the sensitivity of the crescent wavelength to the various physical parameters.

5. Conclusion

Field measurements, satellite imagery and numerical modelling undertaken around Truc Vert Beach were combined to provide a synthesis of our knowledge on the Aquitanian coast high energy double sandbar system. The inner bar received considerable attention recently with many shoreline maps, topographic surveys and remote sensing. The LBT morphology requires at least 10days of fair weather condition, most of the time during summer, to reach a LTT morphology with an alongshore average wavelength of about 400m which migrates downdrift at a mean rate of 2–3 m/day. The outer bar system received less attention with just a handful of satellite images during the past 15years and occasional bathymetric surveys. Despite crescentic having been reported in the literature in nontidal to microtidal settings, the outer bar exhibits long term persistent crescentic patterns at a narrow range of wavelength (mean of 700m) at the meso-macrotidal Truc Vert Beach. The crescent shape varies from a symmetric to an asymmetric shape, likely to be the result of a long period of NW waves. The outer bar is inactive and stagnates for $H_s < 3$ m, while its behaviour is still poorly understood during high wave conditions.

Various aerial photographs and visual observations suggest that a decadal storm may be required to straighten the outer bar, as it was observed in other sites (Van Enckevort et al., 2004; Certain and Barusseau, 2005). According to these findings, a beach state model is proposed for meso-macrotidal beach system of Truc Vert Beach which ranges from a modal double bar configuration to an occasional triple bar configuration. This model can be extended to the whole Aquitanian

Coast, despite some significant differences which may exist concerning the wavelengths and the morphological response times of the system.

The present beach state model, like all the other ones proposed in the literature (Short, 1999), does not take into account the occasional strong morphological coupling between the inner and outer bars, which may have an underestimated role on the entire system behaviour. At Truc Vert Beach, this coupling occurs when the outer crescentic bar is well developed i.e. welded, or almost welded, to the inner bar and, likely, after a significant period of shore–normal wave conditions. The requirement of a well developed outer bar is in agreement with Ruessink et al. (2006, 2007). As the distance of the bar crest to shore is a key parameter for the alongshore wavelength (Deigaard et al., 1999), this study also suggests that the distance between the outer bar and the inner bar may also be a key parameter for the morphological coupling. The role of tidal range may also have a significant influence on double sandbar system morphology which is still poorly understood. Indeed, previous studies on single or multiple alongshore rhythmic sandbar systems dealt with micro-mesotidal environments. Truc Vert Beach exhibits both strong and long term persistent rhythmic bedform features, which shows that intermediate beach state models have to be extended and developed to meso-macrotidal settings.

Significant knowledge gaps remain on Truc Vert Beach sandbar behaviour, such as the variation of the outer bar distance to the shore (particularly during storm events), the short-term variations of both sandbar systems during high wave events and post-storm events and the morphological time response to varying wave forcing. The model proposed on Fig. 11 also has to be tested rigorously. The frequency of occurrence of each morphological configuration (Fig. 11) is barely known and has to be explored through permanent video imagery and compared with other environments. Alongshore migration rates of both systems are poorly understood, particularly for $H_s > 3$ m, as alongshore migration rates of only 0 (1 m/day) were computed during low to moderate wave energy periods. Thus, field measurements and video imagery during high wave events will provide key information for the overall understanding of this high energy meso-macrotidal environment.

This study also results in numerous modelling work perspectives. The various recent advances in the understanding of the cross-shore sandbar dynamics (Drake and Calantoni, 2001; Elgar et al., 2001; Hoefel and Helgar, 2003) have to be implemented in nonlinear 2DH models as not only the distance of the bar to the shore but the distance between each bar may play a key role in the entire system dynamics. The numerical simulation of both the outer bar straightening and decay have to be explored as it remains, at the time of writing this paper, an open problem. Nonlinear modelling has been previously undertaken in tideless environments (Damgaard et al., 2002; Reniers et al., 2004; Calvete et al., 2005; Dronen and Deigaard, 2007) and now needs to be undertaken with varying tide level. Consequently, swash zone processes need to be accurately parameterized in the model to be able to simulate the inner bar dynamics which is often located in the intertidal domain.

The Aquitanian coast is a well developed high energy meso-macrotidal environment which deserves further field experiments combined with numerical modelling. It will be attempted during a 6 week international field campaign to be held at Truc Vert Beach in early 2008 including high quality bathymetric surveys, satellite and video imagery, and a large array of deployed pressure sensors and current meters. These measurements combined with numerical modelling and the implementation of a permanent video station at Biscarrosse Beach on the Aquitanian Coast may bridge some important knowledge gaps highlighted in this paper.

Acknowledgments

This study was initially performed within the framework of the “Programme National d’Envirronement Côtier” (PNEC), “Action de Recherche Thématique” (ART) 7 “Hydrodynamique sédimentaire en zone côtiere”, sponsored by the CNRS/INSU. This study was also supported by the ECORS program (Research contract SHOM no. CA/2006/06/CMO). The two anonymous reviewers are acknowledged for their expertise and constructive comments which substantially improved the content of this paper. Finally, we sadly dedicate this work to our colleague and friend Denis Michel, who was among the first ones to investigate the Aquitanian Coast beaches, and who tragically passed away during a recent field experiment at Biscarrosse Beach. We love and miss you Denis.

References

Aagaard, T., 1991. Multiple-bar morphodynamics and its relation to low frequency edge waves. J. Coastal Res. 7, 810–813.

Aagaard, T., Greenwood, B., Nielsen, J., 1997. Mean currents and sediment transport in a rip channel. Mar. Geol. 140, 25–45.

Abadie, S., Butel, R., Dupuis, H., Brière, C., 2005. Paramètres statiqtiques de la houle directionnelle au large de la côte sud aquitaine. C.R. Geoscience 337 (8), 769–776.

Abadie, S., Butel, R., Mauriet, S., Morichon, D., Dupuis, H., 2006. Wave climate and longshore drift on the South Aquitaine coast. Cont. Shelf Res. 26, 1924–1939.

Anthony, E.J., 1998. Sediment-wave parametric characterization of beaches. J. Coast. Res. 14, 347–352.

Aubié, S., Tastet, J.P., 2000. Coastal erosion, processs and rate : an historical study of the Gironde coastline, Southwestern France. J. Coast. Res. 16 (3), 756–767.

Bauer, B.O., Greenwood, B., 1988. Surf-zone similarity. Geogr. Rev. 78, 137–147.

Bonneton, N., Bonneton, P., Senechal, N., Castelle, B., 2007. Very low fre-quency rip current pulsations during high-energy wave conditions on a meso-macro tidal beach. In : Proc. 30th Int. Conf. on Coastal Eng.

Bonneton, P., Dupuis, H., 2001. Transformation of irregular waves in the inner surf zone. Proc. of the 27th Int. Conf. on Coastal Eng., vol. 1, pp. 745–754.

Bonneton, P., Marieu, V., Dupuis, H., Sénéchal, N., Castelle, B., 2004. Wave transformation and energy dissipation in the surf zone: Comparison between a non-linear model and field data. J. Coastal Res. SI 39, 329–333.

Bowen, A.J., Inman, D.L., 1971. Edge waves and crescentic bar. J. Geophys. Res. 76, 8662–8671.

Brander, R.W., 1999. Field observations on the morphodynamic evolution of low-energy rip current system. Mar. Geol. 157, 199–217.

Brander, R.W., 2000. Morphodynamics of a large-scale rip current system at Muriwai Beach, New Zealand. Mar. Geol. 165, 27–39.

Butel, R., 2000. Botido, une boïte à outils pour le traîtement et l'imagerie des données de bouées océanographiques. Internal Report D.G.O. 35pp.

Butel, R., Dupuis, H., Bonneton, P., 2002. Spatial variability of wave conditions on the French Aquitanian coast using in-situ data. J. Coastal Res. SI 36, 96–108.

Calvete, D., Dodd, N., Falquès, A., van Leeuwen, S.M., 2005. Development of rip channel systems: normal and near normal wave incidence. J. Geophys. Res. 110, C10006. doi:10.1029/2004JC002803.

Castelle, B., 2004. Modélisation de l'hydrodynamique sédimentaire au-dessus des barres sableuses soumises à l'action de la houle : application à la côte aquitaine. Ph.D. thesis, University Bordeaux I, in French, unpublished, 340p.

Castelle, B., Bonneton, P., 2004. Nearshore waves and currents over crescentic bars. J. Coast. Res. SI 39, 687–691.

Castelle, B., Bonneton, P., 2006. Modeling of a rip current induced by waves over a ridge and runnel system on the Aquitanian Coast, France. C.R. Geosciences 338 (10), 711–717.

Castelle, B., Bonneton, P., Butel, R., Dupuis, H., 2005. Nearshore modeling of nearshore crescentic bar dissymetry on an open coast, france. In : Proceeding of Coastal Dynamics '05, [CD-ROM], Barcelona, Spain.

Castelle, B., Bonneton, P., Butel, R., 2006a. Modeling of crescentic pattern development of nearshore bars: Aquitanian coast, france. C.R. Geosciences 338 (11), 795–801.

Castelle, B., Bonneton, P., Sénéchal, N., Dupuis, H., Butel, R., Michel, D., 2006b. Dynamics of wave-induced currents over a multiple-barred sandy beach on the Aquitanian Coast. Cont. Shelf Res. 26 (1), 113–131.

Castelle, B., Turner, I.L., Ruessink, B.G., Tomlinson, R.B., 2007. Impact of storms on beach erosion: Broadbeach (Gold Coast, Australia). J. Coast. Res. SI 50, 534–539.

Cayocca, F., 2001. Long-term morphological modeling of a tidal inlet: the Arcachon Basin, France. Coast. Eng. 42, 115–142.

Certain, R., Barusseau, J.-P., 2005. Conceptual modeling of sand bars morpho-dynamics for a microtidal beach (Sètes, France). Bull. Soc. géol. Fr. 176 (4), 343–354.

Damgaard, J.S., Dodd, N., Hall, L., Chesher, T.J., 2002. Morphodynamic modeling of rip channel growth. Coast. Eng. 45, 199–221.

De Melo Apoluceno, D., 2003. Morpho-hydrodynamique des plages à barres en domaine méso macro-tidal : exemple de la plage du Truc Vert, Gironde, France. Ph.D. thesis, Université Bordeaux I, in French, unpublished.

De Melo Apoluceno, D., Howa, H., Dupuis, H., Oggian, G., 2002. Morphody-namics of ridge and runnel systems during summer. J. Coastal Res. SI 36, 222–230.

Deigaard, R., Dronen, N., Fredsoe, J., Hjelmager Jensen, J., Jorgensen, M.P., 1999. A morphological stability analysis for a long straight barred coast. Coast. Eng. 36, 177–195.

Dolan, R., Vincent, L., Hayden, B., 1985. Crescentic coastal landforms. Z. Geomorphol. 18, 1–12.

Drake, T.G., Calantoni, J., 2001. Discrete particle model for sheet flow sedi-ment transport in the nearshore. J. Geophys. Res. 106 (C9), 19859–19868.

Dronen, N., Deigaard, R., 2007. Quasi-three-dimensionnal modelling of the morphology of longshore bars. Coast. Eng. 54, 197–215.

Dupuis, H., Michel, D., Sottolichio, A., 2006. Wave climate evolution in the bay of biscay over two decades. J. Mar. Syst. 63, 105–114.

Elgar, S., Gallagher, E.L., Guza, R.T., 2001. Nearshore sandbar migration. J. Geophys. Res. 106 (C6), 11623–11627.

Falquès, A., Montoto, A., Iranzon, V., 1996. Bed-flow instability of the long-shore current. Cont. Shelf Res. 16, 1927–1964.

Falquès, A., Coco, G., Huntley, D.A., 2000. A mechanism for the generation of wave-driven rhythmic patterns in the surf zone. J. Geophys. Res. 105 (C5), 24071–24088.

Froidefond, J.-M., Gallissaires, J.-M., Prud'homme, R., 1990. Spatial variation in sinusoidal on a crescentic nearshore bar: application to the Cap Ferret Coast. J. Coastal Res. 6, 927–942.

Hoefel, F., Helgar, S., 2003. Wave-induced sediment transport and sandbar migration. Science 299 (5614), 1885–1887.

Howa, H., De Resseguier, A., 1994. Application of a fluorescent grain detector/counter for sand transport evaluation in the littoral zone. Proc. Int.Conf. Ocean Osates '94, vol. 3, pp. 254–257.

King, C.A.M., 1972. Beaches and Coasts. Edward Arnold, London.

Lafon, V., Dupuis, H., Howa, H., Froidefond, J.-M., 2002. Determining ridge and runnel longshore migration rate using spot imagery. Oceanologica Acta 25, 149–158.

Lafon, V., De Melo Apoluceno, D., Dupuis, H., Michel, D., Howa, H., Froi-defond, J.-M., 2004. Morphodynamics of nearshore rhythmic sandbars in a mixed-energy environment (Sw France):i. mapping beach changes using visible satellite imagery. Estuar. Coast. Shelf Sci. 61 (2), 289–299.

Lafon, V., Dupuis, H., Butel, R., Castelle, B., Michel, D., Howa, H., De Melo Apoluceno, D., 2005. Rhythmic sub-tidal and inter-tidal bar morphology and dynamics in a mixed-energy environment. part II: physical forcing analysis. Estuar. Coast. Shelf Sci. 65 (3), 449–462.

Lippmann, T.C., Holman, R.A., 1990. The spatial and temporal variability of sand bar morphology. J. Coast. Res. 95, 575–590.

Masselink, G., Short, A.D., 1993. The effect of tide range on beach morpho-dynamics and morphology: a conceptual model. J. Coast. Res. 9, 785–800.

Michel, D., Howa, H., 1994. Morphological evolution of a littoral sand bank, modelisation of its dynamics. Annals Geophysical, European Geophysical Union, Part II, 12, p. 240.

Michel, D., Howa, H., 1999. Short-term morphodynamic response of a ridge and runnel system on a mesotidal sandy beach. J. Coast. Res. 15, 428–437.

Michel, D., Howa, H., Tastet, J.-P., 1995. Essai de modélisation de l'évolution morphologique d'un banc sableux intertidal (sud du Bassin d'Arcachon, France). C.R.A.S. 321, 497–504.

Nafaa, N., Frihy, O.E., 1993. Beach and nearshore features along the dissipative coastline of the nile delta. J. Coastal Res. 9, 423–433.

Pedreros, R., 2000. Quantification et modï£¡isation du transport éolien au niveau des zones côtières-application au littoral aquitain. Ph.D. thesis, University Bordeaux I, in French, unpublished.

Pedreros, R., Howa, H., Michel, D., 1996. Application of grain-size-trend analysis for the determination of sediment transport pathways in intertidal areas. Mar. Geol. 135, 35–49.

Ranasinghe, R., Symonds, G., Black, K., Holman, R., 2004. Morphodynamics of intermediate beaches: a video imaging and numerical modelling study. Coast. Eng. 51, 629–655.

Reniers, A.J.H.M., Roelvink, J.A., Thornton, E.B., 2004. Morphodynamic modeling of an embayed beach under wave group forcing. J. Geophys. Res. 109, C01030. doi:10.1029/2002JC001586.

Ribas, F., Falques, A., Montoto, A., 2003. Nearshore oblique sand bars. J. Geophys. Res. 108 (C4), 3119. doi:10.1029/2001JC000985.

Ruessink, B.G., Kroon, A., 1994. The behavior of a multiple bar system in the nearshore zone of terschelling, the netherlands. Mar. Geol. 21, 187–197.

Ruessink, B.G., Terwindt, J.H.J., 2000. The behaviour of nearshore bars on the time scale of years: a conceptual model. Mar. Geol. 163, 289–302.

Ruessink, B.G., Coco, G., Ranasinghe, R., Turner, I.L., 2006. A cross-wavelet study of alongshore nonuniform nearshore sandbar behavior. In : Proc. of the 2006 International Joint Conference on neural networks [DVD-ROM], Vancouver, Canada. pp. 8743–8750.

Ruessink, B.G., Coco, G., Ranasinghe, R., Turner, G., 2007. Coupled and noncoupled behavior of three-dimensional morphological patterns in a double sandbar system. J. Geophys. Res. 112, C07002. doi:10.1029/2006JC003799.

Sallenger, A.H., Holman, R.A., Birkemeier, W., 1985. Storm-induced response of a nearshore-bar system. Mar. Geol. 64, 237–257.

Shepard, F.P., 1952. Revised nomenclature for depositional coastal features. Bull. Am. Assoc. Petrol. Geol. 36, 1902–1912.

Short, A.D., 1979. Three-dimensional beach-stage model. Journal of Geology 87, 553–571.

Short, A.D., 1991. Meso-macro tidal beach morphodynamics—an overview. J. Coast. Res. 7 (2), 417–436.

Short, A.D., 1992. Beach systems of the central netherlands coast: processes, morphology and structural impacts in a storm driven multi-bar system. Mar. Geol. 107, 103–137.

Short, A.D., 1999. Handbook of Beach and Shoreface Morphodynamics. Wiley.

Short, A.D., Aagaard, T., 1993. Single and multi-bar beach change models. J. Coast. Res. SI 15, 141–157.

Sénéchal, N., Bonneton, P., Dupuis, H., 2002. Field experiment on secondary wave generation on a sbarred beach and the consequent evolution of energy dissipation on the beach face. Coast. Eng. 46, 233–247.

Sénéchal, N., Dupuis, H., Bonneton, P., Howa, H., Pedreros, R., 2001. Observation of wave transformation in the surf zone over a gently sloping beach. Oceanologica Acta 24 (6), 545–546.

Sénéchal, N., Dupuis, N., Bonneton, P., 2003. Preliminary hydrodynamic results of a field experiment on a barred beach, truc vert beach on October. Ocean Dynamics 54, 408–414.

Sonu, C.J., 1973. Three-dimensional beach changes. J. Geology 81, 42–64.

Thornton, E.B., MacMahan, J., Sallenger Jr., A.H., 2007. Rip currents, mega-cusps, and eroding dunes. Mar. Geol. 240, 151–167.

Van Enckevort, I.M.J., Ruessink, B.G., 2003. Video observations of nearshore bar behaviour. Part 2: alongshore non-uniform variability. Cont. Shelf Res. 23, 513–532.

Van Enckevort, I.M.J., Ruessink, B.G., Coco, G., Suzuki, K., Turner, I.L., Plant, N.G., Holman, R.A., 2004. Observations of nearshore crescentic sandbars. J. Geophys. Res. 109, C06028. doi:10.1029/2003JC002214.

Wright, L.D., Short, A.D., 1984. Morphodynamic variability of surf zone and beaches: a synthesis. Mar. Geol. 56, 93–118.

Wright, L.D., Short, A.D., Green, M.O., 1985. Short term changes in the morphodynamic of beaches and surf zones: an empirical predictive model. Mar. Geol. 62, 339–364.

D.3 Near-shore swell estimation from a global wind-wave model : Spectral process, linear and articficial neural network models

Matthew Browne, Bruno Castelle, Darrell Strauss, Rodger Tomlinson, Michael Blumenstein, Chris Lane

Coastal Engineering, Vol. 54, pp. 445-460, 2007

Available online at www.sciencedirect.com
ScienceDirect
Coastal Engineering 54 (2007) 445–460
Coastal Engineering
An International Journal for Coastal, Harbour and Offshore Engineers
www.elsevier.com/locate/coastaleng

Near-shore swell estimation from a global wind-wave model: Spectral process, linear, and artificial neural network models

Matthew Browne [a,*], Bruno Castelle [a], Darrell Strauss [a], Rodger Tomlinson [a], Michael Blumenstein [b], Chris Lane [c]

[a] Griffith Centre for Coastal Management, Gold Coast campus, Griffith University, PMB 50 Gold Coast Mail Centre QLD 9726, Australia
[b] School of Information and Communications Technology, Griffith University, Australia
[c] CoastalWatch Australia, Suite 3, 66 Appel Street, Surfers Paradise QLD 4217, Australia

Received 10 March 2006; received in revised form 23 October 2006; accepted 13 November 2006
Available online 22 January 2007

Abstract

Estimation of swell conditions in coastal regions is important for a variety of public, government, and research applications. Driving a model of the near-shore wave transformation from an offshore global swell model such as NOAA WaveWatch3 is an economical means to arrive at swell size estimates at particular locations of interest. Recently, some work (e.g. Browne et al. [Browne, M., Strauss, D., Castelle, B., Blumenstein, M., Tomlinson, R., 2006. Local swell estimation and prediction from a global wind-wave model. IEEE Geoscience and Remote Sensing Letters 3 (4), 462–466.]) has examined an artificial neural network (ANN) based, empirical approach to wave estimation. Here, we provide a comprehensive evaluation of two data driven approaches to estimating waves near-shore (linear and ANN), and also contrast these with a more traditional spectral wave simulation model (SWAN). Performance was assessed on data gathered from a total of 17 near-shore locations, with heterogenous geography and bathymetry, around the continent of Australia over a 7 month period. It was found that the ANNs out-performed SWAN and the non-linear architecture consistently out-performed the linear method. Variability in performance and differential performance with regard to geographical location could largely be explained in terms of the underlying complexity of the local wave transformation.

Keywords: Artificial neural networks; Near-shore wave transformation; Wave modeling; Wave estimation

1. Introduction

Knowledge of swell conditions at specific near-shore locations is important for coastal research, marine engineering, and policy development. Although global swell models are an effective approximation of open swell conditions, they become less accurate in the near-shore zone. Many forms of remote sensing suffer from similar issues; satellite observations, for example, due to the manner in which they are sensed and averaged, normally pertain only to deeper ocean locations, typically 30 km away from the shoreline (Kalra et al., 2005). Variations in near-shore bathymetry, local wind-generated seas and the effects of artificial structures transform deep water swell due to reflection, shoaling, refraction, diffraction and breaking (Londhe and Deo, 2004). At a particular location, local topography may lead to attenuation or accentuation of long or short period swells, either directly, or by the contribution of local wind conditions. This makes the estimation of onshore wave heights, even given reliable offshore swell measurements, a non-trivial exercise.

The ability to estimate and predict onshore wave heights at the shore is of significant public interest in countries such as Australia, due to the high level of public activity in or near the break zone. There is a clear need for this data both as a general advisory to the public concerned with recreational use of the near-shore zone, and for life-guards concerned with providing advice in order to ensure public safety. Much of the Australian coastline is characterised by both high density structures and highly dynamic sediment evolution, and monitoring of onshore wave heights is important for monitoring and managing coastal development. Finally, scientific and engineering evaluations of particular locations and structures in this zone depend on reliable data on wave action.

* Corresponding author. Tel.: +61 7 3826 7267.
E-mail address: matthew.browne@csiro.au (M. Browne).

0378-3839/$ - see front matter © 2006 Elsevier B.V. All rights reserved.
doi:10.1016/j.coastaleng.2006.11.007

Currently, estimation of onshore wave heights from visual inspection is carried out on a regular basis, and this information is broadcast through private and commercial channels. The conventional approach is for this estimation to be performed and recorded manually by human observers, using a combination of heuristics, local knowledge, and offshore wind and wave models published by government agencies. Numerical models based on wave propagation theory have been neglected as a practical onshore wave height estimation tool due to a combination of factors: complexity of implementation, high amounts of processor time required, the need for accurate local bathymetric surveys, and general inaccuracy, even when the previous conditions are met. However, there is a clear need to substitute an objective and automated approach for human observations of onshore wave activity, which are expensive, time consuming, and prone to the usual forms of human failure and error.

In academic research, the propagation of swell in near-shore areas is conventionally studied by running either an actual, or a virtual simulated physical model (Londhe and Deo, 2004). Physical scale models require a significant investment of resources for their construction and simulation. For this reason, physical modeling using numerical computer simulation incorporating the local physical environment and local swell conditions is often used. The Simulating Waves NearShore (SWAN) numerical model is an example of a popular approach for modeling wave propagation in the near-shore zone. However, numerical models themselves require care and expertise in their implementation. For example, a wave prediction system based on a numerical model must often contend with physical processes on a wide range of scales. These techniques are also sensitive to accuracy of the bathymetric data for the study area, and the quality of driving data at the model boundaries. Typically, hours of processing time are required for simulation of a region with adequate temporal and spatial resolution. Due to technical issues that may arise, results are sometimes unsatisfactory, especially in the break-zone.

Empirical wave recordings and observations are used to calibrate and validate theoretical (Booij et al., 1999a) and empirical (Komar and Gaughan, 1972; Caldwell, 2004) approaches to modelling the wave transformations that occur as they progress from deep to shallow water. The method of Caldwell (2004), for instance, was based on comparisons between buoy-measured H_s in deep water in close proximity to locations where visual observations were taken of trough to crest vertical wave height at the break point. There has been interest in developing empirical, data-driven models of near-shore wave characteristics for many years (Booij et al., 1999a). For example, an empirical method of obtaining surf height at the breakpoint from offshore wave data was derived from observations by Komar and Gaughan (1972). Following this approach, an alternative measure of surf height, H_{surf}, was developed for coastal zones with narrow shelves, steep bottom slopes and high refraction,

$$H_{surf} = H_b K_r(H_b), \tag{1}$$

where K_r is the empirical estimation of the refraction coefficient as a function of shoaling and buoy-estimated breaker height, H_b:

$$K_r = -0.0013H_b^2 + 0.1262H_b + 0.3025. \tag{2}$$

The method is based on comparisons between buoy-measured H_s in deep water in close proximity to locations where visual observations were taken of trough to crest vertical wave height at the break point. We note the particular operational definitions of wave height in the break zone (e.g. tough-crest height, assessed visually): it should be recognised that it is usually impossible to measure breaking wave height using a fixed wave gauge, since the spatial point of breaking varies with incident wave conditions. Estimating near-shore wave height through modelling the shallow-water wave transformation via simplified equations that are optimised using real-world data might be termed a 'semi-empirical' approach.

In their application to analysis in the physical sciences, artificial neural networks (ANNs) can be regarded as a strongly empirical, as opposed to a model-based approach to estimate and predict wave behaviour (Deo and Jagdale, 2003). ANNs are a flexible learning architecture which rely on the presentation of input and target data, rather than a theoretical model, for the estimation of an underlying physical relationship. As general purpose function approximators, ANNs purposely impose no constraints on the final model generated, although the size of the neural network necessarily limits the overall complexity of the modelled function. In their role of associating temporally, spatially, or modally distinct measurements of wind-wave activity, they must approximate the physical propagation of wave energy. The effect of local geography or bathymetry is inferred from the co-variation of input-target pairs, rather than explicitly determined. Thus, a representative corpus of training data is essential for the function approximation potential of an ANN to be realised.

The use of ANNs has been reported for numerous applications in the geological and marine sciences, and in particular have been used for forecasting wave climate time series (Deo et al., 2001; Agrawal and Deo, 2002). Tsai and Lee (1999) utilised neural networks for forecasting tidal variability and Tsai et al. (1999) used neural networks for forecasting wave heights at near-shore locations, using measurements from other locations as input, finding that using multiple sites as input increased the accuracy of predictions. Some work has tested ANNs for specific oceanic structural and engineering tasks: (Mase and Kitano, 1999) used feed-forward networks to estimate wave force impact on a marine structure, and (Mase et al., 1995) found that a similar ANN architecture accurately predicted damage levels on a breakwater resulting from wave action. ANNs have recently been shown to produce superior estimates of wave spectra from wave parameters than those provided by theoretical or statistical predictions (Naithani and Deo, 2005). Non-linear empirical models have been shown to approximate well the underlying wave physics (Tolman et al., 2005).

ANNs have been applied to estimating missing wave buoy data (Balas et al., 2004), and recently Kalra et al. (2005) have

detailed an ANN-based effort to map offshore wave data to coastal locations, reporting superior performance of ANNs compared to a linear statistical approach. The authors estimated wave activity in the near-shore region from satellite monitoring at offshore locations. Scotto and Soares (2000) concluded that in estimating significant wave height of sea-states using non-linear autoregressive (AR) models, linear models satisfactorily modelled the lower statistical moments, but non-linear models better approximated the higher moments such as skewness and kurtosis. Also using an AR model, Ho and Yim (2005), recently demonstrated the feasibility of interpolating missing buoy data between two wave measuring stations.

Neural networks have been demonstrated to be superior to conventional approaches for forecasting significant wave height in open water, in a variety of situations (Deo et al., 2002, 2001; Deo and Kumar, 2000; Balas et al., 2004). Rao and Mandal (2005) focused on ANNs as an alternative to numerical modelling for estimating wave-fields generated by cyclone events. Browne et al. (2006) emphasised the use of ANNS for bridging of modes of observation (i.e. global model output/logged buoy data/visual observations) in the context of bringing offshore estimates to estimate activity in the near-shore zone. It has been shown that non-linear ANN approaches outperformed linear statistical and numerical modelling, in the estimation of both human observations at the beach, and wave-rider buoy data.

Apart from the welcome comparison of ANN performance with that of linear regression by Kalra et al. (2005), there have been insufficient comparisons of ANNs with other forms of swell estimation, such as linear predictors, and numerical modelling. Work reported by Browne et al. (2006) represented a first step towards a systematic comparison between ANNs, statistical, and numerical modelling approaches. However, this work needs to be extended to include a greater variety of geographical areas, and longer study time periods.

As neural networks are unconstrained general-purpose function approximators, with potentially a very large number of degrees of freedom, care must be taken in their application in order to ensure that the underlying function is in fact well approximated, allowing in turn for good generalisation to new data. *Over-fitting*, which results from a high ratio of model degrees-of-freedom to presented data, is a particularly common pitfall for engineering and scientific applications of ANNs. These issues have led to concerns being raised regarding the validity of previous work in applying ANNs to wave estimation. For example, a method of wave forecasting using neural networks was recently reported by Makarynskyy (2004), and subsequently challenged by Medina (2005) due to issues related to over-fitting, lack of baseline performance comparisons, and an insufficient degree of cross-validation. Inappropriate application of ANNs often leads to spuriously high performance estimates. It must be also noted that as a strongly empirical approach, ANNs do not provide the insight into wave propagation processes that is provided by full-scale numerical modelling. However, the advantages include computational efficiency and potentially greater predictive power, without the need for detailed geographic information, or the laborious testing of a range of physical model parameters.

Recent research is increasingly focusing on the use of neural networks in the role of an unconstrained empirical function approximation tool for estimating the relationship between geographically or temporally displaced observations of wave height. However, to-date little attention has been paid to applying them to approximate the deep-to-shallow water wave transformation. The current paper is focused on mapping offshore global wind-wave observations to activity observed at particular onshore locations. This requires the model to incorporate the effects of a number of physical processes such as bottom friction, diffraction and refraction, generated by an interaction of local geography and bathymetry with the offshore wave field. Recent studies by Kalra et al. (2005) and Browne et al. (2006), have reported superior performance by ANNs. However, each study considered only a single geographical location for a relatively short time, which prevented strong conclusions regarding the relative efficacy of ANNs to be drawn.

The present study attempts definitive testing of ANNs for modeling the near-shore wave transformation: bringing global ocean wave model output to near-shore locations, and demonstrating a potentially useful tool for emulating expensive surf reporter observations. A comprehensive evaluation of empirical methods is attempted by considering a total of 17 onshore locations across 5 geographical regions distributed across the continent of Australia, for a period of 8 months. ANNs are compared with baseline, linear and model-based approaches and explanations for the differential performance are provided. Detail is provided on the technical implementation and validation of ANN performance, which as discussed above, is critical for establishing an accurate benchmark of performance. The SWAN numerical model is applied for performance comparisons, and in order to investigate the characteristics of the study areas.

2. Methods

2.1. Study regions

As noted above, in order to achieve a comprehensive evaluation of spectral, linear, and ANN based modeling, the present study considered five regions in Australia, each with distinct properties, in both in terms of bathymetry and wave climate. This is illustrated in the regional maps (Figs. 1–3). The red filled circles denote the onshore locations considered in this study, while the red stars indicate the theoretical location of the NOAA WW3 grid point. Fig. 1 maps the bathymetry of each region, which shows a range of profiles, from open, exposed beaches, to sheltered bays, along with a range of island and headland features. Fig. 2 plots the mean wave height, as estimated by the SWAN model from the NOAA data over the time period of interest: this may be considered in conjunction with Table 1 to provide a view of regional and intra-regional wave climate variability. Finally, Fig. 3 shows the degree of linear relationship (correlation r) of the SWAN model output at each point within each region, to that region's NOAA WW3 grid point, over the study period. Lighter values indicate a

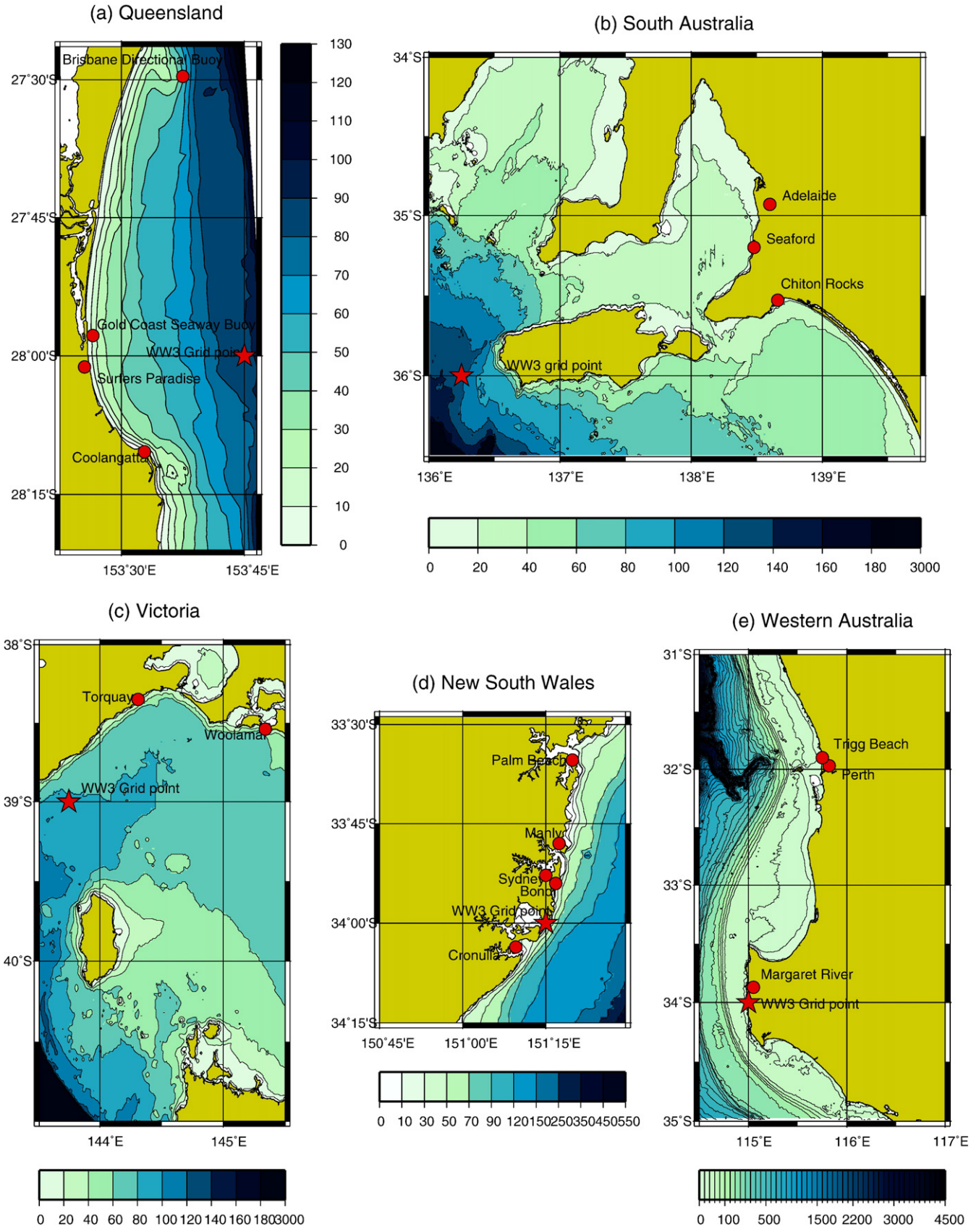

Fig. 1. Bathymetry for five of the study regions.

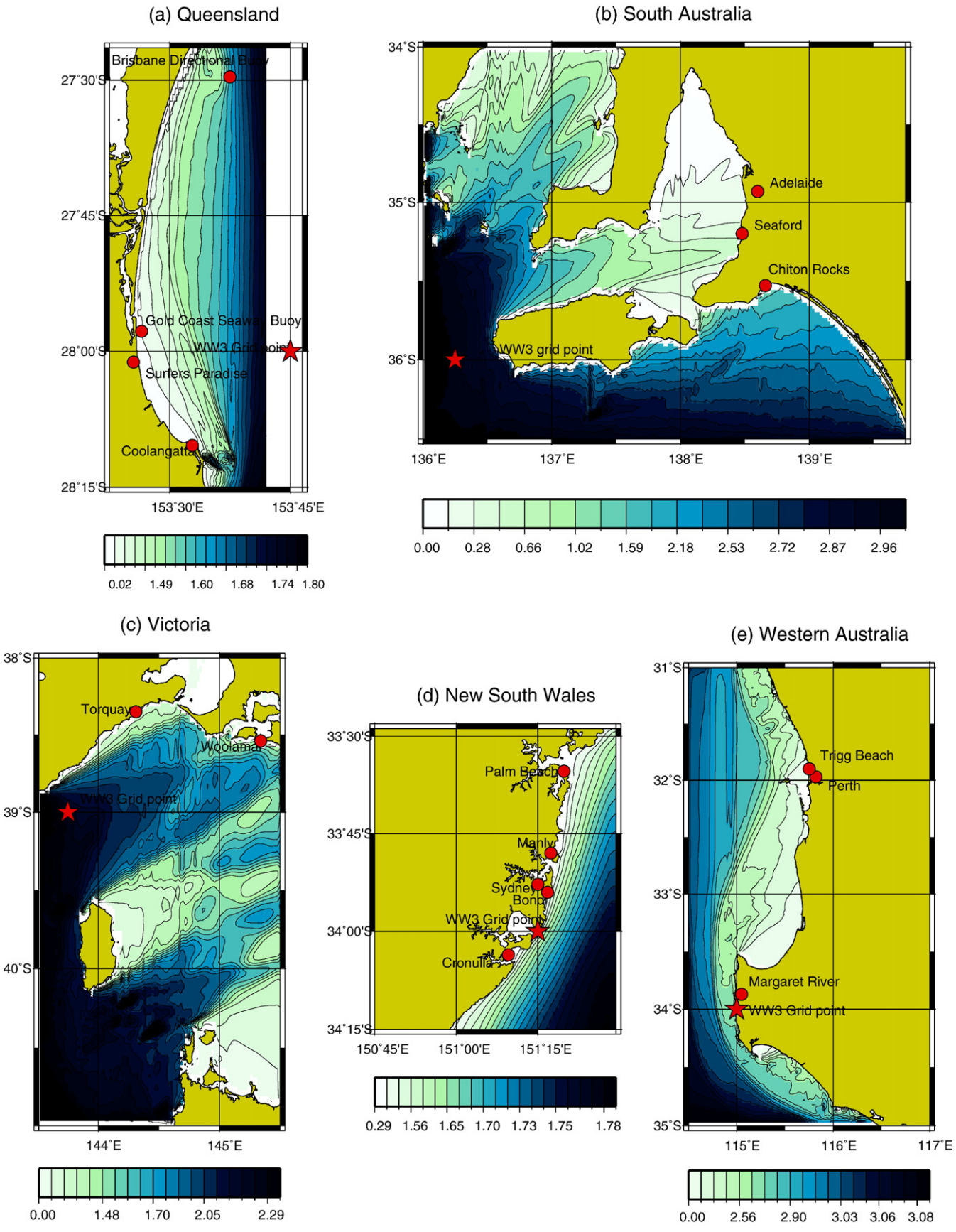

Fig. 2. Mean significant wave height as estimated by the SWAN model when driven by NWW3 over the study period.

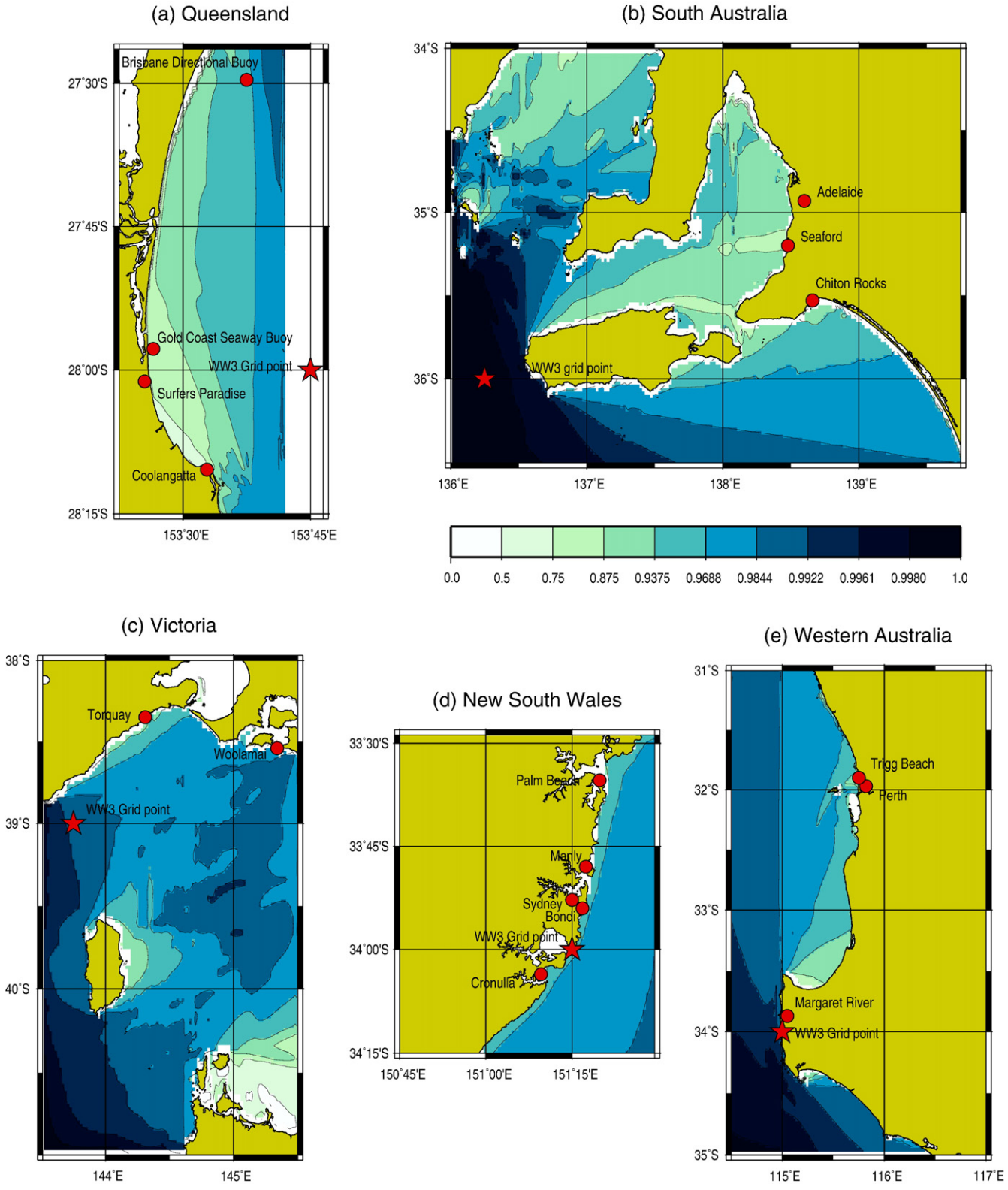

Fig. 3. Normalised correlation coefficient r between the NOAA driving input and SWAN output significant wave height over the study period. Lighter shades indicate local regions affected by more complex wave transformations: i.e. a greater proportion of observed wave height variability is not linearly related to the wave height at the model boundaries.

smaller proportion of the variability being explained by a linear relationship with offshore conditions, and hence indicate a greater proportion of non-linear wave effects in the SWAN model output at that point. We consider this to be a useful guide to the model-estimated complexity in the wave-transformation over each locale with each study region.

Table 1
Cross-correlation matrix and univariate mean and higher moments of significant wave heights H_s recorded at NOAA WW3 grid points from 12/01/05 to 9/8/05

	NNSW	QLD	SA	SNSW	VIC	WA
North New South Wales (153.75 −31)	–					
Queensland (153.75, −28)	.75	–				
South Australia (136.25, −36)	−.23	−.24	–			
South New South Wales (151.25, −34)	.80	.49	−.24	–		
Victoria (143.75, −39)	−.16	−.23	.77	−.17	–	
Western Australia (115.00, −34)	−.02	.12	.21	−.11	−.02	–
Mean $\bar{H}_s$	1.95	1.89	2.91	1.47	2.31	3.06
Standard deviation $\sigma^2(H_s)$	0.85	0.65	1.01	0.78	0.84	1.20
Skewness $\sigma^3(H_s)$	1.48	0.84	0.65	1.87	0.98	1.06
Kurtosis $\sigma^4(H_s)$	6.02	4.26	3.02	8.32	3.88	4.23

2.2. Data

In the following sections we describe the various forms of data used in this study; bathymetric surveys used as input to the numerical physical model, driving variables from NOAA WaveWatch 3 (NWW3), and visual surf reporter estimates of H_s.

2.2.1. NOAA WaveWatch 3

The driving variables for all models tested in this study were drawn from global wave model data gathered from the NWW3 model at 6 grid locations in various regions off the coast of Australia from 12/01/05 to 9/8/05. The NWW3 model provided updates four times daily, at 4 am, 12 pm (midday), 6 pm, and 12 am (midnight). The NWW3 variables were; significant wave height, primary swell direction, primary swell period, wind direction, wind speed, secondary swell direction, secondary swell period, wind wave direction, and wind wave period. NWW3 generates swell forecasts at every 3 h from +3 to +180 h ahead of the current time as well as a single analysis at 0 h, which represents the model state, given current measured data. In the present study, only the 0 h state information was used. For the purpose of presenting the NWW3 variables to the ANNs for empirical prediction, variables in degree format present an issue because of the discontinuity at the 0°/360° point. Each of the directional variables; primary swell direction, wind direction and wave direction were transformed to Cartesian co-ordinates ('northerliness' D^N and 'easterliness' D^E):

$$D^N = \cos\left(\frac{\pi D}{180}\right), D^E = \sin\left(\frac{\pi D}{180}\right). \quad (3)$$

The locations of the NWW3 grid points are shown in Table 1. Table 1 displays the cross-correlation matrix between H_s at the various grid points. As expected, there are correlations between nearby grid points; i.e. between Queensland (QLD) and North New South Wales (NNSW) regions, and between the South Australia (SA) and Victorian (VIC) grid points. However, 11 of the 15 cross-correlations are below 0.3, indicating that overall, the swell conditions around the continent had a relatively high degree of statistical independence during the study period. This entails that to a large extent, although the regions were considered over the same time period, the study regions represent independent sources of data for the purpose of testing the estimation methods. The univariate statistics of the NWW3 estimated H_s in Table 1 also illustrate the heterogeneous nature of the offshore swell conditions around Australia. Southern areas (i.e. VIC, SA and Western Australia (WA)) had higher and more variable seas, whilst NNSW and QLD were characterised by greater skewness in H_s, primarily due to the large contribution that intermittent tropical storm events make to the overall variability of H_s in these areas.

2.2.2. Bathymetric data

Bathymetric data is a key parameter to undertake near-shore wave modelling. Bathymetric data were required for 5 areas of the Australian Coast from deep water to shallow water in order to compute the wave propagation from the NWW3 output grid points to the surf reporter locations. The publicly available Geoscience Australia bathymetric database (www.ga.gov.au) was used to generate the whole bathymetry of 4 areas.

The database contains data around the Australian margin since 1963 from a variety of systems and levels of accuracy. A total of 931 surveys are currently registered, whose extent is 34N–79S, 90–180E. The typical point data spacing is 25–200 m. Approximately 20% of these surveys were acquired by Geoscience Australia, the other component being surveys from other institutions, such as oil exploration companies and the National Geophysical Data Centre to which various institutions have contributed. Swath bathymetry in deep water, laser airborne depth sounder (LADS) data, points digitised from Australian Hydrographic Service charts on the shelf and predicted bathymetry from satellite altimetry (Smith and Sandwell, 1997) have been brought together. The database grid was computed at a cell size of 0.01 (36″ or 1111 m) as a compromise between conveying detail and limiting the file size.

For the Gold Coast area, accurate bathymetry data were provided by the Gold Coast City Council. ETA lines covering the Gold Coast from the Gold Coast Seaway to Tweed Heads

Table 2
Counts of surf reporter observations and total number of days monitored from 12/01/05 to 9/8/05

Region	Beach	Observations (N)	Days (N)
QLD	Surfer's Paradise	231	201
	Sunshine Coast	228	203
WA	Margaret River	229	202
	Perth	223	204
SA	Seaford	222	206
	Chiton Rocks	210	206
NNSW	Mid Coast	361	206
	North Coast	216	206
SNSW	Bondi	374	200
	Cronulla	362	204
	Manly	377	207
	Palm Beach	330	200
	South Coast	236	200
VIC	Woolamai	275	200
	Portsea	268	200
	Torquay	305	206
	Warrombool	243	200

Observations were recorded more than once/day during more dynamic surf conditions.

Table 3
Mean and higher moments of surf reporter significant wave height H_s observations (in metres) from 12/01/05 to 9/8/05

Region	Beach	$\bar{H}_s$	$\sigma^2(H_s)$	$\sigma^3(H_s)$	$\sigma^4(H_s)$
QLD	Surfer's Paradise	0.96	0.35	0.0076	0.0475
	Sunshine Coast	0.91	0.33	0.0086	0.0540
WA	Margaret River	2.02	0.66	0.0009	0.0177
	Perth	0.60	0.28	0.0092	0.0354
SA	Seaford	0.45	0.22	0.0068	0.0324
	Chiton Rocks	1.37	0.31	0.0003	0.0231
NNSW	Mid Coast	0.66	0.43	0.0128	0.0419
	North Coast	1.03	0.33	0.0116	0.0627
SNSW	Bondi	0.88	0.38	0.0132	0.0592
	Cronulla	0.88	0.39	0.0139	0.0608
	Manly	0.88	0.38	0.0126	0.0577
	Palm Beach	0.89	0.38	0.0128	0.0570
	South Coast	0.87	0.45	0.0081	0.0349
VIC	Woolamai	1.40	0.44	0.0002	0.0259
	Portsea	1.46	0.46	0.0034	0.0344
	Torquay	0.85	0.39	0.0085	0.0366
	Warranambool	0.89	0.41	0.0066	0.0360

and refined bathymetric surveys around Burleigh Heads and Currumbin Creek estuary were combined with the Geoscience Australia database for the offshore information (typically used from 20 to 80 m depth).

2.2.3. Surf reporter data

In collaboration with the Australian surf monitoring firm CoastalWatch™, the study relied on a network of professional surf reporters for performing daily visual estimates of significant wave height at each of the 17 beach locations. Estimates were made using a mobile internet link and time-stamped. Visual inspection was usually performed once per day, between 6 am and 8 am, but during dynamic periods a second visual estimate was made in the afternoon. Table 2 displays the number of observations and number of days for which observations were recorded for each of the 17 beaches. As the surf reports were the limiting source of data for optimizing the models, this table also summarizes the number of input/target data pairs available for analysis. Table 3 displays the univariate statistics for the surf reporter observations at each beach study site. As expected, both overall significant wave height and variability are significantly less than the open ocean estimates produced by NWW3. With reference to the regional maps and the NWW3 statistics, it may be seen that there is variability between the various study areas corresponding to both offshore swell characteristics between regions, and local geographic features. At certain nearby beaches, where local geography and bathymetry is relatively homogeneous, there is a high degree of similarity between the univariate statistics of the beaches. This is supported by Table 4, which displays the normalised bivariate correlations in H_s between the surf reporter sites. The Sydney, New South Wales (SNSW) beaches in particular, which are grouped in a relatively small region in and around Sydney, and similar exposure to offshore swell, have a high degree of interdependence. However, in general there is wide variability in the univariate moments due to the different swell conditions prevailing in the different continental locations, and considerable variety in local geography and bathymetry.

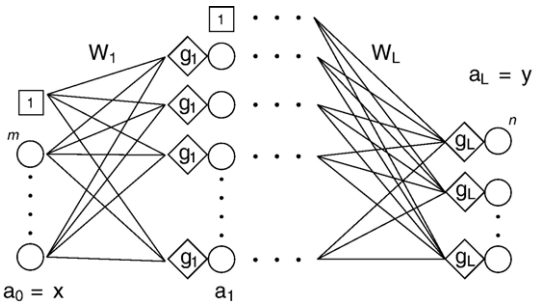

Fig. 4. Standard feed-forward ANN architecture.

Table 4
Cross-correlation matrix r of significant wave H_s at NOAA WW3 grid points from 12/01/05 to 9/8/05

		Queensland		Western Australia		South Australia		North NSW		South NSW					Victoria			
		SP	SC	MR	PE	SF	CR	MC	NC	BI	CR	MY	PB	SC	WO	PO	TO	WL
QLD	Surfer's Paradise SP	–																
	Sunshine Coast SC	**.96**	–															
WA	Margaret River MR	.13	.08	–														
	Perth PE	.12	.09	**.89**	–													
SA	Seaford SF	.15	.15	.12	.14	–												
	Chiton Rocks CR	.12	.12	−.10	−.09	**.45**	–											
NNSW	Mid Coast MC	**.41**	.37	−.01	−.03	−.11	−.05	–										
	North Coast NC	**.77**	.71	.27	.24	.05	.03	**.39**	–									
SNSW	Bondi BI	.20	.11	.04	.01	−.31	−.23	**.65**	.36	–								
	Cronulla CR	.16	.07	.01	−.01	−.32	−.23	**.64**	.33	.98	–							
	Manly MY	.21	.11	.03	.01	−.31	−.23	**.65**	.37	.99	.97	–						
	Palm Beach PB	.21	.12	.04	.02	−.30	−.22	**.66**	.36	.99	.97	.99	–					
	South Coast SC	.12	.05	.06	.07	−.20	−.23	**.59**	.37	.74	.76	.74	.73	–				
VIC	Woolamai WO	−.01	.01	−.20	−.22	.30	**.62**	−.10	−.07	−.12	−.12	−.12	−.12	−.18	–			
	Portsea PO	−.01	−.01	−.13	−.19	.27	**.59**	−.13	−.06	−.10	−.11	−.11	−.10	−.17	**.91**	–		
	Torquay TO	−.00	.00	−.21	−.25	.15	**.67**	−.04	−.02	−.06	−.06	−.08	−.07	−.10	**.83**	.83	–	
	Warranambool WL	−.08	−.08	−.24	−.30	.10	**.54**	−.01	−.07	−.02	−.01	−.04	−.03	−.07	**.71**	.69	.79	–

Boldface indicates correlation r>.30.

Table 5
Mean absolute error (MAE) in cm of NOAA WW3 derived significant height estimates with respect to surf reporter observations

Region	Beach	Baseline		Linear ANN				Non-linear ANN				Ensemble	t**	SWAN
		Raw	Scaled	Training		Validation		Training		Validation				
		MAE	MAE	$\overline{MAE}$	σ(MAE)	$\overline{MAE}$	σ(MAE)	$\overline{MAE}$	σ(MAE)	$\overline{MAE}$	σ(MAE)	MAE		
QLD	Surfer's Paradise	91.77	23.30	17.70	0.12	17.84	1.32	14.93	0.96	16.12	1.05	13.60	3.22*	32.31
	Sunshine Coast	96.33	22.78	16.75	0.07	16.77	0.73	14.17	0.93	15.51	0.96	12.40	3.32*	
WA	Margaret River	102.89	36.64	34.20	0.17	34.74	1.30	23.75	1.46	26.69	1.64	21.34	12.17*	65.51
	Trigg Beach	244.11	13.32	13.46	0.13	13.80	0.55	11.15	0.67	12.05	0.89	10.16	5.25*	62.77
SA	Seaford	245.64	13.82	14.28	0.06	14.49	0.98	11.92	0.48	12.83	0.96	11.12	3.83*	15.20
	Chiton Rocks	152.84	21.15	20.56	0.04	20.64	0.52	16.17	0.76	17.42	0.76	15.12	11.02*	40.93
NNSW	Mid Coast	127.92	22.91	23.42	0.06	22.97	1.19	18.65	1.03	19.62	1.13	17.19	6.46*	
	North Coast	90.93	21.41	20.28	0.22	19.98	0.67	17.13	1.35	18.15	1.17	15.08	4.30*	
SNSW	Bondi	59.54	19.47	21.64	0.13	21.73	1.31	18.12	0.52	19.41	1.04	16.96	4.38*	
	Cronulla	60.26	19.94	22.22	0.15	21.85	1.09	18.76	0.75	20.25	0.93	17.26	3.53*	
	Manly	60.18	19.86	21.71	0.09	21.40	1.50	18.41	0.65	19.49	1.19	17.33	3.15*	50.06
	Palm Beach	58.97	19.72	21.96	0.19	22.26	0.88	17.69	0.65	19.75	1.34	16.42	4.95*	
	South Coast	64.73	28.06	26.97	0.11	27.45	1.33	22.14	1.70	24.20	1.53	20.56	5.06*	
VIC	Woolamai	89.94	29.62	27.88	0.09	28.30	1.05	23.93	0.86	25.64	1.47	22.70	4.67*	38.72
	Portsea	83.22	28.81	28.61	0.14	28.72	1.44	24.49	0.89	26.61	1.78	22.62	2.92*	
	Torquay	143.57	24.18	23.73	0.13	24.34	1.15	19.16	1.00	21.03	1.45	17.83	5.66*	34.98
	Warranambool	141.49	27.93	26.00	0.11	25.96	1.07	23.90	0.72	25.29	1.23	22.78	1.30	

* indicates 1-tailed t-statistics significant (N=5, p<0.01) ** t-statistics: two sample, one-tailed t-test testing $H(\overline{MAE}^{val}_{nl} < \overline{MAE}^{val}_{lin})$.

2.3. Analysis and simulation

2.3.1. ANN background

ANNs are widely accepted as a valuable tool for modeling, approximation, and classification (Kostanic, 2001; Bishop, 1995; Ripley, 1996). The common fully inter-connected feed-forward architecture implements a mapping $\mathbf{y}=f(\mathbf{x}):\Re^m \rightarrow \Re^n$ and is optimized by providing multiple (assumed noisy) paired samples of the input and target output $\{\mathbf{i}_p \in \Re^m, t_p \in \Re^n\}$. The transfer function g, which generates a unit's output given net activation from connections to units in the previous layer, should generally be smooth and have a well bounded range for any input; e.g. $g:(-\infty, \infty)\rightarrow(-1, 1)$ for the tan-sigmoidal case (logistic and gaussian functions are also common basis functions). Assuming the activation function at each layer $\mathbf{i}=\{1, \ldots, L\}$ is homogenous, an ANN implements the function

$$f(\mathbf{x}) = f(\mathbf{a}_0) = h_L(h_{L-1}(h_{L-\ldots}(h_1(\mathbf{a}_0)))) \quad (4)$$

with the layer transformation h defined by

$$\mathbf{a}_i = h_i(a_{i-1}) = g_i(\mathbf{W}_i[\mathbf{a}^T_{i-1}1]) \quad (5)$$

where the set of free parameters (termed weights) in the system $\{\mathbf{W}_i\}$ determine the particular non-linear mapping, noting that

Table 6
Correlation R of NOAA WW3 derived surf height estimates with surf reporter observations

Region	Beach	Baseline		Linear ANN				Non-linear ANN				Ensemble	$H(\bar{r}^{val}_{nl} > \bar{r}^{val}_{lin})$	SWAN
		Raw	Scaled	Training		Validation		Training		Validation				
		$\bar{r}$	$\bar{r}$	$\bar{r}$	$\sigma(r)$	$\bar{r}$	$\sigma(r)$	$\bar{r}$	$\sigma(r)$	$\bar{r}$	$\sigma(r)$	$\bar{r}$	t-statistic	
QLD	Surfer's Paradise	.49	.49	.73	.008	.71	.036	.83	.027	.79	.037	.86	4.84*	.72
	Sunshine Coast	.46	.46	.72	.008	.71	.026	.83	.025	.80	.029	.87	7.42*	
WA	Margaret River	.77	.77	.79	.005	.78	.018	.88	.011	.86	.022	.90	8.23*	.73
	Trigg Beach	.79	.79	.80	.015	.80	.028	.87	.018	.85	.023	.89	4.82*	.72
SA	Seaford	.67	.67	.63	.030	.61	.045	.75	.020	.70	.027	.78	5.81*	.63
	Chiton Rocks	.58	.58	.62	.008	.64	.029	.77	.021	.74	.028	.81	8.63*	.40
NNSW	Mid Coast	.72	.72	.74	.004	.73	.040	.83	.021	.80	.039	.86	3.90*	
	North Coast	.34	.34	.52	.014	.52	.042	.74	.058	.68	.070	.81	6.28*	
SNSW	Bondi	.81	.81	.75	.005	.76	.019	.84	.0093	.82	.021	.86	6.86*	
	Cronulla	.80	.80	.75	.005	.75	.026	.84	.011	.79	.016	.87	4.63*	
	Manly	.80	.80	.75	.004	.75	.036	.84	.0093	.81	.025	.86	4.55*	.76
	Palm Beach	.81	.81	.75	.006	.75	.035	.85	.011	.81	.036	.87	4.15*	
	South Coast	.69	.69	.72	.006	.70	.047	.80	.029	.76	.032	.84	3.16*	
VIC	Woolamai	.67	.67	.69	.003	.68	.033	.78	.018	.74	.034	.80	3.97*	.62
	Portsea	.70	.70	.69	.007	.69	.029	.78	.015	.74	.030	.81	3.53*	
	Torquay	.68	.68	.70	.007	.71	.016	.81	.019	.78	.030	.84	7.35*	.70
	Warranambool	.59	.59	.63	.004	.64	.040	.71	.022	.69	.031	.75	2.91*	

* indicates 1-tailed t-statistic significant (N=5, p<.01).

$\mathbf{a}_0=\mathbf{x}$ is an m element vector, $\mathbf{a}_L=\mathbf{y}$ an n element vector, and necessarily the dimensions $\{d_i^1, d_i^2\}$ of $\mathbf{W}_i$ have the constraints $d_i^1=m+1$, $d_L^2=n+1$, and $d_i^1=d_{i-1}^2$. This notation represents the constant or bias term as a unit input appended to the output vector of the previous layer. ANNs are usually conceptualised as a series of neural layers, with forward interconnections between subsequent layers, as shown in Fig. 4.

A common application of feed-forward networks for estimation involves a fixed architecture or topology, with two or three layers L, and an arbitrary number of neurons (defined by d_i^2) in each layer. Training a neural network usually involves minimising an error function (e.g. for mean-square error (MSE), $\epsilon_n=\sum_p(\mathbf{y}_p-\mathbf{t}_p)^2$), utilising local gradient search algorithms operating on $-\delta\epsilon_n/\delta\{\mathbf{W}_i\}$, the derivative of the error function with respect to the free weight parameters in the network. Sophisticated and efficient search algorithms, such as the Levenburg-Marquardt method or conjugate gradient descent (Marquardt, 1963; Kan and Timmer, 1989), along with modern computational resources, allow for fast optimisation of medium sized networks. Single layer, or linear feed-forward networks converge to a global optimum. The function-approximation power of non-linear ANNs with one or more hidden layers is based on the non-linearity of the basis functions in the hidden layers. However, this property also entails the presence of *local minima* in the error function. ANN implementation requires acknowledgement that optimisation based on local gradients may be expected to yield solutions located in some form of local minima: i.e. good but not optimal solutions. Multiple runs with random initial $\{\mathbf{W}_i\}$ are a straight-forward way to alleiviate this issue. Further, since ANN architectures can involve a large number of free parameters, *over-fitting* of the training data is common: this must be taken into account both in model optimization, and in estimating model effectiveness.

2.3.2. ANN implementation

In the present study, the basic feed-forward ANN architecture was used to implement three empirical estimates of surf reporter readings of significant wave height, H_s^{sr}. In each case, the 9 NWW3 parameters (given in Section 2.2.1) were used as inputs to the model, with the four directional angle variables transformed to 2D Cartesian coordinates on the unit circle, leading to a total of 13 inputs. Firstly, a simple linear scaling of NWW3 derived H_s, H_s^N was implemented:

$$\hat{H}_s^{sr} = w_1 H_s^N + w_0 \tag{6}$$

with the model weights w determined empirically. Because of the extreme simplicity of this model, we refer to this as the

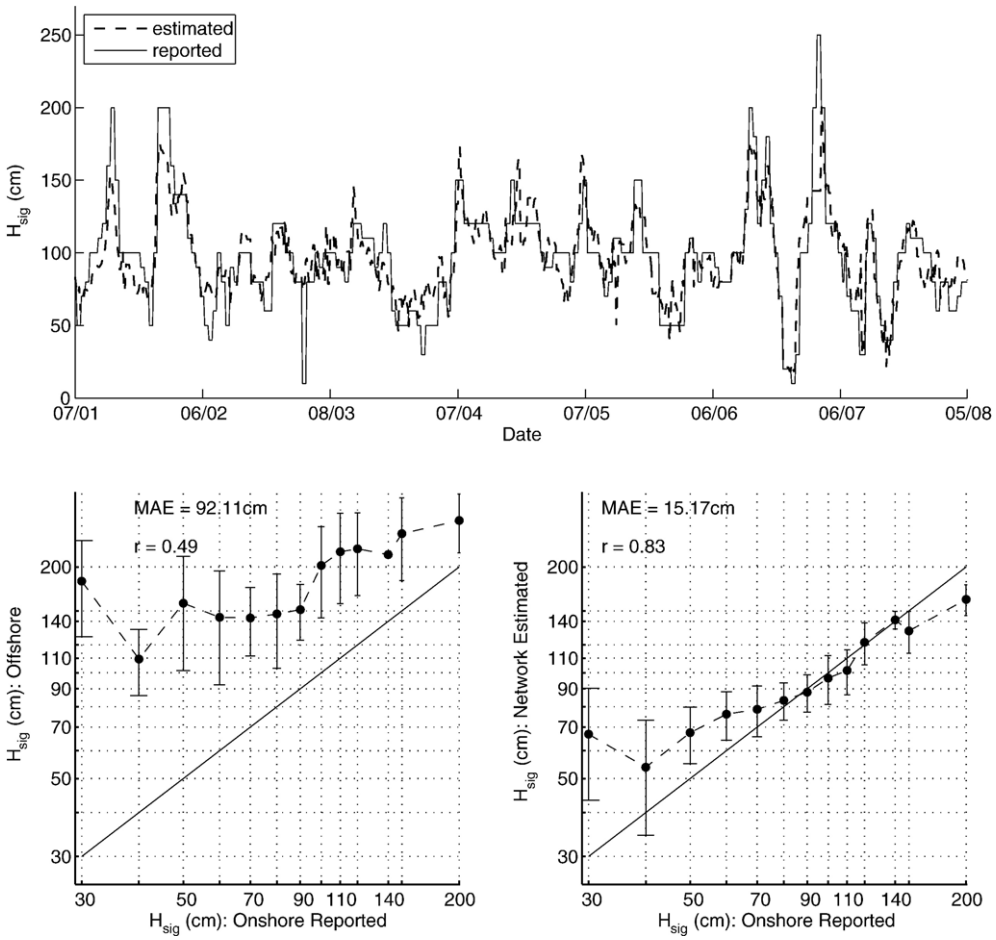

Fig. 5. ANN estimation performance at Surfer's Paradise, Queensland.

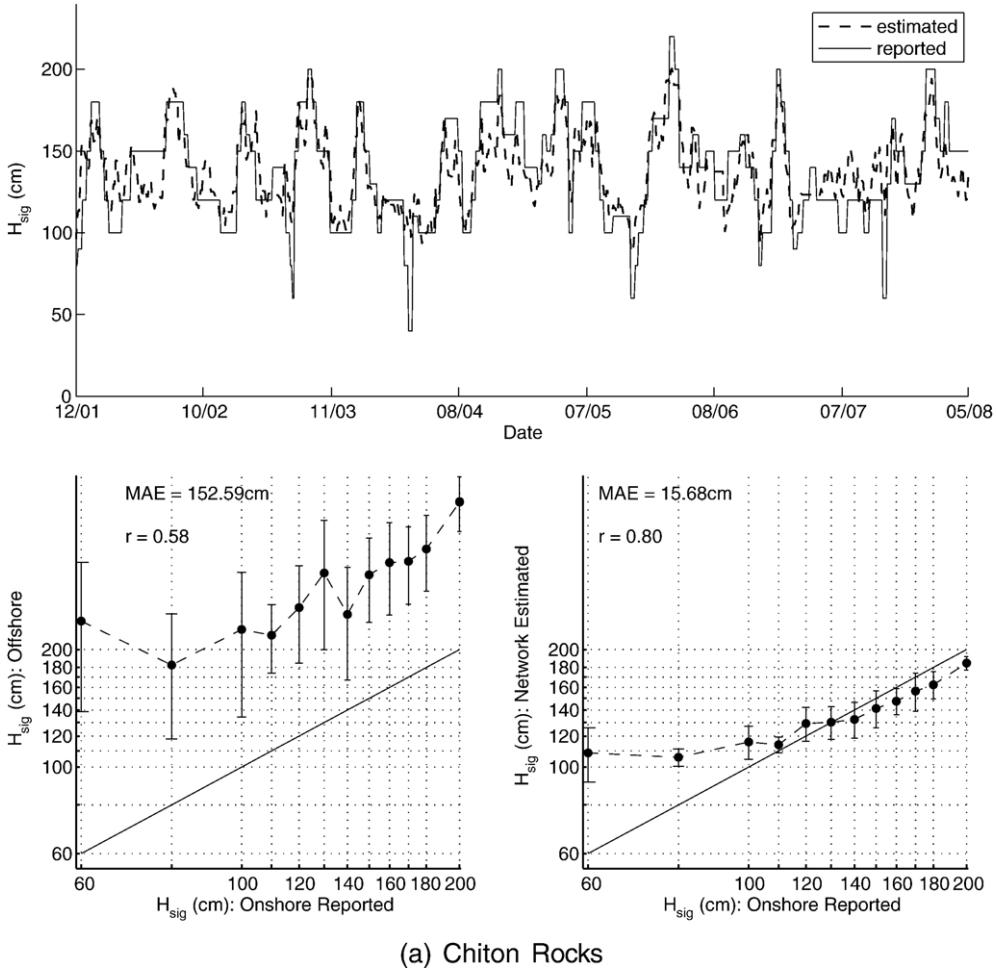

Fig. 6. ANN estimation performance on a South Australian beach.

baseline-scaled estimate. In order to reduce the number of input variables, and hence the number of free weights in the networks, principle components analysis (PCA) was applied as a pre-processing step.[1] Using a form of scree plot, it was decided that retaining the first 6 orthogonal projections of the data retained a reasonable level (>92%) of total (normalised) variability in the NWW3 data. Given the vector of normalised NWW3 driving variables **n**, and the 13×6 PCA transformation matrix **P**, the linear empirical model is given by

$$\widehat{H}_s^{sr} = \langle \mathbf{w}^T, [\mathbf{n}^T\mathbf{P}\ 1]^T \rangle \tag{7}$$

where $\langle\cdot\rangle$ denotes the inner product operation, and the 6-element weight vector **w** is optimized with respect to the training data. All feed-forward ANN and non-ANN model optimization was done using the Levenburg-Marqhardt (LM) algorithm implemented in MATLAB. Like other iterative optimization algorithms, the LM method finds parameter values that minimize the sum of squares using local gradient information of the objective function. It is a more robust form of Gauss-Newton algorithm (which utilizes first derivative information in estimate updates).

The final empirical model is a non-linear feed-forward neural network utilising tan-sigmoid activation functions

$$h(x) = \frac{2}{1+e^{-2x}} - 1 \tag{8}$$

in the hidden layer, and linear activation in the output layer. The non-linear ANN model used a single hidden layer of 6 neurons, the equation being:

$$\widehat{H}_s^{sr} = \left\langle \mathbf{w}_2^T, \left[h([\mathbf{n}^T\mathbf{P}\ 1]\mathbf{W}_1)1\right] \right\rangle \tag{9}$$

with the 6×7 input-to-hidden connection matrix $\mathbf{W}_1$ and the 1×7 hidden-to-output weight vector $\mathbf{w}_2^T$ being determined empirically.

The multi-layer ANNs used in the study were purposely made as small as possible in order to reduce the potential for over-fitting the data: the non-linear architecture involved 49 free weights. It was assumed that a reasonable approximation to the shallow-water transformation for a single location would not require an overly complex model. The available data for the surf reporters at each onshore location varied from 800 to 900 data points. The ANNs were trained using a 5-fold combined early-

[1] As PCA is a standard data pre-processing technique for reducing data dimensionality, it will not be discussed. For more details the reader is directed to Joliffe (2002).

stopping and cross-validation method. That is, 80% of the data was used for optimising the free weights in the model, with 20% used for cross-validation of the data, and early stopping of training. This approach is intended to prevent over-fitting of the training data, and for generating reliable estimates of performance on unseen data. For the non-linear model given in Eq. (9), each partition of the data was used to train 10 ANNs with identical topology, but different random weight initialisations, and the best performing neural net used in each case. Finally the *ensemble* ANN output was calculated by averaging the output of the 10 ANNs upon presentation of the entire data set. The ensemble method is known to improve performance and generalisation of ANNs, but the performance in this case is known to be an overestimate, as the performance calculation is necessarily performed on the combined training and test data subsets for all the trained neural networks. Therefore, in Tables 5 and 6, the validation performance column may be treated as a conservative estimate of future ensemble ANN performance, whilst the reported ANN ensemble performance is rather more optimistic.

2.3.3. SWAN background

SWAN (version 40.41) is a spectral wave model based on the action density balance equation (Hasselmann et al., 1973) that describes the evolution of two-dimensional wave energy spectra under specified conditions of winds, currents, and bathymetry (Booij et al., 1999b; Ris et al., 1998).

SWAN can be used on any scale, even if this model is specifically designed for coastal applications. This model requires no restriction on wave approach angle or directional width. SWAN is able to simulate accurately the wave field in coastal areas where reflection and diffraction are not significant. The SWAN Cycle III User Manual by Holthuijsen et al. (2002) provides a detailed account of the theoretical background, program structures, and implementation. SWAN modeling has been used successfully for storm-induced coastal flooding assessment applications (Cheung et al., 2003), to drive near-shore wave-induced current near-shore models (Castelle et al., in press), for wind generated waves in lakes (Jin and Z.-G., 2001) and in coastal regions (Ou et al., 2002; Castelle et al., 2006), and to model the evolution of wave spectra in a wave tank (Wood et al., 2001).

2.3.4. SWAN implementation

In the present study, SWAN is used in stationary mode. The model considers a steady state situation that requires the time of propagation of the waves through the domain to be short compared to the variation of water level, currents and changes

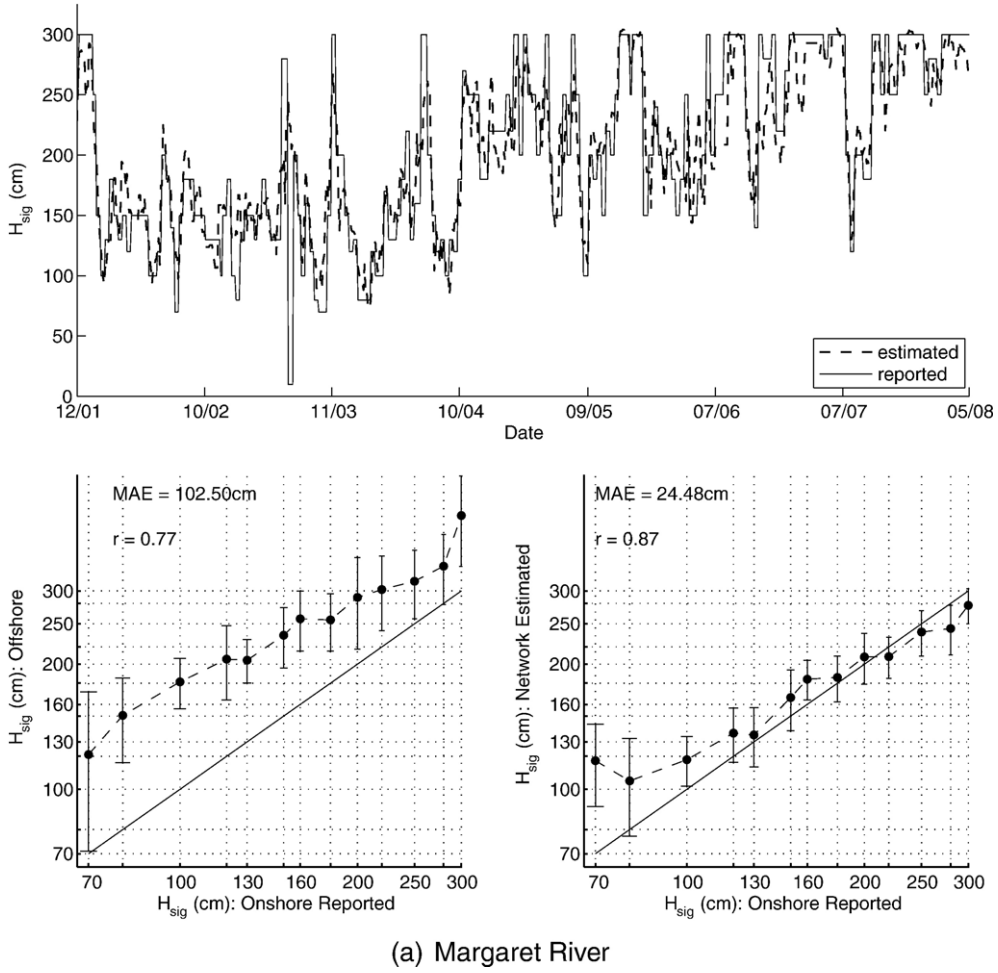

Fig. 7. ANN estimation performance on a Western Australian beach.

in offshore wave conditions. Triad interaction is taken into account in the computations. The breaking wave model chosen herein is the bore-based model of Battjes and Janssen (1978), with a constant breaker parameter $\gamma=0.73$ following Battjes and Stive (1985). The wave forcing provided by the NWW3 nearest output point is to the offshore and lateral boundaries of the model. For Western Australia, South Australia, Victoria and New South Wales areas, the computational grid is concurrent with the Geoscience Australia grid i.e. a regular grid at a cell size of 0.01. For the Queensland area, a curvilinear grid is used for computations with grid cell size of O(100 m). During the simulations, the wave information is requested at each surf reporter location. The outputs are given in 10 m depth in order to avoid an underestimation of wave height due to wave breaking during high energy conditions. The tide level is treated as constant equal to 0 in the Admiralty Height Datum (AHD), i.e. at mid tide. Stationary computations are done every 6 h, concurrent with the NWW3 output data.

3. Results

Table 5 presents the performance of the various empirical models in terms of mean absolute error (MAE) for the 17 surf reporter locations, organised according to study area. A single NOAA WW3 grid point served as input to models for all the surf reporter locations in each study area. For ease of presentation, the MAEs are provided in cm rather than metres. The first column displays the difference between the raw significant wave heights H^s recorded at the offshore NOAA grid point and the surf reporter observations. This base- line difference ranged from approximately 0.6 m at the Sydney, New South Wales beaches, to approximately 2.4 m at Trigg Beach, WA and Seaford, SA. The next column displays the MAE after linear scaling of offshore H^s using Eq. (6). At all locations, linear scaling resulted in a significant decrease in the MAE. This baseline measure represents the error after linear attenuation of wave energy is accounted for. Because of the insignificant degrees of freedom for this model (i.e. 1), division of the data into training and validation subsets was not performed. For the linear and non-linear ANNs (Eqs. (7) and (9)), data was split into training and validation and test sets, and the results of both are shown. The incremental improvement of the linear and non-linear ANNs varied over the test sites. The ensemble ANN performance is also shown. Two sample t-tests ($N=5$) were performed in order to explicitly test the hypothesis that the non-linear ANN MAE was less than the linear version. Despite

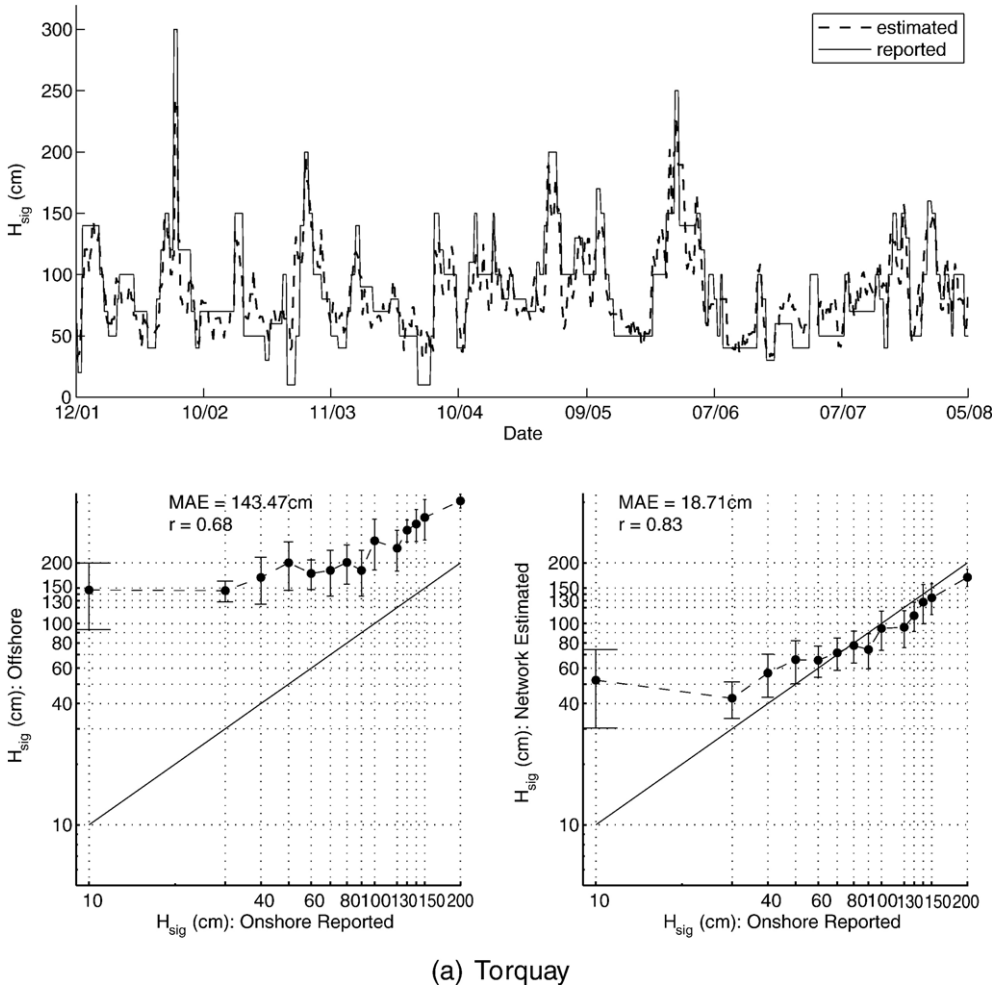

Fig. 8. ANN estimation performance on a Victorian beach.

relatively small incremental improvements in performance in some cases, the *t*-statistics were significant at the .01 probability level for all locations except for Warranambool, VIC.

Table 6 shows similar results for the normalised correlation coefficient *R* between empirical model estimates and surf reporter observations. The *R* coefficient provides a more sensitive measure of estimation performance. For consistency, raw and scaled correlations are included, although they are identical due to the fact that *R* is normalised with respect to univariate variance, and linear scaling therefore has no effect of the observed *R*. Here the improvement is estimation performance over the baseline is more apparent, and so too is the differential improvement over the various locations. Despite the greater degrees of freedom in the non-linear versus linear models, generalisation performance, as measured by the validation columns was consistently better for the non-linear networks. This is confirmed by the *t*-statistics, which indicate significant improvement in performance in almost every case.

Figs. 5–9 compare graphically the output of the best performing non-linear neural network with the surf reporter observations. A time series over the study time period is shown on the left hand side of each plot. The two error-bar plots on the right hand side summarise the relationship between either H^s offshore baseline (middle plot) or ANN network estimated H^s (right plot). In both cases, the diagonal line represents H^s as reported by the human observer, whilst the mean and standard error at each wave height is summarised by the error bars.

The full page illustrations provided in Fig. 1 shows the bathymetric profiles for each of the study regions for which bathymetry was available.

4. Discussion

We first consider the effectiveness of SWAN modeling for near-shore wave estimation. For each area, there is a significant improvement of the wave estimation in terms of the mean absolute error (MAE) at the surf-reporter locations in comparison with the NOAA outputs. Thus, the overall degree of wave bottom friction over the continental shelf and wave energy shadowing behind headlands and islands appears to be correctly estimated. However, the results are generally not comparable with either the linear or non-linear empirical models.

The effectiveness of SWAN modeling is, not surprisingly, more effective when accurate bathymetry are available and a more refined computational grid is used. In the Queensland area, for which this was the case, the correlation factor significantly

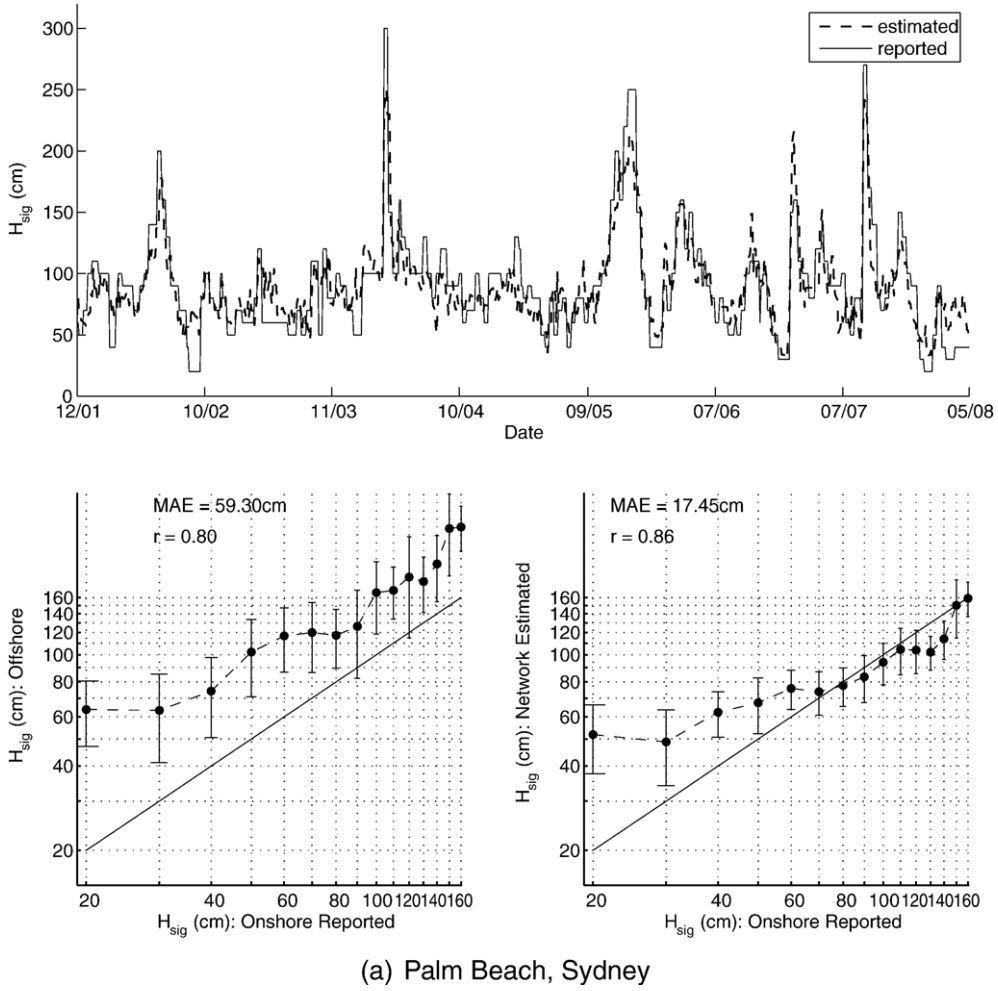

Fig. 9. ANN estimation performance on a New South Wales beach.

improves in comparison with NOAA output data (from 0.49 to 0.72), as does the mean absolute error (MAE) (0.94 m to 0.32 m). This area is exposed to moderate to high energy southerly to south-easterly swell during the winter period. During these wave conditions, the surf reporter location is partially sheltered by the Coolangatta headlands. This sheltering and resulting wave refraction patterns are mostly responsible for the significant improvement of the correlation factor.

For the other areas, SWAN performance in terms of the correlation statistics is significantly worse in comparison to the ANN estimators, and even the baseline. This can be explained by many factors. The main concern is the bathymetric data, and consequently the coarse computational grid. In the Queensland region, comparison of Geoscience Australia bathymetric data and bathymetric surveys provided by the Gold Coast City Council showed that errors of the order of sometimes a few meters could be measured. The main processes affecting the wave propagation exist in the near-shore zone, usually between 30–40 m depth. For example, in the New South Wales area, there is significant longshore variability of the seabed between 0 and 50 m depth which are poorly revealed by Geoscience Australia database. Mid-scale processes such as refraction are poorly simulated by SWAN in the present study. Furthermore, for areas with a large and shallow continental shelf such as the Western Australia area, calibration of bottom friction is a key parameter for an accurate estimation of wave height to the shore. Finally, one of the main reasons why SWAN results are not in very good agreement with surf reporter wave height estimation is the wave forcing format. Indeed, significant wave height, mean period and mean wave angle are provided by NWW3 outputs in our areas of interest. Directional wave spectra, which were not available in the present study, are necessary for optimal performance of model-based estimation techniques.

The ANN based empirical method used, on the other hand, does not depend on careful adjustment of physical parameters (such as bottom friction) and handles gracefully sub-optimal input data (i.e. swell parameters in lieu of the complete directional spectrum). It was expected that the non-linear ANN architecture would perform better than the linear models, and this was borne out by the results. Tables 4 and 5 show that non-linear networks consistently out-performed linear networks over the study regions both in terms of standard error, and correlation with the surf reporter targets. This need for a non-linear model was in accordance with predictions, as a non-linear model was expected to be necessary to take into account the interaction of variable offshore forcing conditions and complex local bathymetries. From Figs. 1–3, it is clear that a significant proportion of the shared variability in offshore and onshore observed swell heights is modulated by non-linear physical processes in the form of refraction, wave interactions, and local wind effects.

The simultaneous prediction of near-shore wave heights over a large number of study regions, along with the use of SWAN modeling of wave propagation in the region (Figs. 1–3) allows us to consider the reasons for differential prediction performance in each study area. The Queensland region, for instance, is subject to variability in swell direction, biased towards the southeast. For these beaches, the relationship between offshore and onshore swell height is moderated strongly by swell direction, with more southerly swells experiencing a higher degree of sheltering and refraction. In the case of Seaford SA, both linear and non-linear ANNs failed to markedly improve onshore swell estimation. This may be explained by the fact that offshore and onshore activity is highly decoupled: the highly dynamic offshore wave climate has limited propagation to the onshore site due to sheltering. Poor performance at this site also results from the inherent difficulty in monitoring small changes in wave height, and the fact that a higher proportion of this variability is due to unpredictable effects such as localized winds. The utility of non-linear estimation was more apparent at Chiton Rocks SA, which may be explained by its more exposed aspect, yielding a more consistent relationship between offshore and onshore activity, which the empirical models were able to emulate. A non-linear model was more effective because it was able to take into account differential attenuation due to swell direction. The empirical estimation methods were less useful on Sydney (SNSW) beaches, where the baseline relationship between NOAA and the surf-reporters was very high. The lack of complexity in the offshore-onshore wave transformation meant that there was little further improvement that the linear or non-linear models could make on the baseline prediction. The South Coast NSW study site was a slight exception to this rule, that we explain by its greater distance from the NOAA grid point (it is located further south, off-map). The best performance overall, in terms of ANN improvement over baseline, was observed at Margaret River and Trigg beach, WA. This is consistent with the general relationship observed between local site characteristics and the improvement of estimation performance over baseline. That is, non-linear ANNs are most effective for estimation when there is a systematic yet complex coupling of offshore and onshore wave climates. Best performance is observed when local transformative processes such as shoaling, attenuation and refraction moderate, but do not completely decouple, the onshore from the offshore wave climate. ANNs tended to over-estimate smaller swells. We believe this is due to the fact that the ANN models assume a Gaussian error distribution. However, this is unrealistic since; a) it is impossible to observe negative wave heights, and b) the wave height distribution is positively skewed. This could be addressed in future work by utilising a zero-truncated, or quasi-binomial error distribution, which would more accurately reflect acutal wave height distributions.

5. Conclusions

The methodologies considered here have immediate application for near-shore wave height estimation. This is significant because the vast majority of human activity occurs in the near-shore zone, and swell conditions in this area are therefore of greatest interest to coastal managers and the public. When combined with a near-shore model, existent global wave models such NWW3 can provide a reliable and cost-effective source of offshore data in absence of *in situ* measurements. Compared with linear and spectral modeling, this study has concluded that near-shore conditions can be

inferred from WW3 parameters most effectively using ANN-based estimation. As well as explicit and implicit modeling of the near-shore wave transformation, the paper establishes quite strong relationships between an open ocean global wind-wave model and onshore visual estimates of wave height provided by experts. The empirical approach presented here relies on the availability of a corpus of target data for model training: the use of a nationwide database of expert surf reporter records is a unique characteristic of this study. The practical application rests on the ability to replace the manual ratings, with the automatic estimates generated by the ANN model. The high correlations and relatively small standard-errors obtained by the ANN model on the *validation* data set indicates that 6–12 months of daily observations is sufficient to build a model that generalizes well.

References

Agrawal, J.D., Deo, M., 2002. Online wave prediction. Marine Structures 15, 57–74.

Balas, C.E., Koc, L., Balas, L., 2004. Predictions of missing wave data by recurrent neuronets. Journal of Waterway, Port, Coastal, and Ocean Engineering 256–265 (Sept/Oct).

Battjes, J., Janssen, J., 1978. Energy loss and set-up due to breaking of random waves. Proceeding of the 16th International Conference on Coast. Eng. ASCE, pp. 569–587.

Battjes, J., Stive, M., 1985. Calibration and verification of a dissipation model for random breaking waves. Journal of Geophysical Research 90 (C5), 9159–9167.

Bishop, C., 1995. Neural Networks for Pattern Recognition. Clarendon Press.

Booij, N., Ris, R., Holthuijsen, L., 1999a. A third-generation wave model for coastal regions. 1. Model description and validation. Journal of Geophysical Research 104 (7), 649–666.

Booij, N., Ris, R., Holthuijsen, L., 1999b. A third-generation wave model for coastal regions, part i: model description and validation. Journal of Geophysical Research 104 (C4), 7649–7666.

Browne, M., Strauss, D., Castelle, B., Blumenstein, M., Tomlinson, R., 2006. Local swell estimation and prediction from a global wind-wave model. IEEE Geoscience and Remote Sensing Letters 3 (4), 462–466.

Caldwell, P.C., 2004. An empirical method for estimating surf heights from deep water significant wave heights and peak periods in coastal zones with narrow shelves, steep bottom slopes, and high refraction. Proceedings of the 8th International Workshop on Wave Hindcasting and Forecasting. North Shore, Oahu, Hawaii, pp. 14–19 (November).

Castelle, B., Cope, M., Abbs, D., Tomlinson, R., 2006. Wave modelling for the gold coast: down-sizing from global to near-shore. 13th National Conference: Climate, Water and Sustainability, Newcastle, Feb 6–8. The Australian Meteorological and Oceanographic Society.

Castelle, B., Bonneton, P., Senechal, N., Dupuis, H., Butel, R., Michel, D., in press. Dynamics of wave-induced currents over an alongshore non-uniform multiple-barred sandy beach on the aquitanian coast, France. Continental Shelf Research.

Cheung, K., Phadke, A., Wei, Y., Rojas, R.D.-M., Martino, C., Houston, S., Liu, P.-F., Lynett, P., Dodd, N., Liao, S., Nakasaki, E., 2003. Modeling of storm-induced coastal flooding for emergency management. Ocean Engineering 30, 1353–1386.

Deo, M.C., Jagdale, S.S., 2003. Prediction of breaking waves with neural networks. Ocean Engineering 30, 1163–1178.

Deo, M., Kumar, N.K., 2000. Interpolation of wave heights. Ocean Engineering 27, 907–919.

Deo, M.C., Jha, A., Chaphekar, A.S., Ravikant, K., 2001. Neural networks for wave forecasting. Ocean Engineering 28 (7), 889–898.

Deo, M., Godane, D., Kumar, V.S., 2002. Analysis of wave directional spreading using neural networks. Journal of Waterways, Port and Coastal Engineering 128 (1), 30–37.

Hasselmann, K., Barnett, T., Bouws, E., Carlson, H., Cartwright, D., Enke, K., Ewing, J., Gienapp, H., Hasselmann, D., Kruseman, P., Meerburg, A., Miller, P., Olbers, D., Richter, K., Sell, W., Walden, H., 1973. Measurements of wind-wave growth and swell decay during the joint north sea wave project (jonswap). Deutsche Hydrographische Zeitschrift 12 (A8).

Ho, P., Yim, J.Z., 2005. A study of the data transferability between two wave-measuring stations. Coastal Engineering 52, 313–329.

Holthuijsen, S., Booij, N., Ris, N., Haagsma, I., Kieftenburg, A., Kriezi, E., 2002. Swan cycle iii version 40.11 user manual. Delft University of Technology, The Netherlands.

Jin, K.-R., Z.-G., J., 2001. Calibration and verification of a spectral wind-wave model for lake okeechobee. Ocean Engineering 28, 571–584.

Joliffe, I., 2002. Principal Component Analysis. Springer.

Kalra, R., Deo, M., Kumar, R., Agarwal, V.K., 2005. Artificial neural network to translate offshore satellite wave data to coastal locations. Ocean Engineering 32, 1917–1932.

Kan, A.R., Timmer, G., 1989. Global Optimization: A Survey, International Series of Numerical Mathematics. Birkhauser Verlag, Basel.

Komar, P.D., Gaughan, M.K., 1972. Airy wave theory and breaker height prediction. Proc. of the 13th Conf. on Coastal Eng. Vol. ASCE, pp. 405–418.

Kostanic, F.M.H.I., 2001. Principles of Neurocomputing for Science and Engineering. McGraw Hill.

Londhe, S.N., Deo, M.C., 2004. Artificial neural networks for wave propagation. Journal of Coastal Research 20 (4), 1061–1070.

Makarynskyy, O., 2004. Improving wave predictions with artificial neural networks. Ocean Engineering 31 (5–6), 724–907.

Marquardt, D., 1963. An algorithm for least-squares estimation of nonlinear parameters. SIAM Journal on Applied Mathematics 11, 431–441.

Mase, H., Kitano, T., 1999. Prediction model for occurence of impact wave force. Ocean Engineering 26, 949–961.

Mase, H., Sakamoto, M., Sakai, T., 1995. Neural network for stability analysis of rubble mound breakwaters. Journal of Waterway, Coastal, and Ocean Engineering 121 (6), 294–299.

Medina, J.R., 2005. Improving wave predictions with artificial neural networks, by O. Makarynskyy. Ocean Engineering 32 (1), 101–103.

Naithani, R., Deo, M.C., 2005. Estimation of wave spectral shapes using ANN. Advances in Engineering Software 36, 750–756.

Ou, S.-H., Liau, J.-M., Hsu, T.-W., Tzang, S.-Y., 2002. Simulating typhoon waves by SWaN wave model in coastal waters of Taiwan. Ocean Engineering 29, 947–971.

Rao, S., Mandal, S., 2005. Hindcasting of storm waves using neural networks. Ocean Engineering 32, 667–684.

Ripley, B.D., 1996. Pattern Classification and Neural Networks. Cambridge.

Ris, R., Booij, N., Holthuijsen, L., 1998. A third-generation wave model for coastal regions, part II: verification. Journal of Geophysical Research 104 (C4), 7649–7666.

Scotto, M., Soares, C.G., 2000. Modelling the long-term time series of significant wave height with non-linear threshold models. Coastal Engineering 313–327.

Smith, W., Sandwell, D., 1997. Global seafloor topography from satellite altimetery and ship depth soundings. Science 277, 1956–1962.

Tolman, H.L., Krasnopolsky, V.M., Chalikov, D.V., 2005. Neural network approximations for nonlinear interactions in wind wave spectra: direct mapping for wind seas in deep water. Ocean Modelling 8, 253–278.

Tsai, C.P., Lee, T.L., 1999. Back-propagation neural network in tidal-level forecasting. Journal of Waterway, Coastal, and Ocean Engineering 125 (4), 195–202.

Tsai, C., Shen, J.N., Kerh, T., 1999. Wave forecasting using neural network model. In: Kumar, Topping (Eds.), Artificial intelligence applications in civil and structural engineering. Civil-Comp. Press, pp. 123–130.

Wood, D., Muttray, M., Oumeraci, H., 2001. The SWaN model used to study wave evolution in a flume. Ocean Engineering 28, 805–823.

D.4 Beach nourishments at Coolangatta Bay over the period 1987-2005 : Impacts and lessons

Bruno Castelle, Ian Turner, Xavier Bertin, Rodger Tomlinson
Coastal Engineering, Vol. 56, pp. 940-950, 2009

Coastal Engineering 56 (2009) 940–950

Contents lists available at ScienceDirect

Coastal Engineering

journal homepage: www.elsevier.com/locate/coastaleng

Beach nourishments at Coolangatta Bay over the period 1987–2005: Impacts and lessons

Bruno Castelle [a,d,e,*], Ian L. Turner [b], Xavier Bertin [c], Rodger Tomlinson [a]

[a] Griffith Centre for Coastal Management, Gold Coast Campus, Griffith University, PMB 50 Gold Coastal Mail Centre, Queensland 9726, Australia
[b] Water Research Laboratory, School of Civil and Environmental Engineering, University of New South Wales, Sydney NSW 2052, Australia
[c] National Civil Engineering Laboratory, Estuaries and Coastal Zones Division, 1700-066, Lisbon, Portugal
[d] CNRS, UMR EPOC 5805, Talence, F-33405, France
[e] Université de Bordeaux, UMR EPOC 5805, Talence, F-33405, France

ARTICLE INFO

Article history:
Received 30 July 2008
Accepted 1 May 2009
Available online 4 June 2009

Keywords:
Artificial sand bypassing
Beach nourishment
Dredging
Sand supply
Embayment
Video-imaging

ABSTRACT

Erosion of the southern Gold Coast beaches (SE Queensland, Australia) was exacerbated after the extension of the Tweed River training walls in the early 1960s. To achieve the objective of restoring and maintaining beach amenity, significant nourishment works have been undertaken in Coolangatta Bay over the past 30 years. Particularly, under the Tweed River Entrance Sand Bypassing Project (TRESBP) since 1995, a number of nourishment campaigns and the implementation of a permanent sand bypass system in 2001 have resulted in significant changes of Coolangatta Bay morphology. The present case study investigates the influence of both wave climate and nourishment works on the area extending from the updrift Snapper Rocks area to downdrift Kirra Beach. SWAN spectral wave model is implemented at Coolangatta Bay area and forced by the global wave model WW3 to estimate wave forcing and the potential natural longshore drift entering in Coolangatta. Specific transects extracted from accurate bathymetric surveys are used to investigate and quantify Coolangatta Bay sedimentation for the period 1987–2005. A network of Argus video stations provides high sample rate information on the shoreline evolution. Results show that, over the past 10 years, Coolangatta Bay has infilled rapidly. Sedimentation reached up to 6 m in some areas between 1995 and 2005, with beach width increasing by 200 m at Kirra Beach. Rapid seaward shoreline migration is consistent with the intense over-pumping of sand relative to the natural potential to move sand alongshore. The nourishment strategy used during this project has successfully delivered large amounts of sand to the southern Gold Coast embayment, although it has been up to now controversial from many community perspectives. The artificial sand bypassing process proved to be much more efficient than depositing the dredged sand in the nearshore area which requires a significant period of low energy condition in order for the deposited sediment to migrate shoreward and weld to the shore. This case study confirms that, when carefully undertaken, sand bypassing is a sustainable and flexible soft engineering approach which can work in concert with natural processes.

1. Introduction

Coastal erosion is a worldwide occurrence along sea shores, and has been reported in the literature for several decades. Traditionally, eroding coastlines have been protected by civil engineering structures involving groynes, seawalls, breakwaters and the like (Charlier et al., 2005). This approach, while providing local relief, can also result in the transfer of the problem from one geographical site to another. Major advances in the technology of beach nourishment have been made over the past 3 decades (Dean, 1996; Houston, 1991, 1996; Elko et al., 2005). Generally speaking, beach nourishment involves the placement of sediment on an eroding beach to migrate the shoreline seaward in order to promote storm protection, natural habitat and beach amenity. Due to the widespread use of beach nourishment worldwide (Hamm et al., 2002; Hanson et al., 2002), it is now important that not only coastal engineers but also geoscientists investigating coastal processes understand the performance of beach nourishments. Various numerical models, both simple (Dean and Yoo, 1992; Elko et al., 2005) and more complex (Van Duin et al., 2004; Li et al., 2006), have been developed to predict the impact of nourishment projects. However, the impact of beach nourishments on both short-term and long-term evolution of complex coastlines warrants continued investigation.

Coolangatta Bay (Fig. 1), located on the east coast of Australia just north of the state border between Queensland and New South Wales, is a major international and national tourism destination. In the early

* Corresponding author. Griffith Centre for Coastal Management, Gold Coast Campus, Griffith University, PMB 50 Gold Coastal Mail Centre, Queensland 9726, Australia.
E-mail address: b.castelle@epoc.u-bordeaux1.fr (B. Castelle).

0378-3839/$ – see front matter © 2009 Elsevier B.V. All rights reserved.
doi:10.1016/j.coastaleng.2009.05.005

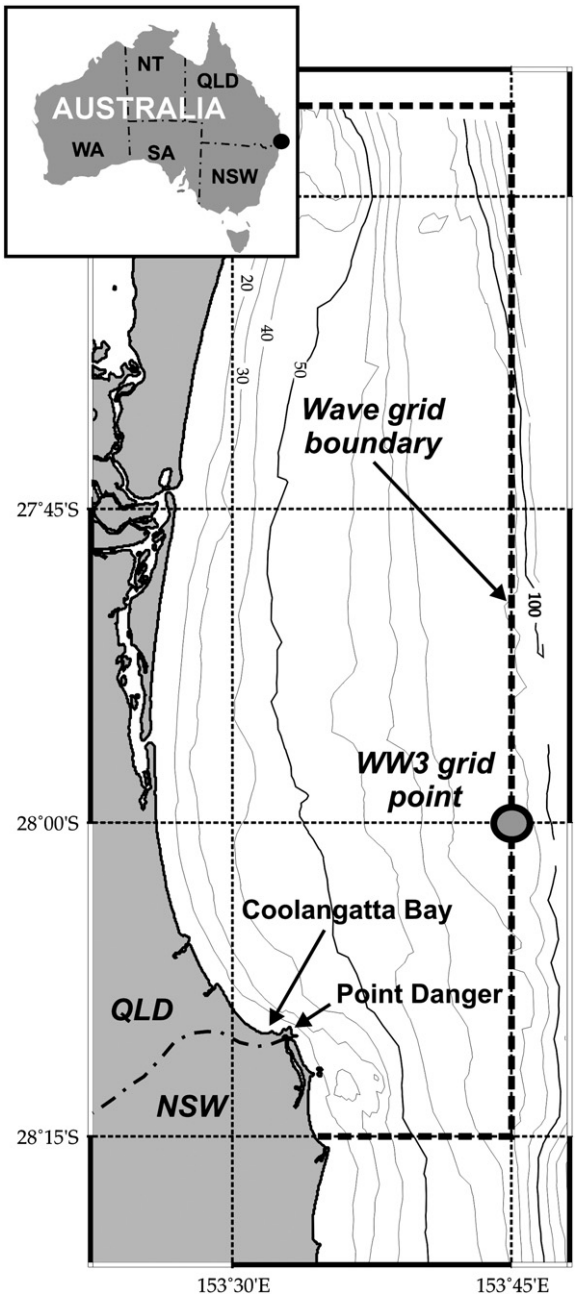

Fig. 1. Location of Coolangatta Bay (Queensland, Australia) with indication of the WW3 grid point and the SWAN grid boundary used for wave modeling.

60s, the Tweed River entrance training walls, located immediately to the south of Coolangatta Bay (Fig. 2), were extended seaward approximately 380 m to improve navigation conditions at the entrance. These walls also created a trap for the natural northward longshore drift, resulting in loss of sand supply to the southern Gold Coast beaches (DHL, 1970), particularly in Coolangatta Bay. Coolangatta Bay beaches eroded to an extent that sea walls were constructed to protect property and infrastructure. Coolangatta Bay beaches had not recovered by the early 1990s, despite various groyne constructions and beach nourishment campaigns. These works, culminating in the implementation of a permanent sand bypassing system in 2001, have resulted in significant and complex changes of Coolangatta Bay morphology.

This case study investigates the influence of wave climate, nourishment works and permanent sand bypassing on Coolangatta Bay coastline morphology. The study focuses on the period 1987–2005 which coincides with the implementation of a number of coastal protection measures, and more particularly the period 1995–2005, when the most important changes to the embayment were observed. This work combines accurate bathymetric surveys, video imagery, quantification of beach nourishment and artificial sand bypassing and wave and longshore drift modeling.

2. Study area

2.1. Location and settings

The 70 km long Gold Coast has been the state of Queensland's premier coastal holiday resort destination for more than 40 years. Coolangatta Bay is located at the southern end of the Gold Coast (Fig. 1). The area is characterized by the presence of the Tweed River entrance and a major headland called Point Danger immediately to the south. Fig. 2 shows the configuration of Coolangatta Bay including the different coastal structures that have been built over the past few decades: the training walls on both sides of the Tweed River entrance and two groynes (Kirra Point groyne and Miles Street groyne). The area of investigation covers approximately 6 km of coastline, comprising 3 distinct embayments within Coolangatta Bay: Rainbow Bay, Coolangatta Beach and Kirra Beach. Tides are semi-diurnal, with a tidal range varying from 0.2 to 2 m, with a mean of 1 m. The area is exposed to high energy waves. South to SE waves are generated by intense low pressure systems off the New South Wales coast in winter and spring, and contribute to the main component of the northerly longshore drift. From December to April, tropical cyclones can generate NE to E waves, sometimes with a destructive power (Hobbs and Lawson, 1982), with significant wave height up to 8 m. The sediment consists of fine sand, with $d_5 = 200$ µm. The estimated net rate of littoral sand transport within the general Gold Coast region is of the order of 500,000 m^3/y toward the north (Turner et al., 2006). The Tweed River itself is considered to be a net sink for sediment, as the river discharges minor quantities only of fluvial sand to the littoral system.

In the early 1960s, the Tweed River entrance training walls were extended seaward approximately 380 m to improve navigation. The wall extensions improved navigation conditions for almost 20 years before a sand bar moved past the end of the southern training wall to infill the channel once more. The loss of longshore sand supply from the south resulted in the progressive recession of the Coolangatta Bay beaches. The Gold Coast also experienced severe storms in 1967 (McGrath, 1967), 1972 and 1974, resulting in major erosion along the entire SE Australian coastline. As outlined in further details below, a number of measures have been undertaken in an attempt to restore and maintain the southern Gold Coast beaches.

2.2. Nourishment works

To achieve the objectives of restoring and maintaining beach amenity, two major nourishment projects were completed to combat beach erosion in Coolangatta Bay over the study period 1987–2005. The first major nourishment project, called the southern Gold Coast Beach Nourishment Project, took place between November 1989 and May 1990. This project involved nourishment of the nearshore and upper beach extending from Kirra East to several kilometers north using sand sourced from inactive offshore deposits in water depths of 20 to 28 m. 400,000 m^3 of sand was bottom dumped in nearshore areas in water depths of 6 to 9 m, and an upper beach nourishment of 3,200,000 m^3 from January to May 1990.

The second phase of nourishment was initiated as a component of the Tweed River Entrance Sand Bypassing Project (TRESBP) commencing in 1995. This project was formulated to overcome the significant erosion of the southern Gold Coast beaches as well as to address the

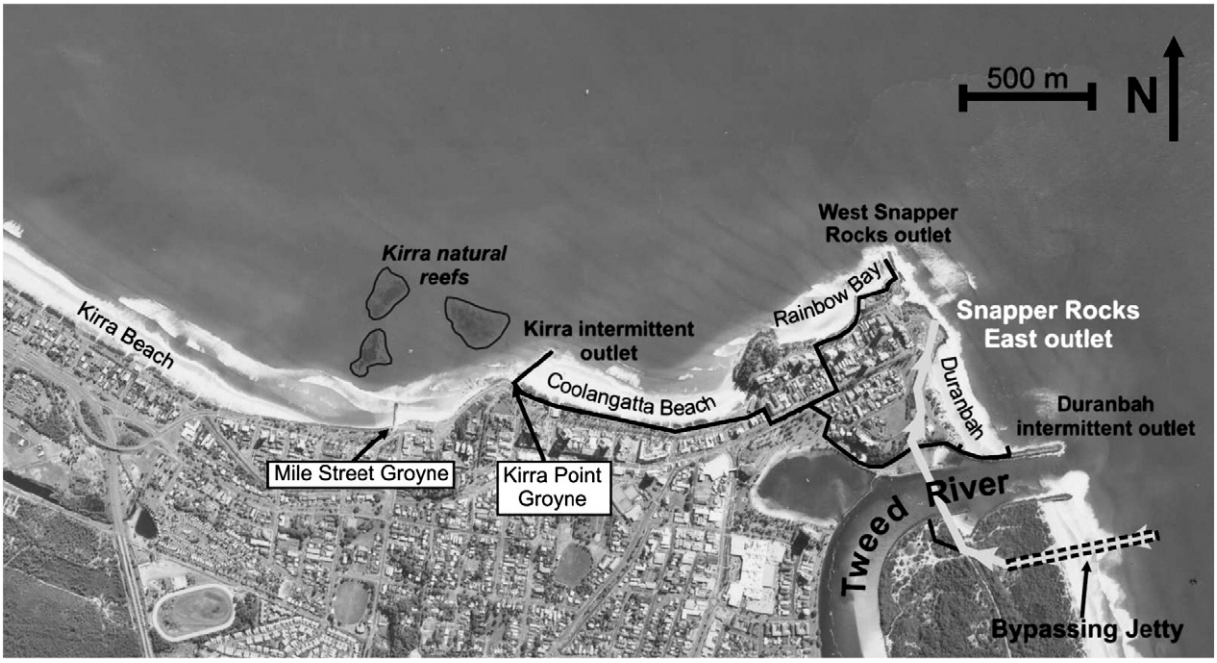

Fig. 2. Aerial photograph of Coolangatta Bay (July 1998) with general settings and superimposed permanent sand bypassing system layout.

navigation issues due to the Tweed River entrance infilling. Stage 1 involved removing the sand bar from the Tweed River entrance to provide material for the initial restoration of the southern Gold Coast beaches. As part of this campaign, 600,000 m^3 of sand was placed on the upper beaches from Rainbow Bay in the east to North Kirra in the west. Additional sand quantities were placed in the nearshore (Dyson et al., 2001). Stage 2 resulted from refinements to the Stage 1 placement areas (Boswood et al., 2001; Colleter et al., 2001). An exclusion deposition zone also provided a 100 m buffer around Kirra natural reef. Most of the sand was placed in an area to the east of Snapper Rock (see deposition areas on Fig. 3). Sand placed in this area was transported by the longshore drift and naturally fed the sandbanks and beaches of the southern Gold Coast. The innovative aspect of the TRESBP (Stage 2) was the implementation in 2001 of a permanent sand bypassing system (see Fig. 2) to collect sand from the southern side of the Tweed River entrance and transport it to the southern Gold Coast beaches in perpetuity (Dyson et al., 2001). The sand was pumped to 5 different locations within Coolangatta Bay (see outlet locations on Fig. 2). The majority of the sand during the period 2001–2005 was pumped to the Snapper Rock outlet, at the eastern (updrift) extremity of Coolangatta Bay.

The nourishments during the period 1987 to 2005 are summarized below, with specific location and placement quantities indicated in Tables 1 and 2:

- 1989–1990: Southern Gold Coast Nourishment Project (3,600,000 m^3).

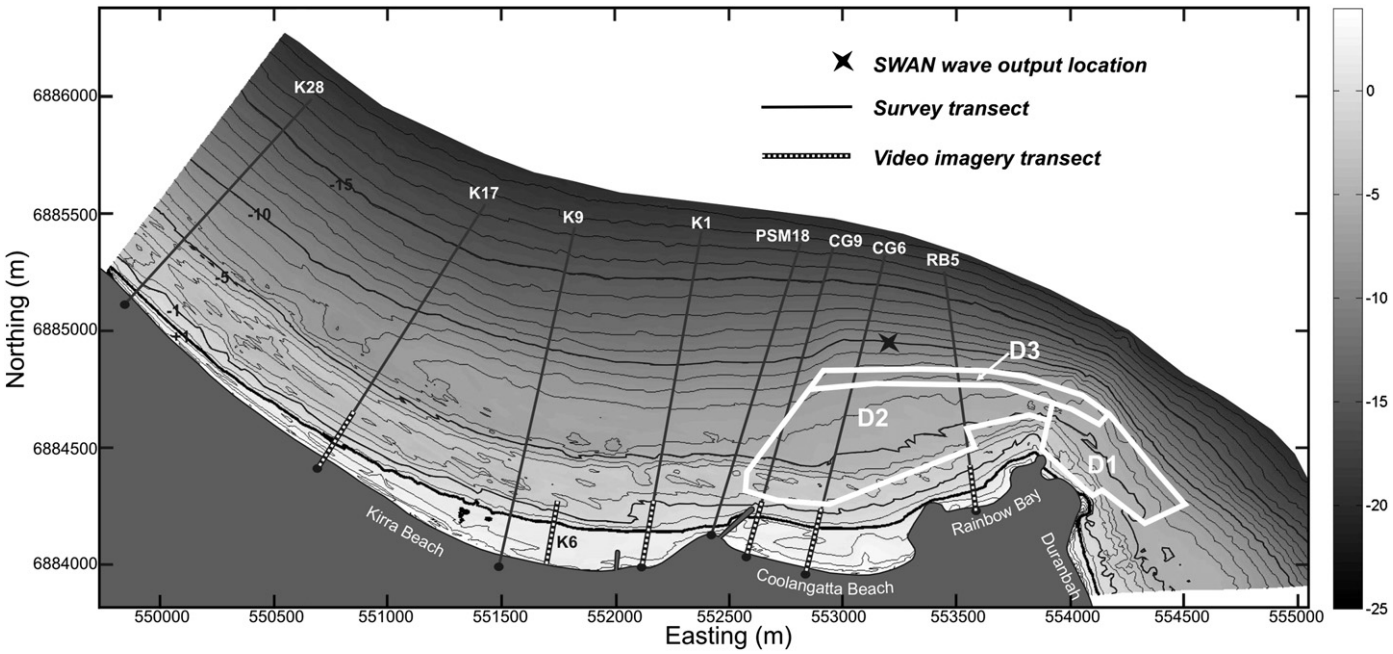

Fig. 3. Coolangatta Bay morphology (October 2004) with locations of the specific survey transect lines, video imagery transect lines, the SWAN wave output point and the 3 main deposition areas D1, D2 and D3 (KB=Kirra Beach, CGB=Coolangatta Beach, RBB=Rainbow Bay Beach).

Table 1
Dredging quantities (m^3) and placement area over the period 1995–2005.

Year	D1	D2	D3	Total
1995	?	?	?	1,731,949
1996	?	?	?	572,403
1997/1998	?	?	?	800,407
2000	237,266	73,010	96,007	405,853
2001	9721	257,996	148,490	416,207
2002	190,285	9014	40,831	240,130
2003	146,628	57,425	26,839	230,892
2004	123,771	11,200	34,955	169,926
2005	111,483	38,573	26,133	176,189

D1, D2, and D3 are defined in Fig. 3.

- 1995–1996: TRESBP Stage 1A, dredging of Tweed River Entrance and associated nourishment of the southern Gold Coast beaches (2,300,000 m^3).
- 1997–1998: TRESBP Stage 1B, dredging of Tweed River Entrance and associated nourishment of the southern Gold Coast beaches (800,000 m^3).
- 2000–2002: TRESBP Stage 2A, dredging of Tweed River Entrance and associated nourishment of the southern Gold Coast beaches (1,100,000 m^3).
- 2001: Start of the permanent sand bypassing system.
- 2003–2006: TRESBP Stage 2B, dredging of Tweed River Entrance and associated nourishment of the southern Gold Coast beaches (500,700 m^3).

3. Methods and materials

3.1. Quantities of delivered sand, potential natural longshore drift and over-pumping estimation

The spectral wave model SWAN (Booij et al., 1999) is used in stationary mode. The wave forcing provided by the global wave model WW3 (Tolman, 1991) nearest output point (see Fig. 1) is applied to the offshore and lateral boundaries of the model. The ability of this modeling strategy to estimate nearshore waves within the Gold Coast region has been successfully demonstrated (Browne et al., 2006, 2007). Accurate bathymetric surveys were used to build a numerical bathymetry with a curvilinear grid at a cell size of $O(100\ m)$. A more refined rectangular grid (mesh size of 5 m) was nested within the coarser curvilinear grid updrift of the Tweed walls on the Leatitia Spit area (Fig. 4). Three hour time-series of wave parameters were generated along two representative cross-shore profiles *T*1 and *T*2 (Fig. 4) where the breaking point was defined as the point for which $H_s/depth = 0.6$. The empirical formula developed by Kaczmarek et al. (2005), using time-series of H_s and wave angle to the shore at the breaking point, was used to estimate the corresponding time-series of potential (without training walls) longshore drift entering into the Coolangatta Bay region. Although these sand transport predictions were not directly calibrated with field data, their integration over the study period resulted in values of the order of 500,000 m^3, which matches the generally accepted alongshore transport rate for this area (Turner et al., 2006). The same methodology has been successfully applied at a dissipative beach (Bertin et al., 2008) and at a sandspit (Allard et al., 2008) located on the western coast of France. In the following, only the longshore drift computed in *T*1 is used, as the cross-shore wave parameter profiles at *T*2 were substantially perturbated by the presence of a shallow shoal (immediately to the Est of *T*2, see Fig. 4) during SE wave events.

Table 2
Pumping quantities (m^3) and outlet locations over the period 2001–2005.

Year	OSRE	OSRW	OK	OD	OG	Total
2001	409,746	1586	97,279	67,258	0	575,869
2002	564,577	0	84,915	71,872	0	721,364
2003	602,953	0	81,918	70,224	31,931	787,026
2004	459,554	0	0	36,813	0	496,367
2005	683,244	0	0	41,687	0	724,931

OSRE: Snapper Rock East Outlet; OSRW: Snapper Rock East Outlet; OK: Kirra Outlet; OD: Duranbah Outlet; OG: Greenmount Outlet (see Fig. 2).

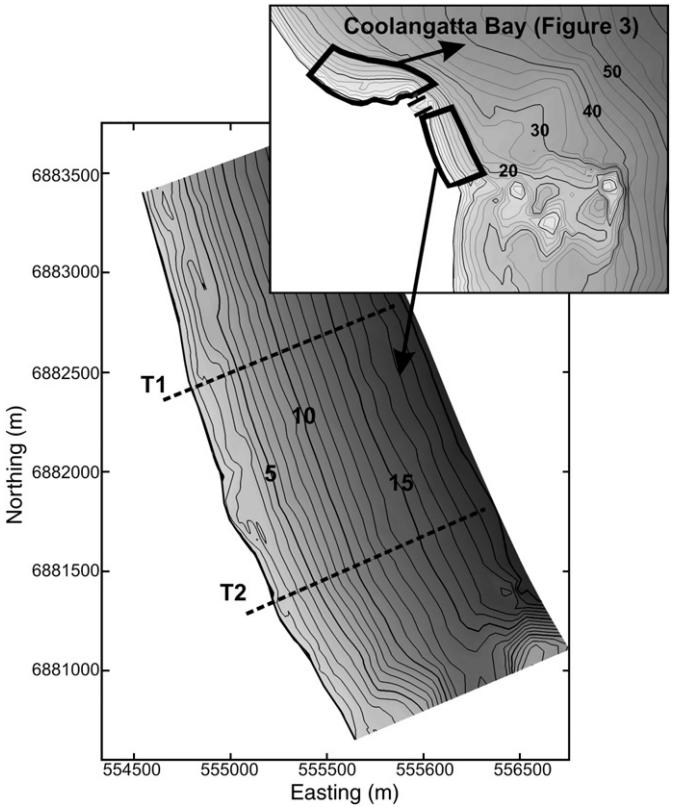

Fig. 4. Refined nested SWAN computational domain and location of the cross-shore profile T1 used to compute wave-beaking conditions and resulting potential natural longshore drift entering Coolangatta Bay.

Monthly quantities of delivered sand since the beginning of the permanent sand bypassing system, with associated deposition and pumping locations, were collated from the TRESBP website (www.tweedriverbypass.nsw.gov.au). These monthly sand quantities were used in the present study to assess the impact of dredging and pumping on both the short-term (weekly–monthly) and longer-term (seasonal–multi-year) evolution of Coolangatta Bay morphology. Using computed monthly potential natural sand supply from the downdrift coast and real delivered sand quantities, monthly over-pumping quantities from the TRESBP were estimated.

3.2. Surveys

Fig. 3 shows the area of interest for the present study, and the period of survey data availability is from 17/9/1987 to 15/7/2005. Survey data were collected in this area by a number of organizations for a variety of investigations and projects. Not all the surveys have been taken on the same survey lines and not all the survey data collected are available for the present study. In the 1970s and 1980s, in response to the severe erosion of Coolangatta Bay, the Gold Coast City Council established survey lines at Coolangatta Beach (CG lines), Kirra Beach (K lines) and Rainbow Bay (RB line). Specific survey lines were chosen to compute the shoreline position. There is an extensive range of shoreline indicators reported in the literature (Boak and Turner,

2005). In the present study, the shoreline position is defined as the intersection of the beach profile with the Mean Sea Level (MSL), which corresponds approximately to 0 m Australian Height Datum (AHD) at the Gold Coast beaches.

The location of the 8 specific survey lines used for this study is shown on Fig. 3. The survey lines cover the bay from North Kirra in the west (transect K28) to Rainbow Bay in the east (RB5). These survey lines were chosen because they are representative of the Coolangatta Bay alongshore variations, and importantly, because a large number of surveys were undertaken on these specific transects. At all 8 transect locations, shoreline position has been normalised so that a shoreline position of 0 m equates to erosion of the beach back to the boulder wall.

3.3. Video imagery

Commencing in mid-2002 a network of Argus coastal imaging stations (Holman and Stanley, 2007) has been operating on a continuous basis, providing full coverage of Coolangatta Bay and vicinity. A total of 16 cameras are used, located atop three beach front buildings and a lighthouse, encompassing the southern region of Kirra Beach, Coolangatta Beach, Rainbow Bay/Snapper Rocks, as well as the up-drift Duranbah Beach located on the southern side of Point Danger (refer Fig. 2). Two additional and landward-looking cameras are located on the sand bypassing pier, to monitor the localised beach changes in the immediate vicinity of this structure. The cameras were installed for the primary purpose of providing continuous and real-time monitoring capabilities to the TRESBP management team (Turner et al., 2004, 2006). Image analysis is undertaken and updated on a regular (weekly) basis, to document and quantify the longer-term impacts of the bypassing and nourishment operations, and to assess the current beach conditions against a range of target indicators, for the purpose of determining the location and quantity of regular sand delivery (Turner and Anderson, 2007).

The key feature of coastal imaging systems that distinguish them from conventional 'surfcams' is the ability to extract quantitative information from a time-series of digital images. This core capability is achieved through the solution of a set of camera model parameters (Holland et al., 1997), that enable the determination of three-dimensional real-world [x,y,z] position from two-dimensional [U,V] image coordinates. These geo-referenced images are then subjected to a range of digital image analysis techniques, to identify, enhance and quantify the particular coastal processes or features of interest. For the present study, the key analysis is determination of the weekly alignment of the shoreline corresponding to mean sea-level. The 'PIC' (Pixel Intensity Clustering) shoreline detection and modeling method is used for this purpose across all Coolangatta Bay sites (Aarninkhof et al., 2003; Plant et al., 2007). Weekly beach widths are then extracted from the time-series of shorelines, corresponding to the same 8 locations for each of the longer-term (pre-2002) but less frequent survey transects, identified in the previous section.

4. Results

4.1. Pre-TRESBP Coolangatta Bay evolution

Fig. 5 shows the temporal morphological variability of the 8 specific cross-shore transects gathered from the bathymetric surveys throughout the study period. In particular, it shows that there is no significant bathymetric change deeper than 15 m depth. Difference in beach profile sometimes reached 8 m showing the strong variabilities of both the bay morphology and shoreline positions over the study period. Fig. 6 shows the time-series of the shoreline evolution between 1987 and 2005 for these 8 cross-shore transects. This figure shows that, prior to the southern Gold Coast Nourishment Project in 1989, the shoreline positions were experiencing a generally slow decreasing trend. This progressive erosion was resulting from the re-establishing of sand transport pathways at the Tweed Entrance. In the late 80s, both the spit southward (updrift) of the Tweed River training walls and the Tweed bar were approaching a new equilibrium, and the Tweed River was also approaching the pre-1962 situation. Thus, natural sand bypassing had greatly increased resulting in a weaker rate of shoreline retreat that was experienced in the 1960s and 1970s (DHL, 1992). However, Coolangatta Bay and particularly Kirra, was still at this time the top Gold Coast nourishment priority and the beach zone identified as in most need of storm protection (Smith and Jackson, 1993).

The 1989 beach nourishment was quite unique as compared with previous Gold Coast nourishment works. To satisfy community demand, it was chosen to place only 11% of the total amount of sand in the nearshore area, with the bulk of the sand placed at the beachface in order to create an 'instant' and visibly wider beach. The onshore nourishment (89%) substantially offset the erosion of the beaches from Kirra to a few kilometers to the North, though the nourishment volume had not fully offset the severe erosion at Kirra and the eastern beaches of Coolangatta Bay (DHL, 1992). This beach response is obvious on Fig. 6: the western part of Coolangatta Bay (transects K1, K9, K17 and K28) experienced a seaward shoreline migration of 120 m on average, while the eastern part (PSM18, CG9, CG6 and RB5) experienced a very weak accretive event. During the period 1990–1995, the beach width remained relatively stable, with a 50 m shoreline retreat on average westward to Kirra groyne.

In 1995, Stage 1A of the TRESBP resulted in a marked beach width increase in the whole bay. This was particularly evident for Coolangatta Beach and the eastern part of Kirra Beach. A 40 m reduction in the length of the Kirra Point groyne was also implemented at this same time. The most significant evolution of Coolangatta Bay is observed from 2001, which coincided with the start of the permanent sand bypassing. This period 1995–2005 is described in more details below.

4.2. Annual morphological evolution of Coolangatta Bay 1995–2005 (TRESBP)

Fig. 7 shows the evolution of the computed Coolangatta Bay morphology during the TRESBP, and reveals significant changes of the sub-aerial beach. Rainbow Bay beach experienced the least significant changes over the study period, while Coolangatta beach and particularly Kirra Beach intensively evolved. Vertical accretion reached 6 m over the period in some areas of Kirra Beach and Miles Street groyne was mostly buried by sand in 2005. The water line reached Kirra Point groyne only at high tide. In 2005, both Coolangatta and Kirra Beach were about 200 m wide with non-vegetated dunes reaching 6 m above AHD. In contrast, since 2002, Rainbow beach has experienced a weak erosive state, Coolangatta Beach appears to have reached a quasi-equilibrium state and Kirra Beach continued to infill rapidly.

The nearshore area also experienced intense changes. Referring to Fig. 7, before 2001, the nearshore bar was mirroring the shape of the crenulated embayments, but this feature has now both widened and straightened. This straight nearshore bar development started in 2001 and coincided with the start of the permanent sand bypassing. The nearshore bar changed its orientation westward to Kirra groyne

Fig. 5. Superimposed beach profiles over the period 1987–2005 for the specific survey lines, with indication of the Lowest Astronomical Tide (LAT) level, Mean Sea Level (MSL) and Highest Astronomical Tide (HAT) level.

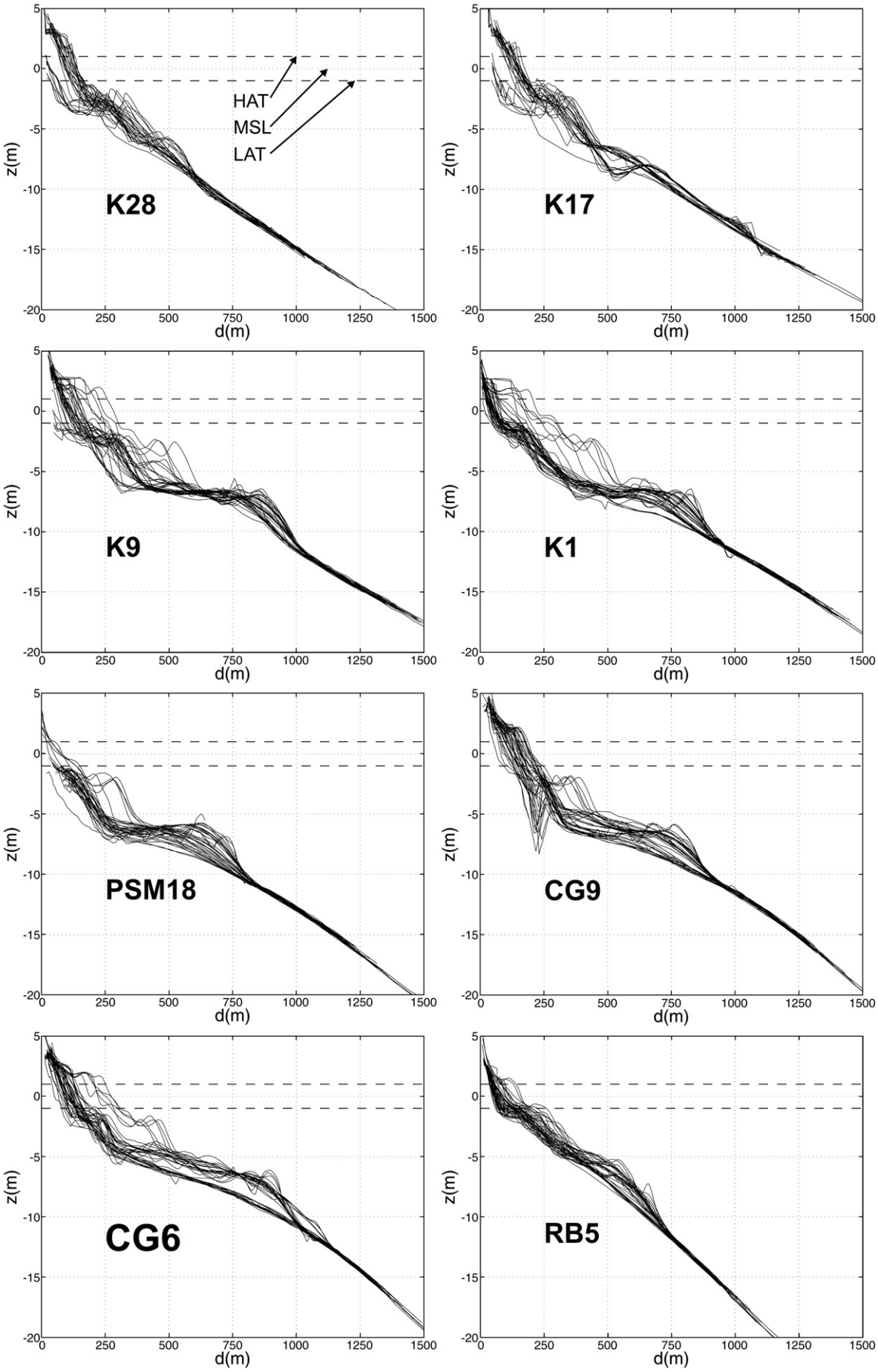
HAT
MSL
LAT
K28
K17
K9
K1
PSM18
CG9
CG6
RB5
z(m)
d(m)

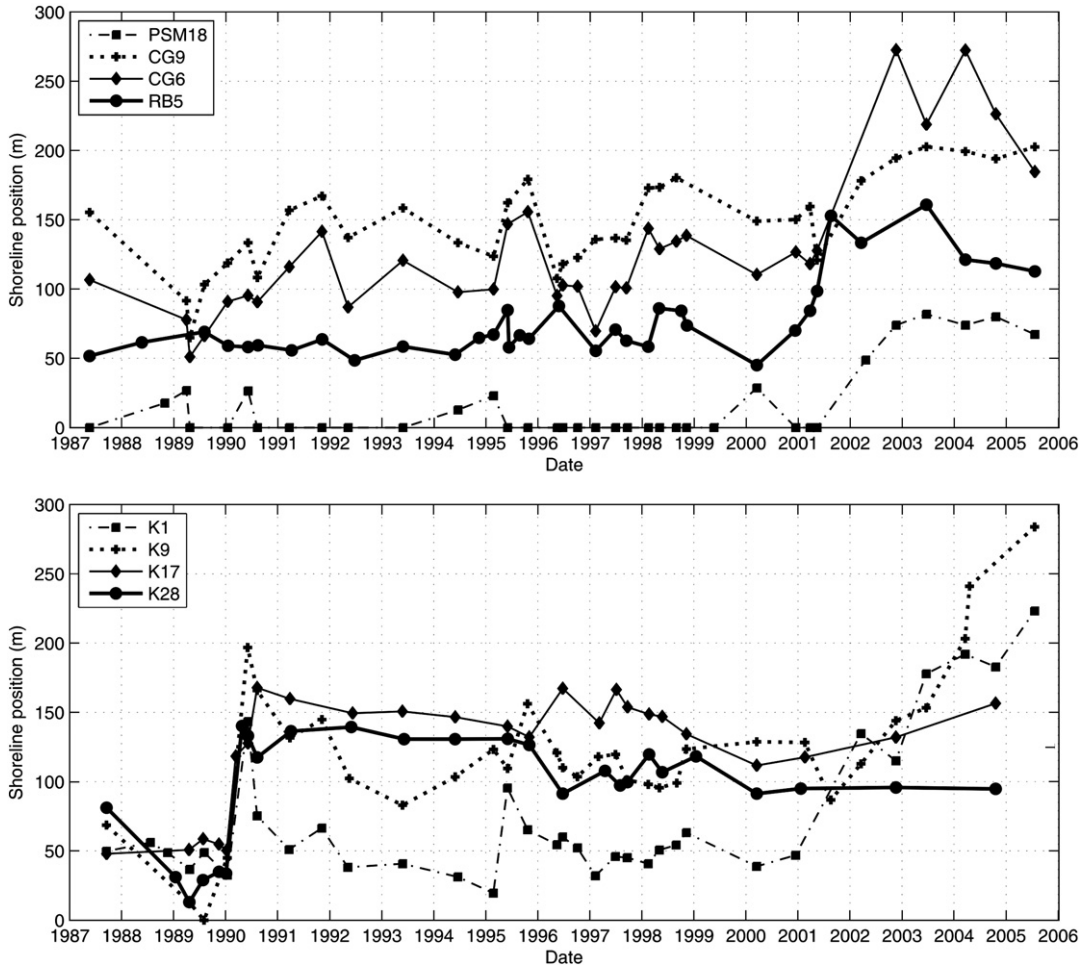

Fig. 6. Shoreline evolution at the specific survey lines over the period 1987–2005.

between 2002 and 2005. This change in the nearshore bar configuration was associated with an intense beach width growth of Kirra Beach.

Fig. 8 shows the time-series of the shoreline position for each of the 8 beach profiles, together with offshore wave conditions and the monthly volume (including placement areas) of both pumped and deposited sand in the bay. This figure clearly shows the coincidence of significant evolution of Coolangatta Bay and the implementation of the TRESBP, as expected, given that there has been significant over-pumping of sand relative to the natural potential to move sand alongshore (Tables 1 and 2). Indeed, offshore wave conditions during this five year monitoring period do not appear to have had a significant impact on the global evolution of the bay, as this interval coincided with a relatively calm period for the Gold Coast beaches, with no severe erosive event(s) observed.

Both Stage 1A and Stage 1B dredging had a significant impact on the shoreline position of the eastern part of Coolangatta Bay. The western part of Coolangatta Bay did not experience significant change of the shoreline position over the period prior to the artificial sand bypassing plant implementation (Figs. 7 and 8). The start of the artificial sand bypassing resulted in an almost immediate seaward migration of the shoreline in the whole bay (except the eastern extremity: K17 and K28). At the beginning (early 2001), increasing beach width was observed at the eastern extremity of Coolangatta Bay i.e. Rainbow Bay (RB5 on Fig. 4). In late 2001, beach width increased at Coolangatta Beach (CG6 and CG9), then at Kirra in 2002. Since 2002, the shoreline position in the eastern part of Coolangatta Bay (RB5, CG9, CG6) was almost stable, with a slight downward trend, while Kirra continues to infill from the east to the west.

4.3. Short-term (weekly) shoreline evolution in response to over-pumping

Fig. 9 shows time-series of both monthly over-pumped quantities of sand relative to the natural potential to move sand alongshore and weekly shoreline position computed from the video imagery. This figure reveals the impact of over-pumping on the shoreline position within the bay on the time scale of days to months which was impossible to grasp from the previous (annual) beach survey analysis.

These monitoring data show that over- or under-pumping have an almost immediate impact in Rainbow Bay (transect RB5). For instance, it only takes a few days for the RB5 shoreline position to migrate seaward when substantial over-pumping occurred. As soon as under-pumping or weak over-pumping occurs, the RB5 shoreline position migrated shoreward. When the delivered sand quantities remain close to the potential natural longshore drift for a few months, for instance early 2005 (Fig. 9), the RB5 shoreline position seems to oscillate around an equilibrium position at about 50 m. The impact of over-pumping on Coolangatta Beach can also be noticed for the transect CG6. A substantial lag exists between the over-pumping peaks and the CG6 shoreline evolution (Fig. 8). Most of the peaks can be identified on Fig. 8, with a lag estimated to be of about 5 to 6 months. Given the CG6 and RB5 transects are about 500 m spaced, the bulk of sand migration rate can be estimated to be on the order of 100 m/month between Rainbow Bay and Coolangatta Beach. The impact on the CG9 shoreline position is barely shown on Fig. 8 as the Kirra Point groyne (Fig. 2) acts as a sand trap and tends to filter the sand bulk migration.

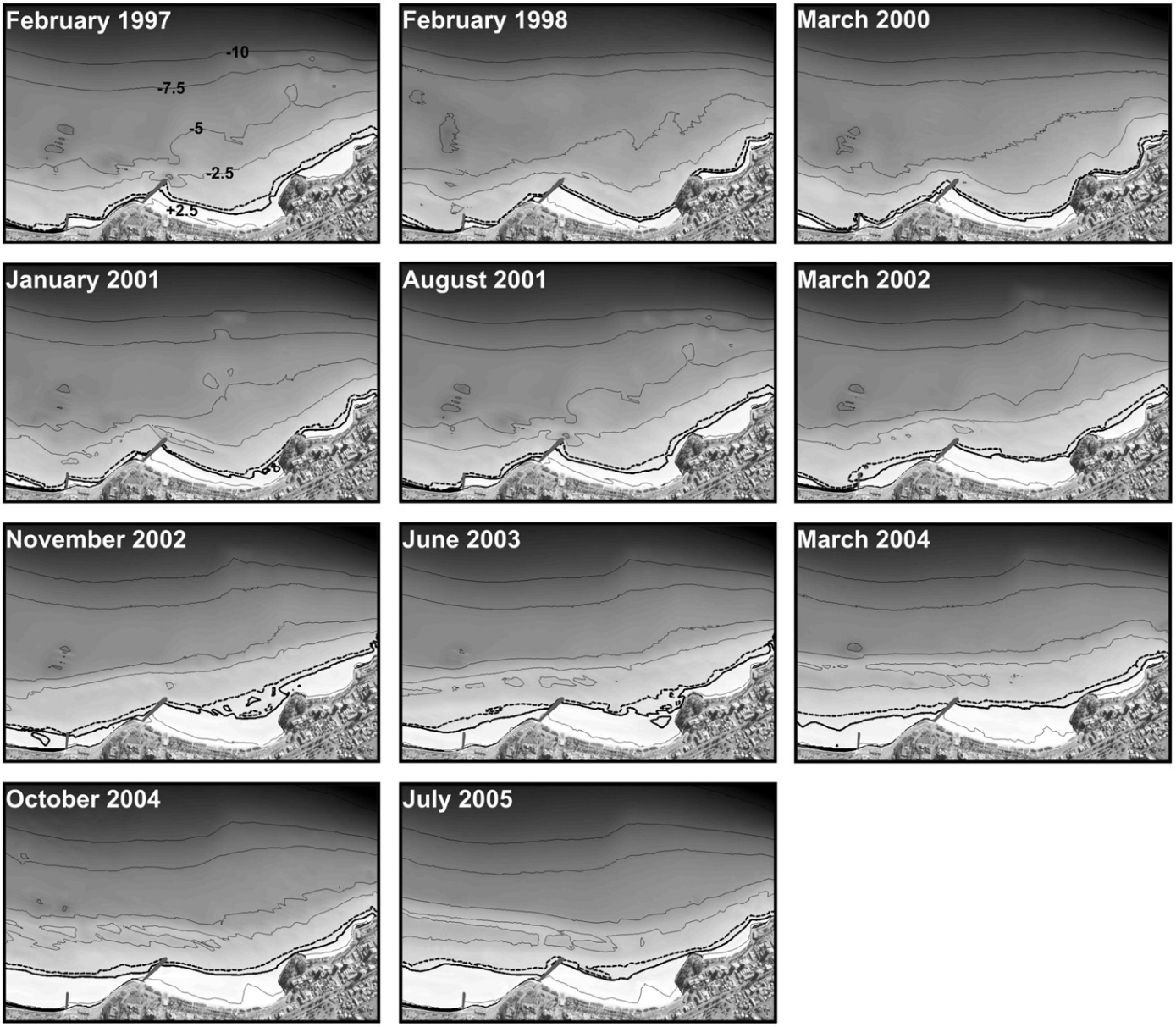

Fig. 7. Evolution of Coolangatta Bay from 1997 to 2005: beach widening and formation of a straight and wide nearshore bar. The thick dot line is the shoreline location (0 AHD) and the thick line is the spring high tide sea level.

This sand bulk migration is much more difficult to identify within the Kirra Beach embayment. The overall observed trend is characterized by a quasi-steady seaward migration of the shoreline from Kirra Point groyne to the K17 transect, as observed from the beach survey analysis (Fig. 7). This behavior shows once again that Kirra Beach seems to act as a sediment sink and keeps infilling to a significant degree.

5. Discussion and conclusions

5.1. Site specific outcomes

Coolangatta Bay experienced significant morphological changes over the past decade, extending from 15 m water depth landward to the subaerial beach. Vertical accretion has reached 6 m in some areas such as Kirra Beach, where the seaward shoreline migration attained 200 m. In comparison to the depleted beach conditions in the 1980s, it is evident that the TRESPB has been successful in both increasing the beach width and enhancing the ability of the southern Gold Coast beaches to accommodate future extreme events. From a local perspective, the principal outcomes of the present study are:

(1) The Coolangatta Bay beaches are very wide. The shoreline seaward migration ranged from 50 m in Rainbow Bay to more than 200 m at Kirra Beach in comparison to the shoreline prior to the TRESBP. The subaerial beach is currently a significant buffer against a severe storm event. The beaches of Kirra and Coolangatta seem to be currently the most able to withstand extreme event of all the Gold Coast beaches (Castelle et al., 2008).
(2) Kirra Beach appears to act as a downdrift sink. This is not surprising given that this section of coastline experienced the greatest negative impact of the erosion wave that followed the construction of the Tweed walls.
(3) Rapid evolution (weekly to monthly) seems to be strongly correlated to the over-pumping of sand relative to the natural potential to move sand alongshore. The resulting bulk of sand

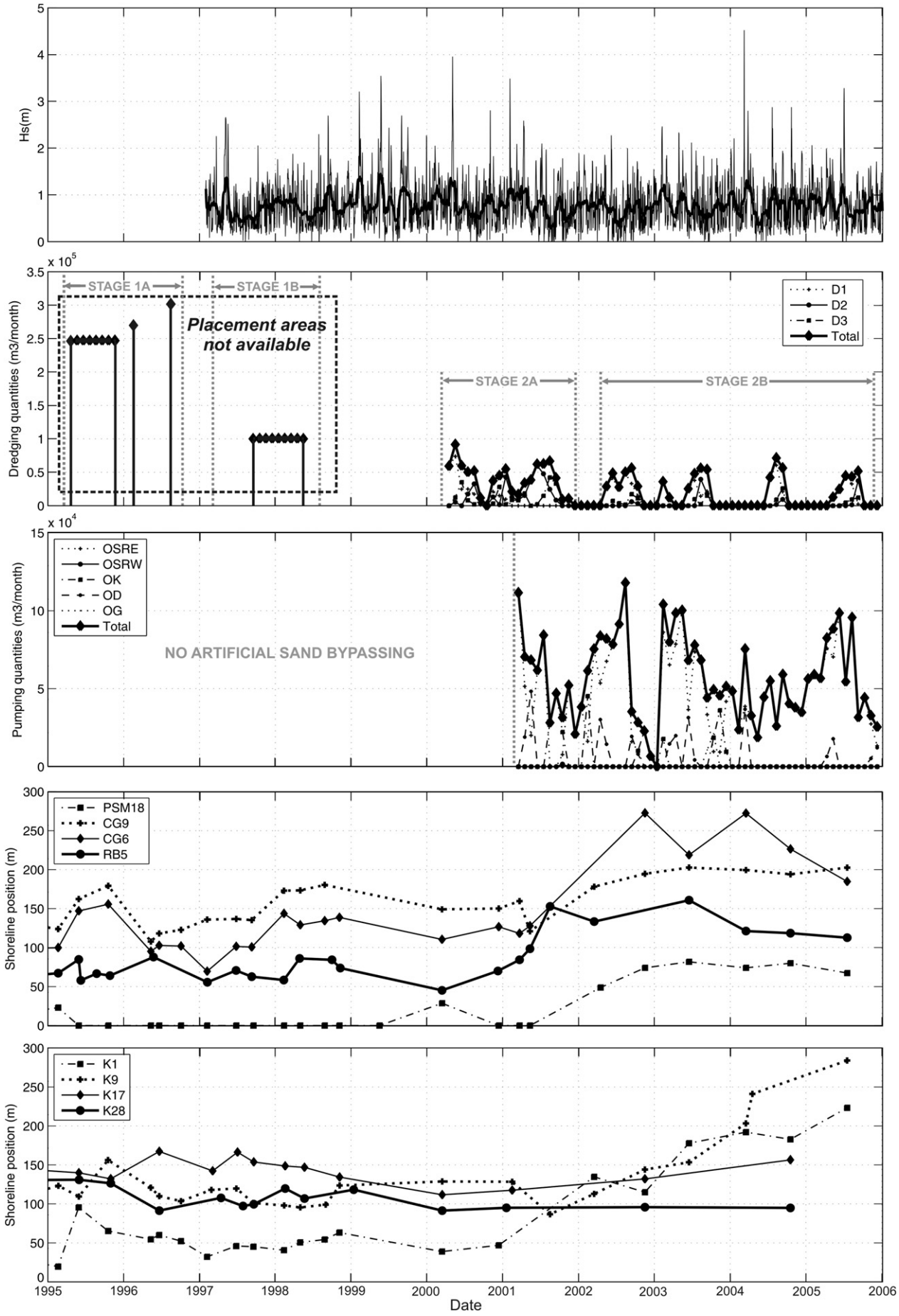
Hs(m)
x 10^5
Dredging quantities (m3/month)
STAGE 1A
STAGE 1B
Placement areas not available
STAGE 2A
STAGE 2B
D1
D2
D3
Total
x 10^4
Pumping quantities (m3/month)
OSRE
OSRW
OK
OD
OG
Total
NO ARTIFICIAL SAND BYPASSING
Shoreline position (m)
PSM18
CG9
CG6
RB5
Shoreline position (m)
K1
K9
K17
K28
1995
1996
1997
1998
1999
2000
2001
2002
2003
2004
2005
2006
Date

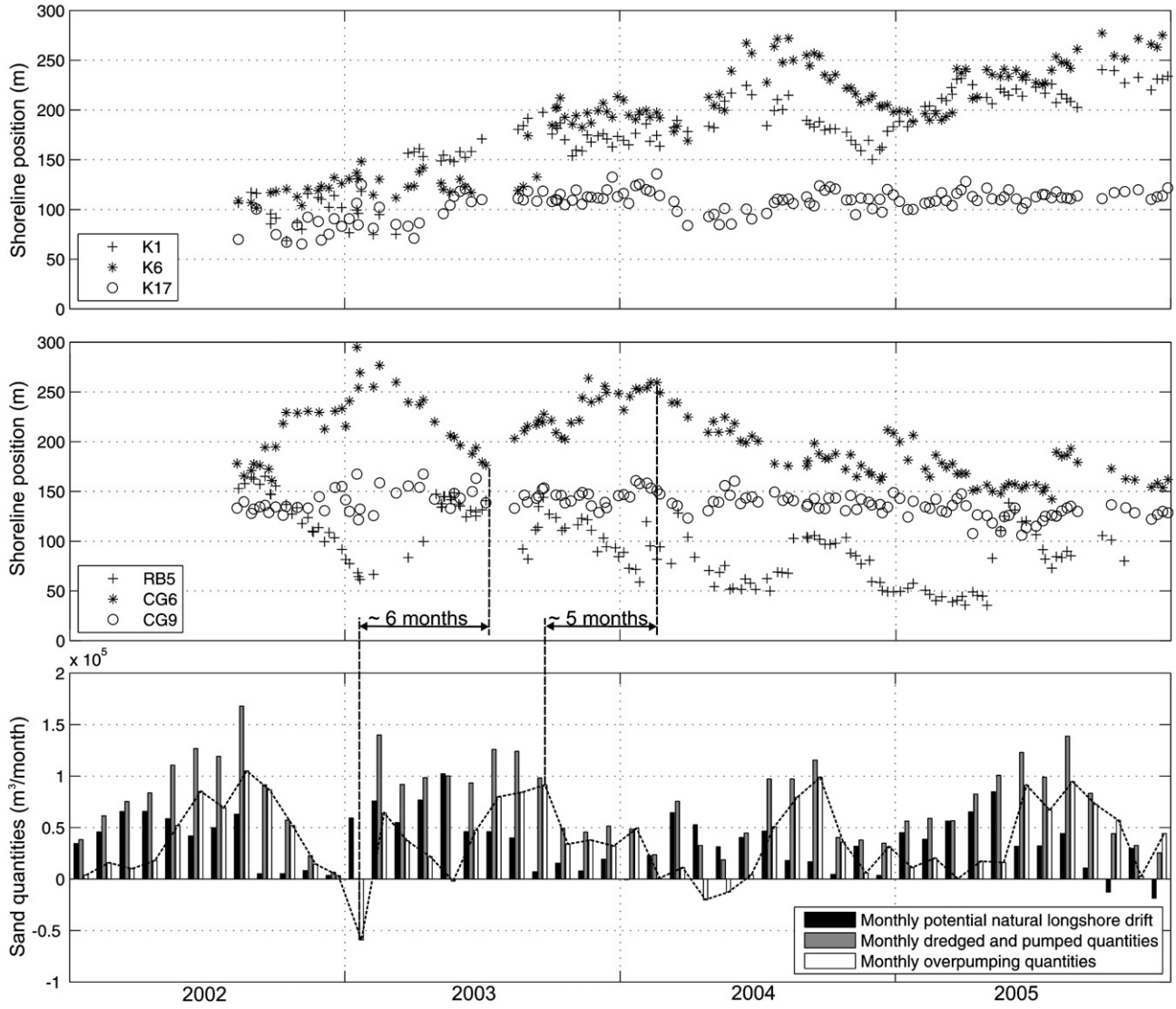

Fig. 9. Time-series of over-pumping quantities and shoreline positions using video imagery during the TRESBP.

observed from Snapper Rocks to Kirra Point groyne migrates toward the Kirra section at a rate of the order of 100 m/month. The bulk of sand is then trapped in the Kirra Beach embayment.

In 2005, the TRESBP had been successful in providing wide and healthy beaches within Coolangatta Bay. However, worldwide no beach nourishment or coastal engineering works program will ever meet everybody's expectations. The TRESBP is another example, as several issues have been raised recently by the community, despite the overall success of the engineering components of the project. Some local and tourist opinions are that beaches are currently too wide (especially at Kirra), and that surfing, swimming, fishing, diving and beach use amenity have been compromised as a result of over-pumping. The width of the nearshore bar has increased such that the natural rock reef seaward of Kirra Beach (Fig. 1) is threatened to be fully covered by sand, which raises both fishing and ecological integrity issues. The formation of the straight and wide nearshore bar along the whole bay, known by the surfers as "Superbank", is regarded by some to have resulted in the disappearance of Kirra Point's world-class surf break.

5.2. Generic lessons learnt

This case study at Coolangatta Bay demonstrates that artificial sand bypassing can have a significant and rapid impact on beach and nearshore morphology. Sand that is pumped to shallow water is readily transported by the longshore current and can naturally feed the sandbanks and beaches. This process has proven to be much more efficient than depositing the dredged sand in the nearshore area, which requires a significant period of low energy conditions in order for the deposited sediment to migrate shoreward and weld to the shore.

Several arguments support the use of sand bypassing systems in coastal areas where significant net longshore drift is observed, and where this sand supply has been interrupted. Indeed, nourishment works often result from the desire to both dispose of available sand dredged to maintain navigable depths in a nearby harbor or inlet, and widen the beach (for storm damage-reduction purposes and/or

Fig. 8. Time-series of significant wave height H_s in the Bay with superimposed 15 days low-pass-filtered H_s (thick line), pumping and dredging quantities, and shoreline position at the specific transects over the period 1995–2005. OSRE: Snapper Rock East Outlet; OSRW: Snapper Rock East Outlet; OK: Kirra Outlet; OD: Duranbah Outlet; OG: Greenmount Outlet.

recreational space). Permanent sand bypassing systems can potentially offer the possibility to both remediate these issues and later prevent them in a sustainable way. If properly formulated and managed, this strategy can remove the requirement for regular refills, dredging and additional hard structures. Collecting sand at the updrift coast also means that the same grain size as the native one is deposited, which is generally favoured. As illustrated in this case study, behavior oriented numerical models can be used to estimate potential natural longshore drift along sandy coastlines. Therefore, it is possible to pump sand quantities comparable to the natural longshore drift. This can allow permanent sand bypassing systems to work in concert with natural processes. These possible dynamic and flexible characteristics of the implementation of permanent sand bypassing system may have to be taken into greater account in future practices.

It must also be recognised that sand bypassing may be ineffective or inappropriate, dependant upon site specific considerations. For example, over-pumping can have negative consequences on natural habitats. In the case of Coolangatta Bay, a large amount of natural reefs were buried under tons of sand, which raised both fishing and ecological integrity issues. Coarser sand than the native beach material is sometimes preferably used in beach fill practices, particularly when there is requirement for offsetting serious erosion and stabilizing the upper part of the beach. This cannot be achieved with sand bypassing alone.

Hamm et al. (2002) strongly recommended the development of monitoring strategy and techniques together with sustainable soft engineering approach. Use of innovative techniques such as video-imaging, accurate bathymetric surveys, and the properly documented quantities of delivered sand quantities, offers a great potential for obtaining very valuable operational and long-term monitoring data at Coolangatta Bay and other coastal management sites worldwide.

Acknowledgements

The research presented in this paper was performed within the framework of the development of a Gold Coast Shoreline Management Plan (GCSMP) on behalf of the Gold Coast City Council (GCCC). Xavier Bertin was funded by the European Commission through a Marie Curie Intra-European Fellowship (contract IMMATIE MEIF-CT-2006-041171). The authors wish to acknowledge the permission of the Tweed River Entrance Sand Bypassing Project (TRESBP), NSW Department of Lands and Queensland Environmental Protection Agency (QEPA). The authors wish to thank GCCC for providing some of the field surveys and Debbie Abbs for providing the WW3 forcing for the study period. Funding to UNSW to operate the ARGUS stations is jointly provided by the NSW and QLD state governments.

References

Aarninkhof, S.G.J., Turner, I.L., Dronkers, T.D.T., Caljouw, M., Nipius, L., 2003. A video-based technique for mapping intertidal beach bathymetry. Coastal Engineering 49 (4), 275–289.

Allard, J., Bertin, X., Chaumillon, E., Pouget, F., 2008. Sandspit rhythmic progradation: a potential record of wave climate variation? The Arçay Sandspit, Western Coast of France. Marine Geology 253, 107–131.

Bertin, X., Castelle, B., Chaumillon, E., Butel, R., Quique, R., 2008. Longshore drift estimation and inter-annual variability at a high-energy dissipative beach: St. Trojan Beach, SW Oléron Island, France. Continental Shelf Research 28, 1316–1332.

Boak, E.H., Turner, I.L., 2005. Shoreline definition and detection: a review. Journal of Coastal Research 21 (4), 688–703.

Booij, N., Ris, R.C., Holthuijsen, L.H., 1999. A third-generation wave model for coastal regions, part I: model description and validation. Journal of Geophysical Research 104 (C4), 7649–7666.

Boswood, P., Victory, S., Lawson, S., 2001. Placement strategy and monitoring of the Tweed River Entrance Sand Bypassing Project nourishment work. Proc. Coasts and Ports Conference 2001, pp. 253–258.

Browne, M., Castelle, B., Strauss, D., Tomlinson, R.B., Blumenstein, M., Lane, C., 2007. Estimating onshore break size from a global wind-wave model: an empirical approach using artificial neural networks. Coastal Engineering 54 (5), 445–460.

Browne, M., Strauss, D., Castelle, B., Blumenstein, M., Tomlinson, R.B., Lane, C., 2006. Empirical estimation of nearshore waves from a global deep-water wave model. IEEE Geoscience and Remote Sensing Letters 3 (4).

Castelle, B., Le Corre, Y., Tomlinson, R.B., 2008. Can the Gold Coast beaches withstand extreme events? Geo-Marine Letters 28, 23–30.

Charlier, R.H., Chaineux, M.C.P., Morcos, S., 2005. Panorama of the history of coastal protection. Journal of Coastal Research 21 (1), 79–111.

Colleter, G., Cummings, P., Aguilar, P., Walters, R., Boswood, P., 2001. Monitoring of Tweed River Entrance dredging and nourishment activities. Proc. Coasts and Ports Conference 2001, pp. 259–264.

Dean, R.G., 1996. Beach nourishment performance: planform consideration. Shore and Beach 64 (3), 36–39.

Dean, R.G., Yoo, C.H., 1992. Beach nourishment performance predictions. Journal of Waterway, Port, Coastal and Ocean Engineering 118 (6), 567–586.

DHL, 1970. Gold Coast, Queensland Australia — coastal erosion and relative problems. Tech. Rep. R257. InDelft Hydraulics Laboratory, The Netherlands.

DHL, 1992. Southern Gold Coast littoral sand supply. Tech. Rep. H85. InDelft Hydraulics Laboratory, The Netherlands.

Dyson, A., Victory, S., Connor, T., 2001. Sand bypassing the Tweed River Entrance: an overview. Proc. Coasts and Ports Conference 2001, pp. 310–315.

Elko, N.A., Holman, R.A., Gelfenbaum, G., 2005. Quantifying the rapid evolution of a nourishment project with video imagery. Journal of Coastal Research 21 (4), 633–645.

Hamm, L., Capobianco, M., Dette, H.H., Lechuga, A., Spanhoff, R., Stive, M.J.F., 2002. A summary of European experience with shore nourishment. Coastal Engineering 47, 237–264.

Hanson, H., Brampton, A., Capobianco, M., Dette, H.H., Hamm, L., Laustrup, C., Lechuga, A., Spanhoff, R., 2002. Beach nourishment projects, practices, and objectives — a European overview. Coastal Engineering 47, 81–111.

Hobbs, J.E., Lawson, S.W., 1982. The tropical cyclone threat to the Queensland Gold Coast. Applied Geography 2, 207–219.

Holland, K.T., Holman, R.A., Lippman, T.C., Stanley, J., Plant, N.G., 1997. Practical use of video imagery in nearshore oceanographic field studies. IEEE Journal of Oceanic Engineering 22 (1), 81–92.

Holman, R.A., Stanley, J., 2007. The history and technical capabilities of ARGUS. Coastal Engineering 54 (6–7), 477–491.

Houston, J.R., 1991. Beachfill performance. Shore and Beach 59 (3), 15–24.

Houston, J.R., 1996. Engineering practice for beach-fill design. Shore and Beach 64 (3), 27–35.

Kaczmarek, J.M., Ostrowski, R., Pruszak, Z., Rozynski, G., 2005. Selected problems of sediment transport and morphodynamics of a multi-bar nearshore zone. Estuarine, Coastal and Shelf Science 62, 415–425.

Li, F., Dyt, C., Griffiths, C., 2006. Multigrain sedimentation/erosion model based on cross-shore equilibrium sediment distribution: application to nourishment design. Estuarine, Coastal and Shelf Science 67, 664–672.

McGrath, B.L., 1967. Erosion of Gold Coast beaches. Journal of the International Engineers. Australia 40, 155–166.

Plant, N.G., Aarninkhof, S.G.J., Turner, I.L., Kingston, K., 2007. The performance of shoreline detection models applied to video imagery. Journal of Coastal Research 23 (3), 658–670.

Smith, A.W.S., Jackson, L.A., 1993. A review of Gold Coast nourishment 1972–1992. Tech. Rep. 181, Gold Coast City Council, Australia.

Tolman, H.L., 1991. A third-generation model for wind waves on slowly varying, unsteady and inhomogeneous depths and currents. Journal of Physical Oceanography 21, 782–797.

Turner, I.L., Anderson, D.J., 2007. Web-based and 'real-time' beach management system. Coastal Engineering 54, 555–565.

Turner, I.L., Aarninkhof, S.G.J., Holman, R.A., 2006. Coastal imaging applications and research in Australia. Journal of Coastal Research 22 (1), 37–48.

Turner, I.L., Aarninkhof, S.J.D., Dronkers, T.D.T., MacGrath, J., 2004. GZM applications of ARGUS Coastal Imaging at the Gold Coast, Australia. Journal of Coastal Research 20 (3), 947–971.

Van Duin, M.J.P., Wiersma, N.R., Walstra, D.J.R., Van Rijn, L.C., Stive, M.J.F., 2004. Nourishing the shoreface: observations and hindcasting of the Egmond case, The Netherlands. Coastal Engineering 51, 813–837.

D.5 Field observations of an evolving rip current on a meso-macrotidal well-developed inner bar and rip morphology

Nicolas Bruneau, Bruno Castele, Philippe Bonneton, Rodrigo Pedreros, Rafael Almar, Natalie Bonneton, Patrice Bretel, Jean-Paul Parisot, Nadia Sénéchal

Continental Shelf Research, Vol. 29, pp. 1650-1662, 2009

Continental Shelf Research 29 (2009) 1650–1662

Contents lists available at ScienceDirect

Continental Shelf Research

journal homepage: www.elsevier.com/locate/csr

Field observations of an evolving rip current on a meso-macrotidal well-developed inner bar and rip morphology

Nicolas Bruneau [a,b,c,*], Bruno Castelle [a,b], Philippe Bonneton [a,b], Rodrigo Pedreros [c], Rafael Almar [a,b], Natalie Bonneton [a,b], Patrice Bretel [a,b], Jean-Paul Parisot [a,b], Nadia Sénéchal [a,b]

[a] CNRS, UMR EPOC 5805, Talence, F-33405, France
[b] Université de Bordeaux, UMR EPOC 5805, Talence, F-33405, France
[c] BRGM, 3 Avenue Claude-Guillemin, BP 36009, 45060 Orléans Cedex2, France

ARTICLE INFO

Article history:
Received 30 June 2008
Received in revised form
21 April 2009
Accepted 13 May 2009
Available online 28 May 2009

Keywords:
Rip current
Meso-macrotidal beach
Field experiment
Mean circulations
Very low-frequency motions
Morphodynamics

ABSTRACT

The Aquitanian Coast (France) is a high-energy meso-macrotidal environment exhibiting a highly variable double sandbar system. The inner and the outer bar generally exhibit a bar and rip morphology and persistent crescentic patterns, respectively. In June 2007, an intense five-day field experiment was carried out at Biscarrosse Beach. A large array of sensors was deployed on a well-developed southward-oriented bar and rip morphology. Daily topographic surveys were carried out together with video imaging to investigate beach morphodynamic evolution. During the experiment, offshore significant wave height ranged from 0.5 to 3 m, with a persistent shore-normal angle. This paper identifies two types of behavior of an observed rip current: (1) for low-energy waves, the rip current is active only between low and mid tide with maximum mean rip current velocity reaching 0.8 m/s for an offshore significant wave height (H_s) lower than 1 m; (2) for high-energy waves ($H_s \approx 2.5$–3 m), the rip current was active over the whole tide cycle with the presence of persistent intense offshore-directed flows between mid and high tide. For both low and high-energy waves, very low-frequency pulsations (15–30 min) of the mean currents are observed on both feeder and rip channels.

A persistent slow shoreward migration of the sandbar was observed during the experiment while no significant alongshore migration of the system was measured. Onshore migration during the high-energy waves can be explained by different sediment transport processes such as flow velocity skewness, wave asymmetry or bed ventilation. High-frequency local measurements of the bed evolution show the presence of significant (in the order of 10 cm) fluctuations (in the order of 1 h). These fluctuations, observed for both low- and high-energy waves, are thought to be ripples and megaripples, respectively and may play an important but still poorly understood role in the larger scale morphodynamics. The present dataset improves the knowledge of rip dynamics as well as the morphological response of strongly alongshore non-uniform meso-macrotidal beaches.

1. Introduction

Rip currents are narrow, intense, seaward-flowing currents which extend beyond the surf zone, and are commonly observed on many beaches. They can transport large quantities of sediment seaward, shape and interact with the sandy shoreline (Thornton et al., 2007). Understanding the dynamics of rip currents remains a scientific challenge for beach hydro and morphodynamics and for human safety. While rips have received increasing attention (MacMahan et al., 2006) in the scientific literature, there are remaining areas of uncertainty due to a lack of field measurements that need to be addressed to improve model validations in topographically-controlled rip current settings.

Various laboratory and field measurements have been carried out during the last decades to understand rip current dynamics. Haas and Svendsen (2002) studied the vertical distribution of rip currents. They found that vertical profiles of horizontal velocities are nearly depth-uniform inside the channel and depth-varying further offshore with higher velocities at the surface than near the bottom. Within field experiments, Brander and Short (2001) mentioned the non-uniform structure of rip currents with maximum velocities occurring in the middle of the water column. A quasi-three-dimensional modeling study was carried out and compared to experimental data by Haas et al. (2003). The authors highlighted the important role of wave/current interactions in rip current systems, particularly for the generation of low-frequency

* Corresponding author.
E-mail address: n.bruneau@epoc.u-bordeaux1.fr (N. Bruneau).

0278-4343/$ - see front matter © 2009 Elsevier Ltd. All rights reserved.
doi:10.1016/j.csr.2009.05.005

pulsations. Rip current pulsations can arise from wave group forcing at the infragravity band (MacMahan et al., 2004a) and can also be observed in the far-infragravity band (MacMahan et al., 2004b; Bonneton et al., 2006), the latter being referred as very low-frequency (VLF) motions. The spatial distribution of the VLF velocities within rip current systems is still poorly understood. In addition, debates remain about the mechanisms of rip current VLF source (Haller and Dalrymple, 2001; Reniers et al., 2007).

Several authors reported the strong tidal modulation of rip currents, with maximum velocities occurring during low tides (LTs) in micro-mesotidal settings (Brander, 1999; Brander and Short, 2000; MacMahan et al., 2005). Studies on the Aquitanian Coast (Castelle and Bonneton, 2006; Castelle et al., 2006) also showed the presence of strong tidally modulated rip currents with maximum rip velocities close to mid tide (MT) for low-energy waves. High-energy rip currents are still poorly understood, particularly over strongly alongshore non-uniform beaches. Brander and Short (2000) measured mean currents reaching 1 m/s near a rip neck of an oblique sandbar system for moderate/energetic conditions. Documented rip studies have mainly focused on low-energy wave conditions over small alongshore bed non-uniformities, suggesting that low waves could only induce low-energy rip currents with most of these rip current velocities on the order of $\sim 0.2-0.4\,\mathrm{m/s}$ (MacMahan et al., 2006). This present paper aims to study an intense rip current system, for both low- and high-energy waves, over a well-developed inner bar and rip morphology in a meso-macrotidal setting.

Conceptual models have been developed to predict three-dimensional beach changes associated with variations in environmental conditions. The classification schemes presented by Wright and Short (1984) are widely accepted. This conceptual model has been modified by several authors to fit the classification to their own studied beach (Masselink and Short, 1993; Brander, 1999; Castelle et al., 2007). For the Aquitanian Coast, a complete description of the observed and expected morphologies is given in Castelle et al. (2007). In this type of classification, the beaches are divided into three main different states as dissipative, intermediate and reflective (with sub-states). During high-energy conditions, the beach evolves from a more reflective state towards a more dissipative state (up-state transition). These models predict down-state transitions (towards a more reflective state) for low-energy wave conditions. Surprisingly, during the present field experiment, an onshore bar migration was observed during high-energy conditions, which is discussed in this paper.

The double-barred intermediate high-energy Aquitanian Coast beaches exhibit strongly alongshore non-uniform and variable inner bar morphologies (Castelle et al., 2007). Previous rip current studies on the Aquitanian Coast suffered from the lack of measurements in the rip. Despite the overall morphodynamics of the inner bar system being quite well understood (Castelle et al., 2007), areas with a paucity of high sample rate data remain, particularly during high-energy conditions. The present study presents an intensive five-day field experiment undertaken over a well-developed bar and rip morphology exposed to a large range of shore-normal waves ($0.5 < H_s < 3\,\mathrm{m}$, where H_s is the significant wave height) and involving a substantial onshore migration of the bar. We show that rip current can be reasonably intense ($\approx 0.8\,\mathrm{m/s}$) for low-energy waves ($H_s \approx 0.8\,\mathrm{m}$) if the morphology is strongly alongshore non-uniform. Two specific wave events are selected (one during low-energy conditions, one during high-energy conditions) to investigate the evolving rip current system behavior. In addition, the difference of tidal modulation with earlier studies in micro-mesotidal environment settings is discussed. Then, the morphodynamics of the inner bar and rip system is investigated on this meso-macrotidal beach.

2. Field experiment description

2.1. Field site

The field experiment was performed in June 2007, at Biscarrosse Beach (France), located about 10 km southward of the Arcachon Lagoon inlet (Fig. 1). The Aquitanian Coast is a wave-dominated environment, except near the Arcachon Lagoon inlet and the estuaries of Adour and Gironde which are tide-dominated environments. At Biscarrosse Beach, a persistent crescentic subtidal outer bar and an intertidal inner bar and rip morphology are observed most of the time. This wave-dominated beach is exposed to high-energy North Atlantic swells coming mainly from the W–NW direction within offshore wave height reaching 10 m during severe storm. The annual mean H_s is about 1.4 m and the mean period around 6.5 s (Butel et al., 2002). Finally, the annual mean spring tidal range is approximately 3.7 m with maximum tidal range reaching 5 m. While previous studies on Aquitanian Coast beaches were undertaken at Truc Vert Beach (Fig. 1) (Michel and Howa, 1999; Castelle et al., 2006; Masselink et al., 2008; Sénéchal et al., 2009), this experiment took place at Biscarrosse because of the recent implementation of a permanent video imagery station (Almar et al., in press).

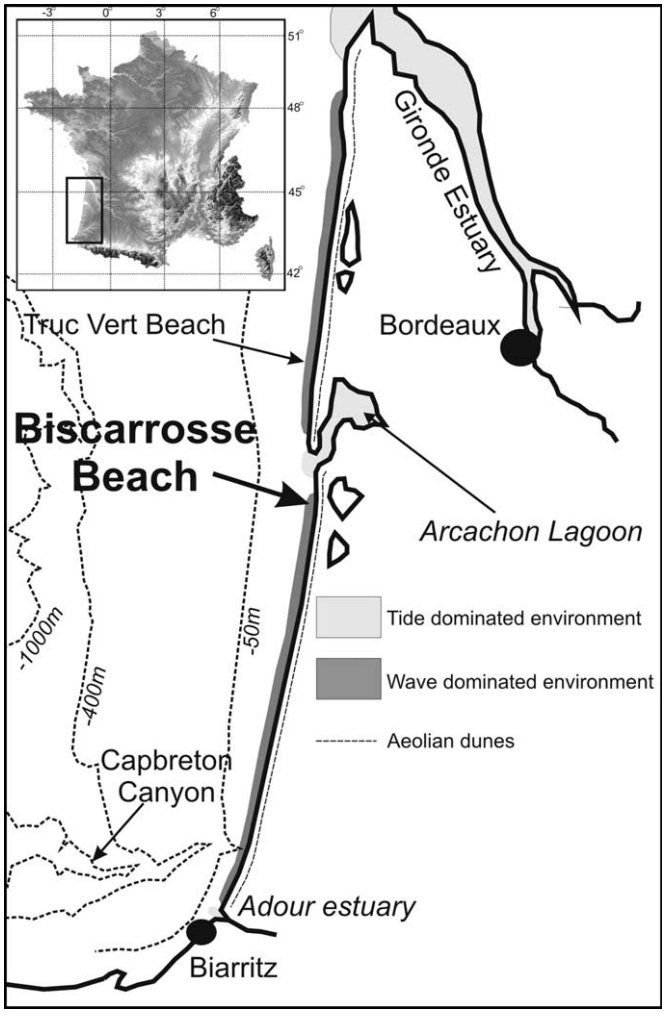

Fig. 1. The French Aquitanian Coast indicating the Biscarrosse field site and locations of wave-dominated and tide-dominated environments.

2.2. Field experiment: Biscarrosse 2007

In high-energy environments like the Aquitanian Coast, the deployment of instruments in the main body of the rip current system is a logistical challenge due to strong currents and the intense morphological evolution. Thus, an array of 12 in-situ stationary instruments (Fig. 2) were deployed on a well-developed inner bar and rip system, in the intertidal zone, between June 13 and June 17. The deployment strategy aimed at capturing the rip current circulation patterns. Four pressure sensors (noted PS1-4, sampled at 8 Hz), four acoustic doppler velocimeter (ADV1-4, 8 Hz), one acoustic Doppler current profiler (ADCP-1, profile interval 20 s), one acoustic wave and currentmeter (AWAC, profile interval 300 s) and one S4 interocean current velocimeter (2 Hz) were deployed. The S4 was deployed in three different locations in the vicinity of the rip neck (Fig. 2, S4-1, -2, -3 correspond to the three deployment locations). Two ADVs (ADV2 and ADV4) and the S4 were deployed in both northern and southern feeder channels and close to the rip channel, respectively. Finally, during the first tide cycle of the experiment, a human drifter experiment was carried out in the rip current system. Table 1 shows the schedule of the sensor deployment as all the instruments were not deployed at the same time.

To measure offshore wave conditions, another ADCP (ADCP-2, 10 min, Fig. 2) was deployed at 10 m depth (at low tide) seaward of the study area. Offshore wave conditions remained very close to shore-normal incidence, favoring rip current formation rather than sinuous longshore currents. Offshore significant wave height ranged from 0.5 to 3 m (Fig. 3) with persistent swell and sometimes a superimposed wind sea. The peak wave period (T_p) ranged from 8 to 11 s. The experiment took place during spring tides, with a tidal range varying from 3.3 to 3.8 m. Thus, in the reference system of coordinates (0 bathymetry), the water level ranged between about 0.9 and 4.7 m.

Daily, topographic surveys were carried out at low tide with 15 m spacing transects on an area covering about 1 km and 250 m in the longshore and cross-shore directions, respectively. The real-time kinematics GPS used herein for measuring the topography with a centimetric precision was a Trimble 5700. In addition, coarser 3 km alongshore topographic surveys were undertaken (25 m spacing transects). To analyze the high-frequency bottom level evolution, an altimeter (ALTUS in Fig. 2, 2 Hz) was placed shoreward of the rip channel. The camera video-imaging system, developed at the NIWA (New Zealand), was implemented in April 2007 at Biscarrosse Beach. The station is composed of five high-resolution cameras which provide high sample rate information of an about 2 km alongshore stretch of beach covering the field experiment area (Almar et al., in press). The "Service Hydrographique et Oceanographique de la Marine Nationale" (SHOM) undertook a large high-resolution bathymetric survey of the area (Fig. 2, bottom right) showing the presence of an almost straight subtidal outer crescentic bar and a well-developed, poorly rhythmic, inner bar and rip morphology.

The instrumented bar and rip morphology was characterized by a narrow and deep rip channel. Fig. 4 describes the studied morphology with the cross-sections of the feeder and rip channels (following the work of Brander and Cowell, 2003). The cross-shore section of the rip-neck channel (Fig. 4b) reached about 110 m wide and 1.4 m deep. Water depth in the rip channel ranged from 1.3 to 5.1 m depending on the tide elevation. The northern longshore-oriented feeder channel was characterized by a cross-section depth and width of around 0.9 and 60 m, respectively (Fig. 4c). The southern longshore-oriented feeder channel was less developed than the northern feeder, with a cross-section depth and width of 0.3 and 50 m, respectively (Fig. 4d). The water depth in both the northern and southern feeder channels ranged from 0.5 to 4.3 m and from 0.1 to 3.9 m, respectively. The rip current did not extend to the outer bar. This morphology can be identified as a transverse bar and rip morphology (TBR) according to the Wright and Short (1984) classification.

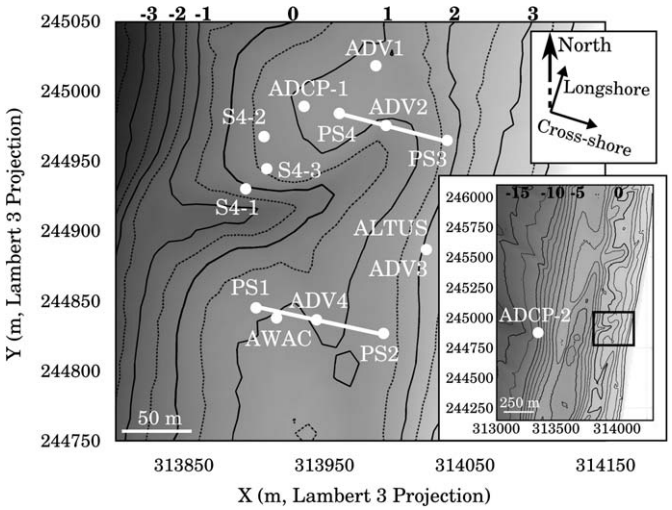

Fig. 2. Bathymetry of the instrumented bar and rip morphology showing the locations of the sensors. The extensive topography-bathymetry of Biscarrosse Beach with the position of the offshore ADCP deployed at 10 m water-depth at low tide is shown in the right hard panel. The system of coordinates is the Lambert 3 projection. The 0 isobath indicates the lowest astronomical tide.

Table 1
Instrumentation deployment schedule during Biscarrosse field experiment.

Sensors	Days of the field experiment									
	13/06/07		14/06/07		15/06/07		16/06/07		17/06/07	
	am	pm	am	pm	am	pm	am	pm	am	pm
ADV1	–	–	–	–	X	X	–	X	X	–
ADV2	–	X	X	X	X	–	X	X	X	–
ALTUS/ADV3	–	–	–	X	X	X	X	–	–	–
ADV4	–	–	X	X	X	X	X	–	–	–
PS-(1,2)	–	–	X	X	X	X	–	–	–	–
PS-3	–	X	X	X	X	–	X	X	X	–
PS-4	–	X	X	X	X	–	–	–	–	–
ADCP-1	–	–	–	X	X	X	X	–	–	–
ADCP-2	X	X	X	X	X	X	X	X	X	X
AWAC	–	–	–	X	X	X	X	X	X	–
S4	–	X1	X2	X2	X3	X3	X3	X3	X3	–

–, no deployment and X, deployment.

3. Rip current hydrodynamics

3.1. Mean rip current circulation

As detailed previously, two distinct wave events can be clearly identified during the field experiment. The first three days were characterized by low-energy waves. High-energy waves were recorded during the storm event which started during the afternoon of June 15. To investigate the influence of the offshore wave forcing (significant wave height) on the rip current dynamics, two specific hydrodynamic periods were selected (gray bands in Fig. 3): (1) June 15 from 5 to 10.30 h (UT + 2) with low-energy shore-normal waves ($H_s = 0.85$ m, $T_p = 8$ s); (2) June 15

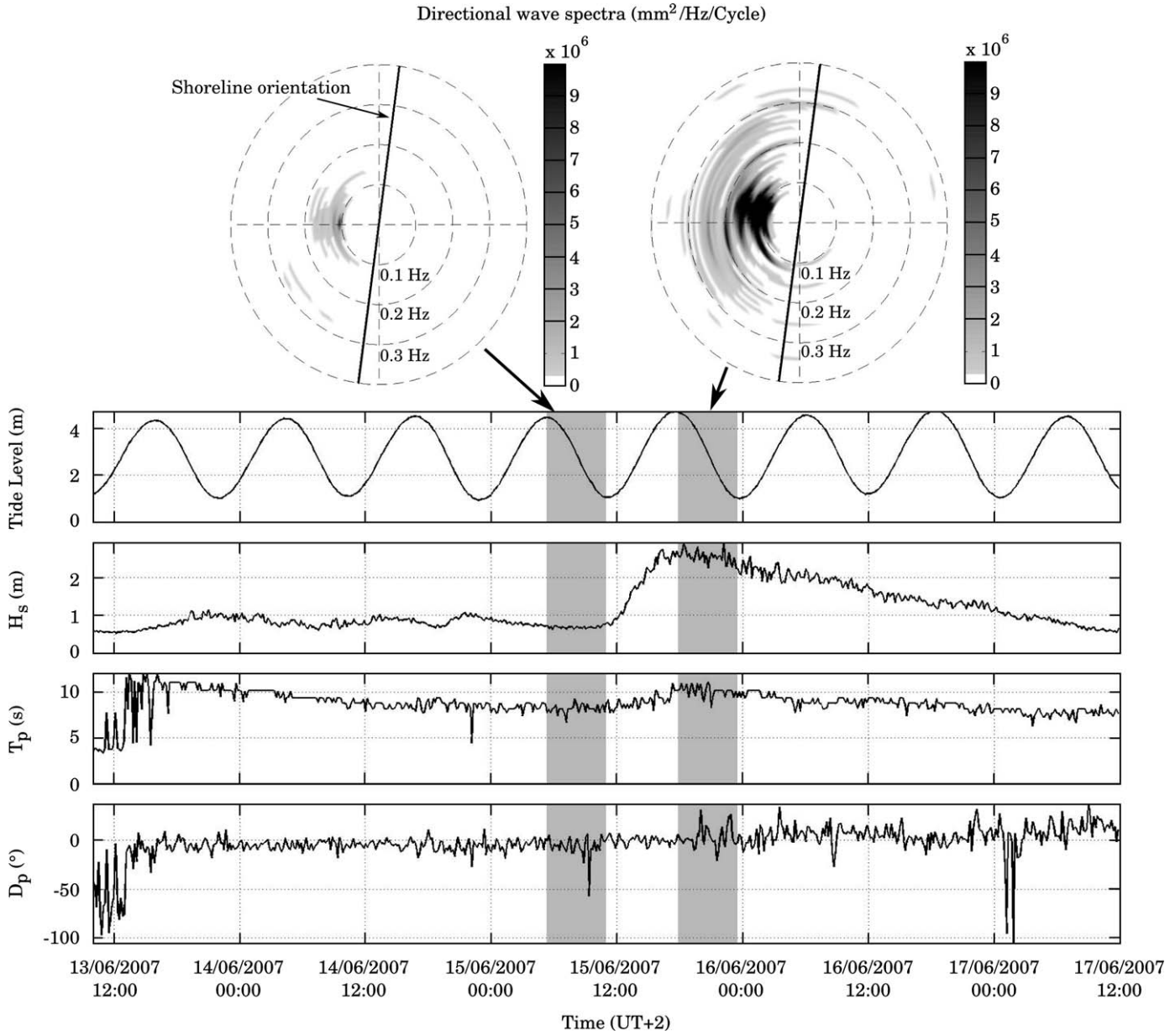

Fig. 3. Offshore wave conditions and tide level measured by the offshore ADCP-2 during the five-day field experiment with indication of the two studied events (shaded areas): (1) June 15 from 5 to 10.30 h (UT + 2) with low-energy shore-normal waves ($H_s = 0.85$ m, $T_p = 8$ s); (2) June 15 from 17 h to 22.30 h (UT + 2) with high-energy shore-normal waves ($H_s = 3$ m, $T_p = 10.5$ s) and superimposed high directional spreading wind sea. The top panels show the directional wave spectrum for each of the two selected events (noted 1 and 2).

from 17 h to 22.30 h (UT + 2) with high-energy shore-normal waves ($H_s = 3$ m, $T_p = 10.5$ s) and superimposed large directional spreading wind sea. Given the strong tidal modulation of observed wave-driven circulations, four representative tidal elevations are selected to investigate the circulation patterns: (1) at high tide (HT), (2) between mid tide and high tide (MTHT), (3) at mid tide and (4) between low tide and mid tide (LTMT). For each wave condition, the four tidal elevations have been chosen during falling tide.

The 1-h mean wave-induced currents with superimposed conceptual circulation patterns for the four tidal elevations described before are shown in Figs. 5 and 6 for events 1 and 2, respectively. The mean flows were averaged on a period larger than VLF motions. Both events show a strong tidal modulation of the wave-induced mean circulation patterns. In particular, during event 1, currents were insignificant between mid tide and high tide as water depth above the bar was too high for the waves break across the bar and to drive rip current circulations. Rip current circulations were significant for lower tide levels (Fig. 5c and d) with persistent onshore flow over the bar on the order of 0.1–0.3 m/s (1-h mean currents), and stronger feeder currents at the southern side of the rip channel. At mid tide, the S4 located on the edge of the main body of the rip channel (S4-3 in Fig. 2) measured 1-h averaged current of about 0.3 m/s and 5-min averaged currents reaching 0.6 m/s (Fig. 7a). Note that for similar wave conditions and with the S4 located closer to the rip channel during the first day of experiment (position S4-1 in Fig. 2, see Fig. 8), mean rip current velocities reached about 0.8 m/s. This suggests that, during event 1, rip current velocities in the main body of the rip channel were larger than those measured by the S4-3. During event 2, mean circulation patterns between low tide and mid tide are similar to those observed during event 1,

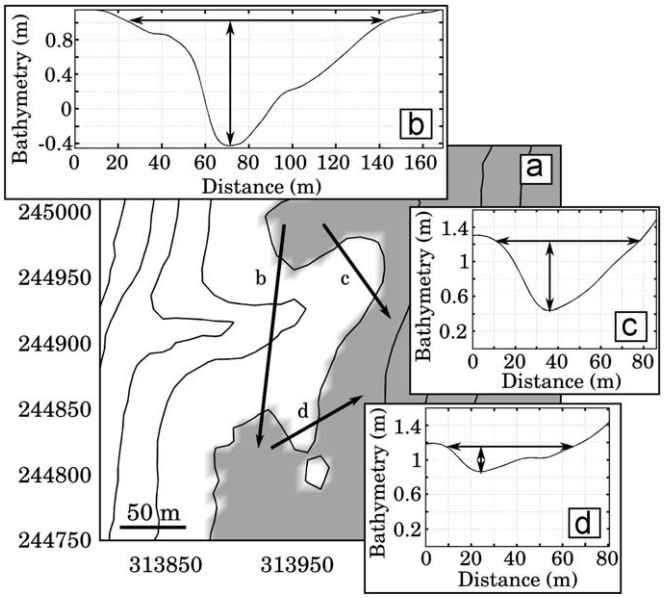

Fig. 4. (a) Description of the bar and rip morphology. Three cross-sections are indicated by the black arrows, (b) cross-section of the rip-neck channel, (c) cross-section of the northern longshore-oriented feeder channel and (d) cross-section of the southern longshore-oriented feeder channel. Black arrows indicate the depth and width of each cross-section.

with more intense velocities (Fig. 6c and d) on the order of 0.3–0.8 m/s for the same tidal water levels. Persistent offshore-directed flows are observed from mid tide to high tide (Fig. 6a and b). The measured mean flow velocities were the result of the superimposition of the rip current circulations and the undertow (also known bed return flow) contribution, as all the current meters were deployed in the surf zone.

Results presented in Fig. 7 show in more detail that, for both high- and low-energy offshore waves, tidal modulation of wave-driven circulation are pronounced. The occurrence of maximum rip current circulation intensity, which is found here to be close to mid/low tide for low-energy waves, shifts toward high tide with increasing wave energy. Strong VLF motions were observed during the whole experiment when the rip current was active.

3.2. Very low-frequency pulsations

Cross-shore and longshore 5-min averaged velocity time series at the S4, ADV3 and ADV4 locations for the two previous events are shown in Fig. 7. The time series corroborate the presence of strong currents for low-energy wave conditions (Event 1, Fig. 7a–c). Velocities measured by the S4 buoy (deployed close to the rip neck but not in the deepest part of the channel) reached 0.6 m/s. Velocities measured in the southern feeder (ADV4) reached 0.4 m/s. During high-energy conditions, 5-min mean currents reached 1.2 and 0.6 m/s, for the rip current and the southern feeder current, respectively (Fig. 7d and e). VLF pulsations were observed when the rip was active. The 15-min pulsations of rip current circulation can be observed for low-energy waves with intensities of about 0.1 m/s (Fig. 7a and b). Fig. 7d and e show 30-min pulsations with intensities on the order of 0.4 m/s (with peak reaching 1 m/s), during the energetic event. Fig. 7c and f illustrate the presence of VLF in the upper beach face where undertow is predominant.

To emphasize the pulsating behavior of rip currents, Fig. 8 shows the velocity spectrum (computed with the S4 measurements recorded during the falling tide June 13 in the afternoon—gray band in Fig. 8) and the velocity time series measured by the S4 during the first day of the experiment when the S4 was deployed in the very close vicinity of the rip neck (S4-1 in Fig. 2). The 5-min averaged currents (Fig. 8b) clearly show the presence of intense VLF pulsations (six significant peaks are observed during this period for both cross-shore and alongshore velocity components) with intensities reaching 0.6 m/s for significant wave height lower than 1 m (wave conditions similar to event 1). Results show that the energy in the infragravity band was insignificant in comparison with that in the far-infragravity band. Two distinct pulsation periods are identified: around 20 and 30 min. During this first day, a human drifter experiment was carried out with a GPS. All the drifters that were caught in the rip passed over the S4 location (Bruneau et al., 2009) which means that the S4-1 was located in the rip current throat, where rip current velocities were the most intense.

3.3. Vertical structure of the currents

Two vertical current profilers were deployed on the northern and southern bars during the experiment (AWAC and ADCP-1 in Fig. 2). Fig. 9a illustrates the vertical structure of the 30-min mean longshore and cross-shore currents for both low- and high-energy conditions between mid and high tide measured by the AWAC. In both conditions, the profiler measured depth-uniform velocities. Onshore currents were observed for low-energy waves, while strong seaward currents were measured during the storm event. This suggests that flow velocities measured by the other (not profiler) currentmeters were representative of the velocities in the water column. Fig. 9b shows 5-min averaged vertical profile in the afternoon of June 14 when strong onshore wind occurred (~20 m/s), which illustrates the presence of an intense shear near the mean free surface elevation.

4. Morphodynamics

Fig. 10 shows daily geo-referenced rectified images of the bar and rip morphology from June 13 to June 17 in the morning, at low tide. Video imaging and topographic survey analysis show an onshore migration of the oblique bar during the whole field experiment. On June 13 (Fig. 10a), the beach exhibited a well-developed southward-oriented bar and rip morphology. A northward-oriented smaller rip channel was observed in the northern part of the system. Another interesting feature was the presence on the upper part of the beach of a small-scale (about 50 m wide in the cross-shore distance) ridge and runnel system with a shore-normal mini-rip opening facing the main rip channel. Before the storm event (Fig. 10a–c), a quasi-steady onshore migration of the bar of about 5 m/day was observed. During the same time, the mini-rip progressively infilled. Fig. 10d and e show the post-storm evolving beach morphology. Surprisingly, during the storm event, the bar continued to migrate shoreward with a slightly higher rate. The upper part of the intertidal domain was entirely flattened.

High-frequency measurements of the bed evolution were carried out with an altimeter deployed in the upper part of the beach (ALTUS, Fig. 2). Fig. 11 shows the measured bed evolution during both low- and high-energy events. During the low-energy event tide cycle, although the mean currents were weak, the altimeter recorded variations on the order of 1-6 cm with a period of 10–90 min (Fig. 11a). These few centimeter fluctuations may be the trace of migrating ripples. Indeed, given the wave conditions, the ripple predictor of Nielsen (1981) predicts ripples with a 20 cm wavelength, a height of about 3 cm and a migration rate of about 0.04 mm/s, which is realistic for weakly asymmetric waves

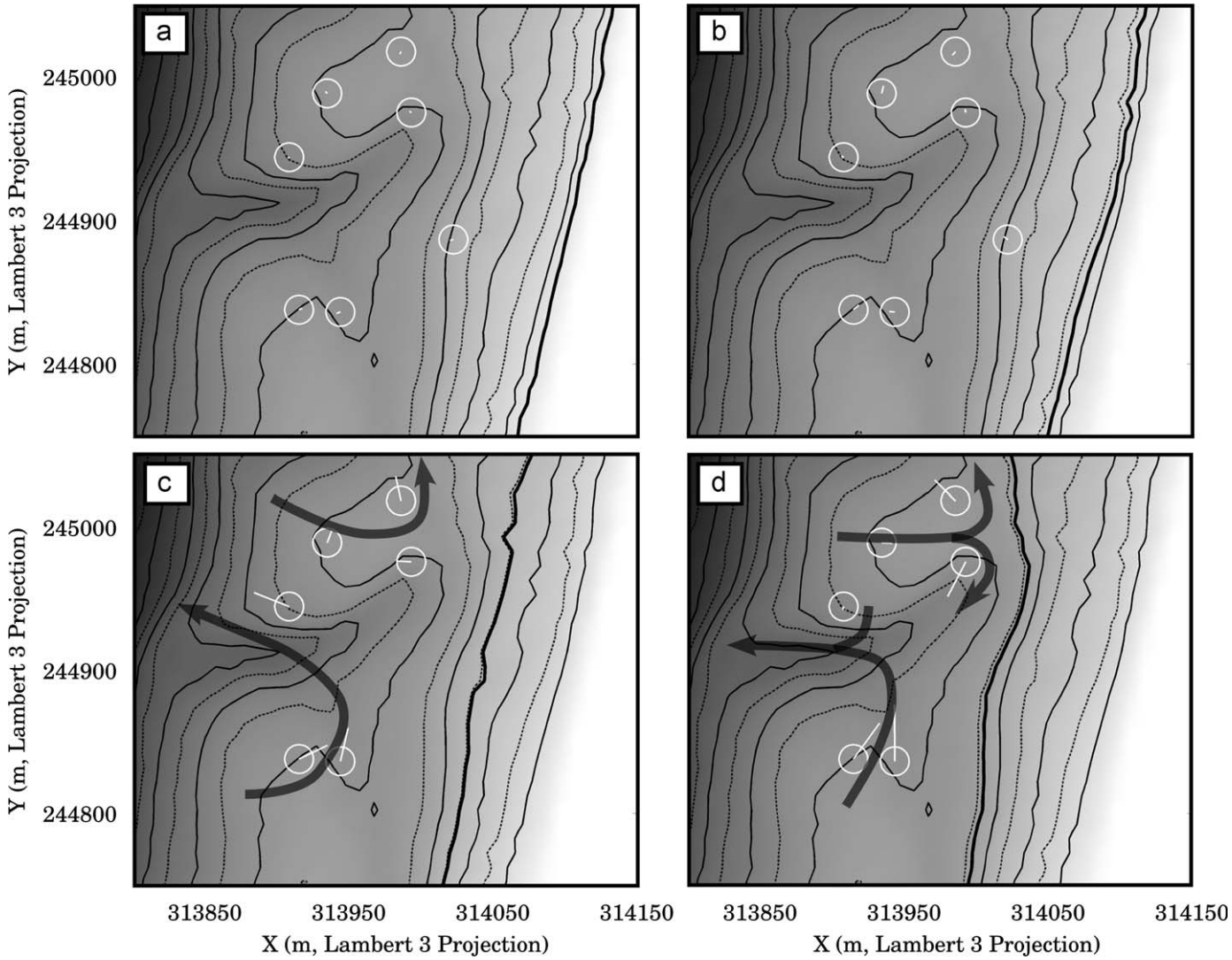

Fig. 5. The 1-h mean current (white line) measured at four different moments of the tide for low-energy wave conditions ($H_s = 0.85$ m, normal incidence and $T_p = 8$ s) during the falling tide of June 15 (from 5 to 11 h (UT + 2), first event in Fig. 3). (a) HT (high tide), (b) MTHT (between mid tide and high tide), (c) MT (mid tide) and (d) LTMT (between low and mid tide). Black arrows show the conceptual circulation patterns. The white lines indicate the directions and the intensities of the 1-h mean currents. Current magnitudes of 0.1 m/s are represented by the white circles. The thick black line represents the water level.

at high tide. For the energetic event (Fig. 11b), the bottom level fluctuations reached 20 cm on time scales of about 1 h which cannot be associated to ripples. Indeed, ripple predictors indicate the presence of sheet flow for these current and wave characteristics. In both cases, the net bed level evolution over the tide cycle was only of about a few centimeters (Fig. 11).

5. Discussion

5.1. Hydrodynamics

Drifter experiments in the laboratory (Kennedy and Thomas, 2004) and in the field (MacMahan et al., in press) showed the presence of circulation cells associated with rip currents. The present paper shows, within a large array of measurements, similar results with the presence of two circulations. In general, previous works focusing on rip hydro and morphodynamics were conducted in low-energy environments with relatively small tidal ranges (Sonu, 1972; Smith and Largier, 1995; Aagaard et al., 1997; Brander, 1999; MacMahan et al., 2005, 2006, 2008, in press). Few studies (Brander and Short, 2000; Castelle et al., 2006) were carried out in more energetic environments (H_s ranging from 1.5 to 2.5 m) where intense rip flow velocities were measured. The present study details a complete dataset on a meso-macrotidal energetic wave-dominated environment. The deployment of the S4 the first day in the close vicinity of the rip neck provided unique information about intensities and VLF motions of rip currents. In particular, intense mean rip current velocities (0.8 m/s) were measured for low-energy conditions ($H_s \approx 0.85$ m) on a well-developed southward-oriented bar and rip system.

Among the studies mentioned above, MacMahan et al. (in press) measured mean rip current velocities of about 0.3 m/s with peak velocities reaching 0.4–0.65 m/s for significant wave height ranging from 0.9 to 1.6 m, over small alongshore bedform non-uniformities. Brander and Short (2000) found mean lagrangian velocities reaching 0.8–1.2 m/s in the rip neck for moderate/energetic conditions. In the present study, rip current velocities during low-energy wave events are stronger than those measured by MacMahan et al. (in press) or similar to those of Brander and Short (2000). Results at Biscarrosse Beach are consistent with previous modeling works and field experiments on Aquitanian

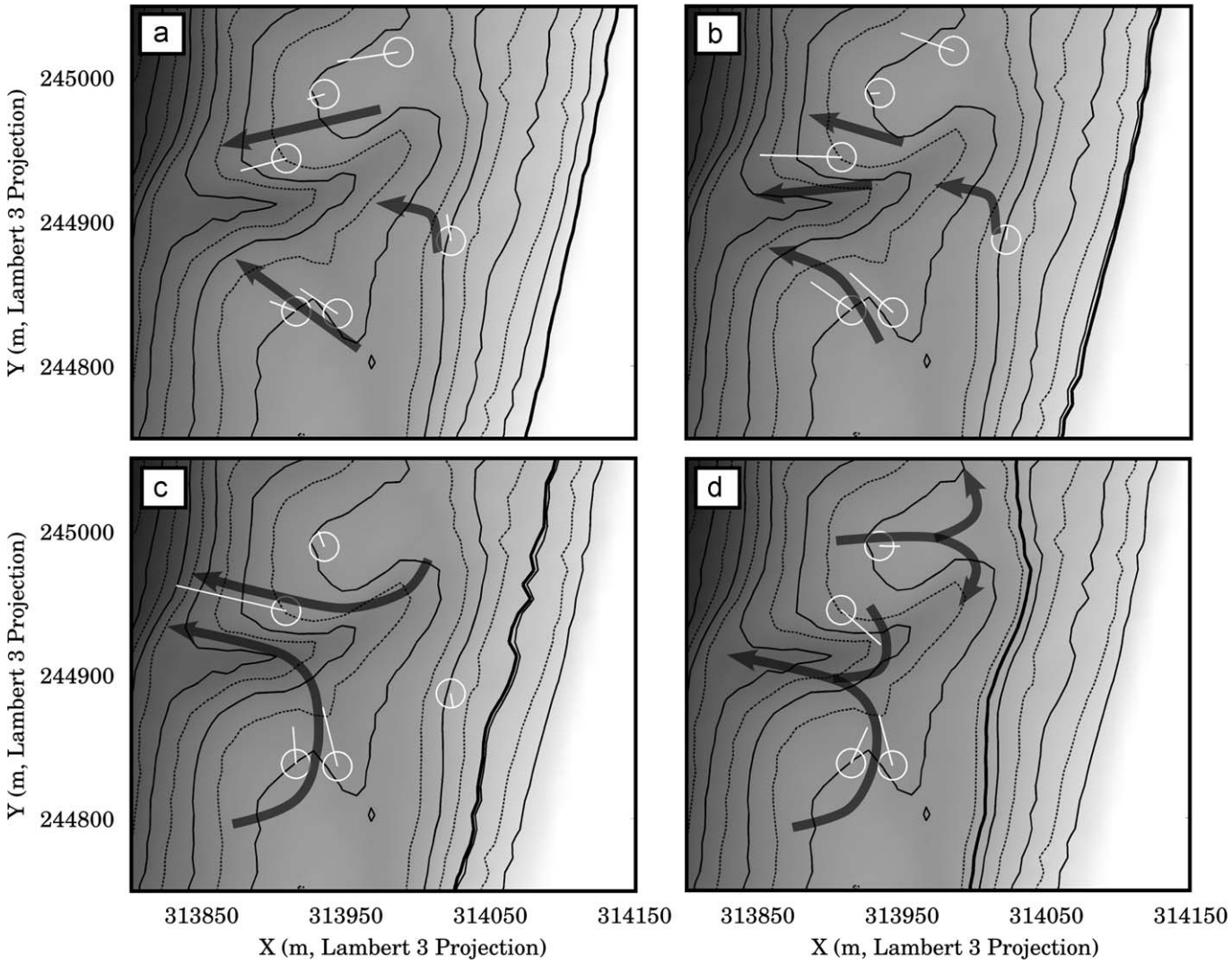

Fig. 6. The 1-h mean current (white line) measured at four different moments of the tide for high-energy conditions ($H_s = 3$ m, normal incidence and $T_p = 10.5$ s) during the falling tide of June 15 (from 17 to 23 h (UT + 2), second event in Fig. 3). (a) HT, (b) MTHT, (c) MT and (d) LTMT. Black arrows show the conceptual circulation patterns. The white lines indicate the directions and the intensities of the 1-h mean currents. Current magnitudes of 0.1 m/s are represented by the white circles. The thick black line represents the water level.

Coast (Castelle and Bonneton, 2006; Castelle et al., 2006). The present work highlights the impact of the bathymetry on rip currents and shows that intense rip currents can be observed on strongly alongshore non-uniform beaches even for low-energy waves.

Tidal modulation of rip current identified by few authors (Aagaard et al., 1997; Brander, 1999; MacMahan et al., 2005, 2006; Castelle and Bonneton, 2006; Castelle et al., 2006) is highlighted in the present work. Aagaard et al. (1997), Brander (1999) and MacMahan et al. (2006) showed that flows in the rip channel and feeders are characterized by an increasing speed with decreasing tidal elevation. Aagaard et al. (1997) showed the presence of a wave state threshold suggesting that rip activity is constrained by some critical amount of wave dissipation across the bar. To characterize the occurrence of wave-breaking, Fig. 12 illustrates the ratio of the offshore significant wave height to the local water depth (both in rip channel and above the sandbar). In Fig. 12, the mean currents are insignificant when the ratio is lower than a given threshold (0.35 on the bar). This clearly confirms the presence of a threshold controlling the activity of the rip current system. For low-energy conditions, the threshold is only exceeded between low and mid tide when waves break across the bar while, during high-energy conditions, the threshold is reached all over the tide cycle. In the present study, when low-energy waves prevailed, maximum rip velocities occurred between low and mid tide which goes with the results of Castelle and Bonneton (2006) and Castelle et al. (2006) using both modeling and experimental studies on other Aquitanian Coast beaches. The occurrence of rip current activity and dynamics is controlled by the rip current system morphology, the offshore wave forcing and the tidal range. The Aquitanian Coast is a meso-macrotidal environment with tidal ranges reaching 5 m during spring tides. At low tide and for a sufficient tidal range, the bar emerges from the water and waves cannot induce feeder and rip currents. When the water level increases, waves break across the bar and drive the rip current circulations. At high tide, low-energy waves do not break across the bar (no rip activity) while energetic waves still break across the bar (rip current activity). This explains why the maximum rip current velocity occurs close to low-mid tide for low-energy waves and shifts to high tide when increasing offshore wave energy. This contrast with earlier rip field studies in lower tidal range settings in which maximum rip current velocity occurred at low tide. The main reason is that the bar did not emerge from the water at low tide.

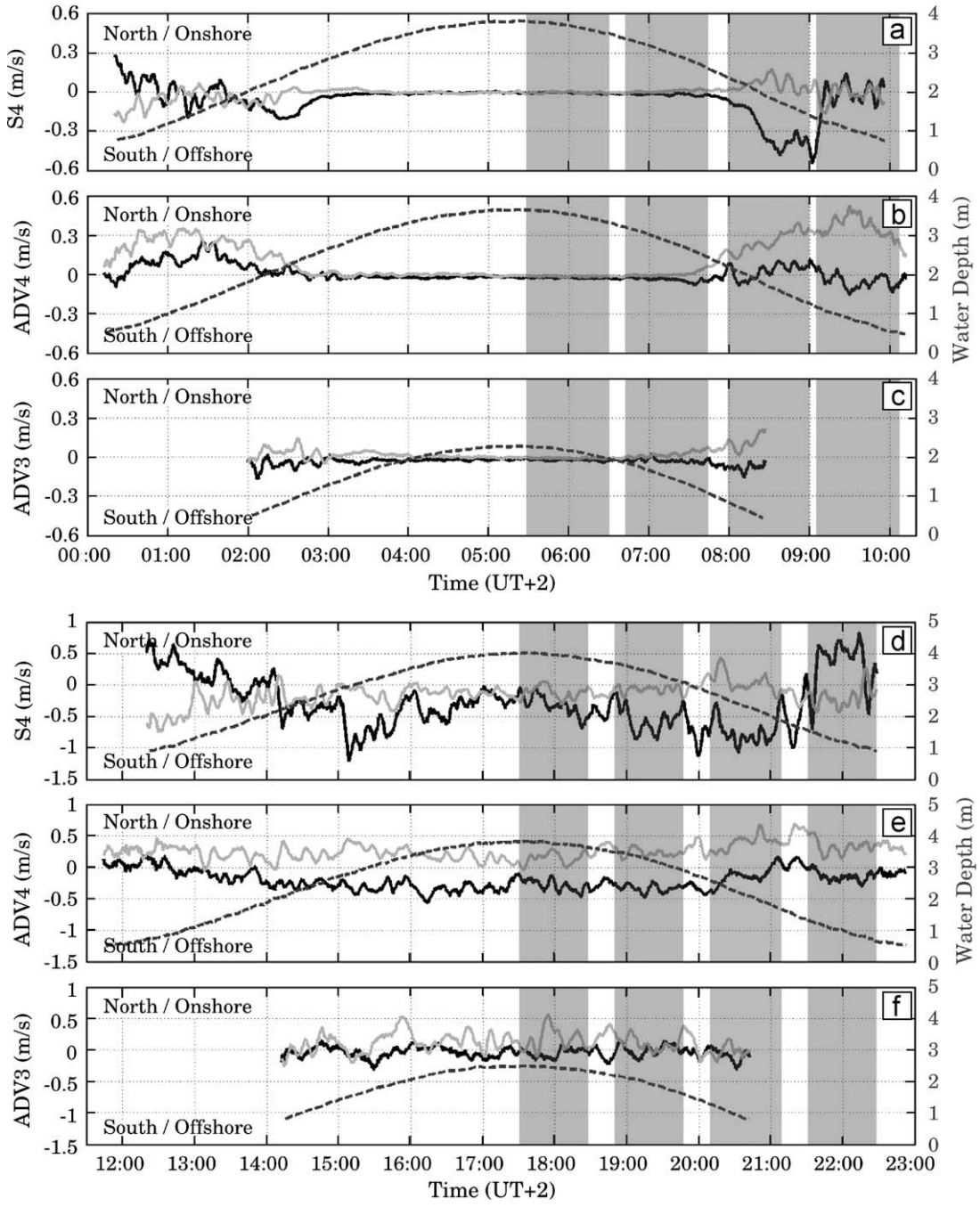

Fig. 7. Flow velocity characteristics on June 15 for the S4 (a, d), the ADV4 (b, e) and ADV3 (c,f). (a, b, c) Time series of 5-min averaged currents for low-energy waves during the first selected event ($H_s = 0.85$ m, normal incidence and $T_p = 8$ s). (d, e, f) Time series of 5-min averaged currents for high-energy waves during the second selected event ($H_s = 3$ m, normal incidence and $T_p = 10.5$ s). The dashed lines represent the water depth. Positive values indicate a shoreward cross-shore current (black) and a northward longshore current (gray).

Recent field experiments (Smith and Largier, 1995; MacMahan et al., 2004a, b, 2006; Bonneton et al., 2006; Reniers et al., 2007) showed infragravity ($0.004 < f < 0.04$ Hz) and/or VLF ($f < 0.004$ Hz) pulsations of rip currents. The present study also underlines the presence of VLF pulsations of the rip currents. The large array of sensors measured both infragravity and VLF motions all over the surf zone, except when the S4 was deployed in the rip throat (S4-1, June 13) when the velocity spectrum clearly highlighted strong energy in the far-infragravity band and insignificant infragravity band contribution. The VLF motions measured in the rip neck reach 0.6 m/s even for low-energy conditions. The results suggest spatial variation of the VLF contribution which is corroborated by the modeling study of Bruneau et al. (2009). The present study also shows that the period and intensity of the VLF pulsations increase with increasing offshore wave conditions, in agreement with the observations of Callaghan et al. (2004) and MacMahan et al. (2004b) on a transverse barred beach. Finally, the study of the drifter trajectories (Castelle et al., 2008; Bruneau et al., 2009) indicated that 80% of the drifters were retained into the circulation patterns associated with the rip current system and the remaining 20% were caught by a pulsating jet which is in agreement with recent observations of MacMahan et al. (in press) on a micro-mesotidal beach. This corroborates the intense pulsating behavior of rip currents. The generation of the VLF

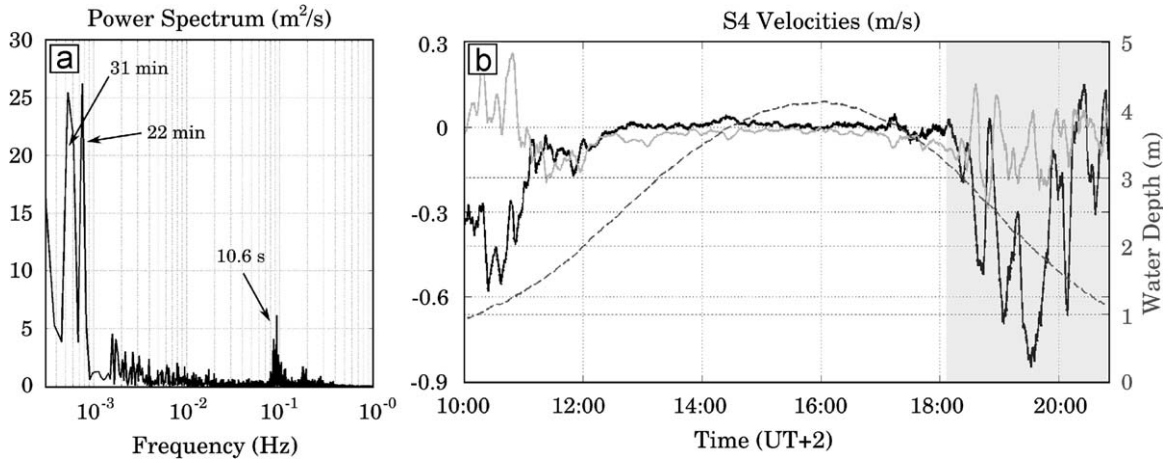

Fig. 8. (a) Velocity power spectrum of rip current measured by the S4 during the afternoon of June 13, when the S4 was deployed in the close vicinity of the rip neck (S4-1 in Fig. 2). (b) The 5-min averaged longshore and cross-shore currents in gray and black, respectively, and superimposed water depth (dashed line). Gray band indicates the section used to compute the spectrum.

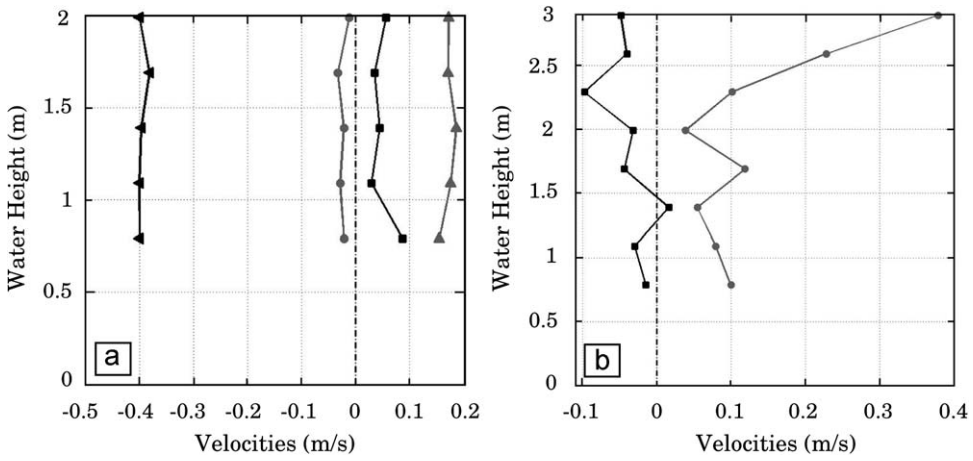

Fig. 9. Vertical profile of averaged current. (a) The 30-min averaged currents measured by the AWAC current profiler between mid tide and low tide. Squares and circles represent the cross-shore and longshore profiles, respectively, during low-energy waves. Triangles represent the profiles during high-energy conditions. (b) The 5-min averaged currents with the presence of wind during calm conditions. Positive values indicate a shoreward cross-shore current (black) and a northward longshore current (gray).

motions are not investigated herein. Understanding the contribution of both wave group (MacMahan et al., 2004b; Reniers et al., 2007) or shear instabilities (Haller and Dalrymple, 2001; Bruneau et al., 2009) is a real scientific challenge to improve our knowledge on the source mechanisms of the VLF.

5.2. Morphodynamics

According to conceptual models (Wright and Short, 1984; Masselink and Short, 1993; Brander, 1999; Castelle et al., 2007), higher wave events result in a rapid up-state transition of beach state, while lower waves result in a slow down-state accretive transition. During the experiment, a shoreward migration of the bar was observed during high-energy waves with H_s reaching 3 m. The observed onshore migration is even more unexpected given that a persistent offshore-directed flow was measured all over the inner bar morphology during the storm. This unexpected onshore bar migration during the storm event can be assumed to be the result of the continuing down-state readjustment of the inner bar resulting from a 6 m storm event which had occurred two weeks before the field campaign. Such accretionary adjustment is in agreement with a previous observation at Truc Vert Beach on the Aquitanian Coast during PNEC 2001 experiment (Castelle et al., 2006, 2007). Recently, Austin et al. (2009) underlined three processes which can cause a net onshore sediment transport: flow velocity skewness, wave asymmetry and bed ventilation. Wave asymmetry or flow acceleration can induce a net onshore transport even in the presence of seaward mean currents. Finally, other recent studies such as Aagaard et al. (2006) or van Maanen et al. (2008) suggest that the bore dynamics in very shallow water (and in swash zone) is responsible for a significant onshore bar migration which may play an important role in the net cross-shore bar migration over a tide cycle. In the present study, given that flow measurements were acquired at about 50 cm above the seabed, there was no information on hydrodynamics when swash processes were predominant.

During the experiment, the altimeter revealed the presence of significant fluctuations of the bed during a tide cycle. This kind of seabed fluctuations has been observed all over the experiment, both inside and outside the surf zone, and for both low- and high-energy conditions. These results provide quite valuable measurements in an energetic wave-dominated environment. During the low-energy period, seabed fluctuations of few centimeters were measured. For such wave conditions, regarding the main ripple characteristics (wavelength, height and migration speed)

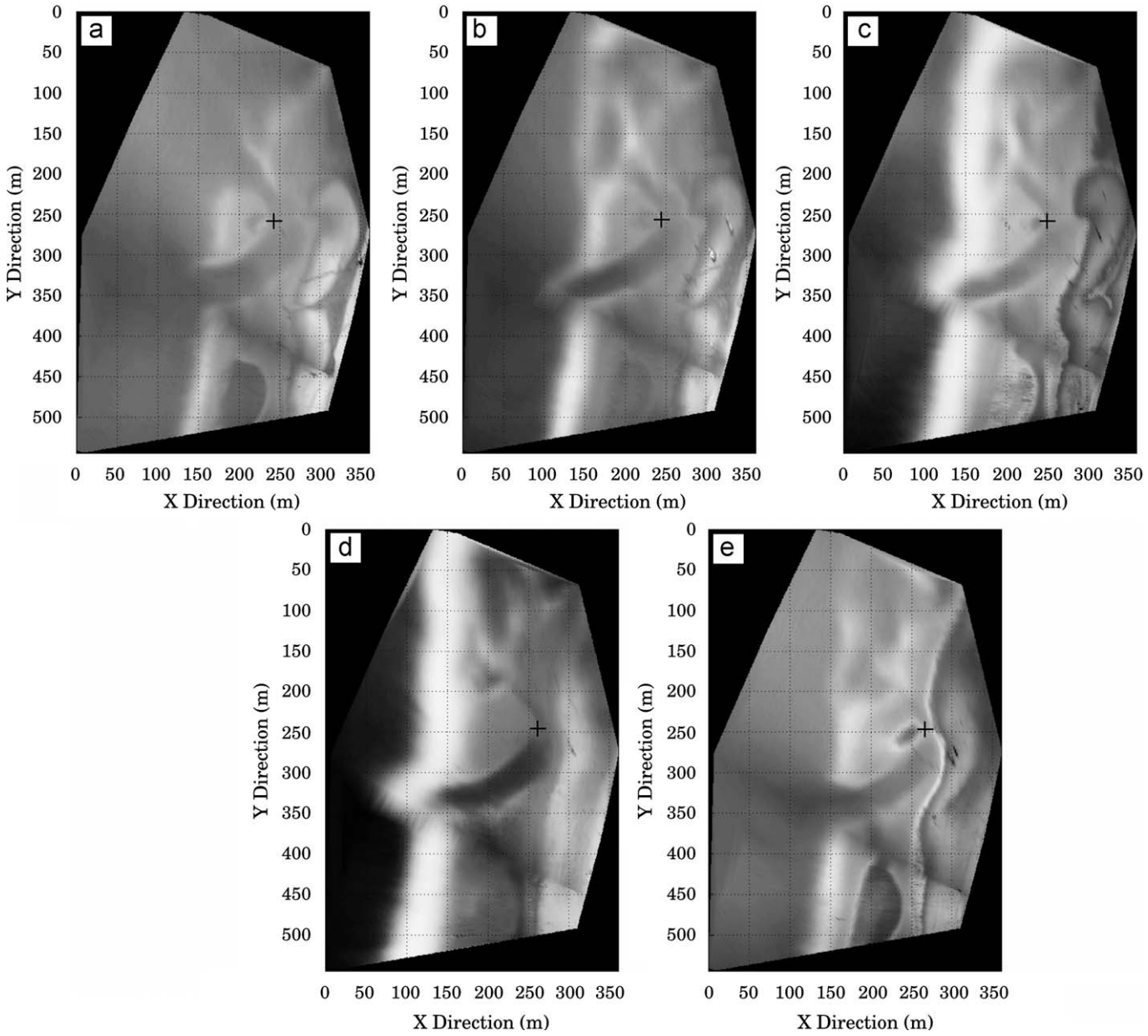

Fig. 10. The 15-min mean camera images (NIWA) combined (cameras 2 and 4) and rectified for each day at low tide during the field experiment centered of the bar and rip system investigated in this study. (a) June 13, (b) June 14, (c) June 15, (d) June 16 and (e) June 17. The black square symbol indicates the position of the bar crest. The time evolution of the crest shows a quasi-steady shoreward migration of about 5 m/day.

given by the Nielsen (1981) ripple predictor, these fluctuations can be caused by migrating ripples. The presence of such bedforms is corroborated by the work of Masselink et al. (2008) in the same environment (Truc Vert Beach). Within two sand ripple profilers, Masselink et al. (2008) observed ripples on the inner bar during calm wave conditions similarly to our observations. In contrast, recorded fluctuations during the energetic event cannot be identified as ripples due to the presence of sheet flow. On a barred beach, Gallagher et al. (1998) measured megaripples in the surf zone with heights of 0.1–0.5 m and widths of 1–5 m for a large range of wave heights (from 0.1 to 4 m) and mean currents (0–2 m/s). Average migration speeds ranged from 0.1 to 1.7 m/h. Wave and flow conditions measured during our experiment and bedform characteristics fit with the observations of Gallagher et al. (1998). This suggests the possibility of megaripple presence. Further measurements of bedform generation and propagation in wave-dominated sandy beach environment have to be done, particularly in meso-macrotidal environments, to identify their potential role in the larger-scale bar dynamics. For example a refined network of altimeters would provide important information on the spatial variabilities of these fluctuations and would help in identifying their natures and their dynamics.

6. Conclusions

The field experiment detailed in the present work provides a unique in-situ dataset on a meso-macrotidal high-energy rip current system. An intense tidal modulation for low-energy conditions was observed with maximum feeder and rip current velocities occurring between low and mid tide. For high-energy waves, the rip current was active during the whole tide cycle. A

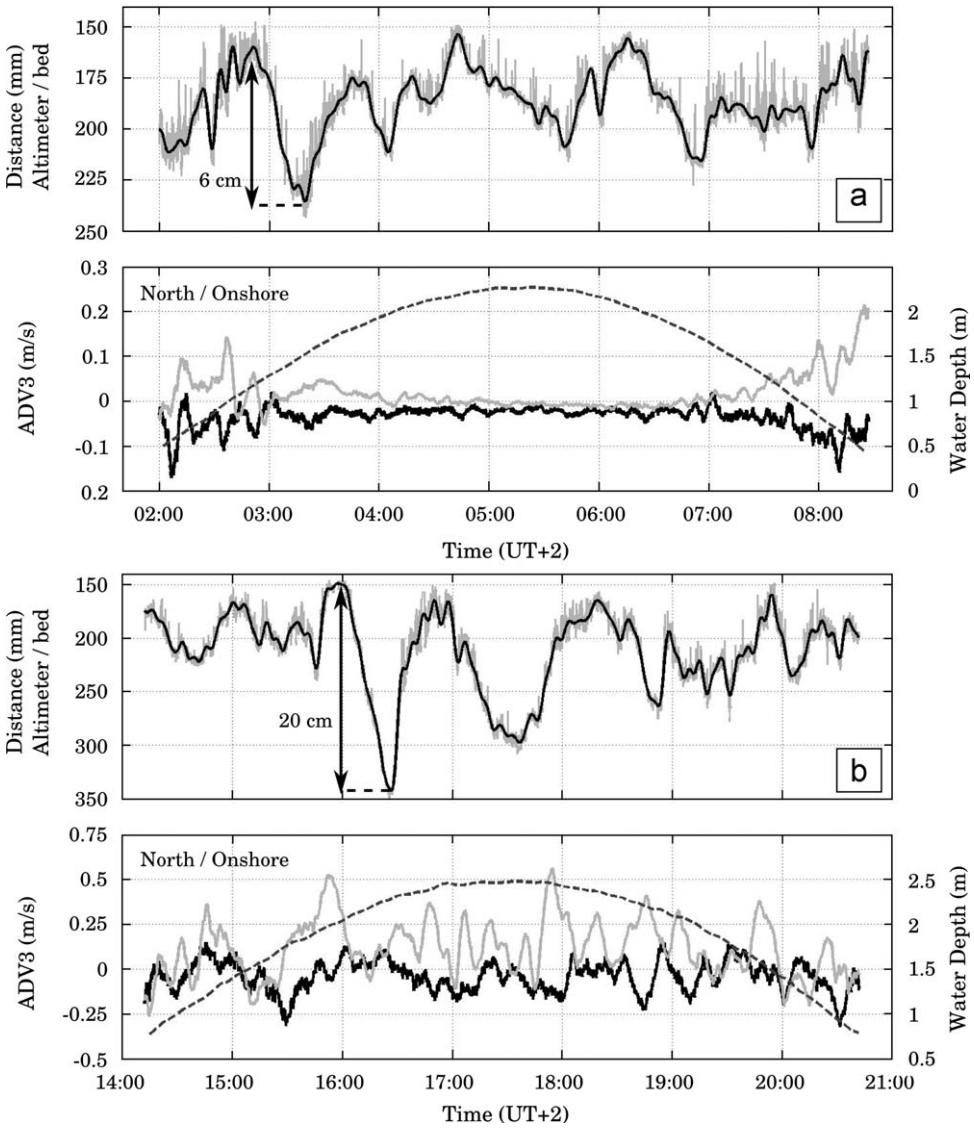

Fig. 11. Time series of the 5-min averaged bed level evolution (black) measured by the altimeter and water depth (dashed line) with superimposed 5-min averaged velocities near the bottom; (a) for low-energy conditions and (b) for energetic conditions.

threshold is identified to characterize rip current activity as a function of offshore wave height and local water depth.

Intense VLF motions of the rip current are also highlighted. The energy of the far-infragravity band can be stronger than this in the infragravity band. In the rip throat when the rip current was active, the infragravity contribution was even found to be insignificant. Intensities and periods of the VLF pulsations reach 0.6 m/s and 15–30 min, respectively, for low-energy conditions ($H_s < 1$ m).

The morphodynamic evolution of this bar and rip morphology was investigated. Using video imagery, we identified a quasi-steady onshore migration of the bar during both low-energy and high-energy conditions. During the high-energy conditions, this onshore bar migration may be explained by sediment transport processes such as velocity skewness, wave asymmetry or in/exfiltration (Austin et al., 2009), that may play a key role in beach morphodynamics; in particular during storm waves when undertow was previously thought to govern the net cross-shore sediment transport.

Finally, the measurements acquired during the Biscarrosse campaign constitute a high quality dataset that will also be useful for model calibration. Previous to this field measurement, high-frequency measurements of wave-induced currents and morphological evolution at a strongly alongshore non-uniform sandy beach were lacking, particularly in meso-macrotidal settings. In addition, the persistent offshore shore-normal wave incidence allows to characterize the rip currents and associated circulations (Bruneau et al., in press) for a large range of offshore wave energy for numerical models to be confronted with.

Acknowledgments

This Biscarrosse 2007 campaign was carried out thanks to the financial support of the BRGM. This study was performed within the framework of the ECORS (SHOM) project and the MODLIT (SHOM and INSU) project that have also sponsored this work. The authors wish to thank all the teams and students involved in the experiment. In particular, they are grateful to Stéphane Bujan, Déborah Idier, Emmanuel Rommieu, Benjamin Francois, Hervé Michallet, Jean-Marc Barnoud, David Hurther, Francois-Xavier Chassagneux, Fabrice Gouaud, Florent Grasso, Frederic Villiers,

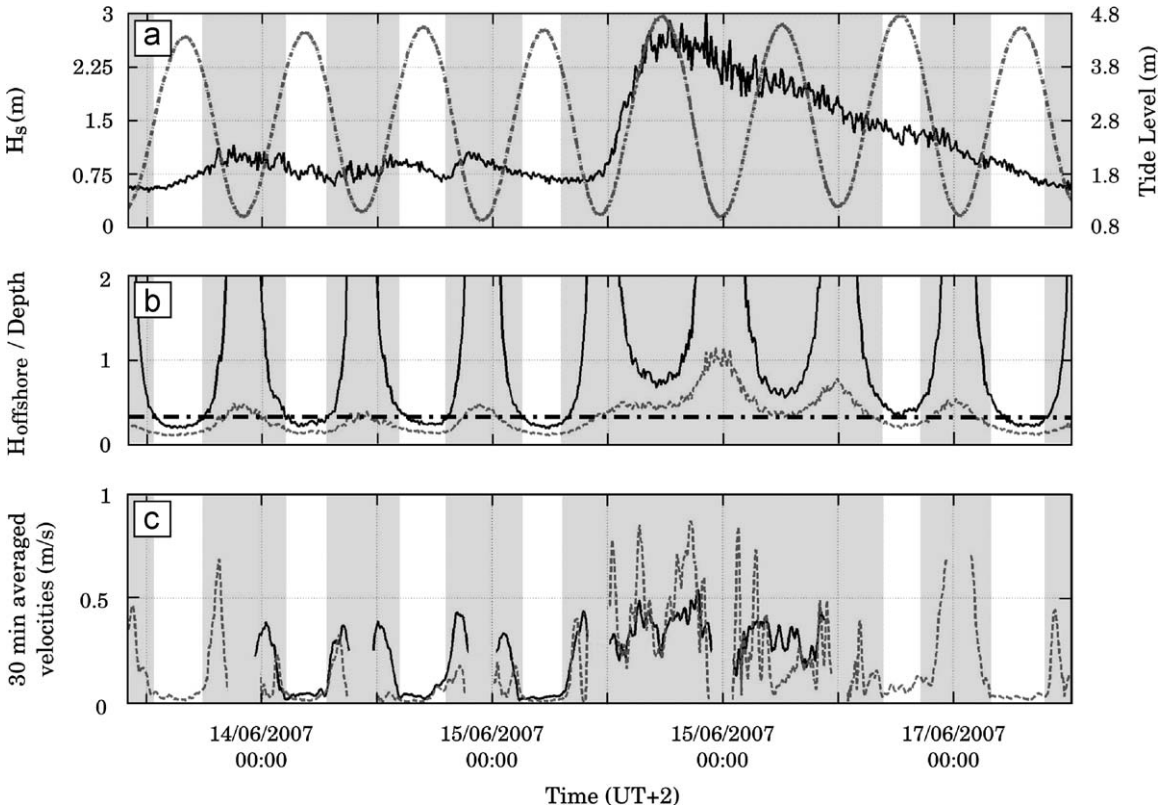

Fig. 12. (a) Offshore significant wave height (black) with superimposed tide level (dashed gray). (b) Ratio of the offshore significant wave height to the local water depth on the bar (black) and in the rip channel (gray). Dashed dot line indicates a threshold (0.35) delimiting rip current activity. (c) The 30-min averaged current magnitudes measured by the ADV4 (black) and by the S4 (gray dashed). Finally the shaded areas illustrate when rip currents are active.

Pierre Ferrer, Simon Morisset, Mathieu Mory, Gael Arnaud, Emanuele Terrile, Silvia Falchetti, Vincent Marieu and Aurélie Dehouck. They also thank the French Navy (SHOM) for the large bathymetry survey carried out on the studied field. Finally, we dedicate this work to our friend and colleague Denis Michel who tragically passed away during this field experiment.

References

Aagaard, T., Greenwood, B., Nielsen, J., 1997. Mean currents and sediment transport in a rip channel. Marine Geology 140, 25–45.

Aagaard, T., Hughes, M., Møller-Sørensen, R., Andersen, S., 2006. Hydrodynamics and sediment fluxes across an onshore migrating intertidal bar. Journal of Coastal Research 22, 247–259.

Almar, R., Sénéchal, N., Bonneton, P., Roelvink, J. Wave celerity from video imaging: validation with in-situ pre-ecors data. In: 31st International Conference on Coastal Engineering (ICCE 2008), Hamburg, Germany, in press.

Austin, M., Masselink, G., O'Hare, T., Russell, P., 2009. Onshore sediment transport on a sandy beach under varied wave conditions: flow velocity skewness, wave asymmetry or bed ventilation? Marine Geology 59, 86–101.

Bonneton, N., Bonneton, P., Sénéchal, N., Castelle, B., 2006. Very low frequency rip current pulsations during high energy wave conditions on a meso-macro tidal beach. In: Proceedings of the 30th International Conference on Coastal Engineering, ASCE, United States, pp. 1087–1096.

Brander, R.W., 1999. Field observations on the morphodynamic evolution of low wave energy rip current system. Marine Geology 157, 199–217.

Brander, R.W., Cowell, P.J., 2003. A trend-surface technique for discrimination of surf-zone morphology: rip current channels. Earth Surface Processes and Landforms 28, 905–918.

Brander, R.W., Short, A.D., 2000. Morphodynamics of a large-scale rip current system at Muriwai Beach, New Zealand. Marine Geology 165, 27–39.

Brander, R.W., Short, A.D., 2001. Flow kinematics of low-energy rip current systems. Journal of Coastal Research 17, 468–481.

Bruneau, N., Castelle, B., Bonneton, P. Pedreros, R., 2009. Very low frequency motions of a rip current system: observations and modeling. Journal of Coastal Research SI 56, 1731–1735. Proceedings of the 10th International Coastal Symposium, Lisbon, Portugal.

Bruneau, N., Castelle, B., Bonneton, P., Pedreros, R., Parisot, J.-P., Sénéchal, N. Modelling of high-energy rip current during Biscarrosse field experiment. In: 31st International Conference on Coastal Engineering (ICCE 2008), Hamburg, Germany, in press.

Butel, R., Dupuis, H., Bonneton, P., 2002. Spatial variability of wave conditions on the French Aquitanian Coast using in-situ data. Journal of Coastal Research 36, 96–108.

Callaghan, D.P., Baldock, T.E., Nielsen, P., Hanes, D.M., Hass, K., MacMahan, J.H., 2004. Pulsing and circulation in a rip current system. In: Proceedings of the 29th International Conference on Coastal Engineering, ASCE, Portugal, pp. 1493–1505.

Castelle, B., Almar, R., Bonneton, N., Bonneton, P., Bretel, P., Bujan, S., Bruneau, N., Parisot, J.-P., Pedreros, R., Sénéchal, N., 2008. Dynamics of a moderate-energy rip current over transverse bar and rip morphology: Biscarrosse 2007 field experiment. In: XI International Symposium on Oceanography of the Bay of Biscay, San Sebastián, Spain, pp. 157–158.

Castelle, B., Bonneton, P., 2006. Modelling of a rip current induced by waves over a ridge and runnel system on the Aquitanian Coast, France. C.R. Geoscience 338, 711–717.

Castelle, B., Bonneton, P., Dupuis, H., Sénéchal, N., 2007. Double bar beach dynamics on the high-energy meso-macrotidal French Aquitanian Coast: a review. Marine Geology 245, 141–159.

Castelle, B., Bonneton, P., Sénéchal, N., Dupuis, H., Butel, R., Michel, D., 2006. Dynamics of wave-induced currents over an alongshore non-uniform multiple-barred sandy beach on the Aquitanian coast, France. Continental Shelf Research 26, 113–131.

Gallagher, E.L., Elgar, S., Thornton, E.B., 1998. Megaripple migration in a natural surf zone. Letters to Nature 394, 165–168.

Haas, K.A., Svendsen, I.A., 2002. Laboratory measurements of the vertical structure of rip currents. Journal of Geophysical Research 107 (C5) 2047, doi:10.1029/2001JC000911.

Haas, K.A., Svendsen, I.A., Haller, M., Zhao, G., 2003. Quasi-three-dimensional modeling of rip current system. Journal of Geophysical Research 108 (C7), 3217, doi:10.1029/2002JC001355.

Haller, M.C., Dalrymple, R.A., 2001. Rip current instabilities. Journal of Fluid Mechanics 433, 161–192.

Kennedy, A.B., Thomas, D., 2004. Drifter measurements in a laboratory rip current. Journal of Geophysical Research 109 (C08005), doi:10.1029/2003JC001927.

MacMahan, J.H., Reniers, A.J.H.M., Thornton, E.B., Stanton, T.P, 2004a. Infragravity rip current pulsations. Journal of Geophysical Research 109 (C01033), 1–9.

MacMahan, J.H., Reniers, A.J.H.M., Thornton, E.B., Stanton, T.P., 2004b. Surf zone eddies coupled with rip current morphology. Journal of Geophysical Research 109 (C07004), doi:10.1029/2003JC002083.

MacMahan, J.H., Thornton, E.B., Reniers, A.J.H.M., 2006. Rip current review. Coastal Engineering 53, 191–208.

MacMahan, J.H., Thornton, E.B., Reniers, A.J.H.M., Stanton, T.P., Symonds, G., 2008. Low-energy rip currents associated with small bathymetric variations. Marine Geology 255, 156–164.

MacMahan, J.H., Thornton, E.B., Stanton, T.P., Measurement of rip current circulation, diffusion and dispersion. In: 31st International Conference on Coastal Engineering (ICCE 2008), Hamburg, Germany, in press.

MacMahan, J.H., Thornton, E.B., Stanton, T.P., Reniers, A.J.H.M., 2005. RIPEX—rip currents on a shore-connected shoal beach. Marine Geology 218, 113–134.

Masselink, G., Austin, M., Tinker, J., O'Hare, T., Russell, P., 2008. Cross-shore sediment transport and morphological response on a macro-tidal beach with intertidal bar morphology, Truc Vert, France. Marine Geology 251, 141–155.

Masselink, G., Short, A.D., 1993. The effect of tide range on beach morphodynamics and morphology: a conceptual beach model. Journal of Coastal Research 9, 785–800.

Michel, D., Howa, H., 1999. Short-term morphodynamic response of a ridge and runnel system on a mesotidal sandy beach. Journal of Coastal Research 15, 428–437.

Nielsen, P., 1981. Dynamics and geometry of wave-generated ripples. Journal of Geophysical Research 86, 6467–6472.

Reniers, A.J.H.M., MacMahan, J.H., Thornton, E.B., Stanton, T.P., 2007. Modeling of very low frequency motions during RIPEX. Journal of Geophysical Research 112 (C07013).

Sénéchal, N., Gouriou, T., Castelle, B., Parisot, J.-P., Capo, S., Bujan, S., Howa, H., 2009. Morphodynamic response of a meso- to macro-tidal intermediate beach based on a long-term data set. Geomorphology 107, 263–274.

Smith, J.A., Largier, J.L., 1995. Observations of nearshore circulation: rip currents. Journal of Geophysical Research 100 (C6), 10967–10975.

Sonu, C.J.,, 1972. Field observation on nearshore circulation and meandering currents. Journal of Geophysical Research 77, 3232–3247.

Thornton, E.B., MacMahan, J.H., Sallenger Jr., A.H., 2007. Rips currents, mega-cusps, and eroding dunes. Marine Geology 240, 151–167.

van Maanen, B., de Ruiter, P.J., Coco, G., Bryan, K.R., Ruessink, B.G., 2008. Onshore sandbar migration at Tairua beach (New Zealand): numerical simulations and field measurements. Marine Geology 253, 99–106.

Wright, L.D., Short, A.D., 1984. Morphodynamic variability of surfzone and beaches: a synthesis. Marine Geology 56, 93–118.

D.6 Coupling mechanisms in double sandbar systems. Part 1 : Patterns and physical explanation

Bruno Castelle, Gerben Ruessink, Philippe Bonneton, Vincent Marieu, Nicolas Bruneau, Timothy Price

Earth Surface Processes and Landforms, Vol. 35, pp. 476-486, 2010

EARTH SURFACE PROCESSES AND LANDFORMS
Earth Surf. Process. Landforms **35**, 476–486 (2010)

Published online 1 February 2010 in Wiley InterScience
(www.interscience.wiley.com) DOI: 10.1002/esp.1929

Coupling mechanisms in double sandbar systems. Part 1: Patterns and physical explanation

Bruno Castelle[1,2]*, B. G. Ruessink[3], Philippe Bonneton[1,2], Vincent Marieu[1,2], Nicolas Bruneau[1,2] and Timothy D. Price[3]
[1] CNRS, UMR EPOC 5805, Talence, F-33405, France
[2] Université de Bordeaux, UMR EPOC 5805, Talence, F-33405, France
[3] Institute for Marine and Atmospheric Research, Department of Physical Geography, Utrecht University, The Netherlands

Received 9 September 2008; Revised 29 July 2009; Accepted 10 September 2009

*Correspondence to: Bruno Castelle, CNRS, UMR EPOC 5805, Talence F-33405, France. E-mail: b.castelle@epoc.u-bordeaux1.fr

ESPL
Earth Surface Processes and Landforms

ABSTRACT: Crescentic sandbars and rip channels along wave-dominated sandy beaches are relevant to understand localized beach and dune erosion during storms. In recent years, a paradigm shift from hydrodynamic template models to self-organization mechanisms occurred to explain the formation of these rhythmic features. In double sandbar systems, both the inner- and outer-bar rip channels and crescentic planshapes are now believed to be free instabilities of the nearshore system arising through self-organization mechanisms alone. However, the occasional occurrence of one or two inner-bar rip channels within one outer-bar crescent suggests a forced, morphologically coupled origin. Here we use a nonlinear morphodynamic model to show that alongshore variability in outer-bar depth, and the relative importance of wave breaking versus wave focussing by refraction across the outer bar, is crucial to the inner-bar rip channel development. The coupling patterns simulated by our model are similar to those observed in the field. Morphological coupling requires a template in the morphology (outer-bar geometry) which, through the positive feedback between flow, sediment transport and the evolving morphology (that is, self-organization) enforces the development of coupling patterns. We therefore introduce a novel mechanism that blurs the distinction between self-organization and template mechanisms. This mechanism may also be extended to explain the dynamics of other nearshore patterns, such as beach cusps. The impact of this novel mechanism on the alongshore variability of inner-bar rip channels is investigated in the companion paper. Copyright © 2010 John Wiley and Sons, Ltd.

KEYWORDS: self-organization; forcing templates; morphological coupling; coupling patterns; double sandbar system

Introduction

Nearshore patterns along sandy wave-dominated beaches cover a wide and intriguing variety of temporal and spatial variability: ripples (Traykovski *et al.*, 1999; Marieu *et al.*, 2008) and megaripples (Clarke and Wermer, 2004; Gallagher *et al.*, 1998), shoreline undulations ranging from a few (beach cusps, Guza and Inman, 1975; Coco *et al.*, 1999) to hundreds (megacusps, Short, 1999) and thousands (coastline features such as cuspate patterns, Ashton *et al.*, 2001; Ruessink and Jeuken, 2002) of metres and three-dimensional (3D, Short, 1999; Van Enckevort *et al.*, 2004) or alongshore-uniform (Greenwood and Davidson-Arnott, 1979; Short, 1991) surfzone sandbars. These striking patterns in the nearshore display complex behaviour seemingly at odds with their simplicity and rhythmicity. Their generation and dynamics have puzzled scientists for decades, and debates and unknowns remain within the nearshore community (Coco and Murray, 2007).

Among these morphological features, surfzone sandbars are some of the most intriguing, dynamical and complex patterns. Surfzone sandbar morphology has been studied for a long time (Shepard, 1952). Most of the time, 3D morphological rhythmic or quasi-rhythmic features are observed, which can be viewed as an alongshore sequence of horns (shoals) and bays (cross-shore troughs) alternating shoreward and seaward of a line parallel to the beach (Van Enckevort *et al.*, 2004). These 3D patterns are often part of an accretionary, down-state sequence developing from an alongshore-uniform beach state (Wright and Short, 1984; Ranasinghe *et al.*, 2004) following a storm event. The resulting nearshore patterns are the so-called crescentic sandbars (Van Enckevort *et al.*, 2004; Castelle *et al.*, 2007), also known as lunate bars (Shepard, 1952), and rip channels (Holman *et al.*, 2006; Thornton *et al.*, 2007), also known as transverse or oblique bars and rips morphology (Wright and Short, 1984; MacMahan *et al.*, 2005).

Coco and Murray (2007) reviewed the paradigm shift from template forcings to self-organization mechanisms that occurred in recent years to explain the generation and subsequent nonlinear evolution of 3D surfzone sandbars. A few decades ago, edge waves (i.e. longshore periodic gravity waves trapped to the shoreline by refraction and reflection) appeared as ideal candidates to explain the formation of

alongshore rhythmic patterns such as crescentic sandbars (Bowen and Inman, 1971) and transverse bars (Holman and Bowen, 1982). The cross-shore and alongshore edge-wave patterns are spatially organized structures in the hydrodynamics that were hypothesized to become imprinted on the seabed. Theoretically, in the bottom boundary layer, the second-order drift velocities induced by the standing edge wave are cellular. Assuming that sediment transport takes place mainly close to the bed, there is a potential for a net sediment transport with a horizontal divergence away from nodal lines and toward antinodal lines (Carter *et al.*, 1973), that is, forming the onshore horns of the bar facing the alongshore nodes of the standing edge wave. This hydrodynamic template forcing became widely accepted (Carter, 1988; Komar, 1998; Short, 1999), despite a number of possible objections progressively raised by several authors (Sonu, 1972; Bryan and Bowen, 1997; Bowen, 1997; Holman, 2000; Van Enckevort *et al.*, 2004). Most importantly, the edge-wave theory, which only assumes a passive response of the incipient sediment patterns to the template in the hydrodynamics, is incompatible with the nonlinear and open nature of natural nearshore systems (Van Enckevort *et al.*, 2004; Coco and Murray, 2007). In other words, the template forcing theory does not take into account the feedback between hydrodynamics (waves and currents), sediment processes and the evolving morphology.

Only recently, this template forcing theory has been challenged by the development of self-organization models based on this feedback. Linear stability models (Deigaard *et al.*, 1999; Falqués *et al.*, 2000; Damgaard *et al.*, 2002; Calvete *et al.*, 2005, among others), restricted to the initial development (linear regime) of the 3D patterns using a number of simplifying assumptions, have established the role of self-organization mechanisms in the development of crescentic sandbars and transverse bars and rips patterns (Caballeria *et al.*, 2002). Nonlinear morphodynamic models (Damgaard *et al.*, 2002; Reniers *et al.*, 2004; Klein and Schuttelaars, 2006; Castelle *et al.*, 2006; Drønen and Deigaard, 2007; Smit *et al.*, 2008; Garnier *et al.*, 2008, among others) were also used to simulate the formation and subsequent nonlinear evolution of crescentic features. In particular, temporal changes in the wavelength and the amplitude of the 3D patterns, resulting from merging and splitting of individual crescents or rip channels (widely observed in the field, e.g. Van Enckevort *et al.*, 2004), were obtained (Garnier *et al.*, 2008). All these complex and more simple models have established that 3D surfzone sandbars can be formed through self-organization mechanisms alone, and do not require a template in the hydrodynamics.

Double sandbar systems often exhibit reasonably regular outer-bar crescentic patterns and inner-bar transverse bar-rip morphology. Although such double-bar patterns are nowadays believed to be free instabilities of the nearshore system and thus to be formed through self-organization mechanisms, some observations suggest inner-bar variability to be a forced response to outer-bar patterns rather than to be local free instabilities (Figure 1). The striking relationship between inner- and outer-bar patterns can be considered as reminiscent of the more commonly observed relationship between inner-bar patterns and shoreline rhythms (Wright and Short, 1984; Short, 1999; Coco *et al.*, 2005; Thornton *et al.*, 2007). For instance, Sonu (1973) observed a 180° out-of-phase relationship of inner-bar patterns and shoreline rhythms, i.e. an inner-bar bay facing a seaward bulge in the shoreline (Figure 2a). An in-phase relationship can also sometimes be observed (Figure 2b) with an inner-bar horn facing a seaward bulge in the shoreline. On the one hand, in many documented observations of double sandbar systems (Hom-ma and Sonu, 1962; Goldsmith *et al.*, 1982; Bowman and Goldsmith, 1983), no phase coupling has been observed, even when the outer-bar horns are welded to the inner bar. On the other hand, Van Enckevort and Wijnberg (1999) observed inner-bar bays to systemati-

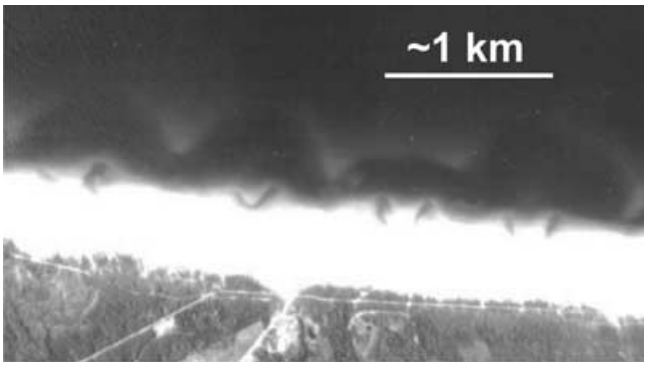

Figure 1. Aerial photograph of a double-barred beach along the Aquitanian Coast revealing the systematic occurrence of two inner-bar rip channels within one outer-bar crescent, suggesting inner-bar variability to be a forced response to outer-bar patterns rather than local free instabilities.

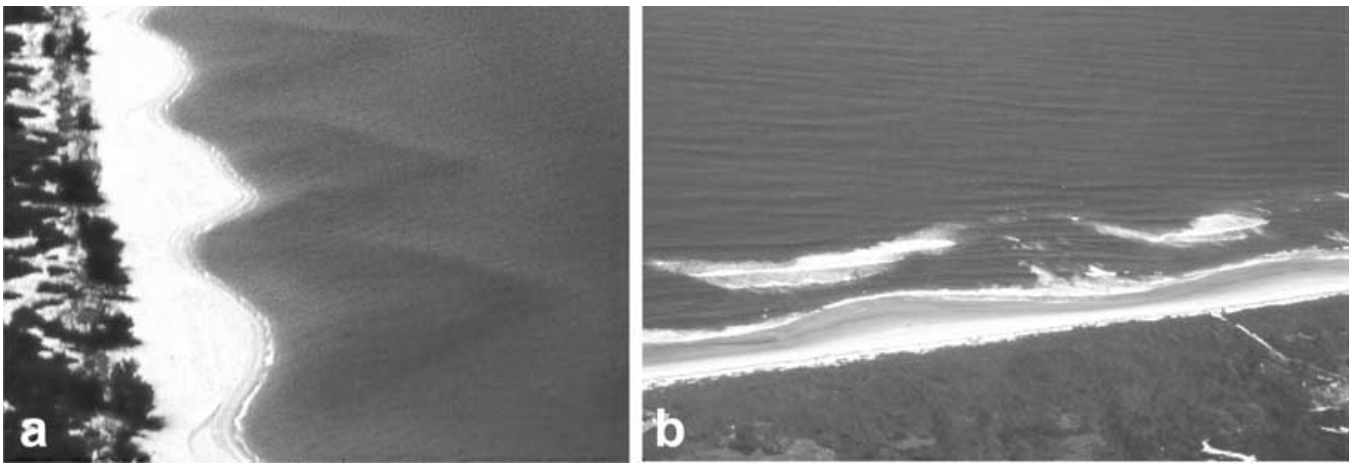

Figure 2. Aerial photographs of a single-barred beach of the New South Wales Coast (Australia) displaying (a) a 180° out-of-phase relationship of inner-bar patterns and shoreline rhythms with inner-bar bays systematically facing a seaward bulge in the shoreline and (b) an in-phase relationship between inner-bar patterns and shoreline rhythms (courtesy of A. D. Short).

cally face outer-bar horns, a situation reminiscent of the commonly observed 180° out-of-phase relationship of inner-bar patterns and shoreline rhythms (Sonu, 1973). Quartel (2009) observed a coupling of the intertidal morphology to the subtidal alongshore variability, with the phase between the two bar variabilities varying from in-phase (0°) to out-of-phase (180°), with gradual phase changes due to different alongshore migration rates of the bars. In addition, Castelle *et al*. (2007) noted the systematic occurrence of two inner-bar rip channels within one outer-bar crescent, revealing the existence of a possible relationship at half of the outer-bar wavelength. Ruessink *et al*. (2007) recently examined an eight-week dataset of daily time-exposure video images and showed that, over time, the inner-bar morphology appeared to couple with the crescentic pattern in the outer bar, with the inner-bar morphology developing in response to the increasingly crescentic, onshore-propagating outer bar. This forced morphological response is presumably due to inner-bar wave height variability and associated circulation patterns enforced by the alongshore variability in depth and position of the outer bar (e.g. Castelle and Bonneton, 2004). At this time, however, previous modelling exercises of double sandbar dynamics (Klein and Schuttlelaars, 2006: Drønen and Deigaard, 2007; Smit *et al.*, 2008) did not investigate the potential role of coupling, and the simulation of the observed coupling patterns in double sandbar systems has never been attempted.

The causative mechanisms leading to the apparent coupled and non-coupled behaviour in 3D patterns of double sandbar systems are not well understood. Here we use a nonlinear morphodynamic model (next section) to demonstrate that, as suggested by observations, the variability in mean water depth along the outer bar is crucial to the evolution of inner-bar rip channels and the generation of coupling patterns, with simulated coupling patterns being in agreement with some observations (Results section). In the final section, we discuss the mechanism leading to coupling in double sandbar systems which appears as a novel mechanism that blurs the distinction between self-organization and template mechanisms. This mechanism may also be applied to other nearshore patterns such as beach cusps.

Nonlinear Morphodynamic Model

Model set-up

We used a nonlinear morphodynamic model (Castelle *et al.*, 2006) that couples a spectral wave model, a time- and depth-averaged flow model, an energetic-type sediment transport model, and the bed level continuity equation to compute bed level changes. The spectral wave model SWAN (Booij *et al.*, 1999) is used to compute the wave field and radiation stress components to drive the flow model. The wave field is described with the 2D wave action density spectrum $N(\sigma, \theta)$, defined as the energy density spectrum divided by the relative frequency σ as observed in a reference frame moving with the current velocity, and with θ being the angle of wave incidence. The spectral wave action balance equation is given by:

$$\frac{\partial N}{\partial t}+\frac{\partial C_x N}{\partial x}+\frac{\partial C_y N}{\partial y}+\frac{\partial C_\sigma N}{\partial \sigma}+\frac{\partial C_\theta N}{\partial \theta}=\frac{S}{\sigma}, \tag{1}$$

with C_x, C_y, C_σ and C_θ the propagation velocities in x-, y-, σ- and θ-space, respectively, and t is time. $S(\sigma,\theta)$ is the sink term, representing the effects of depth-induced breaking and bottom friction dissipation and nonlinear wave–wave interactions as functions of frequency and direction. Default parameter settings and time-invariant offshore wave forcing were used throughout this study.

The flow model is based on the time-averaged and depth-integrated mass and momentum conservation equations. The averaging duration is chosen to be much longer than the wave groups, but significantly shorter than any time-scale associated with changes in incident wave conditions. The hydrodynamics are solved using an implicit method to obtain quasi-steady mean water depth h and water volume fluxes Q_i, with the subscript i referring to the two horizontal coordinates:

$$\frac{\partial Q_i}{\partial t}+\frac{\partial}{\partial x_j}\left(\frac{Q_i Q_j}{h}\right)-gh\frac{\partial \eta}{\partial x_i}-\frac{1}{\rho}\frac{\partial S_{ij}}{\partial x_j}+\frac{1}{\rho}\frac{\partial T_{ij}}{\partial x_j}-\frac{T_i^{\mathrm{b}}}{\rho}, \tag{2}$$

$$\frac{\partial \eta}{\partial t}+\frac{\partial Q_j}{\partial x_j}=0. \tag{3}$$

In Equations (2) and (3), η is the mean free surface elevation, g the gravitational acceleration, ρ the water density, S_{ij} the radiation stress components (Philipps, 1977). With the mean horizontal current velocities given by $U_i = Q_i/h$ following Mei (1989), the bed shear stress τ_i^b according to the weak flow approximation (Liu and Dalrymple, 1978) is given by:

$$\tau_i^{\mathrm{b}}=\rho C_{\mathrm{f}} U_{\mathrm{w}} U_i, \tag{4}$$

with U_{w} the near-bottom orbital velocity and C_{f} a spatially constant bottom friction coefficient. T_{ij} is the lateral shear stress which is the horizontal momentum exchange due to the combined action of turbulence and the mean current, using the formulation proposed by Battjes (1975):

$$T_{ij}=\rho h\left[Mh\left(\frac{D}{\rho}\right)^{1/3}+v_0\right]\left(\frac{\partial U_i}{\partial x_j}+\frac{\partial U_j}{\partial x_i}\right), \tag{5}$$

where D is the rate of energy loss due to depth-induced breaking, and M and v_0 are constants.

The bed and suspended load sediment transport $\vec{Q}_s$ was computed using the formulations of Bailard (1981), using default settings. The new seabed level Z_{f} was computed using the sediment mass conservation equation:

$$\frac{\partial Z_{\mathrm{f}}}{\partial t}+\frac{1}{1-p}\vec{\nabla}\vec{Q}_{\mathrm{s}}=0, \tag{6}$$

where p = 0·4 is the sediment porosity. The morphological time step for the bed update scheme was 1 hour throughout.

All the simulations were run with time-invariant mean water level (no tide). Our model does not include descriptions of the undertow, wave nonlinearity, wave–current interaction and surface rollers to limit model complexity; yet it still contains the essential physics to examine the initial growth and subsequent nonlinear evolution of crescentic patterns in double sandbar systems (Castelle and Bonneton, 2004; Castelle *et al.*, 2006).

Initial bathymetries and grid

We ran the model for different double sandbar geometries on a computational grid with an alongshore length of 4200 m, 20 × 20 m grid cells, and periodic lateral boundary conditions. In each geometry, we implemented an alongshore-uniform inner bar, 100 m from the mean-sea-level shoreline and with its crest in 1 m water depth. Detailed bathymetric

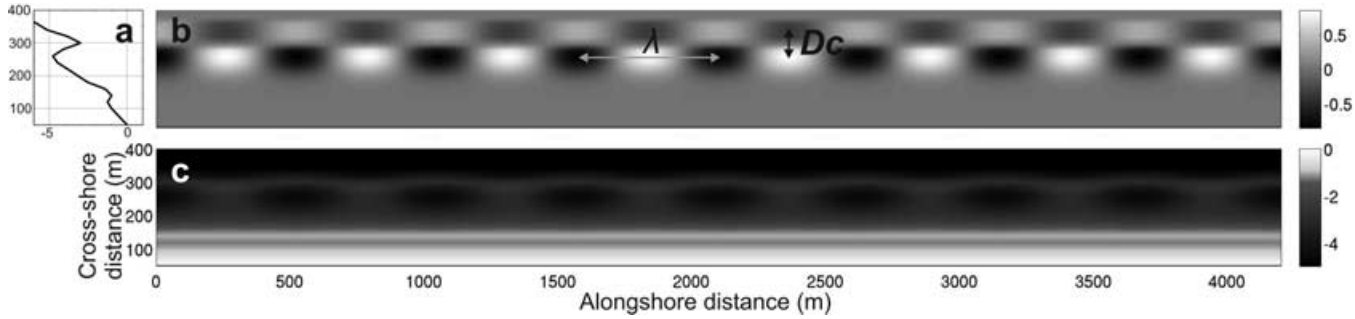

Figure 3. Example of an initial double sandbar geometry used for the simulations with (a) an alongshore-uniform double-barred beach profile with (b) a superimposed horn and bay sequence resulting in (c) outer-bar crescentic patterns, here with $\lambda = 525$ m, $D_c = 60$ m and $D_v = 1{\cdot}7$ m.

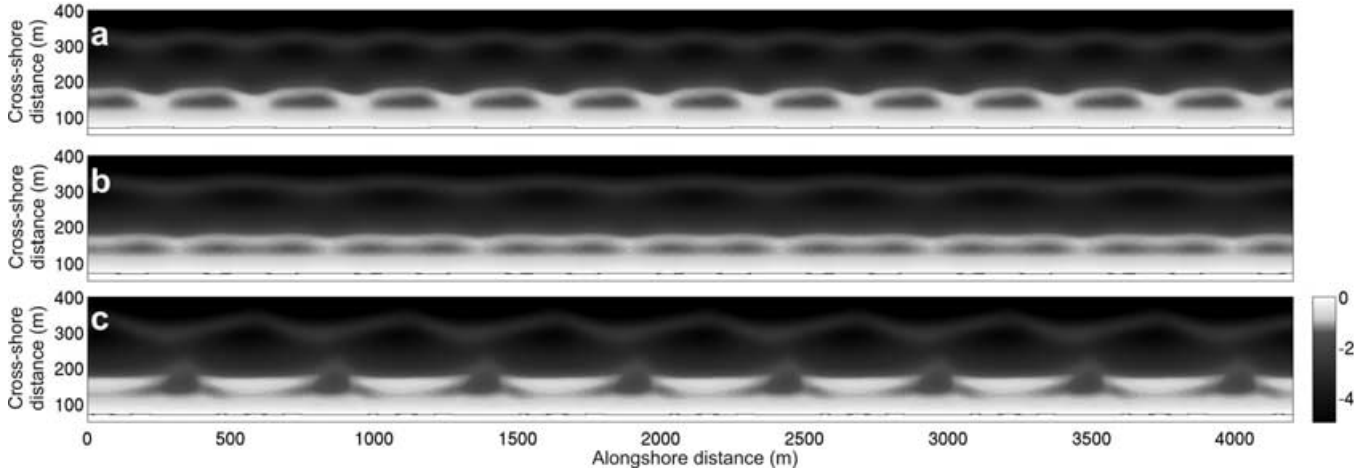

Figure 4. Simulated bathymetry for (a) initially outer-bar crescents with $\lambda = 350$ m, $D_c = 60$ m and $D_v = 1{\cdot}35$ m and constant wave forcing with $H_{s0} = 0{\cdot}8$ m after 7 days, (b) initially outer-bar crescents with $\lambda = 525$ m, $D_c = 60$ m and $D_v = 1{\cdot}7$ m and constant wave forcing with $H_{s0} = 0{\cdot}8$ m after 7 days, and (c) initially outer-bar crescents with $\lambda = 525$ m, $D_c = 60$ m and $D_v = 1{\cdot}7$ m and constant wave forcing with $H_{s0} = 1{\cdot}2$ m after 3 days. Simulated inner- and outer-bar relationship are (a) an in-phase coupling (inner-bar horns facing outer-bar horns), (b) coupling at half of the outer-bar wavelength and (c) 180° out-of-phase coupling (inner-bar horns facing outer-bar bays). The key indicates seabed elevation in metres (light is shallow, dark is deep).

surveys of crescentic bars are scarce. Therefore, the outer-bar geometries were loosely based on existing observations (e.g. Ruessink *et al.*, 2007) but are still considered to be realistic. The outer bar was located 250 m from the mean-sea-level shoreline with its crest in 3 m water depth. Crescentic patterns were superimposed to the alongshore-uniform outer bar as an alongshore sequence of horns and bays alternating shoreward and seaward of the outer-bar crest. Three main parameters were used to characterize the crescentic bar geometry: the alongshore wavelength λ, the cross-shore amplitude between a horn and a bay D_c and the vertical amplitude of the bay/horn sequence D_v (Figure 3). The bars were superimposed on a 1:50 planar sloping depth profile, with its offshore extent in 10·5 m water depth.

Results

Preliminary simulations suggested that D_c does not play a significant role in the simulated coupling patterns except, not surprisingly, for $D_c = 0$ which does not result in coupling patterns. The range of D_c values is strongly limited by the 20 m grid resolution. We set D_c to 60 m for all the initial outer-bar geometries. As the emergence of coupling patterns is favoured by small offshore wave angles with respect to shore normal, only shore-normal waves are considered. To further restrict the number of parameters and the complexity of the sensitivity analysis, we considered shore-normal waves with an offshore peak period T_{p0} of 8 s. In total, 208 simulations were run to investigate the sensitivity of emerging coupling patterns to variations in λ, D_v and H_{s0} only. In our model there is no bed diffusion or bedslope transport (Garnier *et al.*, 2008) likely to damp the instabilities. Continuing the simulations over a long duration would make the bed slope locally too large and the hydrodynamic model would eventually blow up. Accordingly, all the morphological evolutions presented below do not represent a steady state of the double sandbar system and are taken about 1–2 days before the sandbar morphologies become unrealistic.

Figure 4 shows examples of the three main coupling patterns simulated in this study: in-phase coupling (Figure 4a), with inner-bar horns facing outer-bar horns; coupling at half of the outer-bar wavelength (Figure 4b) with two inner-bar rip channels for one outer-bar crescent; 180° out-of-phase coupling (Figure 4c), with inner-bar bays facing outer-bar horns. Figure 5 displays the emerging coupling patterns as a function of λ, D_v and H_{s0}. It is to be noted that, in some simulations, coupling at half of the outer-bar wavelength initially emerges and eventually transforms into an in-phase coupling (which is indicated in Figure 5). This illustrates the strong nonlinear behaviour of the inner-bar dynamics. Results show that in-phase coupling is favoured by low-energy waves (Figures 5a, c), short outer-bar alongshore wavelengths (Figures 5a, c) and small vertical amplitudes of the outer-bar horn/bay sequence

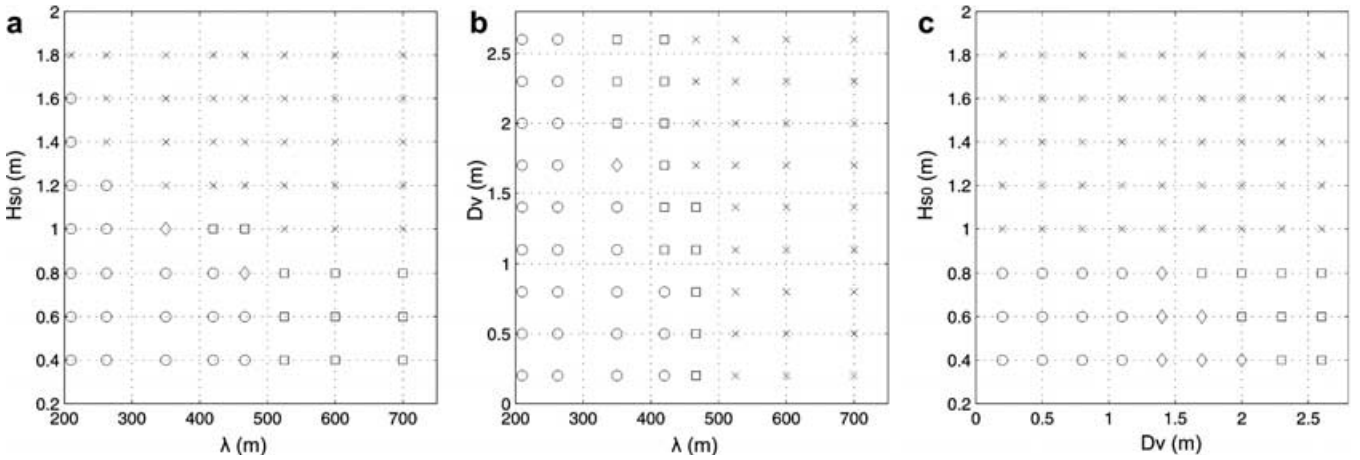

Figure 5. Emerging coupling pattern simulated by the nonlinear morphodynamic model as a function of (a) H_{s0} versus λ for D_v = 1·7 m, (b) D_v versus λ with H_{s0} = 1 m and (c) H_{s0} versus D_v with λ = 525 m. The circles indicate an in-phase coupling (Figure 4a), the squares a coupling at half of the outer-bar wavelength (Figure 4b), the crosses a 180° out-of-phase coupling (Figure 4c), and the diamonds a coupling at half of the outer-bar wavelength that eventually transforms into an in-phase coupling.

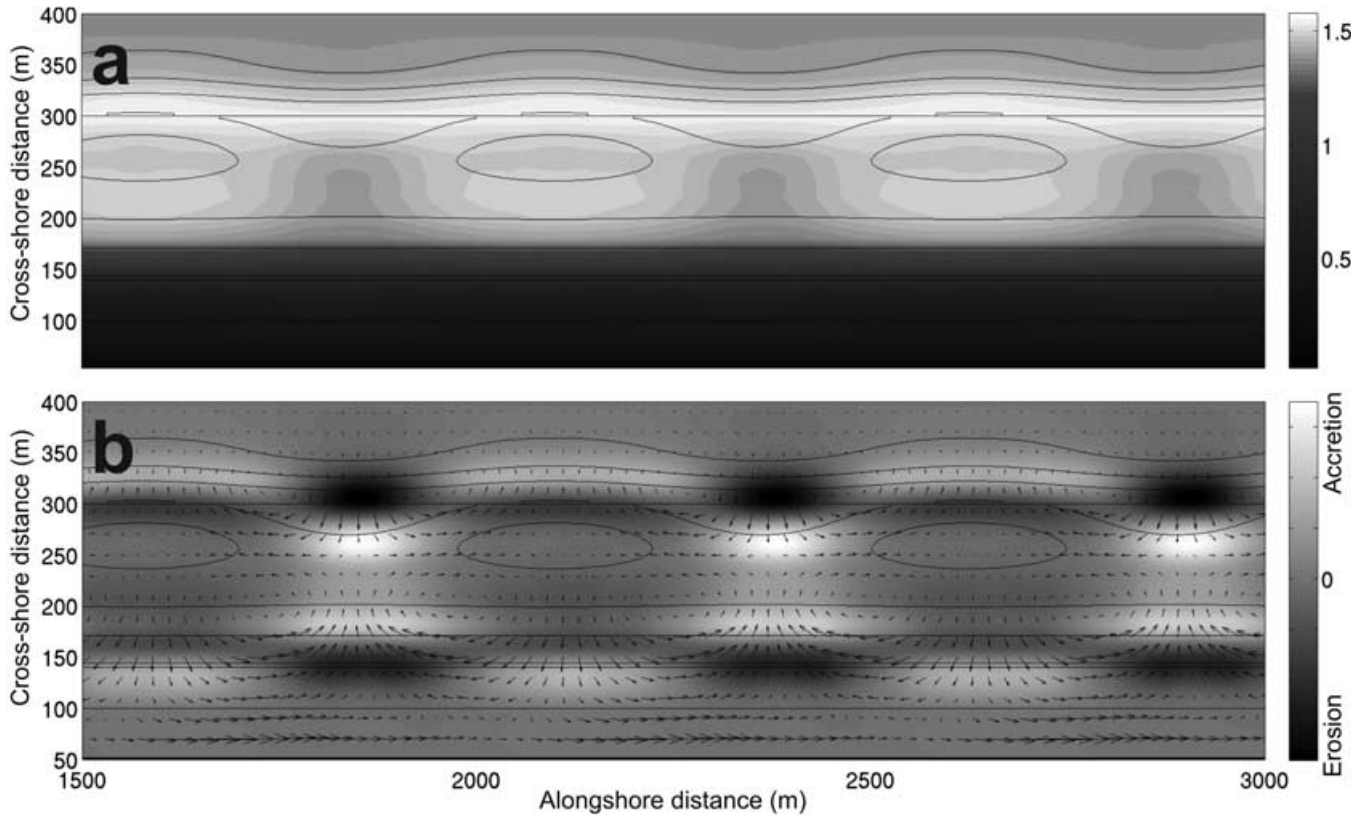

Figure 6. Simulation at t = 0 of (a) significant wave height and (b) resulting wave-induced current (maximum flow velocities reach 0·085 m s^{-1}) and erosion/accretion patterns for outer-bar crescents with λ = 525 m, D_c = 60 m and D_v = 1·7 m and constant offshore wave forcing with H_{s0} = 1·2 m; these settings lead to a 180° out-of-phase coupling (Figure 4c).

(Figures 5b, 5c). Slight increases in H_{s0}, λ or D_v favour a shifting from an in-phase coupling to a coupling at half of the outer-bar wavelength (Figure 5). For larger H_{s0}, λ or D_v, 180° out-of-phase coupling is observed. In other words, in-phase (180° out of phase) coupling can be observed for low (high) energy waves and weakly (well-) developed outer bars with crescentic patterns at small (large) alongshore wavelengths, where coupling at half of the outer-bar wavelength acts as an intermediate (variation of the in-phase) coupling pattern.

A more in-depth investigation of the hydrodynamics shows that wave refraction and depth-induced breaking patterns over the outer bar drive the initial development of coupling patterns. The resulting shoreward variations in wave energy enforce alongshore variations in wave set-up which drive horizontal circulation patterns over the inner bar. Therefore, these inshore horizontal circulation patterns, and resulting initial erosion/accretion patterns, are linked to the more seaward outer-bar geometry.

The degree of wave breaking across the outer bar strongly influences the type of emerging coupling. This is especially true for the distinction between 180° out-of-phase coupling and the two other coupling patterns. Figure 6 shows the initial wave, flow and resulting erosion/accretion patterns leading to the 180° out-of-phase coupling shown in Figure 4c after three

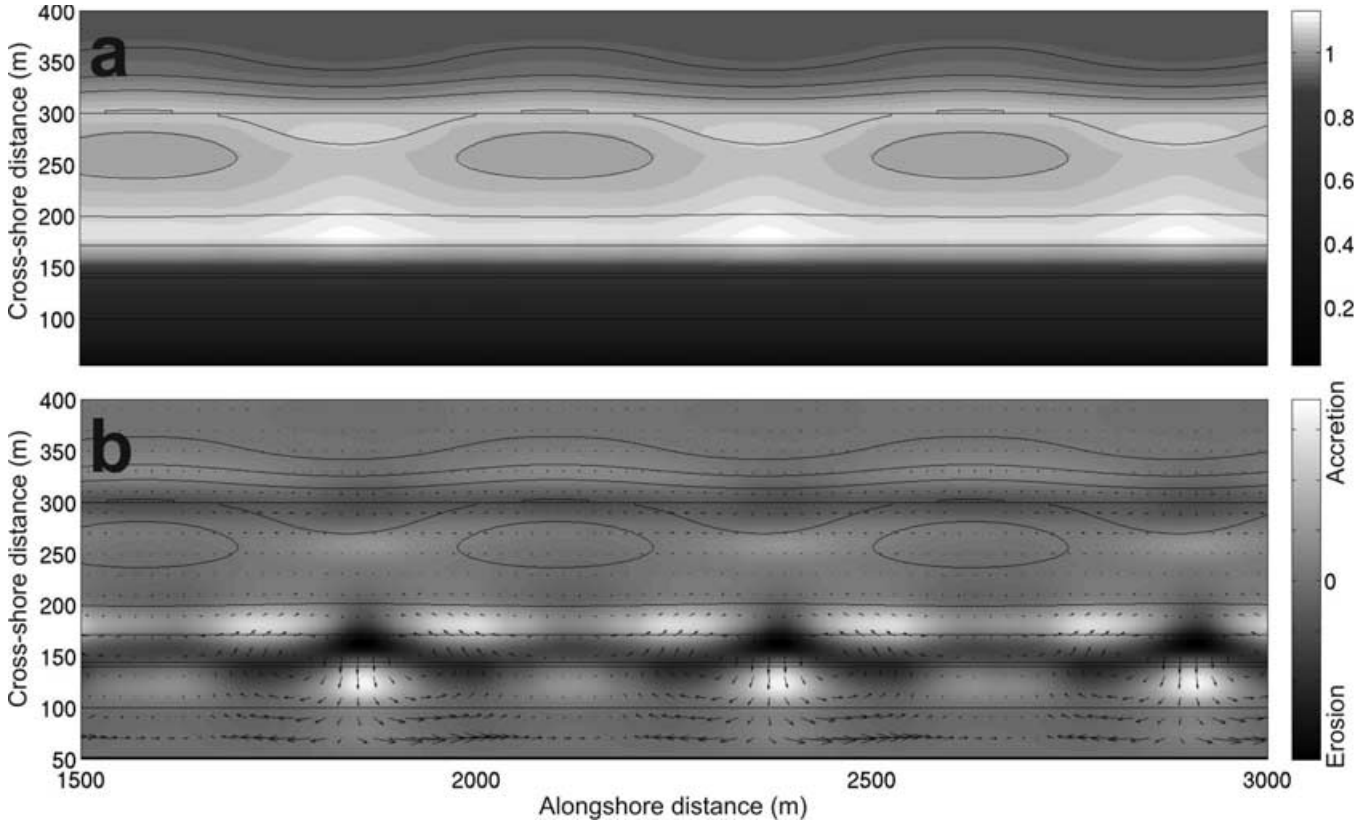

Figure 7. Simulation at $t = 0$ of (a) significant wave height and (b) resulting wave-induced current (maximum flow velocities reach 0·075 m s^{-1}) and erosion/accretion patterns for outer-bar crescents with $\lambda = 525$ m, $D_c = 60$ m and $D_v = 1{\cdot}7$ m and constant offshore wave forcing with $H_{s0} = 0{\cdot}8$ m; these settings lead to a coupling at half of the outer-bar wavelength (Figure 4b).

days of simulations, with wave conditions of $H_{s0} = 1{\cdot}2$ m and $T_{p0} = 8$ s and an outer-bar geometry with $\lambda = 525$ m, $D_c = 60$ m and $D_v = 1{\cdot}7$ m. In this case, depth-induced wave breaking is observed over the outer-bar horns, which results in lower wave energy shoreward of each horn (Figure 6a). The resulting alongshore patterns in wave set-up drives horizontal circulation patterns, with a single rip current over the inner bar (and a resulting erosion area) facing one outer-bar horn (Figure 6b). The temporal evolution of the morphology eventually leads to the 180° out-of-phase coupling observed in Figure 4c. In contrast, with lower offshore wave energy ($H_{s0} = 0{\cdot}8$ m, $T_{p0} = 8$ s) and a similar outer-bar geometry, there is no wave breaking across the outer bar but only refraction which results in wave energy focusing shoreward of the outer-bar horn (Figure 7a). This induces an onshore flow over the inner bar facing an outer-bar horn (Figure 7b). In this case (an outer-bar wavelength λ of 525 m), the distance between each inner-bar onshore flow is large enough for two offshore flows (rip currents) to form for one outer-bar crescent, resulting in two distinct erosion areas over the inner bar (Figure 7b). The temporal evolution of the morphology eventually leads to the coupling patterns at half of the outer-bar wavelength observed in Figure 4b. For shorter outer-bar wavelength and similar D_v and D_c, for instance with $\lambda = 350$ m, the distance between the two onshore flows is too small to drive two sufficiently distinct offshore-directed flows. In this case, the inner-bar morphology, through the positive feedback between hydrodynamics, sediment transport and the evolving morphology, develops a single rip channel facing an outer-bar bay and, eventually, leads to the in-phase coupling observed in Figure 4a, with the two onshore flows only feeding one confined rip current system.

The impact of the degree of wave breaking across the outer bar on the coupling patterns can be assessed in more detail in Figure 8 (for which additional simulations have been made, with H_{s0} values every 0·05 m), here in the case of initial outer bar with $\lambda = 525$ m, $D_c = 60$ m and $D_v = 1{\cdot}7$ m. Results show that change from wave breaking across the outer bar to non-breaking drastically controls alongshore variations of the wave height and resulting onshore and offshore flow patterns along the inner-bar crest. More importantly, this shows that all the shore-normal waves with H_{s0} above a threshold value delimiting wave breaking and non-breaking across the outer bar (in this case 0·95 m), will favour the 180° out-of-phase coupling shown in Figure 4c. Similarly, all the shore-normal waves with H_{s0} below the threshold value will favour the coupling at half of the outer-bar wavelength shown in Figure 4c.

This threshold value of $H_{s0} = 0{\cdot}95$ m is true for outer bars with large wavelengths ($\lambda > 480$ m, Figure 5a). This change in coupling pattern takes place at different H_{s0} values for smaller wavelengths (Figure 5a), which suggests a more complicated process than the onset of wave breaking alone. For smaller outer-bar wavelengths, wave focusing by refraction is more important than for larger outer-bar wavelengths, and the relative importance of wave breaking across the outer bar and wave focusing controls the change in coupling pattern. Figure 9 shows examples of the relative importance of wave breaking and wave focusing by refraction. For an initial outer bar with $\lambda = 525$ m, $D_c = 60$ m and $D_v = 1{\cdot}7$ m (Figure 9a) and for $H_{s0} = 0{\cdot}8$ m, larger waves are observed shoreward of each outer-bar horn (Figure 9b) as the fraction of breaking waves Q_b across the outer bar is not significant (Figure 9c), resulting in the emergence of coupling at half of the outer-bar

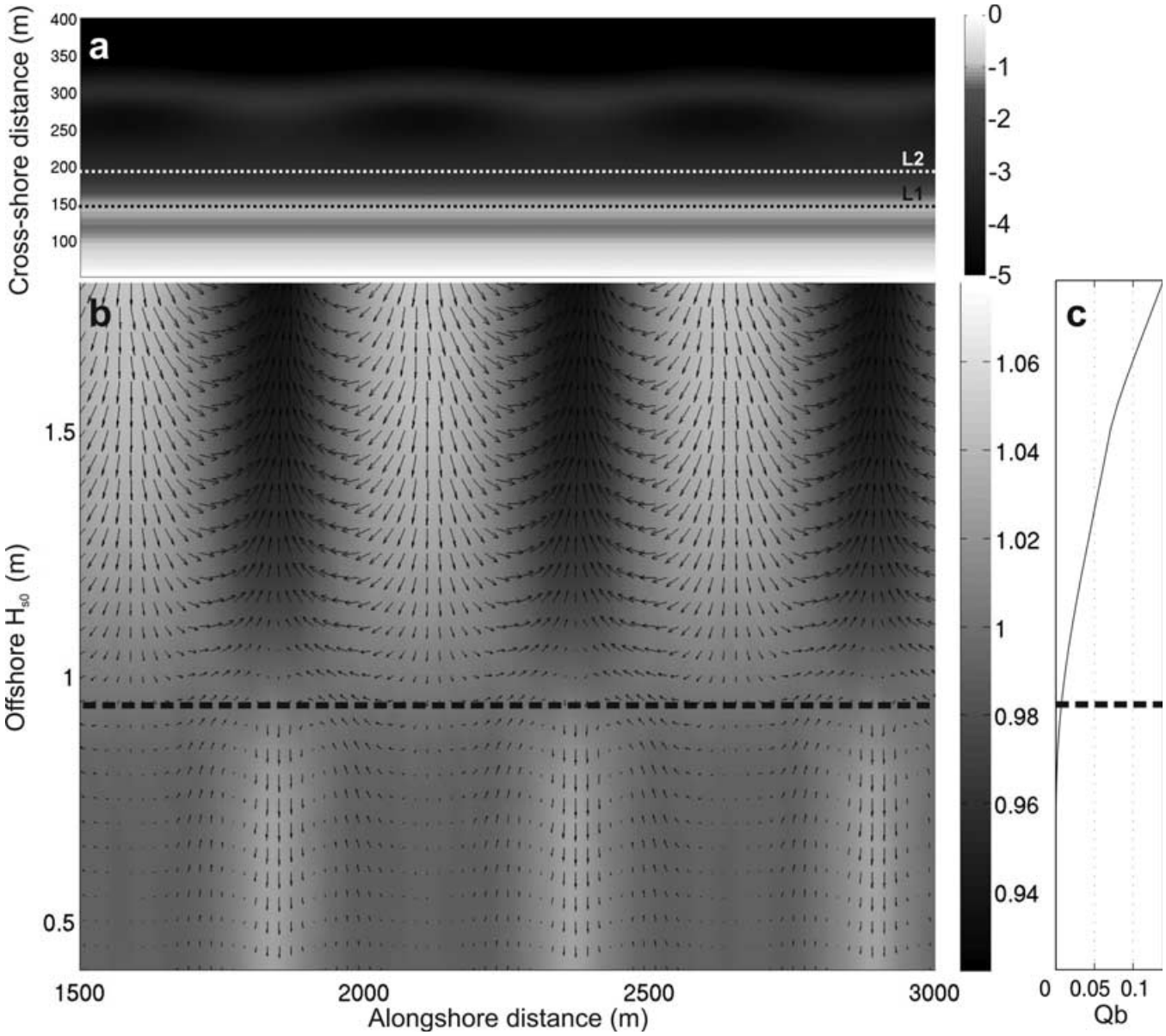

Figure 8. (a) Initial outer bar with $\lambda = 525$ m, $D_c = 60$ m and $D_v = 1{\cdot}7$ m and (b) $H_{s2}/\overline{H_{s2}}$, with H_{s2} denoting the significant wave height H_s along the alongshore line $L2$ located immediately seaward of the inner bar and $\overline{H_{s2}}$ the alongshore average of H_{s2}, versus offshore significant wave height H_{s0}, with superimposed wave-induced currents vectors $\vec{U}_1$ along the alongshore line $L1$ over the bar crest; the dark dashed line in (b) indicates the limit between depth-induced breaking and non-breaking across the outer bar as indicated by (c) the computed fraction of breaking waves Q_b as a function of H_{s0}.

wavelength (Figure 5a). Increasing H_{s0} to 1 m leads to a Q_b of about 0·01 across the outer-bar horns (Figure 9c) which is small but sufficient to overwhelm wave focusing by refraction, resulting in smaller waves shoreward of each outer-bar horn (Figure 5b) and the emergence of a 180° out-of-phase coupling (Figure 5a). For an outer bar with $\lambda = 210$ m (Figure 9d) and for $H_{s0} = 1{\cdot}2$ m, larger Q_b of about 0·035 are computed across the outer-bar horn (Figure 9f). This fraction of breaking wave is not sufficient to overwhelm wave focusing by refraction (Figure 9e) resulting in the emergence of coupling at half of the outer-bar wavelength (Figure 5a). Larger Q_b values are now required for wave breaking to overwhelm wave focusing by refraction. In the case of an outer bar with $\lambda = 210$ m, the overwhelming of wave focusing by wave breaking is observed for $Q_b > 0{\cdot}09$ (Figure 9f), that is for $H_{s0} > 1{\cdot}7$ m, which results in the emergence of 180° out-of-phase coupling (Figure 5a).

Discussion and Conclusions

Our simulations show that coupling patterns arise from horizontal circulation patterns driven by alongshore variations in wave set-up enforced by wave refraction and depth-induced breaking over the outer bar. The relative importance of wave focusing by refraction versus wave breaking across the outer bar controls the inner-bar patterns morphologically forced by the outer bar. For large λ, wave focusing is relatively unimportant and is overwhelmed by wave breaking once waves start to break across the outer bar. For smaller λ, wave focusing by refraction is much more important and a larger fraction of breaking waves across the outer bar is required for overwhelming wave focusing. When wave breaking overwhelms wave focusing, 180° out-of-phase coupling emerges regardless of the outer-bar wavelength. When wave focusing by refraction overwhelms wave breaking, coupling at half of the

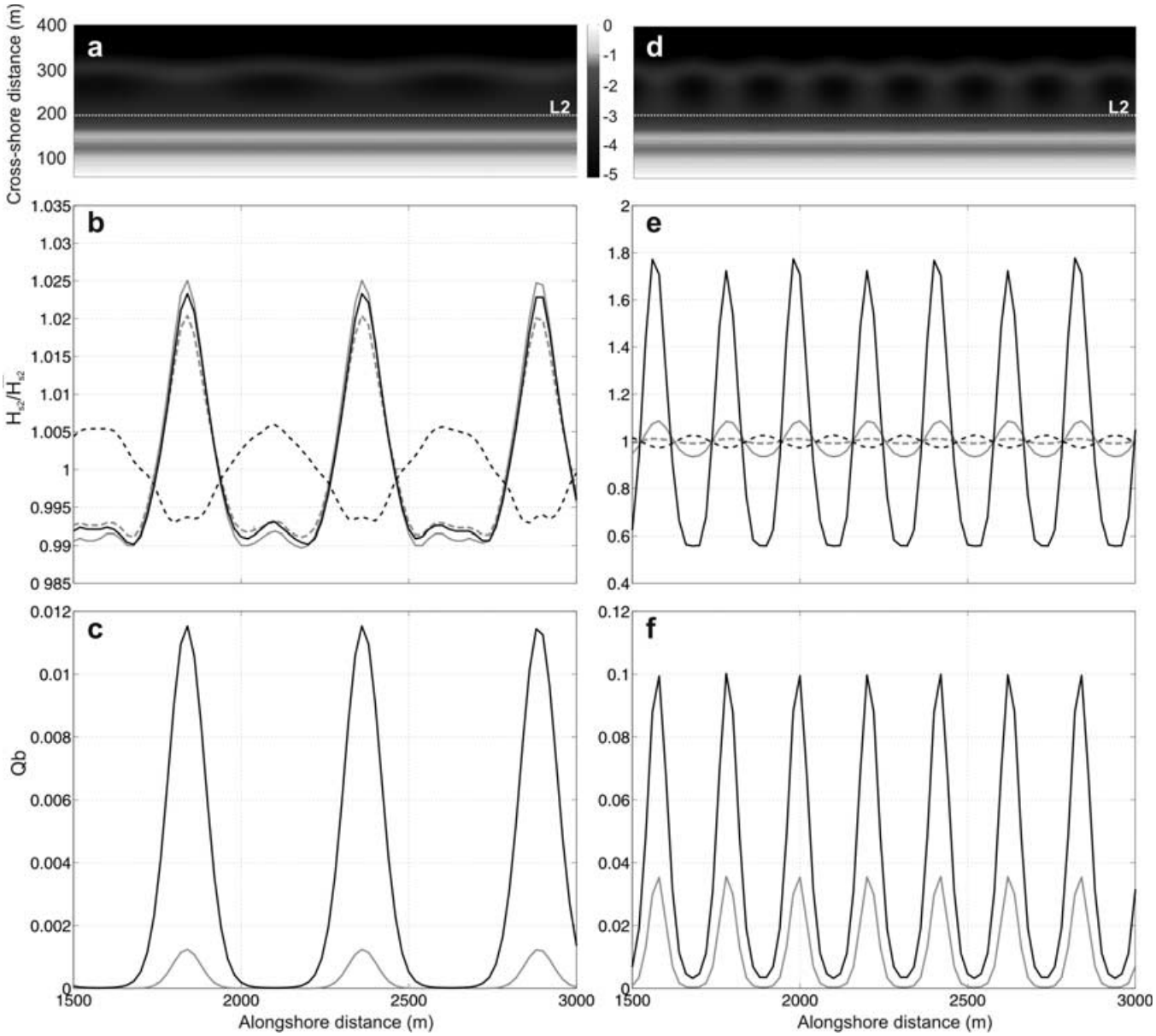

Figure 9. (a) Initial outer bar with λ = 525 m, D_c = 60 m and D_v = 1·7 m, (b) $H_{s2}/\overline{H_{s2}}$, with H_{s2} denoting the significant wave height H_s along the alongshore line *L*2 with deactivated wave breaking (wave refraction alone, solid line) and with wave breaking (dotted line) and (c) fraction of breaking waves along the outer bar, for H_{s0} = 0·8 m and 1 m in grey and black, respectively; (d) Initial outer bar with λ = 210 m, D_c = 60 m and D_v = 1·7 m, (e) $H_{s2}/\overline{H_{s2}}$ with deactivated wave breaking (wave refraction alone, solid line) and with wave breaking (dotted line) and (f) fraction of breaking waves along the outer bar, for H_{s0} = 1·2 m and 1·7 m in grey and black, respectively.

outer-bar wavelength (in phase) is observed for larger (smaller) outer-bar wavelength and larger (smaller) vertical amplitude of the horn and bay sequence.

The simulated 180° out-of-phase coupling patterns are essentially similar to the observations of Van Enckevort and Wijnberg (1999) and Castelle *et al.* (2007) on two contrasting wave-dominated multiple-barred beaches. Figure 10 shows an example of a qualitative comparison of simulated patterns with observations. In the case of no wave breaking across the outer bar, two other coupling patterns can arise. For weakly developed crescents with short alongshore wavelengths and low-energy waves, an in-phase coupling is observed with inner-bar horns facing outer-bar horns. Despite no evidence of such a coupling pattern in double sandbar systems being found in the literature, this coupling can be considered as reminiscent of the more commonly observed in-phase relationship between inner-bar patterns and shoreline rhythms (Figure 2b). When increasing the outer-bar alongshore wavelength, the vertical amplitude of the horn/bay sequence or the offshore wave height (maintaining non-breaking condition across the outer bar), coupling at half of the outer-bar wavelength is observed with the systematic occurrence of two inner-bar rip channels for one outer-bar crescent. Field observations of these simulated coupling patterns (Castelle *et al.*, 2007; also Figures 1 and 11) enforce the confidence we can have in the numerical results and the underlying mechanisms responsible for the emergence of coupling. In the field, the rapid time-varying offshore wave conditions with respect to the slower morphological time response of surfzone sandbars would suggest that such striking coupling patterns can hardly form. In addition, variations in mean water depth induced by tides continuously change the balance between wave breaking and refraction across the outer bar, which was not taken into account in our model. Despite being readily

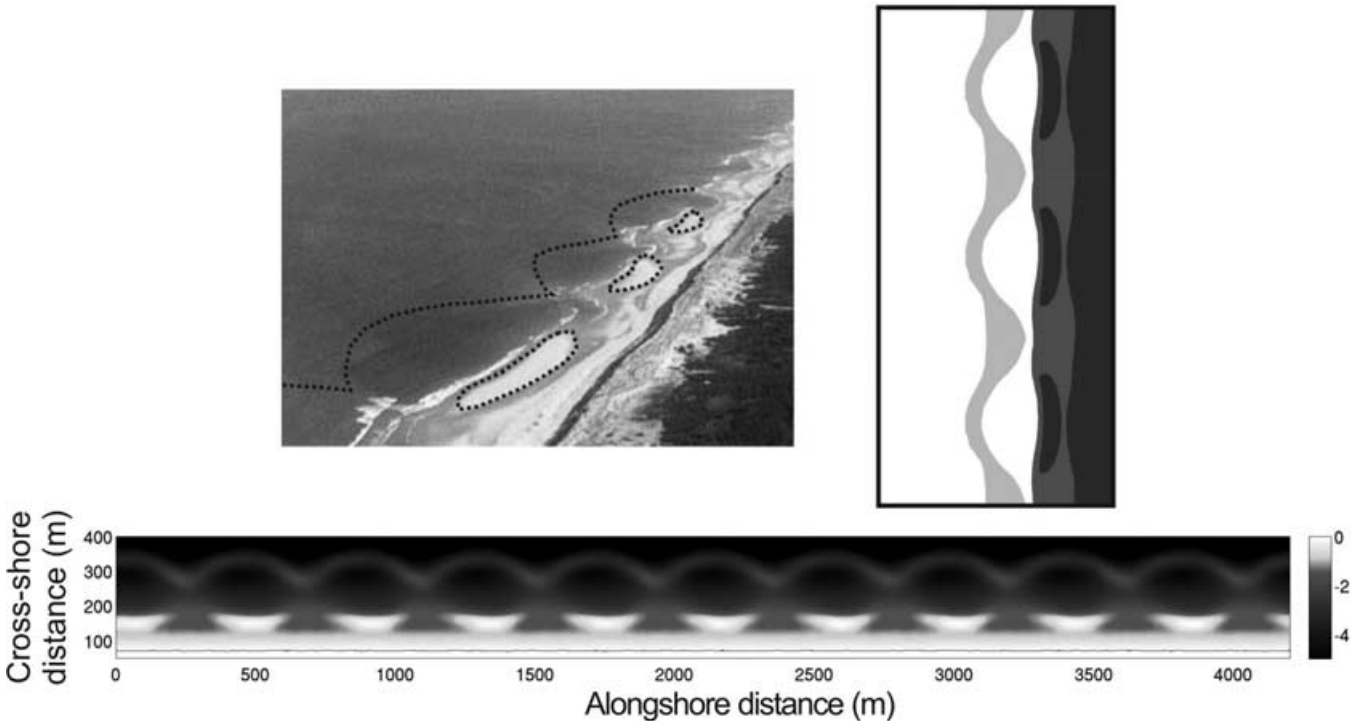

Figure 10. Computed 180° out-of-phase coupling patterns with an outer-bar horn facing an inner-bar bay, favoured in the presence of high-energy shore-normal waves, similar to some observations on a meso- macro-tidal high-energy double-barred beach in Castelle *et al.* (2007).

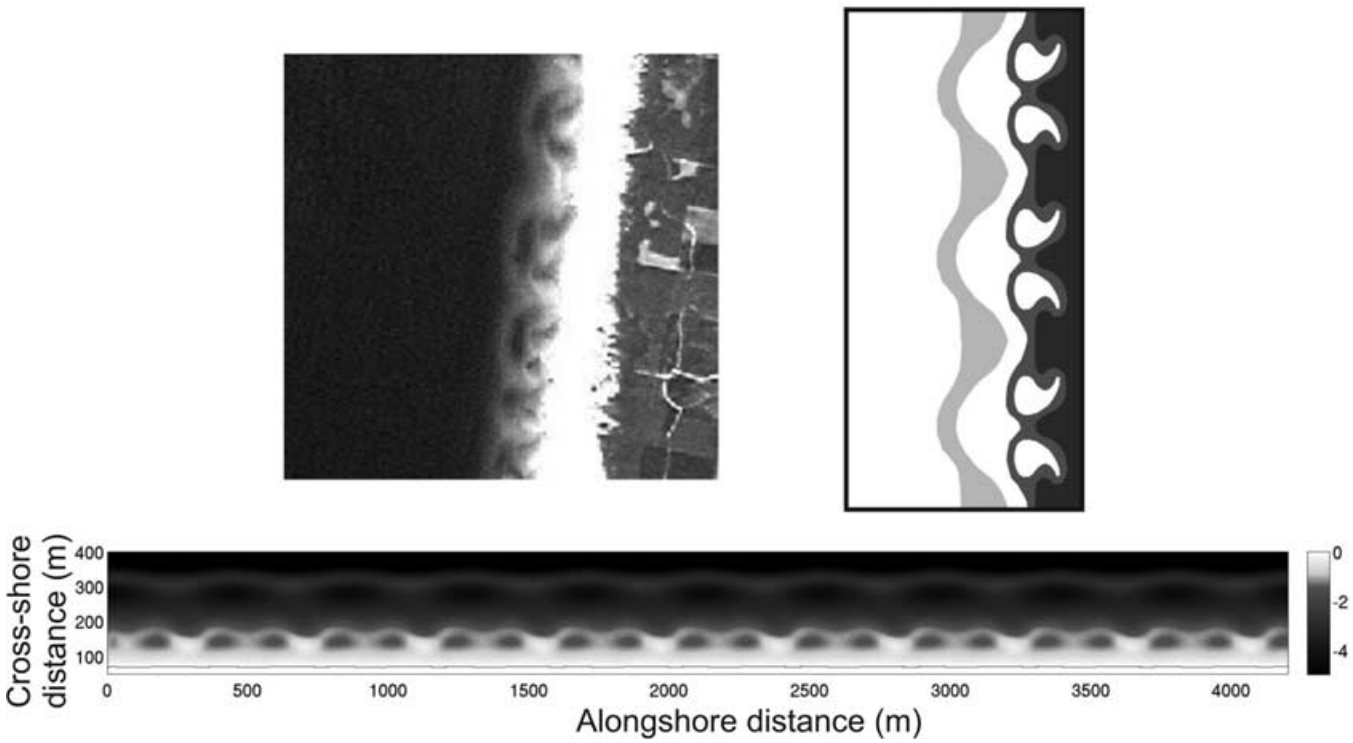

Figure 11. Computed coupling patterns at half of the outer-bar wavelength, favoured in the presence of low-energy shore-normal waves and large outer-bar wavelength, similar to some observations on a meso- macro-tidal high-energy double-barred beach in Castelle *et al.* (2007).

apparent in Figures 10 and 11, emergence of coupling patterns in meso- to macro-tidal environments is potentially more complicated than in the idealized simulations presented in this paper. Further simulations with tides will be required to examine the effects of mean water level variations on the (intertidal) inner-bar dynamics.

Coco and Murray (2007) reviewed the sweeping shift from forcing template to self-organization for explaining the formation of rhythmic surfzone sandbars, among other nearshore patterns. Morphological coupling does not appear to fit in this classification. On the one hand, the inshore horizontal circulation patterns and resulting inner-bar rip channel development are forced by the more seaward outer-bar geometry through wave refraction and wave breaking across the outer bar. Morphological coupling implies the presence of a template in the morphology (outer-bar geometry) which,

therefore, can be seen as a forcing template. On the other hand, the inner-bar rip channels simulated herein with the nonlinear morphodynamic model also form through the positive feedback between hydrodynamics (waves and currents), sediment processes and the evolving bathymetry. In this case, the inner-bar morphology does not passively respond to the template in the hydrodynamics enforced by the outer-bar geometry. Morphological coupling, therefore, can also be seen as self-organization. In the case of sufficient offshore wave energy, the outer bar also evolves significantly (Figure 4c), which means that the forcing template in the morphology is time-varying and governed by self-organization mechanisms. Eventually, the outer-bar horns weld to the inner bar and sections of the forcing template become part of the morphologically forced inner bar.

Morphological coupling can thus be seen as a novel mechanism that blurs the distinction between forcing template and self-organization mechanisms. This mechanism may also be extended to explain the dynamics of other striking morphological patterns exhibited in the nearshore region. For instance, Holland and Holman (1996) observed the formation of shorter-scale cusps with spacings of approximately half that of the most well-developed cusps located at a higher beach level. The authors suggested that a slight change in tidal level or incident wave period might have induced resonantly forced edge waves which, in turn, forced the formation of cusps at half of the larger cusp wavelength. This edge-wave forced response of the smaller beach cusps is not consistent with the recent abandonment of the forcing template explanation. Despite the obvious differences between surfzone sandbar and beach cusp dynamics (beach cusps form in the swash zone, nearshore bars form in the surf zone), the formation of these smaller cusps at half of the larger cusp wavelength may actually be formed through swash zone coupling mechanisms analogous to the surfzone morphological coupling mechanism presented in this paper. In this case, the morphological response of the lower cusps, following a slight decrease in tidal level or a change in incident wave conditions, may be morphologically forced by the higher, larger cusps. This hypothesis cannot be tested with the kind of nonlinear morphodynamic model used in this study and has to be explored further with self-organization models based on swash zone processes (Werner and Fink, 1993; Coco *et al.*, 2004). In addition, our study shows that coupling in double sandbar systems can be considered as reminiscent of the commonly observed relationship between inner-bar patterns and shoreline rhythms. Similarly, sandbar coupling with seaward sorted bedforms (nearshore geological features, i.e. morphological template) may exist, reminiscent of their observed relationship with shoreline undulations (Browder and McNinch, 2006; Schupp *et al.*, 2006). This morphodynamic coupling between other morphological patterns needs to be explored further.

Our numerical model successfully simulated coupling patterns in double sandbar systems observed in the field, and allowed the description of a novel mechanism likely to play an important role in surfzone sandbar dynamics, and for other nearshore patterns. Clear coupling patterns in double sandbar systems, such as in Figures 1, 8 and 9, are however rarely observed in the field (Van Enckevort and Wijnberg, 1999; Castelle *et al.*, 2007; Quartel, 2009). More often, inner-bar rip channels possess remarkably smaller and more variable alongshore scales than the outer bar (e.g. Barusseau *et al.*, 1994; Van Enckevort *et al.*, 2004; Lafon *et al.*, 2004, 2005). This would suggest that morphological coupling does not play a substantial role in the overall double-sandbar dynamics. However, additional simulations with our numerical model show that this variability actually arises from a mixture of morphological coupling and self-organization mechanisms. The general field observation that inner-bar rip channels are more irregularly spaced than outer-bar crescents suggests that morphological coupling may be more important to understanding and predicting the evolution of inner-bar rip channels than previously envisaged. This issue is explored in the companion paper (Castelle *et al.*, 2010).

Acknowledgements—BC and PB gratefully acknowledge funding from the project MODLIT (under the Program RELIEFS/INSU – SHOM/DGA). BGR and TDP acknowledge financial support through the Netherlands Organisation for Scientific Research award 864.04.007 and contract 818.01.009, respectively. The authors wish to thank the two anonymous reviewers for their positive criticism that improved the quality of the paper as well as Professor A. D. Short for kindly providing a set of photographs of the New South Wales coast.

References

Ashton A, Murray AB, Arnault O. 2001. Formation of coastline features by large-scale instabilities induced by high-angle waves. *Nature* **414**: 296–300.

Bailard JA. 1981. An energetics total load sediment transport model for a plane beach. *Journal of Geophysical Research* **86**: C11, 10938–10954.

Barusseau J-P, Radulescu M, Descamps C, Akouango E, Gerbe A. 1994. Morphosedimentary multiyear changes on a barred coast (Gulf of Lions, Mediterranean Sea, France). *Marine Geology* **122**: 47–62.

Battjes JA. 1975. Modelling of turbulence in the surfzone. In *Proc. Symposium on Modelling Techniques* ASCE: New York. 1050–1061.

Booij N, Ris RC, Holthuijsen LH. 1999. A third-generation wave model for coastal regions, Part 1: Model description and validation. *Journal of Geophysical Research* **104**: C4, 7649–7666.

Bowen AJ. 1997. Patterns in the water: Patterns in the sand? In *Proceedings of Coastal Dynamics '97* ASCE: New York. 1–10.

Bowen AJ, Inman DL. 1971. Edge waves and crescentic bars. *Journal of Geophysical Research* **76**: 8662–8671.

Bowman D, Goldsmith V. 1983. Bar morphology of dissipative beaches: an empirical model. *Marine Geology* **51**: 15–33.

Browder AG, McNinch JE. 2006. Linking framework geology and nearshore morphology: correlation of paleo-channels with shore-oblique sandbars and gravel outcrops. *Marine Geology* **231**: 141–162.

Bryan KR, Bowen AJ. 1997. Can bar-trapped edge waves cause bar formation, bar movement or bar growth? In *Proceedings of the 13th Australasian Coastal and Ocean Engineering Conference and the 6th Australasian Port and Harbour Conference* **2**: 1037–1042.

Caballeria M, Coco G, Falqués A, Huntley DA. 2002. Self-organization mechanisms for the formation of nearshore crescentic and transverse bars. Journal of Fluid Mechanics **465**: 379–410.

Calvete D, Dodd N, Falqués A, Van Leeuwen SM. 2005. Morphological development of rip channel systems: Normal and near-normal wave incidence. *Journal of Geophysical Research* **110**: C10006, DOI: 10.1029/2004JC002803.

Carter RWG. 1988. *Coastal Environments* Academic Press:

Carter TG, Liu PL, Mei CC. 1973. Mass transport by waves and offshore bedforms. *Journal of the Waterways, Harbors and Coastal Engineering Division* **99**: 165–184. London, UK.

Castelle B, Bonneton P. 2004. Nearshore waves and currents over crescentic bars. *Journal of Coastal Research* S.I. 39, 687–691.

Castelle B, Bonneton P, Butel R. 2006. Modeling of crescentic pattern development of nearshore bars: Aquitanian Coast, France. *C. R. Geoscience* **338**: 795–801.

Castelle B, Bonneton P, Dupuis H, Sénéchal N. 2007. Double bar beach dynamics on the high-energy meso-macrotidal French Aquitanian Coast: A review. *Marine Geology* **245**: 141–159.

Castelle B, Ruessink BG, Bonneton P, Marieu V, Bruneau N, Price TD. 2010. Coupling mechanisms in double sandbar systems. Part 2: Impact on alongshore variability of inner-bar rip channels. *Earth Surface Processes and Landforms* DOI: 10.1002.esp.1949.

Clarke LB, Wermer BT. 2004. Tidally modulated occurrence of megaripples in a saturated surf zone. *Journal of Geophysical Research* **109**: C1012, DOI: 10.1029/2003JC001934.

Coco G, Murray AB. 2007. Patterns in the sand: from forcing templates to self-organization. *Geomorphology* **91**: 271–290.

Coco G, O'Hare TJ, Huntley DA. 1999. Beach cusps: a comparison of data and theories for their formation. *Journal of Coastal Research* **15**: 741–749.

Coco G, Burnet TK, Werner BT, Elgar S. 2004. The role of tides in beach cusp development. *Journal of Geophysical Research* **109**: C04011, DOI: 10.1029/2003JC002154.

Coco G, Bryan KR, Green MO, Ruessink BG, Turner IL. 2005. Video observations of shoreline and sandbar coupled dynamics. In *Proceedings of Coasts and Ports 2005* 471–476.

Damgaard J, Dodd N, Hall L, Chesher T. 2002. Morphodynamic modeling of rip channel growth. *Coastal Engineering* **43**: 199–221.

Deigaard R, Drønen N, Fredsøe J, Jensen JH, Jørgensen MP. 1999. A morphological stability analysis for a long straight barred coast. *Coastal Engineering* **36**: 171–195.

Drønen N, Deigaard R. 2007. Quasi-three-dimensional modelling of the morphology of longshore bars. *Coastal Engineering* **54**: 197–215.

Falqués A, Coco G, Huntley DA. 2000. A mechanism for the generation of wave-driven rhythmic patterns in the surf zone. *Journal of Geophysical Research* **105**: 24071–24088.

Gallagher EL, Elgar S, Thornton EB. 1998. Observations and predictions of megaripple migration in a natural surf zone. *Nature* **394**: 165–168.

Garnier R, Calvete D, Falqués A, Dodd N. 2008. Modelling the formation and the long-term behavior of rip channel systems from the deformation of a longshore bar. *Journal of Geophysical Research* **113**: C07053, DOI: 10.1029/2007JC004632.

Goldsmith V, Bowman D, Kiley K. 1982. Sequential stage development of crescentic bars: HaHoterim Beach, Southeastern Mediterranean. *Journal of Sedimentary Petrology* **52**: 233–249.

Greenwood B, Davidson-Arnott RGD. 1979. Sedimentation and equilibrium in wave-formed bars: A review and case study. *Canadian Journal of Earth Sciences* **16**: 312–332.

Guza RT, Inman DL. 1975. Edge waves and beach cusps. *Journal of Geophysical Research* **80**: 21, 2997–3012.

Holland KT, Holman RA. 1996. Field observations of beach cusps and swash motions. *Marine Geology* **134**: 77–93.

Holman RA. 2000. Pattern formation in the nearshore. In *Proceedings of River, Coastal and Estuarine Morphodynamics* Springer-Verlag: New York. 141–162.

Holman RA, Bowen AJ. 1982. Bars, bumps and holes: Models for the generation of complex beach topography. *Journal of Geophysical Research* **87**: 457–468.

Holman RA, Symonds G, Thornton EB, Ranasinghe R. 2006. Rip spacing and persistence on an embayed beach. *Journal of Geophysical Research* **111**: C06006, DOI: 10.1029/2005JC002965.

Hom-ma M, Sonu C. 1962. Rhythmic pattern of longshore bars related to sediment characteristics. In *Proceedings of 8th Internat. Conference on Coastal Engineering* ASCE: New York. 248–278.

Klein MD, Schuttelaars HM. 2006. Morphodynamic evolution of double-barred beaches. *Journal of Geophysical Research* **111**: C06017, DOI: 10.1029/2005JC003155.

Komar PD. 1998. *Beach processes and sedimentation*. Prentice Hall:

Lafon V, De Melo Apoluceno D, Dupuis H, Michel D, Howa H, Froidefond J-M. 2004. Morphodynamics of nearshore rhythmic sandbars in a mixed-energy environment (SW France): I. Mapping beach changes using visible satellite imagery. *Estuarine, Coastal and Shelf Science* **61**: 289–299.

Lafon V, Dupuis H, Butel R, Castelle B, Michel D, Howa H, De Melo Apoluceno D. 2005. Morphodynamics of nearshore rhythmic sandbars in a mixed-energy environment (SW France): II. Physical forcing analysis. *Estuarine, Coastal and Shelf Science* **65**: 449–462.

Liu PL-F, Dalrymple RA. 1978. Bottom frictional stresses and longshore currents due to waves with large angles of incidence. *Journal of Marine Research* **36**: 357–375.

MacMahan JH, Thornton EB, Stanton TP, Reniers AJHM. 2005. RIPEX-observations of a rip current system. *Marine Geology* **218**: 113–134.

Marieu V, Bonneton P, Foster DL, Ardhuin F. 2008. Modeling of vortex ripple morphodynamics. *Journal of Geophysical Research* **113**: C09007, DOI: 10.1029/2007JC004659.

Mei CC. 1989. *Applied dynamics of ocean waves*. World Scientific: Singapore.

Philipps OM. 1977. *The dynamics of the upper ocean*. Cambridge University Press: Cambridge, UK.

Quartel S. 2009. Temporal and spatial behaviour of rip channels in a multiple-barred coastal system. *Earth Surface Processes and Landforms* **34**: 163–176.

Ranasinghe R, Symonds G, Black K, Holman R. 2004. Morphodynamics of intermediate beaches: A video imaging and numerical modelling study. *Coastal Engineering* **51**: 629–655.

Reniers AJHM, Roelvink JA, Thornton EB. 2004. Morphodynamic modeling of an embayed beach under wave group forcing. *Journal of Geophysical Research* **109**: C01030, DOI: 10.1029/2002JC001586.

Ruessink BG, Jeuken MCJL. 2002. Dunefoot dynamics along the Dutch coast. *Earth Surface Processes and Landforms* **27**: 1043–1056.

Ruessink BG, Coco G, Ranasinghe R, Turner IL. 2007. Coupled and noncoupled behavior of three-dimensional morphological patterns in a double sandbar system. *Journal of Geophysical Research* **112**: C07002, DOI: 10.1029/2006JC003799.

Schupp CA, McNinch JE, List JH. 2006. Nearshore shore-oblique bars, gravel outcrops, and their correlation to shoreline change. *Marine Geology* **233**: 63–79.

Shepard FP. 1952. Revised nomenclature for depositional coastal features. *Bulletin of the American Association of Petroleum Geology* **36**: 1902–1912.

Short AD. 1991. Macr-meso tidal beach morphodynamics – An overview. *Journal of Coastal Research* **7**: 2, 414–436.

Short AD. 1999. *Handbook of beach and shoreface morphodynamics*. Wiley: Chichester, UK.

Smit MWJ, Reniers AJHM, Ruessink BG, Roelvink JA. 2008. The morphological response of a nearshore double sandbar system to constant wave forcing. *Coastal Engineering* **55**: 761–770.

Sonu CJ. 1972. Field observation of nearshore circulation and meandering currents. *Journal of Geophysical Research* **77**: 18, 3232–3247.

Sonu CJ. 1973. Three-dimensional beach changes. *Journal of Geology* **81**: 42–64.

Thornton EB, MacMahan JH, Sallenger AH Jr. 2007. Rip currents, mega-cusps, and eroding dunes. *Marine Geology* **240**: 151–167.

Traykovski P, Hay AE, Irish JD, Lynch JF. 1999. Geometry, migration, and evolution of wave orbital ripples at LEO-A5. *Journal of Geophysical Research* **104**: C1, 1505–1524.

Van Enckevort IMJ, Wijnberg KM. 1999. Intra-annual changes in bar plan shape in a triple bar system. In *Proceedings of Coastal Sediments '99* 2548–2558.

Van Enckevort IMJ, Ruessink BG, Coco G, Suzuki K, Turner IL, Plant NG, Holman RA. 2004. Observations of nearshore crescentic sandbars. *Journal of Geophysical Research* **109**: C06028, DOI: 10.1029/2003JC002214.

Werner BT, Fink TM. 1993. Beach cusps as self-organised patterns. *Science* **260**: 968–971.

Wright LD, Short AD. 1984. Morphodynamic variability of surf zones and beaches: A synthesis. *Marine Geology* **56**: 93–118.

D.7 Coupling mechanisms in double sandbar systems. Part 2 : Impact on alongshore variability of inner-bar rip channels

Bruno Castelle, Gerben Ruessink, Philippe Bonneton, Vincent Marieu, Nico las Bruneau, Timothy Price

Earth Surface Processes and Landforms, Vol. 35, pp. 771-781, 2010

EARTH SURFACE PROCESSES AND LANDFORMS
Earth Surf. Process. Landforms **35**, 771–781 (2010)

Published online 1 February 2010 in Wiley InterScience
(www.interscience.wiley.com) DOI: 10.1002/esp.1949

Coupling mechanisms in double sandbar systems. Part 2: Impact on alongshore variability of inner-bar rip channels

Bruno Castelle[1,2]*, B. G. Ruessink[3], Philippe Bonneton[1,2], Vincent Marieu[1,2], Nicolas Bruneau[1,2] and Timothy D. Price[3]
[1] CNRS, UMR EPOC 5805, Talence, F-33405, France
[2] Université de Bordeaux, UMR EPOC 5805, Talence, F-33405, France
[3] Institute for Marine and Atmospheric Research, Department of Physical Geography, Utrecht University, The Netherlands

Received 22 April 2009; Revised 14 September 2009; Accepted 15 October 2009

*Correspondence to: Bruno Castelle, CNRS, UMR EPOC 5805, Talence, F-33405, France. E-mail: b.castelle@epoc.u-bordeaux1.fr

ESPL
Earth Surface Processes and Landforms

ABSTRACT: Double sandbar systems are common morphological features along sandy, wave-dominated, micro- to meso-tidal coastlines. In the companion paper, we demonstrated how various alongshore inner-bar rip-channel patterns can develop through morphological coupling to an alongshore-variable outer bar. The simulated coupling patterns are, however, scarcely observed in the field. Instead, inner-bar rip channels more often possess remarkably smaller and more variable alongshore length scales, suggesting that coupling mechanisms do not play a substantial role in the overall double-sandbar dynamics. Here we use a numerical model to show that the relative importance of self-organization and morphological coupling changes in favour of the latter with an increase in waterdepth variability along the outer-bar crest. Furthermore, we find that the typical alongshore variability in inner-bar rip-channel scale is indicative of a mixture of self-organization and morphological coupling rather than self-organization alone. Morphological coupling may thus be more important to understanding and predicting the evolution of inner-bar rip channels than previously envisaged. Copyright © 2010 John Wiley and Sons, Ltd.

KEYWORDS: self-organization; forcing templates; morphological coupling; rip channel variability; double sandbar system

1 Introduction

Surf zone sandbars protect beaches from wave attack by dissipating wave energy offshore through depth-induced wave breaking. Their morphology guides and constrains nearshore wave-induced currents such as rip current circulations (MacMahan *et al.*, 2005), resulting in erosion features known as mega-cusps (Short and Hesp, 1982; Thornton *et al.*, 2007). Therefore, understanding and predicting rip channel dynamics is relevant for shoreline evolution, localized beach and dune erosion during storms and safety implications. Sometimes, the alongshore variability of the sandbar geometry is low (Greenwood and Davidson-Arnott, 1979; Short, 1991). This alongshore-uniform shape is often observed during a storm event when the three-dimensional (3D) bar is rapidly reshaped into a shore-parallel linear bar (Wright and Short, 1984; Lippmann and Holman, 1990; Van Enckevort *et al.*, 2004). Most of the time, surfzone sandbars exhibit striking 3D patterns which can be described in the convenient morphodynamic framework of Wright and Short (1984). The rhythmic or quasi-rhythmic 3D patterns can be viewed as an alongshore sequence of horns (shoals) and bays (cross-shore troughs) where horns extend landward and bays seaward (Van Enckevort *et al.*, 2004) with a wavelength on the order of several times the surf zone width. The resulting patterns are the so-called crescentic sandbars and rip channels. Recently, in the framework of the recent paradigm shift from template forcing theory to self-organization mechanisms (Coco and Murray, 2007), both linear stability models (Deigaard *et al.*, 1999; Falqués *et al.*, 2000; Damgaard *et al.*, 2002; Calvete *et al.*, 2005) and nonlinear morphodynamic models (Damgaard *et al.*, 2002; Reniers *et al.*, 2004; Castelle *et al.*, 2006; Klein and Schuttelaars, 2006; Drønen and Deigaard, 2007; Garnier *et al.*, 2008; Smit *et al.*, 2008) have established that these 3D surfzone sandbars can be formed through self-organization mechanisms alone, and do not require a template in the hydrodynamics, as was previously proposed with the edge wave theory (Bowen and Inman, 1971; Holman and Bowen, 1982).

Double sandbar systems are common morphological features along sandy, wave-dominated, micro- to meso-tidal coastlines (Lippmann *et al.*, 1993; Barusseau *et al.*, 1994; Ruessink *et al.*, 2003; Van Enckevort *et al.*, 2004; Castelle *et al.*, 2007). In the cross-shore direction, the interactions between bars in multiple-barred settings have been recently touched upon. The observations of Ruessink and Terwindt (2000) and numerical modelling of Aarninkhof *et al.* (1998) and Masselink (2004) indicated that the morphodynamic feedback, driven for example by the position and geometry of one sandbar with respect to a second, might be a critical parameter

governing the behaviour of the whole system. Surprisingly, both the inner- and outer-bar rip channels and crescentic planshapes are nowadays believed to be free instabilities of the nearshore system arising through self-organization mechanisms alone, with the interaction of a given bar with respect to another barely touched upon until very recently. In double sandbar systems, the inner bar has been observed to possess remarkably smaller and more variable alongshore scales than the outer bar (e.g. Bowman and Goldsmith, 1983; Van Enckevort *et al.*, 2004), suggesting the absence of interaction and a self-organization at the scale of the individual bar (Houser and Greenwood, 2005). In the companion paper (Castelle *et al.*, 2010, noted as Part 1 below), we showed that the dynamics of inner-bar rip channels are potentially more complicated than they would be if they were governed by self-organization mechanisms alone. The authors showed that alongshore variability in outer-bar depth, and the relative importance of wave breaking versus wave focusing by refraction across the outer bar is crucial to the inner-bar rip channel development. A new mechanism that blurs the distinction between self-organization and template forcing theories (Coco and Murray, 2007) was proposed to explain the formation of previously observed coupling patterns in the field (Van Enckevort and Wijnberg, 1999; Castelle *et al.*, 2007). The simulated coupling patterns, emerging from morphological coupling mechanisms, were essentially similar to the existing observations.

Clear coupling patterns in double sandbar systems, such as those presented in Van Enckevort and Wijnberg, 1999; Castelle *et al.*, 2007; Quartel, 2009 and Part 1), are however rarely observed in the field (Hom-ma and Sonu, 1962; Goldsmith *et al.*, 1982; Bowman and Goldsmith, 1983). More often, inner-bar rip channels possess remarkably smaller and more variable alongshore scales than the outer bar (Barusseau *et al.*, 1994; Van Enckevort *et al.*, 2004; Lafon *et al.*, 2004, 2005). Figure 1 shows a typical double sandbar system geometry with an outer bar exhibiting crescentic patterns at a narrow range of wavelength, which contrasts with highly alongshore-variable inner-bar rip channels. This widely observed characteristic would suggest that morphological coupling does not play a substantial role in the overall double-sandbar dynamics. Ruessink *et al.* (2007) recently examined an eight-week dataset of daily time-exposure video images, starting from an alongshore-uniform double sandbar configuration following a storm event. Using a wavelet analysis, the authors showed that the initial inner bar and outer bar 3D pattern developments were spatially non-coupled. However, over time, the inner-bar morphology appeared to couple with that of the outer bar, with the inner bar patterns developing in response to the increasingly three-dimensional, onshore propagating outer bar. This suggests that the outer-bar geometry is a critical parameter governing the morphological evolution of the composite double sandbar system.

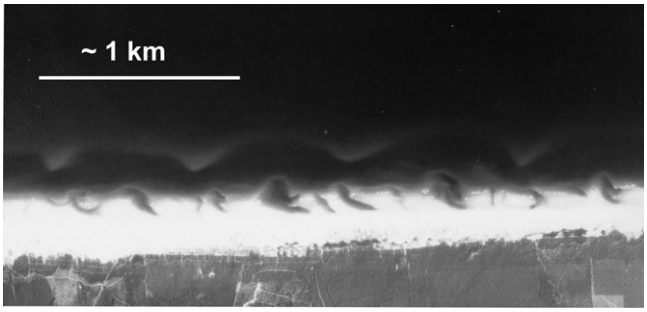

Figure 1. Aerial photograph of a double sandbar system on the French Aquitanian Coast displaying alongshore regularly spaced outer-bar crescentic patterns which contrast with highly alongshore-variable inner-bar rip channels.

This is Part 2 of a two-part paper on morphological coupling in the nearshore. In Part 1, we introduced and explored morphological coupling. Here, we examine the relative importance of morphological coupling and self-organization to the generation of inner-bar rip channels. We use the same numerical model as in Part 1, but now add small initial perturbations to the seabed to allow for the growth of inner-bar rip channels through self-organization mechanisms. Our model results and a wavelet analysis (next section) demonstrate that, as suggested by the observations of Ruessink *et al.* (2007), the variability in mean water depth along the outer bar controls the relative importance of self-organization mechanisms versus morphological coupling mechanisms and, hence, is crucial to the evolution of inner-bar rip channels (Results section).

2 Method

2.1 Model set-up, initial bathymetries and grid

The modelling strategy used in this study is essentially similar to that detailed in Part 1: a nonlinear morphodynamic model that couples a spectral wave model (Booij *et al.*, 1999), a time- and depth-averaged flow model (Castelle *et al.*, 2006), an energetic-type sediment transport model (Bailard, 1981), and the bed level continuity equation to compute bed level changes.

We ran the model for three different double sandbar geometries on a computational grid with an alongshore length of 4200 m, 20 × 20 m grid cells, and periodic lateral boundary conditions. In each geometry, we implemented an alongshore-uniform inner bar, 100 m from the mean-sea-level shoreline and with its crest in 1 m water depth. The three different outer-bar geometries were an alongshore-uniform outer bar, a well-developed outer crescentic bar, and a weakly developed outer crescentic bar. For the alongshore-uniform geometry, the outer bar was located 250 m from the mean-sea-level shoreline with its crest in 3 m water depth. In the two non-uniform geometries, crescentic patterns with a wavelength of 600 m were superimposed on the alongshore-uniform configuration as an alongshore sequence of horns and bays alternating shoreward and seaward of the outer bar crest. In both geometries, the cross-shore distance between a horn and a bay amounted to 60 m. For the weakly developed geometry, the vertical amplitude of the bay/horn sequence was 0·2 m, which we increased to 1·5 m for the well-developed geometry. The bars are superimposed on a 1 : 50 planar sloping depth profile, with its offshore extent in 10·5 m water depth. In contrast with the simulations in Part 1, we superimposed random perturbations with a magnitude of a few centimetres in the seabed to investigate the relative importance of self-organization at the scale of the individual bar versus coupling mechanisms. We note that the alongshore-uniform geometry is essentially similar to previous modelling experiments (Klein and Schuttelaars, 2006; Drønen and Deigaard, 2007; Smit *et al.*, 2008), who all examined the initial growth of crescentic patterns in double sandbars but did not investigate the potential importance of morphological coupling to inner-bar patterns in case of pre-existing outer-bar crescentic patterns.

We ran all the simulations for offshore significant wave heights H_{s0} of 0·8 m and 1 m, a peak period of 8 s, shore-normal incidence and time-invariant mean water level (no tide). These offshore wave conditions were motivated by the

simulations in Part 1, which showed that coupling patterns arise from horizontal circulation patterns driven by alongshore variations in wave set-up enforced by wave refraction and depth-induced breaking over the outer bar. The relative importance of wave focusing by refraction versus wave breaking across the outer bar was proven to control the inner-bar patterns morphologically forced by the outer bar. The authors additionally showed that, when wave breaking overwhelms wave focusing by refraction across the outer bar, 180° out-of-phase coupling emerges regardless of the outer-bar wavelength. When wave focusing by refraction overwhelms wave breaking, coupling at half of the outer-bar wavelength (in phase) is observed for larger (smaller) outer-bar wavelength and larger (smaller) vertical amplitude of the horn and bay sequence. According to Part 1, for the given outer-bar wavelength $\lambda = 600$ m and when investigating coupling mechanism alone (i.e. without initial superimposed perturbations of the seabed), waves with H_s = 0·8 m (1 m) are likely to favour coupling at half of the outer-bar wavelength (180° out-of-phase coupling). In this paper we ran, as mentioned in section 3, an additional simulation with an outer-bar crest in 2 m water depth and H_s = 1·6 m for the alongshore-uniform case to investigate the change of the double sandbar system behaviour from non-coupled to coupled, as observed in Ruessink *et al.* (2007). As we will see below, both H_s = 0·8 and 1·0 m are too low to modify the initial outer-bar morphology. The larger H_s in the non-coupled to coupled run was invoked to cause the initially alongshore-uniform outer bar to develop 3D patterns in time, which may potentially cause the inner-bar rip channels to change from self-organized into morphologically coupled features. As detailed in Part 1, there is no bed diffusion or bedslope transport in our model to damp the seabed instabilities. Continuing the simulations over a long duration would make the bed slope locally too large and the sandbar morphology unrealistic. Accordingly, when investigating the relative importance of self-organization mechanisms versus morphological coupling, we analysed the double sandbar morphology when the mean alongshore height variation of the alongshore depth line Z_{inner} (Figure 2), representative of the inner-bar morphology, reached about 0·5 m. This means that here we do not consider any steady state of the double sandbar system. Given that we ran the model for different wave conditions and initial alongshore non-uniformities (outer-bar geometry), the run durations given below ranged from 4 to 12 days.

2.2 Wavelet Analysis

To examine inner-bar rip channels and their potential coupling to the outer-bar crescents in more detail, we used a wavelet analysis. We applied the continuous wavelet transforms $W_n^z(s)$ defined as the convolution of a discrete sequence z_n ($n = 0, \ldots, N-1$) with a scaled and normalized mother wavelet function ψ_0:

$$W_n^z(s) = \left(\frac{dz}{s}\right)^{1/2} \sum_{n'=0}^{N-1} z_{n'} \psi_0^* \left\{\frac{(n'-n)\,dz}{s}\right\}, \quad (1)$$

where dz is the uniform spacing in z_n, n is the alongshore coordinate, s is the alongshore scale (Torrence and Compo, 1998) and * is the complex conjugate. In addition, we used normalized bivariate extension of the continuous wavelet transform for two discrete sequences z_n ($n = 0, \ldots, N-1$) and y_n ($n = 0, \ldots, N-1$), wavelet-squared coherency, $R_n^2(s)$ (Jevrejeva *et al.*, 2003; Grinsted *et al.*, 2004):

$$R_n^2(s) = \frac{|S\{s^{-1}W_n^{zy}(s)\}|^2}{S\{s^{-1}W_n^{z}(s)\}\,S\{s^{-1}W_n^{y}(s)\}}, \quad (2)$$

where S is a smoothing operator detailed in Torrence and Webster (1999) and Grinsted *et al.* (2004).

The wavelet analysis was on two alongshore lines of sea bed level (Figure 2), denoted $Z_{inner}(n)$ and $Z_{outer}(n)$ in the following. We chose the cross-shore location of $Z_{inner}(n)$ and $Z_{outer}(n)$ to be representative of the inner-bar evolution and outer-bar morphology, respectively. The $W_n^z(s)$ is used to decompose Z_{inner} and Z_{outer} into energy at a given alongshore scale and at a given alongshore distance. This enables both the detection of the dominant spatial modes of variability and how these modes vary in space. $R_n^2(s)$ is used to measure the linear relationship between $Z_{inner}(n)$ and $Z_{outer}(n)$ as a function of alongshore location and scale. A wavelet squared-coherency of 1 means a perfect linear relationship between $Z_{inner}(n)$ and $Z_{outer}(n)$ at a specific scale and alongshore distance, whereas a value of 0 is approached for vanishing linear correlation. As in a previous wavelet application to sandbar data (Ruessink *et al.*, 2007), we used the Morlet wavelet as the mother wavelet ψ_0 because of its good localization characteristics in both the space and frequency domains. Its scale is almost identical to the corresponding Fourier wavelength $\lambda = 1{\cdot}03\ s$ (Torrence and Compo, 1998). In all results below, the term wavelength refers to the Fourier wavelength λ equivalent to the wavelet scale s. We determined the statistical significance of $W_n^z(s)$ and $R_n^2(s)$ against synthetic red noise series, as detailed in Torrence and Compo (1998). The edge-affected part of $W_n^z(s)$ and $R_n^2(s)$ is termed the cone of influence (COI). The COI progressively reduces the useful alongshore region of analysis as the wavelength scale increases. The spatial averages (outside of the COI) of $W_n^z(s)$ and $R_n^2(s)$ are denoted $\overline{W^z}(s)$ and $\overline{R^2}(s)$.

3 Results

Figure 2 shows the bathymetry after a 12-day simulation starting from the alongshore-uniform geometry with H_{s0} = 0·8 m. The inner bar developed rip channels. The outer bar remained alongshore uniform as waves were too small with respect to the water depth above the outer-bar crest to drive sufficiently intense horizontal circulations likely to form 3D patterns. The inner-bar rip spacing is weakly alongshore variable. This alongshore variability is detailed in Figure 3 through the wavelet analysis. The alongshore non-uniform variabity of the seabed along Z_{inner} has a typical amplitude on the order of one

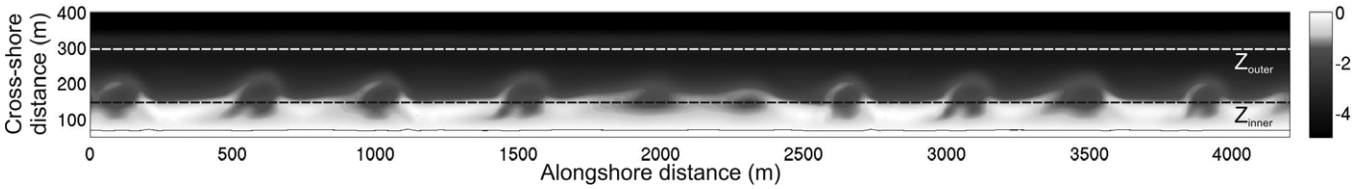

Figure 2. Evolution of the double sandbar morphology after a 12-day simulation period with constant shore-normal waves with H_s = 0·8 m and T_p = 8 s starting from the alongshore-uniform bathymetry, together with locations of $Z_{inner}(n)$ and $Z_{outer}(n)$. The key indicates elevation in m.

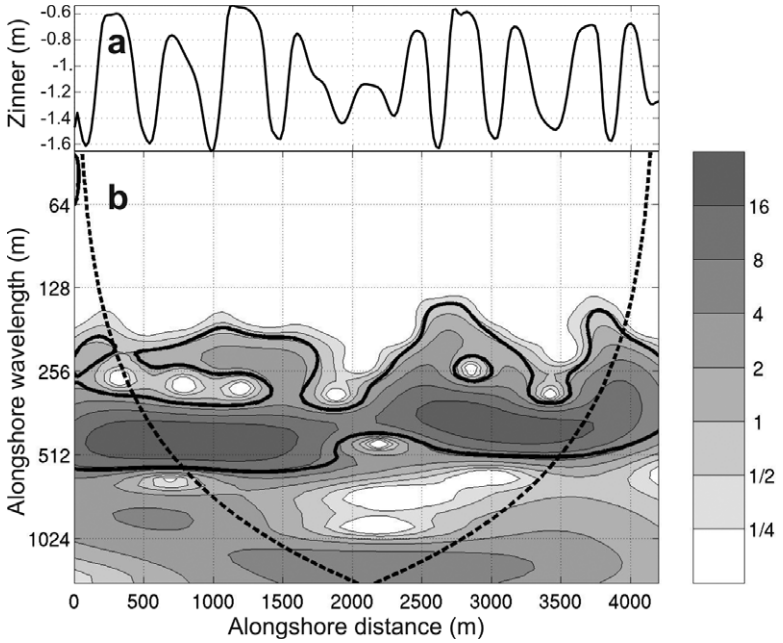

Figure 3. (a) Alongshore depth line Z_{inner} for the morphology given in Figure 2 and (b) the corresponding inner-bar local wavelet spectrum $W_n^z(s)$ normalized by the variance (shading), with the 5% significance level against red noise (bold solid contours) and the cone of influence (bold dotted curves).

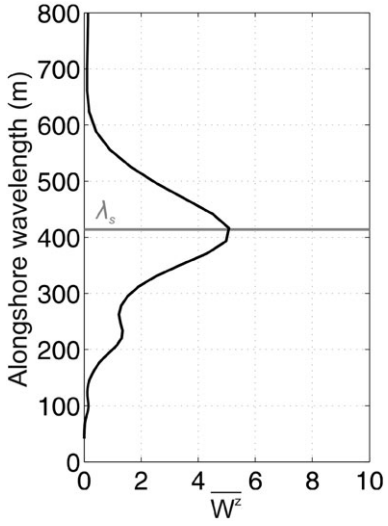

Figure 4. Alongshore-averaged wavelet spectra $\overline{W^z}(s)$ for Z_{inner} normalized with the variance in Z_{inner}, excluding local wavelet values within the COI, for the morphology given in Figure 2 and Z_{inner} in Figure 3. λ_s denotes the self-organization inner-bar emerging wavelength.

metre (Figure 3a). The local wavelet spectrum for this simulation indicates that Z_{inner} contains statistically significant power at the alongshore wavelengths λ between about 300 and 500 m, with slightly larger wavelengths at x = 0–2000 m than at x = 2500–4200 m, as is readily apparent in Figure 2. At x = 2000–2500 m, two less-developed inner-bar rip channels are observed. This alongshore variability in the inner-bar rip channel spacing is expected to be due to edge effects resulting from the periodic lateral boundary conditions imposed by the flow model. Given this restriction, the strong nonlinear behaviour of the inner-bar dynamics tends to self-organize into a more uniform spacing through mergings and splittings. The alongshore-averaged local wave spectrum of Z_{inner} (Figure 4) shows that the inner bar contains statistically high power at λ = 420 m. This corresponds to the self-organization mechanism emerging wavelength at the inner bar and is hence denoted λ_s in Figure 4. It is to be noted that a similar λ_s is observed for H_{s0} = 1 m, with a similar weak alongshore variability.

In Figure 5, the bathymetries of the four situations (weakly and well-developed outer-bar crescents, both with H_s = 0·8 m and 1·0 m) after a few-day simulation period show remarkable differences (Figures 5b, c, e, f) in comparison with the inner-bar variability when self-organization mechanisms prevail (Figure 2). When the outer bar was initially well-developed (Figure 5a), regular features developed for H_s = 0·8 m with two inner-bar rip channels within one outer-bar crescent (coupling at half of the outer-bar wavelength; Figure 5b), reminiscent of the observations in Castelle *et al.* (2007). For a similar initial outer-bar geometry, with H_s = 1 m, regular features also developed, in this case with one rip channel facing one outer-bar horn (180° out-of-phase coupling; Figure 5c), like the patterns observed by Van Enckevort and Wijnberg (1999), Castelle *et al.* (2007) and Quartel (2009). For both H_s = 0·8 and 1 m, coupling mechanisms readily overwhelm self-organization mechanisms at the scale of the individual inner bar, as the inner-bar morphology is fully coupled to the outer-bar geometry. In contrast, when the outer bar was initially weakly developed (Figure 5d), highly irregular inner-bar features formed for both H_s = 0·8 m (Figure 5e) and H_s = 1 m (Figure 5f). Neither of the three regular length scales observed in the other three simulations (Figures 2, 5b and 5c) are readily apparent.

Alongshore-averaged local wave spectra and wavelet coherency-squared are shown in Figure 6 for the four final situations shown in Figure 5. When the outer crescentic bar is well-developed, $Z_{inner}(n)$ contains statistically significant high wavelet power at λ = 300 m (Figure 6a, denoted $\lambda_c/2$) and λ = 600 m (Figure 6b, denoted λ_c) for the H_s = 0·8 m and 1 m simulation, respectively, with λ_c the coupling wavelength (outer-bar wavelength). Both the λ = 300 m and 600 m peaks result from morphological coupling, as indicated by the high wavelet-squared coherency values for λ = 600 m in Figure 6b. Note that bivariate wavelet transforms cannot capture the coupling at 300 m by definition; this is equally true for other

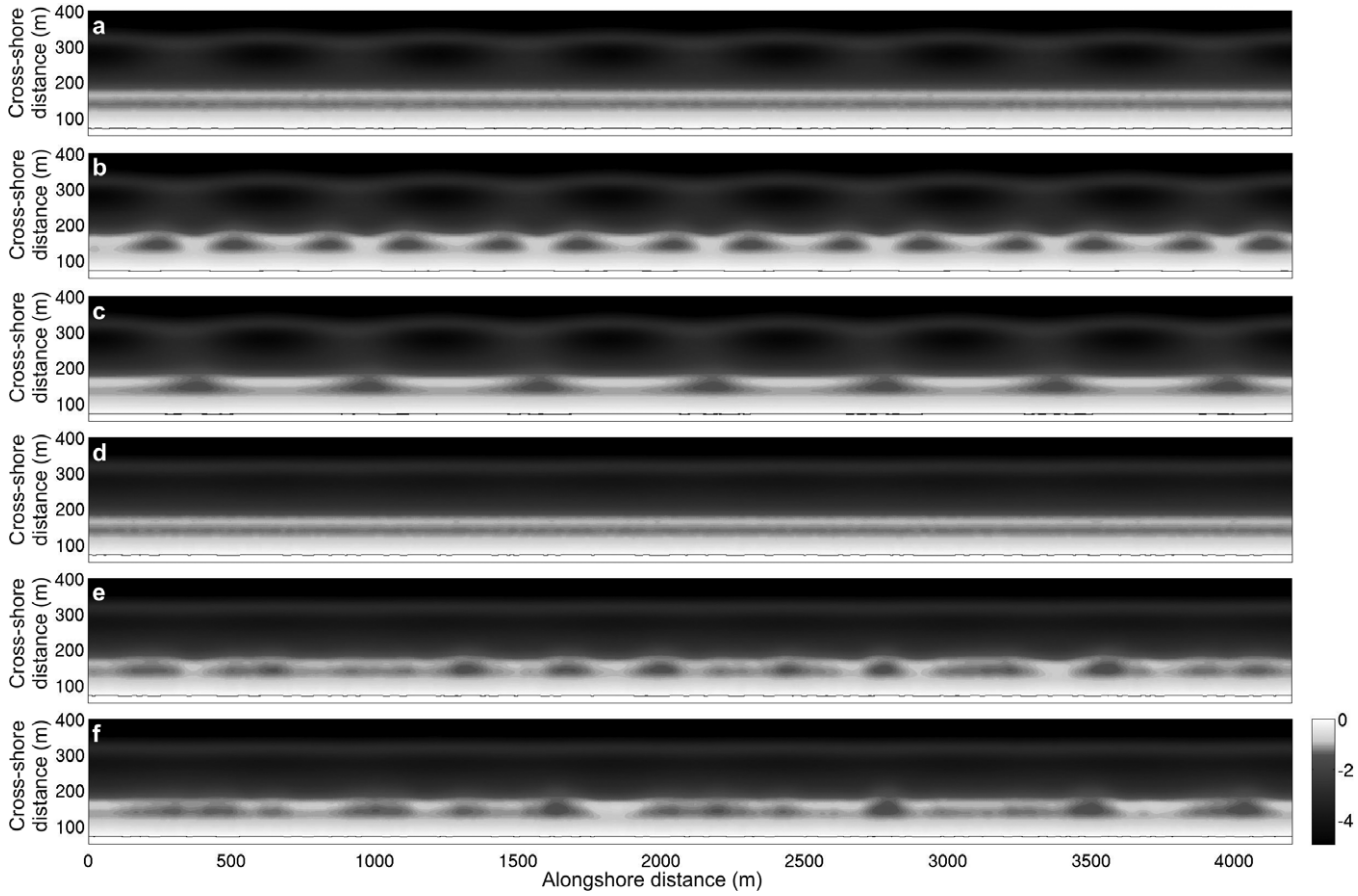

Figure 5. Evolution of the double sandbar morphology with constant shore-normal waves and $T_p = 8$ s: (a) initial well-developed outer crescentic bar, (b) evolution of (a) after a 6-day simulation period with $H_s = 0{\cdot}8$ m, (c) evolution of (a) after a 4-day simulation period with $H_s = 1$ m, (d) initial weakly-developed outer crescentic bar, (e) evolution of (d) after an 8-day simulation period with $H_s = 0{\cdot}8$ m, and (f) evolution of (d) after a 6-day simulation period with $H_s = 1$ m. The key indicates elevation in m.

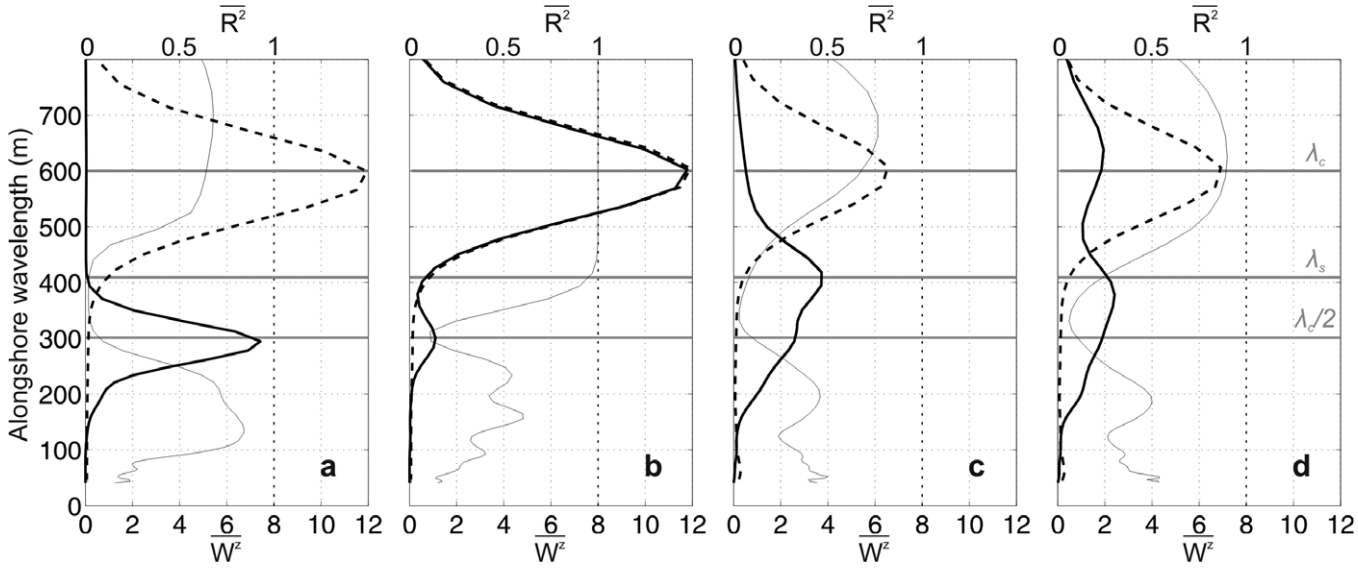

Figure 6. Alongshore-averaged wavelet spectra $\overline{W^z}(s)$ for Z_{inner} (bold solid line) and Z_{outer} (bold dashed line) and wavelet-coherency squared $\overline{R^2}(s)$ between Z_{inner} and Z_{outer} (thin solid line). (a), (b), (c) and (d) correspond to the alongshore depth lines in Figures 5b, 5c, 5e and 5f, respectively. In each panel the wavelet power has been normalized with the variance in Z_{inner} and Z_{outer} respectively. We excluded local wavelet and coherency-squared values within the COI, the region of (n,s) space influenced by wavelet edge effects, in the computation of $\overline{W^z}(s)$ and $\overline{R^2}(s)$. The horizontal grey lines are explained in the text.

techniques potentially suitable to detect morphological coupling, such as cross-correlation and cross-spectral analysis. For the $H_s = 0{\cdot}8$ m run with weakly-developed crescentic outer-bar patterns, $Z_{inner}(n)$ contains statistically significant power at $\lambda = 300$ m and 420 m (Figure 6c). For $\lambda = 300$ m, the statistically high power for the inner bar is indicative of coupling at half of the outer-bar wavelength, reminiscent of the coupling patterns in Figure 5b. In contrast, the $\lambda = 420$ m

is most likely due to self-organization mechanisms, as indicated by both the low $\overline{R^2}(s)$ values (Figure 6c) and the wavelet results for the simulation with prevailing self-organization mechanism (Figure 4). For the $H_s = 1$ m run with weakly-developed crescentic outer-bar patterns, $Z_{inner}(n)$ contains statistically significant power at $\lambda = 600$ m and in the range of 300–420 m (Figure 6d). For $\lambda = 600$ m the $\overline{R^2}(s)$ is large (Figure 6d), which, together with statistically high wavelet power for both inner and outer bars, is indicative of morphological coupling reminiscent of the 180° out-of-phase coupling observed in Figure 5c. The $\lambda = 300$–420 m statistically high power is most likely due to self-organization mechanisms with a significant contribution of coupling at $\lambda_c/2$ reminiscent of the weak statistical power at $\lambda_c/2$ observed in Figure 6b for the well-developed situation. It is to be noted that the 300 m and 420 m peaks are distinct during the first hours of the simulation and eventually tend to merge. For both the $H_s = 0{\cdot}8$ m and $H_s = 1$ m runs, the superposition of both self-organized and morphological features results in the rather irregular inner-bar rip spacing observed in Figures 5e and 5f. The general field observation of highly alongshore-variable inner-bar rip channels contrasting with the more regular outer-bar crescents, previously thought to be a proof of no morphological coupling, is actually indicative of a mixture of self-organization and morphological coupling mechanisms. In addition, the superimposition of the two mechanisms results in smaller alongshore-averaged inner-bar rip spacing than with self-organization mechanisms alone as shown for the $H_s = 1$ m run (Figure 5f) and particularly the $H_s = 0{\cdot}8$ m run (Figure 5e).

The alongshore variations of the relative importance of self-organization mechanism versus morphological coupling is assessed through the non-averaged local spectra. The non-averaged local spectra for the $H_s = 1$ m and well-developed outer-bar crescent run (Figure 7) show that inner-bar power at the coupling wavelength λ_c and local coherency-squared diagram are alongshore uniform, as expected from the regular spacing of the inner-bar rip channels in Figure 5c. A similar alongshore uniformity is observed for the $H_s = 0{\cdot}8$ m and well-developed outer-bar crescent run. In contrast, the wavelet analysis for the weakly-developed outer-bar crescent run with $H_s = 1$ m ($H_s = 0{\cdot}8$ m) given in Figure 8 (Figure 9) indicates that, when there is a mixture of both mechanisms, the relative importance of self-organization mechanisms versus morphological coupling is alongshore variable. For instance, in Figure 8, at alongshore distance $x = 1500$–4000 m, high power can be found at λ_c while high power at $\lambda_c/2 < \lambda < \lambda_s$ is restricted at $x = 1000$–2000 m. The alongshore variability in the relative importance of self-organization versus morphological coupling enforces the apparent highly alongshore-variable inner-bar rip channels that are observed in Figures 5e and f. Initially we suspected that the alongshore variability of the respective contributions of the two mechanisms was a lateral-boundary effect. However, when we ran an additional simulation with the alongshore domain extended to 8400 m, we found (not shown) the relative importance of self-organization mechanism versus morphological coupling to still be strongly alongshore variable, even in the (alongshore) centre of the computational domain. At this stage we do not know why the relative importance of self-organization mechanism versus morphological coupling is alongshore variable.

We also examined the ability of the model to simulate the observed double sandbar behaviour change from non-coupled to coupled (Ruessink *et al.*, 2007). To investigate this potential change, we ran an additional simulation with an initial alongshore-uniform outer bar with its crest in 2 m water depth and $H_s = 1{\cdot}6$ m. The temporal evolution of the double

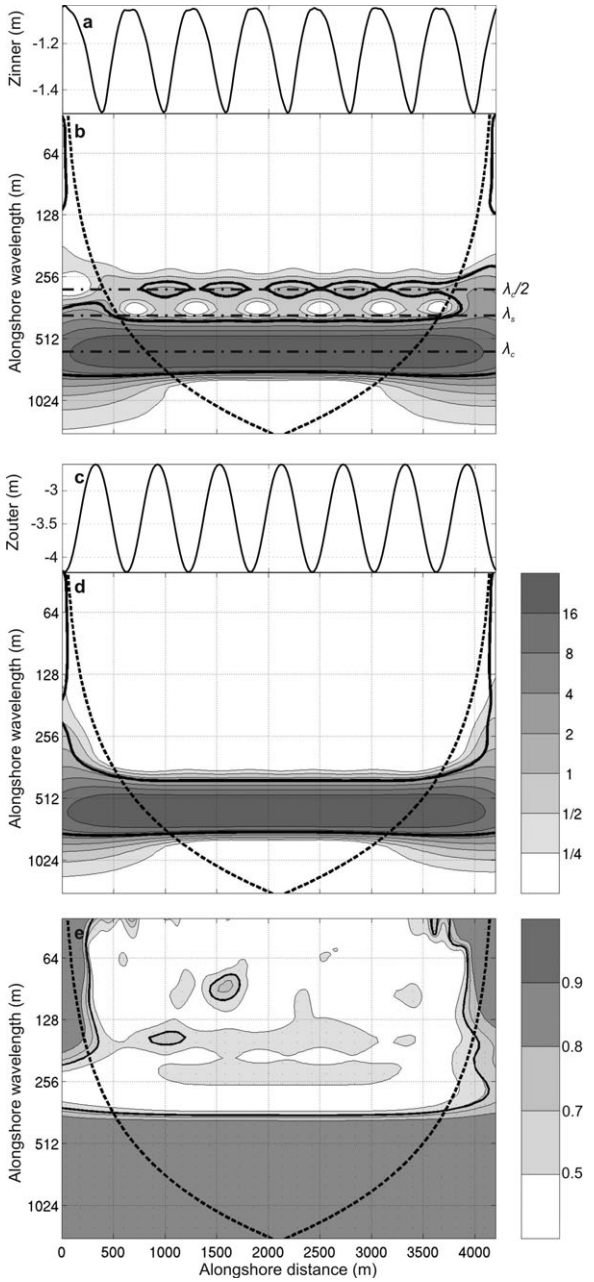

Figure 7. Wavelet analysis corresponding to Figure 5c: (a) alongshore depth line Z_{inner}, (b) inner-bar local wavelet spectrum $W_n^z(s)$, (c) alongshore depth line Z_{outer}, (d) outer-bar local wavelet spectrum $W_n^z(s)$ and (e) wavelet coherency-squared diagram $R_n^2(s)$. In each wavelet panel, the wavelet power has been normalized with the variance in Z_{inner} and Z_{outer} respectively, with the 5% significance level against red noise shown as the bold solid contours and the bold dotted curves depicting the COI beyond which edge effects become important. The horizontal black dash-dotted lines in (b) are explained in the text.

sandbar system morphology is given in Figure 10 with corresponding evolution of the non-averaged local spectra and local coherency-squared diagrams in Figure 11. Results show that after a 2-day simulation period (Figure 10a), a wide range of wavelengths is present at the beginning of inner-bar rip channel and outer-crescentic sandbar formation (Figures 11a and b). Small statistically significant coherency-squared values are observed in the whole (n,s) space, with only occasionally large statistically significant coherency-squared values for some narrow wavelength bands (for instance in Figure 11c, at $x = 3200$–3500 m for $\lambda \approx 120$ m) in which, however, both the

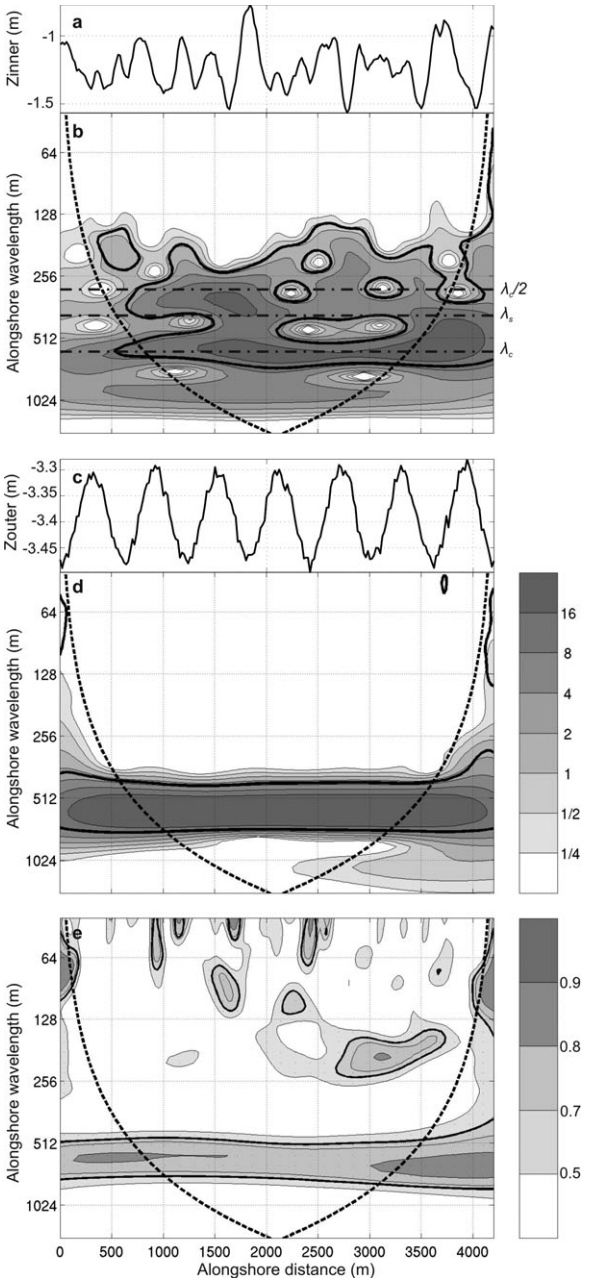

Figure 8. Wavelet analysis corresponding to Figure 5f: (a) alongshore depth line Z_{inner}, (b) inner-bar local wavelet spectrum $W_n^z(s)$, (c) alongshore depth line Z_{outer}, (d) outer-bar local wavelet spectrum $W_n^z(s)$ and (e) wavelet coherency-squared diagram $R_n^2(s)$. In each wavelet panel, the wavelet power has been normalized with the variance in Z_{inner} and Z_{outer} respectively with the 5% significance level against red noise shown as the bold solid contours and the bold dotted curves depicting the COI beyond which edge effects become important. The horizontal black dash-dotted lines in (b) are explained in the text.

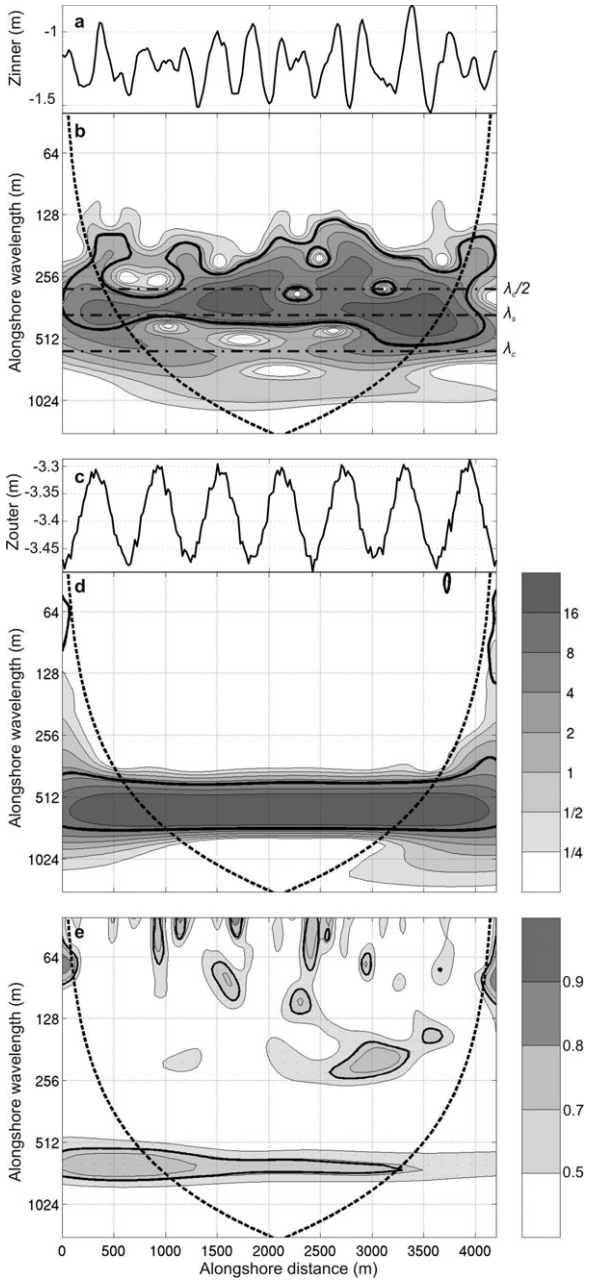

Figure 9. Wavelet analysis corresponding to Figure 5e: (a) alongshore depth line Z_{inner}, (b) inner-bar local wavelet spectrum $W_n^z(s)$, (c) alongshore depth line Z_{outer}, (d) outer-bar local wavelet spectrum $W_n^z(s)$ and (e) wavelet coherency-squared diagram $R_n^2(s)$. In each wavelet panel, the wavelet power has been normalized with the variance in Z_{inner} and Z_{outer} respectively, with the 5% significance level against red noise shown as the bold solid contours and the bold dotted curves depicting the COI beyond which edge effects become important. The horizontal black dash-dotted lines in (b) are explained in the text.

local wavelet power for the inner and outer bar were not significant, which is indicative of non-coupling. This suggests that the development of inner bar and outer bar 3D patterns are initially spatially non-coupled. However, over time the inner-bar morphology appears to couple with that of the outer bar. After a 4-day simulation period (Figure 10b), such coupling becomes apparent at x = 2000–3500 m for $\lambda \approx 350$ m (Figure 11f) in which, however, the inner-bar local wavelet power is reasonably weak. After a 6-day simulation period (Figure 10c), the alongshore extent of coupling is significantly larger together with higher power for the local coherency-squared diagram (Figure 11i) and statistically higher wavelet power in both the inner-bar (Figure 11g) and outer-bar (Figure 11h) local wavelet spectra. After an 8-day simulation period, the band with large coherency-squared values increased to lower wavelengths (Figure 11i), also encompassing regions with high inner-bar (Figure 11j) and outer-bar (Figure 11k) local wavelet power. Furthermore, statistically significant linear coupling can now be found all along the computational domain (Figure 11i). This results in the striking coupling patterns observed in Figure 10d with inner-bar rip channels systematically facing outer-bar horns (180° out-of-phase

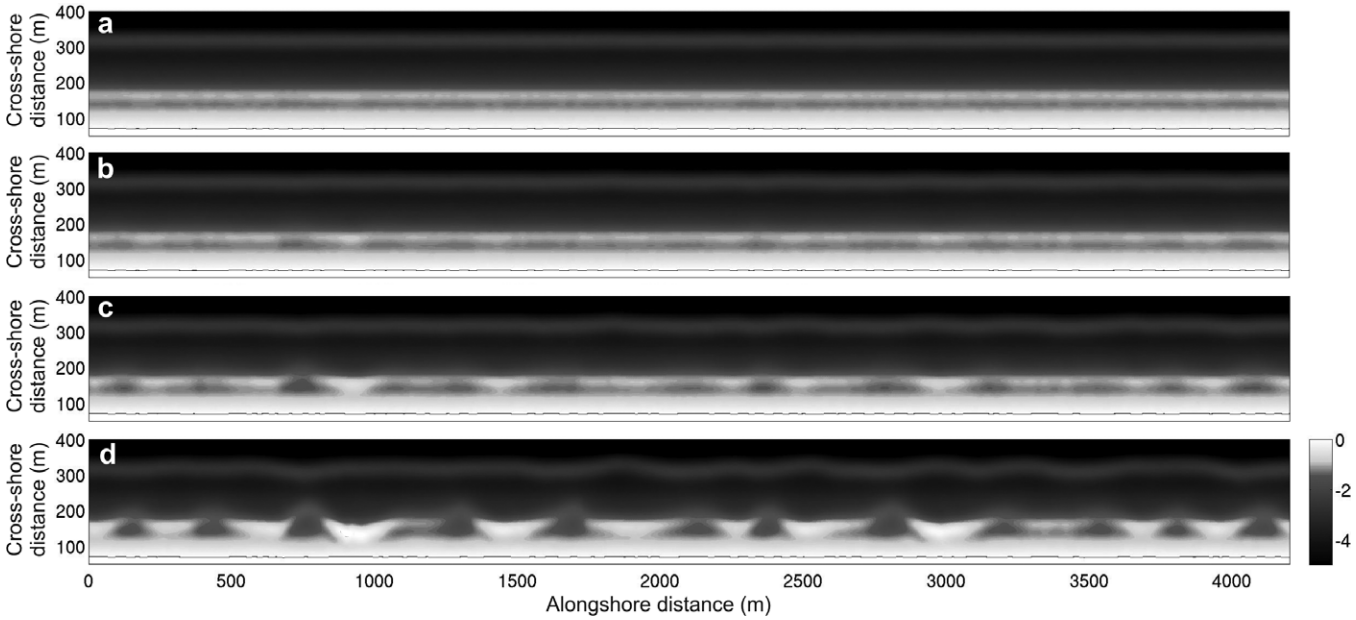

Figure 10. Evolution of the double sandbar morphology for constant shore-normal waves with H_s = 1·6 m and T_p = 8 s showing the temporal development of alongshore variability in the inner and outer bars from non-coupled to coupled. (a) t = 2 days, (b) t = 4 days, (c) t = 6 days, (d) t = 8 days. At the end of the simulation, the inner-bar rip channels systematically face the outer-bar horn (180° out-of-phase coupling).

coupling). The alongshore wavelength of the inner and outer bars are reasonably alongshore non-uniform.

4 Discussion and Conclusions

With our numerical simulations we have established that the relative importance of self-organization mechanisms and morphological coupling to the generation of inner-bar morphological variability is governed by the magnitude of the depth variations along the outer-bar crest. When the outer bar is alongshore uniform, self-organization mechanisms are predominant and the inner bar develops a rhythmicity arising from this mechanism of instability alone. This rhythmicity is found to be reasonably alongshore uniform. The small alongshore variations in the inner-bar wavelength are supposed to be due to the combination of edge effects resulting from the periodic lateral boundary conditions of the depth-averaged flow model and the strong nonlinear behaviour of the inner-bar dynamics, which tend to self-organize into a more uniform spacing through mergings and splittings (the equilibrium state is not reached). In contrast, when the outer-bar crescents are well-developed, self-organization mechanisms are overwhelmed by coupling mechanisms. In this case, inner-bar rip channels arise from horizontal circulation patterns driven by alongshore variations in wave set-up enforced by wave refraction and wave breaking across the outer bar. The relative importance of wave focusing by refraction versus wave breaking across the outer bar controls the inner-bar patterns morphologically forced by the outer bar (Part 1).

For the weakly-developed crescents, both mechanisms coexist as shown by the wavelet analysis, resulting in highly alongshore-variable inner-bar rip channel spacing. Although such irregular variability is generally considered as proof of no morphological coupling, our work demonstrates that this variability actually arises from a mixture of self-organization and morphological coupling mechanisms. The superimposition of the two mechanisms also results in smaller spatially averaged inner-bar rip spacing than when self-organization mechanism or morphological coupling prevails. The general field observation that inner-bar rip channels are more irregularly spaced and with smaller alongshore scales than outer-bar crescents suggests that morphological coupling may be more important to understanding and predicting the evolution of inner-bar rip channels than previously envisaged. In addition, the fact that the relative importance of each mechanism is strongly alongshore variable enforces the highly irregular alongshore variability in the inner bar.

Our model also successfully simulated the main characteristics of the coupled-noncoupled nature of double sandbar systems observed by Ruessink *et al.* (2007) under continued low-energy wave conditions following a morphological reset event (alongshore-uniform double sandbar system). A wide range of wavelengths is observed at the beginning of the 3D pattern development (for both the inner bar and outer bar), with alongshore non-uniformity development at the scale of the individual bar. A temporal change from non-coupled to coupled behaviour occurs in response to the increasingly three-dimensional outer bar. At the end of the simulation, statistically significant linear coupling can now be found along the entire computational area with inner-bar rip channels systematically facing outer-bar horns (180° out-of-phase coupling). These numerical results are essentially similar to the observations of Ruessink *et al.* (2007), despite the fact that they are highly idealized with time-invariant offshore wave conditions and mean water level. We note that, without the presence of the inner bar and with the same wave forcing, the outer bar develops reasonably similar alongshore scales as in Figure 10, confirming that in the double-bar case the inner bar couples to the outer bar, and not the other way around.

This change from non-coupled to coupled behaviour, together with the realistic coupling patterns simulated in Part 1 starting from idealized double sandbar geometry, enforce the confidence we can have in the numerical model. The nonlinear morphodynamic models used in the nearshore community (Damgaard *et al.*, 2002; Reniers *et al.*, 2004; Klein and Schuttelaars, 2006; Castelle *et al.*, 2006; Drønen and Deigaard, 2007; Smit *et al.*, 2008; Garnier *et al.*, 2008) contain the essential physics to examine the initial growth and subsequent nonlinear evolution of 3D surfzone sandbars. Limitations of

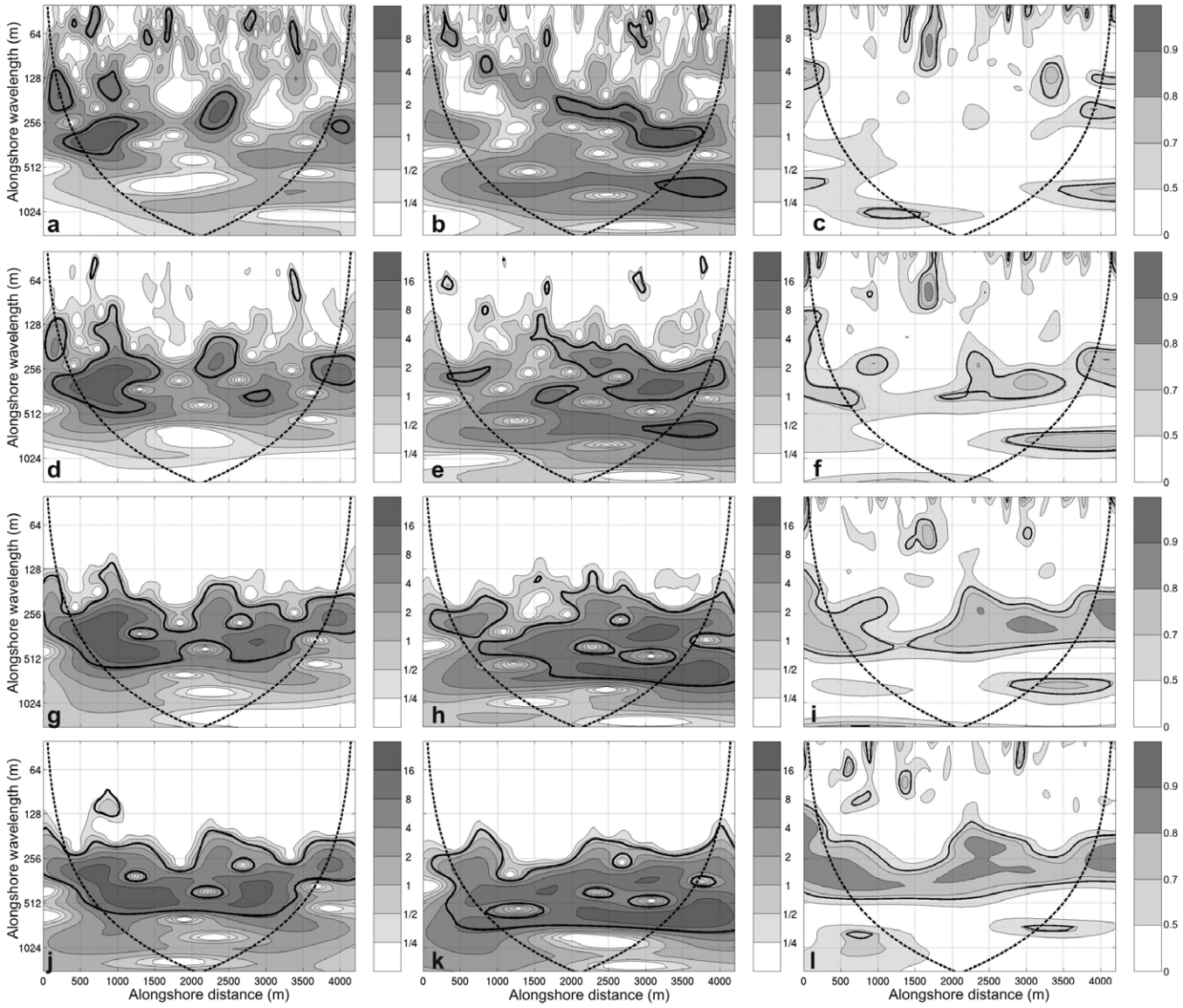

Figure 11. Wavelet analysis corresponding to Figure 10: (a, d, g, j) show the inner-bar local wavelet spectra $W_n^z(s)$, (b, e, h, k) the outer-bar local wavelet spectra $W_n^z(s)$ and (c, f, i, l) the wavelet coherency-squared diagrams $R_n^2(s)$. In each panel, the wavelet power has been normalized with the variance in Z_{inner} and Z_{outer} respectively, with the 5% significance level against red noise shown as the bold solid contours and the bold dotted curves depicting the COI beyond which edge effects become important. (a, b, c) correspond to Figure 10a, (d, e, f) to Figure 10b, (g, h, i) to Figure 10c and (j, k, l) to Figure 10d.

the modelling study undertaken in this paper for the assessment of the relative importance of self-organization mechanisms versus morphological coupling must be pointed out. The contribution of self-organization mechanisms is strongly dependent on the initial random perturbation height initially superimposed on the double sandbar geometry. For instance, for a given offshore wave height H_s and a given vertical amplitude of the horn/bay sequence D_v, decreasing the initial perturbation height favours a change from a mixture of both mechanisms to morphological coupling mechanisms overwhelming self-organization mechanisms. However, the initial random perturbation height does not have any physical sense. Therefore, the simulations and study outcomes presented in this paper constitute a proof of concept rather than a comprehensive extensive modelling exercise. The model will have to be confronted with further field data starting from an accurately surveyed bathymetry and comprising time-varying offshore wave conditions and tidal elevation.

All the simulations were run with time-invariant mean water level (no tide). However, the role of continuously changing tidal elevation in the field may be significant to the development of inner-bar rip channels. A slight variation in mean water level results in a change of the balance between wave breaking and refraction across the outer bar. This induces a change in the driven inshore horizontal circulation patterns which are crucial to the development of inner-bar rip channels. Emergence of coupling patterns in meso- to macro-tidal environments is potentially more complicated than in the idealized simulations presented in both this paper and the companion paper, despite the fact that they were observed in such tidal settings (Ruessink *et al.*, 2007; Castelle *et al.*, 2007; Quartel, 2009). Even more importantly, tide-induced continuously changing balance between breaking and refraction across the 3D outer bar can be hypothesized to enforce the inner-bar rip channel alongshore variability. Further simulations with tides are required to examine the effects of tidal range on the alongshore variability of inner-bar rip-channel scale and how it mixes with self-organization and coupling mechanisms.

Our simulations showed that coupling mechanisms are important for understanding and predicting the evolution of

inner-bar rip channels, and the whole system, during down-state transitions (post-storm periods). Conversely, the potential role of coupling during up-state transitions is poorly documented. For instance, Wijnberg and Holman (2007) observed at a single-barred beach (Duck, USA) that, during storm events, a crescentic bar may shed a bar-like feature that later transits the trough and merges with the subaerial beach within a few days. The authors named this spatially isolated feature a Shoreward Propagating Accretionary Wave (SPAW). Almar *et al*. (in press) observed a similar SPAW event on the double-barred meso- to macro-tidal Truc Vert Beach, southwest France, during a 10-year return storm. They showed that the SPAW connected to the inner bar and subsequently influenced the inner-bar dynamics. The mechanism leading to both the formation and migration of the SPAW and its subsequent interaction with the inner-bar dynamics is not understood. In general, the role of coupling mechanisms during down-state sequence has been highlighted here and in the companion paper, but understanding and reproducing the interaction between the inner and outer bars during up-state sequence remains a challenge for future numerical studies.

Acknowledgements—The wavelet computations in this paper were based on software developed by Aslak Grinsted and co-workers (version wtc-r14, available from http:// www.pol.ac.uk/home/research/waveletcoherence/). BC and PB gratefully acknowledge funding from the project MODLIT (under the Program RELIEFS/INSU – SHOM/DGA). BGR and TDP acknowledge financial support through the Netherlands Organisation for Scientific Research award 864.04.007 and contract 818.01.009, respectively. The authors wish to thank the two anonymous reviewers for their positive criticism that improved the quality of the paper.

References

Aarninkhof SGJ, Hinton C, Wijnberg KM. 1998. On the predictability of nearshore bar behaviour. In *Proceedings of 26th Internat. Conference on Coastal Eng.* ASCE: New York. 2409–2422.

Almar R, Castelle B, Ruessink BG, Sénéchal N, Bonneton P, Marieu V. in press. Two- and three-dimensional double-sandbar system behaviour under intense wave forcing and a meso-macro tidal range. *Continental Shelf Research*.

Bailard JA. 1981. An energetics total load sediment transport model for a plane beach. *Journal of Geophysical Research* **86**: C11, 10938–10954.

Barusseau J-P, Radulescu M, Descamps C, Akouango E, Gerbe A. 1994. Morphosedimentary multiyear changes on a barred coast (Gulf of Lions, Mediterranean Sea, France). *Marine Geology* **122**: 47–62.

Booij N, Ris RC, Holthuijsen LH. 1999. A third-generation wave model for coastal regions, Part 1: Model description and validation. *Journal of Geophysical Research* **104**: C4, 7649–7666.

Bowen AJ, Inman DL. 1971. Edge waves and crescentic bars. *Journal of Geophysical Research* **76**: 8662–8671.

Bowman D, Goldsmith V. 1983. Bar morphology of dissipative beaches: an empirical model. *Marine Geology* **51**: 15–33.

Calvete D, Dodd N, Falqués A, Van Leeuwen SM. 2005. Morphological development of rip channel systems: Normal and near-normal wave incidence. *Journal of Geophysical Research* **110**: C10006, DOI: 10.1029/2004JC002803.

Castelle B, Bonneton P, Butel R. 2006. Modeling of crescentic pattern development of nearshore bars: Aquitanian Coast, France. *C. R. Geoscience* **338**: 795–801.

Castelle B, Bonneton P, Dupuis H, Sénéchal N. 2007. Double bar beach dynamics on the high-energy meso-macrotidal French Aquitanian Coast: A review. *Marine Geology* **245**: 141–159.

Castelle B, Ruessink BG, Bonneton P, Marieu V, Bruneau N, Price TD. 2010. Coupling mechanisms in double sandbar systems. Part 1: Patterns and physical explanation. *Earth Surface Processes and Landforms*, DOI: 10.1002/esp.1929.

Coco G, Murray AB. 2007. Patterns in the sand: from forcing templates to self-organization. *Geomorphology* **91**: 271–290.

Damgaard J, Dodd N, Hall L, Chesher T. 2002. Morphodynamic modeling of rip channel growth. *Coastal Engineering* **43**: 199–221.

Deigaard R, Drønen N, Fredsøe J, Jensen JH, Jørgensen MP. 1999. A morphological stability analysis for a long straight barred coast. *Coastal Engineering* **36**: 171–195.

Drønen N, Deigaard R. 2007. Quasi-three-dimensional modelling of the morphology of longshore bars. *Coastal Engineering* **54**: 197–215.

Falqués A, Coco G, Huntley DA. 2000. A mechanism for the generation of wave-driven rhythmic patterns in the surf zone. *Journal of Geophysical Research* **105**: 24071–24088.

Garnier R, Calvete D, Falqués A, Dodd N. 2008. Modelling the formation and the long-term behavior of rip channel systems from the deformation of a longshore bar. *Journal of Geophysical Research* **113**: C07053, DOI: 10.1029/2007JC004632.

Goldsmith V, Bowman D, Kiley K. 1982. Sequential stage development of crescentic bars: HaHoterim Beach, Southeastern Mediterranean. *Journal of Sedimentary Petrology* **52**: 233–249.

Greenwood B, Davidson-Arnott RGD. 1979. Sedimentation and equilibrium in wave-formed bars: A review and case study. *Canadian Journal of Earth Sciences* **16**: 312–332.

Grinsted A, Moore JC, Jevrejeva S. 2004. Application of the cross wavelet transform and wavelet coherence to geophysical time series. *Nonlinear Processes in Geophysics* **11**: 561–566.

Holman RA, Bowen AJ. 1982. Bars, bumps and holes: Models for the generation of complex beach topography. *Journal of Geophysical Research* **87**: 457–468.

Hom-ma M, Sonu C. 1962. Rhythmic pattern of longshore bars related to sediment characteristics. In *Proceedings of 8th Internat. Conference on Coastal Engineering* ASCE: New York. 248–278.

Houser C, Greenwood B. 2005. Hydrodynamics and sediment transport within the inner surf zone of a lacustrine multiple-barred nearshore. *Marine Geology* **218**: 37–63.

Jevrejeva S, Moore JC, Grinsted A. 2003. Influence of the Arctic Oscillation and El Niño–Southern Oscillation (ENSO) on ice conditions in the Baltic Sea: The wavelet approach. *Journal of Geophysical Research* **108**: D21, DOI: 10.1029/2003JD003417.

Klein MD, Schuttelaars HM. 2006. Morphodynamic evolution of double-barred beaches. *Journal of Geophysical Research* **111**: C06017, DOI: 10.1029/2005JC003155.

Lafon V, De Melo Apoluceno D, Dupuis H, Michel D, Howa H, Froidefond J-M. 2004. Morphodynamics of nearshore rhythmic sandbars in a mixed-energy environment (SW France): I. Mapping beach changes using visible satellite imagery. *Estuarine, Coastal and Shelf Science* **61**: 289–299.

Lafon V, Dupuis H, Butel R, Castelle B, Michel D, Howa H, De Melo Apoluceno D. 2005. Morphodynamics of nearshore rhythmic sandbars in a mixed-energy environment (SW France): II. Physical forcing analysis. *Estuarine, Coastal and Shelf Science* **65**: 449–462.

Lippmann TC, Holman RA. 1990. The spatial and temporal variability of sand bar. *Journal of Geophysical Research* **95**: (C7), 11575–11590.

Lippmann TC, Holman RA, Hathaway KK. 1993. Episodic, nonstationary behaviour of a double bar system at Duck, North Carolina, USA, 1986–1991. *Journal of Coastal Research* Special issue **15**: 49–75.

MacMahan JH, Thornton EB, Stanton TP, Reniers AJHM. 2005. RIPEX-observations of a rip current system. *Marine Geology* **218**: 113–134.

Masselink G. 2004. Formation and evolution of multiple intertidal bars on macrotidal beaches: Application of a morphodynamic model. *Coastal Engineering* **51**: 713–730.

Quartel S. 2009. Temporal and spatial behaviour of rip channels in a multiple-barred coastal system. *Earth Surface Processes and Landforms* **34**: 163–176.

Reniers AJHM, Roelvink JA, Thornton EB. 2004. Morphodynamic modeling of an embayed beach under wave group forcing. *Journal of Geophysical Research* **109**: C01030, DOI: 10.1029/2002JC001586.

Ruessink BG, Terwindt JHJ. 2000. The behaviour of nearshore bars on the time scale of years: A conceptual model. *Marine Geology* **163**: 289–302.

Ruessink BG, Wijnberg KM, Holman RA, Kuriyama K, Van Enckevort IMJ. 2003. Intersite comparison of interannual nearshore bar behavior. *Journal of Geophysical Research* **108**: C8, DOI: 10.1029/2002JC001505.

Ruessink BG, Coco G, Ranasinghe R, Turner IL. 2007. Coupled and noncoupled behavior of three-dimensional morphological patterns in a double sandbar system. *Journal of Geophysical Research* **112**: C07002, DOI: 10.1029/2006JC003799.

Short AD. 1991. Macr-meso tidal beach morphodynamics – An overview. *Journal of Coastal Research* **7**: 2, 414–436.

Short AD, Hesp PA. 1982. Wave, beach and dune interactions in southeastern Australia. *Marine Geology* **48**: 259–284.

Smit MWJ, Reniers AJHM, Ruessink BG, Roelvink JA. 2008. The morphological response of a nearshore double sandbar system to constant wave forcing. *Coastal Engineering* **55**: 761–770.

Thornton EB, MacMahan JH, Sallenger AH Jr. 2007. Rip currents, mega-cusps, and eroding dunes. *Marine Geology* **240**: 151–167.

Torrence C, Compo GP. 1998. A practical guide to wavelet analysis. *Bullettin of the American Meteorological Society* **79**: 61–78.

Torrence C, Webster PJ. 1999. Interdecadal changes in the ENSO–Monsoon system. *Joubnal of Climate* **12**: 2679–2690.

Van Enckevort IMJ, Wijnberg KM. 1999. Intra-annual changes in bar plan shape in a triple bar system. In *Proceedings of Coastal Sediments '99* 2548–2558.

Van Enckevort IMJ, Ruessink BG, Coco G, Susuki K, Turner IL, Plant NG, Holman RA. 2004. Observations of nearshore crescentic sandbars. *Journal of Geophysical Research* **109**: C06028, DOI: 10.1029/2003JC002214.

Wijnberg KM, Holman RA. 2007. Video-observation of shoreward propagating accretionary waves. In *Proceedings of River, Coastal and Estuarine Morphodyanmics '07*. ASCE: New York. 737–743.

Wright LD, Short AD. 1984. Morphodynamic variability of surf zones and beaches: A synthesis. *Marine Geology* **56**: 93–118.

D.8 Two- and three-dimensional double-sandbar system behaviour under intense wave forcing and a meso-macro tidal range

Rafael Almar, Bruno Castelle, Gerben Ruessink, Nadia Sénéchal, Philippe Bonneton, Vincent Marieu

Continental Shelf Research, Vol. 30, pp. 781-792, 2010

Continental Shelf Research 30 (2010) 781–792

Contents lists available at ScienceDirect

Continental Shelf Research

journal homepage: www.elsevier.com/locate/csr

Two- and three-dimensional double-sandbar system behaviour under intense wave forcing and a meso–macro tidal range

R. Almar [a,b,*], B. Castelle [a,b], B.G. Ruessink [c], N. Sénéchal [a,b], P. Bonneton [a,b], V. Marieu [a,b]

[a] Université de Bordeaux, CNRS, UMR EPOC 5805, Av. de Facultés, Talence F33405, France
[b] CNRS, UMR EPOC 5805, Talence F33405, France
[c] Department of Physical Geography, Faculty of Geosciences, Institute for Marine and Atmospheric Research, Utrecht University, P.O. Box 80.115, 3508 TC Utrecht, The Netherlands

ARTICLE INFO

Article history:
Received 26 May 2009
Received in revised form
19 January 2010
Accepted 1 February 2010
Available online 6 February 2010

Keywords:
Double-sandbar system
Meso–macro tidal environment
Storm impact
Nearshore
Video imaging
Short-term morphodynamics
Truc Vert Beach

ABSTRACT

Five weeks of hourly, 10-min time-exposure video images were used to analyze the meso–macro-tidal double-barred Truc Vert Beach, SW France, under intense wave forcing. The four storms experienced, one of which with an offshore significant wave height over 8 m, induced dramatic changes in the double sandbar system. The subtidal outer bar migrated offshore rapidly (up to 30–50 m/day) and its pre-existing crescentic pattern was wiped out. The seaward-protruding parts of the outer bar barely migrated offshore during the most intense storm, whereas a landward-protruding part was shed off. Over the entire study period, the outer-bar dynamics was dominated by alongshore-averaged changes rather than alongshore non-uniform changes, while the opposite was observed for the inner bar. In addition, the outer-bar dynamics was predominantly controlled by the time-varying offshore wave conditions, whereas the inner-bar dynamics was influenced largely by the tide-range variations. Our observations put forward the key role of morphological settings (the presence of a subtidal bar and its shape) and tidal range in governing inner-bar behaviour within a double sandbar dynamics, and provide strong support for previous suggestions that sandbars cannot be studied in isolation.

1. Introduction

Double nearshore sandbar systems are common morphological features along sandy, wave-dominated, micro- to meso–macro-tidal coastlines (Ruessink et al., 2003; Van Enckevort et al., 2004; Castelle et al., 2007). Both bars can exhibit a wide range of planshapes, varying from linear to undulating. Alongshore non-uniformities in nearshore sandbars are traditionally classified into discrete states within the conceptual model of Wright and Short (1984). Initially developed for single-barred, micro-tidal beaches, this conceptual model identifies three main beach states from dissipative to reflective with, in-between, an intermediate state further divided into 4 sub-states. Within this intermediate state, immediately below the dissipative state is the Longshore Bar and Trough (LBT), next the Rhythmic Bar and Beach (RBB), then the Transverse Bar and Rip (TBR) and finally the Low Tide Terrace (LTT). High-energy wave conditions generally induce an up-state transition toward the LBT or the fully dissipative state, which is associated with rapid seaward bar migration of up to 10–20 m/day (e.g., Gallagher et al., 1998). During post-storm, decreasing wave-energy conditions, undulating patterns develop (down-state transition); also, the bar slowly propagates shoreward (Sallenger et al., 1985; Gallagher et al., 1998). In double bar systems, both bars are expected to go through all the states within the intermediate classification and independently follow the same up-state and down-state schemes as single-barred systems (Short and Aagaard, 1993).

Alongshore-averaged (or two-dimensional 2D) cross-shore bar migration has primarily been considered as a morphologic adjustment to the hydrodynamic forcing (among others, King and Williams, 1949; Aagaard et al., 1998). However, this theory has been recently challenged by observations (Ruessink and Terwindt, 2000; Plant et al., 2001) and numerical modelling (Aarninkhof et al., 1998; Masselink, 2004) which put forward that 2D bar behaviour is more complicated than previously envisaged. Bar dynamics may be driven by an interaction of the evolving bar itself and the hydrodynamic forcing. A bar strongly controls the wave breaking location (Lippmann and Holman, 1989) and, hence, cross-shore sediment transport patterns; this may reinforce or suppress further bathymetric modifications (e.g., Plant et al., 2001). For instance, wave-breaking across an outer bar affects the hydrodynamics and hence the evolution of an inner bar. Observations (Ruessink et al., 2007a) suggest that the distance between the inner and outer bars might be a critical parameter governing the behaviour of the composite double-bar system

* Corresponding author at: Université de Bordeaux, CNRS, UMR EPOC 5805, Av. de Facultés, Talence F33405, France. Tel.: +33 5 40 00 88 32; fax: +33 5 56 84 08 48.
E-mail address: r.almar@epoc.u-bordeaux1.fr (R. Almar).

0278-4343/$ - see front matter © 2010 Elsevier Ltd. All rights reserved.
doi:10.1016/j.csr.2010.02.001

during down-state transitions. However, the 2D, cross-shore response of double bar systems to storms is still poorly understood (e.g., Castelle et al., 2007), especially that of the inner bar.

The role of morphological feedback in forming alongshore non-uniform (three-dimensional, 3D) bar patterns is now also widely acknowledged (Coco and Murray, 2007). In double-bar systems, the outer bar often exhibits a reasonably regular crescentic pattern (Van Enckevort et al., 2004), defined as an alongshore sequence of horns and bays where horns and bays are, respectively, landward- and seaward-protruding parts. Recent observations (Ruessink et al., 2007a) and numerical modelling (Castelle et al., in press-a, in press-b) showed that the generation of 3D inner-bar patterns may be more complicated, typically being a mixture of self-organization and outer–inner-bar interactions (or "morphological coupling") rather than self-organization alone. On the contrary to the relatively well-known down-state sequence, up-state double-bar system interactions during storms, whereby pre-existing 3D patterns disappear into an alongshore 2D bar, are still poorly understood. It is possible that during up-state transitions the inner and outer bar may also strongly interact. For instance, during intense (storm) wave forcing, Wijnberg and Holman (2007) observed at a single-barred beach (Duck, USA) that a crescentic bar may shed a bar-like feature that later on merged with the subaerial beach. They named this spatially isolated feature a Shoreward Propagating Accretionary Wave (SPAW). Similar features have been described for Wanganui, New Zealand (Shand, 2007). It is possible that a SPAW shed off from an outer bar may similarly affect the evolution of an inner bar. The link between 2D and 3D changes has never been investigated for up-state transition in double-bar systems.

Recent studies have shown that the tidal range can affect bar dynamics by changing the type and duration of shoaling-wave, surf and swash processes across the bar (Masselink and Turner, 1999; Masselink et al., 2006; Price and Ruessink, 2008). A small tidal range is expected to increase surf zone and swash processes and thus to result in rather short response times to time-varying incident wave conditions, whereas a large meso- to macro-tidal range favours shoaling-wave processes and, hence, increases the response time. Curiously, despite their common occurrence (Short, 1991), double-barred systems exposed to a large tidal range have barely been studied (among others; Masselink et al., 2007, 2008). In particular, the effect of such a large tidal range on the double-bar system response to storms is poorly understood.

In this paper, we present the first high-frequency (~daily) observations of double bar dynamics in a high-energy, meso–macro-tidal environment. In Section 2, we present the hydrodynamic and video data gathered during a 5-week period of intense wave forcing at Truc Vert Beach, SW France. In Section 3, we describe the temporal evolution of this system. Also, we investigate outer–inner-bar interactions as well as the link between waves and tidal levels well seaward of the surf zone and the observed double-bar evolution. The observed complexity of the double-bar system response to storm and tide conditions is discussed in Section 4.

2. Data

2.1. Study area description

The field site is Truc Vert Beach (TVB), located along the southern part of the French Atlantic Coast (Fig. 1) and typical of the relatively undisturbed coast extending 100 km between the Gironde Estuary (90 km to the North) and the Arcachon Lagoon inlet (10 km to the south). TVB's straight sandy coastline is almost

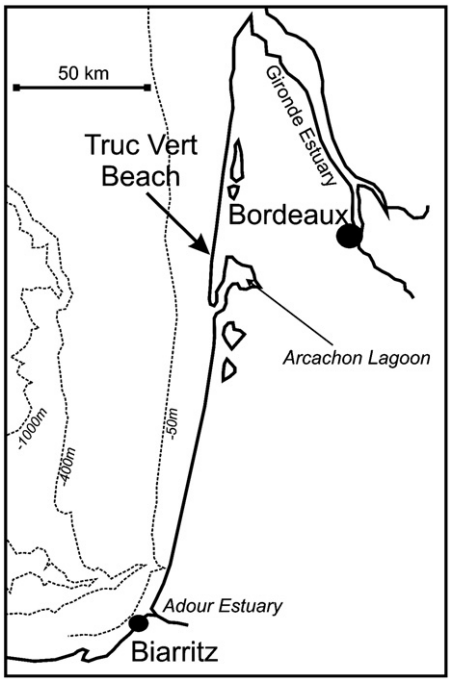

Fig. 1. Location of the field study site, Truc Vert Beach, on the French Aquitanian Coast.

N–S-oriented and bordered by high aeolian dunes. The sediment consists of quartz sand with a mean grain size ranging from 200 to 400 μm (Pedreros et al., 1996). TVB is a wave-dominated environment characterized by mainly low-steepness waves associated with long-distance swell travelling from the W-NW direction. The seasonal modulation of the incoming wave energy is strong, with a minimum in wave energy during summer; in winter the offshore significant wave height (*Hs*) may reach 10 m during severe storms. The mean annual *Hs* is 1.4 m with a corresponding mean period of 6.5 s (Butel et al., 2002). The tide is semi-diurnal with a neap and spring tidal range of about 1.5 and 5 m, respectively. TVB is a highly dynamic, intermediate double-barred beach (Castelle et al., 2007; Sénéchal et al., 2009) following the classification of Wright and Short (1984) and Short and Aagaard (1993).

Long-term satellite monitoring and monthly topographic surveys showed that the inner bar can go through all the intermediate sub-states within the classification of Wright and Short (1984). The inner intertidal bar usually exhibits a TBR morphology with a mean alongshore-averaged wavelength of about 400 m (Lafon et al., 2002; De Melo Apoluceno et al., 2002; Sénéchal et al., 2009). From recurrent observations, De Melo Apoluceno (2003) established that a significantly longer period than for other sites (Owens and Frobel, 1977) was required for the down-state transition from LBT to LTT to occur at TVB. De Melo Apoluceno (2003) suggested that waves with $Hs > 3$ m were required for enforcing an up-state from the LTT morphology, despite some observations (De Melo Apoluceno, 2003) have shown that LTT morphology can persist during storm events with $Hs > 3$ m and TBR morphology during storm events with $Hs > 5$ m. Alongshore southward migration rates of 0.5–4.5 m/day were deduced from sparse satellite images and shoreline maps, and are limited to fair weather conditions.

Most of the time the outer bar exhibits crescentic patterns with a mean alongshore wavelength of about 700 m (Froidefond et al., 1990; Castelle 2004; Lafon et al., 2004). Sparse bathymetric surveys have shown that the shallowest landward-protruding section of the bar, the deepest seaward-protruding section of the

bar and the trough are on the order of 2, 4.5 and 6 m above the Lowest Astronomical Tide (LAT), respectively (Desmazes et al., 2002). These values are likely to vary significantly given the highly-variable wave conditions TVB is exposed to, and given that the available bathymetric surveys were undertaken during fair weather conditions only. The outer-bar shape can vary from a regular crescentic shape to a strongly skewed crescentic shape (Lafon et al., 2004), presumably related to angle of wave incidence. Over a 3-month period of relatively fair weather, Lafon et al. (2004) reported a southerly migration rate of about 1 m/day.

2.2. ECORS08 wave and tide data

The ECORS (DGA-SHOM) field experiment took place at TVB from March 1 to April 9, 2008, and involved 120 scientists from 16 international institutions. One of the aims of the experiment was to study short-term TVB response to storms (more details can be found in Sénéchal et al., 2008). These storm condition expectations were fully satisfied as, during the experiment, the Aquitanian Coast was exposed to 4 severe storms with *Hs* larger than 4 m, comprising a 10-year return storm with *Hs* larger than 8 m coinciding with spring tidal ranges. Wave characteristics (*Hs*, peak period (*Tp*) and direction) were sampled half-hourly from a waverider buoy, located offshore in 54-m depth (SHOM-"Service Hydrographique et Oceanographique de la Marine"). The tidal level was obtained from prediction (SHOM). Time series of the offshore wave and tide parameters during the experiment are shown in Fig. 2.

Nearshore subtidal bathymetric surveys have been carried out by the SHOM on February 14 and April 7–9. Intertidal and subaerial beach surveys were performed daily with centimetric accuracy using DGPS (Parisot et al., 2009). Fig. 3 shows the combination of the topographic and bathymetric data on February 14, in which strikingly well-developed outer-bar crescents with a wavelength of about 600 m can be seen.

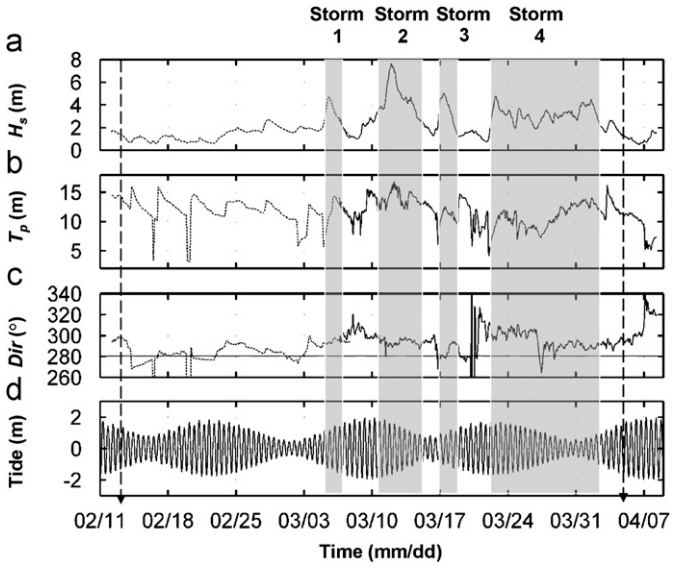

Fig. 2. Time series of offshore (a) significant wave height *Hs*, (b) peak period *Tp*, (c) angle of incidence and (d) water level (tide) versus time at Truc Vert Beach. The horizontal line in (c) indicates the shore-normal direction. Vertical grey bands correspond to the 4 storm periods described in the text. Vertical dashed arrows correspond to the initial and final bathymetric surveys.

2.3. ECORS08 video data

A video system (Cam-Era technology-NIWA) was set up for the duration of the experiment, mounted on an 8-m high scaffolding implemented on the top of the dune (27 m above the Mean Sea Level (MSL)). The system contained two high-resolution cameras (3.5 MPixel) covering an alongshore distance of the inner- and outer-bar of 1200 and 2500 m, respectively. The system collected full frames continuously at 2 Hz during daylight hours for the entire experiment. Because the storm on March 5 damaged the scaffolding, images are available from March 6 to April 9 only.

Time-exposure images were generated by averaging over 1200 consecutive images (10 min) every hour. The two camera images were rectified from pixel to world coordinates (Holland et al., 1997) and merged to yield a single plan view image, referenced to the tidal level. The grid resolution in the plan view images was $2 \times 2\,m^2$. In the inner-bar area, in front of the video cameras (x=0 m, y=0 m), the pixel footprint dimensions were about 0.5 and 1 m in the alongshore y and cross-shore x directions, respectively. These dimensions increase to about 10 and 20 m at both alongshore ends of the field site.

On the selected time-exposure images, white bands are present due to predominant wave-breaking over the underlying bar morphology (Lippmann and Holman, 1989; Van Enckevort and Ruessink, 2001). The bar-crest locations were digitalized by manually tracking the cross-shore location of the image intensity peaks in the alongshore direction. Following Van Enckevort and Ruessink (2003a, 2003b), a matrix $X(t,y)$ was constructed for both bars, consisting of bar crest locations in cross-shore direction X at time t and alongshore location y. The remotely sensed bar crest position varies in time because of time-varying offshore waves and tidal levels (Van Enckevort and Ruessink, 2001) even when the bar crest itself does not migrate. We removed this artificial migration following the approach of Pape and Ruessink (2008). On the whole, the difference between tracked and real bar-crest position depends on (1) the quality of the bar tracking, (2) the pixel footprint, (3) the photogrammetric error that mainly results from the difference between actual elevation and tidal level and (4) the tide- and wave-induced artificial shift (corrected). For the daily averaged bar crest positions, the resulting overall uncertainty in the cross-shore direction is estimated as about 20 and 10 m for the outer bar and the inner bar, respectively.

The bar-crest data were used to describe both the alongshore averaged cross-shore bar crest location $\langle X \rangle$ and the cross-shore distance D between horns and bays positions which indicates how well crescentic patterns and rip channels are developed. In addition to bar-crest lines, the alongshore position of each outer-bar horn, and the seaward exit and landward end of each inner-bar rip channel was manually digitized from the available video time-exposure images.

As we will demonstrate below, we observed a SPAW during part of the field experiment. Information on the observed SPAW morphology and evolution were derived from wave-breaking pattern on video time-exposure images. As described in Wijnberg and Holman (2007), the maximum alongshore length (L) and area of a SPAW were computed from digitized SPAW contours.

2.4. Hydro- and morphological indexes

To link offshore hydrodynamic forcing to nearshore bar morphological changes, specific indexes were computed. A new offshore hydrodynamic forcing parameter has been created, the Hydrodynamic Forcing Index (HFI) that allows representing the cumulative effect of wave and tide forcing. The HFI index is defined as the ratio of offshore significant wave height *Hs*

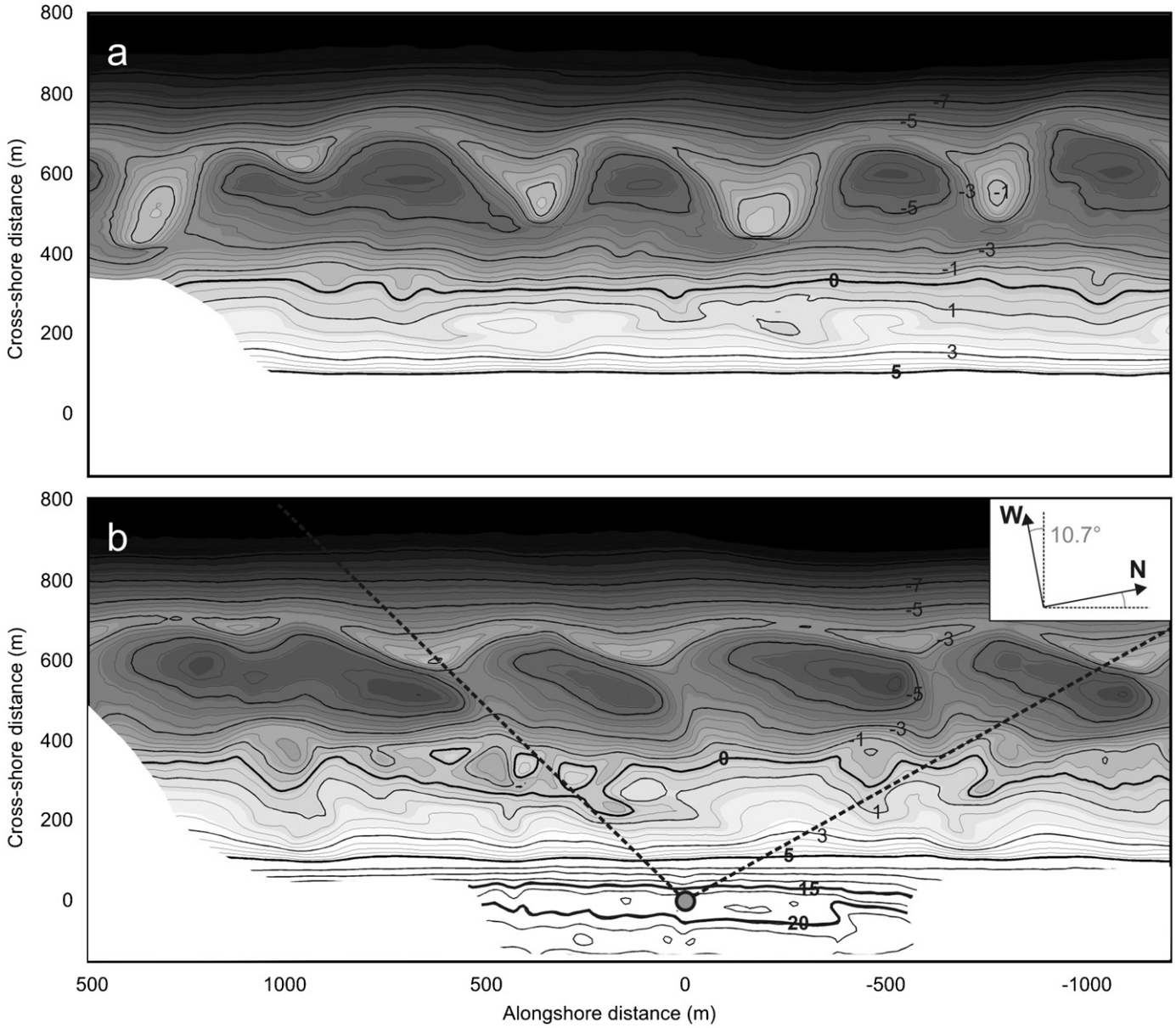

Fig. 3. Truc Vert Beach bathymetry surveyed (a) on February 14, 2008, 3 weeks before the experiment and (b) on April 6, 2008, at the end of the experiment. In (a) the circle at the origin (0,0) indicates the camera system location, and the 0- and 5-m iso-contour stand for the Lowest Astronomical Tide (LAT) and the Highest Astronomical Tide (HAT), respectively. Black dashed lines indicate the camera view field.

(averaged over a tidal cycle) to d_{min} the lowest offshore water level experienced over a tidal cycle (high–low–high tide) above the lowest astronomical tide:

$$HFI = \frac{Hs}{d_{min}} \tag{1}$$

HFI is large for large *Hs* and large tidal range, when d_{min} is low. Our choice to use a new index is motivated by the fact that the existing RTR index (ratio of *Hs* to tide range, see Masselink and Short, 1993) commonly used in inter-tidal morphodynamic studies (among others; Kroon and Masselink, 2002; Masselink et al., 2006; Price and Ruessink, 2008) is not appropriate when considering the observed enhanced impact of a storm in association with a large tide range. This would result in a rather low RTR, indistinguishable from a situation of moderate Hs and neap-tide conditions.

A simple Morphological Index (MI) was computed with the objective to represent the changes of both the inner (MI_i) and the outer-bar (MI_o). The 2D bar changes (MI_{2D}) were determined as the absolute value of the alongshore-averaged cross-shore bar migration rate:

$$MI_{2D} = \left|\frac{d\langle X\rangle}{dt}\right| \tag{2}$$

The 3D bar changes (MI_{3D}) were determined by computing the absolute variation rate of the cross-shore amplitude $A=D/2$ (mathematical definition, half the distance D between bays and horns cross-shore positions) over time,

$$MI_{3D} = \left|\frac{dA}{dt}\right| \tag{3}$$

We did not consider alongshore migration of crescentic and rip patterns in MI_{3D}. The MI index combines MI_{2D} and MI_{3D},

$$MI = \frac{MI_{2D} + MI_{3D}}{\max(MI_{2D} + MI_{3D})} \tag{4}$$

Its maximum value of 1 occurs when the combined cross-shore migration rate and amplitude change are maximum.

3. Results

3.1. Description of the evolution of the double bar system

Prior to the storm sequence, on February 14, the outer bar was characterized by well-developed and regular crescentic patterns (Fig. 3a). The alongshore-averaged wavelength was about 600 m and D_o was about 370 m, which is the largest value in our dataset and is substantially larger than observed elsewhere (e.g., Van Enckevort et al., 2004). The mean vertical difference between shallowest landward-protruding sections of the bar horns and the troughs was about 4 m. In contrast, the inner bar was reasonably alongshore uniform A 1-day storm ($Hs > 4$ m, $Tp = 14$ s) hit TVB on March 5 (Fig. 2). The tidal range during this day was intermediate, close to 3 m. Moderate wave angle with respect to shore-normal (8°, W-NW) coupled with moderate Hs induced a southerly longshore current that resulted in a southward migration of the outer-bar crescentic pattern by 20–30 m without any substantial change in the outer-bar shape (Fig. 4a). This migration was inferred by comparing the video images of March 8–February 14 survey.

The second storm that hit TVB, from March 10–13, was severe with maximum Hs of about 8 m and a corresponding Tp of 18 s, with $Hs > 4$ m during 3 days (Fig. 2). The wave angle with respect to shore-normal was about 15° (W-NW). The tidal range was close to 4 m (spring tide). Morphologic changes associated to this storm are shown in Fig. 4a and b, on March 8 and 14, respectively. The high-energy wave conditions induced an up-state transition (Wright and Short, 1984) of the outer-bar geometry that evolved from well-developed crescentic patterns to a more alongshore linear shape (D_o decreased from ~350 to ~90 m, Fig. 5a). In addition to this outer-bar straightening, the bar migrated some 100 m offshore (Fig. 5a). Interestingly, an isolated bar-like feature (that we henceforth refer to as a SPAW) shed from one of the outer-bar horns, visible as an isolated and coherent patch of foam between the inner and outer bar (Fig. 4b and c). This phenomenon and its evolution are explored in the next subsection. Due to the combined effects of large Hs and wave angle, a 150 m southward migration of the outer bar was observed (see tracked outer-bar horn positions in Fig. 6). Not following an expected up-state transition (Wright and Short, 1984), the inner-bar alongshore non-uniformity increased during the storm (D_i increased from ~30 to ~80 m, Fig. 5b), with the formation of a bulk of sand facing the transverse bar (which can be deduced from the undulating inner-bar wave-breaking pattern at about $x = 200$ m, Fig. 4c).

From March 16 to 17, TVB was exposed to a short-duration storm ($Hs = 6$ m, $Tp = 12$ s), with shore-normal waves during neap tide (tidal range of about 2.5 m). Fig. 4c and d show the plan-view images before and after this third storm, respectively. The outer bar was not substantially affected as no significant outer-bar cross-shore migration, alongshore migration and amplitude changes were observed (Fig. 5a). The SPAW that had appeared during the previous storm welded to the inner bar. As a consequence the inner-bar morphology changed significantly, with increasing alongshore non-uniformities and a slight smoothing of the inner-bar bulk of sand (Fig. 4d). The inner bar did not migrate significantly in the cross-shore direction during this storm.

After a 5-day low-energy period, the fourth storm hit TVB from March 21 to 31, which constitutes a very uncommon long period of high-energy waves for this stretch of coastline, combined with high wave angle with respect to shore-normal (between 15° and 20° W-NW). During this period the tidal range varied from spring (3.8 m) to neap (1.5 m) tide. During this 10-day period of high-energy waves ($Hs > 3$ m, $Tp > 12$ s), because of lower energy in comparison to the two previous storms, the outer bar developed crescentic patterns (down-state transition, D_o increased from 100 to 250 m, see Fig. 5b) and migrated some 200 m southward (Fig. 6). The outer-bar cross-shore migration was only minor. An up-state sequence of the inner-bar was observed, with decreasing alongshore non-uniformities (Figs. 4e and 5b).

Following this 4-storm sequence, waves remained low from April 1 to 9 with Hs lower than 2 m (Fig. 2). During this calm period, the outer bar was inactive, showing a moderate developed crescentic pattern (Fig. 3b), whereas the inner bar developed alongshore short-scale (~300 m) non-uniformities (Fig. 5a and b) (D_i increased to 80 m, Fig. 4f), with the development of shore-normal well-developed rip channels.

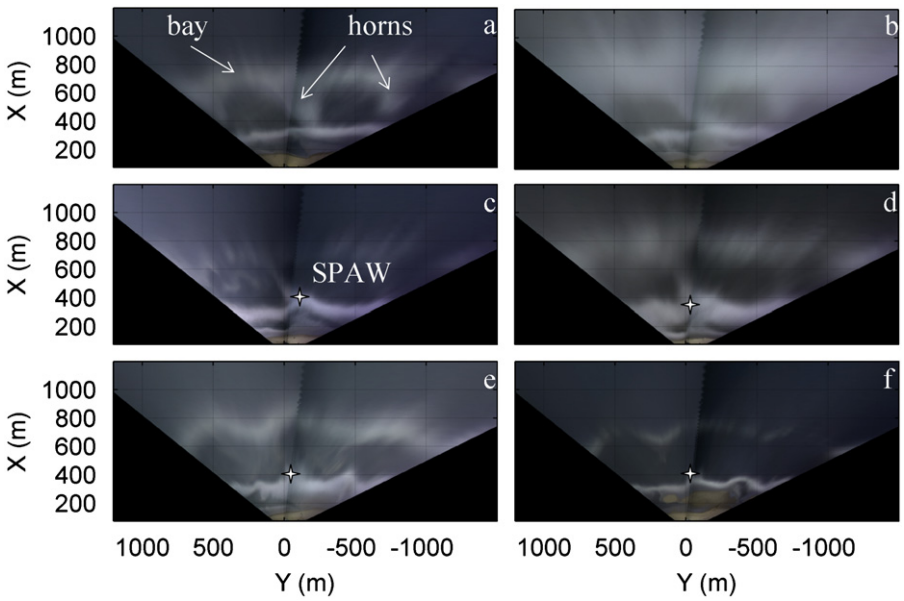

Fig. 4. Truc Vert Beach planview images on March (a) 8, (b) 12, (c) 14, (d) 22, April (e) 2 and (f) 7. The SPAW location is marked with a white star.

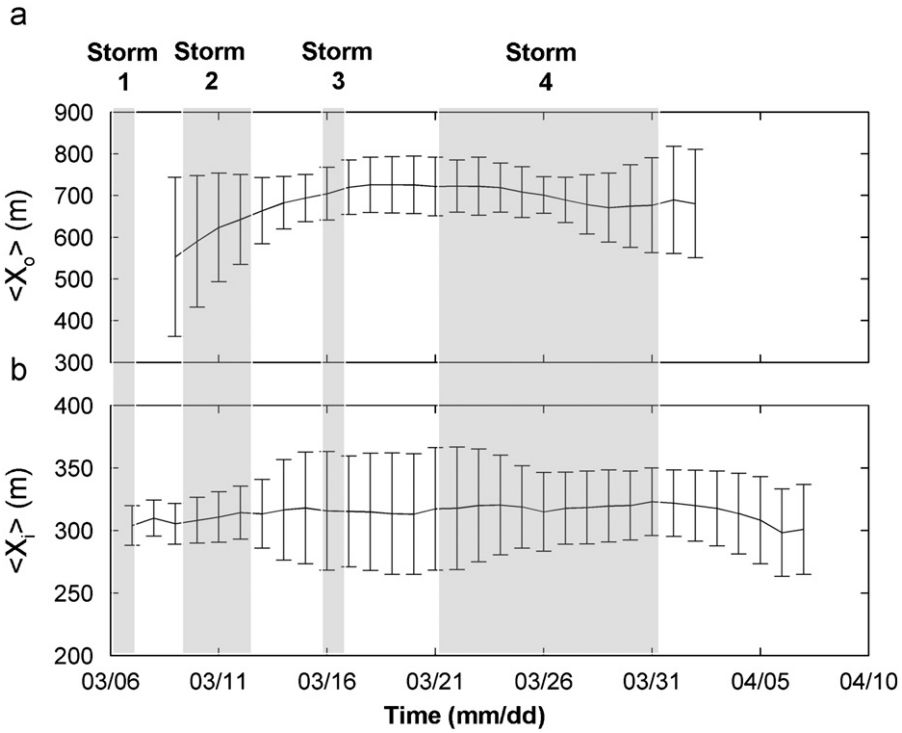

Fig. 5. Time series of outer (o) and inner bar (i) alongshore-averaged crest line cross-shore position ($\langle X \rangle$) with corresponding amplitudes (A) as errorbars for the (a) outer bar and (b) the inner bar.

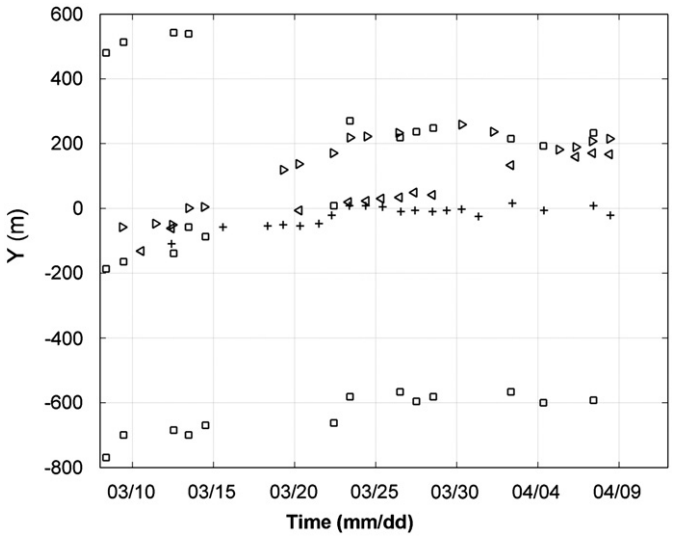

Fig. 6. Evolution over time of the alongshore position of the outer bar horns (squares), SPAW mean position (pluses) and rip feeder (left pointing triangles) and rip head (right pointing triangles).

3.2. SPAW dynamics

The destruction and evolution of the outer-bar horns initiated by the 10-year return storm on March 11–12 is further analyzed here. Prior to this storm, the outer-bar crescentic pattern was strongly developed with horns almost welded to the inner-bar (see Fig. 3). During the 10-year return storm, hourly video images showed that the outer bar experienced a clear reshaping into a more alongshore-uniform bar, comprising crescent horn shedding of bar-like feature from its shoreward facing side, whereas the seaward part migrated offshore. The SPAW transited the trough and merged with the inner bar (Fig. 4b and c). Despite its rapid creation (∼ hours) during the severe storm, the SPAW later evolved continuously and was clearly present until the end of the experiment, 3 weeks later (Fig. 4f).

During its existence, the SPAW did not migrate significantly in the alongshore direction, despite persistent high-energy oblique waves. The evolution of the SPAW contours shown in Fig. 7 indicates that, while the alongshore location remained constant, the area covered by the SPAW decreased continuously over time. The erosion of the feature was mainly localised at its seaward protruding part whereas the whole feature's geometry maintained alike, exhibiting a straight shore-normal oriented face. The SPAW's erosion is also indicated, in Fig. 8, by the evolution of its maximum length (L), which reduced from about 250 to 100 m (∼ −5 m/day).

To assess the longer-term (∼weeks) contribution of the SPAW to the intertidal morphology, the alongshore position of the SPAW was compared over time to the inner- and outer-bar feature positions (Fig. 6). From March 12 to 15, an outer-bar horn, the SPAW and an inner-bar rip channel were approximately aligned. During the long-duration storm from March 20 to 31, characterised by a 15° wave-incidence angle, both the outer-bar horns and the rip channels migrated southward whereas the SPAW and the inner-bar rip feeder channels did not migrate noteworthy. The following calm period induced a southward migration of the rip feeder channels, the rip channels orienting shore-normal. During this period, it is to be noted that inner-bar rip channels were facing the outer-bar horns (Fig. 4f). In contrast, the SPAW did not migrate. The fact that the inter-tidal bar migrated independently of the SPAW (located in the subtidal domain) during the following weeks after the SPAW generation clearly indicates that the SPAW did not control the weekly evolution of the inter-tidal morphology.

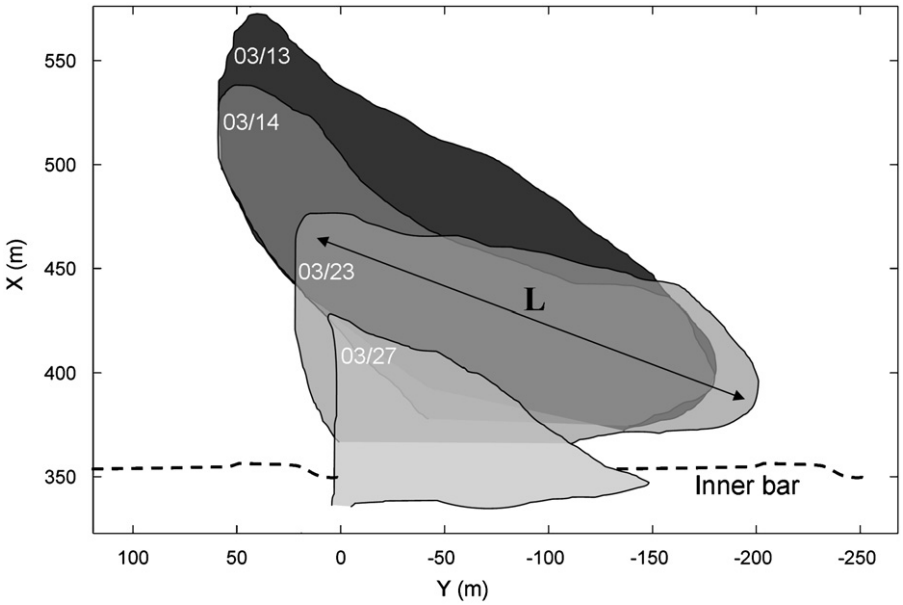

Fig. 7. Evolution over time of the SPAW geometry on March 13, 14, 23 and 27, ranging from dark to bright. The double-arrow represents the maximum length (L) of the SPAW.

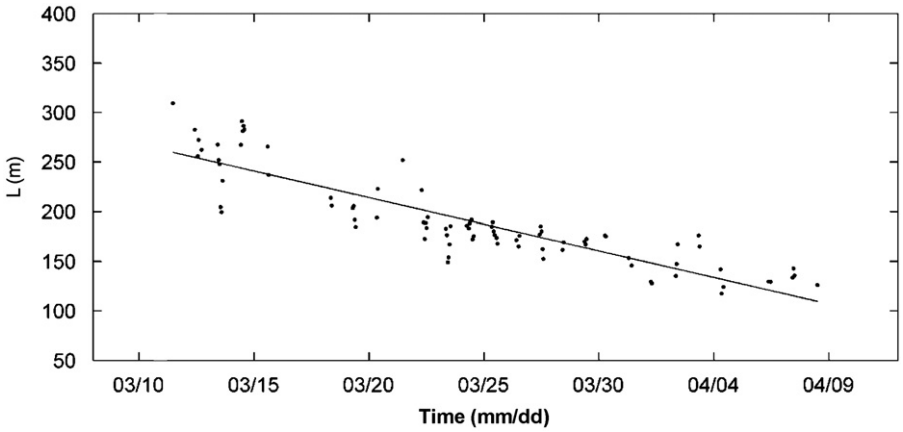

Fig. 8. Time evolution of the SPAW maximum length, L. The solid line represents the linear regression of L time series (slope = -5 m/day, R^2=0.58). SPAW was first observed on images from March 11.

3.3. *Morphological changes and link with offshore wave and tide forcing*

The offshore hydrodynamic HFI index (Eq. (1)) exhibited a large peak during the 10-year return storm (Fig. 9), due the combined effect of large *Hs* and large tidal range ($\sim$4 m). For the following storm (March 16), even though *Hs* was large ($Hs > 5$ m), the smaller tidal range ($\sim$2 m) substantially reduced HFI. During the long-duration storm (from March 21 to 31), moderate *Hs* reduced HFI even during large tidal range. On the whole study period, 52% of the MI variance was explained by *Hs* and 48% by d_{min} (Fig. 9).

In the meantime, the morphological change index MI (Eq. (4)) was maximum for the outer-bar (MI_o) during the 10-year return storm (Fig. 9) and minimum during the relatively calm period (from March 17 to 20). On the whole, 56% of the MI_o variability is explained by MI_{o2D} and 44% by MI_{o3D} (Eqs. (2) and (3), respectively). For the inner bar, the MI_i index time-evolution was clearly different, presenting maxima on March 14–15 and 24–25. In contrast to MI_o, the MI_i variability was rather more related to MI_{i3D} (71%) than to MI_{i2D} (29%).

Cross-correlation analysis was performed over the study period (35 points, 1 day^{-1}) between offshore wave- and tide-based indexes (*Hs*, HFI) and morphological indexes (MI_o and MI_i). Outer-bar changes (MI_o) are well correlated with *Hs* and HFI, as are MI_{o2D} and MI_{o3D} with a correlation maximum ($\sim$0.6, significant at the 95% level) at a 1–2 day time-lag. The fact that the correlation with HFI was not larger than with *Hs* indicates that tide-induced outer-bar changes were limited. In contrast, inner-bar changes (MI_i) were not significantly correlated with *Hs* (<0.2, not significant at the 95% level). Correlation was much larger with HFI, showing a maximum ($\sim$0.5, significant at the 95% level) at a 4–5 day time-lag. We found that correlation with HFI was larger for MI_{i3D} (0.7) than for MI_{i2D} (0.2). Thus, the inner-bar changes, and more particularly the 3D changes, were predominantly related to tidal range variations. This is discussed further in Section 4.3.

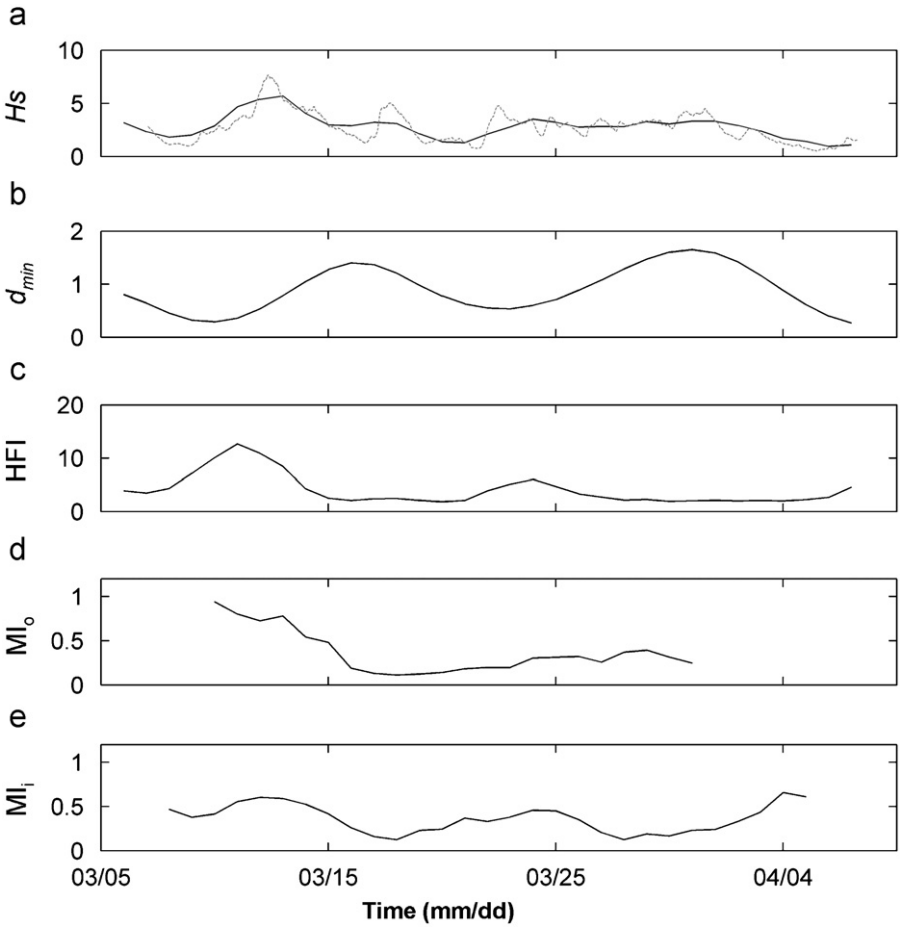

Fig. 9. Time evolution of (a) offshore significant wave height, H_s, (b) the lowest offshore water level experienced over a tidal cycle, d_{min}, (c) the HFI index, (d) the outer bar morphological variation indexes, MI_o, and (e) the inner bar morphological variation indexes, MI_i. The solid lines represent daily interpolated data and the dashed line in (a) represents the non daily-averaged offshore significant wave.

4. Discussion

4.1. Short term evolution of morphology

Our analysis of the ECORS08 TVB hourly video images dataset clearly shows that the double bar system response was highly variable with respect to which storm the beach was exposed to. This, together with the small correlation time-lag (~1–2 days) between the outer-bar changes (MI_o) and *Hs* contrasts with earlier studies at double-barred beaches that mentioned longer bar time response to storms. Observations reported in Ruessink et al. (2000) suggested a minor individual storm impact on the bars, the bars reacting to a sequence of storms rather to individual storm at a double-barred beach of Noordwijk (2–3 days smoothed observation by Van Enckevort and Ruessink, 2003a) and even longer time response spanning from 20 days to 1 year (Plant et al., 1999, 2006). The small response time observed at TVB may result from the exceptionally large waves experienced.

The distance between the inner bar and the outer-bar was close to 400 m at TVB which represents one of the largest observed values at double-barred beaches (~230 m at Noordwijk, Netherlands and ~100 m on the Gold Coast, Australia; Van Enckevort et al., 2004). Noteworthy, distances between bars in triple-barred systems can exceed 500 (Ruessink and Kroon, 1994; Ruggiero et al., 2005). The outer-bar seaward migration reached 30–50 m/day during high-energy wave conditions on March 11–12, a value close to the highest observed values at other sites (10–50 m/day, Van Enckevort and Ruessink, 2003a; Van Enckevort et al., 2004). These observations are not surprising given that TVB was exposed to a 10-year return storm. The rapid and large offshore migration, assumed to be the result of a breakpoint adjustment mechanism, was increased by the large distance between bar position and offshore located breakpoint at the beginning of the storm.

The observed large offshore alongshore-averaged bar migration resulted from the straightening of the pre-existing crescentic pattern rather than from the offshore migration of the entire bar. In other words, the bays did not significantly migrate in the cross-shore direction but the outer-bar amplitude decreased, the horns being more dynamic than the bays (Fig. 10). We developed a simple model to describe the alongshore-averaged cross-shore bar migration by separating the contributions of the two processes: the bar cross-shore migration and the bar three-dimensional development. The first contribution is defined in the model as the position of the bays, $\langle X_{bays} \rangle$, and the second contribution is kD, a linear dependence on the distance between bays and horns. The alongshore-averaged bar position can be approximated as

$$\langle X \rangle = \langle X_{bays} \rangle - kD \quad (5)$$

Fitting the data from the outer bar to Eq. (5) results in k=0.3 with a good agreement between the reconstructed and actually observed alongshore-averaged outer-bar position (Fig. 11): Eq. (5) captures 92% of the total variance in $\langle X \rangle$. This indicates that our

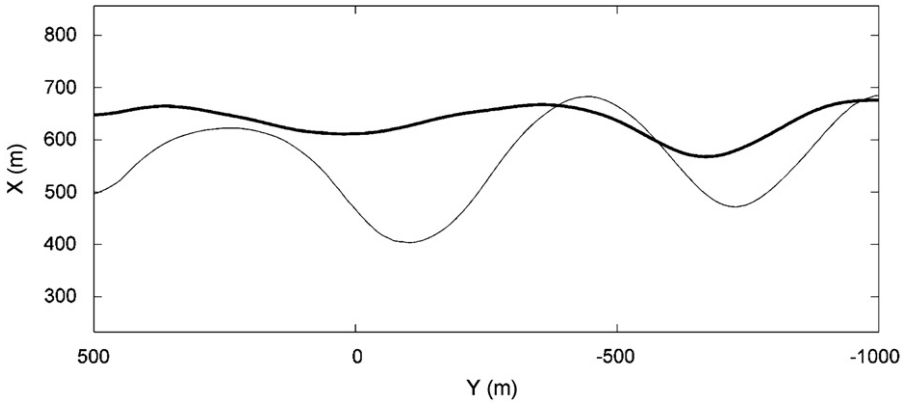

Fig. 10. Video-digitized position of the TVB outer bar crest on March 8 (thin line) and March 13 (thick line), respectively, before and after the 10-year return storm.

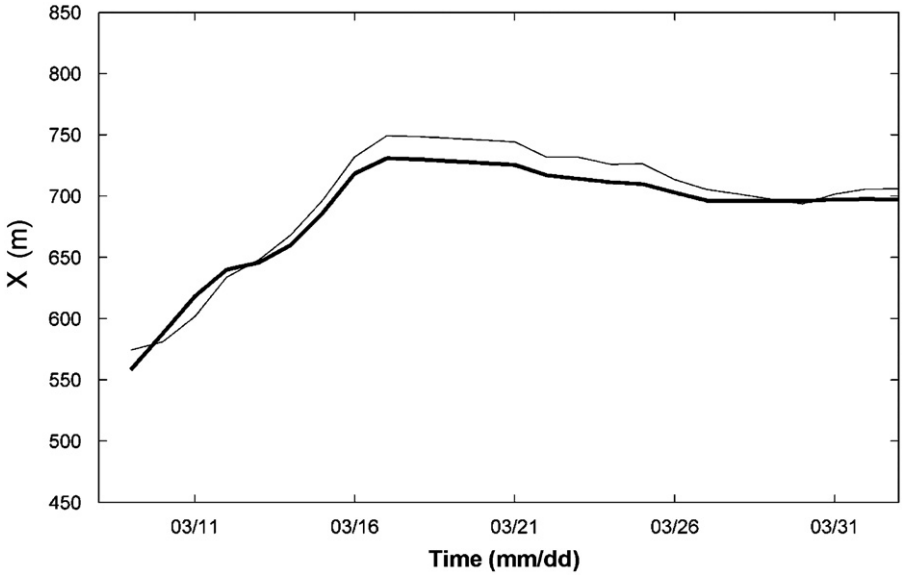

Fig. 11. Time series of outer-bar alongshore-averaged position ($\langle X \rangle$) (thin line) and reconstructed position from Eq. (5), with k=0.3 (thick line).

simple model is appropriate for the description of the bar position, the coefficient k being a good descriptor for the separation of 2D and 3D contributions to the bar migration. Most certainly, this coefficient is site-dependent. For the study period, $\langle X_{bays} \rangle$ and kD explained 55% and 37% of the observed $\langle X \rangle$ variance, respectively. Thus, the different response of horns and bays contributed considerably to the observed overall cross-shore migration of the outer bar. This observed non-linear evolution suggests that bar behaviour is even more complex than previously envisaged, in particular when considering the bar response to storms, which is different from a whole migration or a symmetric (bar horns) amplitude reduction. Our observation that offshore sandbar migration during a storm might result from a differential response of bays and horns contrasts with the commonly held view from field (e.g., Gallagher et al., 1998) and model studies (e.g., Ruessink et al., 2007b) that offshore migration is purely 2D.

With respect to the inner bar, we observed large inner-bar 3D changes (71% of total changes) associated with small alongshore-averaged cross-shore migration. This result can be related to the findings of Ruessink et al. (2000) who showed that, for the inner bar at Egmond aan Zee (Netherlands), 85% of the variance in the inner-bar crest short-term changes corresponded to alongshore non-uniformity variations or alongshore migration whereas only 10% were associated to alongshore-averaged cross-shore migration.

4.2. Morphological interactions

4.2.1. SPAW generation

The mechanism leading to the formation of the SPAW is not understood. Existing SPAW observations (Wijnberg and Holman, 2007; Shand, 2007) report the presence of well developed 3D bar geometries prior to the SPAW formation. In a study on transverse-bars dynamic, Konicki and Holman (2000) found that, under some conditions, well developed 3D bar horns may detach and either dissipate within the trough or migrate landward. Wave incidence angle and resulting alongshore current are believed to play a key role in the SPAW formation and trough transiting. The conditions at TVB and Duck during SPAW formation are intense wave forcing combined with well-developed outer-bar crescents. This is confirmed tentatively by the numerical modelling study of Castelle (2004). In a model run with Hs=4 m and a well-developed crescentic outer-bar (vertical amplitude of the horn/bay sequence of about 3.5 m) at t=7 days, he obtained a local shoreward propagation of sediment resulting from horn degeneration, similar to the observed SPAW events. This behaviour was not

observed for lower (yet energetic) waves (for instance, Hs=3 m), neither for weakly- to reasonably-developed crescentic patterns (for the Hs=4 m run, for instance at t=5 days when the vertical amplitude of the horn/bay sequence amounted 2 m). Castelle (2004) numerical study was not set up specifically to study SPAW behaviour and the SPAW generation mechanism, therefore, remains unclear.

At TVB, the SPAW required only 1 day to transit the trough and merge to the inner-bar whereas a much longer time was reported for Duck (17 days on average, Wijnberg and Holman, 2007). This rapid propagation is believed to be related to exceptionally large waves at TVB, but also to the pre-existing well-developed crescentic outer-bar geometry comprising horns that were, prior to the severe storm, already very close to the inner bar (~50 m).

4.3. SPAW control on the inner bar

The SPAW represented a large input of sediment for the inner bar and the whole intertidal area. This suggestion has been verified with the computation of the surveyed intertidal beach volume changes facing the SPAW. Local total accretion was up to +30 000 m^3 at a rate that reached 10 000 m^3/day rapidly after the peak of the storm (on March 12–13; Capo et al., 2009) whereas the remainder of the intertidal beach (outside of the SPAW influence) eroded (up to −27 m^3/m; Capo et al., 2009). In line with observations reported by Shand (2007), this clearly suggests that a SPAW causes a major input of sand into the intertidal domain, preventing a stretch of beach from eroding even during intense wave forcing.

During the storm (March 16–17) following the SPAW generation, the alongshore non-uniformity in the inner bar evolved from being large-scale and low-amplitude into short-scale and high-amplitude. The formation of intertidal non-uniformities has previously been related to a nearshore topography readjustment of excess sediment (Komar, 1998). This point suggests that the massive input of sand to the inter-tidal area during the large storm (March 11) re-arranged during the following storm (March 16–17). Moreover, the fact that the outer bar was almost alongshore uniform during the second storm acts in favour of a self-organization origin of the development of the inner-bar non-uniformities rather than a morphological coupling (template) origin.

The SPAW was still present 3 weeks later at the same location (Fig. 7). However, the longer-term (~weeks) impact of the SPAW on the inner-bar morphology is less understood. More generic conclusions about the SPAW contribution on the double bar dynamics are limited by the short alongshore distance of the video monitored inner-bar area (~1000 m, Fig. 3). Yet, the fact that intertidal features migrated southward and that the subtidal SPAW feature remained at the same position suggests that the inter-tidal bar rapidly evolved independently of the SPAW. In addition, our results indicate that during the storm from March 20 to 30, the tracked inner-bar rip channel migrated southward, facing an outer-bar horn (Fig. 6). This is consistent with observations by Van Enckevort and Wijnberg (1999) and numerical modelling (Castelle et al., in press-a) who indicated that inner- and outer-bar out-of-phase coupling can occur in the presence of well-developed outer-bar crescentic patterns and moderate energy waves. Our results suggest that the short-term contribution of the SPAW event to the inner-bar was a large input of sediment that re-arranged within days into short-scale features. The longer-term (~weeks) contribution was not substantial although the SPAW remained present after 3 weeks. The evolution of inter-tidal morphology during the storm from March 20 to 30 is assumed to be rather controlled by the developing outer-bar crescents, in a similar manner as documented by Ruessink et al. (2007a).

4.4. Tidal influence

The outer-bar changes were predominantly linked to Hs, and although the correlation was slightly higher considering a combination of Hs and d_{min} (HFI) there was no clear evidence of any tide contribution to outer-bar changes. In our data, we believe that the effect of d_{min} may have been negligible because waves were always breaking when the bar was morphologically most active. In contrast, the inner-bar changes were more strongly related to HFI than to Hs, similar to findings in the intertidal-bar dynamics study of Kroon and Masselink, (2002) where intertidal-bar dynamics was found to be controlled by both Hs and the tidal range. We hypothesise that, in our observations, the observed stronger influence of tide on the inner-bar dynamics was caused by the combined effects of large tidal range variations, large waves and the presence of the subtidal bar. Firstly, as reported in Masselink et al. (2008) for TVB, the large subtidal bar protects the intertidal beach from exposure to extreme wave conditions, thus, inshore significant wave heights are generally less than 2.5 m. During almost the entire campaign, waves broke on the outer bar. When the tidal range was small, the inner bar was persistently in the surf zone. During mid to spring tidal conditions, the inner bar experienced swash conditions at low tide. Thus, in contrast to the outer bar, the tidal range affected the residence times of breaking waves and swash processes, and this likely explains the larger effect of HFI on inner than on outer-bar behaviour. For these reasons, tidal range variations were crucial to the evolution of the inner bar.

We found an even higher correlation coefficient value for MI_i and d_{min} (0.6) than with HFI or Hs. Noteworthy, the peak of correlation between MI_i and d_{min} was present for a 5-day lag. This time-lag is close to a quarter of the neap-spring tide cycle period (28 days) indicating that inner-bar changes maxima occurred when the tide range changed from spring tide to neap tide ($\max(\partial d_{min}/\partial t)$). The observed peaks in MI_i may thus be attributed to transitions from a persisting high-tidal range regime to a small-tidal range regime. This peak of MI_i did not appear from neap to spring tide (near March 20), presumably because the waves were too small ($Hs < 1$ m) to induce beach change.

5. Conclusions

We analyzed a 5-week dataset of hourly, 10-min time-exposure video images of the double-barred meso–macro tidal Truc Vert Beach during intense wave forcing, comprising a 10-year return storm. The short-term (days) response of the outer, subtidal bar to the storms was significant and rapid (1–2 days) for both the dominant (56% of total changes) 2D component with an observed 30–50 m/day maximum seaward migration rate, and for the 3D component (44%), comprising a reshaping of the crescentic patterns into a shore-parallel linear bar. We found that the 3D behaviour influenced the 2D behaviour (37%). In particular, the rapid seaward migration of the alongshore-averaged crest position was partially due to the seaward migration of the horns (reshaping crescents into a shore-parallel linear bar), while the bays did not migrate substantially. This contrasts with the common perception that the bar, as a whole, migrate seaward during storm events. Inner-bar dynamics was dominated by 3D changes (71% of total changes) comprising the local merging of a SPAW (a former outer-bar horn) and the development of alongshore non-uniformities. The inner-bar 2D component (29% of total changes) was associated with cross-shore migration

rates of less than 5 m/day. Whereas outer-bar changes were primarily governed by *Hs* variability, the tidal range appeared to be the steering parameter for inner-bar changes.

The straightening of the outer bar during the most intense storm strongly affected the subsequent evolution of the inner bar. The SPAW represented a large input of sediment for the inter-tidal area. Three weeks later, although the subtidal SPAW remaining feature was still present and attached to the intertidal bar, inter-tidal bar pattern showed no evidence of forcing by the SPAW template any more. We believe that the generation of the SPAW was stimulated by the well-developed outer-bar crescentic pattern before the storm.

In summary, our results indicate that inner-bar behaviour depends on the morphological setting prior to the main storm (the presence of a subtidal bar and its well-developed crescentic shape) and the tide range rather than on storm characteristics only. Inner and outer bars should, therefore, not be studied in isolation.

Acknowledgments

The ECORS experiment and TVB video system were supported by the French "Service Hydrographique et Oceanographique de la Marine" (SHOM). RA's Ph.D. work is funded by the French "Délégation Générale de l'Armement" (DGA). BC and PB acknowledge financial support from the Project MODLIT (RELIEFS/INSU). BGR was supported by the Netherlands Organisation for Scientific Research NWO under project 864.04.007.

References

Aagaard, T., Nielsen, J., Greenwood, B., 1998. Suspended sediment transport and nearshore bar formation on a shallow intermediate-state beach. Mar. Geol. 148, 203–225.

Aarninkhof, S.G.J., Hinton, C.L., Wijnberg, K.M., 1998. On the predictability of breaker bar behaviour. In: Proceedings of the 26th International Conference on Coastal Engineering, Copenhagen, Denmark, ASCE, pp. 2409–2422.

Butel, R., Dupuis, H., Bonneton, P., 2002. Spatial variability of wave conditions on the French Atlantic coast using in-situ data. J. Coastal Res. SI 36, 96–108.

Capo, S., Parisot, J.-P., Bujan, S., Senechal, N., 2009. Short time morphodynamics response of the Truc Vert Beach to storm conditions. J. Coastal Res. SI 36, 1741–1745.

Castelle, B., 2004. Modélisation de l'hydrodynamique sédimentaire au-dessus des barres sableuses soumises à l'action de la houle: application à la côte aquitaine. Ph.D. thesis, Université Bordeaux I, pp. 340 (in French).

Castelle, B., Bonneton, P., Dupuis, H., Sénéchal, N., 2007. Double bar beach dynamics on the high-energy meso–macrotidal French Aquitanian Coast: a review. Mar. Geol. 245, 141–159.

Castelle, B., Ruessink, B.G., Bonneton, P., Marieu, V., Bruneau, N., Price, T.D. (in press-a). Coupling mechanisms in double sandbar systems, Part 1: physical explanation and coupling patterns. Earth Surf. Processes Landforms, doi:10.1002/esp.1929.

Castelle, B., Ruessink, B.G., Bonneton, P., Marieu, V., Bruneau, N., Price, T.D. (in press-b). Coupling mechanisms in double sandbar systems, Part 2: impact on alongshore variability of inner-bar rip channels. Earth Surf. Processes Landforms, doi:10.1002/esp.1949.

Coco, G., Murray, A.B., 2007. Patterns in the sand: from forcing templates to self-organization. Geomorphology 91, 271–290.

De Melo Apoluceno, D., Howa, H., Dupuis, H., Oggian, G., 2002. Morphodynamics of ridge and runnel systems during summer. J. Coastal Res. SI 36, 222–230.

De Melo Apoluceno, D., 2003. Morpho-hydrodynamique des plages à barres en domaine méso à macrotidal: exemple de la plage du Truc Vert-Gironde. Ph.D. Thesis, Université Bordeaux I (in French).

Desmazes, F., Michel, D., Howa, H., Pedreros, R., 2002. Etude morphodynamique du domaine pré-littoral nord-aquitain, site atelier du Truc Vert. In: Proc. 7ème Journées Nationales GCGC, Anglet, pp. 155–162 (in French).

Froidefond, J.-M., Gallissaires, J.-M., Prud'homme, R., 1990. Spatial variation in sinusoidal on a crescentic nearshore bar: application to the Cap Ferret Coast. J. Coastal Res. 6, 927–942.

Gallagher, E.L., Elgar, S., Guza, R.T., 1998. Observations of sand bar evolution on a natural beach. J. Geophys. Res. 103, 3203–3210.

Holland, K.T., Holman, R.A., Lippmann, T.C., Stanley, J., Plant, N., 1997. Practical use of video imagery in nearshore oceanographic field studies. IEEE J. Oceanic Eng. Oceanic Eng. 22, 81–92.

King, C.A.M., Williams, W.W., 1949. The formation and movement of sand bars by wave action. Geogr. J. 112, 70–85.

Komar, P.D., 1998. Beach Processes and Sedimentation. Prentice-Hall, Englewood Cliffs, New Jersey.

Konicki, K.M., Holman, R.A., 2000. The statistics and kinematics of transverse sand bars on an open coast. Mar. Geol. 169, 69–101.

Kroon, A., Masselink, G., 2002. Morphodynamics of intertidal bar morphology on a macrotidal beach under low-energy wave conditions, North Lincolnshire, England. Mar. Geol. 190, 573–591.

Lafon, V., Dupuis, H., Howa, H., Froidefond, J.-M., 2002. Determining ridge and runnel longshore migration rate using spot imagery. Oceanol. Acta 25, 149–158.

Lafon, V., De Melo Apoluceno, D., Dupuis, H., Michel, D., Howa, H., Froidefond, J.-M., 2004. Morphodynamics of nearshore rhythmic sandbars in a mixed-energy environment (Sw France).i. mapping beach changes using visible satellite imagery. Estuarine Coastal Shelf Sci. 61, 289–299.

Lippmann, T.C., Holman, R.A., 1989. Quantification of sandbar morphology: a video technique based on wave dissipation. J. Geophys. Res. 94, 995–1011.

Masselink, G., Short, A.D., 1993. The effect of tide range on beach morphodynamics and morphology: a conceptual beach model. J. Coastal Res. 9, 785–800.

Masselink, G., Turner, I.L., 1999. The effect of tides on beach morphodynamics. In: Short, A.D. (Eds.), Handbook of Beach and Shoreface Morphodynamics Wiley.

Masselink, G., 2004. Formation and evolution of multiple bars on macrotidal beaches: application of a morphodynamic model. Coastal Eng. 51, 713–730.

Masselink, G., Kroon, A., Davidson-Arnott, R.G.D., 2006. Intertidal bar morphodynamics in wave-dominated coastal settings: a review. Geomorphology 73, 3349.

Masselink, G., Auger, N., Russel, P., O'Hare, T., 2007. Short-term morphological change and sediment dynamics in the intertidal zone of a macro-tidal beach. Sedimentology 54, 39–53.

Masselink, G., Austin, M., Tinker, J., O'Hare, T., Russell, P., 2008. Cross-shore sediment transport and morphological response on a macro-tidal beach with intertidal bar morphology, Truc Vert, France. Mar. Geol. 251, 141–155.

Owens, E.H., Frobel, D.H., 1977. Ridge and runnel systems in the Magdalen Islands. Que. J. Sediment Petrol. 47, 191–198.

Pape, L., Ruessink, B.G., 2008. Multivariate analysis of nonlinearity in sandbar behavior. Nonlinear Processes Geophys. 15, 145–158.

Parisot, J.-P., Capo, S., Bujan, S., Sénéchal, N., Moreau, J., Réjas, A., Hanquiez, V., Almar, R., Marieu, V., Castelle, B., Gaunet, J., Gluard, L., George, I., Nahon, A., Dehouck, A., Certain, R., Gervais, M., Barthe, P., Ardhuin, F., Le Gall, F., Bernardi, P.J., Le Roy, R., Pedreros, R., Delattre, M., Mac Mahan, J., 2009. Sedimentary processes and morphodynamics of sandy beaches on short time response. J. Coastal Res. SI 56, 1786–1790.

Pedreros, R., Howa, H.L., Michel, D., 1996. Application of grain size trend analysis for the determination of sediment transport pathways in intertidal areas. Mar. Geol. 135, 35–49.

Plant, N.G., Holman, R.A., Freilich, M.H., Birkemeier, W.A., 1999. A simple model for interannual sandbar behavior. J. Geophys. Res. 104 (15), 755–776.

Plant, N.G., Freilich, M.H., Holman, R.A., 2001. Role of morphologic feedback in surf zone sandbar response. J. Geophys. Res. 106 (C1), 973–989.

Plant, N.G., Holland, K.T., Holman, R.A., 2006. A dynamical attractor governs beach response to storms. Geophys. Res. Lett. 33, L17607.

Price, T.D., Ruessink, B.G., 2008. Morphodynamic zone variability on a microtidal barred beach. Mar. Geol. 251, 98–109.

Ruessink, B.G., Kroon, A., 1994. The behaviour of a multiple bar system in the nearshore zone of Terschelling: 1965–1993. Mar. Geol. 121, 187–197.

Ruessink, B.G., Terwindt, J.H.J., 2000. The behaviour of nearshore bars on the time scale of years: a conceptual model. Mar. Geol. 163, 289–302.

Ruessink, B.G., Van Enckevort, I.M.J., Kingston, K.S., Davidson, M.A., 2000. Analysis of observed two- and three-dimensional nearshore bar behaviour. Mar. Geol. 169, 161–183.

Ruessink, B.G., Wijnberg, K.M., Holman, R.A., Kuriyama, Y., Van Enckevort, I.M.J., 2003. Intersite comparison of interannual nearshore bar behavior. J. Geophys. Res. 108, 3249.

Ruessink, B.G., Coco, G., Ranasinghe, R., Turner, I.L., 2007a. Coupled and noncoupled behavior of three-dimensional morphological patterns in a double sandbar system. J. Geophys. Res. 112, C07002.

Ruessink, B.G., Kuriyama, Y., Reniers, A.J.H.M., Roelvink, J.A., Walstra, D.J.R., 2007b. Modeling cross-shore sandbar behavior on the time scale of weeks. J. Geophys. Res. 112, F03010, doi:10.1029/2006JF000730.

Ruggiero, P., Kaminsky, G.M., Gelfenbaum, G., Voigt, B., 2005. Seasonal to interannual morphodynamics along a high-energy dissipative littoral cell. J. Coastal Res. 21 (3), 553–578.

Sallenger, A.H., Holman, R.A., Birkemeier, W.A., 1985. Storm-induced response of a nearshore-bar system. Mar. Geol. 64, 237–257.

Sénéchal, N., Ardhuin, F., and others, 2008. ECORS-TRUC VERT, 2008. Qualification des modèles de houle et de morphodynamique. In: Proc 10èmes Journées Nationales GCGC, pp. 635–654 (in French).

Sénéchal, N., Gouriou, T., Castelle, B., Parisot, J.P., Capo, S., Bujan, S., Howa, H., 2009. Morphodynamic response of a meso- to macro-tidal intermediate beach based on a long-term data-set. Geomorphology 107, 263–274.

Shand, R.D., 2007. Bar splitting: system attributes and sediment budget implications for a net offshore migrating bar system. J. Coastal Res. SI 50.

Short, A.D., 1991. Macro–Meso tidal beach morphodynamics—an overview. J. Coastal Res. 72, 417–436.

Short, A.D., Aagaard, T., 1993. Single and multi-bar beach change models. J. Coastal Res. IS 15, 141–157.

Van Enckevort, I.M.J., Ruessink, B.G., 2001. Effect of hydrodynamics and bathymetry on video estimates of nearshore sandbar position. J. Geophys. Res. 106, 16969–16980.

Van Enckevort, I.M.J., Ruessink, B.G., 2003a. Video observations of nearshore bar behaviour. Part 1: alongshore uniform variability. Cont. Shelf Res. 23, 501–512.

Van Enckevort, I.M.J., Ruessink, B.G., 2003b. Video observations of nearshore bar behaviour. Part 2: alongshore non-uniform variability. Cont. Shelf Res. 23, 513–532.

Van Enckevort, I.M.J., Ruessink, B.G., Coco, G., Suzuki, K., Turner, I.L., Plant, N.G., Holman, R.A., 2004. Observations of nearshore crescentic sandbars. J. Geophys. Res. 109, C06028.

Van Enckevort, I.M.J., Wijnberg, K.M., 1999. Intra-annual changes in bar plan shape in a triple bar system. In: Proceedings of the Coastal Sediments '99, ASCE, pp. 2548–2558.

Wijnberg, K.M., Holman, R.A., 2007. Video-observations of shoreward propagating accretionary waves. In: Proceedings of the RCEM 2007, Enschede, The Netherlands, pp. 737–743.

Wright, L.D., Short, A.D., 1984. Morphodynamic variability of surf zones and beaches: a synthesis. Mar. Geol. 56, 93–118.

D.9 Laboratory experiment on rip current circulations over a moveable bed : Drifter measurements

B. Castelle, H. Michallet, V. Marieu, F. Leckler, B. Dubardier, A. Lambert, C. Berni, P. Bonneton, E. Barthélemy, and F. Bouchette

Journal of Geophysical Research - Oceans, Vol. 115, C12008, doi :10.1029/2010JC006343, 2010

Laboratory experiment on rip current circulations over a moveable bed: Drifter measurements

B. Castelle,[1] H. Michallet,[2] V. Marieu,[1] F. Leckler,[1] B. Dubardier,[1] A. Lambert,[2,3] C. Berni,[2] P. Bonneton,[1] E. Barthélemy,[2] and F. Bouchette[3]

Received 15 April 2010; revised 10 August 2010; accepted 15 September 2010; published 2 December 2010.

[1] This study describes a laboratory experiment on rip current circulations over a moveable bed. Rip current characteristics over eight contrasting nature-like beach morphologies are investigated. The seabed varied from reasonably alongshore uniform to strongly alongshore nonuniform with crescentic patterns and bar-rip morphologies, representative of a full morphological down-state sequence. The same offshore shore-normal waves were generated by the wavemaker for the eight situations with the same mean water level to study the sensitivity of rip current characteristics as a function of the beach morphology only. In each case, a 30 to 60 min video run was used to track a large number of drifters released within the surf zone. Results show the presence of classic rip current patterns with counterrotating cells and a relatively narrow offshore-directed jet varying from shore-normal to strongly skewed. Wave-driven circulations were strongly unstable. Computed standard deviations of flow intensity and direction provide high-resolution information on the spatial variability of rip current instabilities. Highly pulsating and weakly directionally variable offshore-directed flow is observed in the rip neck for well-developed bar-rip morphologies that turns into a weakly pulsating and highly directional variable rip current flow with decreasing beach alongshore nonuniformity. Proposing a definition of rip current intensity based on the rip current circulation geometry, rip current intensity was found to linearly increase with increasing measure of beach alongshore nonuniformity within both the low-energy and moderate-energy rip current regimes. To date, our laboratory experiment provides the first extensive quantitative rip current information during a full down-state sequence for a given wave condition.

Citation: Castelle, B., H. Michallet, V. Marieu, F. Leckler, B. Dubardier, A. Lambert, C. Berni, P. Bonneton, E. Barthélemy, and F. Bouchette (2010), Laboratory experiment on rip current circulations over a moveable bed: Drifter measurements, *J. Geophys. Res.*, *115*, C12008, doi:10.1029/2010JC006343.

1. Introduction

[2] Rip currents are narrow, intense seaward flowing jets that originate within the surf zone and broaden outside the breaking zone. These ubiquitous flow patterns along wave-dominated beaches have been observed by coastal scientists for many years [*Shepard et al.*, 1941; *McKenzie*, 1958; *Sonu*, 1972]. In recent years, rip currents have received increasing interest [*MacMahan et al.*, 2008; *Reniers et al.*, 2009; *Scott et al.*, 2009; *Bruneau et al.*, 2009b; *MacMahan et al.*, 2010; *Austin et al.*, 2010; *Reniers et al.*, 2010]. They are associated with cell circulations, also known as rip current circulations. These nearshore circulations are thought to produce a continuous interchange between the waters of the surf zone and the shelf, acting as both a distributing mechanism for nutrients and a dispersing mechanism for land runoff.

[3] Rip current circulations permanently interact with the surf zone sandbars and shoreline rhythms. The positive feedback between these wave-driven circulations, sediment processes and the evolving morphology leads to the development of striking nearshore patterns [*Falqués et al.*, 2000] that are the so-called crescentic sandbars [*Van Enckevort et al.*, 2004; *Castelle et al.*, 2007] and bar-rip morphologies [*Holman et al.*, 2006]. These three-dimensional (3-D) morphological rhythmic or quasi-rhythmic patterns are part of an accretionary, down-state sequence developing from an alongshore beach state (longshore bar trough) following a storm event [*Wright and Short*, 1984]. Within the intermediate beach states, immediately after the longshore bar trough substate is the rhythmic bar and beach substate (crescentic bar), next the transverse bar and rip and finally the low tide terrace. Both the rhythmic bar and beach and transverse bar and rip substates are characterized by the presence of intense rip currents. Rip current systems often result in erosion features known as megacusps [*Short and Hesp*, 1982; *Thornton*

[1]CNRS, UMR 5805 EPOC, Université de Bordeaux, Talence, France.
[2]Laboratoire des Ecoulements Géophysiques et Industriels (UJF-INPG-CNRS), Grenoble, France.
[3]UMR 5243, Université Montpellier 2, Montpellier, France.

0148-0227/10/2010JC006343

et al., 2007]. Therefore, understanding and predicting rip current dynamics is relevant for shoreline evolution and localized beach and dune erosion [*Thornton et al.*, 2007]. In addition, rip currents are known to be a major hazard to beach users as they are the cause of the majority of rescues and fatalities within the beach environment [*Short*, 1999; *Scott et al.*, 2009]. Accordingly, rip currents also have significant implications from the perspective of beach safety and life guarding.

[4] A classic explanation for rip current generation is that rip current circulations are driven by alongshore variations of wave-induced radiation stress [*Longuett-Higgins and Stewart*, 1964]. These gradients can be due to spatial variability of the incident wavefield due to wave groups [*Dalrymple*, 1975], wave-current interactions [*Dalrymple and Lozano*, 1978], wavefield interaction with lower-frequency waves such as edge waves [*Symonds and Ranasinghe*, 2001] or local topographic variations [*Bowen*, 1969]. The latter is called "topographically controlled rip current," while the three other ones refer to "transient rip currents" [*Johnson and Pattiaratchi*, 2004a]. More recently, using the general theoretical analysis of wave-driven currents and vortex dynamics due to dissipating waves by *Buhler* [2000], *Bonneton et al.* [2010] showed that wave-averaged vertical vorticity associated with rip current circulations are controlled by alongshore differential broken-wave energy dissipation. In this paper, we are essentially dealing with topographically controlled rip current systems, that is, rip current circulations that are guided and constrained by the 3-D surf zone sandbar morphology.

[5] Within the last decade, a significant number of field rip current investigations have been made [*Aagaard et al.*, 1997; *Brander*, 1999; *Brander and Short*, 2000, 2001; *MacMahan et al.*, 2004a, 2004b, 2005, 2008; *Bruneau et al.*, 2009b; *MacMahan et al.*, 2010; *Austin et al.*, 2010]. These wave-driven circulations were found to be strongly unstable and subject to pulsations over a large range of temporal scales. Rip current pulsations within the infragravity band have been widely observed. While groupiness of the incoming waves [*Shepard and Inman*, 1950] or infragravity standing waves [*Sonu*, 1972; *MacMahan et al.*, 2004a] were hypothesized to explain the presence of these pulsations, the causative mechanism has yet to be conclusively found. Pulsations at much lower frequency have also been reported [*Smith and Largier*, 1995; *Brander and Short*, 2001; *MacMahan et al.*, 2004b; *Callaghan et al.*, 2005; *Bruneau et al.*, 2009a; *Reniers et al.*, 2007]. Explanations based on shear instabilities, detached surf zone eddies in the rip head and rip circulation cell oscillations challenged over the past few years. Similarly, the causative mechanism of far-infragravity rip current pulsations has yet to be conclusively found. Of note, the spatial distribution of rip current circulation variability at these different temporal scales is poorly understood.

[6] Field rip current studies showed that rip currents are strongly influenced by tidal elevation with rip current activity and maximum rip current velocities around low tide in microtidal [*Brander*, 1999], mesotidal [*Brander and Short*, 2000] and macrotidal [*Austin et al.*, 2010] wave-dominated beaches. Conversely, on the meso-macrotidal high-energy Aquitanian Coast beaches (SW France), *Bruneau et al.* [2009b] found that maximum rip current velocities shifted toward higher tides with increasing offshore wave height, corroborating earlier numerical exercises by *Castelle and Bonneton* [2006] and *Castelle et al.* [2006] on this stretch of coastline. Because of these persistent changes in tidal elevation and wave conditions, an in-depth investigation of rip current circulations as a function of beach morphology for a given wave condition and tidal elevation is a challenging task in the field. To overcome time varying both offshore wave conditions and tidal elevation, rip current intensity has mostly been investigated as a function of the dimensionless variable H/h (offshore wave height/water depth on the sandbar) which is considered as a measure of the forcing intensity. Not surprisingly, it was found that rip velocities increase with increasing wave height and decreasing water elevation. Conversely, the sensitivity of rip velocities to the relative depth of the rip channel for a given offshore wave condition and tidal elevation has barely been touched upon [*Nielsen et al.*, 2001] and is therefore poorly understood.

[7] A substantial number of laboratory experiments, all performed with a fixed bed, have been undertaken for easier grasping of topographically controlled rip current circulation information than on natural beaches. Eulerian measurements [*Hamm*, 1992; *Haller and Dalrymple*, 2001; *Haas and Svendsen*, 2002] and more recently Lagrangian techniques [*Kennedy and Thomas*, 2004] have been used to investigate rip current systems. The latter, when a sufficient number of drifters are released during a sufficient duration, can be transformed into a horizontal mean circulation field. The same drifter deployment strategy was recently attempted in the field by *Schmidt et al.* [2005], *Austin et al.* [2009], and *MacMahan et al.* [2010].

[8] A limitation of the existing laboratory experiments of rip current circulations is the configuration of beach used. While most of the field observations of rip currents were undertaken on incised rip channels inshore-connected shoals or depressions on near-planar beaches [*MacMahan et al.*, 2006] with low to pronounced alongshore nonuniformity, all laboratory measurements, with the exception of *Hamm* [1992], have been done with an alongshore bar-trough beach cut by a deep rip channel [*Drønen et al.*, 2002; *Haas and Svendsen*, 2002; *Kennedy and Thomas*, 2004; *Kennedy et al.*, 2006]. The resulting man-made beach shape in the laboratory resulted in rather unrealistic or very scarcely observed rip-channel morphologies. For instance, the relative depth of the rip channel is in general higher in laboratory (2.5–5) compared to the field (1.2–2.7; see the review of *MacMahan et al.* [2006]). Strong discontinuities in the seabed morphology were additionally observed during these previous laboratory experiments, which resulted in ubiquitous macrovortices being shed from the sharp bar crests in the vicinity of the rip channel and subsequently shed offshore [*Kennedy et al.*, 2006]. Generation of these macrovortices is likely to significantly alter the overall hydrodynamics [*Chen et al.*, 1999].

[9] In order to assess the sensitivity of mean rip current flow characteristics to beach morphology, this study describes a laboratory experiment of drifter observations over a moveable bed in the presence of rip current circulations. Flows across eight contrasting nature-like barred-

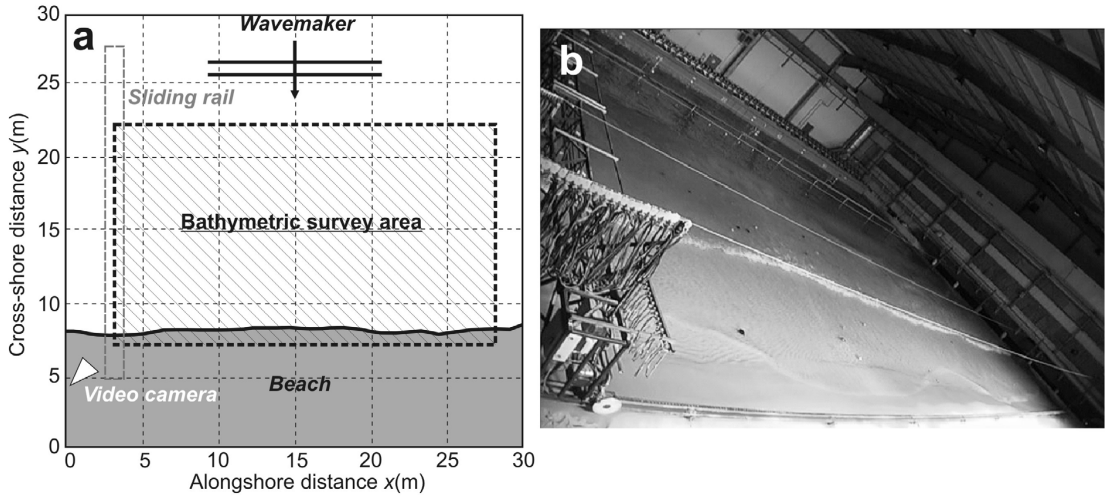

Figure 1. (a) Schematic of setup for the laboratory experiment with delimitations of the bathymetric survey area (dashed box) and location of the video camera. (b) Sample of captured video image with drifters.

beach morphologies consistent with the morphodynamic intermediate beach state classification of *Wright and Short* [1984] are investigated.

2. Experimental Setup

2.1. Laboratory Experiment

[10] The laboratory experiment [*Michallet et al.*, 2010] was undertaken during a 5 week period in a multidirectional wave basin at the SOGREAH (LHF facility, G-INP, France). The basin extended 30 m in both cross-shore (y axis) and alongshore (x axis) directions with an offshore wall constituted of 60 independently controlled piston-type wavemakers (Figure 1). The choice of the general experimental setup (wave conditions, offshore water depth, initial alongshore-uniform beach profile) was based on a previous laboratory experiment of intermediate cross-shore barred-beach morphodynamics in a 36 m long flume [*Michallet et al.*, 2007; *Grasso et al.*, 2009a, 2009b]. To move up to full scale, the length scaling factor and time scaling factor are 10 and 3, respectively. A complete description of the downscaling in hydrodynamics is presented by *Grasso et al.* [2009b]. The still water level at the wavemaker was h_0 = 76.5 cm and the mean beach slope was about 1/25. The moveable bed consisted of fine sand with d_{50} = 164 μm with sediment layer over the rigid bottom of at least 10 cm thick throughout the experiment.

[11] Shore-normal waves were used and the same wave conditions were applied for all cases presented in this paper. Irregular waves were generated according to a JONSWAP spectrum with a significant wave height H_s = 18 cm and a peak period T_p =3.5 s. A linear combination of 350 random sinusoidal components was used to define a 20 min wave sequence. This wave sequence was repeated continuously during the experiment as much as desired. Over the experiment, waves were generated for 102 h [*Michallet et al.*, 2010]. There was neither wave absorption nor second-order correction on the wavemaker motions. Of note, because the primary objective of the experiment was to investigate the formation and subsequent nonlinear evolution of 3-D surf zone sandbar, wave forcing at the wavemaker was not alongshore uniform to initiate sandbar instability. Two 0.5 m long independently controlled pistons centered at x = 15 m were set to half of the wave height at the other pistons. Preliminary investigations showed that, for an alongshore-uniform beach morphology, alongshore variations in wave height at the breaking point were small. Given the substantially alongshore nonuniform beaches investigated, wave-driven circulations were therefore assumed to be essentially guided and constrained by the 3-D sandbar morphology, with negligible effect of the alongshore nonuniform wave generation at the wavemaker.

[12] The seabed morphology was measured using a laser profiler mounted on a motorized trolley located on a sliding rail (Figure 1a). This measurement technique required emptying the basin before recording the bed elevation. During the experiment, the duration between each bathymetric survey varied from 7 to 26 twenty-minute wave sequences. The seabed elevation was recorded with millimeter accuracy every 10 cm and 1 cm in the alongshore and cross-shore direction, respectively. Ambient 3-D beach morphologies were not shaped by the investigators but formed through the positive feedback between flow (waves and currents) sediment transport and the evolving morphology from an initial alongshore-uniform beach geometry. As shown in Figure 1a the bathymetric survey zone was restricted by the sliding rail configuration and covered the area 3.12 m < x < 28.02 m, 7.16 m < y < 22.16 m. The beach morphology both seaward and shoreward of this area was reasonably alongshore uniform and did not evolve significantly throughout the experiment. The beach morphology appeared to be strongly variable during the experiment, ranging from an alongshore-uniform geometry to a well-developed bar-rip morphology, favoring a large range of rip current systems. The present study focuses on a specific period of the experiment when the formation and the subsequent disappearance of rip channels

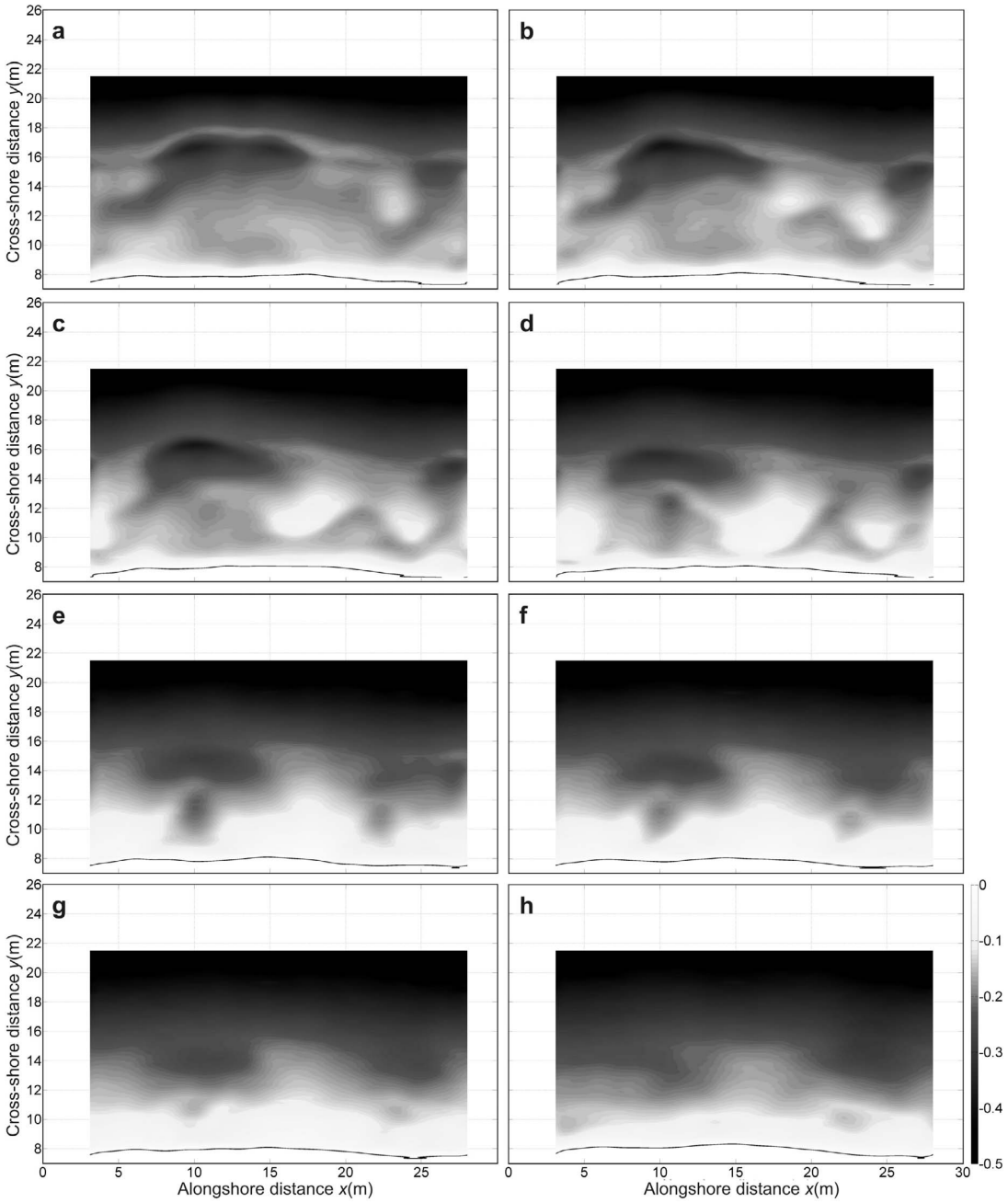

Figure 2. Beach morphologies surveyed with millimeter accuracy (ripples are filtered) corresponding to (a) Run A, (b) Run B, (c) Run C, (d) Run D, (e) Run E, (f) Run F, (g) Run G, and (h) Run H. Grayscale bar and solid black line indicate the seabed elevation in meters and the shoreline position, respectively.

were observed. This period coincided with the deployment of the largest number of drifters to be tracked by the video camera.

2.2. Beach Morphologies

[13] Eight beach morphologies (Figure 2) are considered to assess the rip current circulations as a function of the seabed characteristics only, with corresponding alongshore-averaged beach profiles shown in Figure 3. Following the morphodynamic framework of *Wright and Short* [1984] for intermediate beach states, this morphological sequence appears as a down-state sequence. The beach initially exhibited a typical rhythmic bar and beach morphology (Figure 2a) with a single crescentic bar at about 4 m $< x <$ 18 m

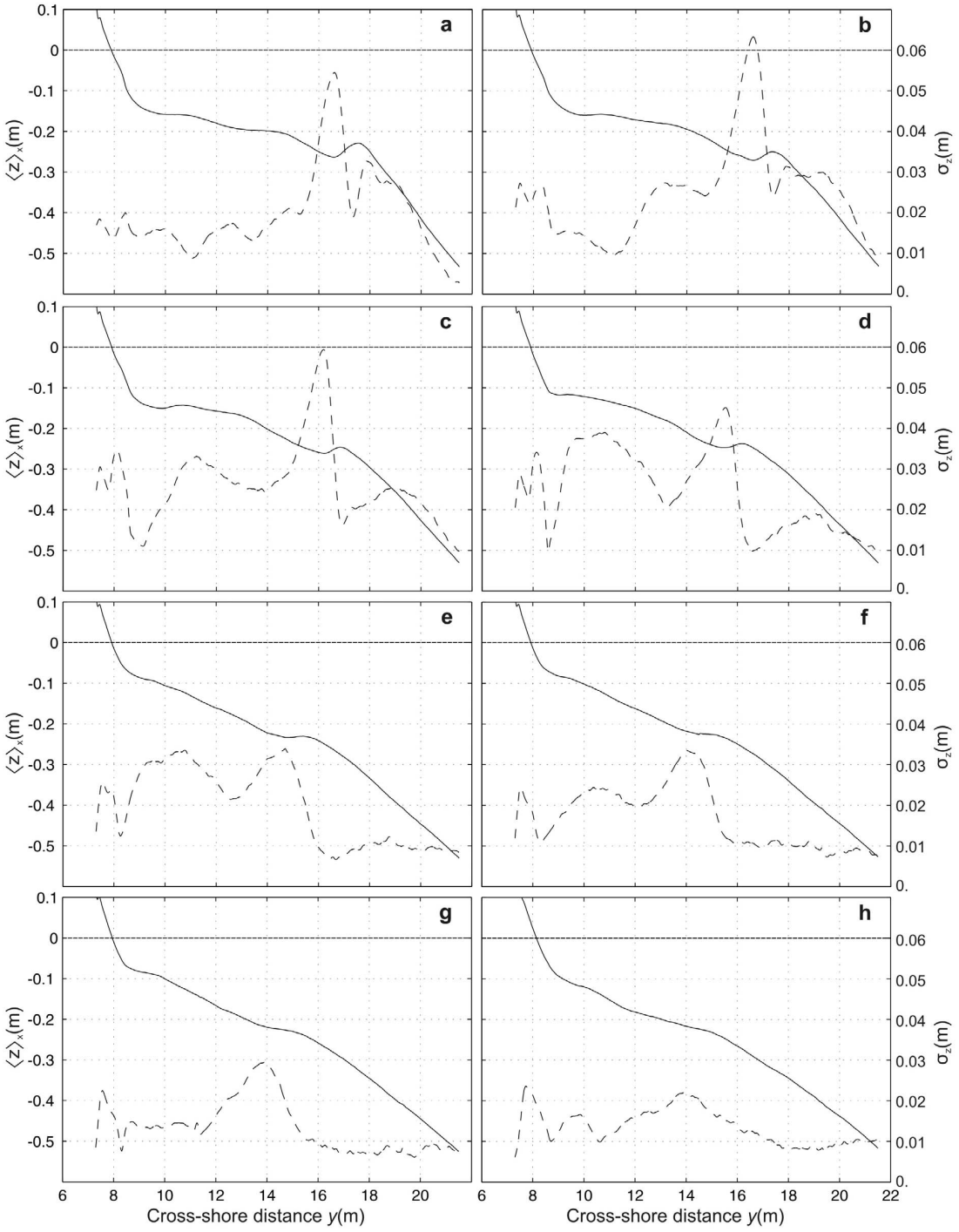

Figure 3. The mean cross-shore bottom profile $\langle z(y)\rangle_x$ (solid line) and its alongshore nonuniformities $\sigma_z(y)$ (dotted line) for (a) Run A, (b) Run B, (c) Run C, (d) Run D, (e) Run E, (f) Run F, (g) Run G, and (h) Run H.

that was not connected to the shore. The bar subsequently migrated shoreward (Figures 2b and 2c; see also Figures 3a–3c) and attached to the beach (Figure 2d) with the formation of shallow shoals alternating with 3 deeper rip channels (at about x = 10 m, 21 m and 26 m) associated with alongshore-oriented feeder channels typical of the transverse bar and rip morphology [*Wright and Short*, 1984]. The two rip channels at about x = 22 m and 26 m then merged to form a single rip channel at x = 22 m together with the infilling of the alongshore-oriented feeder channels (Figure 2e). The following beach morphology (Figure 2f), that can be similarly categorized into the transverse bar and rip morphology, show a continuous overall shoreward migration of the bar (Figure 3) together with the increasing discrimination between the two rip channels (Figure 2). The beach then progressively tended toward an almost featureless terrace-like morphology (Figures 2g and 2h) as the two previously observed rip channels were significantly infilled.

[14] During the whole sequence, the shoreline position did not change significantly. Of note, the beach morphologies in Figure 2 are similar to previously surveyed bar-rip morphologies in the field [see, e.g., *Brander and Cowell*, 2003] or recently surveyed crescentic sandbars [*Almar et al.*, 2010]. Therefore, and conversely to earlier laboratory experiments, the morphologies were characterized by incised rip channels inshore-connected or unconnected shoals, without any sharp discontinuity in the seabed elevation. A preliminary analysis of all the bathymetry, that was corroborated by the observations during the experiment, showed the persistent presence of small-scale variations of the seabed elevation (on the order of 1–2 cm) which were related to the presence of ripples, suggesting bedload sediment transport ubiquity. In the following, ripples were filtered from the bathymetric data.

[15] In this paper we focus on the rip current system that was located at about x = 10 m as, throughout the experiment, both the highest rip current velocities and largest number of drifters were most of the time observed. To examine the evolution of the rip current characteristics as a function of the beach morphology, we quantified the beach geometry for the eight morphologies. While the relative depth of the rip channel has been previously widely used to characterize the rip channel three-dimensionality [*MacMahan et al.*, 2006], here we used the more consistent measure of bathymetric nonuniformities, that is, the alongshore depth standard deviation $\sigma_z(y)$ [*Feddersen and Guza*, 2003; *MacMahan et al.*, 2008]:

$$\sigma_z(y) = \sqrt{\frac{1}{x_2 - x_1}\int_{x_1}^{x_2} \left(z(x,y) - \langle z(y)\rangle_x\right)^2 dx} \qquad (1)$$

where $z(x, y)$ is the seabed elevation at 7.16 m < y < 22 m, x_1 = 3.12 m and x_2 = 18 m, and $\langle z(y)\rangle_x$ is the alongshore mean cross-shore profile between x_1 and x_2. This choice of x_1 and x_2 was motivated by the consideration of the rip current located at about x = 11 m that was hypothesized not to be significantly influenced by the beach morphology at x > 18 m. Figure 3 shows the evolution of $\langle z(y)\rangle_x$ and $\sigma_z(y)$ during the experiment. Corroborating the previous qualitative description of the beach down-state transition in Figure 2, Figure 3 shows the persistent shoreward migration of the bar during the experiment. The beach alongshore nonuniformity is predominantly associated with crescentic patterns and rip morphology. For instance when a crescentic pattern is observed (Figure 2a), the maximum beach alongshore nonuniformity is characterized by two peaks located immediately seaward and shoreward of the bar crest at about y = 17.5 m. This is consistent with the general observation of crescentic patterns that are usually viewed as an alongshore sequence of horns and bays alternating seaward and shoreward of the bar crest [*Van Enckevort et al.*, 2004]. This two-peak feature is also readily apparent for the transverse bar and rip morphology (Figures 3c) with peaks located shoreward and seaward of the cross-shore location $y \approx$ 12–14 m. At the beginning of the sequence, $\sigma_z(y)$ significantly increases (Figures 3a and 3b) and subsequently decreases until the end of the sequence. In the following, we consider the cross-shore averaged beach alongshore nonuniformity $\overline{\sigma_z} = \langle \sigma_z(y)\rangle_y$ as the measure of the bar-rip system three-dimensionality.

2.3. Drifter Observations

[16] Motivated by previous drifter developments for both field and laboratory rip current studies [*Schmidt et al.*, 2003; *Johnson and Pattiaratchi*, 2004a; *Kennedy and Thomas*, 2004; *Schmidt et al.*, 2005], a few drifter designs and shapes were tested prior to the experiment. The best drifter design was a simple balloon filled of water (with a diameter between 5 and 10 cm). Various balloon colors were used for easier discrimination of drifter position when dense clusters were observed. Preliminary tests showed that broken and near-breaking waves passing over the drifters did not significantly push the drifters ashore (i.e., "surfing"). Drifters followed gross water motion in the top 5–10 cm of the water column, except for brief periods when the drifters would sink, when caught in a plunging breaker, and follow deeper portions of the water column for a few seconds. Only during very scarce events did a balloon blow up when caught by a plunging breaker. Note that wave breaking occurred within the rip channel during the higher portions of the wave group, even when the rip channel was the most developed. During the lower portion of the wave group wave breaking occurred in the rip channel only when the rip channel was significantly infilled (Runs G and H). The average surf zone width was about 10 m throughout the experiment.

[17] Drifters were deployed in the surf zone for each run for a 30 to 60 min duration. A bathymetric survey was undertaken immediately after each video run. Generally, wave trains were generated during a few hours between each video run so that the video run duration was short in comparison with timescales associated with the morphological evolution. Therefore the bathymetry was assumed not to change significantly during the video run and the observed rip currents are considered as representative of wave-driven circulations over the subsequently surveyed beach morphology.

[18] For most of the video runs, drifters were manually deployed ashore along the entire domain before the beginning of the wave sequence. Drifters were subsequently caught by the feeder currents and then spread within the surf zone by the wave-driven circulations. For the less-developed rip current systems, drifters were manually deployed at about 5 m seaward of the shoreline before the wave sequence and were further retrieved for redeployment when they came ashore and were trapped in the swash zone for more than about 5 min. Drifters that exited the surf zone and remained

Table 1. Video Run Conditions With the Beach Alongshore Nonuniformity $\overline{\sigma_z}$ and RBB, TBR, and LTT[a]

	Run A	Run B	Run C	Run D	Run E	Run F	Run G	Run H
Video-run duration (min)	40	30	60	60	60	60	60	40
Number of deployed drifters	22	20	25	37	29	39	32	21
Beach morphology	RBB	RBB	TBR	TBR	TBR	TBR	LTT	LTT
$\overline{\sigma_z}$ (m)	0.0186	0.0258	0.0242	0.0224	0.0194	0.0167	0.0134	0.0135

[a]RBB is rhythmic bar and beach, TBR is transverse bar and rip, and LTT is low tide terrace morphology [*Wright and Short*, 1984].

near $y > 22$ m were not retrieved for redeployment. Between 20 and 37 drifters were deployed for each video run. Table 1 lists video run conditions, with the eight video runs further denoted Run A to Run H in the paper.

[19] Drifters were tracked using captured images from a shore-mounted video camera with a captured image resolution of 720 by 576 pixels at 25 frames per second. Image coordinates were then rectified to still water level Cartesian coordinates (see Figure 1b for an example of captured image). Note that because of camera limitations and the presence of the sliding rail (Figure 1), it was impossible to track the drifters at alongshore distance of about $x < 5$ m. The image rectification to Cartesian coordinates was done using a three-dimensional direct linear transformation, the transformation coefficients being calculated by a least squares method on 29 ground control points. The lens optical distortion (radial) was also taken into account. The procedure mean error applied on the control points position is 0.11 m, with a maximum error of 0.26 m at the farther point of the domain. The pixel footprint ranged from less than 0.05 m at the bottom left-hand side of the beach to about 0.35 m at (x, y)=(30 m, 30 m). Within the investigated rip current system that was located close to the camera, the mean errors due to image rectification and identification of the center of the drifter are about 0.1 m and 0.15 m, respectively.

[20] Because of nonoptimized lightning in the laboratory, drifters were tracked using a semiautomatic method in order to avoid difficulties and errors induced by a full automatic method. For each drifter, the drifter position was indicated manually by mouse clicking every 6 s on the original video. Cross-shore and alongshore velocities were estimated from a linear interpolation in position and time of each sequential position of the drifter position at a 1 s time step over a 30 s duration. The study area was further divided into 1 m by 1 m bins in which, according to the drifter position information, the velocity data was sorted into the appropriate bin. Only bins with five or more independent velocity measurements were used for the data processing, which results in statistically confident results [*Spydell et al.*, 2006]. When a sufficient number of velocity measurements were available for a given bin and a required duration, mean current vectors and standard deviations in current angle and intensity were computed to grasp information on the spatial variability of the rip current circulation instabilities. As a drifter followed gross water motions it bobbed up and down with the incoming waves. It resulted in a rectified apparent horizontal motion of the drifter because of the oblique field of view. Some preliminary tests with mouse clicking every 0.2 s showed that these motions were smoothed by the interpolation. Given the quantified errors due to image rectification and identification of the drifter center, the typical maximum drifter velocity error is 0.05 m/s at the furthest basin corner, with a reasonable value of 0.025 m/s within the investigated rip current system. For the mean velocity computations, the expected maximum error decreases with increasing number of samples and is estimated to be about 0.01 m/s when the minimum requirement of five individual measurements is met. Given that a large number of individual samples were systematically observed for a given bin in both the rip neck and within the rip cells (typically between 20 and 200 depending on the video run), the expected maximum error on mean velocity is assumed to be less than 10% of the typical mean velocity within the rip current system.

3. Results

3.1. General Drifter Behavior

[21] Wave-driven circulation patterns were strongly unstable throughout the experiment. Figure 4 shows a sequence of drifter tracks every 120 s for Run D over a well-developed bar-rip morphology with a pronounced shore-normal rip channel at about $x = 10$ m (Figure 2d). Overall, the trajectories show a well-defined offshore flow with two counterrotating cells (Figure 4), with most of the drifters being trapped within the circulations associated with the rip current centered in $x = 10$ m. These circular patterns are essentially coupled with the underlying morphology. Overall the two circulation cells equally occupied half of the shoal and rip channel. There was generally little longshore spreading of the drifters in the rip neck section, indicating a constrained jet-like flow. In contrast, in the rip head, drifters rapidly spread, showing significant variability over a very short distance. Most of the drifters slowly turned right or left with no apparent preference and were subsequently driven across the shoals at an average speed of about 0.1 m/s (instantaneous velocity up to about 0.15 m/s). Only a small number of drifters were ejected from the surf zone (Figures 4f, 4g, 4q, and 4r). When drifters exited the surf zone compartment, they were almost stationary and slowly exited the video camera field. Only a small number slowly turned shoreward before being subsequently caught once again within the rip current circulations, indicating very little onshore flow outside of the surf zone compartment. Rarely a drifter caught in the rip current located at $x = 10$ m was transported sufficiently rightward to be further caught in the rip current located at $x = 22$ m (see, for instance, Figure 4d), suggesting a rather small interchange of water between the two rip current systems. Note that it was not the case for all the video runs. Only three drifters remained ashore at the convergence of the two feeder currents at about $x = 10$ m during most of the sequence. All the other drifters that came ashore were usually rapidly caught by the feeder currents and further transported in the rip current.

[22] The rip jet sometimes changed direction from left to right. For instance, a significant leftward trend is observed at $t = 420$–540 s (Figure 4a) that rapidly changes to a rightward trend at $t = 660$–780 s (Figure 4c) and subsequently a leftward

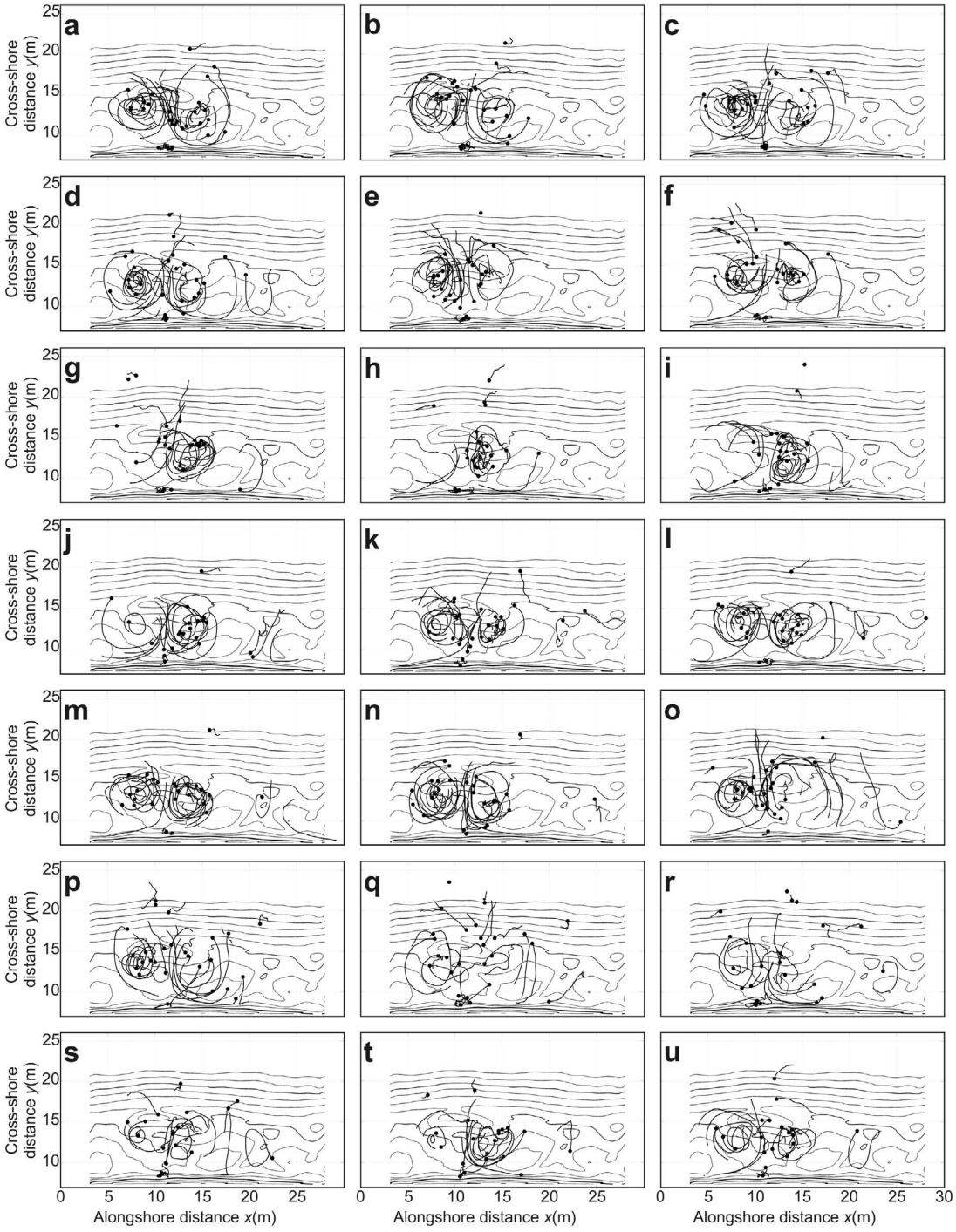

Figure 4. Startup pathlines of the drifters during Run D with the local bottom morphology contoured in the background. (a) 420–540 s, (b) 540–660 s, (c) 660–780 s, (d) 780–900 s, (e) 900–1020 s, (f) 1020–1140 s, (g) 1140–1260 s, (h) 1260–1380 s, (i) 1380–1500 s, (j) 1500–1620 s, (k) 1620–1740 s, (l) 1740–1860 s, (m) 1860–1980 s, (n) 1980–2100 s, (o) 2100–2220 s, (p) 2220–2340 s, (q) 2340–2460 s, (r) 2460–2580 s, (s) 2580–2700 s, (t) 2700–2820 s, and (u) 2820–2940 s. Solid circles give the starting point of each pathline. Drifters were manually deployed ashore at about 5 m < x < 20 m at t = 0 s.

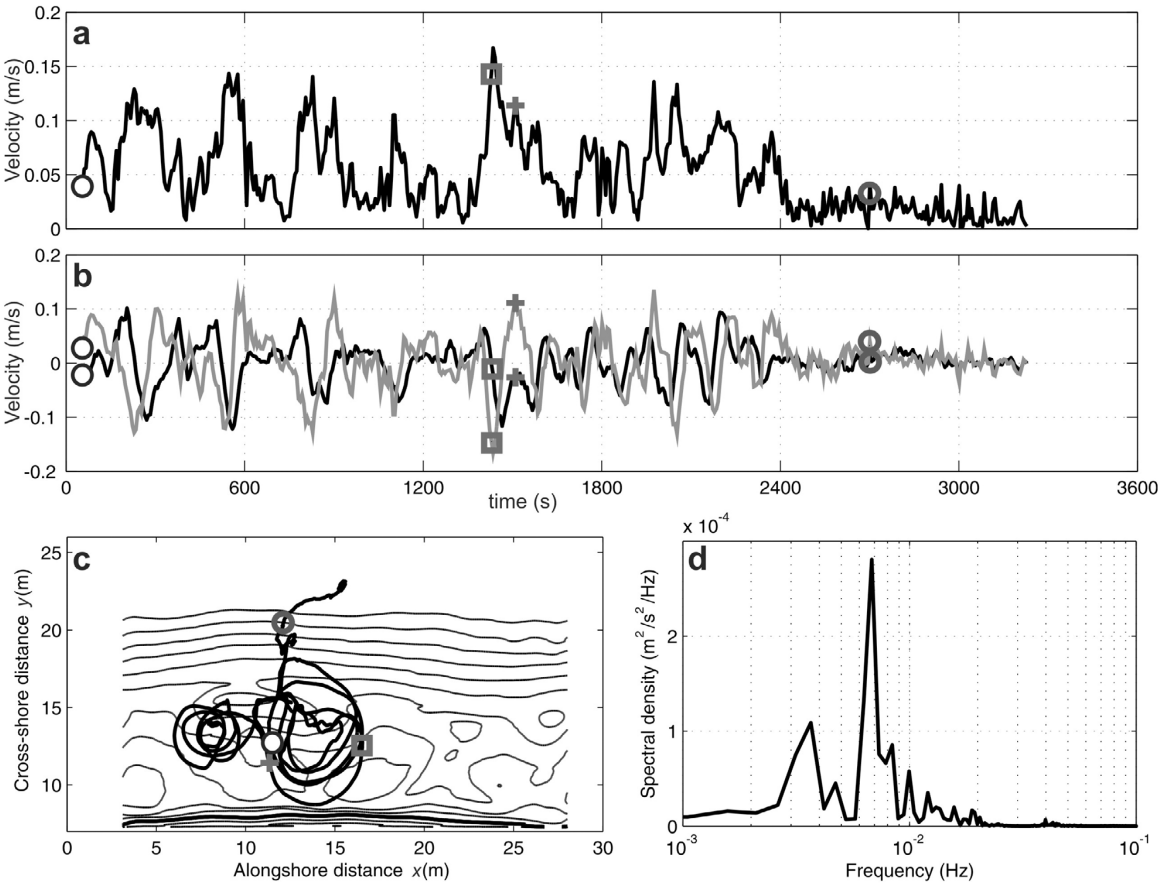

Figure 5. Single drifter data computed during Run D with (a) time series of the drifter velocity, (b) time series of the cross-shore velocity (gray line) and longshore velocity (black line), (c) drifter pathline with the local bottom morphology contoured in the background, and (d) corresponding energy spectrum for cross-shore velocity. In Figures 5a–5c the dark gray cross, circle, and square indicate velocities and locations of the drifter at three different times, and the black circle indicates the starting point.

trend at t = 1020–1140 s (Figure 4f). The circulation cells do not seem to migrate in the alongshore direction, whereas substantial cross-shore migration of the circulation cells is readily apparent. For instance, the rip current circulation centers seem to be located at about y = 14 m at t = 1020–1140 s (Figure 4f) or at t = 2340–2360 s (Figure 4q) while, most of the time, they appear to be located at about y = 12–13 m (Figure 4). Interestingly, this seaward migration of the rip current circulation seems to be associated with subsequent events of drifter expulsion from the surf zone compartment (see at t = 1140–1260 s in Figure 4g and t = 2580–2700 s in Figure 4s).

[23] Unlike other laboratory rip current studies, there was hardly obvious trace of smaller-scale vortices (O(0.5–1 m)) being shed offshore. This can be explained by the choice of our drifter track computation method. The combination of errors in the positioning, the tracking every 6 s and the interpolation in position in time to compute both velocities and tracks are expected to substantially filter these vortices.

[24] Drifters traveled in and out of any 1 m by 1 m bin at irregular intervals. Therefore, like previous field and laboratory rip current studies using Lagrangian measurements, it was impossible to obtain continuous time series of velocity at a given bin. On the other hand, it was possible to compute continuous time series of position and velocity of a given drifter. Figure 5 shows a selected drifter trajectory together with time series of cross-shore and longshore velocities. The selected drifter was initially deployed ashore and was subsequently retained within the rip current circulations. The drifter was caught about 10 times in the rip current and further transported in the rightward or leftward circulation with no apparent preference. As shown in the spectral density plot of the cross-shore velocity (Figure 5d) a clear peak appears at a frequency of about f = 0.007 Hz which means that the selected drifter undertook a full rip current circulation every 2–3 min. The selected drifter was subsequently ejected from the surf zone at about t = 2400 s (Figure 5c). Maximum velocities of about 0.15 m/s were reached when the drifter was in the rip neck or over the shoal (Figures 5a and 5b). Interestingly, the selected drifter did not experience a high offshore-directed velocity in the rip neck immediately before exiting the surf zone (less than

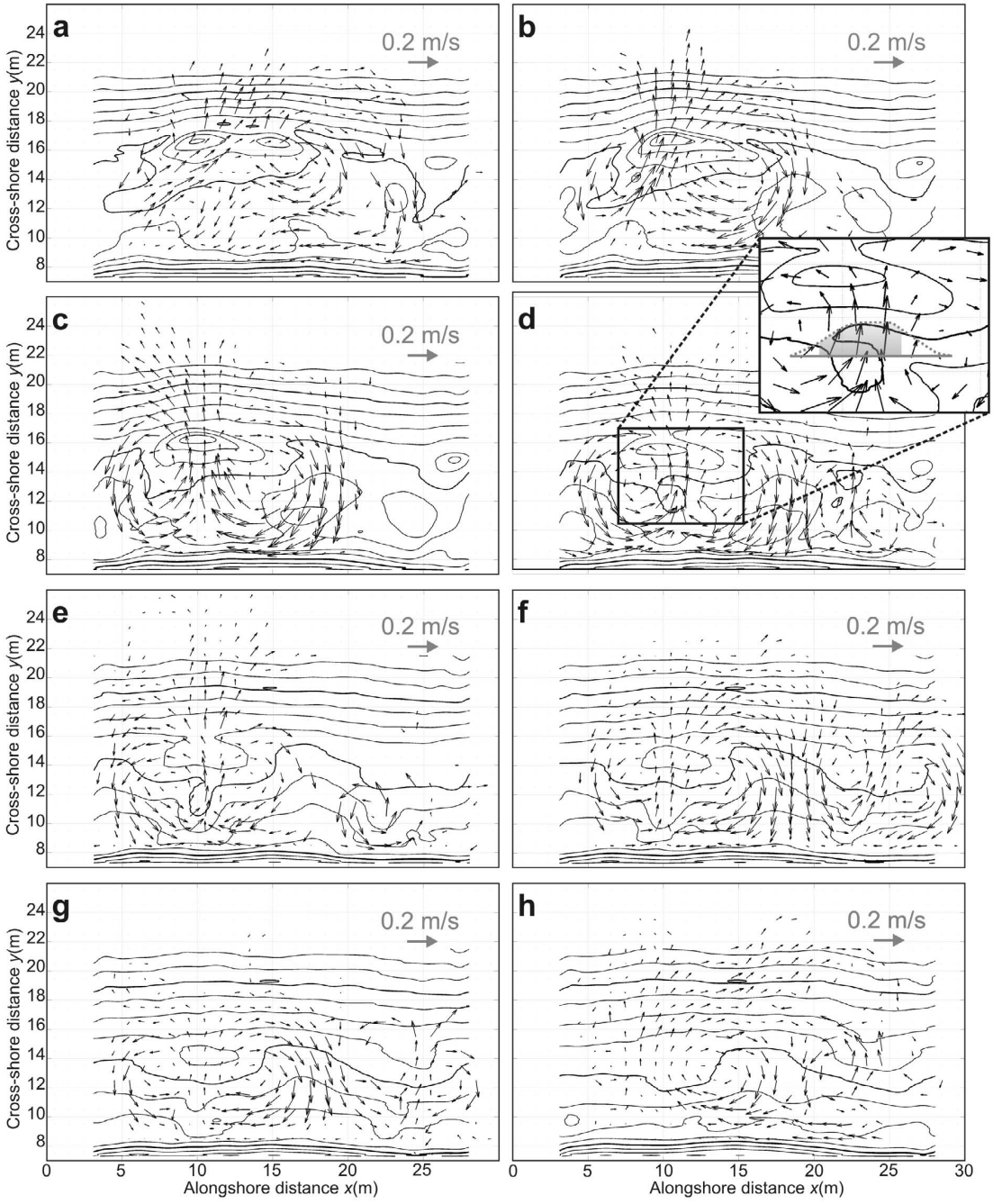

Figure 6. Computed mean flow patterns plotted over the bathymetry for the eight situations (a) Run A, (b) Run B, (c) Run C, (d) Run D, (e) Run E, (f) Run F, (g) Run G, and (h) Run H. Grid spacing resolution is 1 m in both x (cross-shore) and y (alongshore) directions. The local bottom morphology is contoured in the background. The methodology used to compute rip current velocity U_{rip} is shown in Figure 6d and is further detailed in the text.

0.1 m/s, see Figure 5a at $t \approx 2400$ s), which goes against the common perception [*Smith and Largier*, 1995; *Reniers et al.*, 2007] that drifters exiting the surf zone are systematically caught by a pulsating jet.

3.2. Mean Rip Current Circulations

[25] As indicated in section 3.2, rip current circulations were unstable and the velocities were exposed to long-period

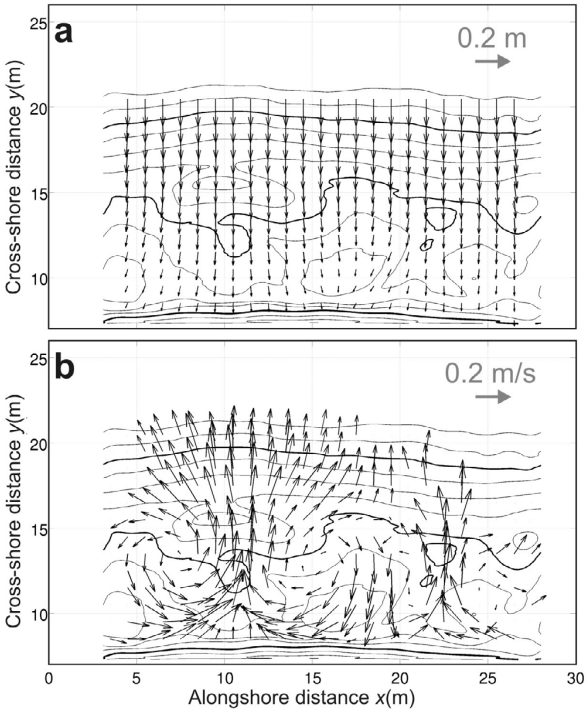

Figure 7. (a) Root-mean-square wave height vector field ($H_{rms}\vec{e}_k$) simulated for Run D with (b) resulting Eulerian velocity field. The local bottom morphology is contoured in the background.

oscillations. The video run durations were long enough to capture a large number of low-frequency periods and, therefore, mean values computed below are assumed not to be affected by infragravity and far-infragravity motions. Figure 6 shows the computed mean rip current circulations for the eight beach morphologies given in Figure 2. Classic rip current patterns are observed for each with alongshore feeder currents, a reasonably intense and narrow offshore-directed jet in the channel, strong onshore-directed flow across the shoals and counterrotating cells to the left and right of the rip current. Only one rip current is observed in the A and B video runs (Figures 6a and 6b) that were constrained by the single crescentic pattern. For all the other video runs two rip current systems are visible at $x \approx 10$ m and $x \approx 23$ m. Note that additional cells closer to the shoreline were persistently seen in previous laboratory experiments over alongshore bar-trough profiles cut by a rip channel [*Drønen et al.*, 2002; *Haas and Svendsen*, 2002; *Kennedy and Thomas*, 2004] and further confirmed trough numerical modeling over similar beach geometries [*Haas et al.*, 2003; *Kennedy et al.*, 2006]. Such circulation cells rotating in the opposite direction of the bar/rip channel circulation were only observed for Run A with a single cell centered at about ($x = 8$ m, $y = 12$ m) when the crescentic bar was sufficiently detached from the beach (Figure 6a).

[26] Because of the contrasting beach morphologies, mean rip current circulation patterns strongly evolved during the course of the experiment. Consistent with the general field observation, rip current intensity readily increases with increasing beach three-dimensionality. More importantly, rip current shape varied from shore-normal (Figures 6d–6h) to strongly skewed rightward (Figures 6a and 6b) and weakly skewed leftward (Figure 6c). The rip current skewness during the first part of the experiment is essentially due to alongshore variability of water depth above the shoals.

[27] From run A to run D, onshore- and offshore-directed flows in the rip channel and on the shoals were in the same order of magnitude (0.1–0.2 m/s). In contrast, when the rip current started to significantly decrease in intensity (Run E, Figure 6e) onshore flows only slightly decreased in intensity (0.1–0.15 m/s) while offshore-directed flows substantially decreased up to being negligible during in Run H (Figure 6h). Similarly to onshore-directed flows, feeder currents only slightly weakened throughout the morphological down-state sequence meanwhile feeder channels appear to have disappeared by Run E. Outside of the breaking region, that is at about $y > 18$–20 m, the computed mean offshore-directed flows are expected to be overestimated because data at these locations was available almost only during events of drifter ejection from the surf, which is not likely to be representative of the overall hydrodynamics at these locations.

[28] Because of persistent changes in waves and tidal conditions in the field and the unrealistic beach geometries in laboratory experiment, rip current intensity U_{rip} has only been quantified as a function of the relative depth of the rip channel or the dimensionless variable H/h representative of the forcing intensity. Because rip current circulations are controlled by alongshore differential broken-wave energy dissipation [*Bonneton et al.*, 2010] that results from nonuniformities of the bathymetry, here we quantify the rip current intensity as a function of the beach alongshore nonuniformity, defined as $\overline{\sigma_z}$ the cross-shore averaged beach alongshore nonuniformity $\sigma_z(y)$ given in equation (1).

[29] In Figure 6, flow patterns were presented using the mean measured drifter velocities. As detailed in [*Kennedy and Thomas*, 2004], measured drifter velocities can significantly differ from true Eulerian velocities because of Stokes drift as drifters responded to orbital motions. We estimated Stokes drift using the spectral wave model SWAN [*Booij et al.*, 1999] to compute the root mean square wave height H_{rms} within the domain for the eight beach morphologies. Default values were chosen in the model with no account for wave-current interactions because of a lack of mean flow information over the whole domain. We estimated the Lagrangian Stokes drift on the drifters using the small-amplitude theory,

$$\vec{U}_{LD} = \frac{ga^2 k \cosh 2kh}{C}\vec{e}_k \tag{2}$$

where g is the gravitational acceleration, a the wave amplitude deduced from H_{rms}, k the wave number, h the local water depth, C is the phase speed and $\vec{e}_k$ the unit vector along wave rays. We subsequently removed the Stokes drift component to the mean drifter velocities to compute the estimated Eulerian velocity field. Figure 7 shows the computed wavefield and resulting mean Eulerian velocity field for Run D (Figure 6d). Note that seaward of the surf zone, at locations where finite amplitude effects (e.g., depth-induced breaking) are not consistent with small amplitude wave theory, the Stokes drift is likely to be significantly overestimated

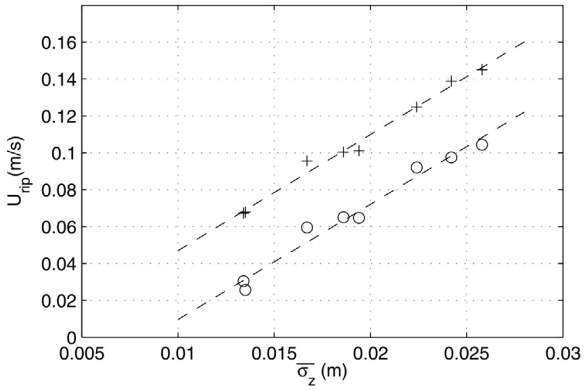

Figure 8. Rip current velocity U_{rip} without (circles) and accounting for (crosses) Stokes drift versus beach alongshore nonuniformity σ_z. The dashed lines represent linear interpolation.

[*Kennedy and Thomas*, 2004]. Within the rip current circulation, the computed velocities are assumed to be representative of the mean Eulerian velocities.

[30] Defining rip current velocity U_{rip} is not that straightforward, especially because strong changes in the general flow structure can occur with the evolving bathymetry, which was the case during our laboratory experiment (Figure 6). Some considerations had to be made on what definition of U_{rip} should be used, that is, where in the rip flow structure to pick up the measurements. Only in the work by *Drønen et al.* [2002] the idealized beach shape together with persistent shore-normal rip current made it natural to define U_{rip} current as the value of the rip current velocity at its maximum. Surprisingly, there was no further discussion on a more generic definition of U_{rip} in the literature than "flow intensity in the rip channel."

[31] Obviously both definitions are hardly applicable herein. For instance during Run B (Figure 6b) the rip current is strongly skewed rightward with both maximum flow velocity and offshore-directed component maximum at (x = 6.5 m, y = 10.5 m) which is not located in the rip channel. Maximum offshore velocity is also found to be located significantly shoreward of the cross-shore position of the rip current circulation centers (located at about x = 15 m, Figure 6b), that is, almost in the feeder current. In contrast maximum offshore velocity is located significantly seaward of the cross-shore position of the rip current circulation centers during Run H (Figure 6h). Therefore, we had to find a consistent definition of U_{rip} based on the geometry of the rip current circulation structure.

[32] We defined U_{rip} as the mean offshore-directed flow along the 3 m long section where the offshore-oriented flow velocity is maximum across the alongshore section joining the two circulation cell centers (see Figure 6d). The two circulation cell centers were manually detected. The choice of a 3 m length was motivated by having a sufficient number of bins to have a representative measure of the offshore flow and avoiding potential odd data at a given bin. Accordingly our computed U_{rip} is substantially less intense than maximum rip current intensity in the rip throat. Figure 8 shows both U_{rip}, with and without accounting for Stokes drift, as a function of beach alongshore nonuniformity $\overline{\sigma_z}$. The overall trend corroborates both the observations in Figure 6 and previous works in the field and in the laboratory as U_{rip} increases with increasing beach alongshore nonuniformity. More importantly, U_{rip} linearly increases with increasing $\overline{\sigma_z}$. Relationship is statistically very good as the R^2 coefficient of determination is 0.97 and 0.98 not accounting and accounting for Stokes drift, respectively. Results are synthesized in Table 2.

[33] The Froude number (Fr), is used to quantify the dimensionless rip current intensity:

$$Fr = \frac{U_{rip}}{\sqrt{gh}} \tag{3}$$

where h is the mean local water depth across the same 3 m section as that along which U_{rip} has been computed. According to *MacMahan et al.* [2006] rip current can be classified into the low-energy ($Fr < 0.1$), moderate-energy ($0.1 < Fr < 0.35$) and high-energy ($Fr > 0.35$) regimes. In the present study, Fr at a given bin in the rip neck region (larger than the 3 m averaged given in Table 2) showed $0.5 < Fr < 1.2$ throughout the experiment, which means that rip currents were within the low- to moderate-energy regime. This suggests weak wave-current interactions throughout our experiment and therefore supports the disregard of wave-current interaction in our SWAN computations.

3.3. Spatial Variability of Rip Current Circulation Infragravity and Far-Infragravity Motions

[34] Information on the spatial variability on how the flow patterns are unstable can be grasped through the standard deviation (σ) of the flow intensity and angle. Because standard deviation is very sensitive to the number of observations at a given bin, there is a strongly varying accuracy in the estimate of the variance. Accordingly, below standard deviations are mostly described in terms of patterns. The patterns of standard deviation of flow intensity (Figures 9a–9h) show that when rip current circulations were the most intense (Figures 9b–9d), highest variations in flow intensity are almost found systematically in the rip neck, suggesting the presence of strong rip current pulsations (on the order of 0.05 m/s). Slightly lower flow intensity variations are found within the rip current circulations throughout the experiment. There is hardly contrasting patterns in flow intensity standard deviation between the eight situations as maximum standard deviations are systematically found in the rip neck and at the onshore flow across the bar. This contrasts with the patterns of standard deviation of velocity angle (Figures 9i–9p). For instance Figure 9 reveals that rip current angle standard deviation within the rip neck increases with

Table 2. Beach Alongshore Nonuniformity $\overline{\sigma_z}$ and Mean Rip Current Characteristics for the Eight Situations With U_{rip}, U^e_{rip}, and Fr^e[a]

	Run A	Run B	Run C	Run D	Run E	Run F	Run G	Run H
$\overline{\sigma_h}$ (m)	0.0186	0.0258	0.0242	0.0224	0.0194	0.0167	0.0134	0.0135
U_{rip} (m/s)	0.0650	0.1044	0.0975	0.0921	0.0647	0.0595	0.0304	0.0256
U^e_{rip} (m/s)	0.1004	0.1450	0.1389	0.1248	0.1012	0.0956	0.0673	0.0679
Fr^e	0.0631	0.0945	0.0997	0.0884	0.0724	0.0691	0.0475	0.0459

[a] U_{rip} is the Lagrangian rip current intensity, U^e_{rip} is the Eulerian rip current intensity, and Fr^e is the nondimensional measure of the Eulerian rip current intensity.

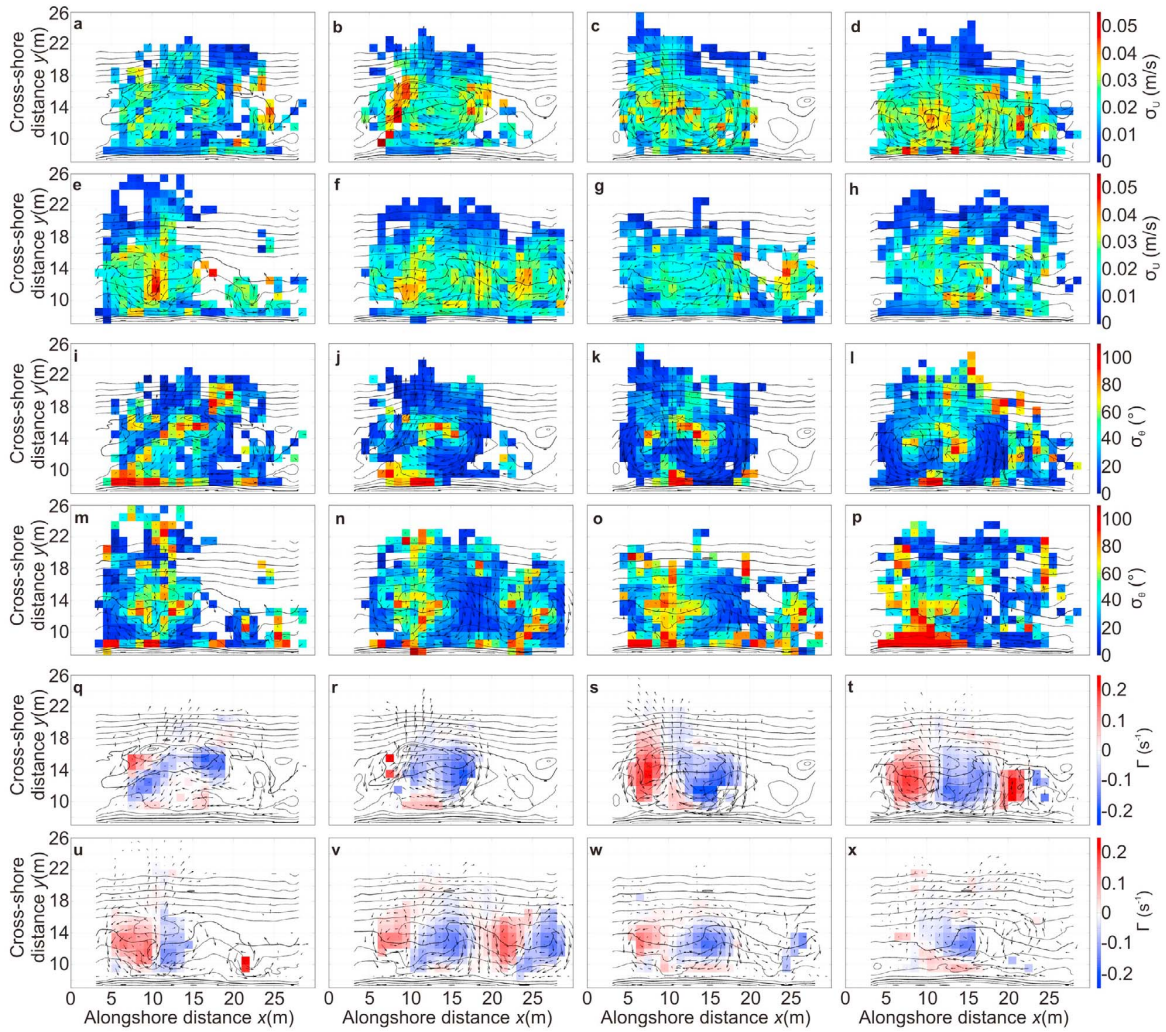

Figure 9. (a–h) Standard deviation of drifter velocity intensity σ_U for (a) Run A, (b) Run B, (c) Run C, (d) Run D, (e) Run E, (f) Run F, (g) Run G, and (h) Run H. (i–p) Standard deviation of drifter velocity angle σ_θ for (i) Run A, (j) Run B, (k) Run C, (l) Run D, (m) Run E, (n) Run F, (o) Run G, and (p) Run H. (q–x) Mean vorticity Γ estimated from drifter observations for (q) Run A, (r) Run B, (s) Run C, (t) Run D, (u) Run E, (v) Run F, (w) Run G, and (x) Run H.

decreasing rip current intensity. When the rip current was the most intense (Figures 9j–9l) the standard deviation of the flow angle within the rip neck is nonsignificant, typical of a highly pulsating and weakly directionally variable offshore-directed flow. Within the rip neck, the flow angle standard deviation increases with decreasing rip current intensity (Figures 9m–9p), which is typical of a reasonably pulsating and highly directionally variable offshore-directed flow. These observations suggest that rip current instabilities display contrasting behavior as a function of how the rip current is intense and sheared. However, the spatial variability in flow angle standard deviation for the eight situations shows some similarities. Flow direction appears rather constant in the feeders and over the shoals where strong alongshore and onshore currents are observed, respectively. This contrasts with the highly variable flow direction within the circulation cells. High standard deviations of flow angle are also observed in the rip head area, because of the observed change of flow direction from left to right that was described in section 3.1. Overall, considering the two counterrotating circulation cells, lower standard deviation of flow angle occurs along the outer edges of the rotational elements (except for weak rip currents for which high standard deviations can be found in the rip neck), with the highest standard deviation occurring both near the circulation centers and in the vicinity of the rip head.

[35] A classic way to investigate rip current circulation characteristics is examining the vertical vorticity defined by $\Gamma = \vec{\nabla} \wedge \vec{u}$, where $\vec{u}$ is the mean flow velocity vector. Here Γ was computed in discrete form using a weighted central difference detailed by *MacMahan et al.* [2010]. The resulting vorticity patterns for the eight situations (Figures 9q–9x) show that the vorticity fields are rather typical in pattern with,

generally, maximum absolute vorticity occurring near the center of the circulation cells. In the rip current neck the vorticity was systematically very low. In contrast, the vorticity drastically increases immediately leftward or rightward of the rip neck. While it was not readily apparent when observing mean flow patterns in Figure 6, Figure 9 actually shows in some cases the presence of four quadrant circulation similar to the observation over bar-trough beach cut by a rip channel [*Kennedy and Thomas*, 2004]. Closer to the shoreline opposite-sign (weak) vorticity were sometimes observed (for instance, in Figures 9q, 9r, 9w, and 9x). Of note, areas with high absolute vorticity are observed in the same locations of the highest standard deviation of flow angle (Figure 9).

4. Discussion and Conclusions

[36] In contrast to earlier laboratory rip current studies, beach morphologies were essentially similar to previous observations of both bar-rip morphologies and crescentic patterns in the field. As far as we are concerned, drifter data gathered during runs A and B are the first flow measurement over crescentic bar systems to date. The seabed varied from reasonably alongshore uniform to strongly alongshore nonuniform with typical rhythmic bar and beach, transverse bar and rip and terrace-like features, representative of the range of sandbar shapes observed within the intermediate beaches [*Wright and Short*, 1984].

[37] As detailed in previous field and laboratory rip current studies based on Lagrangian measurements, drifter design is very important from the perspective of the representativeness of the true near-surface Lagrangian velocity. The most important issue in drifter design is usually addressing the problem of surfing in breaking waves [*Schmidt et al.*, 2003; *Johnson and Pattiaratchi*, 2004b; *MacMahan et al.*, 2009]. Because here we did not have to implement a global positioning system inside the drifter, we chose simple balloons filled of water to minimize surfing as drifters followed gross water motion in the top 5–10 cm of the water column with the same density as that of the water. Throughout the experiment, the visual observation of the drifters in breaking waves was that the balloons were extremely effective in resisting surfing. The only situation in which the drifters did not perform well was when caught at the plunge point of a strongly plunging wave and was subsequently exposed to sinking during 1–2 s. In the rip neck, drifters could rapidly migrate seaward even during the higher portion of the wave group. When approaching the same region, drifters could sometimes stop altogether, but this was visually independent of the presence of breaking or nonbreaking waves. Accordingly, the use of balloons as convenient and low-cost Lagrangian drifters in this laboratory study was successful.

[38] As shown in Figure 5 for the well-developed bar-rip morphology, drifters generally looped back into the same location of the circulation cell after about 140 s (0.007 Hz, Figure 4d). Moving up to full scale means that it would take about 7–8 min to loop back in the field for similar conditions (beach morphology and wave forcing). This is corroborated by recent drifter experiments on an open coast beach at Monterey in similar settings [*MacMahan et al.*, 2010].

[39] Contrary to previous views, and corroborating recent both field experiment of drifter deployment in rip current systems [*MacMahan et al.*, 2010] and numerical modeling [*Reniers et al.*, 2009], only a small number of drifters entering in the rip actually exited the surf zone. As shown in Figure 5, the selected drifter entered 10 times in the rip before exiting the surf zone compartment, which is in agreement with the study of *MacMahan et al.* [2010], who found that only about 10%–20% of the drifters caught in the rip exited the surf zone. The selected drifter did not experience a high offshore-directed velocity in the rip neck immediately before exiting the surf zone (less than 0.1 m/s, see Figure 5a at $t \approx 2400$ s) in comparison with the general 0.1–0.15 m/s velocity in the rip neck. This is intriguing as it was previously hypothesized in the literature [*Smith and Largier*, 1995; *Reniers et al.*, 2007] that drifters exiting the surf zone compartment are systematically caught by a pulsating jet. Some drifters (not presented herein) were actually caught by a pulsating jet before exiting the surf zone but this was by far nonsystematic. Interestingly, the selected drifter that exited the surf zone in Figure 5c has been likely caught in a vortex being shed offshore as it can be deduced from the looped track at about (x = 12.5 m, y = 18 m). This applied for many drifter expulsions throughout the experiment supporting the idea that ejection of surf zone material occurs when surf zone eddies temporarily extend the rip current beyond the surf zone and subsequently detach [*Reniers et al.*, 2010]. Our laboratory rip current study therefore supports recent field and numerical study [*MacMahan et al.*, 2010; *Reniers et al.*, 2010] suggesting that rip flow does not exit the surf zone as much as previously thought and instead is maintained within the surf zone through circulation cells and vorticity. This goes against the traditional paradigm of rip current flow that is now challenged by field, numerical and laboratory studies. Extensive assessment of surf zone retention during this experiment will be explored elsewhere.

[40] According to the morphological framework of *Wright and Short* [1984], here we observed three typical intermediate beach substates that are almost systematically observed along wave-dominated beaches, that are, the rhythmic bar and beach (RBB), transverse bar (TBR) and rip and terrace-like (LTT) morphologies. While the classification of *Wright and Short* [1984] provided very comprehensive qualitative description of the hydrodynamics over these 3-D nearshore patterns, here for the first time quantitative data is provided considering shore-normal constant wave forcing. The present data highlights some contrasting behavior of rip current kinematics depending on the beach morphology. Only low-energy rip currents are driven by waves over LTT morphologies. For the same shore-normal wave conditions rip current circulations are more intense over TBR and RBB morphologies with the presence of classic rip current patterns with counterrotating cells and a relatively narrow offshore-directed varying from shore-normal to potentially strongly skewed. Overall, our measurements are consistent with the qualitative description by *Wright and Short* [1984] except that we suspect that rip current circulations over crescentic patterns are potentially more intense than rip currents over transverse bar and rip morphologies if depth-induced wave breaking is sufficiently intense across the bar. This may also apply to bar and rip morphologies comprising shore-nonconnected shoals. Overall, we found that rip current intensity increases with the beach morphology moving from an alongshore-uniform geometry to a RBB state. For a given

wave height, maximum rip current intensity is observed when the bar is about to attach to the beach. Rip current intensity further decreases with the beach morphology moving from a TBR to a LTT state.

[41] Of note, our results are also in agreement with the model of *Wright and Short* [1984] for the low tide terrace configuration. We measured substantially smaller rip current intensity in Runs G and H, which goes with the usual weak, shallow and ephemeral description of "minirips" in low tide terrace settings [*Wright and Short*, 1984]. This however goes against the observations of *Brander* [1999] who measured increasing rip current intensity from a transverse bar and rip morphology to a low tide terrace morphology on a very similar field situation. The reason for this contrasting behavior remains unclear. Two potential explanations, among others, can be proposed here. First, offshore wave angle to the shore is crucial to the rip current system, which was not assessed by *Brander* [1999] because wave data was nondirectional. Second, the current meter was close to the shore and rather far from the rip throat for the LTT morphology by *Brander* [1999]. The measured cross-shore velocity may have captured undertow and/or feeder effects. Because the pioneer work of *Brander* [1999] contains the only existing field measurements of an evolving rip current during a downstate sequence, our study motivates future intensive field observations of evolving rip currents encompassing a downstate sequence. This will require intensive drifter deployments to accurately capture the entire rip current circulations and subsequently accurately quantify rip current intensity.

[42] In this study we proposed a slightly different definition of rip current intensity than in previous studies. This definition is essentially based on the rip current geometry which can be easily applied elsewhere if there are a sufficient number of available flow measurements. Only using this definition, rip current intensity was found to linearly increase with increasing beach alongshore nonuniformity. This striking relationship was only found within the low- to moderate-energy rip current regime, therefore it has to be extended and confronted with other field and laboratory rip current studies to also further take into account wave period and wave angle to the shore. Given the recent advances in nearshore bathymetry estimation through assimilation of model computations and remote observations [*Van Dongeren et al.*, 2008], beach alongshore nonuniformity could eventually lead to a good predictor of rip current velocity in the field which is of interest from the perspective of beach safety.

[43] The mean vertical vorticity field Γ has been computed for the eight situations (Figures 9q–9x). Despite vorticity fields do not cover the entire domain, from these computations it is readily apparent that Γ increases with beach alongshore nonuniformity. This relationship can be enlightened by the analysis of the mean flow vertical vorticity equation given by *Bonneton et al.* [2010],

$$\frac{\partial \Gamma}{\partial t} + \vec{\nabla}.\left(\Gamma \vec{U}\right) = \vec{\nabla} \wedge \left(D\vec{e}_k\right) + \tau_t \qquad (4)$$

where $\vec{U}$ is the mean transport horizontal velocity, D is the intensity of the depth-induced breaking dissipative force and τ_t the turbulent diffusion of the vorticity. For quasi-stationary rip current circulations ($\partial\Gamma/\partial t \approx 0$), the nonlinear advective term $\vec{\nabla}.(\Gamma\vec{U})$ becomes small in comparison with the wave-induced vorticity forcing term $\vec{\nabla} \wedge (D\vec{e}_k)$ [*Bonneton et al.*, 2010] that can be further approximated as $\vec{\nabla}\mathrm{D} \wedge \vec{e}_k \sim -\partial D/\partial y$ if neglecting wave refraction. This results in a balance between wave-induced vorticity $-\partial D/\partial y$, the alongshore differential broken-wave energy dissipation essentially caused by alongshore depth variations, and the turbulent diffusion of the vorticity $\tau_t \sim \nu_t \vec{\nabla}^2\Gamma$ where ν_t is a turbulent eddy viscosity. As wave dissipation is larger across the shoals than across the rip channel, $-\partial D/\partial y$ drives the strength and the sign of the wave-driven circulation rotational nature (Figure 9).

[44] Despite that it does not provide any information on the involved temporal scales (infragravity or far infragravity), computed standard deviations of flow intensity and direction provide high-resolution information on the spatial variability of the rip current circulation variations. For instance for intense rip current over a RBB or TBR morphology, we highlighted highly pulsating and weakly directionally variable offshore-directed flow in the rip channel, which contrasts with weakly pulsating and highly directional variable flows within the circulation cells. Overall lower standard deviation of flow angle occurs along the outer edges of the rotational elements (except for weak rip currents for which high standard deviations can be found in the rip neck), with the highest standard deviation occurring near the circulation centers and in the vicinity of the rip head. Our laboratory study suggests that spatial distribution of infragravity and far-infragravity motions in rip current settings can vary significantly depending on the rip current regime.

[45] To date the present experiment is the first one involving flow measurements together with an evolving nature-like 3-D sandy beach morphology for a given wave condition and water elevation. Some of the results presented herein are essentially similar to recent field rip current studies, for instance when dealing with surf zone retention and rip current circulations, which brings high confidence in our laboratory results. The data gathered herein will also be eventually used to build a benchmark for the validation of wave-driven circulation and Boussinesq-type models as well as nonlinear morphodynamic models. Our study therefore tends to promote the combination of field, numerical and physical studies to better understand rip current circulations as well as how they interact with the evolving beach morphology.

[46] **Acknowledgments.** This work was undertaken within the framework of the Project MODLIT (RELIEFS/INSU, SHOM-DGA) with additional financial support from COPTER (ANR). BC acknowledges support from BARBEC (ANR). The authors greatly acknowledge SOGREAH Consultants for sharing their facility and for technical support when constructing the physical model, especially the assistance provided by G. Excoffier and L. Marcellin. The authors are also thankful to all the people involved in this experiment. The research presented in this paper was also stimulated by recent fruitful discussions during the First International Rip Current Symposium held in Miami in February 2010. We appreciate the valuable comments by the two anonymous reviewers for making this a better manuscript.

References

Aagaard, T., B. Greenwood, and J. Nielsen (1997), Mean currents and sediment transport in a rip channel, *Mar. Geol.*, *140*, 24–45.

Almar, R., B. Castelle, B. G. Ruessink, N. Sénéchal, P. Bonneton, and V. Marieu (2010), Two- and three-dimensional double-sandbar system behaviour under intense wave forcing and a meso-macro tidal range, *Cont. Shelf Res.*, *30*, 781–792.

Austin, M., T. M. Scott, J. W. Brown, J. A. Brown, and J. H. MacMahan (2009), Macrotidal rip current experiment: Circulation and dynamics, *J. Coastal Res.*, *SI 56*, 24–28.

Austin, M., T. M. Scott, J. W. Brown, J. A. Brown, J. H. MacMahan, G. Masselink, and P. Russell (2010), Temporal observations of rip current circulation on a macro-tidal beach, *Cont. Shelf Res.*, *30*, 1149–1165.

Bonneton, P., N. Bruneau, B. Castelle, and F. Marche (2010), Large-scale vorticity generation due to dissipating waves in the surf zone, *Discrete Contin. Dyn. Syst., Ser. B*, *13*(4), 729–738.

Booij, N., R. C. Ris, and L. H. Holthuijsen (1999), A third-generation wave model for coastal regions: 1. Model description and validation, *J. Geophys. Res.*, *104*, 7649–7666.

Bowen, A. J. (1969), Rip currents: 1. Theoretical investigations, *J. Geophys. Res.*, *74*, 5467–5478.

Brander, R. W. (1999), Field observations on the morphodynamic evolution of a low-energy rip current system, *Mar. Geol.*, *157*, 199–217.

Brander, R. W., and P. J. Cowell (2003), A trend-surface technique for discrimination of surf-zone morphology: Rip current channels, *Earth Surf. Processes Landforms*, *28*, 905–918.

Brander, R. W., and A. D. Short (2000), Morphodynamics of a large-scale rip current system at Muriwai Beach, New Zealand, *Mar. Geol.*, *165*, 27–39.

Brander, R. W., and A. D. Short (2001), Flow kinematics of low-energy rip current systems, *J. Coastal Res.*, *17*, 468–481.

Bruneau, N., B. Castelle, P. Bonneton, and R. Pedreros (2009a), Very low frequency motions of a rip current system: observation and modeling, *J. Coastal Res.*, *SI 56*, 1731–1735.

Bruneau, N., B. Castelle, P. Bonneton, R. Pedreros, R. Almar, N. Bonneton, P. Bretel, J. P. Parisot, and N. Sénéchal (2009b), Field observations of an evolving rip current on a meso-macrotidal well-developed inner bar and rip morphology, *Cont. Shelf Res.*, *29*, 1650–1662.

Buhler, O. (2000), On the vorticity transport due to dissipating or breaking waves in shallow water flows, *J. Fluid Mech.*, *407*, 235–263.

Callaghan, D. P., T. E. Baldock, P. Nielsen, D. M. Hanes, K. A. Haas, and J. H. MacMahan (2005), Pulsing and circulation in a rip current system, in *Coastal Engineering 2004: Proceedings of the 29th International Conference*, vol. 2, edited by J. M. Smith, pp. 1493–1505, World Sci., New York.

Castelle, B., and P. Bonneton (2006), Modelling of a rip current induced by waves over a ridge and runnel system on the Aquitanian Coast, France, *C. R. Geosci.*, *338*, 711–717.

Castelle, B., P. Bonneton, N. Sénéchal, H. Dupuis, R. Butel, and D. Michel (2006), Dynamics of wave-induced currents over an alongshore non-uniform multiple-barred sandy beach on the Aquitanian Coast, France, *Cont. Shelf Res.*, *26*, 113–131.

Castelle, B., P. Bonneton, H. Dupuis, and N. Sénéchal (2007), Double bar beach dynamics on the high-energy meso-macrotidal French Aquitanian Coast: A review, *Mar. Geol.*, *245*, 141–159.

Chen, Q., R. A. Dalrymple, J. T. Kirby, A. B. Kennedy, and M. C. Haller (1999), Boussinesq modelling of a rip current system, *J. Geophys. Res.*, *104*, 20,617–20,637.

Dalrymple, R. A. (1975), A mechanism for rip current generation on an open coast, *J. Geophys. Res.*, *80*, 3485–3487.

Dalrymple, R. A., and C. Lozano (1978), Wave current interaction model for rip current, *J. Geophys. Res.*, *83*, 6063–6071.

Drønen, N., H. Karunarathna, J. Fredsøe, B. M. Sumer, and R. Deigaard (2002), An experimental study of rip channel flow, *Coastal Eng.*, *45*, 223–238.

Falqués, A., G. Coco, and D. A. Huntley (2000), A mechanism for the generation of wave-driven rhythmic patterns in the surf zone, *J. Geophys. Res.*, *105*, 24,071–24,088.

Feddersen, F., and R. T. Guza (2003), Observations of nearshore circulation: Alongshore uniformity, *J. Geophys. Res.*, *108*(C1), 3006, doi:10.1029/2001JC001293.

Grasso, F., H. Michallet, R. Certain, and E. Barthélemy (2009a), Experimental flume simulation of sandbar dynamics, *J. Coastal Res.*, *SI 56*, 54–58.

Grasso, R., H. Michallet, E. Barthélemy, and R. Certain (2009b), Physical modeling of intermediate cross-shore beach morphology: Transient and equilibrium states, *J. Geophys. Res.*, *114*, C09001, doi:10.1029/2009JC005308.

Haas, K. A., and I. A. Svendsen (2002), Laboratory measurements of the vertical structure of rip currents, *J. Geophys. Res.*, *107*(C5), 3047, doi:10.1029/2001JC000911.

Haas, K. A., I. A. Svendsen, M. Haller, and Q. Zhao (2003), Quasi 3D modeling of rip current systems, *J. Geophys. Res.*, *108*(C7), 3217, doi:10.1029/2002JC001355.

Haller, M., and R. A. Dalrymple (2001), Rip current instabilities, *J. Fluid Mech*, *433*, 161–192.

Hamm, L. (1992), Directional nearshore wave propagation over a rip channel: An experiment, in *Coastal Engineering, 1992: Proceedings of the 23rd International Conference, October 4–9, 1992, Venice, Italy*, edited by B. L. Edge, pp. 226–239, Am. Soc. of Civ. Eng., New York.

Holman, R. A., G. Symonds, E. B. Thornton, and R. Ranasinghe (2006), Rip spacing and persistence on an embayed beach, *J. Geophys. Res.*, *111*, C01006, doi:10.1029/2005JC002965.

Johnson, D., and C. Pattiaratchi (2004a), Transient rip currents and nearshore circulation on a swell-dominated beach, *J. Geophys. Res.*, *109*, C02026, doi:10.1029/2003JC001798.

Johnson, D., and C. Pattiaratchi (2004b), Application, modelling and validation of surfzone drifters, *Coastal Eng.*, *51*, 455–471.

Kennedy, A. B., and D. Thomas (2004), Drifter measurements in a laboratory rip current, *J. Geophys. Res.*, *109*, C08005, doi:10.1029/2003JC001927.

Kennedy, A. B., M. Brocchini, L. Soldini, and E. Gutierrez (2006), Topographically controlled, breaking-wave-induced macrovortices. Part 2. Changing geometries, *J. Fluid Mech.*, *559*, 57–80.

Longuett-Higgins, M. S., and R. W. Stewart (1964), Radiation stress in water waves; A physical discussion, with applications, *Deep Sea Res. Oceanogr. Abstr.*, *11*(4), 529–563.

MacMahan, J. H., A. J. H. M. Reniers, E. B. Thornton, and T. P. Stanton (2004a), Infragravity rip current pulsations, *J. Geophys. Res.*, *109*, C01033, doi:10.1029/2003JC002068.

MacMahan, J. H., A. J. H. M. Reniers, E. B. Thornton, and T. P. Stanton (2004b), Surf zone eddies coupled with rip current morphology, *J. Geophys. Res.*, *109*, C07004, doi:10.1029/2003JC002083.

MacMahan, J. H., E. B. Thornton, T. P. Stanton, and A. J. H. M. Reniers (2005), RIPEX-observations of a rip current system, *Mar. Geol.*, *218*, 113–134.

MacMahan, J. H., E. B. Thornton, and A. J. H. M. Reniers (2006), Rip current review, *Coastal Eng.*, *53*, 191–208.

MacMahan, J. H., E. B. Thornton, A. J. H. M. Reniers, T. P. Stanton, and G. Symonds (2008), Low-energy rip currents associated with small bathymetric variations, *Mar. Geol.*, *255*, 156–164.

MacMahan, J. H., J. W. Brown, and E. B. Thornton (2009), Low-cost handheld global positioning system for measuring surf-zone currents, *J. Coastal Res.*, *25*, 744–754.

MacMahan, J. H., et al. (2010), Mean lagrangian flow behavior on an open coast rip channeled beach: A new perspective, *Mar. Geol.*, *268*, 1–15.

McKenzie, P. (1958), Rip-current systems, *J. Geol.*, *66*, 103–113.

Michallet, H., F. Grasso, and E. Barthélemy (2007), Long waves and beach profile evolutions, *J. Coastal Res.*, *SI 50*, 221–225.

Michallet, H., B. Castelle, F. Bouchette, A. Lambert, C. Berni, E. Barthélemy, P. Bonneton, and D. Sous (2010), Modélisation de la morphodynamique d'une plage barrée tridimensionnelle (in French), *Proc. Journée Natl. Génie Côtier-Génie Civ.*, *11*, 379–386, doi:10.5150/jngcgc.2010.045-M.

Nielsen, P., R. W. Brander, and M. G. Hughes (2001), Rip currents: Observations of hydraulic gradients, friction factors and pump efficiency, in *Coastal Dynamics '01: Proceedings of the Fourth Conference on Coastal Dynamics, June 11–15, 2001, Lund, Sweden*, edited by H. Hanson and M. Larson, pp. 483–492, Am. Soc. Civ. Eng., New York.

Reniers, A. J. H. M., J. H. MacMahan, E. B. Thornton, and T. P. Stanton (2007), Modeling of very low frequency motions during RIPEX, *J. Geophys. Res.*, *112*, C07013, doi:10.1029/2005JC003122.

Reniers, A. J. H. M., J. H. MacMahan, E. B. Thornton, T. P. Stanton, M. Henriquez, J. W. Brown, J. A. Brown, and E. Gallagher (2009), Surf zone retention on a rip-channeled beach, *J. Geophys. Res.*, *114*, C10010, doi:10.1029/2008JC005153.

Reniers, A. J. H. M., J. H. MacMahan, F. J. Beron-Vera, and M. J. Olascoaga (2010), Rip-current pulses tied to Lagrangian coherent structures, *Geophys. Res. Lett.*, *37*, L05605, doi:10.1029/2009GL041443.

Schmidt, W. E., B. T. Woodward, K. S. Millikan, R. T. Guza, and B. Raubenheimer (2003), A GPS-tracked surf zone drifter, *J. Atmos. Oceanic Technol.*, *20*, 1069–1075.

Schmidt, W. E., R. T. Guza, and D. N. Slinn (2005), Surf zone currents over irregular bathymetry: Drifter observations and numerical simulations, *J. Geophys. Res.*, *110*, C12015, doi:10.1029/2004JC002421.

Scott, T. M., P. Russell, G. Masselink, and A. Woolers (2009), Rip current variability and hazard along macro-tidal coast, *J. Coastal Res.*, *SI 56*, 895–898.

Shepard, F. P., and D. L. Inman (1950), Nearshore water circulation related to bottom topography and wave refraction, *Trans. Am. Geophys. Union*, *31*, 196–212.

Shepard, F. P., K. O. Emery, and E. C. La Fond (1941), Rip currents: A process of geological importance, *J. Geol.*, *49*, 337–369.

Short, A. D. (1999), Beach hazards and safety, in *Handbook of Beach and Shoreface Morphodynamics*, edited by A. D. Short, pp. 292–304, John Wiley, Chichester, U. K.

Short, A. D., and P. A. Hesp (1982), Wave, beach and dune interactions in South Eastern Australia, *Mar. Geol.*, *48*, 259–284.

Smith, J. A., and J. L. Largier (1995), Observation of nearshore circulation: Rip currents, *J. Geophys. Res.*, *100*, 10,967–10,975.

Sonu, C. J. (1972), Field observation of nearshore circulation and meandering currents, *J. Geophys. Res.*, *77*, 3232–3247.

Spydell, M., F. Feddersen, and R. T. Guza (2006), Observing surf-zone dispersion with drifters, *J. Phys. Oceanogr.*, *37*, 2920–2939.

Symonds, G., and R. Ranasinghe (2001), On the formation of rip currents on a plane beach, in *Coastal Engineering 2000: Conference Proceedings, July 16–21, 2000, Sydney, Australia*, edited by B. L. Edge, pp. 468–481, Am. Soc. of Civ. Eng., Reston, Va.

Thornton, E. B., J. H. MacMahan, and A. H. Sallenger Jr. (2007), Rip currents, mega-cusps, and eroding dunes, *Mar. Geol.*, *240*, 151–167.

Van Dongeren, A. R., N. G. Plant, A. B. Cohen, J. A. Roelvink, M. C. Haller, and P. Catalán (2008), Beach Wizard: Nearshore bathymetry estimation through assimilation of model computations and remote observations, *Coastal Eng.*, *55*, 1016–1027.

Van Enckevort, I. M. J., B. G. Ruessink, G. Coco, K. Susuki, I. L. Turner, N. G. Plant, and R. A. Holman (2004), Observations of nearshore crescentic sandbars, *J. Geophys. Res.*, *109*, C06028, doi:10.1029/2003JC002214.

Wright, L. D., and A. D. Short (1984), Morphodynamic variability of surf zones and beaches: A synthesis, *Mar. Geol.*, *56*, 93–118.

E. Barthélemy, C. Berni, A. Lambert, and H. Michallet, Laboratoire des Ecoulements Géophysiques et Industriels (UJF-INPG-CNRS), BP53, F-38041 Grenoble Cedex, France.

P. Bonneton, B. Castelle, B. Dubardier, F. Leckler, and V. Marieu, CNRS, UMR 5805 EPOC, Université de Bordeaux, Avenue des Facultés, F-33405 Talence Cedex, France. (b.castelle@epoc.u-bordeaux1.fr)

F. Bouchette, UMR 5243, Université Montpellier 2, Place E. Bataillon, F-34095 Montpellier Cedex 5, France.

D.10 Modeling rip current circulations and vorticity in a high-energy mesotidal-macrotial environment

Nicolas Bruneau, Philippe Bonneton, Bruno Castelle, Rodrigo Pedreros
Journal of Geophysical Research - Oceans, Vol. 116, C07026, doi :10.1029/2010JC006693, 2011

Modeling rip current circulations and vorticity in a high-energy mesotidal-macrotidal environment

N. Bruneau,[1,2] P. Bonneton,[2] B. Castelle,[2] and R. Pedreros[3]

Received 29 September 2010; revised 29 March 2011; accepted 7 April 2011; published 28 July 2011.

[1] In June 2007 an intense 5 day field experiment was carried out at the mesotidal-macrotidal wave-dominated Biscarrosse Beach on a well-developed bar and rip morphology. Previous analysis of the field data elucidated the main characteristics of a tide-modulated and strongly evolving rip current driven by low- to high-energy shore-normal waves. Here we present a modeling strategy based on the vertically integrated and time-averaged momentum equations accounting for roller contribution that is applied to the Biscarrosse experiment. Wave and flow predictions in the surf zone improve significantly when using a spatially constant time-varying breaking parameter by Smith and Kraus (1990). The model correctly reproduces the main evolving behaviors of the rip current. An advection-diffusion equation governing the mean wave-driven current vertical vorticity is further derived from the momentum equations. Vertical vorticity is driven by a forcing term that depends on the breaking wave energy dissipation and on the wave propagation direction. Spatial gradients in depth-induced broken-wave energy dissipation therefore determine both the strength and the sign of the wave-driven circulation rotational nature. When applied to the Biscarrosse experiment, the vorticity efficiently predicts the main characteristics of the evolving rip current such as its width, cross-shore extension, and intensity. In addition, good correlations are found between the maximum rip current intensity and the deviation of the forcing term. Thus, we determine precisely the rotational component associated with the wave forcing which is less direct through the traditional radiation stress approach.

Citation: Bruneau, N., P. Bonneton, B. Castelle, and R. Pedreros (2011), Modeling rip current circulations and vorticity in a high-energy mesotidal-macrotidal environment, *J. Geophys. Res.*, *116*, C07026, doi:10.1029/2010JC006693.

1. Introduction

[2] Rip channels are commonly observed along wave-dominated sandy barred beaches. They appear quasi-rhythmically as depressions in shore-connected or unconnected shoals [*Quartel*, 2009]. Counterrotating circulations characterized by seaward flowing jets in the rip channel are driven by waves on these bed forms when waves approach at an angle close to shore normal. These narrow, intense (reaching 1–2 m/s) currents are called rip currents. Understanding and predicting the complex dynamics of rip currents remain a relevant scientific challenge because they play a key role on the beach and surf zone morphodynamics, on the dispersion of material across the surf zone and are a major hazard to swimmers [*Brown et al.*, 2009; *MacMahan et al.*, 2006, 2010; *Thornton et al.*, 2007; *Reniers et al.*, 2009]. While topographically controlled rip currents have received increasing attention these last decades [*MacMahan et al.*, 2006], major advances in the understanding of rip current kinematics that recently challenged traditional views of rip current behaviors [*Reniers et al.*, 2010; *MacMahan et al.*, 2010; *Castelle et al.*, 2010] show that rips are still poorly understood and therefore motivate further rip studies.

[3] Documented rip studies have mostly been restricted to low-energy microtidal rip currents over small alongshore bed nonuniformities [*Brander*, 1999; *MacMahan et al.*, 2005, 2010; *Reniers et al.*, 2007]. Rip current investigations in high-energy environments are still poorly documented [*Brander and Short*, 2000; *Castelle et al.*, 2006; *Bruneau et al.*, 2009a], particularly over strongly alongshore nonuniform beaches. Intense mean rip currents, reaching 1 m/s, were measured near the rip neck by *Brander and Short* [2000] for moderate-energy wave conditions. More recently, *Bruneau et al.* [2009a] measured high-energy topographically controlled mean rip currents (around 0.9 m/s) for low-energy waves ($H_s \approx 0.9$ m). In addition, they highlighted the evolving behavior of rip currents in an energetic mesotidal-macrotidal environment with (1) a strong tidal modulation during low-energy wave conditions ($H_s < 1$ m) and (2) the presence of intense undertow during energetic events ($H_s > 2.5$ m) that dominates the surf zone dynamics.

[1] Laboratório Nacional de Engenharia Civil, Lisbon, Portugal.
[2] Environnements et Paléoenvironnements Océaniques et Continentaux, UMR 5805, Université Bordeaux 1, CNRS, Talence, France.
[3] BRGM, Orléans, France.

0148-0227/11/2010JC006693

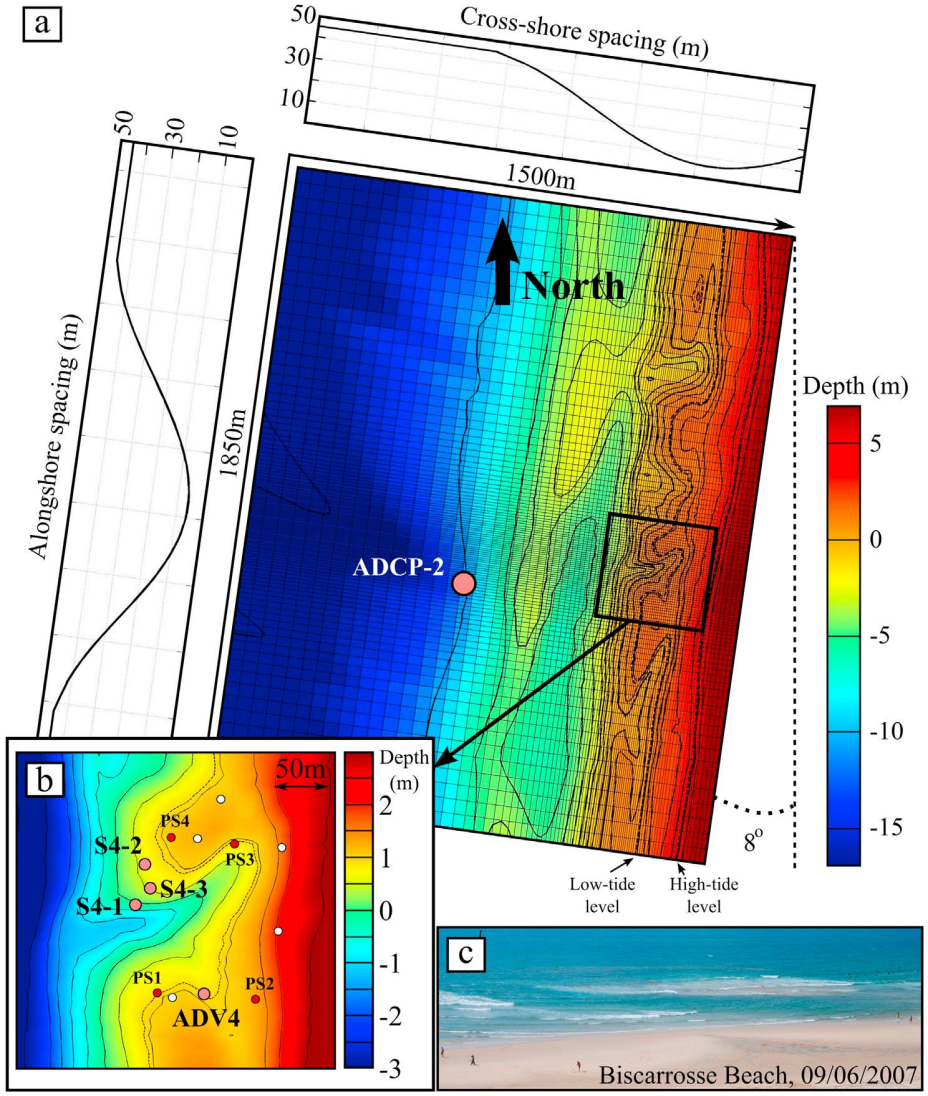

Figure 1. Biscarrosse Beach bathymetry. (a) Irregular rectangular full grid superimposed on the bathymetry with (top) the cross-shore grid spacing and (left) the alongshore grid spacing. (b) Zoom on the instrumented bar and rip morphology showing the locations of the sensors; large light circles for the main sensors involved in the study, small dark circles for other sensors used herein, and small white circles for unused sensors. (c) Photograph of the bar and rip morphology prior to the start of the field experiment.

[4] Combination of field and numerical investigations is currently one of the most promising avenues for rip current analysis because numerical modeling can provide important information when measurements are difficult to obtain. Many modeling studies based on laboratory or field works have focused on the hydrodynamics of rip currents through a depth-averaged or quasi-three-dimensional approach [*Haas et al.*, 2003; *Castelle et al.*, 2006; *Castelle and Bonneton*, 2006; *Bruneau et al.*, 2008, 2009b]. These studies have shown the ability of these models to reproduce the wave-driven horizontal circulations and low-frequency rip current motions generated by shear instabilities [*Haller and Dalrymple*, 2001; *Özkan-Haller and Kirby*, 1999] or forced by wave grouping [*Reniers et al.*, 2007]. Recently, *Reniers et al.* [2009, 2010] used a full three-dimensional model to compute surface flow fields to investigate material dispersion and surf zone retention. However, most of these works were restricted to microtidal environments with low-energy waves over small alongshore seabed nonuniformities.

[5] As shown theoretically by *Peregrine* [1998], nonuniformities along the breaking-wave crest drive vertical vorticity. He modeled the breaking event as the development of a surface and current discontinuity in the nonlinear shallow water equations and proceeded to a direct analysis of the vorticity at the wave time scale. These processes induce mean vorticity with horizontal scales larger than the local water depth; rip currents are a good example of these macrovortices. Retention, dispersion and generally vortical motions associated with topographically controlled rip currents are linked to both quasi-stable rip current, bipolar

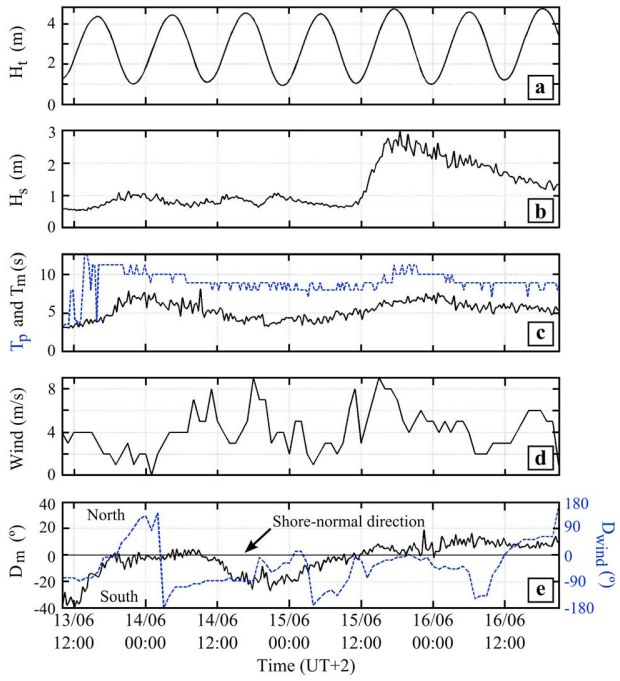

Figure 2. Offshore wave and tide forcings during the 4 days simulated in the study. (a) Tide level H_t, (b) significant wave height H_s, (c) peak T_p (dashed line) and mean T_m (solid line) periods, (d) wind speed and (e) mean wave direction D_m (solid line) and wind direction (dashed line).

circulation cells and unstable, nonstationary jets. *Bühler* [2000] and *Bühler and Jacobson* [2001] described a general theoretical analysis of wave-driven currents and vortex dynamics due to dissipating waves. In addition, they demonstrated that mean flow vorticity generation is controlled by dissipative forces. Based on the system of equations presented by *Smith* [2006], *Bonneton et al.* [2010] identified a vorticity forcing term related to differential, broken-wave energy dissipation as the main source of vorticity.

[6] To examine topographically controlled wave-driven circulations and to investigate evolving rip current behaviors in this study, we use a numerical model based on the nonlinear shallow water equations presented by *Ardhuin* [2005] and *Smith* [2006]. Our model is applied to the Biscarrosse 2007 field experiment [*Bruneau et al.*, 2009a] to validate wave and flow simulations. Next, the mean vorticity conservation equation [*Bruneau et al.*, 2008; *Bonneton et al.*, 2010] is applied to a complex mesotidal-macrotidal high-energy rip current system. The predictive capability of the vertical vorticity conservation equation is further used to investigate the evolving behavior of a rip current for a wide range of tide levels and wave conditions.

2. Study Area

2.1. Regional Setting

[7] The Aquitanian coast is a mesotidal-macrotidal high-energy environment exhibiting a strongly alongshore non-uniform and variable double sandbar system. The outer and the inner bars usually exhibit crescentic patterns, and bar and rip morphologies, respectively [*Castelle et al.*, 2007; *Almar et al.*, 2010]. As with all of the wave-dominated Aquitanian Coast beaches, the Biscarrosse Beach is exposed to high-energy North Atlantic swells coming mainly from the W-NW direction, with an annual mean significant wave height H_s of about 1.4 m and a mean period T_m near 6.5 s [*Butel et al.*, 2002]. During a severe storm, the offshore wave height can reach 10 m. The annual mean spring tidal range is approximately 3.7 m, and the maximum tidal range reaches 5 m.

2.2. Field Experiment: Biscarrosse 2007

[8] An extensive description of the experiment is given by *Bruneau et al.* [2009a]. Figure 1 shows the nearshore bathymetry surveyed during the experiment with concurrent forcing conditions given in Figure 2. During the field experiment, the tidal range varied from 3.3 to 3.8 m (Figure 2a). Offshore significant wave height (H_s) ranged from 0.5 to 3 m (Figure 2b) with persistent swell and only scarcely a superimposed wind sea. Peak wave period (T_p) ranged from 8 to 11 s (Figure 2c) with a wave approach persistently close to the shore normal (Figure 2e). Wind magnitude and direction are given in Figures 2d and 2e, respectively.

[9] The instrumented well-developed bar and rip morphology was characterized by a narrow and deep rip channel (Figures 1b and 1c). As detailed by *Bruneau et al.* [2009a], an array of in situ stationary instruments (Figure 1b) was deployed on this intertidal inner bar and rip system between 13 and 17 June. In the present study, we focus on the S4 and ADV4 records (Figure 1b) because they are the longest samples and were deployed in relevant locations: the rip neck and the southern feeder, respectively. The nearshore morphology did not change significantly during the course of the experiment as only a weak onshore migration of the bar was captured through video imagery [*Bruneau et al.*, 2009a].

3. Modeling Strategy

[10] The modeling strategy consists in coupling the spectral wave model SWAN [*Booij et al.*, 1999] with the nonlinear shallow water model MARS [*Lazure and Dumas*, 2008]. The sediment transport module [*Bruneau et al.*, 2007; *Bruneau*, 2009] is not activated in the present study.

3.1. Wave Model

[11] Wave transformation is computed with the spectral wave model SWAN [*Booij et al.*, 1999] that solves the wave action density balance equation. In our approach, SWAN is used in stationary mode to simulate the wave propagation and deformation. In addition, the effects of generation, dissipation (breaking, bottom friction), nonlinear wave-wave interactions (triad) are taken into account. The wave-current interactions are switched off. An irregular rectangular grid (Figure 1a) is used with a coarse resolution (45 m) along both the offshore and the lateral boundaries. The area of interest is meshed with a 6 m resolution. The computational grid resolution is detailed in Figure 1a. Finally, 36 directions (10° resolution) and 20 frequencies (corresponding to periods varying logarithmically from 2 to 20 s) are used for the directional and spectral discretizations, respectively.

[12] Two parameters are set in the present work: (1) the breaking wave parameter γ_b (wave height-to-depth ratio) and (2) the friction coefficient. The breaking parameter is crucial because it controls the rate of wave energy decay within the surf zone. In the present study, two breaking wave parameters were investigated: (1) a constant γ_b of 0.73 (default value of SWAN) and (2) a spatially constant but time-varying γ_b computed according to the formulation of *Smith and Kraus* [1990]:

$$\gamma_b = \frac{1.12}{1+e^{-60m}} - 5.0\left[1+e^{-43m}\right]s_\infty \tag{1}$$

where m is the mean shoreface slope (herein we use a constant value of 0.02 which allows good wave predictions, as demonstrated later) and s_∞ is the deep-water wave steepness (ratio between the offshore wave height and the offshore wavelength). In addition, γ_b has a minimum threshold of 0.5 to prevent underestimation of the significant wave heights during the energetic period when the model of *Smith and Kraus* [1990] predicts low values of γ_b (which can reach 0.3). This boundary is in agreement (same order) with the work of *Bertin et al.* [2009] which bounded the γ_b with values ranging from 0.4 to 0.8. This formulation is used for its simplicity of implementation (no full-iterative method required; the new breaking parameter is only computed from the previous wave simulation results) and for the good results obtained by *Bertin et al.* [2009]. The equivalent roughness length, K_n, proposed by *Madsen et al.* [1988] is set to 0.04 m to overall fit with the data.

[13] Offshore wave and tide forcing was provided by the ADCP-2 (Figure 1a) deployed in 10 m water depth (at low tide) seaward of the study area and offshore of the subtidal bar. Wave spectra are specified at each boundary (both offshore and lateral) to avoid potential wave energy shadow areas. Finally, both the wave conditions and the water level are updated every 20 min to compute the new wavefield, which is short enough in a mesotidal-macrotidal environment.

3.2. Shallow Water Flow Model

[14] MARS is a finite difference model, originally designed to compute tide- and wind-induced currents. It has been extensively tested on the whole French coast (*http://www.previmer.org/en*). MARS solves the nonlinear shallow water equations in two or three dimensions (it is used in the depth-averaged mode herein).

[15] Most of the depth-averaged models that compute wave-induced currents are based on the radiation stress approach [*Longuet-Higgins and Stewart*, 1964]. *Dingemans et al.* [1987, p. 539] and *Battjes* [1988] showed that the "formulation of the driving forces in terms of the wave dissipation yields more trustworthy results than those obtained by numerical differentiation of the radiation stress tensor." In addition, *Svendsen* [1984] showed the dominance of the roller in dissipating wave energy in the surf zone. During the field experiment, the surf similarity parameter ranged from 0.1 to 0.3 characterizing the dominance of spilling waves which justifies the choice to use a roller model. Thus, according to the works of *Ardhuin* [2005] and *Smith* [2006], and defining $\vec{U}$ as the mean depth-averaged velocity vector and $\overline{\zeta}$ as the mean free surface elevation, the hydrodynamic system of equations can be written as follows (the different stages to obtain these equations with the roller contribution are detailed in Appendix A):

$$\partial_t\overline{\zeta} + \partial_i\overline{h}U_i = -\partial_i\tilde{Q}_i \tag{2}$$

$$\partial_t U_i + U_j\partial_j U_i + g\partial_i\overline{\zeta} = -\partial_i\tilde{J} + \frac{D^r k_i}{\sigma_r\rho\overline{h}} + \frac{\tilde{Q}_j}{\overline{h}}\left(\partial_i U_j - \partial_j U_i\right) + \frac{H_i}{\rho\overline{h}} + \frac{\overline{\tau}_i^S - \overline{\tau}_i^B}{\rho\overline{h}} \tag{3}$$

where t is time, g is the gravitational acceleration, ρ is the fluid density, $\overline{h}$ is the mean water depth, H_i is the lateral turbulent shear stress and, τ_i^S and τ_i^B are the surface and bottom shear stresses, respectively. Finally, defining k_i as the wave number and σ_r as the relative frequency, the terms related to the waves (superscript w for the wave-organized motion and superscript r for the roller) can be described as mass transport of unbroken and broken waves Q_i^w and Q_i^r, respectively:

$$\tilde{Q}_i = Q_i^w + Q_i^r = \left(E^w + E^r\right)\frac{k_i}{\rho c k} \tag{4}$$

and the irrotational contribution to radiation stresses J^w and J^r:

$$\tilde{J} = J^w + J^r = \frac{E^w}{\rho\overline{h}}\left(\frac{c^g}{c} - \frac{1}{2}\right) + \frac{E^r}{2\rho\overline{h}} \tag{5}$$

with E^w and E^r the organized wave motion and roller energy, respectively, c and c^g are the phase and group celerities, respectively, ρ_r is the mass density of the roller and A_r is the area of the roller computed with the following balance equation: $\partial_t E^r + \partial_i[E^r\,(U_i + c_i)] = D^w - D^r$, where D^w is the wave energy dissipation computed according to *Battjes and Janssen* [1978]. The wave energy is classically defined as $E^w = \rho_g {H_{rms}}^2/8$, and the roller energy is evaluated with the formulation proposed by *Stive and De Vriend* [1994] and *Dally* [2001], that is, $E^r = \rho_r c A_r/T_m$. The roller energy dissipation is given by $D^r = g\beta_D E^r/c$ [*Dally and Brown*, 1995; *Dally*, 2001] with β_D a constant set to 1.

[16] The surface and bottom friction are given by

$$\overline{\tau}_i^S = \rho\ 0.0015\ \|\vec{U}^{Wind}\|\ U_i^{Wind} \tag{6}$$

$$\overline{\tau}_i^B = \frac{2}{\pi}\rho\ C_f\ \|\vec{U}^w\|\ U_i \tag{7}$$

where U^{Wind} is the wind velocity at 10 m and U^w is the wave orbital velocity magnitude. The friction coefficient C_f is set to 0.006.

[17] Defining $\nu_{t,i}$ as the horizontal turbulent eddy viscosity coefficient, the mixing term H_i is parameterized as

$$H_i = \rho\overline{h}\partial_j\left(\nu_{t,i}\partial_j U_i\right) \tag{8}$$

According to *Battjes* [1975], the wave breaking is the main process governing the mixing in the surf zone. In addition,

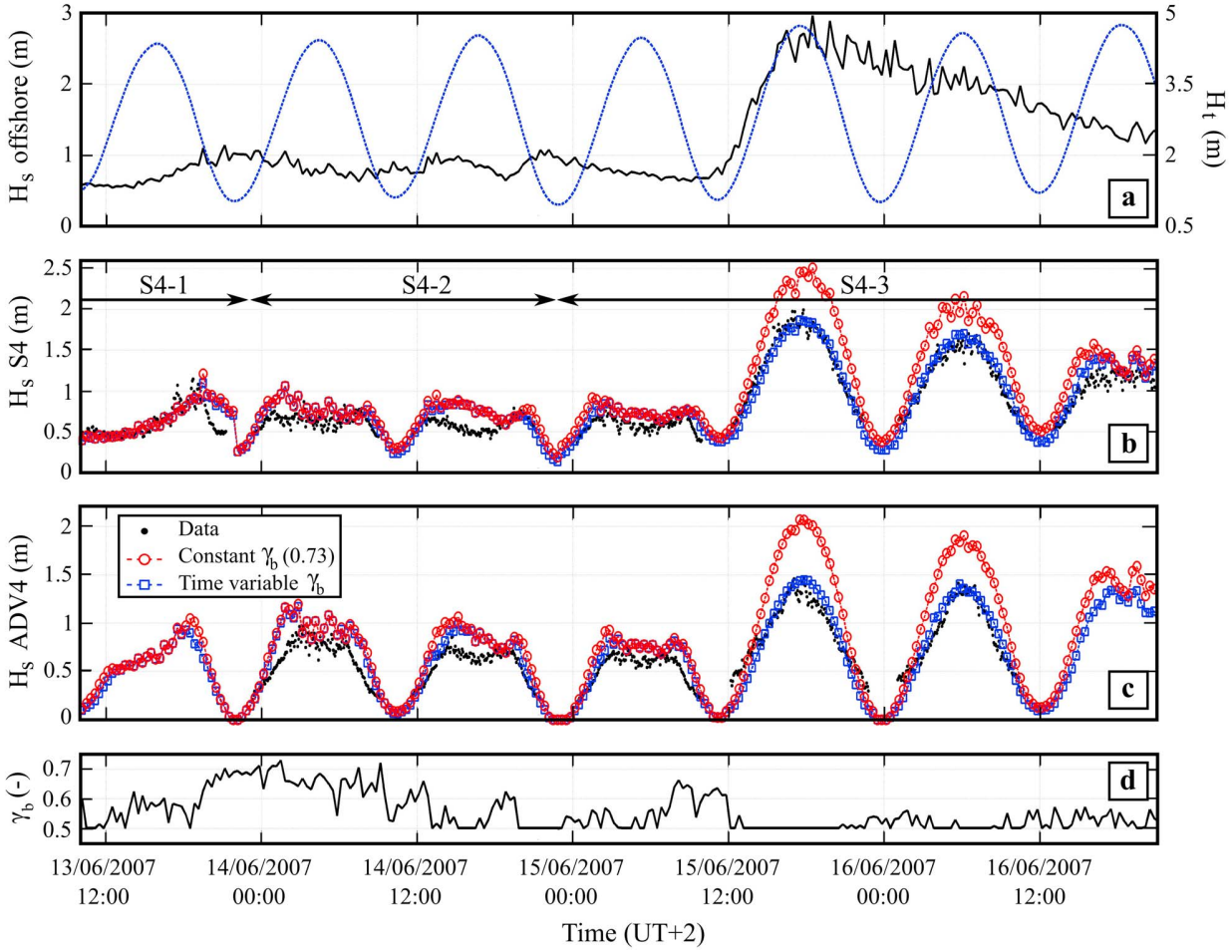

Figure 3. Time series of (a) offshore wave height (solid line) and tidal elevation (dashed line) and the comparisons between measured and modeled significant wave height at (b) the three S4 locations and (c) ADV4 for a constant breaking parameter (dashed line with circles) and for a time-varying breaking parameter (dashed line with squares). (d) The evolution of the computed time-varying breaking parameter γ_b.

considering small scale eddies associated to submesh processes, the global turbulent eddy viscosity $\nu_{t,i}$ coefficient is computed as follows:

$$\nu_{t,i} = M\bar{h}\left(\frac{D^w}{\rho}\right)^{1/3} + f_v\ 0.01\ \Delta_{s,i}^{1.15} \tag{9}$$

where M is a constant set to 7, f_v is 3 $m^{0.85}/s$ and $\Delta_{s,i}$ is the spacing in the i direction.

[18] To account for tide level variations, the signal recorded by the ADCP-2 (denoted H_t in Figure 2a) is imposed at the offshore boundary. Periodic lateral conditions are used. Thus, only a cross-shore propagation of the tide is modeled in this approach. Finally, a constant hydrodynamic time step of 0.8 s is used to solve the nonlinear shallow water equations on the same irregular rectangular grid as for SWAN (Figure 1a). To compute the mean currents and to filter the far-infragravity and infragravity current motions, a 20 min averaging is applied to the computed currents.

4. Application to the Biscarrosse Beach

4.1. Wave Simulations

4.1.1. Significant Wave Heights

[19] Figure 3 shows the comparison of the simulated significant wave height with that measured at the two sensors for both constant and time-varying breaking parameter. Results show that wave heights are significantly overestimated during the energetic event ($H_s > 2$ m) when using the constant default breaking parameter ($\gamma_b = 0.73$). The overestimation reaches 0.7 m for offshore significant wave heights of 2.5–3 m (25%). Using a time-varying γ_b improves the model ability to reproduce wave heights in the surf zone. The values of γ_b are illustrated in Figure 3d. During the low-energy period (the four first tidal cycles), γ_b ranges from 0.5 to 0.75 with a mean value of around 0.6–0.65 while

Table 1. RMS Errors Between the Significant Wave Height Measured and the Modeled

Sensors	S4	ADV4	PS1	PS2	PS3	PS4
Constant γ_b	29 cm	33 cm	27 cm	22 cm	15 cm	20 cm
Variable γ_b	14 cm	16 cm	16 cm	14 cm	11 cm	17 cm

it remains close to 0.5–0.55 during the energetic event. Table 1 summarizes the root-mean-square (RMS) errors obtained with the two γ_b parameterizations for a larger set of sensors. The use of the spatially constant but time-varying γ_b improves the results considerably (RMS errors of about 15 cm) with a halving of the RMS errors (about 30 cm with the constant γ_b). In addition, the correlation coefficients obtained between the data and the model predictions are greater than 0.9.

[20] For the time-varying γ_b, the results (Figure 3) show that (1) for both low-energy and high-energy conditions the model underestimates the wave heights at low-tide levels and (2) for low-energy waves the model overestimates wave heights around the midtide levels. The third cycle shows a contrasting behavior with a strong overprediction at high tide that is correlated with a significant wind event.

4.1.2. Ratio Between Wave Height and Depth: γ

[21] Figure 4 shows the time series of $\gamma = H_s/\bar{h}$ at two representative locations. Similar to previous comparisons of wave heights, the model is in good agreement with field data. During low-energy periods, both constant and time-varying γ_b curves fit well with the data while during the energetic event, the use of a time-varying γ_b substantially improves the model accuracy. Particularly, the ADV4 recordings (Figure 4b) highlight a threshold with a value $\gamma = 0.35$. This threshold is well represented with the variable γ_b but is strongly overestimated when using a constant γ_b that induces a saturation of γ at a value of 0.5. This behavior clearly shows that wave-energy dissipation through depth-induced breaking over a complex bar and rip morphology cannot be accurately modeled if using a time-invariant breaking parameter γ_b.

[22] Overall, the wavefields predicted by SWAN using a spatially constant and time-varying breaking parameter are in good agreement with the data obtained during the field experiment for both low-energy and high-energy periods. The RMS errors are on the order of 15 cm, which is reasonably low to subsequently investigate the topographically controlled wave-driven circulations.

4.2. Hydrodynamic Simulations

4.2.1. Offshore Mean Currents

[23] Wave and flow data were acquired outside the surf zone throughout the experiment by ADCP-2 deployed offshore of the crescentic subtidal outer bar (Figure 1a). The comparison between these (depth-averaged) mean flow data and the model results is given in Figure 5. For the cross-shore mean velocities (Figure 5a), the order of magnitude is well reproduced with currents lower than 5 cm/s and a clear tidal signal. For energetic conditions, weak offshore currents (undertow of about 15 cm/s) due to wave breaking over the outer bar are modeled, while no undertow is present in the measured sample. Figure 5b illustrates the major impact of wind on the alongshore currents. The data-model agreement improves significantly when wind is taken into account. Hence, only the simulations accounting for wind stresses are presented below. Of note, the tide signal is weakly visible (Figures 5b and 5c).

[24] To investigate the hydrodynamics above the outer bar during the full campaign, Figure 6 details the temporal evolution of the modeled cross-shore currents along an alongshore profile, located offshore of the outer bar (Figure 6a). During low-energy conditions, when waves do not break across the outer bar, flows are characterized by weak tide-induced

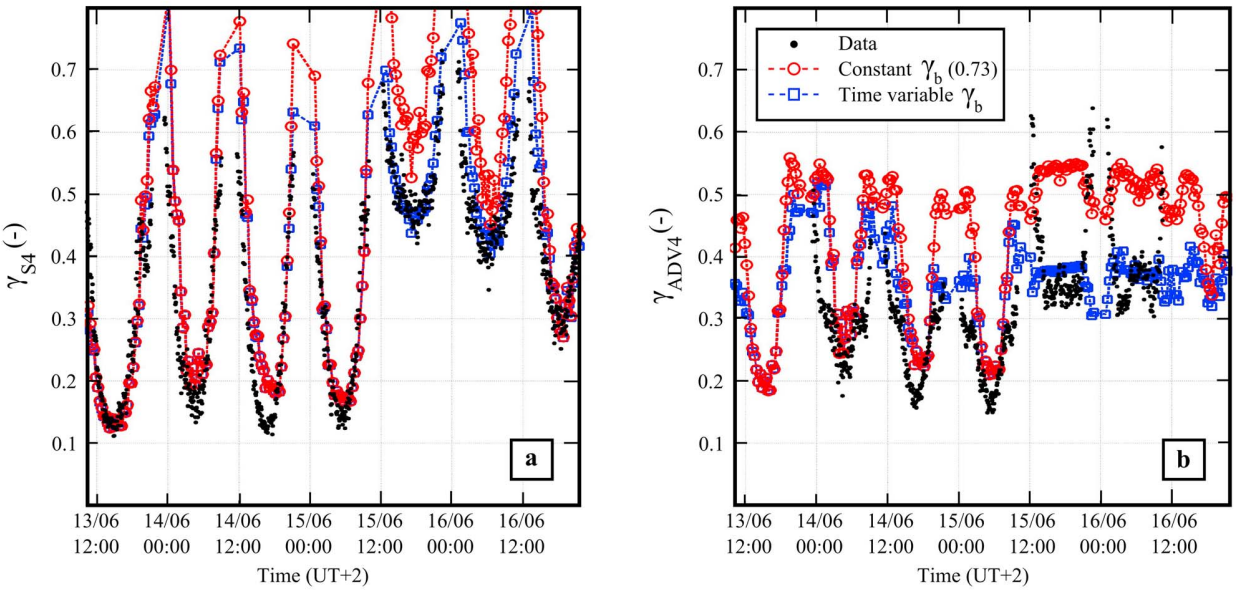

Figure 4. Time series of γ at (a) S4 and (b) ADV4. Black dots represent the measurements; the dashed line with squares (circles) illustrates the model results for a time-varying (constant) breaking parameter.

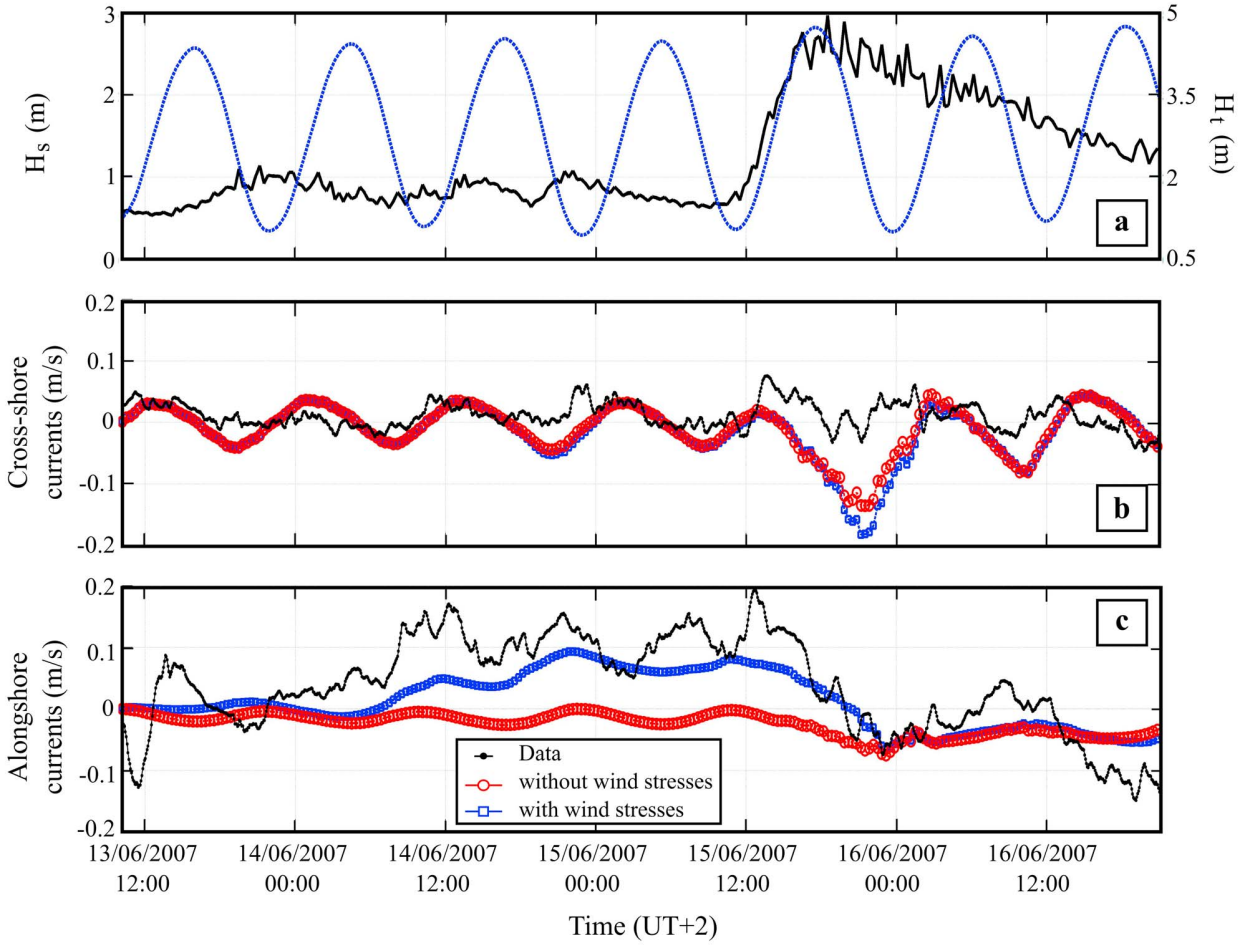

Figure 5. Time series of offshore 20-min-averaged currents (depth-averaged) at the ADCP-2 location. Time series of (a) offshore wave height (solid line) and tidal elevation (dashed line) and (b) cross-shore 20-min-averaged and depth-integrated velocity measured (black dots) and modeled without wind surface stresses (circles) and with wind surface stresses (squares). (c) Time series of 20-min-averaged and depth-integrated alongshore velocity. By convention, positive (negative) cross-shore currents indicate onshore- (offshore-) directed currents and positive (negative) alongshore currents indicate northward (southward) directed currents.

currents. With increasing offshore wave heights, waves break across the outer bar inducing a large offshore wave-driven circulation with onshore-directed currents across the crescent horn and offshore currents across the crescent bay. Figure 6c shows the strong alongshore variability of the cross-shore currents during the energetic conditions. Particularly, offshore (onshore) currents are weaker (stronger) at 50 m northward of the ADCP-2 (inducing better comparisons with the data in Figure 5).

4.2.2. Rip Current Behavior on a Mesotidal-Macrotidal Beach

[25] Figure 7 shows both the cross-shore and the alongshore components of the 20-min-averaged currents for the three locations of the S4 current meter (on the edge of the rip neck) and the ADV4 (southern feeder). For both the cross-shore and the alongshore directions and also for both the S4 and the ADV4, the flow behaviors are qualitatively reproduced by the model.

[26] Rip and feeder currents during the low-energy period are characterized by (1) strong mean currents (>0.4 m/s) between low and midtide with a maximum value reached between low and midtide and (2) weak currents between midtide and high tide (<0.05 m/s). This intense tide modulation is well predicted by our approach (RMS error less than 0.1 m/s and correlation coefficients in the order of 0.6–0.85 except for the alongshore currents at the S4 location where the correlation coefficient is of 0.25). When the S4 was deployed close to the rip neck (S4-1), both data and model results show the presence of a strong rip current (reaching 0.75 m/s) despite reasonably low-energy wave conditions (H_s < 1 m). At S4-2 and S4-3 locations (on the edge of the bar), the results (data and model in Figure 7b) indicate onshore-directed currents for low tide levels. With increasing tide levels from low to midtide, the breaking line shifts onshore and both measurements and model results show offshore-directed currents (rip currents). For the alongshore

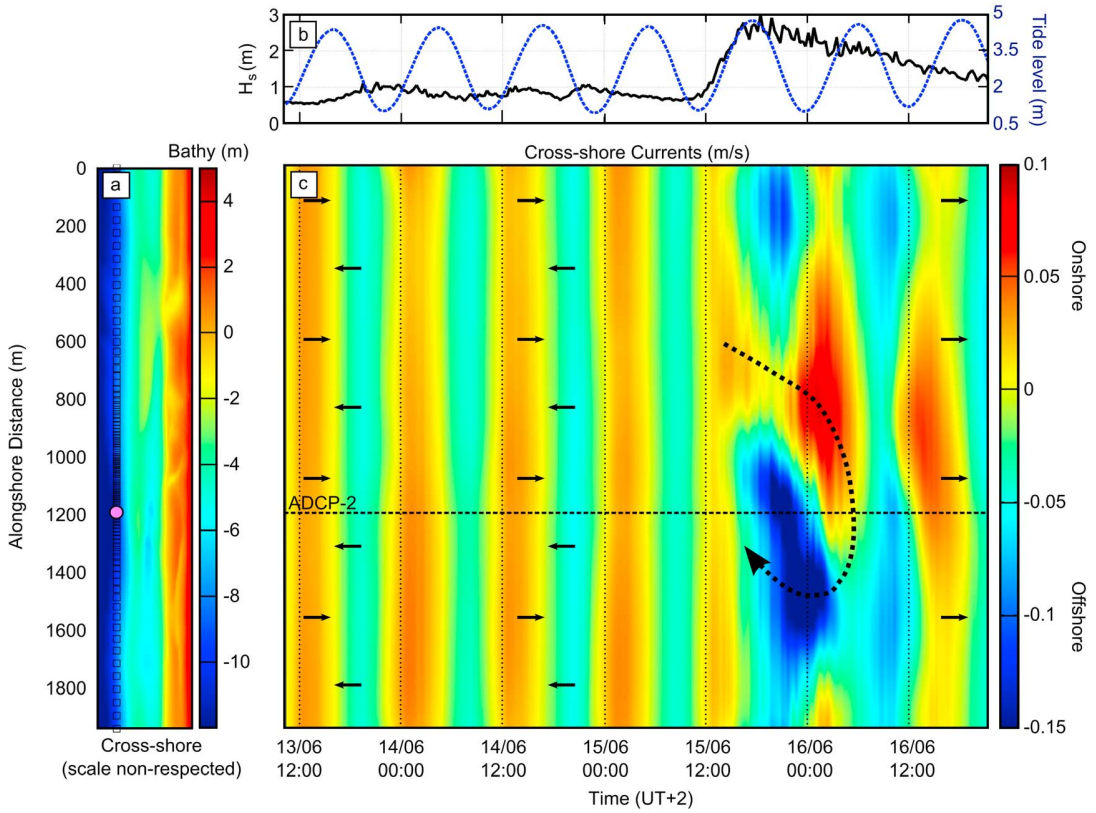

Figure 6. (a) Bathymetry with an unscaled cross-shore direction. Each square represents a node where cross-shore velocities are exported. (b) Time series of offshore significant wave height (solid line) and tidal levels (dashed line). (c) Time series of cross-shore currents along the alongshore profile. Dark and dotted arrows represent current directions.

currents (Figures 7c and 7e), overall, the model predictions are good despite a systematic small underestimation of the velocity (Figure 7e).

[27] When energetic conditions occur (from 15 June, 12:00 LT), strong offshore-directed currents are measured by both the S4 and the ADV4. The model underestimates this behavior with only weak offshore-directed currents (RMS errors <0.20 m/s and correlation coefficients of 0.4–0.7). During the first energetic cycle, the model computes onshore currents when the data show the presence of offshore currents (Figure 7d). On the one hand, these results point out the potential difficulties to model strong undertow with a depth-averaged approach where the vertical variability of the currents is not taken into account (see existing 3D modeling investigations of rip currents by *Haas et al.* [2003], *Reniers et al.* [2009], and *Haas and Warner* [2009]). On the other hand, the alongshore currents (Figures 7c and 7e) are well reproduced by the model. Finally, results obtained 3–4 grid meshes northward of the ADV4 location show better agreement with the data (Figure 10f; flow field during the energetic event with the presence of offshore directed currents northward of the ADV4), which suggests the potential impact of the bathymetry on obtaining good flow predictions. It illustrates the efficiency of the model to reproduce qualitatively the complex dynamics of rip currents even during an energetic event.

[28] Both the model and the data highlight the asymmetric behavior of the currents between the rising and the falling tide (Figures 7b and 7d). During the low-energy period, for similar offshore wave conditions, results at the S4 location show more intense rip current during the decreasing tide. In contrast, the ADV4 (onshore currents) shows lower onshore currents during the decreasing tide than during the rising tide.

5. Analysis of Rip Current Circulation Generation

5.1. Source Terms of the Momentum Equations

[29] As explained in section 3, the wave forcing in the momentum equations is composed by three driving source terms in equation (3): (1) $-\partial_i \widetilde{J}$, (2) $D^r k_i/\sigma_r \rho \overline{h}$ and (3) $(\widetilde{Q_j}/\overline{h})$ $(\partial_i U_j - \partial_j U_i)$. Figure 8 displays the spatial distributions of the intensity and directions of each term for offshore shore-normal waves with H_s = 1 m and T_p = 9 s. The first source force (irrotational), mainly linked to H_s^2, is directed seaward offshore of the breaking point due to the shoaling and onshore in the surf zone (Figure 8a). Further inshore, this term is directed from the edge of the bar to the rip neck due

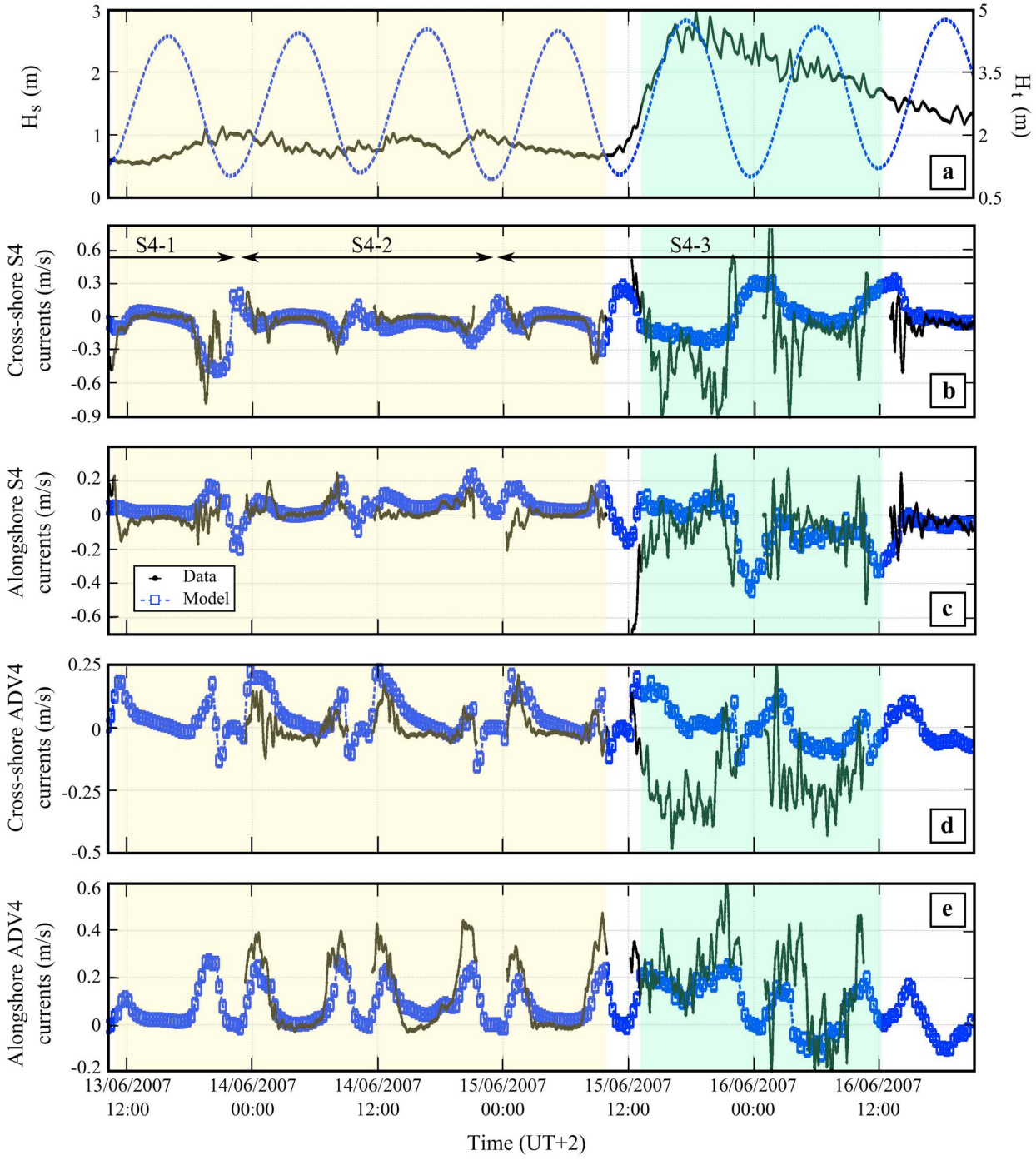

Figure 7. Time series of (a) offshore wave height (solid line) and tidal elevation (dashed line), (b) 20-min-averaged cross-shore current at S4-1, S4-2 and S4-3, (c) 20-min-averaged alongshore current at S4-1, S4-2 and S4-3, (d) 20-min-averaged cross-shore at ADV4, (e) 20-min-averaged alongshore at ADV4. In Figures 7b–7e the data are represented by black dots and model results are represented by the dashed line with squares. By convention, positive (negative) cross-shore currents indicate onshore- (offshore-) directed currents and positive (negative) alongshore currents indicate northward (southward) directed currents. The two shaded areas define two different rip behaviors: tidal modulation for low-energy waves and undertow during energetic conditions.

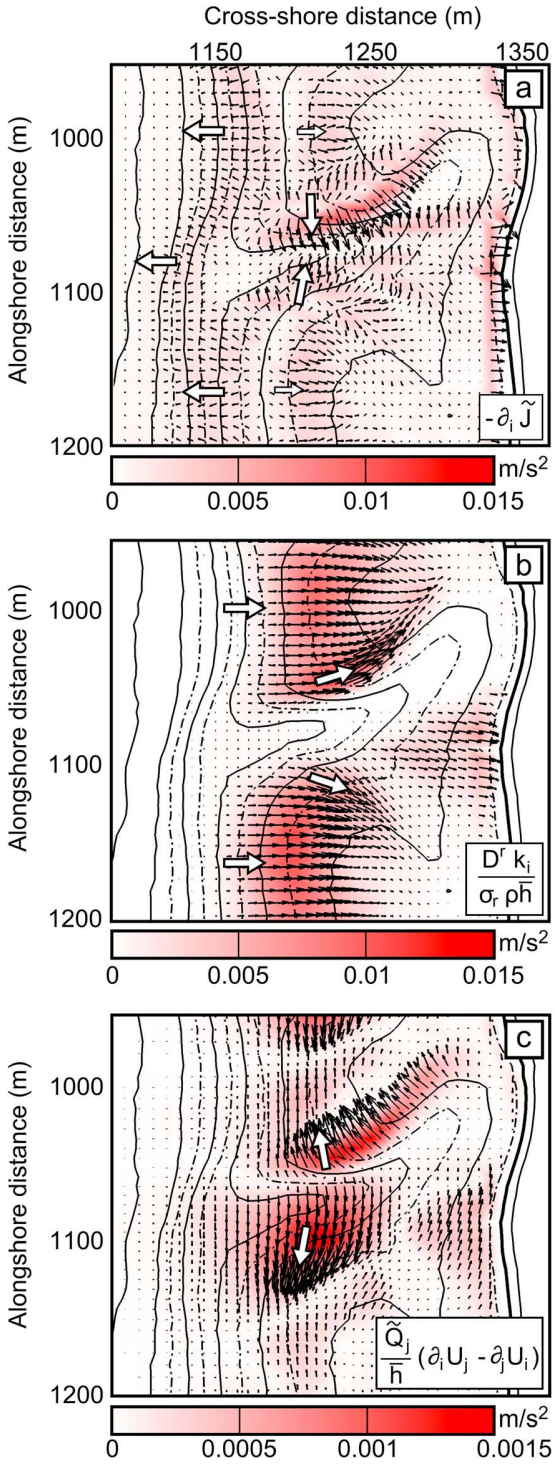

Figure 8. Comparison of the modeled wave source terms of the momentum equations for a midtide condition and a typical wave climate (H_t = 1.75 m, H_s = 1 m, T_p = 9 s with a shore-normal incidence): (a) $-\partial_i \tilde{J}$, (b) $D^r k_i/\sigma_r \rho \bar{h}$ and (c) $(\tilde{Q}_j/\bar{h})(\partial_i U_j - \partial_j U_i)$. The arrows represent the main direction of the forcing.

to wave refraction. The second term, which is driven by the energy dissipation, is significant above the bar where waves break and almost vanishes in the rip channel (Figure 8b). In addition, this term follows the wave propagation rays. Finally, the last term (called vortex force) is only persistent at the rip edges and is directed from the channel to the edges. While this source is smaller than the two previous ones, it tends to compensate the first term and to strengthen the jet as it was suggested by *Ardhuin* [2005]. The formulation used herein provides a decomposition of the driving source forces to interpret wave-induced currents and circulations.

5.2. Vorticity Theory

[30] Previous studies [*Bühler*, 2000; *Bühler and Jacobson*, 2001] presented a general theoretical analysis of wave-driven currents and vortex dynamics due to dissipating waves. In the present approach, as it is defined in equations (2) and (3), irrotational and rotational terms are clearly dissociated (which is not the case when considering the radiation stress approach). According to the previous works of *Bruneau et al.* [2008] and *Bonneton et al.* [2010] and

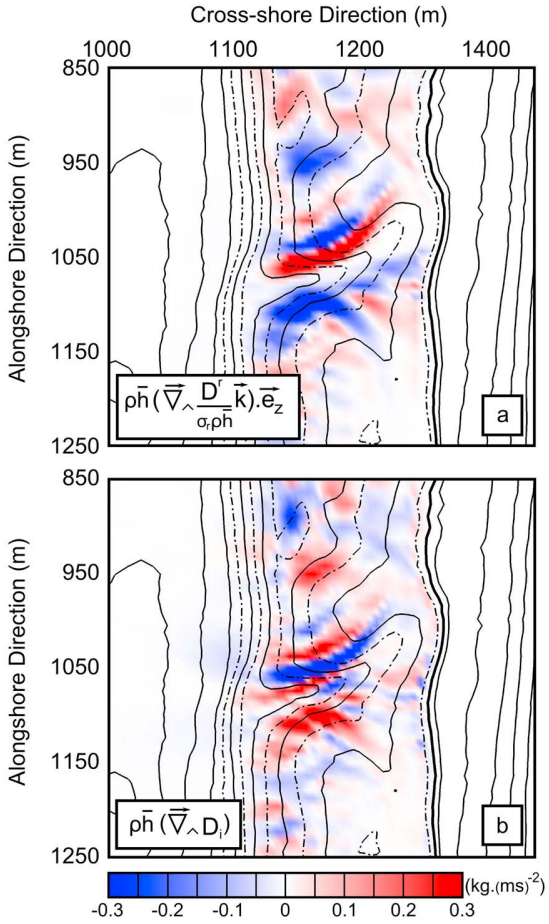

Figure 9. Snapshots of the two main source terms (model) of the vorticity conservation equation for a low-tide/midtide condition and a typical wave climate (H_t = 1.75 m, H_s = 1 m, T_p = 9 s with a shore-normal incidence): (a) the vorticity forcing term and (b) the diffusion term.

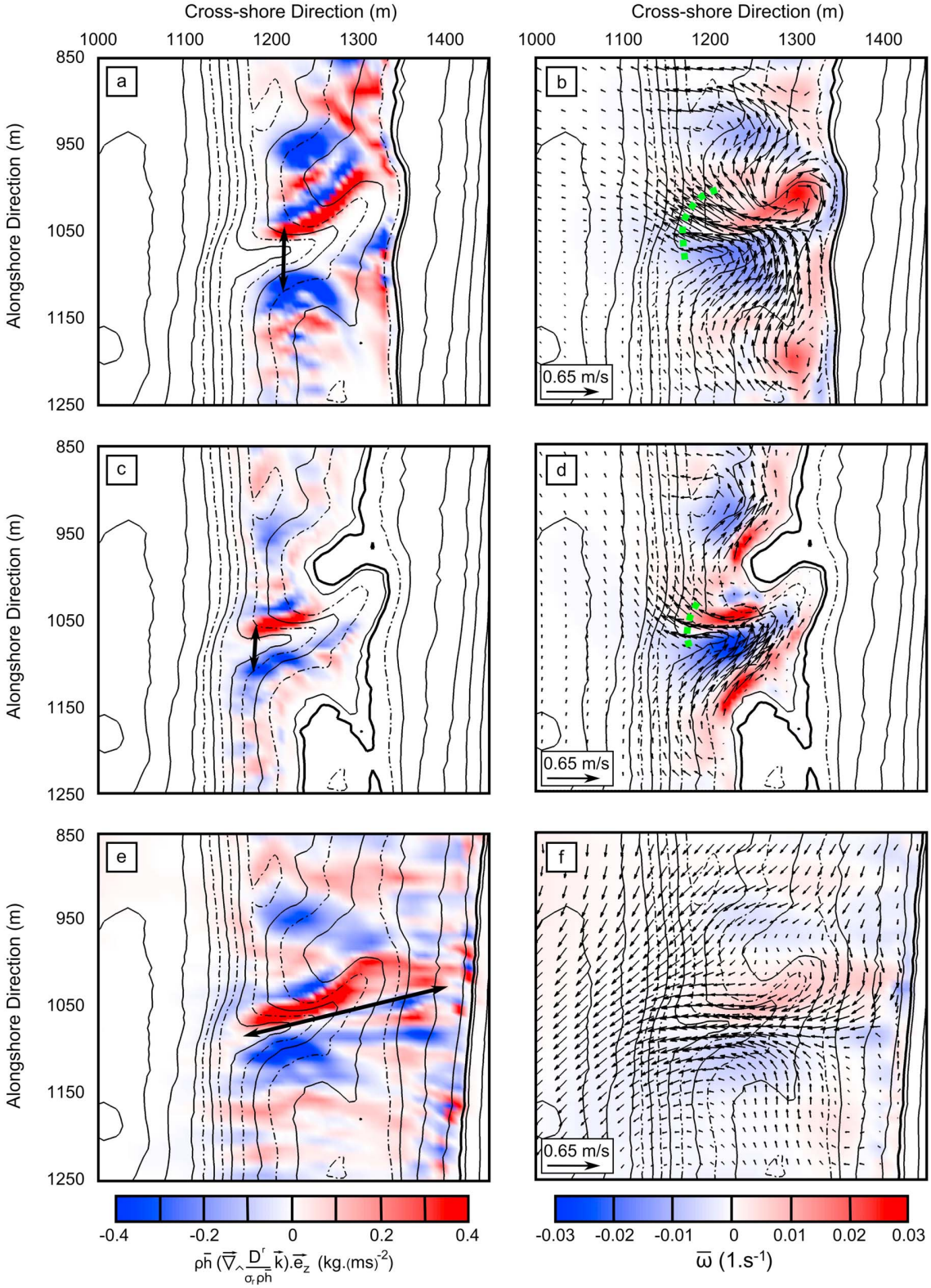

Figure 10. Snapshots of the vorticity forcing term calculated from the modeled wavefield (Figures 10a, 10c, and 10e) and the computed 20-min-averaged vorticity and currents at three contrasting moments (Figures 10b, 10d, and 10f) on (a and b) 14 June at 08:30 LT (UT + 2), (c and d) 14 June at 10:30 LT (UT + 2) and (d and e) 15 June, at 17:50 LT (UT + 2). Black arrows indicate cell separation distance or cell cross-shore extension and dotted green curves, Figures 10b–10d, give the rip width.

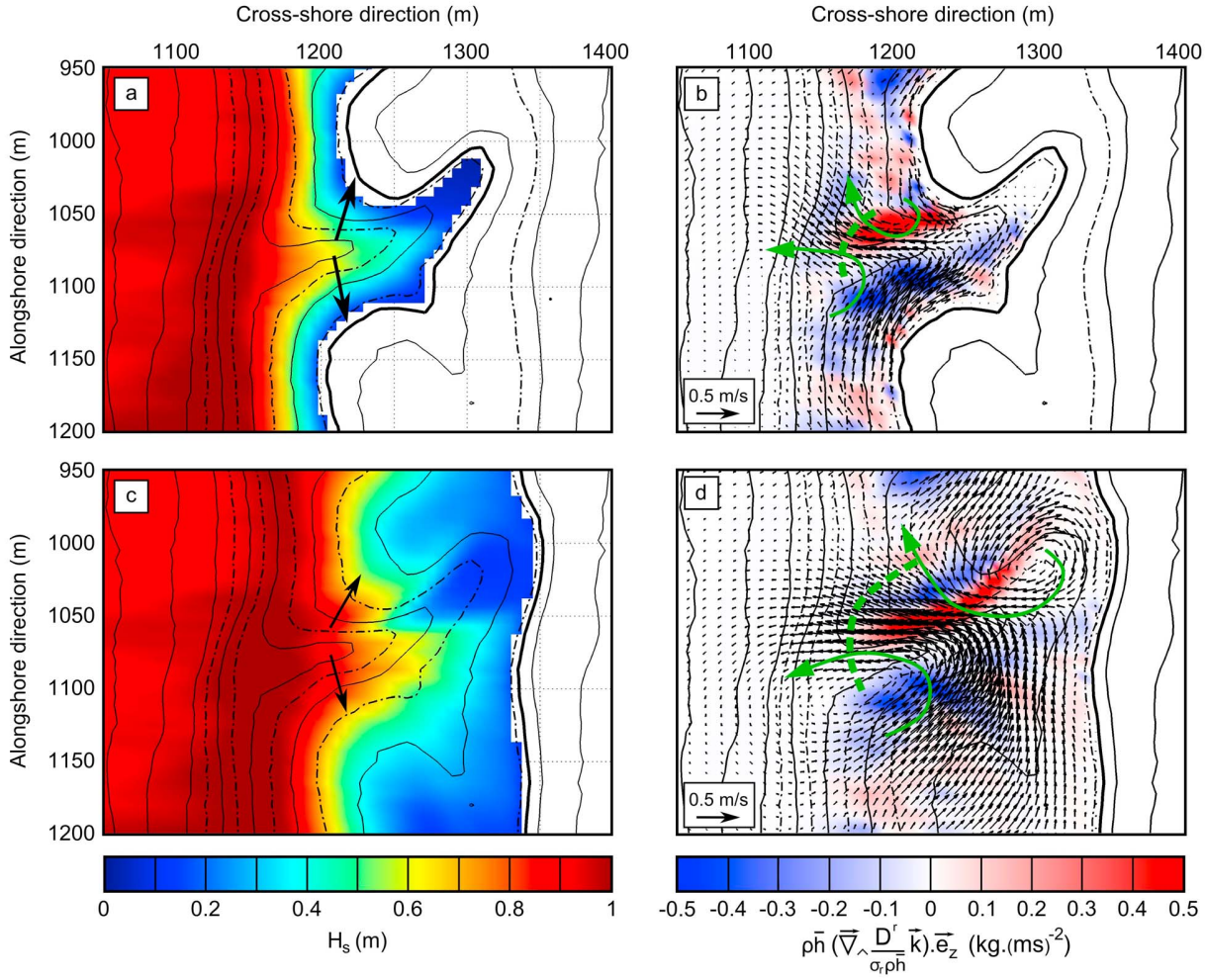

Figure 11. Example of rip current enlargement with increasing tide levels for a typical wave climate, H_s = 1 m, T_p = 9 s with a shore-normal incidence. Snapshots of the significant wave heights (Figures 11a and 11c) and the modeled vorticity forcing term superimposed on the modeled velocity field at two different instants (Figures 11b and 11d) for (a and b) low-tide H_t = 0.75 m and (c and d) low-tide/midtide H_t = 1.75 m. Black arrows indicate the significant wave height gradients, and the large dash-dotted line indicates the position where waves start to break. Dashed green curves show the rip width.

neglecting the friction term (that is around one order of magnitude lower than the two others in the surf zone), we can derive the mean vorticity $\overline{w} = (\vec{\nabla} \wedge \vec{U}) \cdot \vec{e}_z$ conservation equation (only along the vertical in a two-dimensional approach) that reads:

$$\partial_t \overline{w} + \vec{\nabla} \cdot \left[\overline{w} \left(\vec{U} + \frac{\vec{\overline{Q}}}{\overline{h}} \right) \right] = \left(\vec{\nabla} \wedge \left[\frac{D^r}{\sigma_r \rho \overline{h}} \vec{k} \right] \right) \cdot \vec{e}_z + \left(\vec{\nabla} \wedge H_i \right) . \vec{e}_z \tag{10}$$

According to the linear theory, the first term of the right-hand side can be simplified to $(\vec{\nabla}(D^r/\sigma_r \rho \overline{h}) \wedge \vec{k}) \cdot \vec{e}_z$. For a constant eddy viscosity coefficient ν_t, the second source term of equation (10) can be rearranged into a turbulent diffusion term $\nu_t \nabla^2 \overline{w}$. The two terms of the right-hand side describe the production and the dissipation of mean vorticity, respectively. The production term is only active in presence of breaking waves, when the gradient of dissipation is not collinear with the wave propagation direction. Figure 9 presents both the eddy turbulent diffusion term and the term linked to the wave dissipation, which are of the same order of magnitude. The two terms in the left-hand side of equation (10), the local variation of the vorticity and advection, are small when the other two terms are active (not shown). Hence, the two main terms compensate more or less one another and the forcing term associated with the wave dissipation controls the mean flow vorticity. As the wave dissipation forcing term is the source of the vorticity, this modeled forcing and vorticity terms have good correlations (>0.7 and close to 1 near the rip edges).

[31] This formulation is a simple and efficient tool to investigate the generation of circulation cells in the surf zone, such as rip currents. This approach proved its efficiency to understand vortical motions of a rip current above an idealized bar and rip morphology [*Bonneton et al.*, 2010].

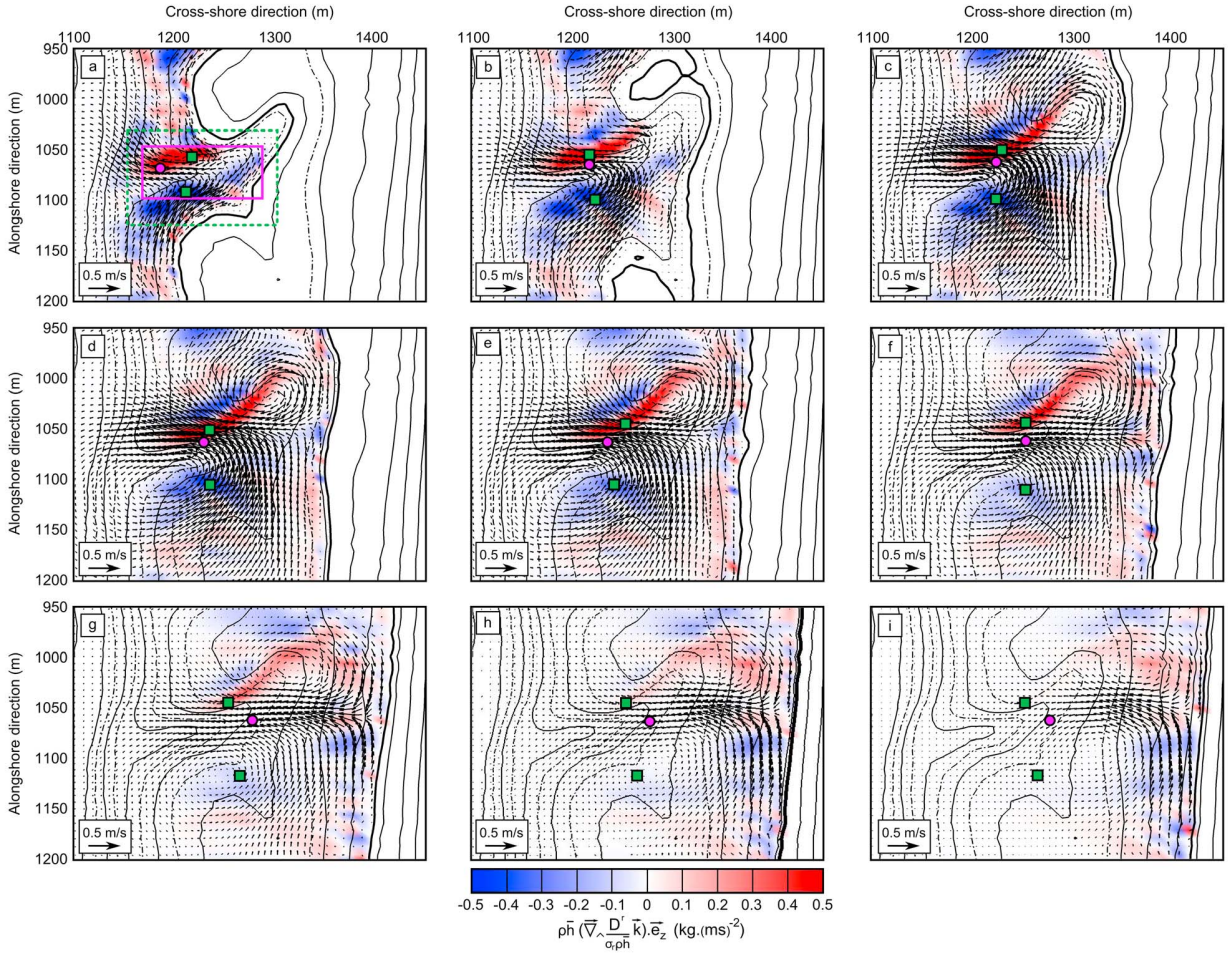

Figure 12. Snapshots of the computed vorticity forcing term superimposed on the modeled currents for different tide levels of (a) H_t = 0.75 m, (b) H_t = 1.25 m, (c) H_t = 1.75 m, (d) H_t = 2.25 m, (e) H_t = 2.75 m, (f) H_t = 3.25 m, (g) H_t = 3.75 m, (h) H_t = 4.25 m and (i) H_t = 4.75 m. Wave conditions are the same as in Figure 11. Squares give the position of the relative maxima and minima of the forcing term, and circles indicate the location of the maximum rip currents. The two boxes in Figure 12a illustrate the domain where local extrema are identified: dashed green box for the vorticity forcing term and purple box for the maximum rip velocity.

In the present work, we focus on a complex field bar and rip morphology (Biscarrosse field experiment presented above), both to investigate the validity of equation (10) and to improve our knowledge on the generation of wave-driven circulation in a high-energy rip current system.

5.3. Application to Biscarrosse Beach

[32] The theory detailed in section 5.2 is now applied to the Biscarrosse experiment to analyze the behavior of the forcing term $(\vec{\nabla} \wedge [\frac{D^r}{\sigma_r \rho h}\vec{k}]) \cdot \vec{e}_z$ and its impact on the mean wave-driven circulations for different wave and tide conditions. Figure 10 describes three different forcing conditions: (1) at midtide, for low-energy waves, 14 June at 08:30 LT (UT + 2) (Figures 10a and 10b), (2) at low tide, for low-energy waves, 14 June at 10:30 LT (Figures 10c and 10d) and (3) close to high tide with energetic waves, 15 June at 17:50 LT (Figures 10e and 10f). In Figure 10c, the distance between the two vorticity cells is very small inducing a narrow and intense rip current (around 30 m wide, Figure 10d). With increasing tide levels (Figure 10a), the distance separating the two main cells increases, widening the rip throat (around 90 m wide, Figure 10b). Finally, Figures 10e and 10f show a cross-shore extension of the forcing term cells due to both the high-tide level and a larger surf zone (energetic waves). These extended and narrow shapes tend to illustrate the weak character of the rotational nature of mean currents with a low alongshore variability which characterizes the presence of undertow.

5.4. Main Predicted Behaviors of the Rip Current

[33] To investigate in depth the physical processes driving rip current circulations, we consider a typical low-energy condition (H_s = 1 m, T_p = 9 s and a shore-normal incidence). As the rip current is not active at high tide for this low-energy wave forcing [*Bruneau et al.*, 2009a], only two tide levels are investigated here: a low-tide level (H_t = 0.75 m)

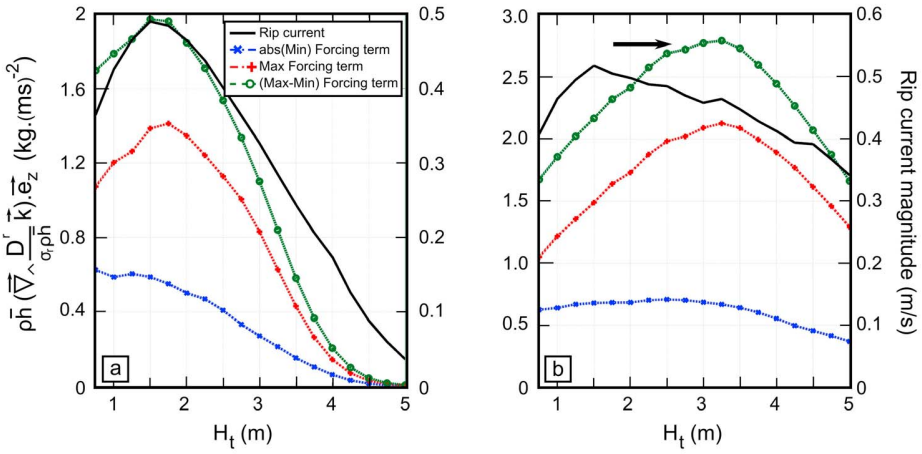

Figure 13. Evolution of both the modeled rip current magnitude (solid line) and the characteristics of the modeled forcing term (minimum (crosses), maximum (pluses) and the gradient maximum-minimum (circles)) function of the tide levels (model results) (a) for low-energy waves (H_s = 1 m, T_p = 9 s with a shore-normal incidence) and (b) for energetic conditions (H_s = 2 m, T_p = 9 s with a shore-normal incidence).

and a low tide/midtide level (H_t = 1.75 m). Figure 11 details both the wavefield (H_s) and the mean vorticity forcing term with superimposed mean currents. At low tide, when sandbars are not submerged, waves mostly break offshore of the bar and rip morphology. Wave refraction close to the bar is weaker (Figure 11a), but an important alongshore gradient of H_s is present between the rip channel and the edges of the bars (Figure 11a) that induces two circulation cells. The centers of these circulations are close and they are located in the edge of the rip current system. The flows are drained from the shoals to the deepest part of the rip channel through a narrow jet (Figure 11b, 40 m wide and rip currents of 0.41 cm/s).

[34] For higher tide levels (mid tide), when sandbars are submerged, wave refraction is stronger over the bar and rip morphology (Figure 11c) but alongshore gradients of H_s are weak. Both the distance between the two cells and the intensity of the forcing term increase. Hence, the rip current widens and its velocity increases (Figure 11d, 80 m wide rip currents of around 0.48 cm/s).

[35] Figure 12 details the spatial evolution of the mean vorticity forcing term during a full tide cycle for low-energy conditions. Except at low tide, the maximum rip current intensity is located between the two extrema of the forcing term (but not systematically in the middle). Even though the rip current maximum is always located close to the most significant extremum, no clear correlation was found between maximum rip current locations and the forcing term intensity. With increasing tide levels, the forcing term cells extend in the cross-shore direction. The maximum rip current magnitude increases from low tide to low-tide/midtide levels (compare Figure 13a, black curve) and subsequently decreases rapidly when waves break onshore of the bar and rip morphology. In the meantime, the intensity of the forcing term also decreases. Both maximum rip current magnitudes and characteristics of the vorticity forcing term are illustrated in Figure 13 as a function of the tide level for low-energy shore-normal waves (Figure 13a, H_s = 1 m) and more energetic waves (Figure 13b, H_s = 2 m). Figure 13 shows the strong correlation between the rip current magnitude and the gradient between the maximum and the minimum of the forcing term (correlation greater than 0.95, except for the energetic wave conditions; Table 2). For low-energy conditions, the occurrence of maximum rip current between low tide and midtide is well predicted by the min/max gradient of the forcing term. For a more energetic event, the peak of the gradient is obtained for a higher tide level than the maximum rip current magnitude. The correlation coefficients for the min/max gradient are very good (correlation > 0.95) except for the shore-normal energetic conditions (0.45). In addition, the quality of the correlation coefficients (between the modeled forcing term and the modeled vorticity field) is not affected by wave direction or period at the offshore boundary (Table 2).

[36] These examples illustrate the potential of the formulation proposed above. From a computed wavefield on a given morphology, it is possible to investigate the shapes of the circulations and some characteristics of the rip current such as its location, its width and its extension. The good correlations obtained between the maximum rip current and the min/max deviation demonstrate the capacity of the approach to characterize the intensity of rip currents. The proposed model provides an useful and simple tool to investigate the vortical motions. Thus, computing the vertical vorticity conservation equation from a wavefield

Table 2. Correlation Coefficient (CC) Between the Rip Current Magnitudes and the Gradient Max-Min of the Forcing Term

H_s (m)	T_p (s)	Wave Type	CC
1	9	shore-normal	0.98
1	6	shore-normal	0.97
1	12	shore-normal	0.97
2	9	shore-normal	0.45
1	9	15° incidence N	0.95
1	9	15° incidence S	0.99

efficiently determines the strength and sign of the wave-driven circulation rotational nature, which is not possible with the traditional radiation stress approach.

6. Conclusions

[37] In this paper, a modeling strategy based on the depth-averaged and time-averaged momentum equations accounting for roller contribution was presented and applied to an evolving rip current system at the mesotidal-macrotidal Biscarrosse Beach. Computed wave heights and wave-driven currents show good agreement with field data using the spatially constant and time-varying breaking parameter suggested by *Smith and Kraus* [1990].

[38] In addition, we derived a conservation equation of the vertical vorticity of the mean wave-driven currents. This equation shows that the vorticity forcing term $(\vec{\nabla} \wedge [(D^r/\sigma_r \rho \overline{h})\,\vec{k}]) \cdot \vec{e}_z$, due to spatial gradients in broken-wave energy dissipation, is the only major source of topographically controlled wave-driven circulations. This term allows a straightforward qualitative prediction of some rip current characteristics such as its width, location, cross-shore extension or intensity. Good correlations are found between maximum rip current intensity and the gradient between the maximum and the minimum of the forcing term. Therefore, spatial gradients in depth-induced broken-wave energy dissipation determine both the strength and the sign of the rip current system rotational nature. Thus, computing this simple vertical vorticity conservation equation from a wavefield provides straightforward information on rip current circulations that was difficult to interpret through the traditional radiation stress approach.

Appendix A: Nonlinear Shallow Water Equations

[39] This appendix details the derivation of equations (2) and (3) given in section 3.2. The following is from the work by *Smith* [2006], where the roller distribution was included. Neglecting the Coriolis forces, the basic system of equations to solve the hydrodynamics in the surf zone, according to *Phillips* [1977] and accounting for the roller contribution [*Dally*, 2001], is given by

$$\partial_t \overline{\zeta} + \partial_i \overline{h} U_i = -\partial_i \tilde{Q}_i \tag{A1}$$

$$\partial_t U_i + U_j \partial_j U_i + g \partial_i \overline{\zeta} = -\frac{1}{\rho \overline{h}} \partial_j \left(S_{ij} + R_{ij}\right) - \frac{1}{\overline{h}} \partial_j \left[U_j \tilde{Q}_j\right] - \frac{\tilde{Q}_j}{\overline{h}} \partial_j U_i + \frac{H_i}{\rho \overline{h}} + \frac{\overline{\tau}_i^S - \overline{\tau}_i^B}{\rho \overline{h}} - \frac{1}{\overline{h}} \partial_t \tilde{Q}_j \tag{A2}$$

where the radiation S_{ij} and roller R_{ij} stresses are expressed as

$$S_{ij} = E^w \left(\frac{k_i k_j}{k^2} \frac{c^g}{c} + \delta_{ij} \left(\frac{c^g}{c} - \frac{1}{2}\right)\right) = \rho Q_i^w c_j^g + \rho \overline{h} J^w \delta_{ij} \tag{A3}$$

$$R_{ij} = c \left(\frac{\rho_r A_r}{T}\right) \left(\frac{k_i k_j}{k^2} + \frac{\delta_{ij}}{2}\right) = \rho Q_i^r c_j + \rho \overline{h} J^r \delta_{ij} \tag{A4}$$

respectively, in which J^w and J^r are defined as in equation (5). These decompositions are integrated into (A2) that becomes

$$\partial_t U_i + U_j \partial_j U_i + g\, \partial_i \overline{\zeta} = -\frac{1}{\overline{h}} \overbrace{\left[\partial_t \left(Q_i^w + Q_i^r\right) + \partial_j \left(Q_i^w \left(c_j^g + U_j\right) + Q_i^r \left(c_j + U_j\right)\right)\right]}^{\text{(WADBE)}} - \frac{Q_j^w + Q_j^r}{\overline{h}} \partial_j U_i - \frac{1}{\overline{h}} \partial_i \left[\overline{h}(J^w + J^r)\right] + \frac{H_i}{\rho \overline{h}} + \frac{\overline{\tau}_i^S - \overline{\tau}_i^B}{\rho \overline{h}} \tag{A5}$$

[40] Using the definitions of Q_i^w and Q_i^r, the term WADBE can be developed as follows:

$$\text{WADBE} = \frac{1}{\rho} \left[\frac{E^w + E^r}{\sigma_r} \partial_t k_i + \left(\frac{E^w}{\sigma_r} \left(c_j^g + U_j\right) + \frac{E^r}{\sigma_r} \left(c_j + U_j\right)\right) \partial_j k_i\right] + \frac{k_i}{\rho} \left[\partial_t \frac{E^w + E^r}{\sigma_r} + \partial_j \frac{E^w}{\sigma_r} \left(c_j^g + U_j\right) + \partial_j \frac{E^r}{\sigma_r} \left(c_j + U_j\right)\right] \tag{A6}$$

[41] The second part of (A6) highlights the wave action density equation due to both wave-organized motion and roller contribution (assuming that the relative frequency varies smoothly in time and space):

$$\partial_t \left(\frac{E^w + E^r}{\sigma_r}\right) + \partial_j \left[\frac{E^w}{\sigma_r} \left(c_j^g + U_j\right)\right] + \partial_j \left[\frac{E^r}{\sigma_r} \left(c_j + U_j\right)\right] = -\frac{D^r}{\sigma_r} \tag{A7}$$

Using the irrotationality of the wave number, the wave crest conservation equation [*Mei*, 1989] is written

$$\partial_t k_i + \left(c_j^g + U_j\right) \partial_j\, k_i = -k_j \partial_i U_j - \partial_{\overline{h}} \sigma_r\, \partial_i \overline{h} \tag{A8}$$

Thus, introducing (A7) in (A5), using the wave crest conservation equation (A8) and assuming that the wave velocity is equal to the group velocity (this approximation is verified in the surf zone), equation (A5) becomes

$$\partial_t U_i + U_j \partial_j U_i + g \partial_i \overline{\zeta} = \frac{k_i D^r}{\rho \overline{h} \sigma_r} + \frac{1}{\rho \overline{h}} \frac{E^w + E^r}{\sigma_r} \partial_{\overline{h}} \sigma_r\, \partial_i \overline{h} + \frac{\tilde{Q}_j}{\overline{h}} \left[\partial_i U_j - \partial_j U_i\right] - \frac{1}{\overline{h}} \partial_i \left[\overline{h} \tilde{J}\right] + \frac{H_i}{\rho \overline{h}} + \frac{\overline{\tau}_i^S - \overline{\tau}_i^B}{\rho \overline{h}} \tag{A9}$$

The dispersion relation enables the treatment of

$$\frac{E^w + E^r}{\sigma_r} \partial_{\overline{h}} \sigma_r = \frac{E^w + E^r}{\sigma_r} \frac{k}{\overline{h}} \left(\partial_k \sigma_r - \frac{\sigma_r}{2k}\right) = \frac{E_w + E_r}{c \overline{h}} \left(c^g - \frac{c}{2}\right) = \rho (J_w + J_r) \tag{A10}$$

[42] Finally, after a last simplification, the system of equations reads

$$\partial_t \overline{\zeta} + \partial_i \overline{h} U_i = -\partial_i \tilde{Q}_i \tag{A11}$$

$$\partial_t U_i + U_j \partial_j U_i + g \partial_i \overline{\zeta} = -\partial_i \tilde{J} + \frac{D^r k_i}{\sigma_r \rho \overline{h}} + \frac{\tilde{Q}_j}{\overline{h}} \left(\partial_i U_j - \partial_j U_i \right) + \frac{H_i}{\rho \overline{h}} + \frac{\overline{\tau}_i^S - \overline{\tau}_i^B}{\rho \overline{h}} \tag{A12}$$

[43] **Acknowledgments.** This Biscarrosse 2007 campaign was carried out thanks to the financial support of the BRGM. This study was performed within the framework of the ECORS (SHOM) project and the MODLIT (SHOM and INSU) project that have also sponsored this study. The authors thank the French Navy (SHOM) for the large bathymetry survey carried out on the studied field that was required for such an experiment. They are also grateful to the teams and students involved in the field experiment. The authors thank the developers of the models SWAN and MARS. The authors also thank André Fortunato for his comments and his help in improving the English quality of the paper. This work was partially funded by a postdoctoral research grant to the first author from the Fundação para a Ciência (SFRH/BPD/67041/2009). The third author acknowledges support from BARBEC (ANR 2010 JCJC 602 01). Finally, this work is dedicated to our friend and colleague Denis Michel, who tragically passed away during this field experiment.

References

Almar, R., B. Castelle, B. G. Ruessink, N. Sénéchal, P. Bonneton, and V. Marieu (2010), Two- and three-dimensional double-sandbar system behaviour under intense wave forcing and a meso–macro tidal range, *Cont. Shelf Res.*, *30*(7), 781–792, doi:10.1016/j.csr.2010.02.001.

Ardhuin, F. (2005), État de mer et dynamique de l'océan superficiel, Habilitation à diriger des recherches, thesis, Univ. de Bretagne Occidental, Brest, France.

Battjes, J. A. (1975), Modeling of turbulence in the surf zone, in *Proceedings of Symposium on Modelling Techniques*, vol. 2, pp. 1050–1061, Am. Soc. of Civ. Eng., San Francisco, Calif.

Battjes, J. A. (1988), Surf-zone dynamics, *Annu. Rev. Fluid Mech.*, *20*, 257–291, doi:10.1146/annurev.fl.20.010188.001353.

Battjes, J. A., and J. P. F. M. Janssen (1978), Energy loss and set-up due to breaking of random waves, in *Proceedings of Sixteenth Coastal Engineering Conference, Hamburg, Germany, Aug. 27–Sept. 3, 1978*, pp. 569–587, Am. Soc. of Civ. Eng., New York.

Bertin, X., A. B. Fortunato, and A. Oliveira (2009), A modeling-based analysis of processes driving wave-dominated inlets, *Cont. Shelf Res.*, *29*, 819–834, doi:10.1016/j.csr.2008.12.019.

Bonneton, P., N. Bruneau, B. Castelle, and F. Marche (2010), Large scale vorticity generation due to dissipating waves in the surf zone, *Discrete Contin. Dyn. Syst., Ser. B*, *13*(4), 729–738, doi:10.3934/dcdsb.2010.13.729.

Booij, N., R. C. Ris, and L. Holthuijsen (1999), A third-generation wave model for coastal regions 1. model description and validation, *J. Geophys. Res.*, *104*(C4), 7649–7666, doi:10.1029/98JC02622.

Brander, R. W. (1999), Field observations on the morphodynamic evolution of low wave energy rip current system, *Mar. Geol.*, *157*, 199–217, doi:10.1016/S0025-3227(98)00152-2.

Brander, R. W., and A. D. Short (2000), Morphodynamics of a large-scale rip current system at Muriwai Beach, New Zealand, *Mar. Geol.*, *165*, 27–39, doi:10.1016/S0025-3227(00)00004-9.

Brown, J., J. H. MacMahan, A. J. H. M. Reniers, and E. Thornton (2009), Surfzone diffusivity on a rip-channeled beach, *J. Geophys. Res.*, *114*, C11015, doi:10.1029/2008JC005158.

Bruneau, N. (2009), Modélisation morphodynamique des plages sableuses, Ph.D. thesis, Université Bordeaux I, Talence, France.

Bruneau, N., P. Bonneton, R. Pedreros, F. Dumas, and D. Idier (2007), A new morphodynamic modelling platform: Application to characteristic sandy systems of the Aquitanian Coast, France, *J. Coastal Res.*, *SI 50*, 932–936.

Bruneau, N., B. Castelle, P. Bonneton, R. Pedreros, J.-P. Parisot, and N. Sénéchal (2008), Modelling of high-energy rip current during Biscarrosse field experiment, in *31st International Conference on Coastal Engineering (ICCE 2008), Hamburg, Germany*, vol. 1, pp. 901–913, Am. Soc. of Civ. Eng., New York, doi:10.1142/9789814277426_0076.

Bruneau, N., B. Castelle, P. Bonneton, R. Pedreros, R. Almar, N. Bonneton, P. Bretel, J. Parisot, and N. Sénéchal (2009a), Field observations of an evolving rip current on a meso-macrotidal well-developed inner bar and rip morphology, *Cont. Shelf Res.*, *29*(14), 1650–1662, doi:10.1016/j.csr.2009.05.005.

Bruneau, N., B. Castelle, P. Bonneton, and R. Pedreros (2009b), Very low frequency motions of a rip current system: Drifter experiment and modeling, *J. Coastal Res.*, *SI 56*, 1731–1735.

Bühler, O. (2000), On the vorticity transport due to dissipating breaking waves in shallow-water flow, *J. Fluid Mech.*, *407*, 235–263, doi:10.1017/S0022112099007508.

Bühler, O., and T. E. Jacobson (2001), Wave-driven currents and vortex dynamics on barred beaches, *J. Fluid Mech.*, *449*, 313–339, doi:10.1017/S0022112001006322.

Butel, R., H. Dupuis, and P. Bonneton (2002), Spatial variability of wave conditions on the French Aquitanian Coast using in-situ data, *J. Coastal Res.*, *36*, 96–108.

Castelle, B., and P. Bonneton (2006), Modelling of a rip current induced by waves over a ridge and runnel system on the Aquitanian Coast, France, *C. R. Geosci.*, *338*, 711–717, doi:10.1016/j.crte.2006.06.003.

Castelle, B., P. Bonneton, N. Sénéchal, H. Dupuis, R. Butel, and D. Michel (2006), Dynamics of wave-induced currents over an alongshore non-uniform multiple-barred sandy beach on the Aquitanian Coast, France, *Cont. Shelf Res.*, *26*, 113–131, doi:10.1016/j.csr.2005.08.027.

Castelle, B., P. Bonneton, H. Dupuis, and N. Sénéchal (2007), Double bar beach dynamics on the high-energy meso-macrotidal french aquitanian coast: A review, *Mar. Geol.*, *245*, 141–159, doi:10.1016/j.margeo.2007.06.001.

Castelle, B., H. Michallet, V. Marieu, F. Leckler, J. Dubardier, A. Lambert, C. Berni, P. Bonneton, E. Barthélemy, and F. Bouchette (2010), Laboratory experiment on rip current circulations over a moveable bed: drifter measurements, *J. Geophys. Res.*, *115*, C12008, doi:10.1029/2010JC006343.

Dally, W. R. (2001), Modeling nearshore currents on reef-fronted beaches, paper presented at Fourth Conference on Coastal Dynamics, Am. Soc. of Civ. Eng., Lund, Sweden.

Dally, W. R., and C. A. Brown (1995), A modeling investigation of the breaking wave roller with application to cross-shore currents, *J. Geophys. Res.*, *100*(C12), 24,873–24,883, doi:10.1029/95JC02868.

Dingemans, M. W., A. C. Radder, and H. J. D. Vriend (1987), Computation of the driving forces of wave-induced currents, *Coastal Eng.*, *11*(5–6), 539–563, doi:10.1016/0378-3839(87)90026-3.

Haas, K. A., and J. C. Warner (2009), Comparing a quasi-3D to a full 3D nearshore circulation model: SHORECIRC and ROMS, *Ocean Modell.*, *26*, 91–103, doi:10.1016/j.ocemod.2008.09.003.

Haas, K. A., I. A. Svendsen, M. C. Haller, and Q. Zhao (2003), Quasi-three-dimensional modeling of rip current systems, *J. Geophys. Res.*, *108*(C7), 3217, doi:10.1029/2002JC001355.

Haller, M. C., and R. A. Dalrymple (2001), Rip currents instabilities, *J. Fluid Mech.*, *433*, 161–192.

Lazure, P., and F. Dumas (2008), An external-internal mode coupling for a 3D hydrodynamical model for applications at regional scale (Mars), *Adv. Water Resour.*, *31*(2), 233–250, doi:10.1016/j.advwatres.2007.06.010.

Longuet-Higgins, M. S., and R. W. Stewart (1964), Radiation stresses in water waves: A physical discussion, with applications, *Deep Sea Res.*, *11*, 529–563.

MacMahan, J. H., E. B. Thornton, T. P. Stanton, and A. J. H. M. Reniers (2005), Ripex—Rip currents on a shore-connected shoal beach, *Mar. Geol.*, *218*, 113–134, doi:10.1016/j.margeo.2005.03.019.

MacMahan, J. H., E. B. Thornton, and A. J. H. M. Reniers (2006), Rip current review, *Coastal Eng.*, *53*, 191–208, doi:10.1016/j.coastaleng.2005.10.009.

MacMahan, J. H., et al. (2010), Mean lagrangian flow behavior on an open coast rip-channeled beach: A new perspective, *Mar. Geol.*, *268*(1–4), 1–15, doi:10.1016/j.margeo.2009.09.011.

Madsen, O. S., Y.-K. Poon, and H. C. Graber (1988), Spectral wave attenuation by bottom friction: theory, paper presented at 21st International Conference on Coastal Engineering, Am. Soc. of Civ. Eng., Torremolinos, Spain.

Mei, C. C. (1989), *The Applied Dynamics of Ocean Surface Waves, Adv. Ser. Ocean Eng.*, vol. 1, World Sci., Singapore.

Özkan-Haller, H., and J. Kirby (1999), Nonlinear evolution of shear instabilities of the longshore current: A comparison of observations and computations, *J. Geophys. Res.*, *104*(C11), 25,953–25,984, doi:10.1029/1999JC900104.

Peregrine, D. H. (1998), Surf zone currents, *Theor. Comput. Fluid Dyn.*, *10*, 295–309, doi:10.1007/s001620050065.

Phillips, O. (1977), *The Dynamics of the Upper Ocean*, Cambridge Univ. Press, Cambridge. U. K.

Quartel, S. (2009), Temporal and spatial behaviour of rip channels in a multiple-barred coastal system, *Earth Surf. Processes Landforms*, *34*, 163–176, doi:10.1002/esp.1685.

Reniers, A. J. H. M., J. H. MacMahan, E. B. Thornton, and T. P. Stanton (2007), Modeling of very low frequency motions during ripex, *J. Geophys. Res.*, *112*, C07013, doi:10.1029/2005JC003122.

Reniers, A. J. H. M., J. H. MacMahan, E. B. Thornton, T. P. Stanton, M. Henriquez, J. W. Brown, J. A. Brown, and E. Gallagher (2009), Surf zone surface retention on a rip-channeled beach, *J. Geophys. Res.*, *114*, C10010, doi:10.1029/2008JC005153.

Reniers, A. J. H. M., J. H. MacMahan, F. J. Beron-Vera, and M. J. Olascoaga (2010), Rip-current pulses tied to Lagrangian coherent structures, *Geophys. Res. Lett.*, *37*, L05605, doi:10.1029/2009GL041443.

Smith, E., and N. Kraus (1990), Laboratory study on macro-features of wave breaking over bars and artificial reefs, *Tech. Rep. CERC-90-12*, U.S. Army Corps of Eng., Waterways Exp. Stn., Vicksburg, Va.

Smith, J. (2006), Wave-current interactions in finite depth, *J. Phys. Oceanogr.*, *36*(7), 1403–1419, doi:10.1175/JPO2911.1.

Stive, M. J. F., and H. J. De Vriend (1994), Shear stresses and mean flow in shoaling and breaking waves, paper presented at 24th International Conference on Coastal Engineering, Am. Soc. of Civ. Eng., (Kobe, Japan).

Svendsen, I. A. (1984), Wave heights and set-up in a surf zone, *Coastal Eng.*, *8*, 303–329, doi:10.1016/0378-3839(84)90028-0.

Thornton, E. B., J. H. MacMahan, and A. H. Sallenger Jr. (2007), Rips currents, mega-cusps, and eroding dunes, *Mar. Geol.*, *240*, 151–167, doi:10.1016/j.margeo.2007.02.018.

P. Bonneton and B. Castelle, Environnements et Paléoenvironnements Océaniques et Continentaux, UMR 5805, Université Bordeaux 1, CNRS, avenue des Facultés, F-33405 Talence, France.

N. Bruneau, Laboratório Nacional de Engenharia Civil, Av. do Brasil 101, P-1700-066 Lisboa, Portugal. (nbruneau@lnec.pt)

R. Pedreros, BRGM, 3 av. Claude-Guillemin, BP 36009, F-45060 Orléans CEDEX 2, France.

D.11 Modeling formation and subsequent nonlinear evolution of rip channels : Time-varying versus time-invariant wave forcing

Bruno Castelle, Gerben Ruessink
Journal of Geophysical Research - Earth Surface, Vol. 116, F04008, doi :10.1029/2010JF001997, 2011

Modeling formation and subsequent nonlinear evolution of rip channels: Time-varying versus time-invariant wave forcing

B. Castelle[1] and B. G. Ruessink[2]

Received 15 February 2011; revised 25 July 2011; accepted 1 August 2011; published 21 October 2011.

[1] We use a nonlinear morphodynamic model to demonstrate that time-varying forcing, in particular the time-varying angle of wave incidence, is crucial to the development of rip channels in terms of rip channel morphology, nonlinear behavior, longshore migration, and mean rip spacing. The time-varying angle of incidence leads to different mean rip spacings than the time-integrated time-invariant forcing and to systematically less developed bar and rip morphologies at more alongshore variable scales. This supports the common field observation of irregular and random alongshore rip spacings, and contrasts with the regular spacing predicted by existing time-invariant template, and instability models. Time-varying wave incidence also generally results in the onset of splitting of shoals and an increase in merging of rip channels. In addition, a time-varying angle of incidence with zero mean can drive a significant net alongshore migration of the rip channels. Abrupt changes in wave conditions are responsible for this net longshore migration through cumulative effects of the mismatch between wave conditions and bar and rip morphology orientation.

Citation: Castelle, B., and B. G. Ruessink (2011), Modeling formation and subsequent nonlinear evolution of rip channels: Time-varying versus time-invariant wave forcing, *J. Geophys. Res.*, *116*, F04008, doi:10.1029/2011JF001997.

1. Introduction

[2] Rip channels are ubiquitous and striking patterns in the sand along wave-dominated beaches. They are important from the perspective of localized beach and dune erosion as well as beach safety and mixing in the nearshore. Rip channels are often part of an accretionary, down-state sequence developing from an alongshore-uniform barred-beach state [*Wright and Short*, 1984] following a storm event. During this extended period of beach recovery, shoals develop from the shallowest sections of the alongshore bar that progressively migrate onshore and in some cases they can even attach to the beach [*Van Enckevort et al.*, 2004]. Depending on the dominant wave-angle to the shore, rip channels can be shore-normal to strongly skewed downdrift [*Wright and Short*, 1984]. During severe storms, or during moderate-energy waves with high angle of incidence [*Price and Ruessink*, 2011], rip channels are reshaped into an alongshore-uniform feature [*Van Enckevort et al.*, 2004], often with concurrent erosion of the beach face.

[3] The emergence and dynamics of rip channels have puzzled scientists for decades. *Coco and Murray* [2007] reviewed the shift from (edge-wave) forcing template to self-organization theories for explaining the formation and subsequent nonlinear evolution of rip channels. Using self-organization models, it was established that rip channels and other three-dimensional (3-D) sandbar patterns, such as crescentic sandbars, form through the positive feedback between flow (waves and currents), sediment processes, and the evolving seabed morphology and that their formation does not require a template in the hydrodynamics.

[4] Linear stability models [*Deigaard et al.*, 1999; *Falqués et al.*, 2000; *Calvete et al.*, 2005; *Klein and Schuttelaars*, 2006], restricted to the initial development of the 3-D patterns using a number of simplifying assumptions, predict rip channels with similar alongshore scales to those observed in the field, with larger length scales for oblique incidence waves. Most importantly, these models allowed both identification of the physical mechanisms that govern feedbacks leading to self-organization [*Falqués et al.*, 2000; *Ribas and Kroon*, 2007] and examination of the role of different parameters such as wave height, period, and direction [*Damgaard et al.*, 2002; *Calvete et al.*, 2007] on characteristic length and timescales. Recently, nonlinear models [e.g., *Damgaard et al.*, 2002; *Reniers et al.*, 2004; *Castelle et al.*, 2006a; *Drønen and Deigaard*, 2007; *Garnier et al.*, 2008; *Smit et al.*, 2008] have been developed to examine the initial growth and subsequent nonlinear evolution of rip channels and crescentic planshapes. Nonlinear morphodynamic models allow temporal changes in the wavelength and the amplitude of the 3-D patterns to be examined.

[5] The recent growing number of high-frequency field observations of sandbar evolution through video imagery has improved our knowledge of rip channel behavior along wave-dominated sandy beaches [e.g., *Van Enckevort and Ruessink*, 2003; *Holman et al.*, 2006; *Turner et al.*, 2007;

[1]CNRS, UMR 5805 EPOC, Université de Bordeaux, Talence, France.
[2]Department of Physical Geography, Faculty of Geosciences, Institute for Marine and Atmospheric Research, Utrecht University, Utrecht, Netherlands.

0148-0227/11/2011JF001997

Ruessink et al., 2007a; *Almar et al.*, 2010; *Price and Ruessink*, 2011; *Gallop et al.*, 2011]. Some studies have tried to identify potential relationships between rip channel wavelength and the prevailing offshore wave conditions [*Huntley and Short*, 1992; *Holman et al.*, 2006; *Turner et al.*, 2007]. Surprisingly, all these studies found poor correlation between rip spacing and wave conditions. Three major arguments can be put forward to explain this lack of correlation. First, rip wavelength may become morphologically controlled soon after a storm reset event [*Turner et al.*, 2007] and is thus unrelated to subsequent variations in offshore wave conditions. Second, rip-channel evolution with time may be much slower than typical timescales associated with changes in offshore wave conditions. In particular, rip channels with a long cross-shore length and wide alongshore spacing have been observed to respond slower to changes in wave conditions than rips with a short cross-shore length and narrower alongshore spacing [*Gallop et al.*, 2011]. Third, rip channel wavelength sensitivity to the initial cross-shore profile is high, implying that the underlying bathymetry is as crucial as wave conditions to the development of rip channels [*Calvete et al.*, 2007].

[6] Because linear stability analysis is restricted to the initial growth of rip channels, time-invariant forcing is an appropriate condition under which to undertake such a modeling exercise. Only *Tiessen et al.* [2010] addressed time-varying wave conditions to show that combining linear stability analysis with an appropriate algorithm which identifies the more physically representative model results resulted in a fair agreement of predicted length scales of the crescentic bed patterns with observations. Surprisingly, all existing nonlinear morphodynamic modeling studies use time-invariant wave forcing, with only two exceptions. First, *Smit et al.* [2005] investigated the dynamics of a double sandbar system to changes in wave conditions. They noted both the important role of the antecedent morphology and that the bathymetry evolved in a similar way for the time-invariant conditions as for rapidly varying wave conditions. This study was limited to a small number of simulations and was further complicated by the feedbacks between the two sandbar systems. Second, *Reniers et al.* [2004] addressed time-varying conditions at the timescales of wave groups (O(100 s)), which is different from addressing time-varying forcing at the change in wave regime timescales (O(1–10 days)). The assumption of time-invariant forcing suggests that rip channel evolution time is shorter than natural variability in the forcing [see, e.g., *Turner et al.*, 2007]. Consequently, all the nonlinear morphodynamic modeling studies to date (except *Smit et al.* [2005]) investigated rip channel evolution as if the wave climate is constant, incompatible with the persistent changes in natural wave conditions. Accordingly, the impact of time-varying wave conditions on finite-amplitude rip channel dynamics remains poorly understood.

[7] In this paper we use a nonlinear morphodynamic model (section 2) to compare predictions of nonlinear rip channel evolution under time-invariant (section 3) and time-varying (section 4) wave forcing and demonstrate that, in particular, a time-varying angle of incidence results in substantially different predictions from those for a time-invariant angle. The discussion and conclusions are presented in section 5.

2. Nonlinear Morphodynamic Model

2.1. Set of Equations

[8] We used a nonlinear morphodynamic model [*Castelle et al.*, 2010a, 2010b] that couples a spectral wave model, a time- and depth-averaged flow model, an energetics-type sediment transport model, and the bed level continuity equation to compute bed level changes. The wavefield and resulting radiation stress components are computed from the spectral wave model SWAN [*Booij et al.*, 1999], which solves the spectral wave-action balance, here with default parameter settings.

[9] The flow model is based on the phase-averaged nonlinear shallow water equations comprising the water mass conservation and momentum conservation equations:

$$\frac{\partial Q_i}{\partial t}+\frac{\partial}{\partial x_j}\left(\frac{Q_iQ_j}{h}\right)=-gh\frac{\partial \eta}{\partial x_i}-\frac{1}{\rho}\frac{\partial S_{ij}}{\partial x_j}+\frac{1}{\rho}\frac{\partial T_{ij}}{\partial x_j}-\frac{\tau_i^b}{\rho} \quad (1)$$

$$\frac{\partial \eta}{\partial t}+\frac{\partial Q_j}{\partial x_j}=0 \quad (2)$$

where h is the mean water depth; Q_i are the water volume fluxes, with the subscript $_i$ referring to the two horizontal coordinates (with x and y the alongshore and cross-shore axis, respectively); η is the mean free surface elevation; g is the gravitational acceleration; ρ is the water density; S_{ij} are the radiation stress components [*Phillips*, 1977]; τ_i^b is the bed shear stress; and T_{ij} is the lateral shear stress which is the horizontal momentum exchange due to the combined action of turbulence and the mean current using the formulation proposed by *Battjes* [1975]. More details on the flow model and the validation with field data are given by *Castelle et al.* [2006b].

[10] In the work of *Castelle et al.* [2010a] the combined bed and suspended load sediment transport $\vec{Q}_s$ was computed using the formulations of *Bailard* [1981], using default settings. This approach cannot be used if one wants to run simulations over long durations, i.e., several times the typical growth time, as the model would blow up when the bar amplitude becomes too large compared to that in nature. Therefore we modified the original code to examine the finite amplitude dynamics through an adequate treatment of the gravitational downslope sediment transport, as in the work of *Garnier et al.* [2008]. In our model the horizontal sediment flux vector $\vec{Q}_s$ is

$$\vec{Q}_s=\alpha\left(\overline{\overline{|\vec{u}_b(t)|^3\vec{u}_b(t)}}-\gamma u_{rms}\vec{\nabla}Z\right) \quad (3)$$

where α is a stirring factor; γ is a bed slope coefficient; u_{rms} is the root mean square wave orbital velocity amplitude at the bottom; $\vec{u}_b$ (t) is the total instantaneous flow velocity at the bottom (mean currents and orbital velocity) with the notation $\overline{()}$ indicating the time-averaging over a duration larger than the typical wave period and Z is the bed level deviation from initial equilibrium, such that $Z = Z_f - Z_f^0$ where Z_f^0 is the initial bed level, i.e., the basic state. The first

term in equation (3) is similar to the suspended sediment load in the work of *Bailard* [1981] while the second term is the downslope sediment transport with respect to the basic state. First, we set α for $\gamma = 0$ to obtain similar rip channel growth time as in existing modeling studies [e.g., *Garnier et al.*, 2006]. Second, we set γ balancing the desire to both prevent any model blow-up in the range of wave conditions used in this study (by increasing γ) and to have a morphodynamic model as nonlinear as possible (by decreasing γ). The latter means increasing the possibility of observing splitting and merging dynamics. In the following we set $\alpha = 2.10^{-4}$ s^3.m^{-2} and $\gamma = 100$ m^2.s^{-1} based on these preliminary tests. Because the advective part in our sediment transport formula $\alpha\,|\vec{u}_b(t)|^3\vec{u}_b(t)$ is different from that in the work of *Garnier et al.* [2006, 2008, 2010] that reads $\alpha\vec{Q}/h$, our reference values of γ and α are not comparable with those in the work of *Garnier et al.* [2006]. Yet, simulated rip channel systems and wave-driven circulations at saturation are similar in patterns.

[11] The new seabed level Z_f was computed using the sediment mass conservation equation:

$$\frac{\partial Z_f}{\partial t} + \frac{1}{1-p}\vec{\nabla}\vec{Q}_s = 0 \tag{4}$$

where $p = 0.4$ is the sediment porosity. The morphological time step for the bed update scheme was 1 h throughout. All the simulations were run for 996 morphological time steps, that is, 41.5 days of morphological evolution. Note that the shoreline is allowed to evolve. This represents a major difference with other nonlinear morphodynamic models applied to 3-D surfzone sandbar behavior.

2.2. Model Setup

[12] We ran the model for one initial single-barred beach geometry. This choice of a single bar setting was motivated by recent studies unraveling the highly complex behavior of inner-bar rip channel systems in multiple-barred settings due to morphological feedbacks between the sandbars [*Masselink et al.*, 2006; *Ruessink et al.*, 2007a; *Castelle et al.*, 2010a, 2010b; *Almar et al.*, 2010; *Price and Ruessink*, 2011]. A single-barred beach setting prevents such complexity. The computational grid had an alongshore length of 5000 m, 20 × 20 m grid cells, and periodic lateral boundary conditions. Additional simulations with a larger domain showed that these periodic boundary conditions did not significantly affect rip channel behavior. About 10 rip channels were typically observed in the 5000-m long domain. This number of simulated rip channels is similar to existing modeling studies of rip channel and crescentic bar with periodic lateral boundaries [e.g., *Garnier et al.*, 2008].

[13] The basic state consisted of a beach with a 1:50 planar sloping depth profile, with its offshore extent in 10.6 m water depth. A bar was superimposed on this planar profile, located 90 m from the mean sea level shoreline at $y = 140$ m with its crest in 0.8 m depth. This choice of bar geometry was motivated by the aim of having a large number of wavelengths in the domain (hence the relatively short distance of the bar crest to the shoreline) and persistent wave breaking across the bar for a range of offshore significant wave heights around 1 m (hence the small water depth at the bar crest). Random perturbations with a magnitude of 1 mm in the seabed were superimposed on the initial alongshore-uniform single-barred beach to excite nearshore instabilities. The initial beach profile together with the cross-shore wave height profiles for $H_s = 0.8$ m, 1 m, and 1.2 m, a peak wave period $T_p = 10$ s and shore-normal wave incidence are shown in Figure 1. These simulations show that the wave height at the bar systematically saturates as a result of intense depth-induced breaking dissipation. According to *Calvete et al.* [2005], this suggests that there will be little dependence of rip spacing on offshore wave height for 0.8 m < H_s < 1.2 m as rip spacing typically increases with offshore wave height up to a saturation value that is reached when the wave height at the bar saturates.

[14] We defined a reference time-invariant wave forcing simulation characterized by $H_s = 1$ m, $T_p = 10$ s and $\theta = 0°$. Additional time-invariant simulations were done with 6 s < T_p < 14 s and 0.8 m < H_s < 1.2 m. This narrow range of H_s values was motivated by the basic state approach in the sediment transport $\vec{Q}_s$ computation. This approach assumes that for the alongshore-uniform basic state, cross-shore sediment transport driven by undertow and wave nonlinearities are in balance for the given reference wave conditions. Given natural variability in the wave forcing, the true equilibrium is never reached in the field [*Pape et al.*, 2010]. Therefore when addressing the formation and nonlinear evolution of rip channels, we assume that rip channels form and evolve more rapidly than the rate at which the beach profile is changing. On the one hand, weakly to nonbreaking wave conditions result in significant onshore sandbar migration together with a typically slow 3-D pattern development. On the other hand, large waves result in significant (O(10 m/day)) offshore sandbar migration, sometimes with reshaping of the 3-D patterns into an alongshore-uniform feature. Accordingly, to be consistent with the assumption that rip channels evolve more rapidly than the rate at which the beach profile is changing, both low and large H_s values were disregarded and a narrow range of wave height values (0.8 m < H_s < 1.2 m), corresponding to the saturated basic states in Figure 1, was considered for both time-invariant and time-varying forcing simulations.

[15] Time-varying wave conditions started after 4 days of time-invariant reference forcing ($H_s = 1$ m, $T_p = 10$ s and $\theta = 0°$). This choice will be discussed in section 5. For a given wave parameter (H_s, T_p or θ), the time-varying forcing was defined by an amplitude A (0.1 and 0.2 m for H_s; 1, 2, 3, and 4 s for T_p; 2, 4, 6, and 8° for θ), a period T (2, 4, 8, and 16 days), and a shape. Four shapes were addressed (Figure 2): sine wave, sawtooth, sawtooth-sine wave, and block function, all with a mean corresponding to the time-invariant reference forcing.

2.3. Rip Channel Evolution

[16] To examine the evolution of the single-barred beach, we computed a number of parameters representative of the morphological evolution. First, we computed at every time step the alongshore beach profile located at $y = 100$ m between the bar crest and the mean-sea level shoreline denoted $Z_f(x,100,t)$ to estimate rip channel time evolution. Fourier analysis of the time evolution of this alongshore profile, i.e., local analysis, has been commonly used to compute the predominant rip spacing when modeling the

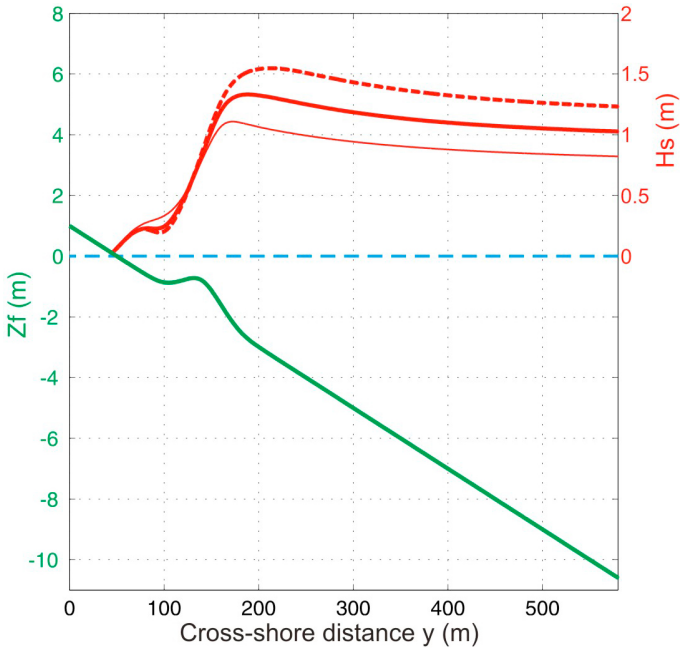

Figure 1. Initial beach profile (basic state) used for all the simulations with cross-shore evolution of the significant wave height profile for H_s = 0.8 m (thin red line), H_s = 1 m (thick solid red line), and H_s = 1.2 m (thick dashed red line). The three simulations show a saturated basic state situation because of intense wave energy dissipation through depth-induced breaking across the bar.

formation and evolution of rip channels [e.g., *Garnier et al.*, 2008]. Here, because in our time-varying simulations rip channels often exhibited significant variability in the alongshore scales and depths, this approach was not suitable. Instead we manually counted the number of rip channels to estimate mean rip spacing λ.

[17] In addition, we used a global analysis of beach evolution [*Garnier et al.*, 2006, 2010] which consists of analyzing variables that are integrated over the whole computational domain. Accordingly, we introduce the overbar notation $\overline{()}$ to define an average over the computational domain, which reads, for a given function $f = f(x, y, t)$:

$$\bar{f}(t) = \frac{1}{L_x L_y} \int_0^{L_x} \int_0^{L_y} f(x,y,t)\,dxdy \tag{5}$$

where L_x and L_y are the longshore and cross-shore length of the computational domain, respectively. By using the same definition as in the work of *Vis-Star et al.* [2008] and *Garnier et al.* [2010] the global growth rate σ is given by

$$\sigma(t) = \frac{1}{2E_z(t)^2} \frac{dE_z(t)^2}{dt} \tag{6}$$

where E_z reads

$$E_z(t) = \sqrt{\overline{Z(x,y,t)^2}} \tag{7}$$

so that E_z^2 can be considered as the potential energy density of the bedforms [*Vis-Star et al.*, 2008; *Garnier et al.*, 2010].

3. Time-Invariant Forcing Simulation

3.1. Reference Time-Invariant Simulation

[18] Figure 3 shows the final beach morphology for the reference time-invariant simulation with H_s = 1 m, T_p = 10 s

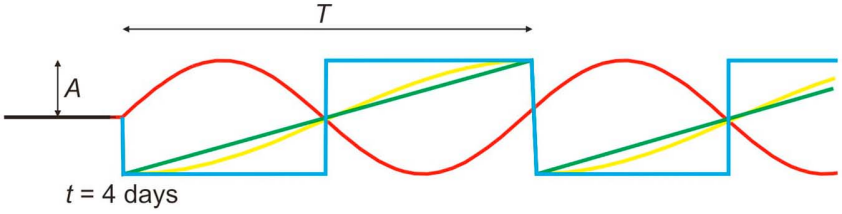

Figure 2. Schematic of time-varying wave forcing starting after 4 days of time-invariant reference forcing with an amplitude A, a period T, and a shape: sine wave (red), sawtooth-sine wave (yellow), sawtooth (green), and block function (blue).

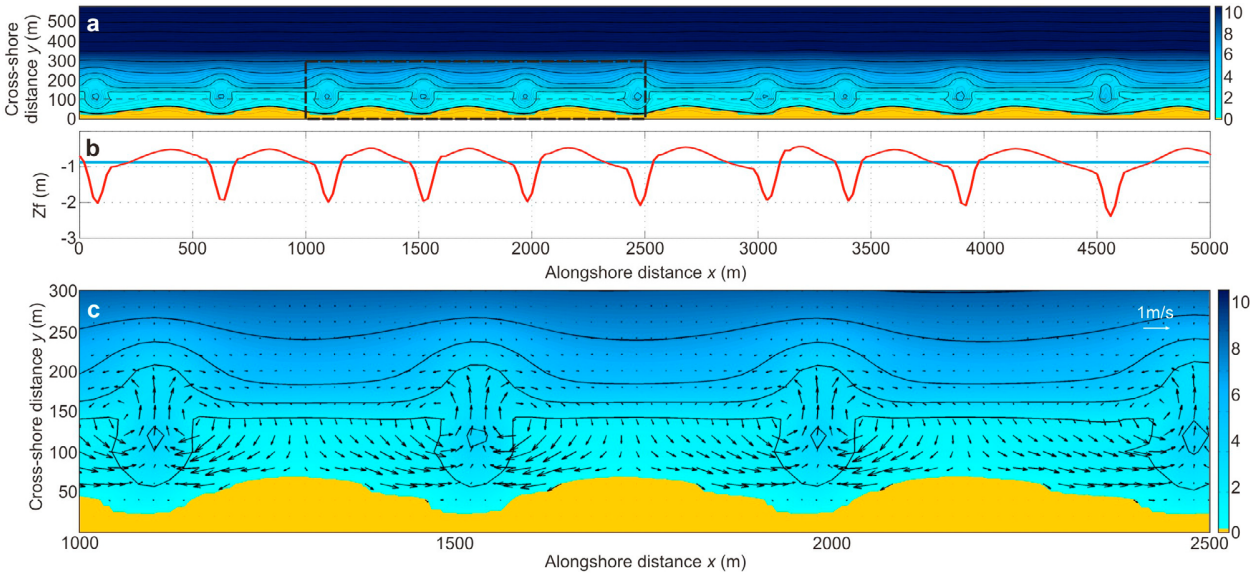

Figure 3. (a) Single barred-beach morphology after 41.5 days of simulation (reference time-invariant wave conditions) for time-invariant forcing with H_s = 1 m, T_p = 10 s, and θ = 0° together with (b) the alongshore line at y = 100 m (dotted gray line) along which bed profile Z_f (x,100,0) and Z_f (x,100,41.5) are given in blue and red, respectively. (c) Zoom of the bathymetry at 1000 m < x < 2500 m and 0 m < y < 300 m with superimposed wave-induced currents. In Figures 3a and 3c the local bottom morphology is contoured in the background and the color bars indicate water depth in meters.

and θ = 0° at t = 41.5 days. The beach exhibits well-developed rip channels at a reasonably narrow range of wavelengths, with a mean $\lambda \approx$ 500 m (Figure 3a). All the rip channels show a similar shape with a deep and narrow shore-normal neck and a well-developed rip head bar. The alongshore bed level at y = 100 m shows that rip channels are about 1.5 m deep and reasonably narrow with a width of about 50 m (Figure 3b). A zoom on the bathymetry at 1000 m < x < 2500 m, 0 m < y < 300 m with superimposed wave-induced currents is given in Figure 3c. Flow patterns show classic rip current circulations with alongshore feeder currents, reasonably intense and narrow offshore-directed jets in the channel of about 0.5 m/s, strong onshore flows across the shoals and counterrotating cells to the left and the right of the rip current. Because the shoreline is allowed to evolve in our model, erosive features of the rip currents, i.e., megacusps, are clearly present on the beach face, with a cross-shore amplitude of about 40 m. Note that these rip-channel morphologies and wave-driven hydrodynamics are essentially similar to field and laboratory observations of well-developed bar and rip systems exposed to shore-normal low-energy waves [e.g., *Bruneau et al.*, 2009; *Castelle et al.*, 2010c].

[19] Figure 4 shows the time series of Z_f (x, 100, t), E_z and σ for the same simulation. The bars appear at day 2–3 (Figure 4a) as E_z starts to be nonzero (Figure 4b). From about day 2–3 to day 5, an initial mode seems to dominate with a mean wavelength $\lambda \approx$ 350 m (Figure 4a) with concurrent strongly and linearly increasing E_z (Figure 4b). This corresponds to the linear regime. From day 5 to day 10 rips merge with concurrent less rapidly increasing E_z. For instance, at day 7 two clear mergings occur at x = 2400 m and x = 3900 m. The same applies at day 8 at x = 200 m. From day 10 to the end of the simulation, the predominant wavelength $\lambda \approx$ 500 m stabilizes. At day 15 we can consider that the bars have reached a quasi-equilibrium state as bars reached their maximum amplitude. Note that there are no splitting of rip channels throughout this simulation.

3.2. Influence of Time-Invariant H_s, T_p, and θ

[20] We ran a number of simulations to address the influence of H_s and T_p for the given basic state. Simulations show that both H_s and T_p have an influence on the global growth rate as σ increases with increasing H_s and increasing T_p. Both H_s and T_p also have a significant influence on rip channel morphology. Rip channel depth and width increase and decrease, respectively, with increasing H_s and T_p. This is illustrated in Figure 5, which shows examples of time series of Z_f (x,100,t) for different H_s and T_p. For shore-normal waves with T_p = 10 s and H_s = 0.8 m rip channels are less well developed (Figure 3b) than for H_s = 1.2 m (Figure 5b, rip channel depth ≈2 m).

[21] The same applies for T_p, because for shore-normal waves with H_s = 1 m and T_p = 6 s (Figure 5c, rip channel depth <0.8 m) rip channels are less developed than for T_p = 14 s (Figure 5d, rip channel depth ≈1.5 m). Not surprisingly, H_s has no significant influence on mean rip spacing λ because of the saturated basic state for 0.8 m < H_s < 1.2 m (Figure 1), which agrees with *Calvete et al.* [2005]. This is slightly different for T_p as λ typically weakly increases with wave period for shore-normal waves according to *Calvete et al.* [2005]. This is apparent in our simulations as nine rip channels are observed for T_p = 14 s (Figure 5d) instead of 10 rip channels for both T_p = 6 s (Figure 5c) and T_p = 10 s (Figure 4a).

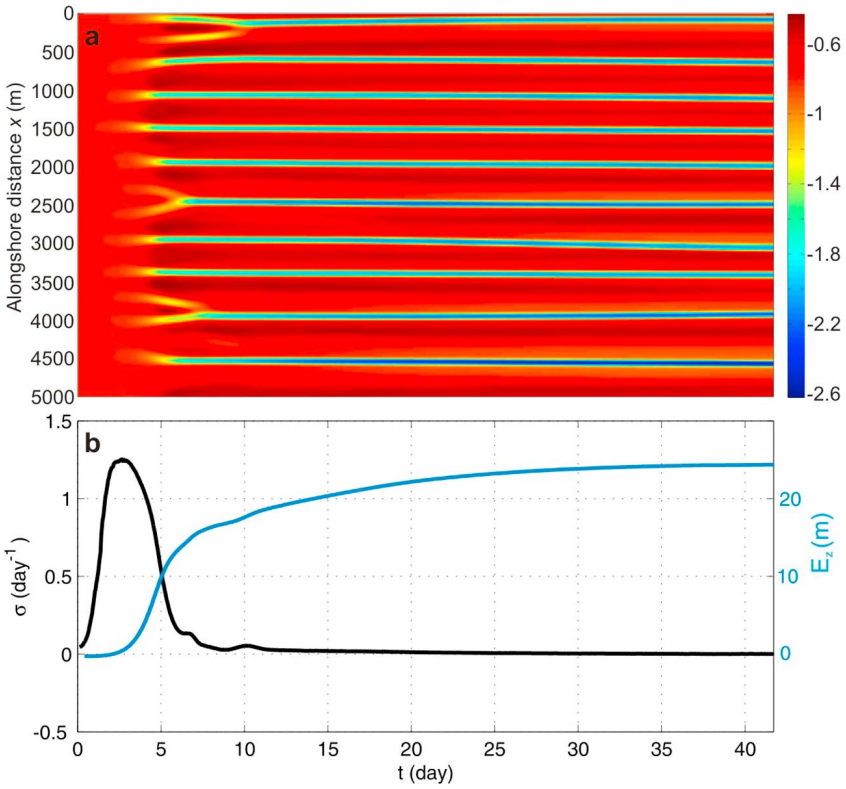

Figure 4. Reference time-invariant simulation with (a) time evolution of the alongshore profile Z_f (x,100,t) with corresponding time series of (b) global growth rate σ and potential energy density of the bedforms E_z.

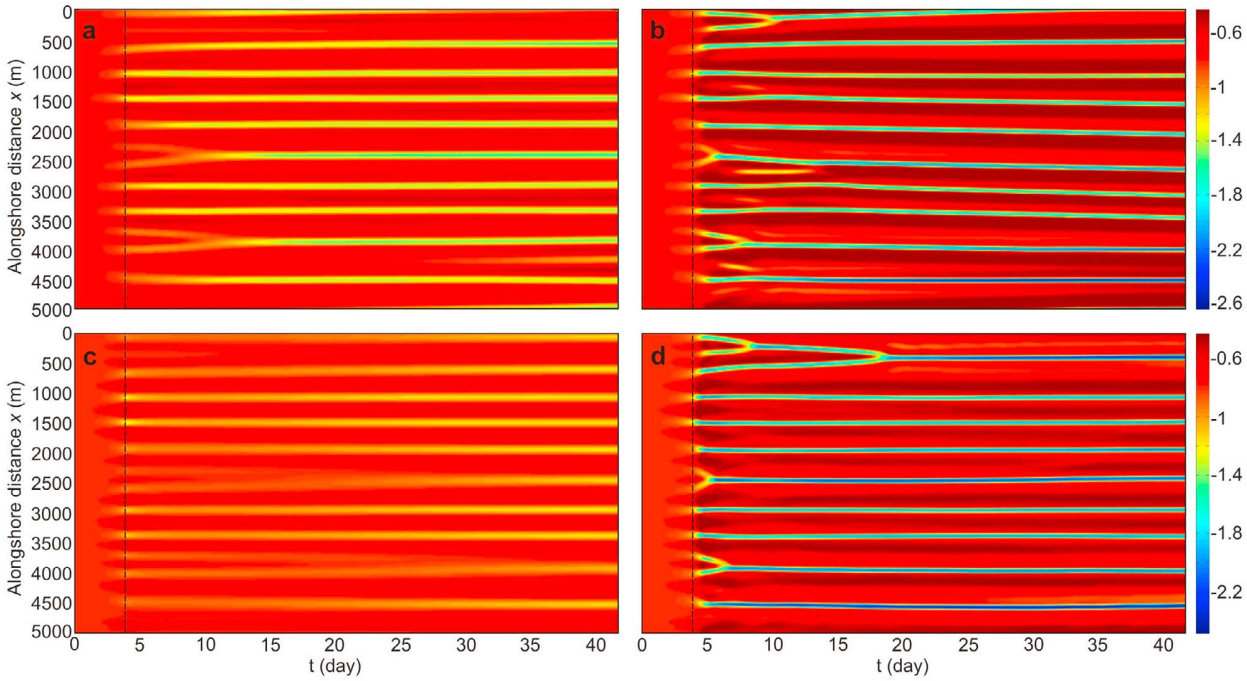

Figure 5. Time evolution of the alongshore profile Z_f (x,100,t), starting at t = 0 with H_s = 1 m, T_p = 10 s and θ = 0°, with changing significant wave height H_s at t = 4 days with (a) H_s = 0.8 m and (b) H_s = 1.2 m, and changing peak wave period T_p at t = 4 days with (c) T_p = 6 s, and (d) T_p = 14 s. Color bars indicate seabed elevation in meters.

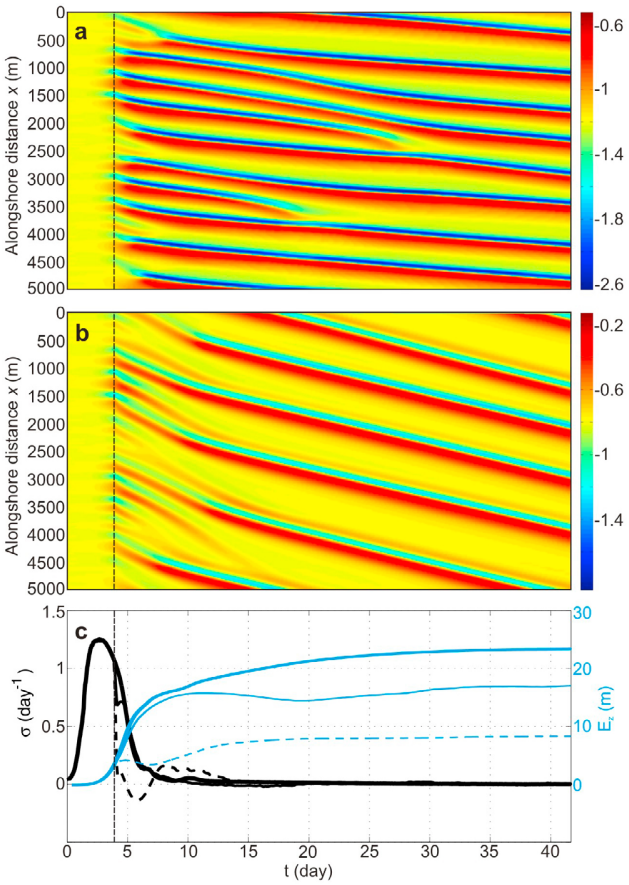

Figure 6. Time evolution of the alongshore profile Z_f (x,100,t), starting at t = 0 with H_s = 1 m, T_p = 10 s and θ = 0°, and changing wave angle to the shore at t = 4 days with (a) θ = 2° and (b) θ = 4°, the color bars indicate seabed elevation in meters. (c) Global growth rate σ (black) and potential energy density of the bedforms E_z (blue) for the reference time-invariant simulation (thick solid line), θ = 2° (thin solid line), and θ = 4° (thin dotted line).

[22] Importantly, splittings are observed for only one of our time-invariant simulations for H_s = 1.2 m at about t = 7 days at x = 2700 m and 4300 m (Figure 5b). This is actually not the splitting of a rip channel into two rip channels but the splitting of a shoal (the shallowest section of the sandbar) through the formation of a rip channel in its center. Note that the two rip channels emerging from splitting at $t \approx 7$ days in Figure 5b subsequently merge to another rip channel. The development of channels in the center of a shoal will be referred to as a splitting in the following and will be discussed later in the paper.

[23] In contrast with H_s and T_p, θ is crucial to the formation and subsequent nonlinear evolution of rip channels. Figure 6 shows the rip channel formation and subsequent nonlinear evolution for two wave angles to the shore. The model shows that for θ = 2° and θ = 4° rip channels stabilize for $\lambda \approx$ 600 m and 1000 m, respectively. These two simulations show that rip spacing increases with θ. Mergings of rip channels are ubiquitous for the two simulations and splittings are nonexistent. Figure 6c additionally shows that the typical equilibrium timescale increases with increasing wave obliquity. Our finding that both rip spacing and equilibrium time increase with increasing θ is in agreement with existing modeling studies [e.g., *Deigaard et al.*, 1999; *Calvete et al.*, 2005; *Garnier et al.*, 2008].

4. Time-Varying Forcing Simulations

4.1. Wave Height and Period

[24] Consistent with the main time-invariant forcing results synthesized in the previous section, time-varying H_s and T_p had a limited influence on the evolution of rip channels. Therefore below we only show simulations with different values of the amplitude A of sine wave time-varying H_s and T_p and the influence of the shape and period T of the time-varying forcing is not addressed. Figure 7 shows the influence of the amplitude A of H_s variations on the evolution of rip channels for sine wave time-varying H_s with a mean of 1 m (Figure 7a). The time evolution of the alongshore profile Z_f (x,100,t) for time-varying H_s starting at t = 4 days is shown with A = 0.1 m (Figure 7b) and A = 0.2 m (Figure 7c). Results show that final mean rip spacing is the same as for the time-invariant forcing (Figure 4a) for both A = 0.1 and 0.2 m. Three-dimensional patterns systematically decay and grow during periods of low and high H_s values, respectively. Overall, beach three-dimensionality decreases with increasing amplitude of H_s variations (Figure 7d).

[25] The same applies for the influence of the time-varying T_p simulations with a mean of 10 s (Figure 8). The time evolution of the alongshore profile Z_f (x,100,t) is shown for time-varying T_p starting at t = 4 days (Figure 8a) with A = 2 s (Figure 8b) and A = 4 s (Figure 8c). Results are essentially similar to those with time-varying H_s, because both final rip spacing is the same as for the time-invariant reference simulation (Figure 4a) and beach three-dimensionality decreases with increasing A (Figure 8d). Note that for the range of H_s and T_p values tested in this study, rip channels more rapidly respond to changes in T_p than to changes in H_s (e.g., larger σ values in Figure 8e with respect to Figure 7e). Overall, the simulations show that both time-varying H_s and T_p have a negligible influence on mean rip spacing and that rip channels are systematically less developed for the time-varying simulations than for the time-invariant simulation. Similar results were obtained for different T and shapes.

4.2. Wave Angle

[26] Below we address the impact of periodic time-varying θ with the influence of the amplitude A, the period T and the shape of θ variations.

4.2.1. Influence of the Amplitude A of θ Time Evolution

[27] Figure 9 shows the influence of A on the evolution of rip channels for sine wave time-varying, zero-mean θ, with a period T = 4 days, H_s = 1 m and T_p = 10 s starting at t = 4 days. The time evolution of the alongshore profile Z_f (x,100,t) is shown with A = 2° (Figure 9a), A = 4° (Figure 9b), A = 6° (Figure 9c), and A = 8° (Figure 9d). Results show that low A values do not significantly affect rip channel behavior with only small alongshore migration of the rip channels (Figure 9a) and a with final rip channel configuration with λ essentially similar to that with time-invariant forcing (compared to Figure 4a).

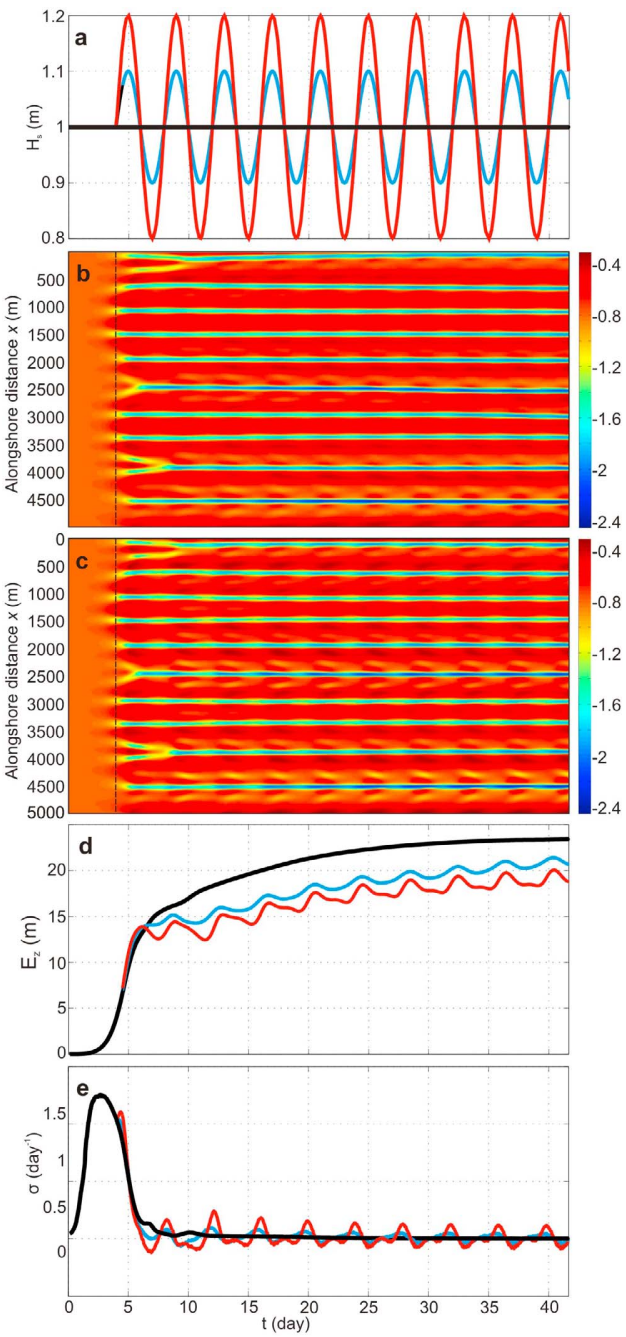

Figure 7. Influence on rip channel evolution of the amplitude A of time-varying offshore significant wave height H_s starting at $t = 4$ days, with a 1-m mean, a sine wave shape, $T = 4$ days, $\theta = 0°$, and $T_p = 10$ s. (a) Time series of H_s, (b, c) time evolution of the alongshore profile $Z_f(x,100,t)$ and corresponding time series of (d) potential energy density of bedforms E_z and (e) global growth rate σ: $A = 0.1$ m (Figure 7b, in blue in Figures 7a, 7d, and 7e), $A = 0.2$ m (Figure 7c, in red in Figures 7a, 7d, and 7e). In Figures 7b and 7c the color bar indicates seabed elevation in meters and the vertical black dashed line indicates the start of time-varying H_s. In Figures 7a, 7d, and 7e the thick black line is the time-invariant simulation ($H_s = 1$ m).

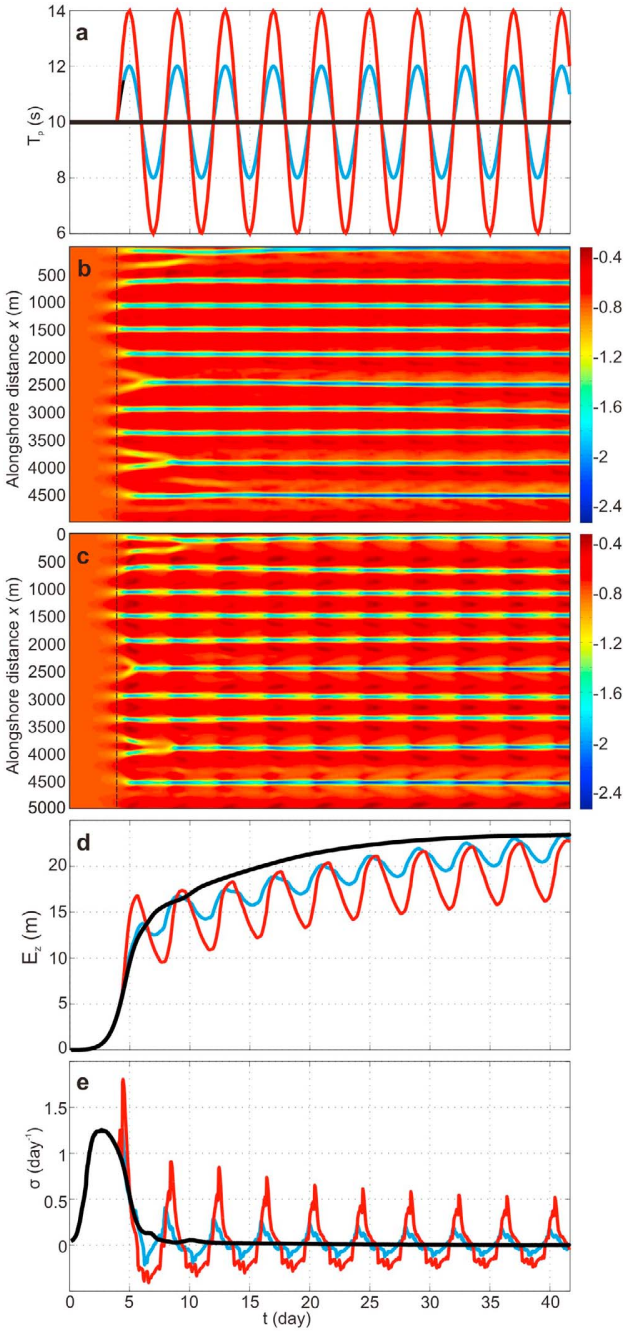

Figure 8. Influence on rip channel evolution of the amplitude A of time-varying peak wave period T_p starting at $t = 4$ days, with a 10-s mean, a sine wave shape, $T = 4$ days, $\theta = 0°$, and $H_s = 1$ m. (a) Time series of T_p, (b, c) time evolution of the alongshore profile $Z_f(x,100,t)$ and corresponding time series of (d) potential energy density of bedforms E_z, and (e) global growth rate σ: $A = 2$ s (Figure 8b, in blue in Figures 8a, 8d, and 8e), $A = 4$ s (Figure 8c, in red in Figures 8a, 8d, and 8e). In Figures 8b and 8c the color bar indicates seabed elevation in meters and the vertical black dashed line indicates the start of time-varying T_p. In Figures 8a, 8d, and 8e the thick black line is the time-invariant simulation ($T_p = 10$ s).

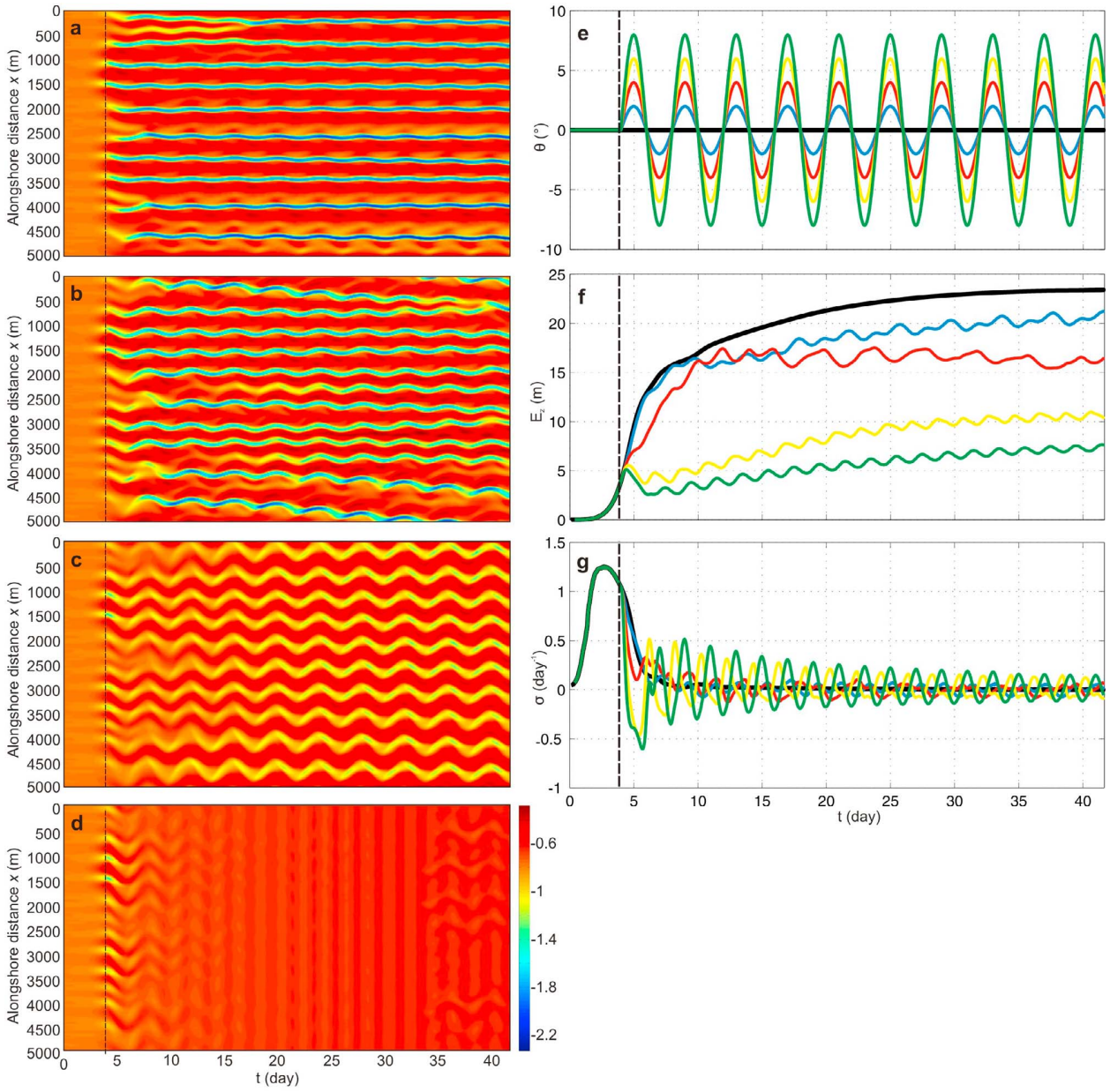

Figure 9. Influence on rip channel evolution of the amplitude A of time-varying wave offshore wave angle to the shore θ starting at $t = 4$ days, with a 0-mean, a sine wave shape, $T = 4$ days, $H_s = 1$ m, and $T_p = 10$ s. (a–d) Time evolution of the alongshore profile $Z_f(x,100,t)$ and corresponding time series of (e) offshore wave angle to the shore θ, (f) potential energy density of bedforms E_z, and (g) global growth rate a: $A = 2°$ (Figure 9a, in blue in Figures 9e–9g), $A = 4°$ (Figure 9b, in red in Figures 9e–9g), $A = 6°$ (Figure 9c, in yellow in Figures 9e–9g), $A = 8°$ (Figure 9d, in green in Figures 9e–9g). In Figures 9a–9d the color bar indicates seabed elevation in meters. In Figures 9a–9g the vertical black dashed line indicates the start of time-varying θ. In Figures 9e–9g the thick black line is the time-invariant simulation ($\theta = 0°$).

[28] Increasing the amplitude in the θ variations to 4° increases the number of mergings with odd rapid alongshore migration of some rip channels (Figure 9b) as rip channels try to self-organize into more regular alongshore scales. Interestingly, splittings are observed at about $t = 15$ days at $x = 2300$ m and 3700 m. The two rip channels that arise through splitting do not subsequently merge and have become two well-developed rip channels by the end of the simulation (Figure 9b). Despite rip spacing increasing with increasing θ in the time-invariant simulations, here rip spacing decreases with respect to the $\theta = 0°$ time-invariant simulation. For $A = 4°$ (Figure 9b), 11 to 12 rip channels are observed throughout the simulation (e.g., 12 rip channels for 15 days $< t <$ 27 days) instead of 10 in the time-invariant simulation (Figure 4a).

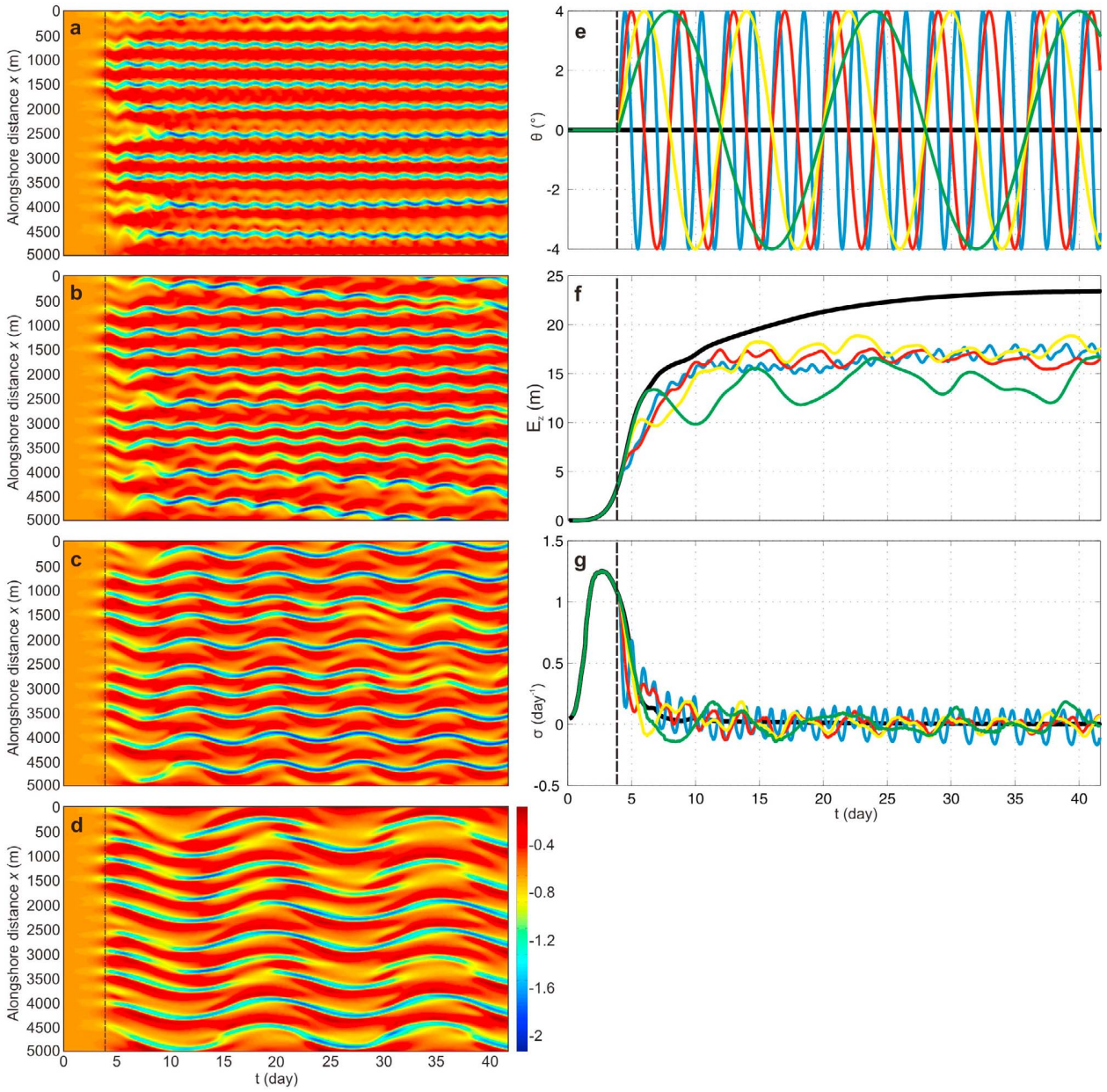

Figure 10. Influence on rip channel evolution of the period T of time-varying offshore wave angle to the shore θ starting at t = 4 days, with a 0-mean, a sine wave shape, A = 4°, H_s = 1 m, and T_p = 10 s. (a–d) Time evolution of the alongshore profile Z_f (x,100,t) and corresponding time series of (e) offshore wave angle to the shore θ, (f) potential energy density of bedforms E_z, and (g) global growth rate σ: T = 2 days (Figure 10a, in blue in Figures 10e–10g), T = 4 days (Figure 10b, in red in Figures 10e–10g), T = 8 days (Figure 10c, in yellow in Figures 10e–10g), T = 16 days (Figure 10d, in green in Figures 10e–10g). In Figures 10a–10d the colormbar indicates seabed elevation in meters. In Figures 10a–10g the vertical black dashed line indicates the start of time-varying θ. In Figures 10e–10g the thick black line is the time-invariant simulation (θ = 0°).

[29] Further increasing A to 6° drastically prevents mergings and splittings (Figure 9c) with a final rip spacing similar to that of the θ = 0° time-invariant simulation. Finally, higher A values result in a progressive bar straightening at the beginning of the simulation (4 days < t < 10 days) driven by a strong longshore current (≈0.8 m/s) when $|\theta|$ temporarily exceeds about 6° during a sufficient duration (≈1 day). Overall, beach three-dimensionality decreases with increasing A (Figure 9f) and increasingly keeps the morphology away from equilibrium (Figure 9g).

4.2.2. Influence of the Period T of θ Time Evolution

[30] Figure 10 shows the influence of T on the evolution of rip channels for sine wave time-varying θ with an amplitude

$A = 4°$, $H_s = 1$ m, and $T_p = 10$ s. The time evolution of the alongshore profile $Z_f(x,100,t)$ for time-varying θ starting at $t = 4$ days is shown for $T = 2$ days (Figure 10a), $T = 4$ days (Figure 10b), $T = 8$ days (Figure 10c), and $T = 16$ days (Figure 10d). The results show that for $T = 2$ days the rip channels are not significantly affected by the time-varying θ as they seem not to be able to adapt to the persistent rapid changes in θ (Figure 10a). This results in a final rip channel configuration and λ that are essentially similar to those with time-invariant forcing. This agrees with *Smit et al.* [2005].

[31] For higher values of T rip channels have more time to adapt to the changes in θ. Rip channels and shoals therefore merge and split more frequently, respectively, which results in smaller rip spacing for $T = 4$ days (Figure 10b). Further increasing T (Figures 10c–10d) results in a rather complicated behavior. For instance, for $T = 16$ days mergings and/or formations of rip channels become increasingly complex to discriminate from the quasiperiodic deepening and filling of rip channels (Figure 10d). Splittings are observed but rip channels subsequently merge rapidly or remain reasonably shallow throughout the simulation. Overall, changes in T do not have any significant influence on beach three-dimensionality and all these simulations result in less-developed bar and rip morphologies compared to time-invariant $\theta = 0°$ forcing (Figure 10f). In addition, for $T = 2$, 4, and 8 days, 10 to 13 rip channels are observed throughout the simulations (Figures 10a, 10b, and 10c) which results in a generally smaller mean rip spacing than for the time-invariant simulation. The situation for $T = 16$ days is different because, as a result of the more slowly varying θ, rip channels have more time to adapt to wave conditions which results in a situation that gets closer to the time-invariant forcing with oblique waves, i.e., with a larger mean rip spacing. Alongshore variability in rip channel depth and morphology is also found to increase with increasing T. In contrast, T has a limited influence on the evolution of the global growth rate σ (Figure 10g).

4.2.3. Influence of the Shape of θ Time Evolution

[32] Figure 11 shows the influence of the shape on the evolution of rip channel for time-varying θ, with $T = 4$ days, $A = 4°$, $H_s = 1$ m, and $T_p = 10$ s. Four shapes are addressed: sine wave (Figure 11a), sawtooth (Figure 11b), sawtooth-sine wave (Figure 11c), and block function (Figure 11d), all with a zero mean θ. A number of important results arise from these simulations.

[33] 1. The global growth rate decreases with increasing abruptness in θ variations. If the model is run for sufficient duration the θ shape does not have a significant influence on the, in quasi-equilibrium, beach three-dimensionality (Figure 11f).

[34] 2. In all these simulations with the same T and A, rip spacing is generally smaller (10 to 13 rip channels, Figures 11a–11d) than that with $\theta = 0°$ time-invariant forcing (10 rip channels, Figure 4a).

[35] 3. Splittings are observed for the four situations, with for instance four to five splittings for the sawtooth-sine wave forcing in Figure 11c. The only exception is for the block function forcing for which only one splitting is observed at the end of the simulation at $x \approx 2700$ m (Figure 11d).

[36] 4. Surprisingly, when the time variation is asymmetric (sawtooth and sawtooth-sine wave), a strong net (T-averaged) alongshore migration of rip channels is observed (Figures 11b and 11c), despite a zero-mean θ.

5. Discussion and Conclusions

[37] In this paper we investigated whether the nonlinear evolution of rip channels is influenced by time-varying wave height, period, and angle of incidence. Considering time-invariant forcing for a given basic state, H_s and T_p were found to have a significant influence on global growth rate and beach three-dimensionality as both σ and E_z typically increase with increasing T_p and H_s in the range of values tested in this study. This agrees with earlier linear or nonlinear stability analyses [e.g., *Calvete et al.*, 2005; *Garnier et al.*, 2008] that showed that the conditions most prone to rip channel formation occur for large wave height, long wave period, and normal incidence. In addition, H_s does not have any significant influence on mean rip spacing as a result of a saturated basic state, which once again corroborates an earlier study [*Calvete et al.*, 2005]. In this paper our model was used for the first time to address long-term rip channel behavior. Overall, all our time-invariant forcing results agree with existing, time-invariant, modeling studies [e.g., *Deigaard et al.*, 1999; *Calvete et al.*, 2005; *Garnier et al.*, 2008], which supports the use of this numerical model to subsequently address the impact of time-varying wave forcing.

[38] The tuning parameters α and γ in equation (3) were set to a small number of time-invariant simulations to have saturation of rip channels for the range of wave conditions used in this study. Using these parameters for time-varying forcing showed a systematic dynamic equilibrium of rip channels. While the effect of time-varying wave height and period was limited (in the range of conditions tested here), the influence of a time-varying angle of incidence was profound. Rip channels behave similarly (same rip spacing) to time-invariant forcing with $\theta = 0°$ only when the amplitude A and/or the period T of variation was very small, except that the final potential energy density of the bedforms was systematically lower than that for time-invariant forcing. Increasing A or T resulted in more complex behavior throughout the simulation. While rip spacing increases with increasing θ in time-invariant simulations, mean rip spacing decreases with increasing θ variability. The alongshore variability in rip channel depth and alongshore scales is also found to increase with increasing θ variability. This supports the common field observation of irregular and random spacing of rips alongshore [e.g., *Van Enckevort et al.*, 2004; *Turner et al.*, 2007] that is inconsistent with the regular spacing of rips alongshore predicted by existing, time-invariant, template, and instability models. Further increasing A results in a progressive damping of the bed instability as rip channels become both increasingly obliquely oriented and decreasingly three-dimensional. This is similar to the development of the erosive transverse bar and rip state (eTBR) described by *Price and Ruessink* [2011].

[39] Time-varying wave incidence also generally resulted in the onset of splittings. In our simulations, we did not observe the splitting of the rip channel (i.e., bay) into two rip channels but the splitting of a shoal (the shallowest section of the sandbar) through the formation of a rip channel in its center. The only detailed field study of splittings deals with

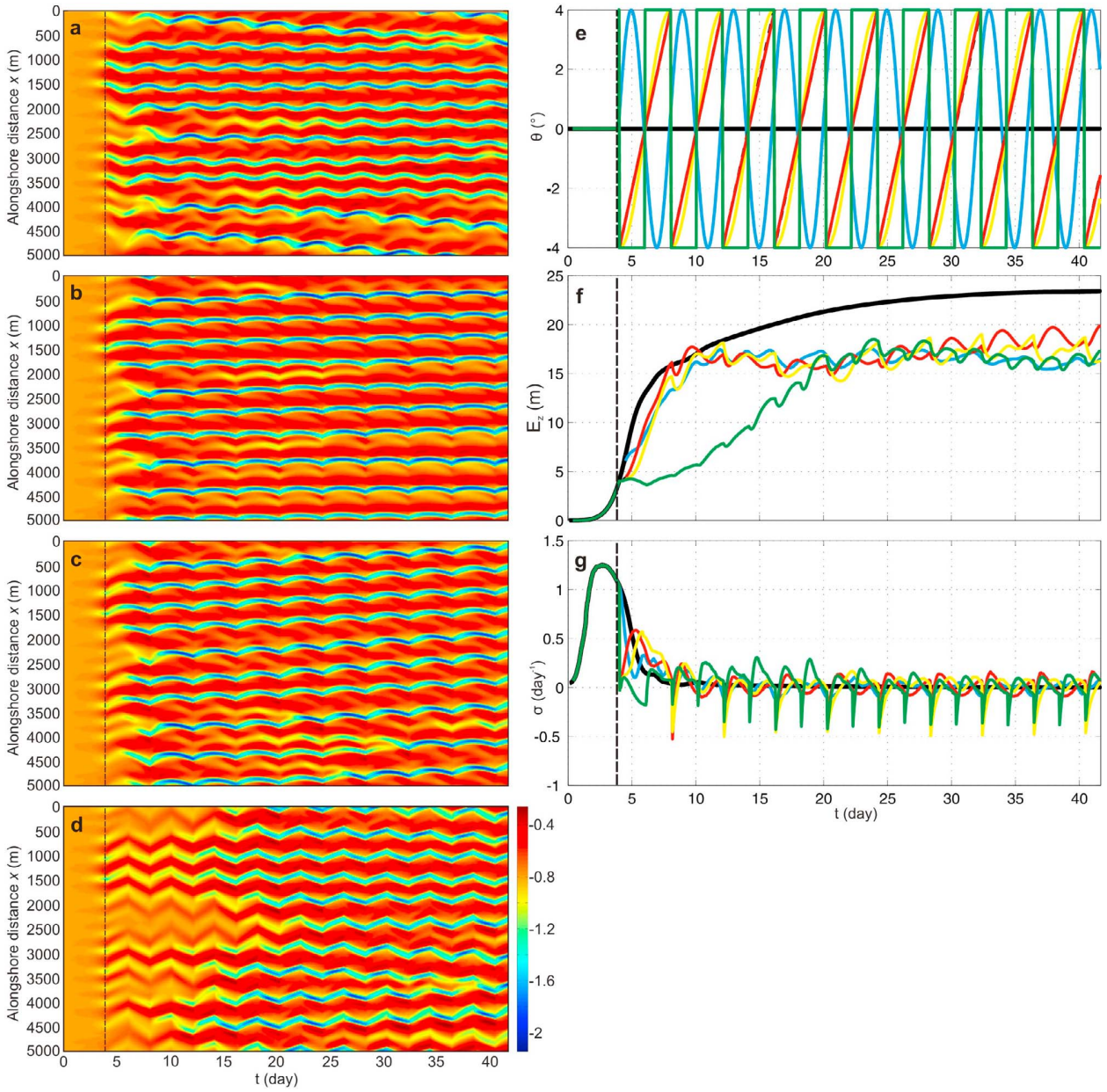

Figure 11. Influence on rip channel evolution of the shape of time-varying offshore wave angle to the shore θ starting at $t = 4$ days, with a 0-mean, a sine wave shape, $A = 4°$, $H_s = 1$ m, and $T_p = 10$ s. (a–d) Time evolution of the alongshore profile $Z_f(x, 100, t)$ and corresponding time series of (e) offshore wave angle to the shore θ, (f) potential energy density of bedforms E_z, and (g) global growth rate σ: sine wave (Figure 11a, in blue in Figures 11e–11g), sawtooth (Figure 11b, in red in Figures 11e–11g), sawtooth-sine wave (Figure 11c, in yellow in Figures 11e–11g), block function (Figure 11d, in green in Figures 11e–11g). In Figures 11a–11d the color bar indicates seabed elevation in meters. In Figures 11a–11g) the vertical black dashed line indicates the start of time-varying θ. In Figures 11e–11g the thick black line is time-invariant simulation ($\theta = 0°$).

crescentic sandbars [*Van Enckevort et al.*, 2004]. In their observations, splittings are characterized by the separation of a bay (seaward perturbation) into two crescentic patterns, that is, the other way around with respect to our simulations. However, despite not being focused on splittings, the time-evolution of the video-derived rip channel positions in the work of *Holman et al.* [2006] shows that splittings occur in the same way as in our simulations. We noted that splittings were almost nonexistent in our time-invariant simulations. The same applies for existing time-invariant nonlinear morphodynamic modeling of rip channel evolution [e.g., *Garnier et al.*, 2008] in which, although sometimes claimed, there is no clear evidence of any splitting. Time-varying wave incidence generally resulted in the onset of splittings

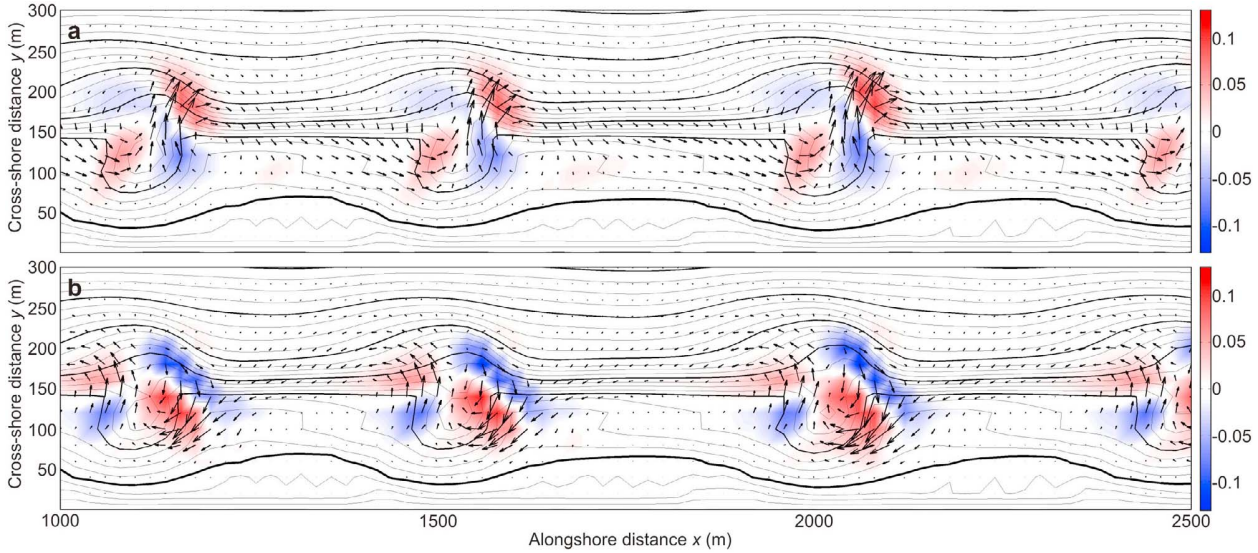

Figure 12. Zoom of the bathymetry at 1000 m < x < 2500 m and 0 m < y < 300 m with superimposed sediment transport field $\vec{Q}_s$ and resulting erosion $\partial Z/\partial t < 0$ (blue) and accretion $\partial Z/\partial t > 0$ (red) patterns for the sawtooth-sine wave time-varying wave angle (simulation in in Figure 11c) at $t \approx 36$ days (a) immediately before the abrupt change with $\theta = 4°$ and (b) immediately after with $\theta = -4°$. The local bottom morphology is contoured in the background and the color bars indicate $\partial Z/\partial t$ in meters per hour.

and an increased number of mergings. This agrees with *Van Enckevort et al.* [2004] who suggested that splittings and mergings are related to time-variations in the forcing. Our simulations are supported by additional field evidence: in our simulations, mergings and splittings are an attempt of the rip channels to self-organize into a more alongshore-uniform pattern as splitting is confined to the longest shoals, whereas merging usually combines the smaller rip spacings into a longer shoal (e.g., Figures 11a–11d). Only rarely did the rip channels arising through splittings develop into channels with a water depth similar to that of the other existing channels (e.g., Figure 11a). Most of the time rip channels arising through splittings remained reasonably shallow and subsequently (typically after 10–20 d) merged with another rip channel (e.g., Figures 11b and 11c).

[40] When θ variability is asymmetric (sawtooth and sawtooth-sine waves), the net (T-averaged) alongshore migration can be non-zero despite zero-mean θ (Figures 11b and 11c). As shown in Figure 11, all abrupt changes are characterized by a rapid decrease in beach three-dimensionality (Figure 11f) and a negative global growth rate (Figure 11g), which is the result of a rapid decrease in rip channel depth (see for instance in Figure 11d after each abrupt change). This is further emphasized in Figure 12, which shows the sediment transport field and resulting erosion/accretion patterns immediately before the abrupt change at $t \approx 36$ days for $\theta = 4°$ (Figure 12a) and immediately after (Figure 12b), corresponding to the sawtooth-sine wave simulation given in Figure 11c. Before the abrupt change, rip channels are skewed downdrift as they progressively adapted to the increasingly oblique wave approach. As a result, wave conditions before the abrupt change match the bar and rip orientation which results in classical sediment transport and erosion/accretion patterns with erosion and accretion at the downdrift and updrift part of the rip channel, respectively, and a reasonably small accretion of the bar (Figure 12a). This both drives an alongshore migration of the rip channel and maintains rip channel three-dimensionality. Immediately after the abrupt change in wave conditions, rip channels are skewed updrift. Wave conditions mismatch the rip channel morphology as the angle of wave approach (and resulting wave-driven rip current skewness) is not in accordance with the bar/rip orientation. As a result, there is a reversal in the roles of each patch of accretion and erosion together with an increase in intensity (Figure 12b) that drive a switch in the migration direction and an increase in rate, respectively. In addition, this drives a rapid decrease in rip channel depth (see the significant decrease of E_z in Figure 11b after each abrupt change). Given that, for a given oblique incidence wave condition, rip channel alongshore migration rate decreases with increasing rip channel depth, rip channel migration is enhanced after each abrupt change. Therefore rip migration is larger after an abrupt change in wave angle than before an abrupt change which, all cumulative, results in a net longshore migration of the rip channel system. The role of this mismatch between sandbar morphology and prevailing wave conditions has previously been discussed in terms of nearshore circulations [e.g., *Sonu*, 1972; *Masselink and Hegge*, 1995]. Here we show that this mismatch may lead to a rapid decrease in rip channel volume, which facilitates a strongly increased alongshore migration rate of the rip channel directly after an abrupt change in wave angle.

[41] Our results imply that using mean wave conditions (typically averaged over O(weeks)) can be misleading when investigating alongshore migration of rip channels. Mean wave conditions have often been used to understand surf-zone sandbar alongshore migration [e.g., *Lafon et al.*, 2005; *Sénéchal et al.*, 2009; *Orzech et al.*, 2010]. While this approach sometimes proved to be a success [e.g., *Ruessink et al.*, 2000; *Orzech et al.*, 2010], correlations were not

that high as events of odd migration rates were common. More frequently poor correlation is found when quantifying rip channel alongshore migration rates as a function of prevailing wave conditions. *Turner et al.* [2007] measured a large number of rip channel migrations along the Gold Coast. The authors even found that migrations did not always occur in the direction consistent with the prevailing offshore swell direction and resulting alongshore current. We suspect that when rip channels are sufficiently well-developed, abrupt changes in wave conditions (particularly wave angle to the shore), can drive contrasting net rip channel migration because of the cumulative effects of the mismatch between hydrodynamics and sandbar morphology.

[42] The present nonlinear modeling exercise relies on a number of simplifying assumptions. For instance, we neglected the wave groupscale forcing that is known to influence rip spacing [*Reniers et al.*, 2004] as well as the 3-D structure of wave-driven circulations that can become significant in rip current settings [e.g., *Haas and Svendsen*, 2002]. These assumptions are commonly used for modeling 3-D surfzone sandbar behavior [e.g., *Garnier et al.*, 2008; *Smit et al.*, 2008]. More importantly, there are two key assumptions that need to be discussed. Simulations (not presented herein) showed that changing the basic state drastically impacts rip channel characteristics with similar results as in the work of *Calvete et al.* [2007]. Therefore our statement that changes in H_s do not impact on rip spacing in the model is likely not to be relevant for situations where rip channels form and evolve similarly or less rapidly than the rate at which the beach profile is changing, that is, for large-amplitude changes in offshore wave heights. Correspondingly, *Van Enckevort et al.* [2004] indicated that most merging and splitting events took place during a significant increase and decrease in wave height, which was not possible to test with our model. A second assumption in our modeling study is that changes in wave conditions systematically occur at $t = 4$ days, that is, with a preexisting (yet slightly developed) sequence of horns and bays superimposed to the bar. The motivation for this choice was that, when starting time-varying wave angle forcing from the alongshore-uniform geometry, the dynamic equilibrium of rip channels systematically started later, typically at about $t = 20$–25 days for the 4°-amplitude simulations. For $A > 4°$, rips sometimes did not even have the time to saturate by the end of the 41.5 day simulation. Thus we started the time-varying conditions at $t = 4$ days to keep the computation cost reasonable and to be able to accurately address merging/splitting dynamics for a large range of A. These preexisting bedforms may have impacted the subsequent evolution of rip channels. *Tiessen* [2010]showed that the influence of preexisting bedforms was limited if the initial bedform amplitude was small, the final dominant rip spacing always close to the dominant rip spacing found by linear stability analysis (i.e., without preexisting bedforms). The additional simulations starting with time-varying forcing at different times showed similar rip channel behavior as in the simulations presented in this paper. Therefore we think that the weakly developed preexisting pattern at $t = 4$ days does not influence our study outcomes significantly.

[43] Despite the limitations of our modeling approach, our results imply that the use of wave-climate mean values can be potentially misleading when investigating alongshore migration of surfzone sandbars, mean rip spacing, and beach three-dimensionality, and that sandbar response becomes increasingly complex when conditions change abruptly. The present nonlinear morphodynamic model has never been validated with field data, so the threshold values in A and T are to be considered in a qualitative way. Given the recent advances in process knowledge and numerical techniques in the nonlinear modeling of 3-D surfzone sandbar patterns, so far with application to academic cases only, a new step will be to study the response of a real-time sandbar system to natural changes in wave regimes. To do so, a crucial step is starting from an accurate nearshore bathymetry. Both the recent development of data-assimilation techniques [e.g., *Van Dongeren et al.*, 2008] and improvements in the understanding of cross-shore sandbar behavior [e.g., *Ruessink et al.*, 2007b], that should eventually prevent using the basic state assumption, will facilitate the emergence of data model comparisons.

[44] **Acknowledgments.** This work was done within the framework of the project BARBEC (ANR N2010 JCJC 602 01). BGR acknowledges additional funding by the Netherlands Organisation for Scientific Research (NWO) under contract 818.01.009. We thank Timothy Price for his corrections and acknowledge the three anonymous reviewers, the Associate Editor, and the Editor for their insightful comments.

References

Almar, R., B. Castelle, B. G. Ruessink, N. Sénéchal, P. Bonneton, and V. Marieu (2010), Two- and three-dimensional double-sandbar system behaviour under intense wave forcing and a meso-macro tidal range, *Cont. Shelf Res.*, *30*, 781–792.

Bailard, J. A. (1981), An energetics total load sediment transport model for a plane beach, *J. Geophys. Res.*, *86*(C11), 10,938–10,954.

Battjes, J. A. (1975), Modelling of turbulence in the surfzone, paper presented at Symposium on Modelling Techniques, Am. Soc. of Civ. Eng., Reston, Va.

Booij, N., R. C. Ris, and L. H. Holthuijsen (1999), A third-generation wave model for coastal regions: 1. Model description and validation, *J. Geophys. Res.*, *104*(C4), 7649–7666.

Bruneau, N., B. Castelle, P. Bonneton, R. Pedreros, R. Almar, N. Bonneton, P. Bretel, J. P. Parisot, and N. Sénéchal (2009), Field observations of an evolving rip current on a meso-macrotidal well-developed inner bar and rip morphology, *Cont. Shelf Res.*, *29*, 1650–1662.

Calvete, D., N. Dodd, A. Falqués, and S. M. Van Leeuwen (2005), Morphological development of rip channel systems: Normal and near-normal wave incidence, *J. Geophys. Res.*, *110*, C10006, doi:10.1029/2004JC002803.

Calvete, D., G. Coco, A. Falqués, and N. Dodd (2007), (Un)predictability in rip channel systems, *Geophys. Res. Lett.*, *34*, L05605, doi:10.1029/2006GL028162.

Castelle, B., P. Bonneton, and R. Butel (2006a), Modeling of crescentic pattern development of nearshore bars: Aquitanian Coast, France, *C. R. Geosci.*, *338*, 795–801.

Castelle, B., P. Bonneton, N. Sénéchal, H. Dupuis, R. Butel, and D. Michel (2006b), Dynamics of wave-induced currents over an alongshore non-uniform multiple-barred sandy beach on the Aquitanian Coast, France, *Cont. Shelf Res.*, *26*, 113–131.

Castelle, B., B. G. Ruessink, P. Bonneton, V. Marieu, N. Bruneau, and T. D. Price (2010a), Coupling mechanisms in double sandbar systems, Part 1: Patterns and physical explanation, *Earth Surf. Processes Landforms*, *35*, 476–486.

Castelle, B., B. G. Ruessink, P. Bonneton, V. Marieu, N. Bruneau, and T. D. Price (2010b), Coupling mechanisms in double sandbar systems, Part 2: impact on alongshore variability of inner-bar rip channels, *Earth Surf. Processes Landforms*, *35*, 771–781.

Castelle, B., et al. (2010c), Laboratory experiment on rip current circulations over a moveable bed: Drifter measurements, *J. Geophys. Res.*, *115*, C12008, doi:10.1029/2010JC006343.

Coco, G., and A. B. Murray (2007), Patterns in the sand: from forcing templates to self-organization, *Geomorphol.*, *91*, 271–290.

Damgaard, J., N. Dodd, L. Hall, and T. Chesher (2002), Morphodynamic modeling of rip channel growth, *Coastal Eng.*, *43*, 199–221.

Deigaard, R., N. Drønen, J. Fredsøe, J. H. Jensen, and M. P. Jørgensen (1999), A morphological stability analysis for a long straight barred coast, *Coastal Eng.*, *36*, 171–195.

Drønen, N., and R. Deigaard (2007), Quasi-three-dimensional modelling of the morphology of longshore bars, *Coastal Eng.*, *54*, 197–215.

Falqués, A., G. Coco, and D. A. Huntley (2000), A mechanism for the generation of wave-driven rhythmic patterns in the surf zone, *J. Geophys. Res.*, *105*(C10), 24,071–24,088.

Gallop, S. L., K. R. Bryan, G. Coco, and S. Stephens (2011), Storm-driven changes in rip-channel patterns on an embayed beach, *Geomorphol.*, *127*, 179–188.

Garnier, R., D. Calvete, A. Falqués, and M. Caballeria (2006), Generation and nonlinear evolution of shore-oblique/transverse sand bars, *J. Fluid Mech.*, *567*, 327–360.

Garnier, R., D. Calvete, A. Falqués, and N. Dodd (2008), Modelling the formation and the long-term behavior of rip channel systems from the deformation of a longshore bar, *J. Geophys. Res.*, *113*, C07053, doi:10.1029/2007JC004632.

Garnier, R., N. Dodd, A. Falqués, and D. Calvete (2010), Mechanisms controlling crescentic bar amplitude, *J. Geophys. Res.*, *115*, F02007, doi:10.1029/2009JF001407.

Haas, K. A., and I. A. Svendsen (2002), Laboratory measurements of the vertical structure of rip currents, *J. Geophys. Res.*, *107*(C5), 3047, doi:10.1029/2001JC000911.

Holman, R. A., G. Symonds, E. B. Thornton, and R. Ranasinghe (2006), Rip spacing and persistence on an embayed beach, *J. Geophys. Res.*, *111*, C01006, doi:10.1029/2005JC002965.

Huntley, D. A., and A. D. Short (1992), On the spacing between observed rip currents, *Coast. Eng.*, *17*, 211–225.

Klein, M. D., and H. M. Schuttelaars (2006), Morphodynamic evolution of double-barred beaches, *J. Geophys. Res.*, *111*, C06017, doi:10.1029/2005JC003155.

Lafon, V., H. Dupuis, R. Butel, B. Castelle, D. Michel, H. Howa, and D. De Melo Apoluceno (2005), Morphodynamics of nearshore rhythmic sandbars in a mixedenergy environment (SW France): II. Physical forcing analysis, *Estuarine Coastal Shelf Sci.*, *65*, 449–462.

Masselink, G., and B. Hegge (1995), Morphodynamics of meso- and macrotidal beaches: Examples from central Queensland, Australia, *Mar. Geol.*, *129*, 1–23.

Masselink, G., A. Kroon, and R. G. D. Davidson-Arnott (2006), Morphodynamics of intertidal bars in wave-dominated coastal settings—A review, *Geomorphol.*, *73*, 33–49.

Orzech, M. D., E. B. Thornton, J. H. MacMahan, W. C. O'Reilly, and T. P. Stanton (2010), Alongshore rip channel migration and sediment transport, *Mar. Geol.*, *271*, 278–291.

Pape, L., N. G. Plant, and B. G. Ruessink (2010), On cross-shore sandbar behavior and equilibrium states, *J. Geophys. Res.*, *115*, F03008, doi:10.1029/2009JF001501.

Phillips, O. M. (1977), *The Dynamics of the Upper Ocean*, Cambridge Univ. Press, Cambridge, U. K.

Price, T. D., and B. G. Ruessink (2011), State dynamics of a double sandbar system, *Cont. Shelf Res.*, *31*, 659–674.

Reniers, A. J. H. M., J. A. Roelvink, and E. B. Thornton (2004), Morphodynamic modeling of an embayed beach under wave group forcing, *J. Geophys. Res.*, *109*, C01030, doi:10.1029/2002JC001586.

Ribas, F., and A. Kroon (2007), Characteristics and dynamics of surfzone transverse finger bars, *J. Geophys. Res.*, *112*, F03028, doi:10.1029/2006JF000685.

Ruessink, B. G., I. M. J. Van Enckevort, K. S. Kingston, and M. A. Davidson (2000), Analysis of observed two- and three-dimensional nearshore bar behaviour, *Mar. Geol.*, *169*, 161–183.

Ruessink, B. G., G. Coco, R. Ranasinghe, and I. L. Turner (2007a), Coupled and noncoupled behavior of three-dimensional morphological patterns in a double sandbar system, *J. Geophys. Res.*, *112*, C07002, doi:10.1029/2006JC003799.

Ruessink, B. G., Y. Kuriyama, A. J. H. M. Reniers, and J. A. Roelvink (2007b), Modeling cross-shore sandbar behavior on the timescales of weeks, *J. Geophys. Res.*, *112*, F03010, doi:10.1029/2006JF000730.

Sénéchal, N., T. Gouriou, B. Castelle, J.-P. Parisot, S. Capo, S. Bujan, and H. Howa (2009), Morphodynamic response of a meso- to macro-tidal intermediate beach based on a long-term dataset, *Geomorphol.*, *107*, 263–274.

Smit, M. W. J., A. J. H. M. Reniers, and M. J. F. Stive (2005), Nearshore bar response to time-varying conditions, paper presented at Coastal Dynamics '05, Am. Soc. of Civ. Eng., New York.

Smit, M. W. J., A. J. H. M. Reniers, B. G. Ruessink, and J. A. Roelvink (2008), The morphological response of a nearshore double sandbar system to constant wave forcing, *Coast. Eng.*, *55*, 761–770.

Sonu, C. J. (1972), Field observation of nearshore circulation and meandering currents, *J. Geophys. Res.*, *77*, 3232–3247.

Tiessen, M. C. H. (2010), The influence of pre-existing bed-forms on the development of crescentic bed patterns, paper presented at Linear stability analysis in coastal morphodynamics: Essential or useless?, Tech. Univ. of Catelonia, Barcelona, Spain.

Tiessen, M. C. H., S. M. Van Leeuwen, D. Calvete, and N. Dodd (2010), Field test of a linear stability model for crescentic sandbar, *Coast. Eng.*, *57*, 41–51.

Turner, I. L., D. Whyte, B. G. Ruessink, and R. Ranasinghe (2007), Observations of rip spacing, persistence and mobility at a long, straight coastline, *Mar. Geol.*, *236*, 209–221.

Van Dongeren, A. R., N. G. Plant, A. B. Cohen, J. A. Roelvink, M. C. Haller, and P. Catalán (2008), Beach Wizard: Nearshore bathymetry estimation through assimilation of model computations and remote observations, *Coastal Eng.*, *55*, 1016–1027.

Van Enckevort, I. M. J., and B. G. Ruessink (2003), Video observation of nearshore bar behaviour. Part 2: alongshore non-uniformity variability, *Cont. Shelf Res.*, *23*, 513–532.

Van Enckevort, I. M. J., B. G. Ruessink, G. Coco, K. Susuki, I. L. Turner, N. G. Plant, and R. A. Holman (2004), Observations of nearshore crescentic sandbars, *J. Geophys. Res.*, *109*, C06028, doi:10.1029/2003JC002214.

Vis-Star, N., H. de Swart, and D. Calvete (2008), Patch behaviour and predictability properties of modelled finite-amplitude sand ridges on the inner shelf, *Nonlinear Proc. Geophys.*, *15*, 943–955.

Wright, L. D., and A. D. Short (1984), Morphodynamic variability of surf zones and beaches: A synthesis, *Mar. Geol.*, *56*, 93–118.

B. Castelle, CNRS, UMR 5805 EPOC, Université de Bordeaux, Avenue des Facultés, F-33405 Talence CEDEX, France. (b.castelle@epoc.u-bordeaux1.fr)

B. G. Ruessink, Department of Physical Geography, Faculty of Geosciences, Institute for Marine and Atmospheric Research, Utrecht University, NL-3508 Utrecht, Netherlands.

D.12 On the impact of an offshore bathymetric anomaly on surf zone rip channels

Bruno Castelle, Vincent Marieu, Giovanni Coco, Philippe Bonneton, Nicolas Bruneau, Gerben Ruessink

Journal of Geophysical Research - Earth Surface, Vol. 117, F01038, doi :10.1029/2011JF002141, 2012

On the impact of an offshore bathymetric anomaly on surf zone rip channels

B. Castelle,[1] V. Marieu,[1] G. Coco,[2] P. Bonneton,[1] N. Bruneau,[3] and B. G. Ruessink[4]

Received 4 July 2011; revised 6 February 2012; accepted 10 February 2012; published 31 March 2012.

[1] We use a nonlinear morphodynamic model to demonstrate that the presence of a single persistent offshore bathymetric anomaly strongly affects the formation, nonlinear evolution and saturation of surf zone rip channels. In the case of an offshore bump or trough and waves with oblique incidence, a rip channel shoreward of the anomaly is enforced by the more seaward alongshore variability in depth. The degree of rip channel enforcement is controlled by the strength of the rotational nature of surf zone rip current circulations, which is, in turn, driven by differential broken wave energy dissipation induced by wave refraction across the offshore bathymetric anomaly. The alongshore location of this forced rip channel is more stable with increasing offshore anomaly amplitude, decreasing offshore wave obliquity and decreasing bathymetric anomaly distance to the shore. Simulations show that rip channel behavior downdrift and updrift of the offshore perturbation are different. In our numerical experiments, downdrift rip channels have systematically larger alongshore scales, smaller alongshore migration rates and more erosive megacusps than those updrift. Rip channels therefore self-organize into patterns of different alongshore scales and migration rates as a result of an alongshore perturbation in the wave forcing enforced by wave refraction across an offshore bathymetric anomaly. These simulations are qualitatively corroborated by video observations of sandbar behavior during a down-state sequence at a site with a persistent offshore trough.

Citation: Castelle, B., V. Marieu, G. Coco, P. Bonneton, N. Bruneau, and B. G. Ruessink (2012), On the impact of an offshore bathymetric anomaly on surf zone rip channels, *J. Geophys. Res.*, *117*, F01038, doi:10.1029/2011JF002141.

1. Introduction

[2] Rip channels along wave-dominated beaches are ubiquitous and striking patterns in the sand. They typically consist of both longshore-oriented feeder channels and an offshore-directed rip neck channel that extends throughout the surf zone and incises shallow shore-connected or non-connected shoals [*Brander and Cowell*, 2003]. A rip head bar is also commonly observed seaward in a relatively shore-normal orientation aligned with the rip neck [*Brander and Short*, 2000]. Rip channels prevail as a rhythmic or quasi-rhythmic pattern with an alongshore wavelength of typically several times the surf zone width, i.e., O(100 m). Breaking waves on rip channel morphology force strong jet-like offshore-directed currents called rip currents [*MacMahan et al.*, 2006]. The resulting surf zone circulations are both a key element of mixing in the nearshore and a major hazard to beachgoers [*Scott et al.*, 2009; *Dalrymple et al.*, 2011].

[3] Self-organization models based on linear stability analysis [e.g., *Deigaard et al.*, 1999; *Falqués et al.*, 2000; *Calvete et al.*, 2005; *Klein and Schuttelaars*, 2006] or nonlinear solution of the shallow water equations coupled to sediment transport [e.g., *Reniers et al.*, 2004; *Garnier et al.*, 2006; *Drønen and Deigaard*, 2007; *Smit et al.*, 2008; *Castelle and Ruessink*, 2011] have established that rip channels and other three-dimensional (3-D) sandbar patterns, such as crescentic sandbars, form through the positive feedback between flow (waves and currents), sediment processes and the evolving seabed morphology without requiring a template (edge wave) in the hydrodynamics [*Coco and Murray*, 2007]. Nonlinear morphodynamic models allow examination of temporal changes in the wavelength and the amplitude of the 3-D patterns resulting from merging and splitting of rip channels that are typically observed in the field [*Van Enckevort et al.*, 2004]. So far, all the existing nonlinear analysis studies assumed alongshore-uniform initial beach geometry and wave forcing, with three notable exceptions. First, *Reniers et al.* [2004] used an alongshore nonuniform wavefield by including directional spreading in the initial wave conditions. They showed that the directional spreading affects the behavior of rip channels. Second, *Castelle et al.* [2010a, 2010b] addressed the impact of a crescentic outer bar on inner bar rip channel formation. This

[1]UMR EPOC 5805, CNRS, Université de Bordeaux, Avenue des Facultés, Talence, France.
[2]Environmental Hydraulic Institute, IH Cantabria, Universidad de Cantabria, Santander, Spain.
[3]National Laboratory of Civil Engineering, Estuaries and Coastal Zones Division, Lisbon, Portugal.
[4]Institute for Marine and Atmospheric Research, Department of Physical Geography, Faculty of Geosciences, Utrecht University, Utrecht, Netherlands.

0148-0227/12/2011JF002141

numerical study showed that alongshore variability in outer bar depth, and the relative importance of wave breaking versus wave focusing by refraction across the outer bar, is crucial to the inner bar rip channel development. For well-developed outer bar crescentic patterns, inner bar rip channels ultimately couple to the outer alongshore length scales, corroborating existing observations [e.g., *Ruessink et al.*, 2007; *Price and Ruessink*, 2011]. Third, *Tiessen et al.* [2011] addressed the influence of preexisting rhythmic surf zone bed forms on the subsequent nonlinear evolution of rip channels. They showed that the final dominant rip spacing was most of the time different than that obtained by running the numerical model with the same conditions over an initial alongshore-uniform bathymetry.

[4] Recent observations indicate that morphological features seaward of a surf zone strongly control shoreline variability [*Bender and Dean*, 2003; *McNinch*, 2004; *Schupp et al.*, 2006] and surf zone wave-driven circulations [e.g., *Shepard and Inman*, 1950; *Long and Özkan-Haller*, 2005; *Dalrymple et al.*, 2011]. Most of the studies addressing existing perturbation-shoreline coupling are essentially descriptive [e.g., *McNinch*, 2004; *Browder and McNinch*, 2006; *Schupp et al.*, 2006], with no insight in the underlying physics. Notable exceptions are the theoretical works addressing the development of shoreline instabilities induced by very oblique waves [e.g., *Falqués et al.*, 2011] and potentially low-angle wave incidence [*Idier et al.*, 2011], that are essentially based on the coupling between the surf and shoaling zones. *Bender and Dean* [2003, 2005] investigated wave transformation caused by the processes of wave refraction, diffraction and reflection across an offshore bathymetric anomaly to address the formation of a salient, but they did not compute sediment transport and resulting morphological evolution. Some authors [e.g., *Shepard and Inman*, 1950; *Long and Özkan-Haller*, 2005] examined rip current dynamics for specific beach configurations but did not explore the morphological evolution of rip channels. Overall, nonlinear morphodynamic numerical models have not been used to explore the sensitivity of rip channel behavior to an offshore bathymetric anomaly (i.e., seabed perturbation). This is addressed in this contribution.

[5] In section 2 we present the nonlinear morphodynamic model that describes morphological developments of 3-D surf zone patterns. We present the model by introducing the governing equations and corresponding assumptions, along with an introduction of the methods used to identify the linear/nonlinear/saturation regimes of the rip channels, to quantify rip spacing and alongshore migration rates, and to address the degree of enforcement of initial rip current circulations through wave refraction across the offshore bathymetric anomaly. Results are presented in section 3. We describe in detail a reference case simulation, showing that rip channel behavior downdrift and updrift of the offshore bathymetric anomaly are different. We further qualitatively address the influence of the offshore perturbation characteristics and wave angle on surf zone rip channel evolution. Then, differences in rip spacing and migration rates are quantified at the start of the saturation regime. A discussion is presented in section 4. We link downdrift rip channel behavior with the strength of surf zone rip current circulations enforced by wave refraction across the offshore bathymetric anomaly. Our proof of concept is then qualitatively compared with video observations of sandbar behavior during a down-state sequence at a site with a persistent offshore perturbation; and, furthermore, we discuss the limitations of our model. Finally, conclusions are provided in section 5.

2. Method

2.1. Nonlinear Morphodynamic Model

[6] The nonlinear morphodynamic model used herein couples a spectral wave model, a time- and depth-averaged flow model, an energetic-type sediment transport model, and the bed level continuity equation to compute bed level changes. This model contains the essential physics to describe the formation, nonlinear evolution and the saturation of the growth and the finite amplitude dynamics of rip channels and crescentic sandbars [e.g., *Castelle and Ruessink*, 2011].

2.1.1. Wave Module

[7] The wavefield and resulting radiation stress components are computed from the spectral wave model SWAN [*Booij et al.*, 1999] that solves the spectral wave action balance equation. As depth-induced wave breaking drives nearshore circulation, wave energy dissipation in the surf zone must be accurately computed. We used the parameterization of *Battjes and Janssen* [1978] with the breaker parameter γ_b as proposed by *Battjes and Stive* [1985], here $\gamma_b = 0.73$. These SWAN settings have been extensively validated with field cases [e.g., *Ris et al.*, 1999]. In addition, the reliability of this parameterization to drive nearshore circulation has been proven during low- to moderate-energy wave conditions [*Bruneau et al.*, 2011], which are the conditions considered in our numerical experiments.

2.1.2. Flow Module

[8] The flow model is based on the depth- and phase-averaged nonlinear shallow water equations [*Phillips*, 1977]. The wave group scale forcing [*Reniers et al.*, 2004] is disregarded in the flow model. The vertical structure of the flow was not resolved, despite the potentially significant variation of the velocity profile in rip current settings [e.g., *Haas and Svendsen*, 2002]. These are typical assumptions in nonlinear morphodynamic modeling of 3-D surf zone sandbars [e.g., *Garnier et al.*, 2006]. The nonlinear shallow water equations comprise the water mass conservation and momentum conservation equation that read, using the Einstein summation convention:

$$\frac{\partial Q_i}{\partial t} + \frac{\partial}{\partial x_j}\left(\frac{Q_i Q_j}{h}\right) + gh\frac{\partial \eta}{\partial x_i} + \frac{1}{\rho}\frac{\partial S_{ij}}{\partial x_j} - \frac{1}{\rho}\frac{\partial T_{ij}}{\partial x_j} + \frac{\tau_i^b}{\rho} = 0 \qquad (1)$$

$$\frac{\partial \eta}{\partial t} + \frac{\partial Q_j}{\partial x_j} = 0 \qquad (2)$$

where t is time, h is the mean water depth; $Q_i = hU_i$ is the water volume fluxes with the subscript $_i$ referring to the two horizontal coordinates (with x and y the alongshore and cross-shore axis, respectively), U_i is the wave-driven mass flux velocity according to *Mei* [1989], η is the mean free surface elevation, g is the gravitational acceleration, ρ is the water density, S_{ij} is the radiation stress tensor [*Phillips*, 1977], $\tau_i^b = \rho C_f u_{rms} U_i$ is the bed shear stress, u_{rms} is the

root-mean-square wave orbital velocity at the bottom, C_f is a bottom friction coefficient (equal to 0.0015 in the present study), and T_{ij} is the lateral mixing term which describes the horizontal momentum exchange due to the combined action of turbulence and mean current. Using the formulation proposed by *Battjes* [1975],

$$T_{ij} = \rho h \nu \left(\frac{\partial U_i}{\partial x_j} + \frac{\partial U_j}{\partial x_i} \right) \quad (3)$$

where the eddy viscosity ν is defined as

$$\nu = Mh \left(\frac{D}{\rho} \right)^{1/3} + \nu_0 \quad (4)$$

where D is the rate of energy loss through depth-induced wave breaking; M is a dimensionless coefficient (taken as 5 in the present study) and ν_0 is a constant eddy viscosity (taken as 5 m^2 s^{-1} in the present study). The latter eddy viscosity is used to damp potential hydrodynamic instabilities in the setup and circulation.

[9] In equation (1), the flow is driven by the gradient in radiation stresses S_{ij} of the surface water waves [*Longuett-Higgins and Stewart*, 1964] that read

$$S_{ij} = E \left(\frac{c_g}{c} \frac{k_i k_j}{k^2} + \left(\frac{c_g}{c} - \frac{1}{2} \right) \delta_{ij} \right) \quad (5)$$

where E is the wave energy density defined as $E = \rho g H_{rms}^2/8$; H_{rms} is the root-mean-square wave height; c_g and c are the group and phase velocity using linear wave theory, respectively; k is the wave number; and δ_{ij} is the Kronecker delta. For irregular waves, c, c_g and k are based on the spectral peak period.

2.1.3. Sediment Module

[10] Sediment transport computation is crucial to sandbar evolution as it provides the time-dependent coupling mechanism for adjusting the seabed which, in turn, alters the wavefield and wave-driven currents. Some of the existing sediment transport formulations in nonlinear morphodynamic models result in model blow-up for long-term simulations because the bed slope and bar amplitude become locally too large [e.g., *Drønen and Deigaard*, 2007; *Castelle et al.*, 2010a]. An alternative approach must be used if one wants to run simulations over long durations, i.e., several times the typical 3-D pattern growth time. An efficient and reasonably easy to implement approach is to assume that the cross-shore transport driven by wave nonlinearities and undertow is in balance with the gravitational downslope transport for a given equilibrium cross-shore beach profile Z_f^0 [*Garnier et al.*, 2006, 2008]. In other words, we assume that rip channels evolve more rapidly than the rate at which the beach profile is changing. In addition, as previously done in a number of numerical studies on nearshore bed form formation [e.g., *Falqués et al.*, 2000], we can assume that hydrodynamics plays a dominant role in such a way that accurate and/or complex description of sediment transport [e.g., *Van Rijn*, 1989] is not necessary to give some conceptual insight into the physical mechanisms that govern the bed form dynamics [e.g., *Schielen et al.*, 1993; *Falqués et al.*, 1996]. This type of simplified approach has been previously used in linear stability analysis studies [e.g., *Falqués et al.*, 1996, 2000; *Calvete et al.*, 2005] and more recently in nonlinear stability analysis [e.g., *Garnier et al.*, 2006]. Accordingly, the original sediment transport module [*Castelle et al.*, 2010a] was modified to examine the finite amplitude dynamics. We use a simplified advective sediment flux [*Castelle and Ruessink*, 2011] together with a gravitational downslope sediment transport that causes an increase in morphodynamic diffusivity. The latter produces a damping of the patterns essential for the onset of saturation of the rip channels [e.g., *Garnier et al.*, 2010]. In our model the horizontal sediment flux vector $\vec{Q}_s$ is

$$\vec{Q}_s = \alpha(\overline{\overline{|\vec{u}_b(t)|^3 \vec{u}_b(t)}} - \gamma u_{rms} \vec{\nabla} Z) \quad (6)$$

where α is a stirring factor; γ is a bed slope coefficient and $\vec{u}_b(t) = \vec{U} + (u_{rms} \cos\omega t)\vec{e}_k$ is the total flow velocity at the bottom (mean currents and orbital velocity, here assuming linear waves with ω the wave's angular frequency based on spectral peak) with $\vec{e}_k$ the unit vector along the wave ray (based on spectral peak). The $\overline{\overline{()}}$ notation defines time-averaging over a duration longer than the typical wave period. Finally, Z is the bed level deviation from initial equilibrium, i.e., $Z = Z_f - Z_f^0$, where Z_f and Z_f^0 are the seabed level and the initial equilibrium beach profile, or the basic state, respectively. The first term in equation (6) is the advective part in our sediment transport formula, similar to the suspended sediment load of *Bailard* [1981]. The second term is the downslope sediment transport with respect to the basic state. In the following we set $\alpha = 2.10^{-4}$ s^3 m^{-2} and $\gamma = 100$ m^3 s^{-3}. These settings (for more details, see *Castelle and Ruessink* [2011]) were chosen balancing the desire to both prevent any model blow-up in the range of wave conditions used both by *Castelle and Ruessink* [2011] and herein and to increase the possibility of observing merging and splitting dynamics. Because the advective part in our sediment transport formula is different from that of *Garnier et al.* [2006, 2008, 2010] our reference values of γ and α are not comparable with those of *Garnier et al.* [2006]. Yet, simulated rip channel systems and wave-driven circulations at saturation are similar in patterns and grow over similar timescales.

[11] The new seabed level Z_f was computed every morphological time step using the sediment mass conservation equation:

$$\frac{\partial Z_f}{\partial t} + \frac{1}{1-p} \vec{\nabla} \vec{Q}_s = 0 \quad (7)$$

where $p = 0.4$ is the sediment porosity. The morphological time step for the bed update scheme, which is different from the hydrodynamic time step (1 s), was 1 h throughout. All the simulations were run for 2000 morphological time steps, that is, 83.3 days of morphological evolution. In our model, the shoreline is allowed to evolve, which is a major difference with other nonlinear morphodynamic models applied to 3-D surf zone sandbar behavior. The sediment fluxes are computed at cell centers and further interpolated at the cell interfaces, artificially allowing sediment fluxes to transfer across the interface between dry and wet cells. Even though this is not a real swash zone, this allows the formation of

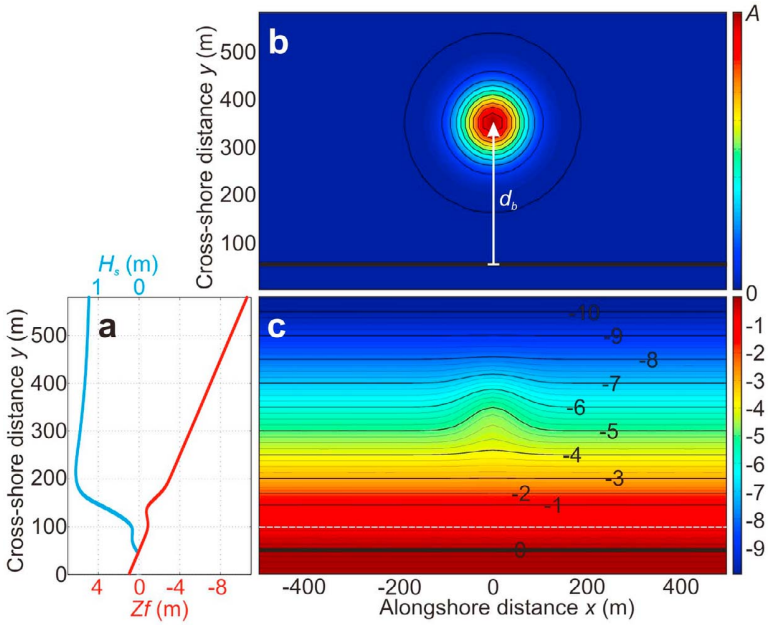

Figure 1. (a) Initial alongshore-uniform beach profile (red) with cross-shore distribution of the significant wave height H_s (H_s = 1.2 m, T_p = 10 s and $\theta = 0°$ at the offshore boundary). (b) Zoom at -500 m < x < 500 m of the superimposed offshore perturbation at a distance d_b from the 0 m sea level shoreline with height A (color bar). (c) Initial bathymetry (basic state) with the white dashed line indicating the location of the alongshore profile Z_b and color bar indicating seabed elevation in meters. In Figures 1b and 1c the thick black line indicates the 0 m sea level shoreline.

shoreline features such as megacusps, which are shoreline signatures of rip current presence.

2.2. Model Setup

[12] We ran the model for a number of different initial single-barred beach bathymetries. The computational grid had an alongshore and cross-shore length of 8000 m and 580 m, respectively, 20 × 20 m grid cells, and periodic lateral boundary conditions whose effect will be discussed later. The basic state consisted of a beach with a 1:50 planar sloping depth profile, with its offshore extent in 10.6 m water depth. A bar was superimposed onto this planar profile, located 90 m from the mean sea level shoreline with its crest in 0.8 m depth (Figure 1a).

[13] First, an alongshore-uniform profile without a bathymetric anomaly was considered. Random perturbations with a magnitude of 1 mm in the seabed were superimposed on the initial alongshore-uniform single-barred beach to excite nearshore instabilities. Hereafter we refer to this initial bathymetry as the alongshore-uniform scenario since there is no preexisting offshore perturbation.

[14] We designed additional initial bathymetries, with the same sandbar characteristics, and with the presence of one offshore bathymetric anomaly. To simplify, the offshore perturbation was described by a two-dimensional Gaussian function at a distance d_b from the 0 m sea level shoreline with a height A (Figure 1b). This perturbation was superimposed on the alongshore-uniform single-barred beach geometry, in the center of the domain at x = 0, to obtain an alongshore nonuniform initial bathymetry (Figure 1c). In our simulations we considered perturbations with -1.5 m ≤ A ≤ 1.5 m to address the influence of both bumps and troughs on the evolution of surf zone rip channels. The offshore bathymetric anomaly was part of the basic state which means that the offshore bump or trough did not significantly flatten or get infilled during the simulations, respectively.

[15] Time-invariant offshore wave conditions were used throughout this study with H_s = 1.2 m and T_p = 10 s. Different values of the offshore wave angle to the shore θ were implemented with $0 \le \theta \le 3.5°$. The simulated rip channel behavior with a preexisting offshore perturbation was very similar for $\theta > 3°$ because of the lateral boundary conditions in the model (this is further discussed in section 4). Therefore simulations with $3.5 < \theta < 7°$ are not presented.

2.3. Model Analysis

[16] Below we detail how we examined surf zone rip channel behavior. First, we used a global analysis of beach evolution (section 2.3.1) to both detect the linear, nonlinear and saturation regimes of rip channels and to quantify rip channel alongshore migration downdrift and updrift of the offshore perturbation. Second, we used a wavelet analysis (section 2.3.2) to estimate updrift and downdrift rip spacing. Finally, the offshore bathymetric anomaly control on surf zone rip currents and resulting initial rip channel formation was examined (section 2.3.3) to explain the contrasting updrift/downdrift rip channel behavior in section 4.

2.3.1. Global Analysis

[17] To examine the evolution of rip channels, a 'global analysis' of beach evolution [*Garnier et al.*, 2006, 2010] was

used. This consists of analyzing variables that are integrated over the whole computational domain. The notation $\overline{()}^g$ is introduced to define an average over the computational domain which, for a given function $f = f(x, y, t)$, reads

$$\bar{f}^g = \frac{1}{L_x L_y}\int_0^{L_x}\int_0^{L_y} f\,dxdy \tag{8}$$

where L_x and L_y are the longshore and cross-shore length of the computational domain, respectively. In addition, because simulations comprising an offshore bathymetric anomaly showed that rip channels often possess remarkably contrasting behavior updrift ($x < 0$) of the perturbation with respect to downdrift ($x > 0$), we discriminated the global analysis updrift of the perturbation ($-3000\ \text{m} \le x \le -1000\ \text{m}$) and downdrift of the perturbation ($1000\ \text{m} \le x \le 3000\ \text{m}$) with the $\bar{.}^u$ and $\bar{.}^d$ notations:

$$\bar{f}^u = \frac{1}{2000 L_y}\int_{-3000}^{-1000}\int_0^{L_y} f\,dxdy \tag{9}$$

$$\bar{f}^d = \frac{1}{2000 L_y}\int_{1000}^{3000}\int_0^{L_y} f\,dxdy \tag{10}$$

[18] Using the same definition as *Garnier et al.* [2010], the global growth rate, σ^i ($i = g$ for the whole computational domain, u for the updrift or d for the downdrift), is given by

$$\sigma^i = \frac{1}{2\|Z\|^{i2}}\frac{d}{dt}\left(\|Z\|^{i2}\right) \tag{11}$$

where $\| Z \|^i$ is the L_2 norm of Z:

$$\|Z\|^i = \sqrt{\overline{Z^2}^i} \tag{12}$$

so that $\| Z \|^i$ is a measure of beach three dimensionality.

[19] An additional variable that is considered in this study is the instantaneous global longshore migration rate V_L^i of the rip channels. According to *Vis-Star et al.* [2008], V_L^i is defined as

$$V_L^i = -\frac{1}{\overline{(\partial Z/\partial x)^2}}\overline{\frac{\partial Z}{\partial x}\frac{\partial Z}{\partial t}}^i \tag{13}$$

[20] Because of the periodic lateral boundary conditions implemented in the model, downdrift rip channels eventually enter the updrift domain for $\theta > 0°$. When running a simulation for a long duration and significant rip channel alongshore migration, V_L^u and V_L^d eventually become inseparable. Therefore, to have a good measure of the updrift and downdrift rip channel migrations, we computed V_L^u and V_L^d when $\sigma^g \approx 0$ for the first time. *Garnier et al.* [2010] called the corresponding state the saturated state. Therefore here we defined the saturation time t_s as the time when for the first time $\sigma^g < 0.01\ \text{d}^{-1}$. Because the detection of the saturation time was sometimes complicated for situations with an offshore bathymetric anomaly (large variability of σ^g close to the expected t_s as a result of merging of rips at $x \approx 0$), we defined the saturation time from the corresponding alongshore-uniform scenario simulation. Hereafter, updrift and downdrift rip channel longshore migration rates at saturation ($t = t_s$) are noted $\tilde{V}_L^u$ and $\tilde{V}_L^d$, respectively.

2.3.2. Rip Spacing

[21] The alongshore profile $Z_b(x, t) = Z_f(x, y = 100\ \text{m}, t)$ between the bar crest and the mean sea level shoreline (Figure 1c) was computed at every time step to estimate rip channel time evolution. This location is considered to be representative of the rip channel evolution. Because simulations with preexisting offshore perturbation often showed large variability in rip channel alongshore scales, the traditional Fourier Transform was not suitable to estimate rip spacing. Instead, we used a wavelet analysis to examine the evolution of rip channels and how rip spacing varies alongshore. Using the toolbox wtc-r14 [*Jevrejeva et al.*, 2003; *Grinsted et al.*, 2004], we applied the continuous wavelet transforms $W_n^z(s)$ defined as the convolution of a discrete sequence z_n ($n = 0, \ldots, N-1$) with a scaled and normalized mother wavelet function ψ_0:

$$W_n^z(s) = \left(\frac{\mathrm{d}z}{s}\right)^{1/2}\sum_{n'=0}^{N-1} z_{n'}\psi_0^*\left(\frac{(n'-n)\mathrm{d}z}{s}\right) \tag{14}$$

where $\mathrm{d}z$ is the uniform spacing in z_n, n is the alongshore coordinate, s is the alongshore scale [*Torrence and Compo*, 1998], and the asterisk is the complex conjugate. The $W_n^z(s)$ is used to decompose Z_b into energy at a given alongshore scale and at a given alongshore distance. This enables both the detection of the dominant spatial modes of variability and how these modes vary in space. As in some previous wavelet applications to sandbar data [e.g., *Ruessink et al.*, 2007; *Castelle et al.*, 2010b], we used the Morlet wavelet ψ_0 because of its good localization characteristics in both the space and frequency domains. In all results below, the term wavelength refers to the Fourier wavelength λ equivalent to the wavelet scale s. We determined the statistical significance of $W_n^z(s)$ against synthetic red noise series, as detailed by *Torrence and Compo* [1998]. The edge-affected part of $W_n^z(s)$ is termed the cone of influence (COI).

[22] We additionally computed the spatial averages (outside of the COI) of $W_n^z(s)$ updrift of the offshore bathymetric anomaly $\overline{W^z}^u(s)$ and downdrift of the perturbation $\overline{W^z}^d(s)$. As for the alongshore rip channel migrations rates, V_L^u and V_L^d, downdrift rip channels eventually enter the updrift domain and the downdrift rip spacing can be progressively disturbed by the downdrift rip spacing. Therefore, we selected the wavelet transform at the end of the saturation process ($t = t_s$) and we computed the corresponding updrift and downdrift spatial averages $\widetilde{W^z}^u(s)$ and $\widetilde{W^z}^d(s)$. The wavelengths for which $\widetilde{W^z}^u(s)$ and $\widetilde{W^z}^d(s)$ are maximum define the updrift rip spacing $\tilde{\lambda}_m^u$ and downdrift rip spacing $\tilde{\lambda}_m^d$ at saturation.

2.3.3. Offshore Bathymetric Anomaly Control on Surf Zone Rip Currents and Resulting Initial Rip Channel Formation

[23] The impact of wave transformation across the offshore perturbation on the generation of inshore rip currents was addressed with two approaches: the traditional radiation stress approach and the more recently introduced vorticity forcing term related to spatial gradients in depth-induced

breaking wave dissipation. The motivation for combining these two approaches is twofold: (1) to address in detail the nearshore wave-induced circulations across the sandbar due to wave refraction offshore and (2) to test the ability of the vorticity conservation equation to provide straightforward quantitative information of the strength and rotational nature of wave-driven circulations without the requirement of running a wave-driven circulation model.

[24] It is commonly stated that alongshore pressure gradients $-\rho g\partial\eta/\partial x$ drive rip current circulations. However, the major driving mechanism for nearshore circulation currents is the combination of the radiation stress gradients $\vec{F}_w$ and the pressure gradients $\vec{F}_p$ [*Haas and Svendsen*, 2002; *Castelle and Bonneton*, 2006]. Thus, the vectorial sum of the two components, that we can derive from equation (1), indicates how much net forcing is available to drive nearshore currents only and reads

$$F_{ri} = -gh\frac{\partial\eta}{\partial x_i} - \frac{1}{\rho}\frac{\partial S_{ij}}{\partial x_j} \tag{15}$$

[25] The second approach is based on the differential broken wave energy dissipation derived from the depth-integrated and time-averaged momentum equations given by *Smith* [2006]. The resulting advection-diffusion mean flow vertical vorticity conservation equation is [*Bonneton et al.*, 2010; *Bruneau et al.*, 2011]

$$\frac{\partial\Gamma}{\partial t} + \vec{\nabla}.(\Gamma\vec{U}) = \left(\vec{\nabla}\wedge(D\vec{e}_k)\right)\cdot\vec{e}_z + \tau_t \tag{16}$$

where $\Gamma = \left(\vec{\nabla}\wedge\vec{U}\right)\cdot\vec{e}_z$ is the mean vertical vorticity; $\vec{e}_z$ is the vertical unit vector; $D = D_b k/\sigma_r$ is the intensity of the depth-induced breaking dissipative force [*Bonneton et al.*, 2010] with D_b the depth-induced wave breaking dissipation; σ_r is the relative frequency (all based on spectral peak) and τ_t the turbulent diffusion of the vorticity. For quasi-stationary rip current circulations ($\partial\Gamma/\partial t \approx 0$), the nonlinear advective term $\vec{\nabla}.(\Gamma\vec{U})$ becomes small in comparison with $\left(\vec{\nabla}\wedge(D\vec{e}_k)\right)\cdot\vec{e}_z$ [*Bruneau et al.*, 2011]. This results in a balance between the spatial gradients in broken wave energy dissipation, and the turbulent diffusion of the vorticity $\tau_t \sim \nu_t\vec{\nabla}^2\Gamma$ where ν_t is a turbulent eddy viscosity. Therefore the strength and rotational nature of nearshore circulations are essentially governed by the wave-induced vorticity forcing term F_v that reads

$$F_v = \left(\vec{\nabla}\wedge(D\vec{e}_k)\right)\cdot\vec{e}_z \tag{17}$$

3. Results

3.1. No Perturbation Versus Perturbation

[26] Below we address two simulations with the same wave conditions (H_s = 1.2 m, T_p = 10 s and θ = 1.5°) but contrasting offshore geometries: the alongshore-uniform scenario (no offshore perturbation) and an alongshore non-uniform scenario characterized by an offshore perturbation with $A = -1$ m (trough) and d_b = 350 m. The latter will be hereafter referred to as the reference case simulation. The same approach was systematically used for all the other simulations from which results are synthesized in section 3.2.

3.1.1. General Behavior

[27] Figure 2 shows the time evolution of the alongshore profile Z_b and corresponding time series of σ^i, $\|Z\|^i$ and V_L^i (i = g, u, d) for the two simulations. For the alongshore-uniform scenario (Figures 2a, 2c, and 2e), the rips appear at $t \approx$ 5–6 days (Figure 2a) with concurrent exponentially increasing $\|Z\|^g$ and highest values of σ^g (Figure 2c). This characterizes the linear regime [*Garnier et al.*, 2010]. From about day 6 to day 10, σ^g strongly decreases with merging of rips and less rapidly increasing $\|Z\|^g$ (Figure 2c). This characterizes the saturation process [*Garnier et al.*, 2010]. Further mergings occur for t > 10 days ($\sigma^g \approx 0$, saturated state) as rips tend to self-organize into more regularly spaced features. For t > 20 days no further rip merging occurs and the rip channel alongshore migration rate stabilizes at $V_L^g \approx 16$ m d^{-1} (Figure 2e). Considering the reasonably small angle of incidence (θ = 1.5°), 16 m d^{-1} is high. The systematic overestimation of rip channel migration rates with nonlinear morphodynamic models has already been pointed out by *Falqués et al.* [2008]. In nature, similar migration rates have been observed only for much higher angle of incidence [e.g., *Van Enckevort and Ruessink*, 2003]. For the alongshore-uniform scenario the saturation time is t_s = 9.37 days.

[28] This rip channel behavior contrasts with that in the experiment with the preexisting offshore bathymetric anomaly (Figures 2b, 2d, and 2f). Within 1–2 days, a rip channel forms shoreward of the perturbation at $x \approx 0$ (Figure 2b). At t = 2 days a second rip channel forms updrift with a third one later at $t \approx 5$ days. Downdrift of the perturbation, rip channels form at $t \approx 4$ and 6 days at $x \approx 900$ m and 1800 m, respectively. In the meantime, rips appear at $x < -1000$ m and $x > 3000$ m from about t = 5–6 days (Figure 2a) with concurrent exponentially increasing $\|Z\|$ and highest values of σ^g (Figure 2d). This is similar to the rip channel behavior in the alongshore-uniform scenario. The latter rip channel formation is not affected by the offshore bathymetric anomaly and these rip channels are hereafter referred to as free rip channels (indicated by white circles in Figure 2b). Downdrift of the perturbation, for t > 10 days, rip channels progressively migrate downdrift at a rate 4 m d^{-1} < V_L^d < 10 m d^{-1} (Figure 2f) which is significantly smaller than for the alongshore-uniform scenario. In addition, the downdrift mean rip spacing is larger than for the alongshore-uniform scenario (Figure 2b). In contrast, updrift of the perturbation for 10 days < t < 60 days, rip channels progressively migrate downdrift at a rate 20 m d^{-1} < V_L^u < 23 m d^{-1}. For t > 60 days V_L^u subsequently decreases (Figure 2f) as the downdrift rip channels progressively enter the updrift domain (Figure 2b). All the updrift rip channels continuously merge to the forced rip channel shoreward of the offshore perturbation at x = 0 with no updrift rip channel entering the downdrift domain throughout the simulation.

[29] This alongshore nonuniform simulation (Figures 2b, 2d, and 2f) illustrates the difficulty of discriminating updrift and downdrift domains when running a simulation over a long duration (downdrift rip channels eventually enter the updrift domain). To more accurately address the downdrift and updrift rip channel behavior, we analyzed rip channels at the saturation time t_s when both forced and free rip channels

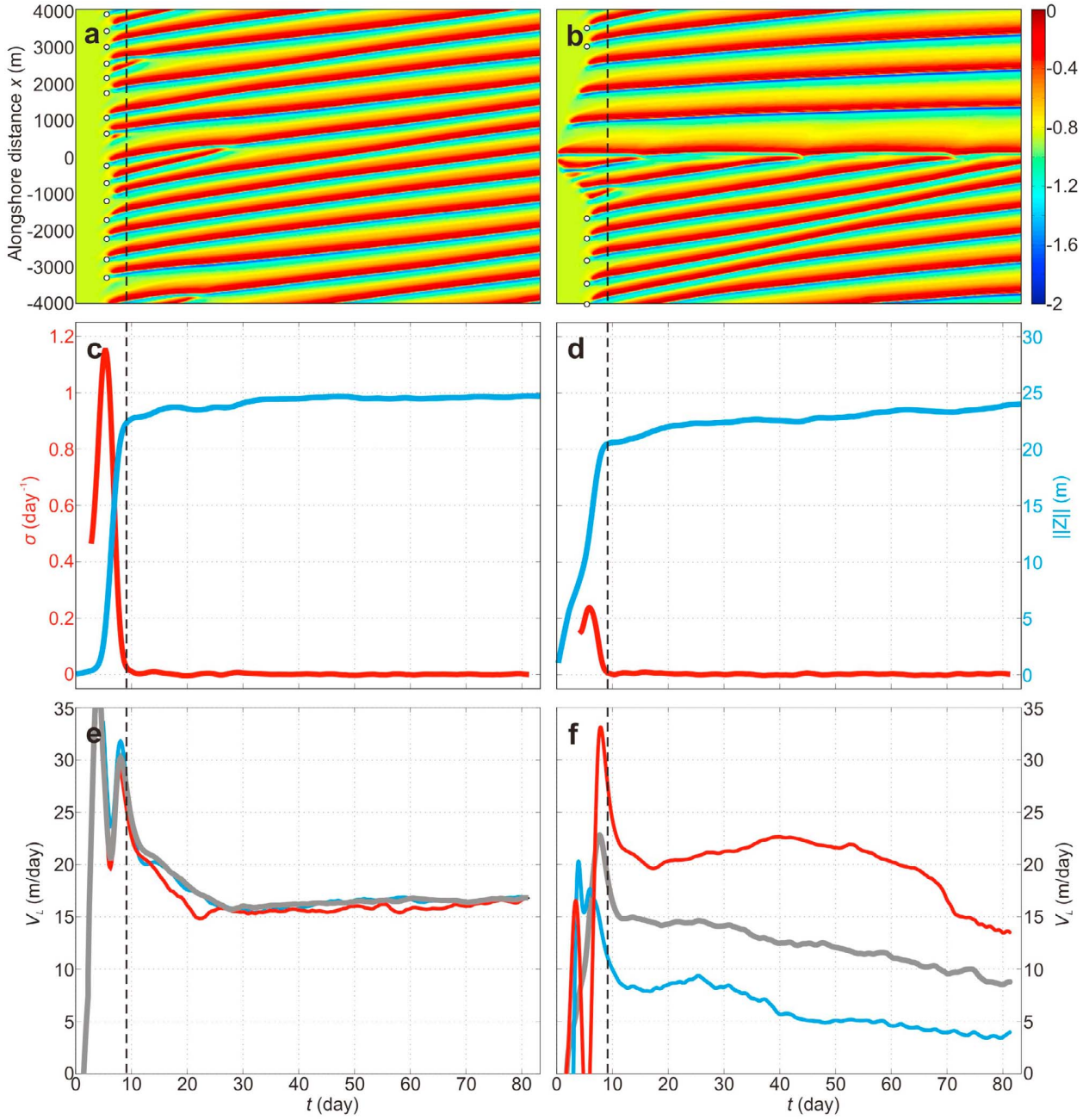

Figure 2. Formation and subsequent nonlinear evolution of rip channels for H_s = 1.2 m, T_p = 10 s and θ = 1.5° starting (left) from an alongshore-uniform beach and (right) with an offshore perturbation at x = 0 with $A = -1$ m (trough) and d_b = 350 m (reference case simulation). (a and b) Time evolution of the alongshore profile Z_b with white circles indicating the formation of free rip channels at $t \approx 6$ days and corresponding time series of (c and d) global growth rate σ^g (red) and $\|Z\|^g$ (blue) and (e and f) global longshore migration rate V_L^g (gray), updrift migration rate V_L^u (red) and downdrift migration rate V_L^d (blue). The vertical dashed line indicates the saturation time t_s = 9.37 days.

saturate and updrift rip channels are unlikely to affect/be affected by downdrift rips.

3.1.2. Configuration at Saturation Time t_s

[30] In this section we analyze the alongshore nonuniform scenario (Figures 2b, 2d, and 2f) at the saturation time (Figure 3). Figure 3a shows the alongshore profile Z_b at t_s = 9.37 days. The alongshore nonuniform variability of the seabed along Z_b has a typical height of 1.2–1.4 meters. The local wavelet spectrum for this situation indicates that Z_b contains alongshore nonuniform statistically significant power (Figure 3b) with larger wavelengths at 1000 m < x < 3000 m (downdrift domain in red in Figure 3b) than at -3000 m < x < -1000 m (updrift domain in blue in Figure 3b). The alongshore-averaged local wavelet spectra

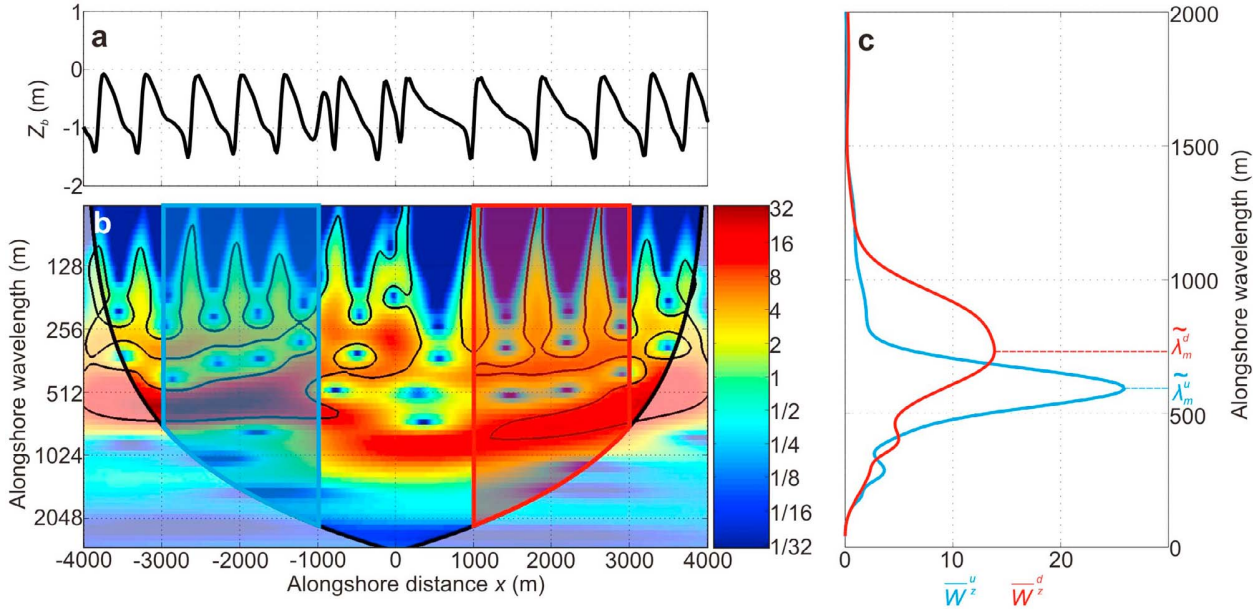

Figure 3. (a) Alongshore profile Z_b at the saturation time t_s = 9.37 days for H_s = 1.2 m, T_p = 10 s and θ = 1.5° starting from the alongshore nonuniform reference case with an offshore perturbation at x = 0 with A = −1 m (trough) and d_b = 350 m (reference case simulation). (b) Corresponding local wavelet spectrum $W_n^z(s)$ normalized by the variance with the 5% significance level against red noise (thick black contours), the cone of influence (COI) (shaded white area), superimposed areas to compute the updrift and downdrift local wavelet spatial averages $\overline{W^z}^u(s)$ and $\overline{W^z}^d(s)$ in blue and red, respectively, excluding local wavelet values within the COI. (c) Resulting $\overline{W^z}^u(s)$ and $\overline{W^z}^d(s)$ and updrift and downdrift mean rip spacing $\widetilde{\lambda}_m^u$ = 525 m and $\widetilde{\lambda}_m^d$ = 742 m defined as the wavelength for which $\overline{W^z}^u(s)$ and $\overline{W^z}^d(s)$ are maximum at the saturation time t_s in blue and red, respectively.

of Z_b in the updrift domain $\widetilde{W^z}^u(s)$ and downdrift domain $\widetilde{W^z}^u(s)$ are shown in blue and red in Figure 3c, respectively. Results show that the sandbar contains statistically high power at $\widetilde{\lambda}_m^u$ = 525 m (mean updrift rip spacing) and at $\widetilde{\lambda}_m^d$ = 742 m (mean downdrift rip spacing).

[31] The presence of the localized peaks of statistically significant power in Figure 3 is in line with our definition of the downdrift (1000 m < x < 3000 m) and updrift (−3000 m < x < −1000 m) domains. In Figure 3b there is a reasonably alongshore nonuniform statistically significant power in the downdrift domain at 1000 m < x < 3000 m and a lack of statistically significant power at −1000 m < x < 0 because rips were merging updrift of the offshore bathymetric anomaly at this time of the simulation. This was rarely the case for the other simulations.

3.1.3. Wave-Driven Circulations and Rip Channel Morphology Beyond Saturation Time t_s

[32] To address downdrift and updrift rip channel morphology and wave-driven circulations, we analyze results at t = 30 days when downdrift rip channels had not yet entered the updrift domain yet. Figure 4 shows a zoom at −2000 m < x < 2000 m of the beach morphology with superimposed wave-driven circulations at t = 30 days for the two scenarios described in Figure 2. For the alongshore-uniform scenario (Figure 4a) rip channels are reasonably regularly spaced alongshore. All the rip channels have a similar shape with a deep and narrow, slightly downdrift skewed neck, and a well-developed rip head bar. Megacusps with a cross-shore amplitude of about 40–50 m are also coupled to the rip channel geometry. These alongshore (O(100 m)) and cross-shore (O(10 m)) scales of megacusps are similar to observations of well-developed bar and rip morphologies [e.g., *Wright and Short*, 1984; *Thornton et al.*, 2007]. The undulations of the bathymetric lines coupled to the bar and rip morphology reach into about Z_f = −6 m. Even though large and detailed bathymetric surveys of well-developed 3-D surf zone sandbars are scarce, there is plenty of evidence that undulations (in the form of either isolated shoals or crescentic sandbars) at water depths of about −6 m are common. For example, *Almar et al.* [2010] measured bathymetric undulations at about Z_f = −9 m coupled to a crescentic sandbar with its crest in about 3 m depth. Similar observations were made at sites exhibiting bar and rip morphologies or crescentic sandbars [e.g., *Wijnberg and Kroon*, 2002; *Bender and Dean*, 2003]. The megacusps have a significantly skewed shape (Figure 4a). To date, the two most comprehensive studies on megacusps were done by *Thornton et al.* [2007] and *Orzech et al.* [2011]. They both addressed megacusps along the southern Monterey Bay (California), which is characterized by persistent near-normal wave incidence due to strongly refracted waves and narrow bay aperture. This results in relatively stationary, shore-normal, rip channels. Accordingly, the authors could not address the impact of wave incidence on the shape of megacusps in the presence of migrating and skewed rip channels. Wave-driven rip current circulations are typical in patterns with alongshore feeder currents, a reasonably

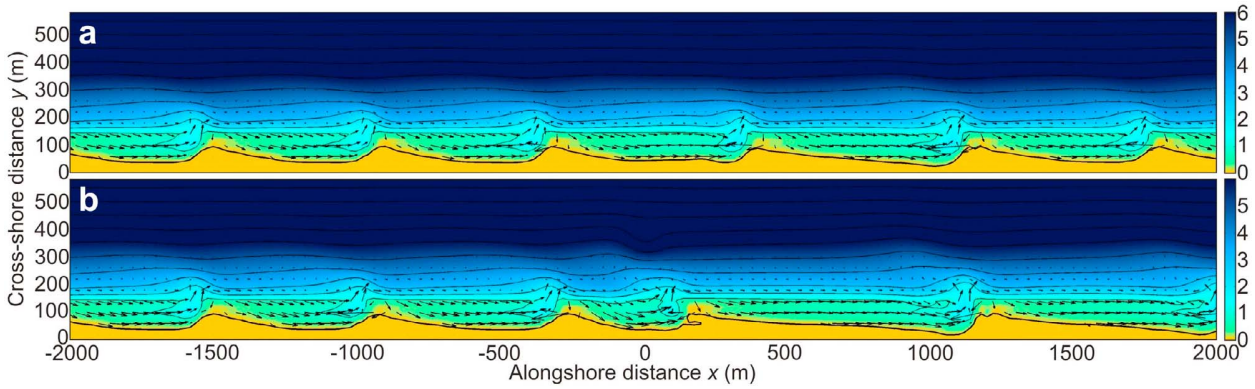

Figure 4. Zoom of the bathymetry at -2000 m $< x <$ 2000 m and $0 < y <$ 300 m with superimposed wave-induced currents (arrows, one out of two vectors are plotted in both directions) at t = 30 days for waves with H_s = 1.2 m, T_p = 10 s and θ = 1.5° (a) starting from the alongshore-uniform beach and (b) starting from the alongshore nonuniform reference case with an offshore perturbation at x = 0 with $A = -1$ m (trough) and d_b = 350 m (reference case simulation). Note the larger rip spacing and more erosive megacusps downdrift of the perturbation than updrift of the perturbation. Color bars indicate seabed elevation in meters, and isobaths (1 m intervals) are contoured in the background.

intense (≈ 0.7 m s^{-1}) and narrow offshore-directed jet in the channel, onshore-directed flow across the shoals and counterrotating cells to the left and right of each rip current. These rip channel morphology and wave-driven hydrodynamics are essentially similar to field and laboratory observations of well-developed bar and rip systems exposed to low- to moderate-energy waves with normal to near-normal incidence [e.g., *Bruneau et al.*, 2009; *Austin et al.*, 2010; *Castelle et al.*, 2010c].

[33] The same applies for the alongshore nonuniform scenario (reference case simulation) at t = 30 days in Figure 4b. As previously shown (Figure 2b), rip spacing is substantially larger downdrift of the offshore bathymetric anomaly than updrift. In addition, rip currents are more shore-normal downdrift of the offshore perturbation than updrift (Figure 4b). Megacusps show alongshore-variable cross-shore scales for the alongshore nonuniform scenario (Figure 4b). Updrift of the offshore perturbation, megacusps have a cross-shore amplitude of about 40–50 m, similar to the alongshore-uniform scenario, while megacusps systematically have a larger cross-shore amplitude of about 60–70 m downdrift of the perturbation (Figure 4b).

3.2. Influence of Perturbation Height, Wave Angle and Offshore Perturbation Distance to the Shore on Surf Zone Rip Channel Evolution

[34] Below we address the influence of the perturbation height A, wave angle θ and offshore perturbation distance to the shore d_b on the formation and subsequent evolution of rip channels. First, we describe the general evolution of the rip channels throughout the simulations for different values of d_b. Second, we set d_b = 350 m and investigate the influence of A and θ on rip spacing and migration rate at saturation time t_s.

3.2.1. General Behavior

[35] Figure 5 shows the time evolution of the alongshore profile Z_b for waves with H_s = 1.2 m, T_p =10 s and θ = 1.5° for an offshore trough with $A = -1$ m and different offshore distances to the shore d_b = 350 m (in about 6 m depth, reference case simulation), 450 m (in about 8 m depth) and 550 m (in about 10 m depth). Results show that, for d_b = 350 m and 450 m, rip channel evolution is similar up to $t \approx$ 30 days (Figures 5a and 5b) as the forced rip channel shoreward of the offshore bathymetric anomaly at $x \approx 0$ does not enter the downdrift domain. Downdrift mean rip spacing and longshore migration rates are about 800 m and 10 m d^{-1}, respectively. For $t >$ 30 days, the forced rip channel enters the downdrift domain for d_b = 450 m (Figure 5b). These two situations contrast with that for d_b = 550 m (Figure 5c), with updrift rip channels continuously entering the downdrift domain. Downdrift rip channels still have a larger mean spacing (about 800 m) than updrift rip channels until $t \approx$ 30 days when updrift and downdrift rip channels become inseparable. Similar results were obtained for an offshore trough. Overall, for a given A, the influence of the presence of an offshore bathymetric anomaly on surf zone rip channels decreases with increasing distance to the shore of the perturbation. In the following we only address situations with d_b = 350 m.

[36] Figure 6 shows the time evolution of the alongshore profile Z_b to address the influence of the presence of an offshore trough ($A = -0.5$ m, -1 m and -1.5 m at x = 0 with d_b = 350 m) on the surf zone rip channels for different wave angles to the shore θ (0°, 1°, 2° and 3°). For shore-normal waves (θ = 0°, Figures 6a–6c) a rip channel systematically forms within a few morphological time steps shoreward of the offshore trough at x = 0. Within a few days, further rip channels progressively form on both sides of the forced rip channel. Later for t = 5–10 days, free rip channels form farther away from the offshore trough (Figures 6a–6c). Overall for shore-normal waves, mean rip spacing is not overly affected by the offshore trough aside from triggering the formation of a "forced" rip (at x = 0).

[37] Rip channel behavior is more complicated for waves with oblique incidence (Figures 6d–6l). If the offshore wave angle to the shore θ is reasonably small and/or the trough

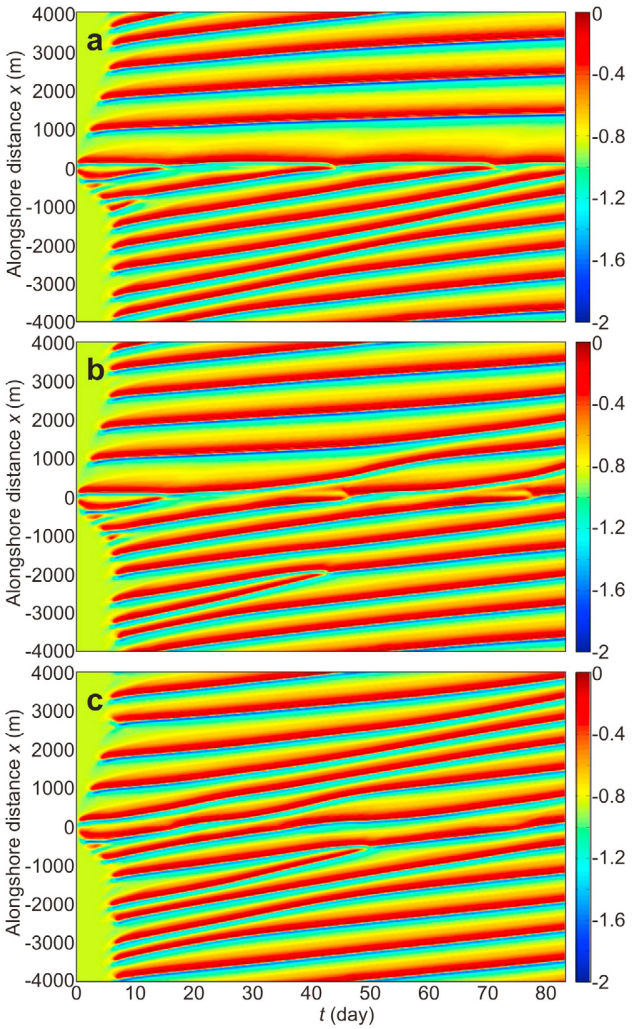

Figure 5. Influence of the offshore perturbation distance to the shore d_b on the formation and subsequent nonlinear evolution of rip channels. The offshore perturbation consists of an offshore trough with $A = -1$ m at $x = 0$. Figures 5a–5c show the time evolution of the alongshore profile Z_b with the color bar indicating seabed elevation in meters for H_s = 1.2 m, T_p = 10 s and $\theta = 1.5°$: (a) d_b = 350 m (reference case simulation), (b) d_b = 450 m and (c) d_b = 550 m.

amplitude $|A|$ is large, then updrift rip channels continuously merge to the forced rip channel at $x = 0$ without entering the downdrift domain (Figures 6e, 6f and 6i, see also Figure 2b). For these situations, rip channel behavior is similar to the alongshore nonuniform scenario described in detail in section 3.1. Updrift rip channels are not affected by the offshore perturbation until downdrift rip channels enter the updrift domain at the end of the simulation for $\theta = 1°$ (Figures 6e and 6f) and earlier for $\theta = 2°$ at $t \approx 30$ days (Figure 6i). Downdrift of the bathymetric anomaly, once formed, rip channels progressively migrate downdrift at a lower rate than updrift. In addition, in these numerical experiments, the downdrift mean rip spacing is systematically larger than the updrift mean rip spacing.

[38] For larger θ and/or smaller trough amplitude $|A|$ (Figures 6d, 6g, and 6h), updrift free rip channels continuously or sporadically enter the downdrift domain. In addition, a forced rip channel shoreward of the perturbation at $x = 0$ is not always present. Downdrift, mean rip spacing and alongshore migration rates are larger and smaller than updrift, respectively (Figures 6d, 6g, and 6h), similar to the situations with smaller θ and/or larger trough amplitude $|A|$ (Figure 6e, 6f and 6i). Further increasing θ and/or decreasing trough amplitude $|A|$ (Figures 6g, 6j, 6k and 6l) results in updrift rip channels continuously entering the downdrift domain without remaining at $x = 0$ for a long duration. In this case, for $\theta = 3°$ (Figures 6j, 6k, and 6l), updrift and downdrift rip channels are inseparable, which is a limitation due to the lateral periodic boundary conditions in the model. All the simulations with $\theta > 3°$ showed the same rip channel behavior.

[39] Figure 7 shows the time evolution of the alongshore profile Z_b to address the influence of the presence of an offshore bump (A = 0.5 m, 1 m and 1.5 m) on the surf zone rip channels for the same wave conditions as in Figure 6. For the shore-normal wave forcing (Figures 7a–7c), overall, rip channels behave the same as for an offshore trough with the same amplitude (Figures 6a–6c), as mean rip spacing is not readily affected by A. In contrast to the situations with an offshore trough, however, a bar forms at $x = 0$ instead of a rip channel for shore-normal waves. The situation with A = 1.5 m is more complicated as the two nearby rips almost merge at $x = 0$ from $t \approx 20$ days to the end of the simulation.

[40] For waves with oblique incidence (Figures 7d–7l), a shoal forms rapidly at $x = 0$ and subsequently migrates downdrift with a rip channel progressively forming immediately updrift at about $x \approx 0$. Therefore, morphology at $x \approx 0$ is reasonably similar for an offshore trough and an offshore bump (Figure 6d–6l). However, for the same perturbation amplitude $|A|$, updrift rip channels migrate more easily beyond the $x \approx 0$ position for an offshore bump than for an offshore trough (Figure 7d–7l). Overall, mean rip spacing and rip channel alongshore migration rate are larger and smaller downdrift of the offshore bump than updrift.

3.2.2. Configuration at Saturation Time t_s

[41] As indicated in section 3.1, investigating rip channels at saturation time t_s is relevant to more accurately address the downdrift and updrift rip channel behavior, as updrift rip channels are unlikely to be affected by downdrift rips (and potentially the other way around). Figure 8 shows the updrift and downdrift mean rip spacing $\widetilde{\lambda}_m^u$ and $\widetilde{\lambda}_m^d$ (Figures 8b and 8c) and longshore migration rate $\widetilde{V}_L^u$ and $\widetilde{V}_L^d$ (Figures 8d and 8e), respectively, at saturation time t_s. In agreement with existing linear and nonlinear stability analysis studies [e.g., *Garnier et al.*, 2008], t_s increases with increasing θ (Figure 8a). Mean rip spacing in the downdrift domain (Figure 8c) increases with increasing θ and is systematically larger than both the updrift (Figure 8b) and the alongshore-uniform scenario (Figures 8b and 8c for $A = 0$). In addition, in the downdrift domain for a given θ, mean rip spacing substantially increases with increasing perturbation amplitude $|A|$ (Figure 8c). In contrast, in the updrift domain, mean rip spacing is weakly influenced by θ or A as, overall, rip spacing only very slightly increases with increasing θ with a larger sensitivity for offshore troughs ($A < 0$ in Figure 8b) than for offshore bumps. In the updrift

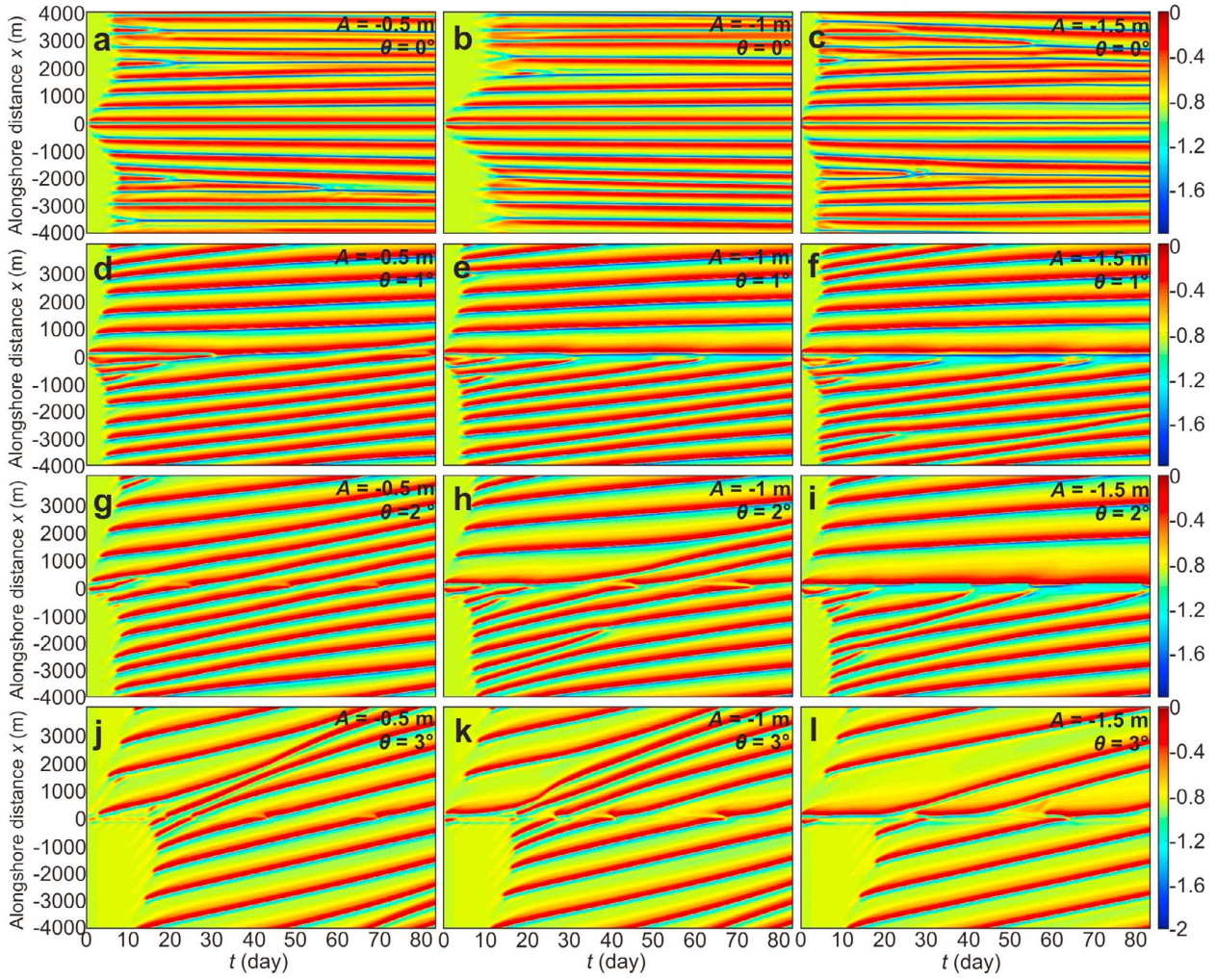

Figure 6. Influence of an offshore trough ($A < 0$) at $x = 0$ with $d_b = 350$ m on the formation and subsequent nonlinear evolution of rip channels. Figures 6a–6l show the time evolution of the alongshore profile Z_b with the color bar indicating seabed elevation in meters for $H_s = 1.2$ m, $T_p = 10$ s. (left) For $A = -0.5$ m, (middle) for $A = -1$ m and (right) for $A = -1.5$ m, with (a, b, c) $\theta = 0°$, (d, e, f) $\theta = 1°$, (g, h, i) $\theta = 2°$ and (j, k, l) $\theta = 3°$.

domain rip channel longshore migration rate increases with increasing θ and is not readily influenced by A (Figure 8d). In contrast, in the downdrift domain (Figure 8e), on the one hand $\widetilde{V}_L^d$ increases with increasing θ and on the other hand $\widetilde{V}_L^d$ decreases with increasing $|A|$ for a given θ. Therefore, for these obliquely incident wave numerical experiment, rip channel alongshore migration rate downdrift of an offshore bathymetric anomaly is systematically smaller than in the alongshore-uniform scenario.

[42] These results are synthesized in Figure 9 that shows the mean rip spacing $\widetilde{\lambda}_m$ versus rip channel migration rate $\widetilde{V}_L$ at saturation time t_s discriminating between the updrift and downdrift behavior. For a given domain (updrift or downdrift, or the whole domain if considering the alongshore-uniform scenario), rip channel migration rate $\widetilde{V}_L$ increases with increasing mean rip spacing $\widetilde{\lambda}_m$. In the downdrift domain, the alongshore migration rate increases with increasing mean rip spacing much more slowly than for both the alongshore-uniform scenario and the updrift domain.

4. Discussion

[43] In this section, we first discuss the links between the initial wave-driven circulations with the subsequent evolution of the rip channels. Second, we qualitatively compare our results with observations at a beach with a persistent offshore trough. We further discuss model limitations and the implications of our modeling exercise.

4.1. Physical Mechanism

[44] We first describe the hydrodynamics and resulting sediment transport patterns at $t = 0$ for different situations to examine the strength and patterns of rip current circulations enforced by wave refraction across the offshore bathymetric anomaly as a function of A and d_b. Second, we examine the time evolution of the hydrodynamics for the reference case

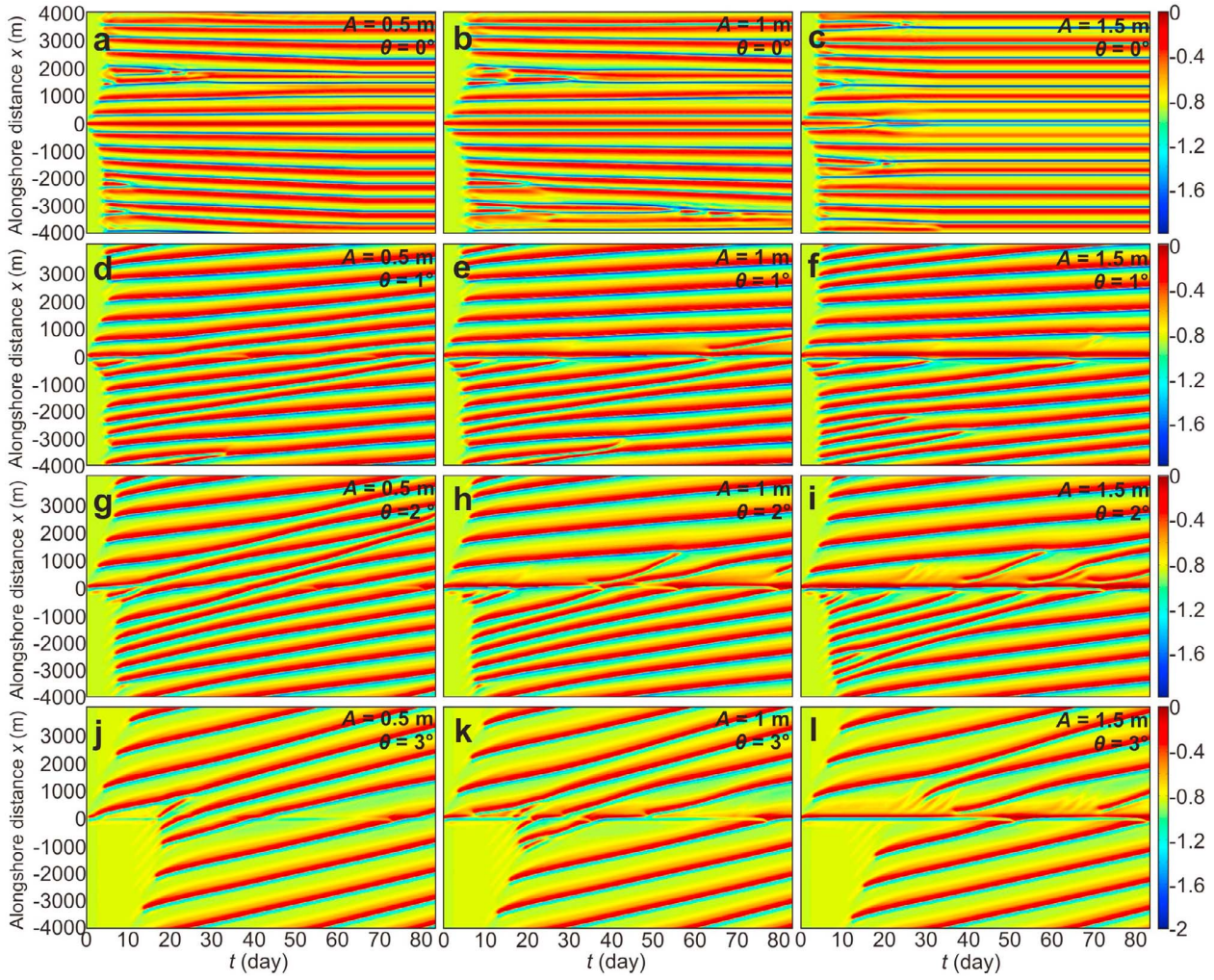

Figure 7. Influence of an offshore bump ($A > 0$) at $x = 0$ with $d_b = 350$ m on the formation and subsequent nonlinear evolution of rip channels. Figures 7a–7l show the time evolution of the alongshore profile Z_b with the color bar indicating seabed elevation in meters for $H_s = 1.2$ m, $T_p = 10$ s. (left) For $A = 0.5$ m, (middle) for $A = 1$ m and (right) for $A = 1.5$ m, with (a, b, c) $\theta = 0°$, (d, e, f) $\theta = 1°$, (g, h, i) $\theta = 2°$ and (j, k, l) $\theta = 3°$.

simulation to explore why updrift and downdrift rip channels behave differently.

4.1.1. Initial Wave-Driven Circulations

[45] Figure 10 shows the hydrodynamics and sediment transport patterns at $t = 0$ for offshore waves with $H_s = 1.2$ m, $T_p = 10$ s and $\theta = 1.5°$ for two alongshore nonuniform configurations with an offshore perturbation at $x = 0$ and $d_b = 350$ m with $A = -1$ m (trough, Figures 10a, 10c, 10e, 10g, and 10l, reference case simulation) and $A = 1$ m (bump, Figures 10b, 10d, 10f, 10h, and 10j). For the two configurations, and also for all the other simulations in this paper, wave-driven circulations and sediment transport are strong on the sandbar where waves break and are negligible in the vicinity of the offshore perturbation.

[46] For the initial situation with an offshore trough (reference case simulation, Figures 10a, 10c, 10e, 10g, and 10i corresponding to temporal evolution of Z_b in Figures 2b and 5a), wave refraction across the trough results in two wave energy focusing locations updrift and downdrift of the bathymetric anomaly at $x \approx -100$ m and 100 m, respectively (Figure 10a). The increasing wave heights at these locations lead to a larger amplitude of setup and set down in the surf and shoaling zone, respectively (Figure 10c). Alongshore gradients in radiation stress (Figure 10a) and pressure (Figure 10c) show slight patterns shoreward of the perturbation, and the vectorial sum resulting in the residual forcing $\vec{F}_r = \vec{F}_w + \vec{F}_p$ shows striking counterrotating patterns (Figure 10e) that characterizes the net forcing available to drive nearshore currents. In Figure 10e the wave-induced vorticity forcing term $F_v = \left(\vec{\nabla} \wedge (D\vec{e}_k)\right) \cdot \vec{e}_z$, which is superimposed, is essentially similar in pattern to $\vec{F}r$ (notice no circulation model has been run). This shows that rip current circulations are essentially driven by differential broken wave energy dissipation, i.e., without having to consider pressure gradients. The wave-driven circulations $\vec{U}$ and vorticity $\Gamma = \left(\vec{\nabla} \wedge \vec{U}\right) \cdot \vec{e}_z$ are shown in Figure 10g.

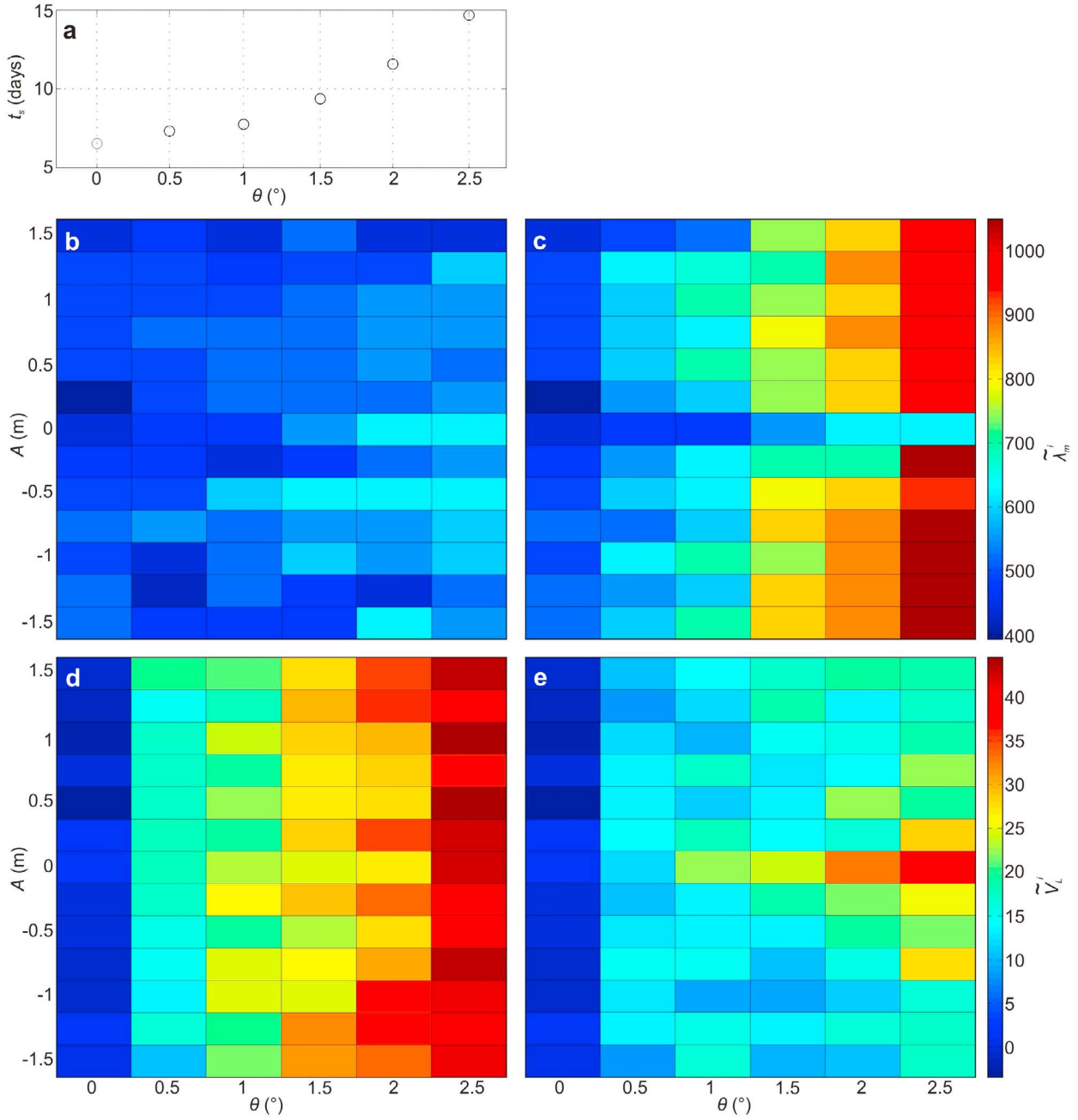

Figure 8. Mean rip spacing and rip channel alongshore migration at saturation time t_s as a function of the offshore perturbation height A and offshore wave angle to the shore θ for $d_b = 350$ m. (a) Saturation time t_s as a function of θ, (b) mean updrift rip spacing $\widetilde{\lambda}_m^u$, (c) mean downdrift rip spacing $\widetilde{\lambda}_m^d$, (d) updrift rip channel migration rate $\widetilde{V}_L^u$ and (e) downdrift rip channel migration rate $\widetilde{V}_L^d$.

A downdrift-skewed rip current is observed at $x \approx 0$ with a slightly undulating longshore current immediately to the right and to the left of the rip current.

[47] The resulting sediment transport fluxes $\vec{Q}_s$ and erosion/accretion patterns are shown in Figure 10i. An erosion area is observed shoreward of the offshore perturbation at $x \approx 0$, with the temporal evolution of the morphology eventually leading to the presence of the forced rip channel at $x \approx 0$ (Figure 6d). Two other erosion areas, yet less intense, are found at $x \approx -300$ m (updrift) and 400 m (downdrift) with the updrift erosion about 3 times larger than the downdrift one.

[48] The same analysis was done for the case of an offshore bump (Figures 10b, 10d, 10f, 10h, and 10j). For this situation wave refraction across the bump results in one localized wave energy focusing location shoreward of the bathymetric anomaly at $x \approx 0$ (Figure 10b). These forcing patterns have an opposite rotational nature with respect to the offshore trough situation (Figure 10e). This results in an onshore flow shoreward of the offshore bump at $x = 0$ and a

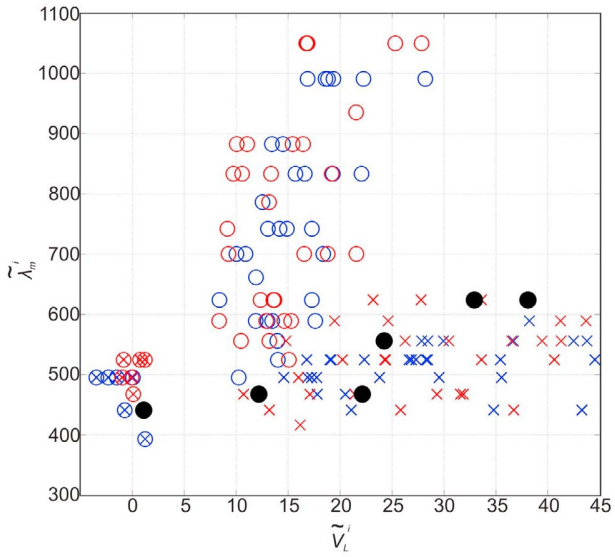

Figure 9. Mean rip spacing versus rip channel migration rate at saturation time t_s for d_b = 350 m: updrift (crosses), downdrift (circles) and alongshore-uniform scenario (thick circles). Red and blue correspond to simulations with an offshore trough and bump, respectively.

rip current immediately updrift at $x \approx -100$ m (Figure 10h). These circulations drive an accretion area shoreward of the offshore bump and two erosion areas to the right and to the left (Figure 10j).

[49] For smaller perturbation amplitude $|A|$ and/or larger wave angle θ, wave-induced vorticity forcing terms are similar in patterns but are less intense (not shown). Therefore, the degree of enforcement of the rip current circulation shoreward of the offshore perturbation decreases. As a result, rip channels can migrate past the $x = 0$ location (e.g., Figures 6g, 6h, 6j, 6k and 6l). For large perturbation amplitude $|A|$ and/or smaller wave angle θ, the degree of enforcement of the rip current circulation shoreward of the offshore bathymetric anomaly is large and the forced rip channel remains at the same alongshore location throughout the simulation.

[50] Figure 11 shows the same hydrodynamic analysis for the three situations addressing the influence of the offshore perturbation distance to the shore d_b in Figure 5. Wave refraction is similar in patterns for d_b = 350 m, 450 and 550 m, with two localized wave energy focusing locations updrift at $x \approx -100$ m and downdrift at $x \approx 100$ m (Figures 11a–11c). These wave focusing patterns are less intense and more diffused alongshore with increasing d_b (Figure 11). Accordingly, both the residual forcing $\vec{F}_r$ and wave-induced vorticity forcing term F_v show a rotational nature of similar pattern with less strength. Accordingly, there is less intense net rotational forcing available to drive nearshore currents with increasing d_b (Figures 11d–11f). Accordingly, nearshore currents are characterized by an undulating longshore current and a downdrift-skewed rip current (Figures 11g and 11h). The intensity of the enforced rip current decreases with increasing d_b. The refraction-induced intensification of net rotational forcing for a more shoreward positioned offshore perturbation explains why, for a given amplitude $|A|$, the influence of an offshore perturbation on surf zone rip channel evolution decreases with increasing perturbation distance to the shore d_b.

4.1.2. Temporal Evolution of Rip Channel Morphology and Wave-Driven Circulations

[51] The larger rip spacing downdrift of the offshore bathymetric anomaly cannot be explained through the examination of the wave-driven circulations and resulting sediment transport patterns at $t = 0$ alone as the presence of an offshore perturbation does not impact wave-driven circulations and resulting sediment transport patterns for $|x| >$ 500 m. Figure 12 shows in detail the evolution of the rip channels and wave-driven circulations for the reference case simulation ($A = -1$ m, $d_b = 350$ m, $H_s = 1.2$ m, $T_p = 10$ s and $\theta = 1°$), from $t = 0$ (Figure 12a) to saturation ($t = 7$ days in Figure 12h). At $t = 0$ (Figure 12a) a weak (≈ 0.2 m s^{-1}) skewed rip current shoreward of the offshore trough is driven by alongshore differential broken wave energy dissipation enforced by wave refraction (Figures 10a, 10c, 10e, 10g, and 10i). This rip current drives the rapid formation of a rip channel shoreward of the offshore perturbation at $t =$ 1 day (Figure 12b). Updrift of the perturbation, the circulation cell to the left of this rip channel is associated with an onshore flow across a rapidly developing shoal at $x \approx -100$ m (Figure 12b). The resulting clockwise circulation to the left of the shoal encounters the rightward longshore currents driven by wave obliquity along the alongshore-uniform section of the beach ($x < -500$ m), enforcing a rip current and the consecutive formation of a rip channel at $x \approx -400$ m (Figure 12b). This process explains the subsequent rapid formation of rip channels updrift (Figures 12b–12f), before free rip channels start to form at $t \approx 6$ days (Figures 12g and 12h).

[52] In contrast, downdrift of the perturbation the anticlockwise circulation cell to the right of the shoal (at $x \approx$ 100 m) is advected by the rightward longshore current (Figure 12b) resulting in a larger alongshore scale of the circulation cell. Downdrift of the perturbation, a rip channel therefore forms less rapidly and farther from the forced rip channel (at $x \approx 700$ m in Figure 12c) than updrift of the perturbation. This seems to drive an increase in the alongshore extent of the circulation associated with the first downdrift rip current. This effect cascades to the following 3–4 downdrift rip channels until it becomes negligible at about the end of the downdrift domain and the spacing goes back to the value associated with the simulations starting with an alongshore-uniform bathymetry. Accordingly, although downdrift rip channels are exposed to an alongshore-uniform wavefield similar to that of the rest of the domain (as the influence of the offshore bathymetric anomaly on hydrodynamics is significant only at about $x < 500$ m) downdrift rip channels self-organize into patterns with different length scales and migration rates than the free rip channels.

4.2. Qualitative Comparison With Observations

[53] Contrasting updrift/downdrift rip channel behavior for an idealized configuration as the one of this study is obviously difficult to find in the field. This requires an accurate high-frequency monitoring of the sandbar geometry with concurrent wave data acquisition at a site exhibiting a

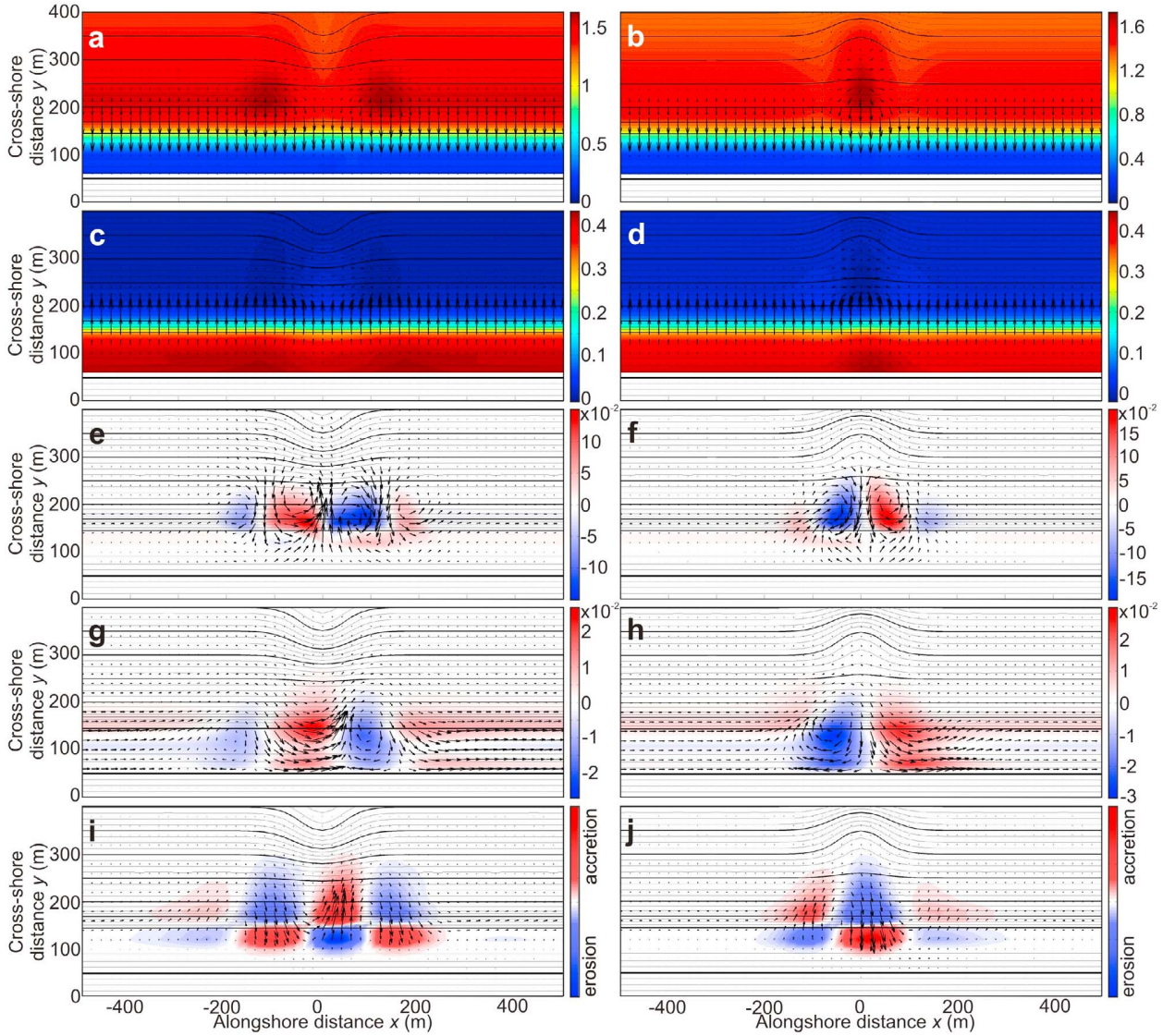

Figure 10. Hydrodynamics and sediment transport patterns at $t = 0$ for offshore waves with $H_s = 1.2$ m, $T_p = 10$ s and $\theta = 1°$ and for two alongshore nonuniform situations with an offshore perturbation at $x = 0$ and $d_b = 350$ m with (left) $A = -1$ m (reference case simulation) and (right) $A = 1$ m (bump). (a, b) Wave-field with color bar indicating significant wave height H_s in meters and resulting gradients in radiation stress $\vec{F}_w$ (arrows). (c, d) Pressure gradients F_p (m^2 s^{-2}) (arrows) superimposed on the η field with color bar indicating η in meters. (e, f) Residual forcing $\vec{F}_r = \vec{F}_p + \vec{F}_w$ (arrows) superimposed on the vorticity forcing term field related to differential broken wave energy dissipation $F_v = \left(\vec{\nabla} \wedge (D\vec{e}_k)\right) \cdot \vec{e}_z$ (kg m^{-2} s^{-2}). (g, h) Resulting wave-driven circulations $\vec{U}$ (arrows) and vorticity $\Gamma = \left(\vec{\nabla} \wedge \vec{U}\right) \cdot \vec{e}_z$ (s^{-1}) and (i, j) sediment transport fluxes $\vec{Q}_s$ (arrows) with erosion (blue) and accretion (red) patterns. Isobaths (0.5 m intervals) are contoured in the background.

single, persistent, offshore perturbation. A wave-dominated beach site meeting these criteria is Duck, North Carolina, extensively described by *Lippmann and Holman* [1990] and monitored with an ARGUS video system [*Holman and Stanley*, 2007]. Figure 13 shows a typical sandbar downstate sequence starting from an alongshore-uniform sandbar geometry (Figure 13a) progressively evolving toward a typical bar and rip morphology (Figure 13k). At Duck, a persistent offshore trough, formed by scouring by the Field Research Facility bridge piers [e.g., *Lee and Birkemeier*, 1993] is located at $x \approx 0$ in Figure 13 with a maximum amplitude of about 1–1.5 m. During the downstate sequence in Figure 13 crescentic patterns develop and subsequently attach to the beach with a rip spacing larger downdrift of the pier ($\lambda \approx 500$ m at $x < 0$ with respect to prevailing wave conditions, see the downdrift bar and rip orientation in Figures 13g–13k) than updrift of the pier ($\lambda \approx 350$–400 m at $x > 0$). This contrasting rip spacing is also readily apparent in

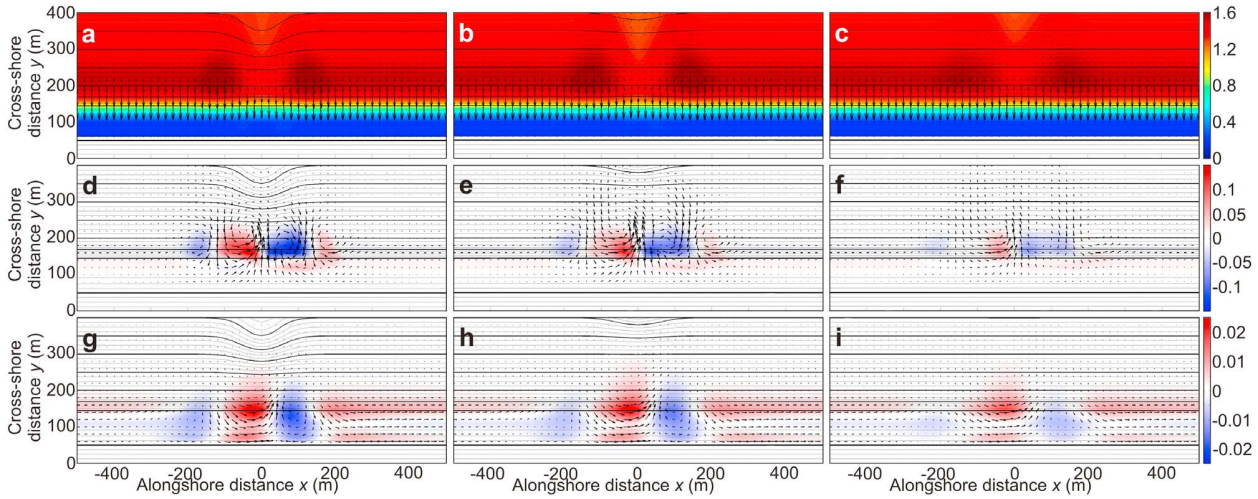

Figure 11. Hydrodynamics at $t = 0$ for offshore waves with $H_s = 1.2$ m, $T_p = 10$ s and $\theta = 1.5°$ and corresponding to the situations given in Figure 5 with an offshore trough ($A = -1$ m) at $x = 0$ and with a distance to the shore (left) $d_b = 350$ m (reference case simulation), (middle) $d_b = 450$ m and (right) $d_b = 550$ m. (a, b, c) Wavefield with color bar indicating significant wave height H_s in meters and resulting gradients in radiation stress $\vec{F}_w$ (arrows). (d, e, f) Residual forcing $\vec{F}_r = \vec{F}_p + \vec{F}_w$ (arrows) superimposed on the vorticity forcing term field related to differential broken wave energy dissipation $F_v = \left(c\vec{\nabla} \wedge (D\vec{e}_k)\right)\cdot\vec{e}_z$ (kg m^{-2} s^{-2}). (g, h, i) Resulting wave-driven circulations $\vec{U}$ (arrows) and vorticity $\Gamma = \left(\vec{\nabla} \wedge \vec{U}\right)\cdot\vec{e}_z$ (s^{-1}). Isobaths (0.5 m intervals) are contoured in the background.

a planview image at Duck of *Plant et al.* [2006]. This 11 day event at Duck 1998 following Hurricane Bonnie at $t \approx$ 237 days is part of a longer sequence that has been extensively studied for other purposes [e.g., *Van Enckevort et al.*, 2004; *Plant et al.*, 2006; *Tiessen et al.*, 2010].

[54] This observation supports qualitatively our numerical results. We cannot rule out that additional processes contribute to the contrasting sandbar behavior updrift and downdrift of the pier. For instance, the mean cross-shore sandbar position at the beginning of the down-state sequence could have been slightly different updrift and downdrift. As rip spacing is highly sensitive to the beach profile prior to pattern development, with typically rip spacing increasing with increasing sandbar distance to the shore [*Calvete et al.*, 2007], alongshore difference in beach profile at the peak of the storm could also explain the contrasting rip spacings observed updrift and downdrift of the offshore trough. Another potential explanation is the presence of preexisting, yet slightly developed, sandbar alongshore rhythmicity at the peak of the storm with different length scales updrift and downdrift. These preexisting patterns can impact the subsequent development of the rip channels [*Tiessen et al.*, 2011].

4.3. Model Limitations

[55] There are a number of model limitations in our study. To simplify, as indicated in section 2.1.2, we neglected the wave group scale forcing (narrow banded swells are used throughout this study) and the 3-D structure of nearshore circulations. As we addressed reasonably low amplitude offshore perturbation ($|A| \leq 1.5$ m), we also neglected wave scattering and reflection that can be significant for the case of an offshore perturbation with abrupt bathymetric changes [e.g., *Bender and Dean*, 2003]. We did not address the impact of the alongshore width of the offshore perturbation on surf zone rip channels. Additional simulations (not shown here) show that increasing the width of the bathymetric anomaly results in wave focusing patterns that are more diffuse alongshore. The less intense and more spread alongshore net rotational forcing available to drive nearshore currents decreases the influence of the offshore perturbation on surf zone rip channel evolution. The impact of the offshore perturbation on rip channels increases with decreasing perturbation width up to a point when wave scattering and reflection becomes significant which is out of bound of the validity of our numerical model. Furthermore, we did not address the effect of multiple offshore anomalies on nearshore rip evolution.

[56] For $\theta \geq 3.5°$ our numerical results are distorted by the lateral boundary conditions as downdrift rip channels rapidly enter the updrift domain before free rip channels have the time to develop. A small number of additional simulations with a longer domain showed that, for $\theta \geq 3°$, the distance from the offshore perturbation at which downdrift rip channels form increases with increasing θ and that the general behavior described in this paper for $\theta < 3°$ is not affected by the alongshore length of the domain.

[57] The typical growth time of 3-D surf zone patterns (here the free rip channels) increases with decreasing initial bed perturbation amplitude and increasing θ [e.g., *Garnier et al.*, 2008]. In our approach the initial random perturbations in the seabed are of the order of 1 mm, which is very small in comparison to the vertical amplitude of preexisting morphology (e.g., ripples) at the beginning of the down-state sequence. As bed form growth time decreases with increasing magnitude of the random perturbations, this explains the large typical growth times computed herein. This also

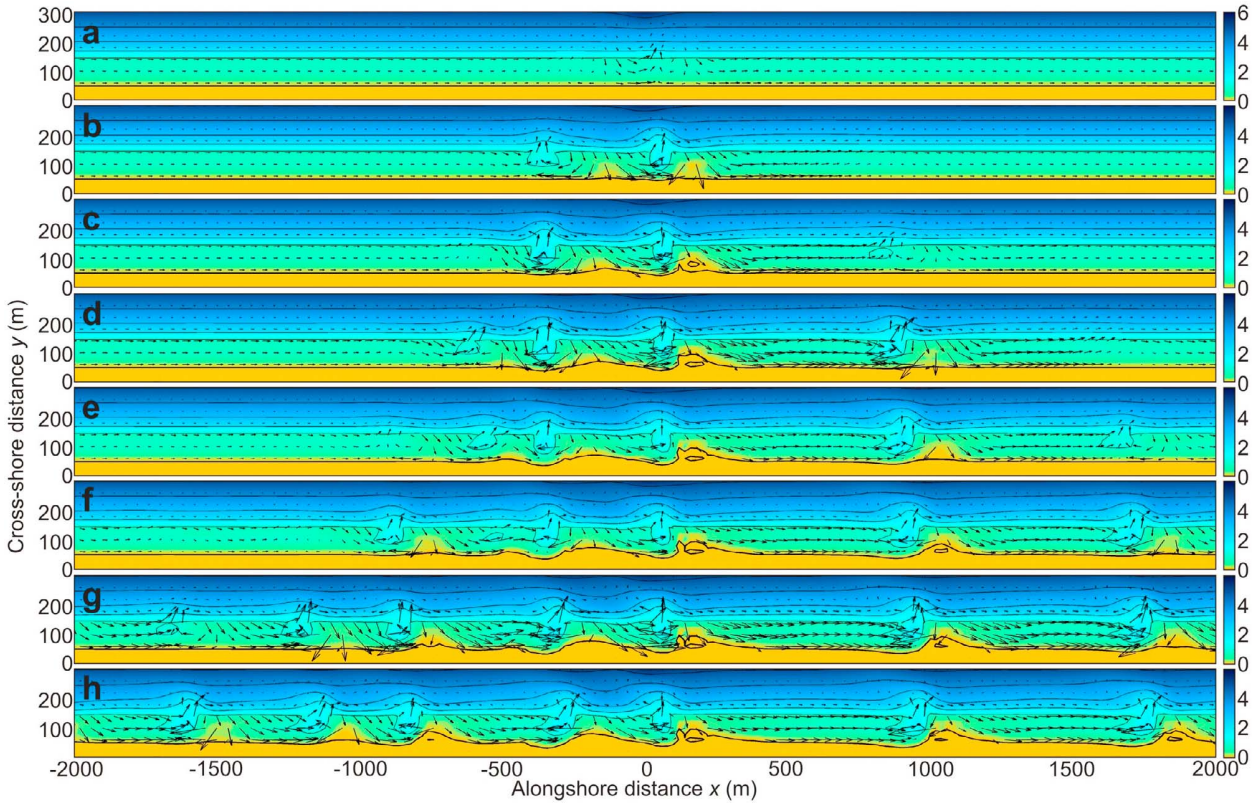

Figure 12. Zoom of the bathymetry at -2000 m $< x <$ 2000 m and $0 < y <$ 300 m with superimposed wave-induced currents (arrows, one out of two vectors are plotted in both directions) for offshore waves with H_s = 1.2 m, T_p = 10 s and $\theta = 1.5°$ starting from the alongshore nonuniform beach with an offshore perturbation at $x = 0$ with $A = -1$ m (trough) and d_b = 350 m (reference case simulation) at (a) $t = 0$, (b) $t =$ 1 day, (c) $t = 2$ days, (d) $t = 3$ days, (e) $t = 4$ days, (f) $t = 5$ days, (g) $t = 6$ days and (h) $t = 7$ days when saturation is reached. Color bars indicate seabed elevation in meters, and isobaths (1 m intervals) are contoured in the background.

explains why, for the 1 mm amplitude initial random perturbations implemented in the model, rip channels do not form for $\theta > 6$–$7°$,whereas field observations suggest that 3-D patterns are progressively damped for about $\theta > 30°$ [*Price and Ruessink*, 2011].

4.4. Proof of Concept and Implications

[58] Despite being exposed to the same wave conditions, downdrift and updrift rip channels self-organize into features with different alongshore scales and migration rates. A similar observation was made by *Tiessen et al.* [2011], who used a nonlinear morphodynamic model to address the influence of preexisting, small-amplitude, rhythmic surf zone bed forms on the subsequent evolution of rip channels. They concluded that, for a given offshore wave forcing, rip channels can self-organize into a range of different alongshore scales depending on the initial bathymetry. *Reniers et al.* [2004] used an alongshore nonuniform wavefield by including directional spreading in the initial wave conditions. They showed that the directional spreading affects the behavior of rip channels, with rip spacing depending on the directional spreading. These results appear to apply also to our study as different alongshore scales and migration rates are excited by the offshore bathymetric anomaly feeding back onto wave forcing through wave refraction.

[59] Overall, our work demonstrates that the behavior of an individual element of the surf zone system, herein rip channels, contrasts with the behavior of the wider nearshore system, suggesting that the approach of studying each nearshore element in isolation can limit our understanding of field observations. It therefore corroborates recent field evidence of interactions between shoreline evolution and offshore geological framework and stimulates further numerical and field studies addressing the nearshore system as a whole, that is, encompassing shoreline undulation (and erosional hot spots), sandbar(s) and offshore slowly evolving features.

5. Conclusion

[60] Using a nonlinear morphodynamic model we showed that the presence of a single offshore bathymetric anomaly strongly affects the formation, subsequent nonlinear evolution and saturation of surf zone rip channels. Despite the enforced wave-driven circulation patterns being highly different for an offshore bump and an offshore trough, a forced rip channel shoreward of the offshore bathymetric anomaly systematically forms under oblique wave incidence. The rip

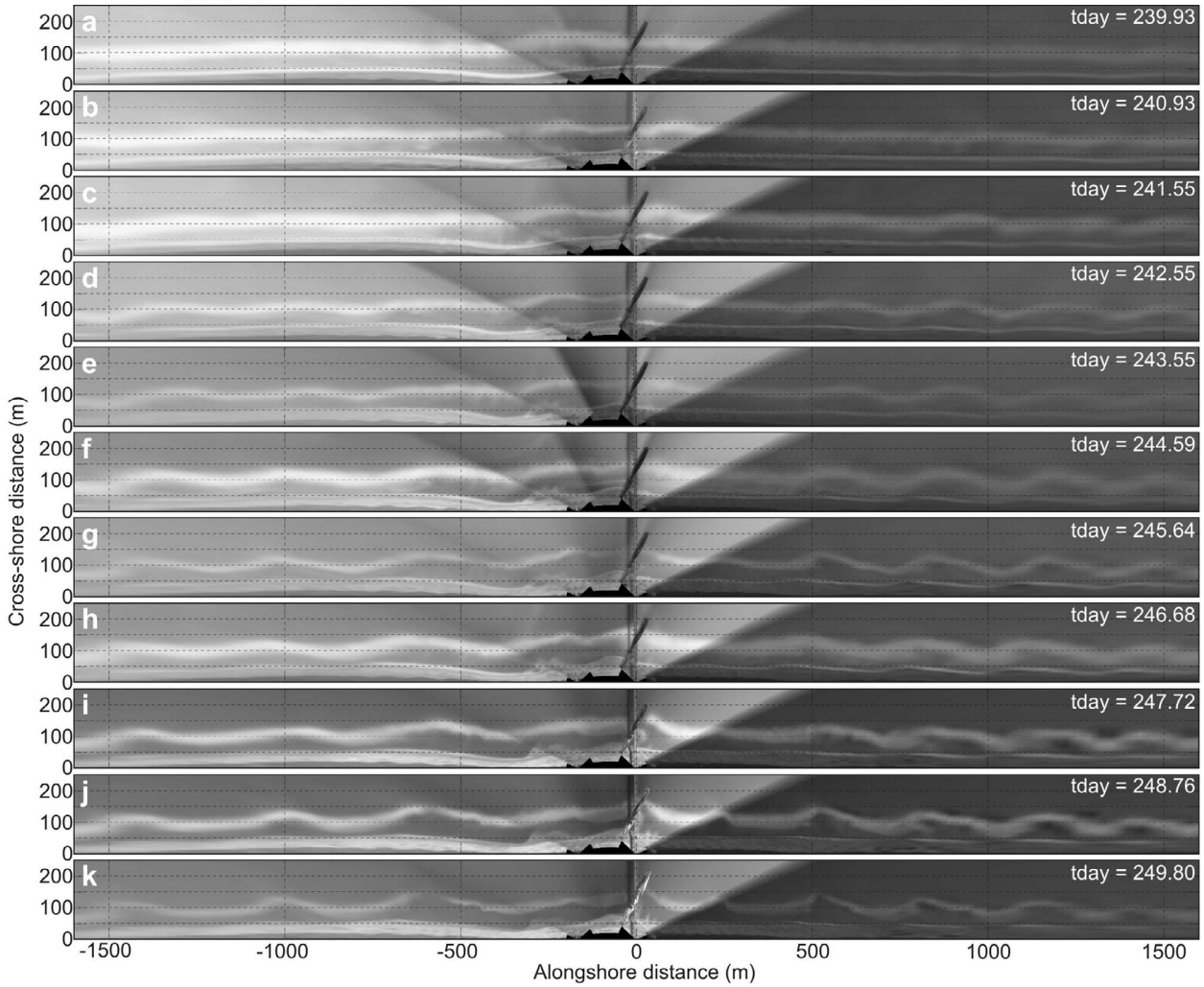

Figure 13. Sequence of rectified time exposure images at Duck Beach from 28 August (tday = 239) to 7 September (tday = 249) 1998 with the rip channels indicated by dark cuts through the white nearshore dissipation patterns across the sandbar. Duck exhibits a persistent offshore trough at the pier ($x \approx 0$). From top to bottom, sandbar evolution is characterized by a typical down-state sequence (3-D patterns develop from an alongshore-uniform sandbar geometry) with smaller rip spacing updrift ($x > 0$) than downdrift ($x < 0$) with respect to the prevailing wave conditions during this event that supports our numerical exercise.

channel can subsequently migrate downdrift or remain at the same alongshore location throughout the simulation. The stability in the location of this forced rip channel increases with increasing perturbation amplitude $|A|$, decreasing offshore wave obliquity, and decreasing perturbation distance to the shore. When the offshore perturbation amplitude $|A|$ is large and wave obliquity θ is small, updrift rip channels continuously merge to the forced rip channel and updrift rip channels cannot enter the downdrift domain. Rip channel behavior is essentially controlled by the strength of surf zone rip current circulations enforced by wave refraction across the offshore bathymetric anomaly. We additionally showed that the strength of initial surf zone rip current circulations is governed by differential broken wave energy dissipation (equation (17)), without having to consider alongshore pressure gradients, as traditionally done in the literature.

[61] Simulations show that, in the range of wave and bathymetric conditions addressed in this study, rip channel behavior downdrift and updrift of the preexisting offshore bathymetric anomaly is highly contrasting. Downdrift rip channels have systematically larger alongshore scales, smaller alongshore migration rates and more erosive megacusps than those updrift. Therefore, for a given offshore wave forcing, rip channels can self-organize into features of different alongshore scales and migration rates. This contrasting behavior can be excited by the presence of preexisting, small-amplitude, rhythmic surf zone bed forms [*Tiessen et al.*, 2011], an alongshore nonuniform wavefield by including directional spreading in the initial wave conditions [*Reniers et al.*, 2004] or an alongshore perturbation in the wavefield enforced by wave refraction across an offshore bathymetric anomaly (present study). Despite being highly idealized, our simulations are qualitatively

corroborated by video observations of sandbar behavior during a down-state sequence for shore-oblique waves at a site with a persistent offshore trough.

[62] **Acknowledgments.** This work was done within the framework of the project BARBEC (ANR 2010 JCJC 602 01). B.G.R. acknowledges additional funding by the Netherlands Organisation for Scientific Research (NWO) under contract 818.01.009. G.C. funded by the Cantabria Campus International (Augusto Gonzales Linares Program) and NIWA. N.B. funded by a postdoctoral research grant from the Fundacao para a Ciencia (SFRH/BPD/67041/2009). The wavelet computations in this paper were based on software developed by Aslak Grinsted and coworkers (version wtc-r14, available from http://www.pol.ac.uk/home/research/waveletcoherence/). We thank Timothy Price for his corrections and acknowledge the two anonymous reviewers, the Associate Editor and the Editor for their insightful comments.

References

Almar, R., B. Castelle, B. G. Ruessink, N. Sénéchal, P. Bonneton, and V. Marieu (2010), Two- and three-dimensional double-sandbar system behaviour under intense wave forcing and a meso-macro tidal range, *Cont. Shelf Res.*, *30*, 781–792.

Austin, M., T. M. Scott, J. W. Brown, J. A. Brown, J. H. MacMahan, G. Masselink, and P. Russell (2010), Temporal observations of rip current circulation on a macro-tidal beach, *Cont. Shelf Res.*, *30*, 1149–1165.

Bailard, J. A. (1981), An energetics total load sediment transport model for a plane beach, *J. Geophys. Res.*, *86*(C11), 10,938–10,954.

Battjes, J. A. (1975), Modeling of turbulence in the surf zone, paper presented at Symposium on Modeling Techniques, Am. Soc. of Civ. Eng., San Francisco, Calif.

Battjes, J. A., and J. Janssen (1978), Energy loss and set-up due to breaking in random waves, paper presented at 16th International Conference on Coastal Engineering, Am. Soc. of Civ. Eng., New York.

Battjes, J. A., and M. J. F. Stive (1985), Calibration and verification of a dissipation model for random breaking waves, *J. Geophys. Res.*, *90*(C5), 9159–9167.

Bender, C. J., and R. G. Dean (2003), Wave field modification by bathymetric anomalies and resulting shoreline changes: A review with recent results, *Coastal Eng.*, *49*, 125–153.

Bender, C. J., and R. G. Dean (2005), Wave transformation by axisymmetric three-dimensional bathymetric anomalies with gradual transitions in depth, *Coastal Eng.*, *52*, 331–351.

Bonneton, P., N. Bruneau, B. Castelle, and F. Marche (2010), Large-scale vorticity generation due to dissipating waves in the surf zone, *Discrete Contin. Dyn. Syst., Ser. B*, *13*(4), 729–738.

Booij, N., R. C. Ris, and L. H. Holthuijsen (1999), A third-generation wave model for coastal regions: 1. Model description and validation, *J. Geophys. Res.*, *104*(C4), 7649–7666.

Brander, R. W., and P. J. Cowell (2003), A trend-surface technique for discrimination of surf-zone morphology: Rip current channels, *Earth Surf. Processes Landforms*, *28*, 905–918.

Brander, R. W., and A. D. Short (2000), Morphodynamics of a large-scale rip current system at Muriwai Beach, New Zealand, *Mar. Geol.*, *165*, 27–39.

Browder, A. G., and J. E. McNinch (2006), Linking framework geology and nearshore morphology: Correlation of paleo-channels with shore-oblique sandbars and gravel outcrops, *Mar. Geol.*, *231*, 141–162.

Bruneau, N., B. Castelle, P. Bonneton, R. Pedreros, R. Almar, N. Bonneton, P. Bretel, J. P. Parisot, and N. Sénéchal (2009), Field observations of an evolving rip current on a meso-macrotidal well-developed inner bar and rip morphology, *Cont. Shelf Res.*, *29*, 1650–1662.

Bruneau, N., P. Bonneton, B. Castelle, and R. Pedreros (2011), Modeling rip current circulations and vorticity in a high-energy mesotidal-macrotidal environment, *J. Geophys. Res.*, *116*, C07026, doi:10.1029/2010JC006693.

Calvete, D., N. Dodd, A. Falqués, and S. M. van Leeuwen (2005), Morphological development of rip channel systems: Normal and near-normal wave incidence, *J. Geophys. Res.*, *110*, C10006, doi:10.1029/2004JC002803.

Calvete, D., G. Coco, A. Falqués, and N. Dodd (2007), (Un)predictability in rip channel systems, *Geophys. Res. Lett.*, *34*, L05605, doi:10.1029/2006GL028162.

Castelle, B., and P. Bonneton (2006), Modelling of a rip current induced by waves over a ridge and runnel system on the Aquitanian Coast, France, *C. R. Geosci.*, *338*, 711–717.

Castelle, B., and B. G. Ruessink (2011), Modeling formation and subsequent nonlinear evolution of rip channels: Time-varying versus time-invariant wave forcing, *J. Geophys. Res.*, *116*, F04008, doi:10.1029/2011JF001997.

Castelle, B., B. G. Ruessink, P. Bonneton, V. Marieu, N. Bruneau, and T. D. Price (2010a), Coupling mechanisms in double sandbar systems, Part 1: Patterns and physical explanation, *Earth Surf. Processes Landforms*, *35*, 476–486.

Castelle, B., B. G. Ruessink, P. Bonneton, V. Marieu, N. Bruneau, and T. D. Price (2010b), Coupling mechanisms in double sandbar systems, Part 2: impact on alongshore variability of inner-bar rip channels, *Earth Surf. Processes Landforms*, *35*, 771–781.

Castelle, B., H. Michallet, V. Marieu, F. Leckler, B. Dubardier, A. Lambert, C. Berni, P. Bonneton, E. Barthélemy, and F. Bouchette (2010c), Laboratory experiment on rip current circulations over a moveable bed: Drifter measurements, *J. Geophys. Res.*, *115*, C12008, doi:10.1029/2010JC006343.

Coco, G., and A. B. Murray (2007), Patterns in the sand: from forcing templates to self-organization, *Geomorphology*, *91*, 271–290.

Dalrymple, R. A., J. H. MacMahan, A. J. H. M. Reniers, and V. Nelko (2011), Rip currents, *Annu. Rev. Fluid Mech.*, *43*, 551–581.

Deigaard, R., N. Drønen, J. Fredsøe, J. H. Jensen, and M. P. Jørgensen (1999), A morphological stability analysis for a long straight barred coast, *Coastal Eng.*, *36*, 171–195.

Drønen, N., and R. Deigaard (2007), Quasi-three-dimensional modelling of the morphology of longshore bars, *Coastal Eng.*, *54*, 197–215.

Falqués, A., A. Montoto, and V. Iranzo (1996), Bed-flow instability of the longshore current, *Cont. Shelf Res.*, *16*, 1927–1964.

Falqués, A., G. Coco, and D. A. Huntley (2000), A mechanism for the generation of wave-driven rhythmic patterns in the surf zone, *J. Geophys. Res.*, *105*, 24,071–24,088.

Falqués, A., N. Dodd, R. Garnier, F. Ribas, L. C. MacHardy, P. Larroudé, D. Calvete, and F. Sancho (2008), Rhythmic surf zone bars and morphodynamic self-organization, *Coastal Eng.*, *55*, 622–641.

Falqués, A., D. Calvete, and F. Ribas (2011), Shoreline instability due to very oblique wave incidence: Some remarks on the physics, *J. Coastal Res.*, *27*, 291–295.

Garnier, R., D. Calvete, A. Falqués, and M. Caballeria (2006), Generation and nonlinear evolution of shore-oblique/transverse sand bars, *J. Fluid Mech.*, *567*, 327–360.

Garnier, R., D. Calvete, A. Falqués, and N. Dodd (2008), Modelling the formation and the long-term behavior of rip channel systems from the deformation of a longshore bar, *J. Geophys. Res.*, *113*, C07053, doi:10.1029/2007JC004632.

Garnier, R., N. Dodd, A. Falqués, and D. Calvete (2010), Mechanisms controlling crescentic bar amplitude, *J. Geophys. Res.*, *115*, F02007, doi:10.1029/2009JF001407.

Grinsted, A., J. C. Moore, and S. Jevrejeva (2004), Application of the cross wavelet transform and wavelet coherence to geophysical time series, *Nonlinear Processes Geophys.*, *11*, 561–566.

Haas, K. A., and I. A. Svendsen (2002), Laboratory measurements of the vertical structure of rip currents, *J. Geophys. Res.*, *107*(C5), 3047, doi:10.1029/2001JC000911.

Holman, R. A., and J. Stanley (2007), The history and technical capabilities of argus, *Coastal Eng.*, *54*, 477–491.

Idier, D., A. Falqués, B. G. Ruessink, and R. Garnier (2011), Shoreline instability under low-angle wave incidence, *J. Geophys. Res.*, *116*, F04031, doi:10.1029/2010JF001894.

Jevrejeva, S., J. C. Moore, and A. Grinsted (2003), Influence of the Arctic Oscillation and El Niño–Southern Oscillation (ENSO) on ice conditions in the Baltic Sea: The wavelet approach, *J. Geophys. Res.*, *108*(D21), 4677, doi:10.1029/2003JD003417.

Klein, M. D., and H. M. Schuttelaars (2006), Morphodynamic evolution of double-barred beaches, *J. Geophys. Res.*, *111*, C06017, doi:10.1029/2005JC003155.

Lee, G., and W. A. Birkemeier (1993), Beach and nearshore survey data: 1985–1991 CERC Field Research Laboratory, *Tech. Rep. CERC-93-3*, U.S. Army Corps of Eng., Waterways Exp. Stn., Vicksburg, Miss.

Lippmann, T., and R. Holman (1990), The spatial and temporal variability of sand bar, *J. Geophys. Res.*, *95*(C7), 11,575–11,590.

Long, J. W., and H. T. Özkan-Haller (2005), Offshore controls on nearshore rip currents, *J. Geophys. Res.*, *110*, C12007, doi:10.1029/2005JC003018.

Longuett-Higgins, M. S., and R. W. Stewart (1964), Radiation stress in water waves, a physical discussion with applications, *Deep Sea Res.*, *11*(4), 529–563.

MacMahan, J. H., E. B. Thornton, and A. J. H. M. Reniers (2006), Rip current review, *Coastal Eng.*, *53*, 191–208.

McNinch, J. E. (2004), Geologic control in the nearshore: shore-oblique sandbars and shoreline erosion hotspots, Mid-Atlantic Bight, USA, *Mar. Geol.*, *211*, 121–141.

Mei, C. C. (1989), *Applied Dynamics of Ocean Waves*, World Sci., Singapore.

Orzech, M. D., A. J. H. M. Reniers, E. B. Thornton, and J. H. MacMahan (2011), Megacusps on rip channel bathymetry: Observations and modeling, *Coastal Eng.*, *58*, 890–907.

Phillips, O. M. (1977), *The Dynamics of the Upper Ocean*, Cambridge Univ. Press, Cambridge, U. K.

Plant, N. G., K. T. Holland, and R. A. Holman (2006), A dynamical attractor governs beach response to storms, *Geophys. Res. Lett.*, *33*, L17607, doi:10.1029/2006GL027105.

Price, T. D., and B. G. Ruessink (2011), State dynamics of a double sandbar system, *Cont. Shelf Res.*, *31*, 659–674.

Reniers, A. J. H. M., J. A. Roelvink, and E. B. Thornton (2004), Morphodynamic modeling of an embayed beach under wave group forcing, *J. Geophys. Res.*, *109*, C01030, doi:10.1029/2002JC001586.

Ris, R. C., L. H. Holthuijsen, and N. Booij (1999), A third-generation wave model for coastal regions: 2. Verification, *J. Geophys. Res.*, *104*(C4), 7667–7681.

Ruessink, B. G., G. Coco, R. Ranasinghe, and I. L. Turner (2007), Coupled and noncoupled behavior of three-dimensional morphological patterns in a double sandbar system, *J. Geophys. Res.*, *112*, C07002, doi:10.1029/2006JC003799.

Schielen, R., A. Doelman, and H. E. De Swart (1993), On the dynamics of free bars in straight channels, *J. Fluid Mech.*, *252*, 325–356.

Schupp, C. A., J. E. McNinch, and J. H. List (2006), Nearshore shore-oblique bars, gravel outcrops, and their correlation to shoreline change, *Mar. Geol.*, *233*, 63–79.

Scott, T. M., P. Russell, G. Masselink, and A. Woolers (2009), Rip current variability and hazard along macro-tidal coast, *J. Coast. Res.*, *SI 56*, 895–898.

Shepard, F. P., and D. L. Inman (1950), Nearshore water circulation related to bottom topography and wave refraction, *Eos Trans. AGU*, *31*, 196–212.

Smit, M. W. J., A. J. H. M. Reniers, B. G. Ruessink, and J. A. Roelvink (2008), The morphological response of a nearshore double sandbar system to constant wave forcing, *Coastal Eng.*, *55*, 761–770.

Smith, J. (2006), Wave-current interactions in finite depth, *J. Phys. Oceanogr.*, *36*, 1403–1419.

Thornton, E. B., J. H. MacMahan, and A. H. Sallenger Jr. (2007), Rip currents, mega-cusps, and eroding dunes, *Mar. Geol.*, *240*, 151–167.

Tiessen, M. C. H., S. M. Van Leeuwen, D. Calvete, and N. Dodd (2010), Field test of a linear stability model for crescentic sandbar, *Coastal Eng.*, *57*, 41–51.

Tiessen, M. C. H., N. Dodd, and R. Garnier (2011), Development of crescentic bars for a periodically perturbed initial bathymetry, *J. Geophys. Res.*, *116*, F04016, doi:10.1029/2011JF002069.

Torrence, C., and G. P. Compo (1998), A practical guide to wavelet analysis, *Bull. Am. Meteorol. Soc.*, *79*, 61–78.

Van Enckevort, I. M. J., and B. G. Ruessink (2003), Video observations of nearshore bar bahaviour. Part 2: alongshore non-uniform variability, *Cont. Shelf Res.*, *23*, 513–532.

Van Enckevort, I. M. J., B. G. Ruessink, G. Coco, K. Susuki, I. L. Turner, N. G. Plant, and R. A. Holman (2004), Observations of nearshore crescentic sandbars, *J. Geophys. Res.*, *109*, C06028, doi:10.1029/2003JC002214.

Van Rijn, L. C. (1989), *Handbook of Sediment Transport by Currents and Waves*, Delft Hydraul., Delft, Netherlands.

Vis-Star, N., H. de Swart, and D. Calvete (2008), Patch behaviour and predictability properties of modelled finite-amplitude sand ridges on the inner shelf, *Nonlinear Processes Geophys.*, *15*, 943–955.

Wijnberg, K. M., and A. Kroon (2002), Barred beaches, *Geomorphology*, *48*, 103–120.

Wright, L. D., and A. D. Short (1984), Morphodynamic variability of surf zones and beaches: A synthesis, *Mar. Geol.*, *56*, 93–118.

P. Bonneton, B. Castelle, and V. Marieu, UMR EPOC 5805, Université de Bordeaux, CNRS, Avenue des Facultés, F-33405 Talence CEDEX, France. (b.castelle@epoc.u-bordeaux1.fr)

N. Bruneau, National Laboratory of Civil Engineering, Estuaries and Coastal Zones Division, Av. do Brasil, 101, P-1700-066 Lisbon, Portugal.

G. Coco, Environmental Hydraulic Institute, IH Cantabria, Universidad de Cantabria, c/Isabel Torres 15, E-39011 Santander, Spain.

B. G. Ruessink, Institute for Marine and Atmospheric Research, Department of Physical Geography, Faculty of Geosciences, Utrecht University, PO Box 80.115, NL-3508 TC Utrecht, Netherlands.

ou

D.13 The morphodynamics of rip channels on embayed beaches

Bruno Castelle, Giovanni Coco
Continental Shelf Research, Vol. 43, pp. 10-23, 2012

Continental Shelf Research 43 (2012) 10–23

Contents lists available at SciVerse ScienceDirect

Continental Shelf Research

journal homepage: www.elsevier.com/locate/csr

Research papers

The morphodynamics of rip channels on embayed beaches

Bruno Castelle [a,*], Giovanni Coco [b]

[a] CNRS, UMR EPOC, Université Bordeaux 1, France
[b] Environmental Hydraulics Institute, IH Cantabria, Universidad de Cantabria, Spain

ARTICLE INFO

Article history:
Received 7 November 2011
Received in revised form
13 April 2012
Accepted 16 April 2012
Available online 17 May 2012

Keywords:
Numerical modelling
Rip current
Morphodynamics
Embayed beach
Self-organization
Headland rip

ABSTRACT

We use a nonlinear morphodynamic model to examine the formation and nonlinear evolution of surfzone rip channels on embayed beaches. Starting from a range of embayed beach bathymetries characterized by different length and curvature, and under different time-invariant and time-varying wave conditions, the numerical model can reproduce the flow circulation and morphological characteristics observed on natural embayed beaches: (1) normal beach circulation, characterized by rips similar to non-embayed beaches and the presence of headland rips, (2) cellular circulation, with either headland rips only occurring at one or both ends of the embayment or a single rip at the centre of the beach and (3) transitional circulation, where both topography and currents influence rip location and behaviour. Time-invariant simulations show that, under oblique-wave forcing, rip spacing is systematically larger updrift than downdrift. Headland rips are preferably observed for straight beaches, with no clear dependence on wave angle. Wave shadowing and resulting alongshore gradients in wave height against the headland are the primary driving mechanism for headland rips. The formation of a single central rip is observed for short, curved embayed beaches, with no clear dependence on the wave angle as well. We use a novel non-dimensional embayment scaling parameter to quantify the degree of headland impact on beach circulation. Our simulations with shore-normal waves and initially alongshore-uniform embayed beaches show the parameter is consistent with observations. Our simulations also suggest that for high wave obliquity or time-varying wave angle to the shore, the influence of the headlands can progressively propagate into the whole domain. A time-varying wave angle results in persistent migration of rips towards the downcurrent headland rip, the splitting of shoals, an increase in merging of rip channels and more alongshore-variable rip spacing. The longshore variability of rip channel wavelength along embayed beaches is consistent with the hypothesis that rips are self-organized patterns and is consistent with recent field observations.

1. Introduction

Embayed sandy beaches are ubiquitous along hilly or mountainous wave-exposed coasts (e.g., Short and Masselink, 1999; Klein et al., 2010; Scott et al., 2011). The geometry of embayed beaches (headland and beach length) depends on the inherited geology or the presence of coastal structures which can deeply affect hydro- and morphodynamic processes. Embayed beaches are common worldwide and have inspired a large number of studies at different temporal scales. A number of models have been developed (e.g., Silvester, 1960; Hsu et al., 1989) to address the long-term behaviour (order of years) of the shoreline shape as a function of the local wave climate and the embayment geometry. At the intermediate scale (order of months) embayed beaches are often characterized by beach rotation (amongst many others, see for example Schyuer-Ming and Komar, 1994) with the alongshore direction of sand movement being associated with the dominant wave direction. Recently, Harley et al. (2011) showed that, at the intermediate scale, the beach rotation signal at Collaroy-Narrabeen Beach (Australia) is dominated by sediment exchange in the cross-shore rather than the alongshore direction, thus suggesting a more subtle conceptual model of beach rotation. Beach rotation is usually seasonal but periodic shifts related to wave climate have also been reported (Komar et al., 2000; Ranasinghe et al., 2004). Beach rotation can also occur as a fast response to individual storms possibly coupled to human activities (e.g., Ojeda and Guillen, 2008). Overall, at short time scales (order of days to weeks) embayed beaches are dynamic environments characterized by a variety of processes and a range of complex behaviours resulting in the presence of morphological patterns and the formation of rips (e.g., Holman et al., 2006; Gallop et al., 2011; Ojeda et al., 2011). The shorter time scale is the scale addressed in this study and is of particular relevance because rips are one of the most lethal hazards in the nearshore and are affected by the presence of headlands.

A study of 25 mostly embayed beaches along the Irish coast indicated the importance of the geological setting on morphological development and beach states (Jackson et al., 2005). In essence, as the geological factors regulate the source of beach material and the

* Corresponding author. Tel.: +33 05 40 00 29 65.
E-mail address: b.castelle@epoc.u-bordeaux1.fr (B. Castelle).

0278-4343/$ - see front matter © 2012 Elsevier Ltd. All rights reserved.
http://dx.doi.org/10.1016/j.csr.2012.04.010

volume of the accommodation space, the range of beach response to changes in wave climate can be limited compared to beaches in open coasts (Jackson et al., 2005; McNinch, 2004). Similarly, Short (2006) assessed the role of waves, sediment and tidal range in contributing to beach type for all the Australian beach systems. In some cases, Short (2006) indicated that geological inheritance was a major factor in defining beach type. Because of the variability in the degree of "control" posed by the geological setting, Short and Masselink (1999) synthesized the typical embayed beach hydrodynamic circulations into two main modes at different ends of the spectra and a third type that encompasses intermediate situations. More specifically: (1) normal beach circulation, where "normal" refers both to the presence of headland rips and the fact that the beach tends to behave as an open coast and therefore can be characterized by a large number of rips; (2) cellular circulation which stands at the opposite end of the spectra and is characterized by the dominance of the geological setting with rips only occurring at either the centre of the embayment or at one or both ends of the embayment; (3) transitional circulation which is an intermediate configuration with headland rip(s) and an increasing influence of the embayment size and shape on the surf zone circulation. In Short and Masselink (1999), there is no clear threshold to distinguish between normal and transitional circulations using observations. In this contribution, if the number of rips along the embayment (excluding headland rips) is larger than or equal to 4, we classify the circulation as "normal" (this is in qualitative agreement with the parameter proposed by Short and Masselink, 1999). Different types of embayed beach circulations are illustrated in Fig. 1.

Short and Masselink (1999) additionally used a non-dimensional embayment scaling parameter to quantify the degree of headland impact on beach circulation. The parameter they proposed depends on wave height and headland characteristics. Yet, in their approach they assumed that wave energy is redistributed along the whole wet–dry contour of the embayment. This implies that on embayed beaches where the headland length is larger than the surfzone width, the headland impact will be systematically overestimated. Another limitation is that the amount of wave energy dissipated against the headland is in most cases small compared to that dissipated along the beach. Accordingly, the non-dimensional embayment scaling parameter designed by Short and Masselink (1999) is misleading when addressing beach circulation for low- to moderate-energy wave conditions for embayed beaches with pronounced headlands. In order to quantify the degree of headland impact on beach circulation, we define a non-dimensional scaling parameter that considers the number, δ, of surf zone widths, X_s, that fit into an embayment of length L. If we consider a beach with a surf zone slope β exposed to

Fig. 1. Examples of typical embayed beach circulations as described in Short and Masselink (1999). (a) Cellular beach circulation with a rip current at the centre of the beach at Tamarama Beach in Sydney (New South Wales, Australia). Rip location is highlighted by the presence of dye (courtesy of R.W. Brander). (b) Cellular beach circulation with one headland rip at the same beach (courtesy of R.W. Brander). (c) Cellular circulation at St. James Point (South Australia). The two headland rips can be deduced from (headland in the upper part of the image) the dark area in the breaker and (headland in the lower part of the image) the sediment plume (source: Google Earth). (d) Transitional beach circulation at Bondi Beach (New South Wales, Australia) with one headland rip and additional rip channels away from the headland. (e) Transitional beach circulation at Blueys Beach (New South Wales, Australia) with one headland rip and two additional rip channels within the embayment (courtesy of A.D. Short). (f) Normal beach circulation at Seal Rocks (New South Wales, Australia) with one headland rip and six to seven additional rip channels along the beach (courtesy of A.D. Short).

waves with a significant wave height H_s, then we can assume $X_s = H_s/(\gamma_b\beta)$ where γ_b is the breaking parameter (here equal to 0.73; Battjes and Stive, 1985). Accordingly, the non-dimensional embayment scaling parameter reads:

$$\delta = \frac{L\gamma_b\beta}{H_s} \quad (1)$$

Studies linking the high-frequency response of rips on embayed beaches to changes in tidal and wave conditions are scarce. Holman et al. (2006) studied surfzone sandbar dynamics on an embayed, single-barred, beach with reasonably large length compared to the offshore extent of the headlands. The study site was located in the central part of the embayment. Thus, rips were likely not directly influenced by the headlands. Gallop et al. (2011) studied an embayed beach characterized by shorter length (especially when compared to the offshore extent of the headlands) and noted the persistent occurrence of headland rips and an evident longshore variability in the spacing between rip channels. On a beach where the ratio between the headland protrusion and the beach length is even larger, Enjalbert et al. (2011) observed the expected headland rips and the common formation of a transient rip channel developing at a fixed location along the embayment. This rip channel subsequently migrates to merge with rips further along the beach. Enjalbert et al. (2011) also noted that, during severe storms, sandbar three-dimensionality rapidly increases which is in contrast with observations on open beaches that are typically characterized by a system reset (i.e., decrease in beach three-dimensionality as a result of an up-state sequence e.g., Wright and Short, 1984; Van Enckevort et al., 2004) and that develop sandbar three-dimensionality only if sustained large waves are present (Van Enckevort et al., 2004; Splinter et al., 2011). Table 1 synthesizes these studies and other existing documented embayed beach sites at which sufficient material is provided to indicate the observed beach circulation and to compute the embayment parameter δ.

Similar to the relatively small number of field observations, only a limited number of numerical studies describe embayed beaches. Rip current development on a semi-elliptical beach has been studied by Silva et al. (2010) and results indicated, for the specific geometry analysed, the presence of cellular circulation characterized by a central rip. In terms of morphodynamics, Yamashita and Tsuchiya (1992) used a numerical model to simulate pocket beach formation and focussed on the evolution of the shoreline position. They found no evident circulation cells except close to the headland. Daly et al. (2011) used the same type of process-based model to investigate beach rotation for one embayed beach configuration and 16 different wave conditions. The authors used a non-barred beach, therefore limiting the range of dynamics related to rip channels. Simulations resulted in the formation of a stable bay shape that was highly dependent on the incident wave conditions. Ribas et al. (2007) applied a nonlinear morphodynamic model to the artificial embayed beaches of Barcelona (Spain). The model was able to simulate two events of crescentic bar formation. Yet, periodic lateral boundary conditions without headland were considered, therefore preventing the investigation of the impact of the embayment on 3D sandbar evolution. Finally, Reniers et al. (2004) studied the effect of wave-groups on the development of rip channels on an embayed beach. The primary objective of their study was to assess the effects of wave group forcing on the surfzone sandbar response, and the impact of the beach geometry was not studied systematically. Addressing the phase resolution of the mean and infragravity motions on a fixed alongshore-uniform bathymetry, Reniers et al. (2004) showed that including directional spreading in the initial wave conditions affects the behaviour of rip channels. They noted no clear evidence of a dominant standing edge wave mode but they further observed an increased contribution of trapped edge waves to the total infragravity motions concurrent with rip channel development. Reniers et al. (2004) concluded that infragravity waves are not required to generate the quasi-periodic rip channels (or crescentic bars) on an embayed beach, and that the observed preference in length scale for the edge wave motions is the result of the underlying bathymetry and not the other way around. This confirms that, on embayed beaches as well as for open beaches, three-dimensional (3D) surfzone sandbar patterns such as rip channels and crescentic bedforms can develop through the positive feedback between flow, sediment transport and the evolving bathymetries (e.g., Deigaard et al., 1999; Falqués et al., 2000; Calvete et al., 2005; Smit et al., 2008; Castelle and Ruessink, 2011) and that the presence of standing edge waves is not a necessary requirement (Coco and Murray, 2007).

Overall, the influence of the embayment geometry (length and shape of the beach, cross-shore extent of the headlands) on the formation and subsequent evolution of surfzone rip channels has never been studied using a nonlinear morphodynamic model. In this paper we address this problem which, aside from its scientific interest, is critical to predict the characteristics of one of the most deadly coastal hazards (e.g., MacMahan et al., 2006; Scott et al., 2007) and a key element of mixing in nearshore hydrodynamics (Dalrymple et al., 2011). A nonlinear morphodynamic model (Section 2) is used herein to simulate the development of surfzone rip channels on a number of embayed beach geometries. Results (Section 3) are discussed in Section 4 in the framework of existing observations of rip channels on embayed beaches.

2. Methodology

2.1. Numerical model

A nonlinear morphodynamic model (detailed in Castelle and Ruessink, 2011; Castelle et al., 2012) is used to simulate the formation, subsequent nonlinear evolution of the rip channels and associated shoreline rhythmic features (megacusps) as well as the saturation of the bedform growth. The model describes nearshore hydrodynamics coupling the spectral wave model SWAN (Booij et al., 1999) and a short-wave averaged and depth-integrated flow model. Hydrodynamics in turn drive a model addressing sediment transport and bottom changes. This approach has already been successfully used to study rip current dynamics (e.g., Castelle and Bonneton, 2006) and 3D

Table 1
Observations of embayed beach circulation ordered by publication year. Wave data correspond to prevailing wave conditions, except in Loureiro et al. (2012) which corresponds to a single storm event resulting in the formation of mega-rips.

	L (m)	β	Hs (m)	δ	Type of rips	Reference
Engine head bay (Jamaica)	350	0.028	0.5	14.3	Transitional; Headland rips and central rip	Huntley et al. (1988)
Palm Beach (Australia)	2000	0.02	1.5	19.5	Normal; No headland rip	Holman et al. (2006)
La Barceloneta (Spain)	1100	0.033	1.1	24.1	Normal; Headland rips	Ribas et al. (2007)
Tairua (New Zealand)	1200	0.03	0.56	46.9	Normal; Headland rips	Gallop et al., 2011
Biarritz (France)	1200	0.02	1.57	11.2	Transitional; Headland rips	Enjalbert et al. (2011)
Arrifana (Portugal)	1340	0.038	5.5	6.8	Cellular; Headland rips	Loureiro et al. (2012)

surfzone sandbar morphodynamics (e.g., Castelle et al., 2010). In this study, the shape of the offshore wave spectrum is the default JONSWAP with a narrow directional spreading of 8° while diffraction is not accounted for. The effect of directional spreading and wave diffraction will be discussed later in the paper.

In the flow model, the nonlinear shallow water equations comprise the continuity equation:

$$\frac{\partial \eta}{\partial t}+\frac{\partial Q_i}{\partial x_i}=0 \tag{2}$$

where t is time; η is the mean free surface elevation; $Q_i=hU_i$ is the water volume fluxes with the subscript $_i$ referring to the two horizontal coordinates (x and y represent the alongshore and cross-shore axis, respectively); U_i is the wave-driven mass-flux velocity according to Mei (1989); h is the mean water depth. The momentum balance equation is defined as:

$$\frac{\partial Q_i}{\partial t}+\frac{\partial}{\partial x_j}\left(\frac{Q_iQ_j}{h}\right)+gh\frac{\partial \eta}{\partial x_i}+\frac{1}{\rho}\frac{\partial S_{ij}}{\partial x_j}-\frac{1}{\rho}\frac{\partial T_{ij}}{\partial x_j}+\frac{\tau_i^b}{\rho}=0 \tag{3}$$

where g is the gravitational acceleration; ρ is the water density; S_{ij} is the radiation stress tensor (Philipps, 1977); $\tau_i^b=\rho C_f u_{rms}U_i$ is the bed shear stress; u_{rms} is the root mean square wave orbital velocity at the bottom; C_f is a bottom friction coefficient (equal to 0.0045 in the present study) and T_{ij} is the lateral mixing term which describes the horizontal momentum exchange due to the combined action of turbulence and mean current using the formulation proposed by Battjes (1975):

$$T_{ij}=\rho h\nu\left(\frac{\partial U_i}{\partial x_j}+\frac{\partial U_j}{\partial x_i}\right) \tag{4}$$

where the eddy viscosity ν is defined as:

$$\nu=Mh\left(\frac{D}{\rho}\right)^{1/3}+\nu_0 \tag{5}$$

where D is the rate of energy loss through depth-induced wave breaking; M is a dimensionless coefficient (taken as 2 in the present study) and ν_0 is a constant eddy viscosity (taken as 2 $m^2\ s^{-1}$ in the present study). The slightly larger eddy viscosity is used to damp, potentially, purely hydrodynamic instabilities in the wave set-up and flow circulation.

The sediment transport $\vec{Q}_s$ is computed as:

$$\vec{Q}_s=\alpha(\overline{\overline{|\vec{u}_b(t)|^3\vec{u}_b(t)}}-\gamma u_{rms}\vec{\nabla}Z) \tag{6}$$

where α is a stirring factor set to 2×10^{-4} $s^3\ m^{-2}$; γ is a bedslope coefficient (equal to 100 $m^3\ s^{-3}$ in the present study); $\vec{\nabla}$ is the horizontal gradient operator and $\vec{u}_b(t)=\vec{U}+(u_{rms}\cos\omega t)\vec{e}_k$ is the total flow velocity at the seabed (mean currents and orbital velocity) assuming linear waves with ω being the wave angular frequency and $\vec{e}_k$ the unit vector along the wave ray, both based on spectral peak. The $\overline{\overline{()}}$ notation defines time-averaging over a duration longer than the typical wave period. Z is the bed level deviation from initial equilibrium calculated as $Z=Z_f-Z_f^0$ where Z_f and Z_f^0 are the seabed level and the initial equilibrium beach profile, i.e. the bed level at the basic state. Consistent with a widely accepted approach (e.g., Garnier et al., 2006, 2008; Castelle and Ruessink, 2011), we assume the presence of a basic state meaning that the cross-shore transport driven by wave nonlinearities and undertow is in balance with the gravitational downslope transport for a given equilibrium cross-shore beach profile Z_f^0. Because the advective part in our sediment transport formula (6), similar to the suspended sediment load in Bailard (1981), is different from that in Garnier et al. (2006, 2008) our reference values of α and γ are not directly comparable. Yet, simulated rip channel systems and wave-driven circulations are similar in patterns and grow over similar timescales.

The new seabed level Z_f was computed using the sediment mass conservation equation:

$$\frac{\partial Z_f}{\partial t}+\frac{1}{1-p}\vec{\nabla}\vec{Q}_s=0 \tag{7}$$

where $p=0.4$ is the sediment porosity. The morphological time step for the bed update scheme, which is different from the hydrodynamic time step (1 s), was 1 h for all the simulations presented herein.

We used periodic lateral boundary conditions and a 0-mass flux boundary condition across the headland. We therefore assumed an infinite number of embayed beaches of similar size and shape. This implies that, ultimately, headland sediment bypassing can occur for long-term simulations with large wave angles (when beach rotation becomes significant). SWAN simulations were run over a bathymetry generated by a sequence of three embayed beaches (the three beaches are exactly the same). Driving forces were extracted at the central embayment to prevent potential edge effects for waves with both high obliquity and large directional spreading.

2.2. Model set-up

Two main configurations were used to apply the model to different initial embayed bathymetries: rectilinear (Fig. 2a) or curved shape (Fig. 2b). The headland length was kept constant (450 m) and the alongshore length was varied (L=500, 1000, 2000, 4000 and 8000 m). A 40-m seaward shoreline extent at the headland was applied to the curved configuration (Fig. 2b). To address the effect of headlands on rip channel morphodynamics, additional simulations on a 8000-m long alongshore-uniform

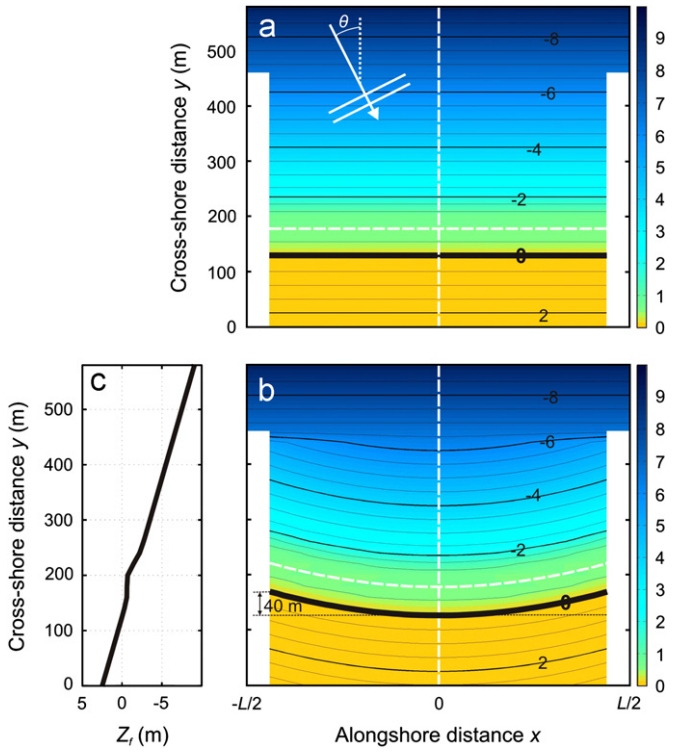

Fig. 2. (a) Initial (basic state) alongshore-uniform embayed beach exposed to waves with an angle of incidence θ. (b) Initial (basic state) curved embayed beach bathymetry. (c) Single-barred beach profile used to build the initial embayed beach bathymetries. The alongshore dotted white line in a and b indicates the location of the alongshore beach profile Z_b used in the analysis, L is the alongshore length of the domain, the thick black line indicates the 0-m sea level shoreline, colour bars show seabed elevation in meters and the cross-shore white dotted line indicates the location of the beach profile in (c).

open beach (no headland) were performed. To avoid the complicated feedbacks governing multi-barred beach dynamics (e.g., Ruessink et al., 2007; Castelle et al., 2010), only the behaviour of single-barred embayed beaches was investigated here. The basic state consisted of a beach with a 1:50 planar sloping depth profile. A sandbar, located 90 m from the mean-sea-level shoreline with its crest in 0.8 m water depth, was superimposed on the planar profile (Fig. 2c). The computational grid had an alongshore and a cross-shore length of L and 580 m, respectively, with 20×20 m grid cells. Random perturbations with a magnitude of 1 mm in the seabed were superimposed on the initial beach bathymetries to excite nearshore feedbacks and the growth of morphological perturbations.

For each initial bathymetry, time-invariant wave forcing is applied at the offshore boundary with a significant wave height $H_s=1$ m, a peak wave period $T_p=10$ s and a wave angle perpendicular to the shore $\theta=0^\circ$, 5° and 10° (anticlockwise is positive for the frame of reference adopted). Additional simulations were done for time-varying wave angle (we used a sine wave shape with a 0-mean θ, amplitude $A=5^\circ$ or 10° and a period $T=4$ days, see Castelle and Ruessink, 2011, for further details). Accordingly, the different alongshore lengths of the embayed beach ($L=500$, 1000, 2000, 4000 and 8000 m) correspond to an embayment scaling parameter $\delta=7.3$, 14.6, 29.2, 58.4 and 116.8. Overall, a total of 50 embayed-beach simulations, each characterized by a 60-day duration, i.e. 1440 morphological time steps, have been performed and analysed. To examine the evolution of rip channels, the alongshore profile at $y=180$ m between the bar crest and the mean-sea-level shoreline denoted $Z_b(x,t)$ (Fig. 2a) was computed at every time step. A curved alongshore profile (Fig. 2b) was applied at the same location for the curved bathymetries. Tests have confirmed this location is representative of the overall rip channel evolution. We additionally counted the number of rip channels (comprising the headland rips) along the beach N_{rip} to estimate the mean rip spacing λ defined as N_{rip}/L. For short embayed beaches (with only one to three rips comprising the headland rips), the term "mean" is inadequate and is only used for consistency with the other simulations.

3. Results

We first briefly describe rip channel morphodynamics along open beaches. Then, we analyse in detail a typical simulation of rip channel formation and evolution on an embayed beach. Finally, we examine rip channel morphodynamics on embayed beaches for time-invariant and time-varying wave forcing, respectively.

3.1. Open beach (no headland) simulations

Fig. 3 shows the time evolution of the alongshore profile Z_b on an open beach for time-invariant forcing with $H_s=1$ m, $T_p=10$ s and $\theta=0^\circ$, 5° and 10°, with a zoom at 2000 m $< x <$ 4000 m of the rip channel morphology and superimposed wave-driven circulation at $t=10$ days. The model shows that for $\theta=0^\circ$, 5° and 10°, rip channels stabilize at a narrow range of wavelengths with a mean λ of about 320, 440 and 600 m, respectively (Fig. 3a–c). A notable difference with Castelle and Ruessink (2011) and Castelle et al. (2012) is the smaller, more realistic, rip spacings obtained as a result of the slight changes in hydrodynamic parameters (M, v_0 and C_f). Rip channel migration rate and beach three-dimensionality increase and decrease with increasing θ, respectively. These results are in line with existing linear or nonlinear stability analyses for open coasts (e.g., Calvete et al., 2005; Garnier et al., 2008). In addition, our model shows that megacusps are more pronounced for shore-normal waves. For $\theta=0$ and 5°, clear shore-normal and skewed rip current circulations are observed, respectively (Fig. 3d and e). In contrast, a meandering longshore current is observed for $\theta=10^\circ$ (Fig. 3f).

3.2. Example of typical rip channel morphodynamics on an embayed beach

Fig. 4 shows the time evolution of rip channels on a curved embayed beach with $L=2000$ m ($\delta=29.2$), for time-invariant forcing with $H_s=1$ m, $T_p=10$ s and $\theta=5^\circ$. Results show that at $t=0$ (Fig. 4a) the longshore current dominates the circulation within the entire embayment. As expected, the longshore current is larger in the updrift (left) part of the beach (≈ 0.55 m s^{-1}) than in the downdrift (right) part (≈ 0.15 m s^{-1}) because of beach curvature. One rip current is observed against each headland. The updrift headland rip is larger (≈ 0.4 m s^{-1}) than the downdrift one (≈ 0.1 m s^{-1}). At $t=5$ days (Fig. 4b), a rip channel formed against each headland. Three additional rip channels are observed within the embayment at $x \approx 0$, 400 and 650 m. The downdrift headland rip is more intense (≈ 0.65 m s^{-1}) than the updrift one (≈ 0.5 m s^{-1}), which is in the same order of magnitude of the three other rips within the embayment (Fig. 4b). A strong longshore current ($\approx 0.6-0.7$ m s^{-1}) dominates the updrift part of the embayment. The same applies at $t=10$ days (Fig. 4c) with the notable exception that the rip channel located at $x=400$ m at $t=5$ days merged to the rip channel at $x=650$ m. Also, the rip that initially appeared at $x=0$ m has further developed and migrated to $x=150$ m. Overall, for the simulation shown in Fig. 4, the resulting beach circulation pattern at $t=10$ days can be referred to as transitional in the Short and Masselink (1999) classification with two headland rips and two additional rips within the embayment.

The corresponding time evolution of the alongshore profile Z_b given in Fig. 4d shows at $t \approx 9$ days the merging of the two rip channels into a rip channel at $x=600$ m that subsequently merges to the downdrift headland rip channel at $t \approx 35$ days. The other rip channel remains quasi stationary for $t > 35$ days. For $t > 25$ days, transient rip channels persistently form, migrate downdrift and subsequently merge to the rip channel further downdrift (Fig. 4d).

Over the course of the simulation, beach rotation increases. Simulations with $\theta=10^\circ$ showed that for larger wave obliquity beach rotation can become a dominant factor by the end of the 60-day simulation. The basic state approach in the model (for more details see Castelle and Ruessink, 2011) is not consistent with a rotated beach and can ultimately result in unrealistic morphodynamic behaviour. Beach rotation will be discussed later in the paper and in the following we focus on the first 20 days of the simulations.

3.3. Time-invariant simulations

Fig. 5 shows the time evolution of the alongshore profile Z_b for time-invariant wave forcing with $H_s=1$ m, $T_p=10$ s and $\theta=0^\circ$ (left-hand panels), 5° (middle panels) and 10° (right-hand panels). Simulations are shown for alongshore-uniform (top panels) and curved (bottom panels) embayed beaches for $L=500$, 1000, 2000 and 4000 m. Simulations with $L=8000$ m are not shown as they are essentially the same as the ones with $L=4000$ m with the exception that more rip channels are observed within the embayment.

Results show that, for alongshore-uniform embayed beaches under shore-normal waves (Fig. 5a, d, g and j), headland rip channels are systematically observed. The impact of the headland on rip spacing λ is important only for short beaches. For $L=500$ m (Fig. 5a), rip channel formation within the embayment is inhibited; for $L=1000$ m (Fig. 5d) one rip forms at the centre of the

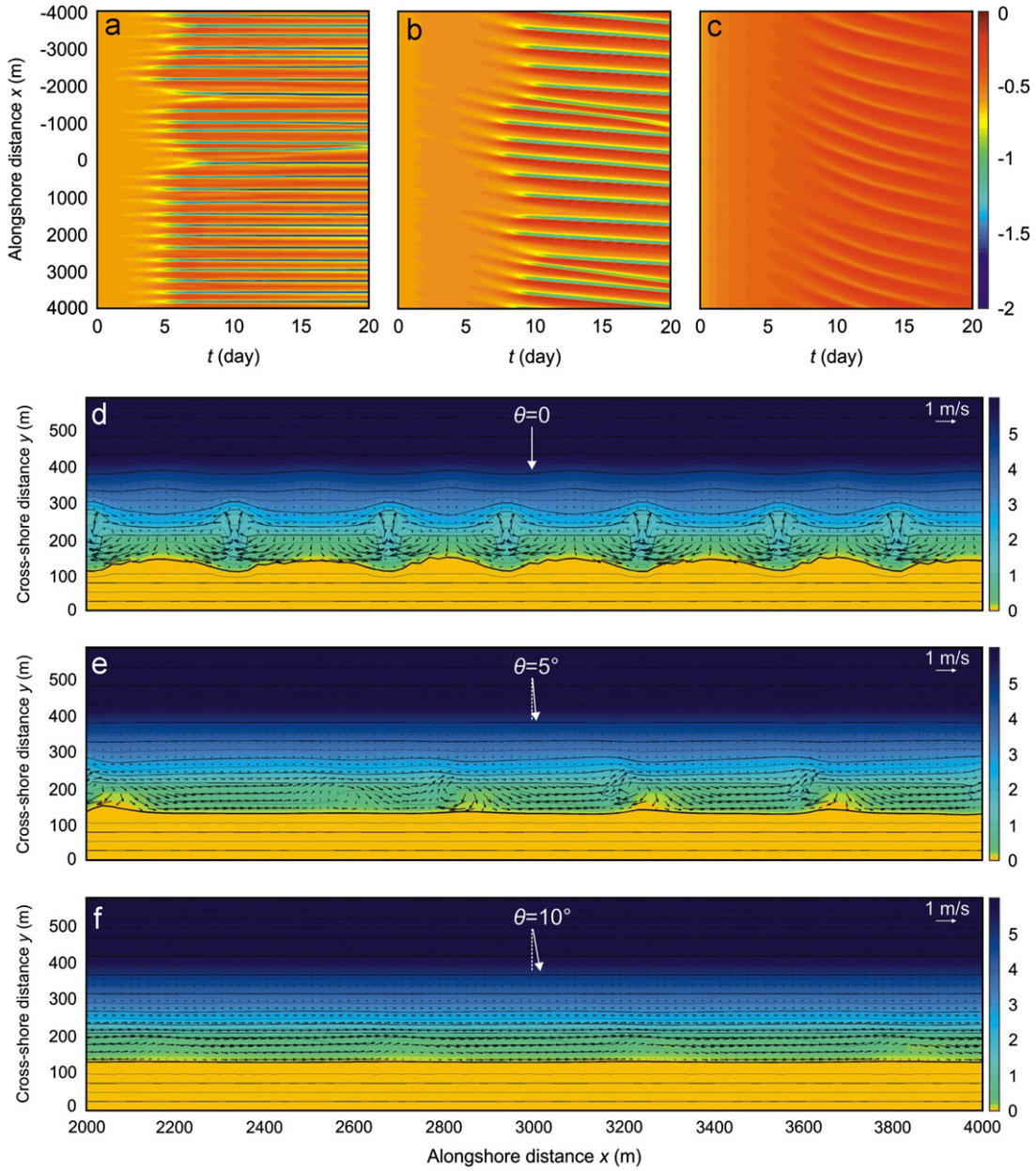

Fig. 3. Evolution of surfzone rip channels starting from an alongshore-uniform open beach (no headland) for time-invariant wave forcing with $H_s=1$ m, $T_p=10$ s and (a,d) $\theta=0^\circ$, (b,e) $\theta=5^\circ$, (c,f) $\theta=10^\circ$. Top panels show the time evolution of the alongshore profile Z_b, and bottom panels show a zoom at 2000 m $< x <$ 4000 m of the beach morphology with superimposed wave-driven circulation at $t=10$ days. In all panels colour bar indicates seabed elevation in meters.

beach ($\lambda=500$ m); for $L=2000$ m (Fig. 5g) and $L=4000$ m (Fig. 5j), a total N_{rip} of 6 and 12 rip channels are observed ($\lambda=333$ m). The latter case is characterized by a similar rip spacing as for the open beach case (Fig. 3) and so falls in the category of normal beach circulation (Short and Masselink, 1999).

Results for alongshore-uniform beaches (Fig. 5a–l) also show that the impact of wave obliquity on rip channel behaviour is large, with the exception of headland rips which are systematically present. As for linear and nonlinear modelling studies of rip channel behaviour on open beaches (e.g., Deigaard et al., 1999; Calvete et al., 2005; Garnier et al., 2008; Castelle and Ruessink, 2011, see also Fig. 3) both rip spacing and rip migration increase with increasing θ. Rip channels often merge with the downdrift headland rip (e.g., Fig. 5k at $t=15$ days). Under oblique waves the impact of headlands on rip spacing is stronger than for shore-normal waves. For instance, for $L=4000$ m and $\theta=5^\circ$ (Fig. 5k) $N_{rip}=7$, corresponding to a mean rip spacing $\lambda\approx570$ m, which is substantially larger than the mean rip spacing of 440 m found in the open-beach (no headlands) scenario (Fig. 3b). In addition, simulations with oblique waves almost systematically result in alongshore variable rip spacing.

Similar results were obtained for curved embayed beaches (Fig. 5m–x) with a few noteworthy exceptions. Rip channels against the two headlands are not systematically observed (e.g., Fig. 5m, n, p). For instance, the simulation starting from a curved embayed beach with $L=500$ m and $\theta=0^\circ$ or 5° results in a cellular beach circulation with one rip channel at the centre of the beach and no headland rip (Fig. 5m and n), which contrasts with the headland rips situations for alongshore-uniform embayed beaches. This different behaviour is illustrated in Fig. 6 that details the hydrodynamics at $t=0$ for the alongshore-uniform and the curved embayed beach. For the alongshore-uniform

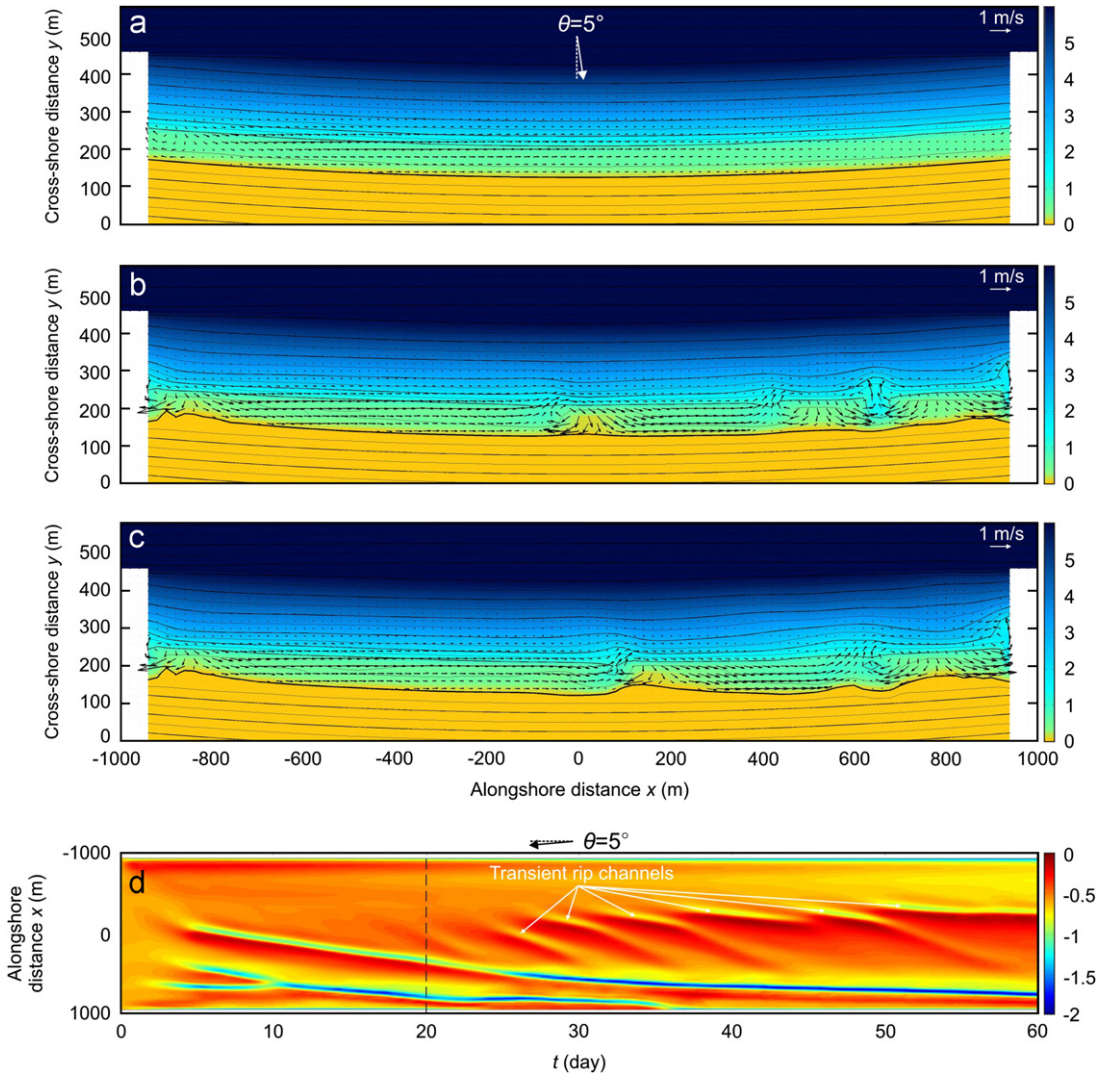

Fig. 4. Evolution of surfzone rip channels with superimposed wave-driven circulations for $H_s=1$ m, $T_p=10$ s and $\theta=5^\circ$, starting from a curved embayed beach with $L=1000$ m. (a) $t=0$, (b) $t=5$ days, (c) $t=10$ days. (d) Resulting time evolution of the alongshore profile Z_b with the vertical dashed line indicating $t=20$ days at which beach rotation is still negligible for all simulations.

embayed beach (left-hand panels), the increasing wave heights at the centre of the beach (Fig. 6a) due to wave shadowing lead to a slightly larger amplitude of set-up and set-down in the surf and shoaling zone, respectively (Fig. 6b). The vectorial sum of the resulting gradients in radiation stress $\overrightarrow{F_w}$ ($F_{wi}=-(1/\rho)\partial S_{ij}/\partial x_j$, Fig. 6a) and pressure gradients $\overrightarrow{F_p}$ ($F_{pi}=-gh\partial\eta/\partial x_i$, Fig. 6b) gives the residual forcing $\overrightarrow{F_r}$ (Fig. 6c). $\overrightarrow{F_r}$, which, for open beaches, is essentially similar to the vorticity forcing term derived from the differential broken wave energy dissipation (Bonneton et al., 2010; Bruneau et al., 2011), indicates how much net forcing is available to drive nearshore currents (Haas et al., 2002; Castelle and Bonneton, 2006). This forcing therefore drives two headland rips (Fig. 6d). The resulting sediment transport patterns result in beach erosion against each headland and lead to the subsequent formation of two headland rip channels at $t=2$ days (Fig. 6e). This contrasts with the results starting from a curved embayed beach (right-hand panels in Fig. 6) for which wave energy focussing through wave refraction across the curved nearshore bathymetry overwhelms wave shadowing near the headlands. This results in slightly larger wave heights at the headlands (Fig. 6f) and slightly smaller amplitude of set-up and set-down in the surf and shoaling zone at the centre of the beach, respectively (Fig. 6g). In turn, there is a reversal in residual forcing (Fig. 6h) that drives a rip current near the centre of the beach (Fig. 6i) and the formation of a rip channel at $t=2$ days (Fig. 6j).

For a given offshore wave forcing and larger beach length L, the number of rip channels N_{rip} is generally the same or smaller for curved beaches than for alongshore-uniform embayed beaches. For shore-normal waves, rip spacing systematically increases with decreasing distance to the headland as rips tend to migrate toward the centre of the beach as a result of beach curvature (e.g., Fig. 5v).

3.4. Time-varying simulations

Fig. 7 shows the time evolution of the alongshore profile Z_b for $H_s=1$ m, $T_p=10$ s and time-varying angle of wave incidence with an amplitude $A=5^\circ$ and 10°. We started the numerical simulations considering an alongshore-uniform embayed beach with $L=500$, 1000, 2000, 4000 and 8000 m. Given that no beach rotation occurs (wave climate is characterized by 0-mean in θ), here we show the results for a 30-day duration simulation. Results show that rip channel evolution for $A=5^\circ$ (left-hand panels in Fig. 7) are similar to that with time-invariant shore-normal waves (Fig. 5a, d, g and j)

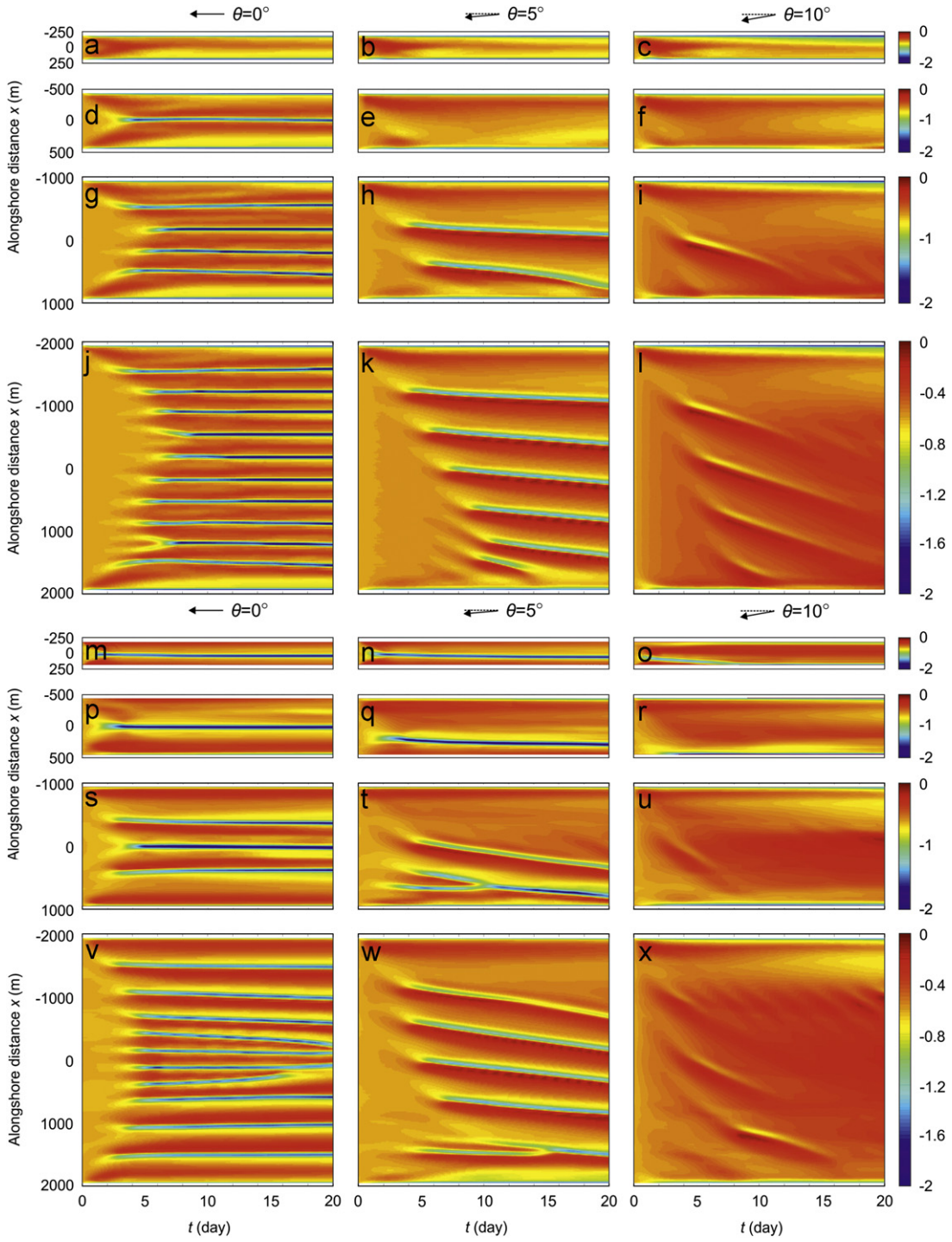

Fig. 5. (a–l) Time evolution of the alongshore profile Z_b starting from an alongshore-uniform embayed beach and for time-invariant wave conditions with $H_s=1$ m, $T_p=10$ s and (left-hand panels) $\theta=0^\circ$, (middle panels) $\theta=5^\circ$ and (right-hand panels) $\theta=10^\circ$. (a–c) $L=500$ m, (d–f) $L=1000$ m, (g–i) $L=2000$ m, (j–l) $L=4000$ m. (m–x) is the same starting from a curved embayed beach.

with few notable exceptions. For $L>1000$ m, time-invariant forcing results in the splitting of shoals (see Fig. 7i for examples of splitting of shoal). This is consistent with the recent modelling exercise of Castelle and Ruessink (2011) who showed that a time-varying wave angle of incidence results in the increase in merging and the splitting, that contrasts with the limited number of mergings and the absence of splitting for time-invariant forcing simulations (see also Fig. 3). This results in slightly different mean rip spacing than for the time-invariant shore-normal wave simulation.

For $A=10^\circ$, the impact of time-varying θ on rip channel morphodynamics is more profound. Rip channel evolution is the same as for the time-invariant forcing only for the case of $L=500$ m with two persistent headland rips. For larger L, splitting of shoals is ubiquitous. For instance, it results in the formation of two rip channels within the embayment for $L=1000$ m (Fig. 7d) instead of the single rip observed for the time-invariant simulation (Fig. 5d). In addition, for $L>1000$ m (Fig. 7f, h and j), rip channels that are located in the vicinity of the headland are systematically drawn towards the headland rip.

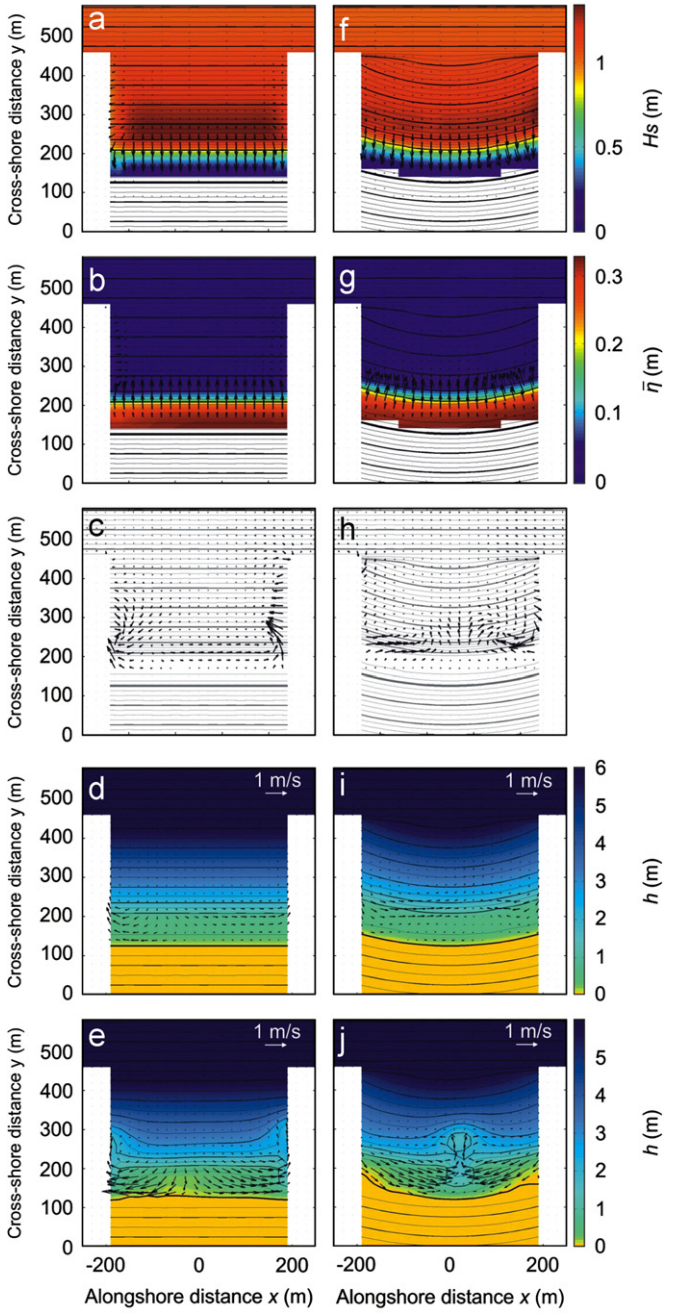

Fig. 6. Hydrodynamics at $t=0$ for offshore waves with $H_s=1$ m, $T_p=10$ s and $\theta=5^\circ$ starting from an embayed beach with $L=500$ m and an alongshore-uniform (left-hand panels) and a curved shape (right-hand panels). (a,f) Wave field with colour bar indicating significant wave height H_s in meters and resulting gradients in radiation stress $\overrightarrow{F_w}$ (arrows) with $F_{wi}=-(1/\rho)\partial S_{ij}/\partial x_j$. (b,g) Pressure gradients $\overrightarrow{F_p}$ (arrows) with $F_{pi}=-gh\partial\eta/\partial x_i$, superimposed on the η field with colour bar indicating η in meters. (c,h) Residual forcing $\overrightarrow{F_r}=\overrightarrow{F_p}+\overrightarrow{F_w}$ (arrows). (d,i) Resulting wave-driven circulation with colour bar indicating water depth in meters. (e,j) Evolution of wave-driven circulation and bottom evolution at $t=2$ days. In all panels is-contours (0.5-m intervals) are contoured in the background.

This feeds back onto the behaviour of the morphology at the larger spatial scale. The increase of rip spacing results in the splitting of the nearby shoals as rip channels continuously attempt to self-organize into a more alongshore-uniform spatial pattern (e.g., Fig. 5h). As a result, at times, the alongshore spacing is not regular and even the mean spacing changes throughout the simulation. For instance, for $L=2000$ m (Fig. 7f) three and five rip channels are observed within the embayment at $t\approx10$ and 25 days, respectively.

Overall, for $L\leq2000$ m, time-varying forcing is crucial to understand sources of variability in rip channel morphodynamics. In fact, simulations with time-varying forcing show drivers of change in mean rip spacing as well as an increase in the nonlinear behaviour of rip channels (i.e. merging and splitting). The simulations starting from curved embayed beaches showed similar results as those given in Fig. 7 except that rips in the vicinity of the headlands are less effective in "attracting" the nearby rips.

4. Discussion and conclusions

In this paper the nonlinear morphodynamic modelling of rip channels on embayed beaches was addressed. Starting from a number of idealized bathymetries and for different synthetic time-invariant and time-varying wave conditions, all the embayed beach circulation patterns deduced from field observations in Short and Masselink (1999) can be reproduced with the present numerical model. Fig. 8 shows some examples of embayed beach circulation patterns (all after 10 days of simulation). We found that cellular circulation with headland rips (Fig. 8a) is favoured by both small beach curvature and short beach length while cellular circulation with a rip at the centre (Fig. 8b) is favoured by large beach curvature and short beach length due to the residual forcing $\overrightarrow{F_r}$ (Fig. 6). Transitional circulation with an updrift headland rip and a rip further along the beach (Fig. 8c) is favoured by large values of wave obliquity and beach curvature, and by a reasonably small beach length. When increasing the beach length further, transitional rip circulation with headland rips and one to three additional rips along the beach is observed (e.g., Fig. 8d). Increasing the beach length even further (or decreasing the angle of wave approach and/or beach curvature) results in normal circulation with the development of four or more rips not affected by the headlands (even though headland rips are still present, Fig. 8e) whose spacing is similar to that observed on open beaches. In this case the circulation of the overall embayment was classified as "normal". The flow patterns as well as the bar and rip morphologies, which are obtained starting from highly idealized embayed beach geometries, are consistent with the observations provided in Fig. 1.

We showed that wave shadowing leads to smaller wave height against the headlands (Fig. 6a) when not overwhelmed by wave refraction in the case of significantly curved embayed beaches (Fig. 6f). Accordingly, wave height patterns, and in turn the presence of headland rips, are influenced by the characteristics of the directional spreading imposed at the seaward boundary. Fig. 9 shows the wave patterns and resulting wave-driven circulation at $t=0$ for an alongshore-uniform embayed beach with $L=500$ m and waves with $H_s=1$ m, $T_p=10$ s, $\theta=5^\circ$, considering a range of directional spreadings from 4° to 37.5°. Simulations show that wave shadowing increases with increasing directional spreading. This suggests that, for a given headland geometry, the presence of headland rips is favoured by waves with large directional spreading. For curved embayed beaches, there is a competition between wave shadowing due to the headlands and wave refraction due to the bathymetry. The balance between the two processes controls the eventual presence of headland rips. For instance, under wave forcing characterized by a directional spreading of 37.5° and a curved beach characterized by $L=1000$ m, wave shadowing becomes the dominant factor and results in the generation of headland rips. This is in contrast with the simulations performed over the same bathymetry but with a directional spreading of 8° as in this case only a central rip developed (not shown). Additional simulations including the effect of wave diffraction (not shown here) indicate that wave

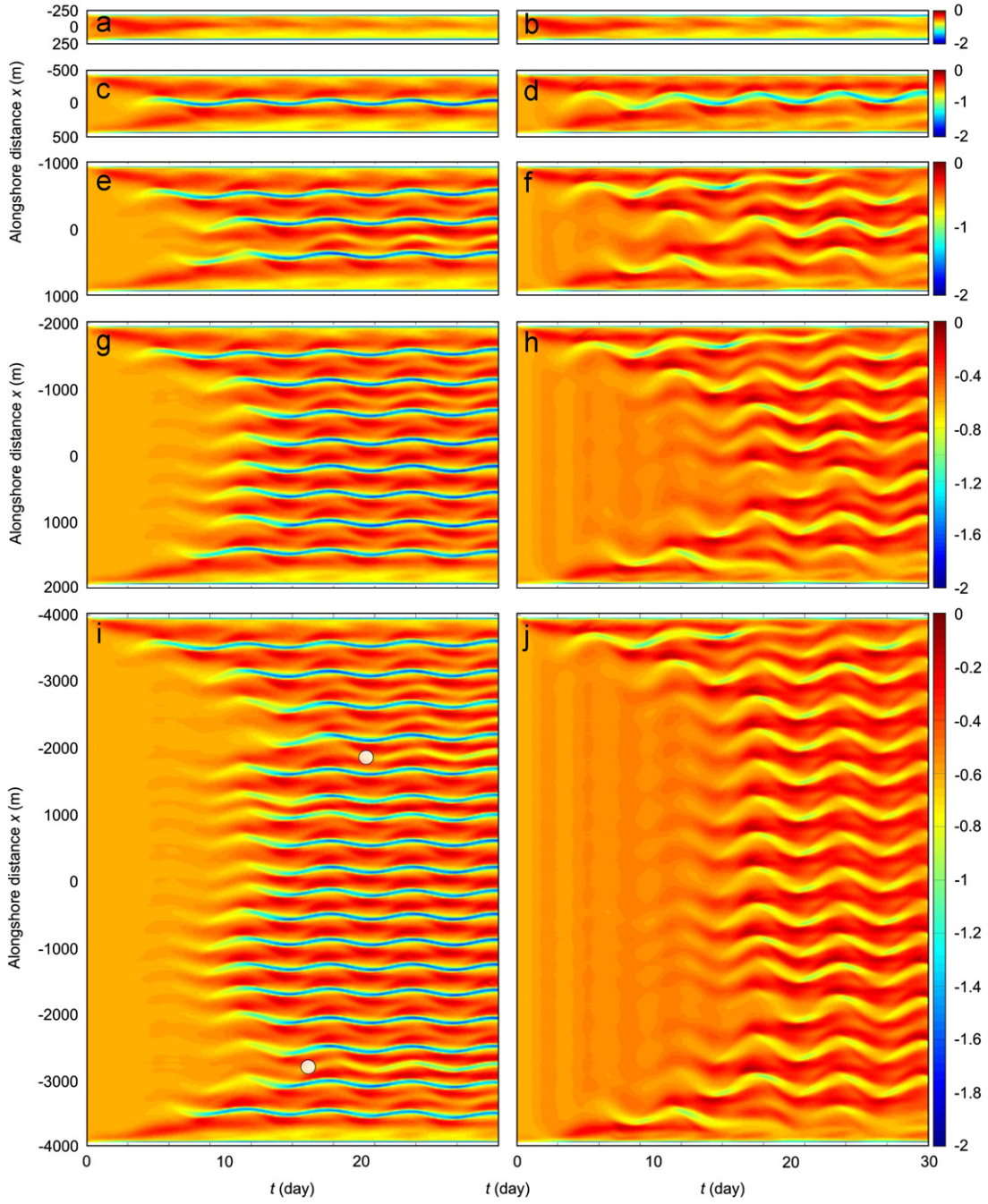

Fig. 7. Time evolution of the alongshore profile Z_b starting from an alongshore-uniform embayed beach and for $H_s=1$ m, $T_p=10$ s and time-varying wave angle θ with an amplitude (left-hand panels) $A=5^\circ$ and (left-hand panels) $A=10^\circ$. (a,b) $L=500$ m, (c,d) $L=1000$ m, (e,f) $L=2000$ m, (g,h) $L=4000$ m and (i,j) $L=8000$ m. In panel i the two white circles indicate the onset of splitting of shoal.

shadowing systematically overwhelms wave diffraction for both narrow banded swells and waves with large directional spreading. Overall, wave shadowing and the resulting alongshore gradients in wave height are the major driving mechanism for headland rips.

Table 1, listing the existing observations of embayed beach circulations with corresponding embayment parameter δ, shows that cellular circulation is generally observed for $\delta \leq 9$, transitional circulation for $9 < \delta < 16$ and normal circulation for $\delta \geq 16$. Fig. 10 synthesized our numerical experiments in terms of embayment parameter δ and λ. In our simulations with $\delta \leq 9$ (i.e., $\delta = 7.3$ for $L=500$ m), cellular beach circulation is always observed and is characterized by either cellular circulation with headland rips (Fig. 8a) or cellular circulation with a rip at the centre (Fig. 8b). Our simulations indicate that this result is not dependent on the wave angle. Accordingly, λ essentially depends on whether one central rip or two headland rips are observed (Fig. 10). For larger beach lengths ($\delta > 9$), beach circulation is influenced by both wave incidence and beach curvature. For shore-normal waves and initially alongshore-uniform embayed beaches, our numerical results are essentially similar to the observations in Table 1 as for $9 < \delta < 16$ (i.e., $\delta = 14.6$ for $L=1000$ m) and $\delta \geq 16$ ($L \geq 2000$ m), transitional and normal circulations are observed. For initially alongshore-uniform embayed beaches, the constant rip spacing $\lambda \approx 350$ m for $\delta > 16$ (Fig. 10) confirms that, for shore-normal waves, the presence of headlands does not impact the overall rip channel behaviour. This corresponds to configurations

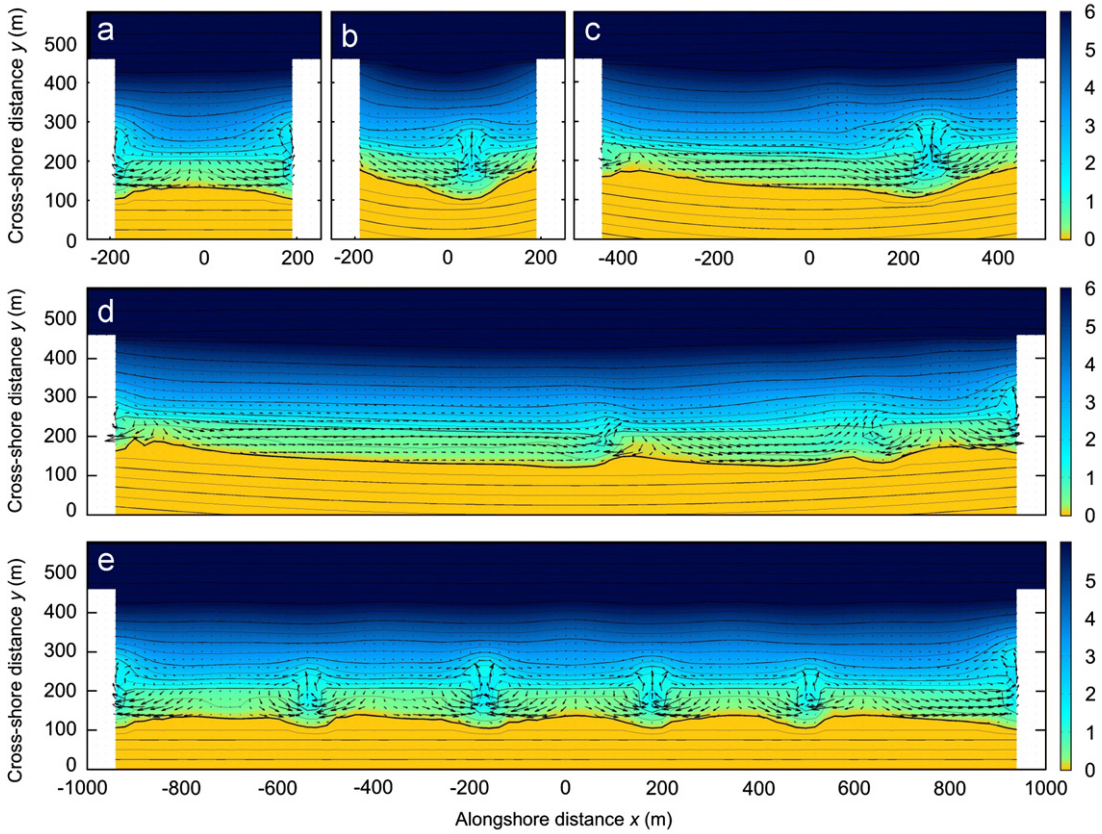

Fig. 8. Surfzone circulation and rip channel configurations: (a) Cellular circulation with headland rips. Simulation starting with an alongshore-uniform embayed beach (L=500 m and $\theta=5^{\circ}$) ; (b) Cellular circulation with a rip developing in the centre of the beach. Simulation starting with a curved embayed beach (L=500 m and $\theta=5^{\circ}$); (c) Asymmetric and transitional configuration with a rip channel/current occurring only at one end of the embayment (the updrift one). Simulation starting with a curved embayed beach (L=500 m and $\theta=5^{\circ}$); (d) Transitional circulation with a rip channel/current occurring at both ends of the embayment and two additional rips along the beach. Simulation starting with a curved embayed beach (L=2000 m and $\theta=5^{\circ}$); (e) Normal circulation with a rip channel/current occurring at both ends of the embayment and four additional rips along the beach. Simulation starting with an alongshore-uniform embayed beach (L=2000 m and $\theta=0^{\circ}$). All morphological configurations at t=10 days.

with a number of rips within the embayment larger than or equal to 4. This is more complicated for curved beaches as for $\delta=14.6$ ($L=1000$ m) and $\delta=29.2$ ($L=2000$ m), cellular circulation (with a central rip) and transitional circulation (3 rip channels along the beach) can be simulated, respectively. This suggests that the threshold values (9 and 16) in δ and the arbitrary threshold of 4 rips within the embayment could increase for increasing beach curvature. The same effect is obtained when the wave angle is changed (threshold values in δ increase with increasing θ and increasing variability in θ) and is the reason for the large variability in rip spacing for simulations characterized by $\delta>20$.

Our embayment parameter δ is slightly different from that (δ') proposed in Short and Masselink (1999). For embayed beaches where the headland length is larger than the typical surfzone width, the degree of embaymentisation predicted by δ' is systematically overestimated which is not the case with δ. We showed that in our simulations with shore-normal waves and initially alongshore-uniform embayed beaches, the degree of embayment predicted by δ is consistent with observations (Table 1). Yet, beach curvature and prevailing wave angle should be accounted for in δ to more accurately predict beach circulation. To some extent, δ should also account for the geometry of the headlands as, together with directional spreading, it controls the presence of headland rip and the dimensions of the shadowed region along the beach.

The impact of the headlands on beach circulation for high wave obliquity or time-varying wave angle to the shore can be addressed in more detail. For time-invariant oblique waves on an embayed beach with $L\leq 2000$ m, rip spacing systematically decreases with increasing distance from the updrift headland. The driving mechanism for the larger downdrift rip spacing is similar to the one described in Castelle et al. (2012) where it was shown that, for a given alongshore perturbation in the wave forcing (here the shadow region at the updrift headland), rip spacing immediately downdrift is larger than without a perturbation. This effect cascades to the following 3-4 downdrift rip channels with the rip spacing progressively decreasing and going back to the same value associated to the situation without a perturbation. This behaviour is exacerbated on curved embayed beaches as a result of the decreasing breaking wave angle to the shore with increasing distance to the updrift headland. Additionally, time varying θ results in persistent merging of free rips to headland rips, the onset of splitting of shoals, an increase in merging of rip channels and more alongshore-variable rip spacing. Similar conclusions were drawn in Castelle and Ruessink (2011) on open beaches. On embayed beaches, rip channel nonlinear behaviour is strengthened by the presence of the headlands as under time-varying wave conditions rip channels that are located in the vicinity of a headland systematically migrate towards and eventually merge with the headland rip. This in turn results in the onset of splitting of the nearby shoals. This effect can potentially cascade further along the embayment (e.g., Fig. 7h) ultimately resulting in different mean rip spacing than for the time-invariant shore-normal wave simulation (Fig. 10).

Simulations with high wave obliquity often resulted in the onset of beach rotation by the end of the 60-day simulation.

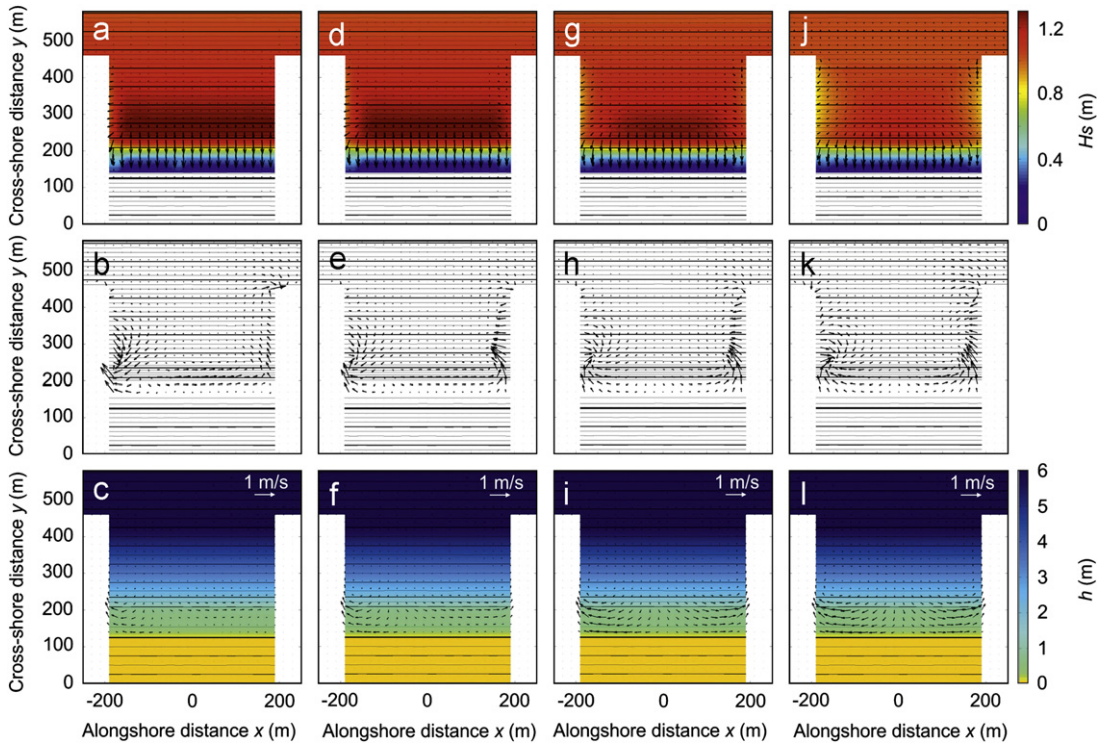

Fig. 9. Hydrodynamics at $t=0$ starting from an embayed beach with $L=500$ m and an alongshore-uniform shape, for offshore waves with $H_s=1$ m, $T_p=10$ s, $\theta=5^\circ$ with a direction spreading of (a,b,c) 4°, (d,e,f) 8° (used throughout the study), (g,h,i) 22.7° and (j,k,l) 37.5°. (a,d,g,j) Wave field with colour bar indicating significant wave height H_s in meters and resulting gradients in radiation stress $\vec{F}_w$ (arrows) with $F_{wi}=-(1/\rho)\partial S_{ij}/\partial x_j$. (b,e,h,k) Residual forcing $\vec{F}_r=\vec{F}_p+\vec{F}_w$ (arrows). (c,f,i,j) Resulting wave-driven circulation with colour bar indicating water depth in meters. In all panels iso-contours (0.5-m intervals) are contoured in the background.

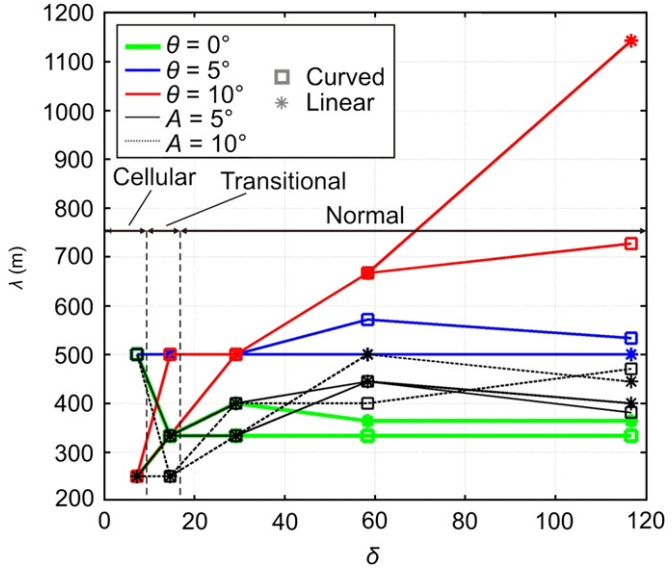

Fig. 10. λ versus the non-dimensional embayment scaling parameter δ. Simulations for $\theta=0^\circ$ are shown in green, $\theta=5^\circ$ in blue, $\theta=10^\circ$ in red, time-varying θ with $A=5^\circ$ in black and time-varying θ with $A=10^\circ$ with the dashed black line. Crosses and squares indicate simulations starting from an alongshore-uniform and a curved embayed beach, respectively. The two vertical dashed lines distinguish the cellular, transitional and normal embayed beach circulations deduced from the observations given in Table 1. (For interpretation of the references to color in this figure caption, the reader is referred to the web version of this article.)

Overall, beach rotation was favoured by large θ and embayed beach length of 1000 m $\leq L \leq$ 4000 m. The shoreline signal was dominated by the megacusps for shorter beach lengths (e.g., $L=500$ m) while longer embayed beaches (e.g., $L=8000$ m) would likely require more time to rotate significantly because of the larger amount of sand that needs to be transported from one side of the beach to the other, and because in this study we do not consider extreme storms but rather low- to moderate-energy conditions that imply a slow transport of sand from the updrift to the downdrift part of the beach. Fig. 11 shows a typical example of beach morphology at $t=60$ days for a simulation with time-invariant waves with $H_s=1$ m, $T_p=10$ s and $\theta=10^\circ$ starting from an alongshore-uniform embayed beach with $L=2000$ m. The simulated morphology shows that beach rotation is a dominant feature as most of the iso-contours rotated to the point that headland bypassing can also be observed. An emerged shoal is observed at $x\approx800$ m and $y\approx200$ m which coincides with the basic state bar crest. Since the down-slope transport depends on the bottom perturbation and beach rotation is not interpreted as a rotation of the basic state, resulting sediment transport fluxes can become unrealistic. In addition, recent observations suggest that cross-shore transport, which is not explicitly considered in the basic state approach, can dominate beach the rotation signal (Harley et al., 2011). Therefore, long-term ($t>20$ days) simulations of rip channel morphodynamics were disregarded in this paper and the role of migrating rip channels on beach rotation signal was not investigated.

The numerical model used in this study relies on a number of simplifying assumptions. These assumptions, which are discussed in more detail in Castelle and Ruessink (2011) are: disregard of both the wave group-scale forcing that is known to influence rip spacing (Reniers et al., 2004) and resolution of the vertical structure of the flow, despite the potentially significant variation of the velocity profile in rip currents (e.g., Haas and Svendsen, 2002). These are the typical assumptions in nonlinear morphodynamic modelling of 3D surfzone sandbars (e.g., Garnier et al.,

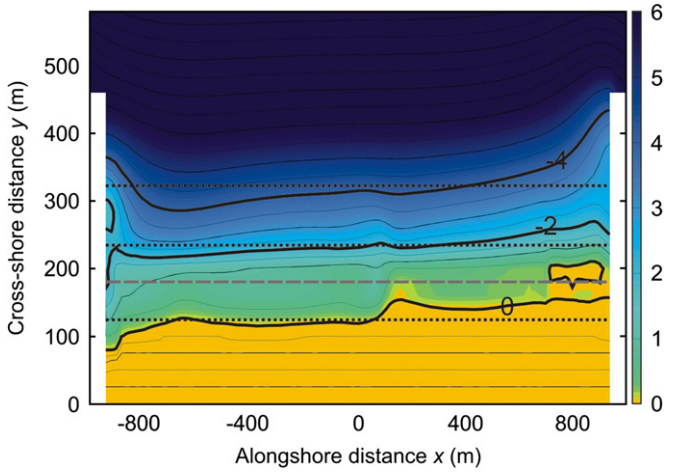

Fig. 11. Embayed beach bathymetry at $t=60$ days for a simulation starting from an alongshore-uniform embayed beach with $L=2000$ m with time-invariant waves with $H_s=1$ m, $T_p=10$ s and $\theta=10^{\circ}$. The thick black lines indicate respresentative iso-contours of the bathymetry with the thick dotted black line indicating the corresponding iso-contours at $t=0$. The thick dotted gray line shows the location of the basic state bar crest and the colour bar indicates seabed elevation in meters. The cross-shore scale is enlarged by a factor of 3.

2006). High curvatures in the planar beach shape were not addressed as large shoreline gradients in the vicinity of the headlands tend to result in numerical instabilities. The details of the shape of the headlands can control the presence and characteristics of rips developing in their proximity while in this study only one regular and simplified headland geometry and length has been considered. Wave diffraction, which is included in an approximate manner in SWAN, wave reflection and breaking against the headlands were not addressed in detail in this paper. Finally, the influence of changes in the flow circulation resulting from different values of H_s has not been addressed but will constitute the topic of a future study. Despite the number of model limitations, the considerable longshore variability of rip channel wavelength simulated on embayed beaches is consistent with the hypothesis that rips are self-organized patterns and is in line with recent field observations (Gallop et al., 2011) and the earlier pioneer work of Reniers et al. (2004).

Overall, the numerical model was capable of reproducing the main rip channel behaviour commonly observed on embayed beaches and the main beach circulation patterns. Simulations show that wave angle and the embayment size are crucial to rip channel morphodynamics on embayed beaches. Future observations on embayed beaches of large-scale rip channel behaviour and detailed field observations are needed to further improve the link between numerical models and reality, and to refine the embayment parameter δ. This will improve our skill to predict the characteristics of this critical and hazardous element of the nearshore system.

Acknowledgments

This work was done within the framework of the project BARBEC (ANR N2010 JCJC 602 01). GC acknowledges funding from NIWA (through NZ FRST) and Cantabria Campus International (Augusto Gonzalez Linares Program). The authors thank both Dr. A.D. Short and Dr. R.W. Brander for kindly providing the fantastic pictures of embayed beach rips shown in Fig. 1. Thanks to B.B. Lopez for prereviewing an earlier version of this manuscript and the reviewers for their constructive comments.

References

Bailard, J.A., 1981. An energetics total load sediment transport model for a plane beach. Journal of Geophysical Research 86 (C11), 10938–10954.
Battjes, J.A., 1975. Modelling of turbulence in the surfzone. In: Proceedings of Symposium on Modelling Techniques, ASCE, pp. 1050–1061.
Battjes, J.A., Stive, M.J.F., 1985. Calibration and verification of a dissipation model for random breaking waves. Journal of Geophysical Research 90 (C5), 9159–9167.
Bonneton, P., Bruneau, N., Castelle, B., Marche, F., 2010. Large-scale vorticity generation due to dissipating waves in the surf zone. Discrete and Continuous Dynamical Systems - Series B 13 (4), 729–738.
Booij, N., Ris, R.C., Holthuijsen, L.H., 1999. A third-generation wave model for coastal regions, Part 1, Model description and validation. Journal of Geophysical Research 104 (C4), 7649–7666.
Bruneau, N., Bonneton, P., Castelle, B., Pedreros, R., 2011. Modeling rip current circulations and vorticity in a high-energy meso-macrotidal environment. Journal of Geophysical Research 116 (C07026), http://dx.doi.org/10.1029/2010JC006693.
Calvete, D., Dodd, N., Falqués, A., Van Leeuwen, S.M., 2005. Morphological development of rip channel systems: normal and near-normal wave incidence. Journal of Geophysical Research 110 (C10006), http://dx.doi.org/10.1029/2004JC002803.
Castelle, B., Bonneton, P., 2006. Modelling of a rip current induced by waves over a ridge and runnel system on the Aquitanian Coast, France. Comptes Rendus Geoscience 338, 711–717.
Castelle, B., Marieu, V., Coco, G., Bonneton, P., Bruneau, N., Ruessink, B.G., 2012. On the impact of an offshore bathymetric anomaly on surfzone rip channels. Journal of Geophysical Research 117 (F01038), http://dx.doi.org/10.1029/2011JF002141.
Castelle, B., Ruessink, B.G., 2011. Modeling formation and subsequent nonlinear evolution of rip channels: time-varying versus time-invariant wave forcing. Journal of Geophysical Research 116 (F04008), http://dx.doi.org/10.1029/2011JF001997.
Castelle, B., Ruessink, B.G., Bonneton, P., Marieu, V., Bruneau, N., Price, T.D., 2010. Coupling mechanisms in double sandbar systems, Part 1: Patterns and physical explanation. Earth Surface Processes and Landforms 35, 476–486.
Coco, G., Murray, A.B., 2007. Patterns in the sand: from forcing templates to self-organization. Geomorphology 91, 271–290.
Dalrymple, R.A., MacMahan, J.H., Reniers, A.J.H.M., Nelko, V., 2011. Rip currents. Annual Review of Fluid Mechanics 43, 551–581.
Daly, C.J., Bryan, K.R., Roelvink, J.A., Klein, A.H.F., Hebbeln, D., Winter, C., 2011. Morphodynamics of embayed beaches: the effect of wave conditions. Journal of Coastal Research SI 64, 1003–1007.
Deigaard, R., Drønen, N., Fredsøe, J., Jensen, J.H., Jørgensen, M.P., 1999. A morphological stability analysis for a long straight barred coast. Coastal Engineering 36, 171–195.
Enjalbert, C., Castelle, B., Rihouey, D., Dailloux, D., 2011. High-frequency video observation of geologically-constrained barred-beach: La Grande Plage de Biarritz (France). Journal of Coastal Research SI 64, 70–74.
Falqués, A., Coco, G., Huntley, D.A., 2000. A mechanism for the generation of wave-driven rhythmic patterns in the surf zone. Journal of Geophysical Research 105, 24071–24088.
Gallop, S.L., Bryan, K.R., Coco, G., Stephens, S.A., 2011. Storm-driven changes in rip channel patterns on an embayed beach. Geomorphology 127, 179–188.
Garnier, R., Calvete, D., Falqués, A., Caballeria, M., 2006. Generation and nonlinear evolution of shore-oblique/transverse sand bars. Journal of Fluid Mechanics 567, 327–360.
Garnier, R., Calvete, D., Falqués, A., Dodd, N., 2008. Modelling the formation and the long-term behavior of rip channel systems from the deformation of a longshore bar. Journal of Geophysical Research 113 (C07053), http://dx.doi.org/10.1029/2007JC004632.
Haas, K.A., Svendsen, I.A., 2002. Laboratory measurements of the vertical structure of rip currents. Journal of Geophysical Research 107 (C5), 5–11, http://dx.doi.org/10.1029/2001JC000911.
Haas, K.A., Svendsen, I.A., Brander, R.W., Nielsen, P., 2002. Modeling of a rip current system on Moreton Island, Australia. In: Proceedings of 28th International Conference on Coastal Engineering, vol. 1, ASCE, New York, pp. 784–796.
Harley, M.D., Turner, I.L., Short, A.D., Ranasinghe, R., 2011. A reevaluation of coastal embayment rotation: the dominance of cross-shore versus alongshore sediment transport processes, Collaroy-Narrabeen Beach, southeast Australia. Journal of Geophysical Research 116 (F04033), http://dx.doi.org/10.1029/2010JF001989.
Holman, R.A., Symonds, G., Thornton, E.B., Ranasinghe, R., 2006. Rip spacing and persistence on an embayed beach. Journal of Geophysical Research 111 (C06006), http://dx.doi.org/10.1029/2005JC002965.
Hsu, J.R.C., Silvester, R., Xia, Y.M., 1989. Generalities on static equilibrium bays. Coastal Engineering 12, 353–369.
Huntley, D.A., Hendry, M.D., Haines, J., Greenidge, B., 1988. Waves and rip currents on a Caribbean pocket beach, Jamaica. Journal of Coastal Research 4, 69–79.
Jackson, D.W.T., Cooper, J.A.G., Rio, L.D., 2005. Geological control of beach morphodynamic state. Marine Geology 216, 297–314.
Klein, A.H.F., Ferreira, O., Dias, J.M.A., Tessler, M.G., Silveira, L.F., Benedet, L., de Menezes, J.T., de Abreu, J.G.N., 2010. Morphodynamics of structurally controlled headland-bay beaches in southeastern Brazil: a review. Coastal Engineering 57, 98–111.

Komar, P.D., Allan, J.C., Dias-Mendez, G.M., Marra, J.J., Ruggiero, P., 2000. El Niño and La Niña: erosion processes and impacts. In: 27th International Conference on Coastal Engineering, ASCE, pp. 2414–2427.
Loureiro, C., Ferreira, O., Cooper, J.A.G., 2012. Extreme erosion on high-energy embayed beaches: influence of megarips and storm grouping. Geomorphology 139–140, 155–171.
MacMahan, J.H., Thornton, E.B., Reniers, A.J.H.M., 2006. Rip current review. Coastal Engineering 53, 191–208.
McNinch, J.E., 2004. Geologic control in the nearshore: shore-oblique sandbars and shoreline erosion hotspots, Mid-Atlantic Bight, USA. Marine Geology 211, 121–141.
Mei, C.C., 1989. Applied Dynamics of Ocean Waves. World Scientific.
Ojeda, E., Guillen, J., 2008. Shoreline dynamics and beach rotation of artificial embayed beaches. Marine Geology 253, 51–62.
Ojeda, E., Guillen, J., Ribas, F., 2011. Dynamics of single-barred embayed beaches. Marine Geology 280, 76–90.
Philipps, O.M., 1977. The dynamics of the upper ocean. Cambridge University Press.
Ranasinghe, R., McLoughlin, R., Short, A.D., Symonds, G., 2004. The Southern Oscillation Index, wave climate, and beach rotation. Marine Geology 204, 273–287.
Reniers, A.J.H.M., Roelvink, J.A., Thornton, E.B., 2004. Morphodynamic modeling of an embayed beach under wave group forcing. Journal of Geophysical Research 109 (C01030), http://dx.doi.org/10.1029/2002JC001586.
Ribas, F., Garnier, R., Ojeda, E., Falqués, A., Guillén, J., Calvete, D., 2007. Observation and modeling of crescentic bars in Barcelona embayed beaches. In: Proceedings of Coastal Sediments '07, ASCE.
Ruessink, B.G., Coco, G., Ranasinghe, R., Turner, I.L., 2007. Coupled and noncoupled behavior of three-dimensional morphological patterns in a double sandbar system. Journal of Geophysical Research 112 (C07002), http://dx.doi.org/10.1029/2006JC003799.
Schyuer-Ming, S., Komar, P.D., 1994. Sediments, beach morphology and seacliff erosion within an Oregon Coast littoral cell. Journal of Coastal Research 10, 144–157.
Scott, T.M., Masselink, G., Russell, P.E., 2011. Morphodynamic characteristics and classification of beaches in England and Wales. Marine Geology 286, 1–20.
Scott, T.M., Russell, P.E., Masselink, G., Woolers, A., Short, A.D., 2007. Beach rescue statistics and their relation to nearshore morphology and hazards: a case study for southwest England. Journal of Coastal Research SI 50, 1–6.
Short, A.D., 2006. Australian beach systems—nature and distribution. Journal of Coastal Research 22, 11–27.
Short, A.D., Masselink, G., 1999. Embayed and structurally controlled embayed beaches. In: Short, A.D. (Ed.), Handbook of Beach and Shoreface Morphodynamics. Wiley, Chichester, pp. 230–250.
Silva, R., Baquerizo, A., Losada, M.A., Mendoza, E., 2010. Hydrodynamics of headland-bay beach-nearshore current circulation. Coastal Engineering 57, 160–175.
Silvester, R., 1960. Stabilization of sedimentary coastlines. Nature 188, 467–469.
Smit, M.W.J., Reniers, A.J.H.M., Ruessink, B.G., Roelvink, J.A., 2008. The morphological response of a nearshore double sandbar system to constant wave forcing. Coastal Engineering 55, 761–770.
Splinter, K.D., Holman, R.A., Plant, N.G., 2011. A behavior-oriented dynamic model for sand bar migration and 2DH evolution. Journal of Geophysical Research 116.
Van Enckevort, I.M.J., Ruessink, B.G., Coco, G., Susuki, K., Turner, I.L., Plant, N.G., Holman, R.A., 2004. Observations of nearshore crescentic sandbars. Journal of Geophysical Research 109 (C06028), http://dx.doi.org/10.1029/2003JC002214.
Wright, L.D., Short, A.D., 1984. Morphodynamic variability of surf zones and beaches: a synthesis. Marine Geology 56, 93–118.
Yamashita, T., Tsuchiya, Y., 1992. Numerical simulation of pocket beach formation. In: Proceedings of 23rd International Conference on Coastal Engineering, ASCE, New York, pp. 2556–2566.